AkO 28415.1-GS-CF

②

ICO 🌐
Topical Meeting on
**Atmospheric,
Volume and
Surface Scattering
and Propagation**

DTIC
ELECTE
D

DIGEST

FLORENCE, ITALY
August 27-30, 1991

92-09883

REPORT DOCUMENTATION PAGE

Form Approved
OMB No. 0704-0188

Public reporting burden for this collection of information is estimated to average 1 hour per response, including the time for reviewing instructions, searching existing data sources, gathering and maintaining the data needed, and completing and reviewing the collection of information. Send comments regarding this burden estimate or any other aspect of this collection of information, including suggestions for reducing this burden, to Washington Headquarters Services, Directorate for Information Operations and Reports, 1215 Jefferson Davis Highway, Suite 1204, Arlington, VA 22202-4302, and to the Office of Management and Budget, Paperwork Reduction Project (0704-0188), Washington, DC 20503.

1. AGENCY USE ONLY (Leave blank)	2. REPORT DATE	3. REPORT TYPE AND DATES COVERED
	January, 1992	Final 30 Sep 90 - 29 Jan 92

4. TITLE AND SUBTITLE

International Conference on Atmospheric, Volume and
Surface Scattering and Propagation

5. FUNDING NUMBERS

DAAL03-90-G-0219

6. AUTHOR(S)

J. Fred Holmes   (principal investigator)

7. PERFORMING ORGANIZATION NAME(S) AND ADDRESS(ES)

Oregon Graduate Institute of Science and Technology
Beaverton, OR 97006-1999

8. PERFORMING ORGANIZATION REPORT NUMBER

9. SPONSORING / MONITORING AGENCY NAME(S) AND ADDRESS(ES)

U. S. Army Research Office
P. O. Box 12211
Research Triangle Park, NC 27709-2211

10. SPONSORING / MONITORING AGENCY REPORT NUMBER

ARO 28415.1-GS-CF

11. SUPPLEMENTARY NOTES

The view, opinions and/or findings contained in this report are those of the author(s) and should not be construed as an official Department of the Army position, policy, or decision, unless so designated by other documentation.

12a. DISTRIBUTION / AVAILABILITY STATEMENT

Approved for public release; distribution unlimited.

12b. DISTRIBUTION CODE

13. ABSTRACT (Maximum 200 words)

The meeting was held as scheduled.   A Digest of the meeting was
published and contains copies of the presentations.

14. SUBJECT TERMS

Atomosphere, Surface Scattering, Optics,
Wave Propagation

15. NUMBER OF PAGES

585

16. PRICE CODE

17. SECURITY CLASSIFICATION OF REPORT	18. SECURITY CLASSIFICATION OF THIS PAGE	19. SECURITY CLASSIFICATION OF ABSTRACT	20. LIMITATION OF ABSTRACT
UNCLASSIFIED	UNCLASSIFIED	UNCLASSIFIED	UL

NSN 7540-01-280-5500

Standard Form 298 (Rev. 2-89)
Prescribed by ANSI Std. Z39-18
298-102

ICO

Topical Meeting on
Atmospheric, Volume and Surface Scattering and Propagation

DIGEST

FLORENCE, ITALY
August 27-30, 1991

92 4 17 029

A Topical Meeting of the

INTERNATIONAL COMMISSION FOR OPTICS

Organized by
- Department of Physics, University of Florence
- Oregon Graduate Institute, Oregon, U.S.A.

Sponsored by
- University of Florence
- CEO-Centro di Eccellenza Optronica-
  Florence Optronics
- CNR-National Research Council, Italy:
  Comitato per le Scienze Fisiche,
  Comitato Tecnologico
- Commission of the European Communities
- Fondazione Ugo Bordoni, Roma, Italy
- OSA - Optical Society of America
- U.S. Army Research Office
- Banca Toscana

Under the Auspices of
- Italian Commission of Optics-CIO
- European Optical Society - EOS
- European Physical Society - EPS
- Gruppo Nazionale di Elettronica Quantistica
  e Plasmi- CNR
- Gruppo Nazionale Fisica dell'Atmosfera e
  dell'Oceano- CNR
- Società Italiana di Ottica e Fotonica - SIOF

ORGANIZERS

Anna Consortini (Chair), *Università di Firenze, Italy*
John Christopher Dainty, *Imperial College, London, UK*
J. Fred Holmes, *Oregon Graduate Institute, USA*
Pierre Chavel - ICO Secretary General, ex officio,
CNRS, Orsay, France

ADVISORY COMMITTEE

Joseph W. Goodman, *Stanford University, USA*
Akira Ishimaru, *University of Washington, USA*
Valeryan I. Tatarskii, *Academy of Sciences, USSR*

PROGRAM COMMITTEE

Reginald J. Hill (Chair), *NOAA, Boulder, Colorado, USA*
Tito F. Arecchi, *Università di Firenze, Italy*
Mark J. Beran, *Tel Aviv University, Israel*
Piero Bruscaglioni, *Università di Firenze, Italy*
Allan I. Carswell, *York University, Toronto, Canada*
John Christopher Dainty, *Imperial College, London, UK*
Walter A. Flood, *U.S. Army Research Office, USA*
David L. Fried, *Optical Sciences Co., Placentia, USA*
Koichi Furutsu, *Nakato 1876, Tokio, Japan*
Alexander S. Gurvich, *Academy of Sciences, USSR*
Benjamin M. Herman, *University of Arizona, USA*
Ivan J. Lahaie, *ERIM, Ann Arbor, Michigan, USA*
Georg Maret, *Max Planck Institute, Grenoble, France*
Daniel Maystre, *Université de Marseille, France*
Fritz Merkle, *European Southern Observatory, FRG*
Manuel Nieto Vesperinas, *C.S.I.C., Madrid, Spain*
François Roddier, *University of Hawaii, USA*
Yi Yi Sun, *Academia Sinica, Heifei, China*
Vladimir E. Zuev, *Academy of Sciences, Tomsk, USSR*

LOCAL ORGANIZING COMMITTEE

Francesco Fedi, *Fondazione Ugo Bordoni, Roma*
Giuseppe Longobardi, *CEO - INO, Firenze*
Luca Pantani, *IROE-CNR, Firenze*
Giancarlo Righini, *IROE-CNR, Firenze*

INDEX

ROUGH SURFACE SCATTERING 1

POSTER SESSION 1

ROUGH SURFACE SCATTERING 2

WAVEGUIDES AS RANDOM MEDIA

POSTER SESSION 3

(Postdeadline papers under separate cover)

TIME - TABLE

	Tuesday, August 27	Wednesday, August 28	Thursday, August 29	Friday, August 30
GREEN ROOM				
8.00	Scintillation 1	Rough surface scattering 1	Scattering	Non linear propagation
9.00				Waveguides as random media
10.30	Scintillation 2			
13.30	Adaptive optics 1	Rough surface scattering 2	Scintillation 3	Lidar 1
15.30				Lidar 2
16.00	Adaptive optics 2	Rough surface scattering 3	Cloud scattering (GNFAO session)	
16.30				Closing statement
ONYX ROOM				
10.45-12.00		Poster session 1	Poster session 2	Poster session 3

SCINTILLATION 1 & 2

Propagation of the Scintillation Index and the Correlation of Intensity Function in the Turbulent Atmosphere

Mark J. Beran
The Catholic University of America*

and

Alan M. Whitman
Villanova University
(INVITED)

Reference [1] details the calculation of the scintillation index σ_I^2 for a plane wave propagating in a random medium. The medium is described by a Kolmogorov spectrum modified to include an inner scale. In the numerical calculations, we used the zero-order approximation of the two-scale procedure. The theoretical formulation presented, however, included formulas for higher-order corrections and formulas to calculate the correlation of intensity function $\langle R_I(r)\rangle$.

Here we will show the effect, of including the first-order correction, on both the scintillation index and the correlation of intensity function. We shall do this principally for the case in which the inner scale is taken to be zero. However, in the scintillation index calculations, we shall include an inner-scale effect. We compare these results with the numerical simulation results obtained by Martin and Flatte [2].

The correlation of intensities $\langle R_I(x_{T1},x_{T2},z)\rangle$ is defined as follows

$$\langle R_I(x_{T1},x_{T2},z)\rangle = \langle I(x_{T1},z)I(x_{T2},z)\rangle \tag{1}$$

where z is the mean propagation direction and x_{Ti} is the transverse coordinate of the ith position. The function $I(x_T,z)$ is the intensity of the light field at the point (x_T,z) in one realization of the turbulent field. The brackets $\langle\ \rangle$ indicate an ensemble average over all realizations of the turbulent field.

The scintillation index σ_I^2 is defined as

$$\sigma_I^2 = [\langle I^2\rangle - \langle I\rangle^2]/\langle I\rangle^2 \tag{2}$$

where

$$\langle I^2(x_T,z)\rangle = \langle R_I(x_T,x_T,z)\rangle \tag{3}$$

The average intensity is denoted $\langle I(x_T,z)\rangle$.

A normalized form of $\langle R_I\rangle$ defined as

$$\langle S_I \rangle = [\langle R_I \rangle - 1]/\sigma_I^2 \tag{4}$$

Scintillation Index

Zero-order approximation

For a plane wave propagating through a turbulent atmosphere that is taken to be locally statistically homogeneous and isotropic, $\langle I(x) \rangle$ is a constant. The expression for the scintillation index σ_I^2 determined by the zero-order approximation of the two-scale method is

$$\sigma_I^2 + 1 = \int_0^\infty \int (xy/\pi) dx dy \int_0^\pi \exp[ixy\cos\theta - \tilde{\zeta}_k^{11/6} Q_o] d\theta$$

$$\tag{5}$$

Here

$$Q_o = \int_0^1 F(xt, y, \cos\theta) dt$$

and $\tilde{\zeta}_k = 1.23 k^{7/11} (C_n^2)^{6/11} z$. The constant C_n^2 is the structure constant and k is the wavenumber.

The general expression for F is

$$F = \langle 2D(xt\zeta^{1/2}) + 2D(y\zeta^{1/2}) - D(r_+(t)\zeta^{1/2}) - D(r_-(t)\zeta^{1/2}) \rangle / \zeta^{5/6} \tag{6}$$

where D is the dimensionless structure function. Here $\zeta = z/k\ell_m^2$ and

$$r_+(t) = [(xt)^2 + y^2 + xyt\cos\theta]^{1/2}$$

$$r_-(t) = [(xt)^2 + y^2 - xyt\cos\theta]^{1/2}$$

For a zero inner scale we use the Kolmogorov structure function. When the inner scale is finite, many expressions have been used to modify the Kolmogorov structure function. For convenience, we shall use a form proposed by Tatarski[3].

First-order approximation

A more exact value of σ_I^2 can be obtained by including the next order approximation of the two-scale procedure. The method given in Ref. 1 for two dimensions may be extended to

18

three dimensions. We find that the first-order correction may be included by replacing the expression $\tilde{\zeta}_k^{11/6} Q_0$ by the expression $\tilde{\zeta}_k^{11/6} Q_0 + i\tilde{\zeta}_k^{11/3} Q_1$ where Q_1 is a two-dimensional integral over the structure functions. Details are given in Ref. [4].

Correlation of Intensities

The function $\langle R_I \rangle$, for a plane wave impinging on a locally statistically homogeneous and isotropic atmosphere, is a function only of the propagation distance and the transverse separation r. The function $\langle R_I(r,z) \rangle$ is calculated from an expression similar to that given in Eq. (5). It is only necessary to multiply the integrand by the Bessel function $J_0[xr(k/z)^{1/2}]$.

Numerical Results

Scintillation index σ_I^2

In Ref. [1] (Fig. 4), we presented curves of the square root of σ_I^2, the standard deviation of the intensity fluctuations σ_I, as a function of $\sigma_0 = [1.23k^{7/6}C_n^2 z^{11/6}]^{1/2}$ for various values of a parameter $\gamma_K = .94(\tilde{\zeta}_k/\zeta)^{11/6}$, where $\gamma_K = 0$ corresponds to a zero inner scale. These curves were evaluated using the zero-order approximation of the two-scale method. Here we would like to compare the $\gamma_K = 0$ and the $\gamma_K = 10$ curves to curves which include the first-order correction and to curves calculated by Martin and Flatte [2] which were obtained using a numerical simulation technique. The three curves for $\gamma_K = 0$ are given in Fig. 1. The curves for $\gamma_K = 10$ are given in Fig. 2.

As we see, the curves in all cases are similar, with the first-order correction curve lying above the zero-order curve and the Martin-Flatte (MF) result lying above both curves. For $\gamma_K = 0$, the first-order correction increases the peak value by about 5% and the peak value of the MF curve is about 7.5% above the peak value of the first-order correction curve. For the $\gamma_K = 10$ curves, the changes are about 11% and 7% respectively.
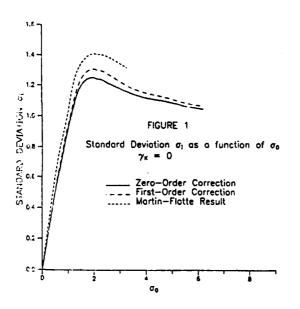
Correlation of intensities
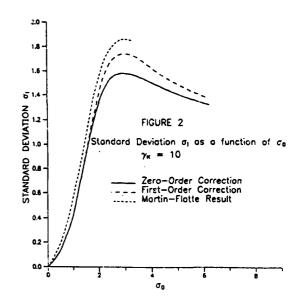
In Fig. 3 we show the result of calculating the normalized form of the correlation of intensities $\langle S_I(r) \rangle$ for a zero inner scale at the peak value $\sigma_0 = 2.06$. We plot $\langle S_I(r) \rangle$ vs. $r/(kz)^{1/2}$. As we see, the zero-order solution and the first-order correction are nearly identical. Similar results are found for other values of σ_0.
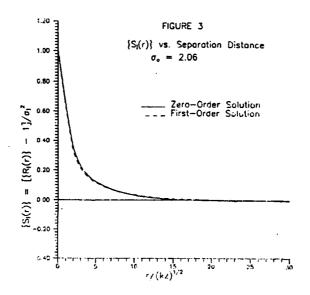
References

[1] Whitman, A.M. and M.J. Beran, "Two-Scale Solution for Atmospheric Scintillation" J. Opt. Soc. Am., A2, 2133-2143, 1985.

[2] Martin, J.M. and S.M Flatte, "Intensity Images and Statistics from Numerical Simulation of Wave Propagation in 3-D Random Media" Applied Optics, 27, 2111-2126, 1988.

[3] Tatarski, V.I., The effects of the turbulent atmosphere on wave propagation TT-68-50464 (Springfield, VA: National Technical Information Service), 1971.

[4] Whitman, A.M. and M.J. Beran, "First-order Correction for the Scintillation Index and Correlation of Intensity Function", Submitted for publication.

FIGURE 1

Standard Deviation σ_1 as a function of σ_0

$\gamma_\kappa = 0$

——— Zero-Order Correction
- - - First-Order Correction
········· Martin-Flatte Result

FIGURE 2

Standard Deviation σ_1 as a function of σ_0

$\gamma_\kappa = 10$

——— Zero-Order Correction
- - - First-Order Correction
········· Martin-Flatte Result

FIGURE 3

$\{S_l(r)\}$ vs. Separation Distance

$\sigma_0 = 2.06$

——— Zero-Order Solution
- - - First-Order Solution

WAVE PROPAGATION IN AN INTERMITTENT TURBULENT MEDIUM

Joseph Gozani
Wave Propagation Laboratory, National Oceanic and Atmospheric Administration (NOAA),
325 Broadway, Boulder, CO 80303, USA; Tel: (303) 497-6283
&
Cooperative Institute of Research in the Environmental Sciences (CIRES),
University of Colorado, Boulder, CO 80309, USA.

INTRODUCTION (INVITED)

The purpose of this paper is to take into account the effect of intermittencies in the propagation of waves in the turbulent atmosphere. Intermittence effects are due to the variability of the medium's parameters. These parameters are specified to have large-scale fluctuations as opposed to the localized dielectric permittivity fluctuations that have a characteristic small scale.

Discarding intermittencies can lead to difficulties in comparison of theories and measurements needed to validate and to predict actual propagation phenomena. Their presence necessitates future common agreement of the definitions of parameters of the medium.

Intermittency's effects were first included in a consistent manner in multiple scattering propagation through random media by Tatarskii and Zavorotny.[1] They studied the problem mainly on the level of governing equations. Their paper also provides a list of references about experimental work on this problem. Our present paper provides a path integral solution for the problem and a specific model that may account for the effects of intermittencies on coherence function propagation.

GOVERNING EQUATION

We begin with the following governing equation,[1,2]

$$\left[2ik\partial_z + \Delta_{\underset{\sim}{x}} - \Delta_{\underset{\sim}{y}} + k^3 \nu\left(z, \underset{\sim}{x}, \underset{\sim}{y}; A\right) \right] \gamma = 0, \quad \underset{\sim}{x}, \underset{\sim}{y} \in \mathbb{R}^{2N}, \tag{1a}$$

$$\gamma(z{=}0) = \gamma_0\left(\underset{\sim}{x}, \underset{\sim}{y}\right). \tag{1b}$$

This equation describes the stochastic evolution of the product of multiple scalar fields

$$\gamma\left(z, \underset{\sim}{x}, \underset{\sim}{y}; \underset{\sim}{A}\right) = \prod_{n=0}^{N} u\left(z, \underset{\sim}{x_n}; \underset{\sim}{A}\right) u^*\left(z, y_n; \underset{\sim}{A}\right). \tag{2}$$

Here, $u\left(z, \underset{\sim}{x}; A\right)$ is the complex field envelope, z signifies the propagation range, x and y are position vectors transverse to the propagation direction, k is the wave number, Δ is a Laplacian operator. The last term of (1a) $\nu\left(z, \underset{\sim}{x}, \underset{\sim}{y}; \underset{\sim}{A}\right)$ accounts for parametric fluctuations, ν being sum and difference of (complex) dielectric permittivities with $\langle \nu \rangle = 0$.

Subsequently we find that for clarity and brevity it is not essential to represent the exact form of $\nu\left(z, \underset{\sim}{x}, \underset{\sim}{y}; \underset{\sim}{A}\right)$ because we confine our present analysis to intermittent effects that depend only on the longitudinal variable z.

CONDITIONAL EXPECTATION

The stochastic dependency of (1a) is signified by the event partition $A = \{A_\ell, A_L\}$, where A_ℓ and A_L, respectively, are the small and large scale events of the total fluctuation causes. Small-scale conditional averaging for a given large-scale variation provides us with the conditional expectation $\gamma_L \equiv \langle \gamma \mid A_L \rangle$. This coherence function is a random process with a characteristic scale $L \gg \ell$. This

coherence function should further be averaged with respect to A_L to get $\langle\gamma\rangle\equiv\langle\langle\gamma\mid A_L\rangle\rangle$. Note that because a double averaging process is made, we must select the ordering of averages as close as possible to the measurement process.[1]

SMALL-SCALE AVERAGING

Following Tatarskii and Zavorotny[1] we consider small-scale fluctuation to be a δ-correlated Gaussian process. This assumption and limits of its validity are well established.[2] This approximation was found to be extremely valuable because of the considerable simplification obtained in (1a) above. The intermittent parameter becomes explicit when we assume that the medium is a locally quasi-homogeneous field.

Following this outline we get

$$\partial_z \gamma_L = \frac{i}{2k}\left[\Delta_{\underset{\sim}{x}} - \Delta_{\underset{\sim}{y}}\right]\gamma_L - \frac{k^2}{4}\alpha^2(z)\, B_\eta\left[\underset{\sim}{x},\underset{\sim}{y}\right]\gamma_L = 0 ,\tag{3a}$$

where

$$\alpha^2(z)\, B_\eta\left[\underset{\sim}{x},\underset{\sim}{y}\right] \equiv \int_{-\infty}^{\infty} d\zeta\, \langle\nu\left[z - \frac{\zeta}{2},\underset{\sim}{x},\underset{\sim}{y};A\right]\nu\left[z + \frac{\zeta}{2},\underset{\sim}{x},\underset{\sim}{y};A\right]\mid A_L\rangle .\tag{3b}$$

Equation (3a) has a formal Green's function solution in terms of a Feynman path integral.

$$g\left(z',\underset{\sim}{\rho}\,'; z'',\underset{\sim}{\rho}\,''; a\right) = \mu^{-1}\int_{z',\underset{\sim}{\rho}\,'}^{z'',\underset{\sim}{\rho}\,''} D\underset{\sim}{x}\,D\underset{\sim}{y}$$

$$x\exp\left\{\frac{i}{2k}\int_{z'}^{z''}d\tau\left[\underset{\sim}{x}\,^2(\tau) - \underset{\sim}{y}\,^2(\tau)\right] - \frac{k^2}{4}\int_{z'}^{z''}d\tau\,\alpha^2(\tau)\, B_\eta\left[\underset{\sim}{x}(\tau),\underset{\sim}{y}(\tau)\right]\right\}\tag{4}$$

Here μ is a normalization factor that insures that a free space result is obtained when no fluctuations are present. This solution is subject to the condition

$$g\left(z',\underset{\sim}{\rho}\,'; z',\underset{\sim}{\rho}\,''; a\right) = \delta\left(\underset{\sim}{\rho}\,' - \underset{\sim}{\rho}\,''\right), \quad \underset{\sim}{\rho} \equiv \left(\underset{\sim}{x},\underset{\sim}{y}\right) \in R^{4N} .\tag{5}$$

Our notation uses a prime ' and double prime " to denote initial and final planes respectively. We also introduce the multi-vetor $\underset{\sim}{\rho}$ merely for notation convenience. The parameter a in Green's function above represents the variability of A_L. This result applies for an arbitrary range z when no intermittent effects are present. When intermittency occurs, this solution is only a local one and needs further averaging with respect to A_L.

GENERAL SOLUTION

We split $\alpha^2(t)$ into average and deviation

$$\alpha^2(\tau) = \langle\alpha^2(\tau)\rangle + \tilde{a}\,(\tau), \quad \langle\alpha^2(\tau)\rangle \geq 0, \quad \langle\tilde{a}\,(\tau)\rangle \equiv 0.\tag{6}$$

We create realizations that depend on the $\tilde{a}\,(\tau)$, $0 \leq \tau \leq z$. Using the group property of the path integral we find that we can insert (6) directly in (4) and smooth it with appropriate probability function. The averaged Green's function is

$$G\left(z', \underset{\sim}{\rho}\,'; z'', \underset{\sim}{\rho}\,''\right) = \mu^{-1} \int_{z',\underset{\sim}{\rho}\,'}^{z'',\underset{\sim}{\rho}\,''} D\underset{\sim}{x}\ D\underset{\sim}{y}$$

$$\times \exp\left\{\frac{i}{2k}\int_{z'}^{z''} d\tau\left[\underset{\sim}{\dot{x}}\,{}^2(\tau) - \underset{\sim}{\dot{y}}\,{}^2(\tau)\right] - \frac{k^2}{4}\int_{z'}^{z''} d\tau\ \langle\alpha^2(\tau)\rangle\ B_\eta\left[\underset{\sim}{x}(\tau), \underset{\sim}{y}(\tau)\right]\right\}$$

$$\times \left\langle\exp\left\{-\frac{k^2}{4}\int_{z'}^{z''} d\tau\ \tilde{a}(\tau)\ B_\eta\left[\underset{\sim}{x}(\tau), \underset{\sim}{y}(\tau)\right]\right\}\right\rangle. \tag{7}$$

The first term is a path integral without intermittency. The second term has to be averaged using an expression of the moment-generating functional.

$$M_a\left[-\frac{k^2}{4}B_\eta\right] \equiv \left\langle\exp\left\{-\frac{k^2}{4}\int_0^z \tilde{a}(\tau)\ B_\eta(\tau)\ d\tau\right\}\right\rangle$$

$$= \exp\left\{\sum_{n=1}^\infty \left(-\frac{k^2}{4}\right)^n \int_0^z d\tau_1 \int_0^{\tau_1} d\tau_2 \dots \int_0^{\tau_{n-1}} d\tau_n\ \langle\tilde{a}(\tau_1)\dots\tilde{a}(\tau_n)\rangle_c\ B_\eta(\tau_1)\dots B_\eta(\tau_n)\right\}, \tag{8}$$

where $\langle\tilde{a}_1\cdots\tilde{a}_n\rangle_c$ is the nth order cumulant. Unless $\tilde{a}(\tau)$ is Gaussian, the moment-generating func-

tional has infinitely many terms. However a Gaussian distribution for $\tilde{a}(\tau)$ is unacceptable because $\alpha^2(\tau)$ is positive. Hence, moments of order greater than 2 are important.

PHYSICAL MEANING OF $\alpha^2(\tau)$

The parameter $\alpha^2(\tau)$, which is proportional to an intermittent variance, usually stands for $C_n^2(\tau)$. In Eq.(3b) the inner scale ℓ_0 dependency is much more complicated than that of the C_n^2. We speculate that its intermittent effects will manifest themselves mainly in the random focusing regime where the inner scale becomes of the order of Fresnel zone, and also in the saturated fluctuations regime where the inner scale becomes of the order of the coherence length. Using asymptotic expansion of (3b) in these regimes will provide us definitions of $\alpha^2(\tau)$ as the factor of the leading term in each regime. The resulting $\alpha^2(\tau)$ will comprise a simpler combination of the medium's parameters C_n^2, inner scale and the order of the coherence function N.

Equation (8) predicts that only a few models will produce tractable results, and there is no guarantee that they will portray a physical model for the intermittency. For example if we consider (9) and a joint log-normal distribution for inner-scale and C_n^2 variability[3] and insert it in (8) we will produce a complicated expression.

SPECIFIC PROCESS

Examining experimental intermittent inner-scale and C_n^2 fluctuations[4,5] we assume that realization of our process can be described as a generalized Poisson field

$$\tilde{a}(z) = \sum_{j=0}^{J(z)} q_j\, h(z - z_j), \tag{10}$$

where $h(z)$ is a given function and $\{z_j\}$ are Poisson-distributed with average density λ. The number

of impulses at range z, $J(z)$, is also Poisson-distributed with the λz. The weight $\{q_j\}$ is a set of independent random variables with moment-generating function $M_q(s) = \langle\exp(s\,q)\rangle$. We hope that this burst-like representation will be flexible enough to simulate intermittency.

We insert the moment-generating functional for a generalized Poisson process[2] in (7) to get

$$G\left[\underset{\sim}{z',\rho'};\underset{\sim}{z'',\rho''}\right] = \mu^{-1}\int_{\underset{\sim}{z',\rho'}}^{\underset{\sim}{z'',\rho''}} D\underset{\sim}{x}\,D\underset{\sim}{y}$$

$$x\exp\left\{\frac{i}{2k}\int_{z'}^{z''}d\tau\left[\underset{\sim}{\dot{x}}{}^2(\tau) - \underset{\sim}{\dot{y}}{}^2(\tau)\right] - \frac{k^2}{4}\int_{z'}^{z''}d\tau\,\langle\alpha^2(\tau)\rangle\,B_\eta\left[\underset{\sim}{x}(\tau),\underset{\sim}{y}(\tau)\right]\right\}$$

$$x\exp\left[\lambda\int_{z'}^{z''}dt'\left\{M_q\left\{-\frac{k^2}{4}\int_{z'}^{z''}d\tau\,h(\tau - t')\,B_\eta\left[\underset{\sim}{x}(\tau),\underset{\sim}{y}(\tau)\right]\right\} - 1\right\}\right], \qquad (11)$$

and finally use of a superposition integral on the initial condition in (1b) produces the coherence function $\langle\gamma\rangle$.

SUMMARY AND FUTURE WORK

We looked for a way to include intermittencies in the propagation model. We adopted a generalized Poisson field to describe the intermittency process. In order to get quantitative results of our model, one has to identify its characteristics using experimental data.

The final expression obviously needs simplification. In the geometrical optics regime we expect that replacing the trajectories $\underset{\sim}{\rho}(\tau)$ by straight lines between source and receiver will be a good approximation.

Three-dimensional variability that emerges out of a locally quasi-homogeneous medium can be included easily in the same way we accounted for the longitudinal variability.

REFERENCES

[1] V.I. Tatarskii and V.U. Zavorotny, "Wave Propagation in Random Media with Fluctuating Turbulent Parameters," J. Opt. Soc. Am. A, 2, 2089-2075 (1985).

[2] S.M. Rytov, Yu. A. Kravtsov and V.I. Tatarskii: *Principles of Statistical Radiophysics*, Vol 3-4, Springer Verlag, Berlin (1989).

[3] S.J.S Khalsa, "Surface-layer Intermittency Investigated with Conditional Sampling," Boundary Layer Meteorology, 19, 135-153 (1980).

[4] A.S. Gurvich and V.P. Kukharets, "The Influence of Intermittence of Atmospheric Turbulence on Scattering of Radio Waves," Scripta Technica, 85, 52-53 (1986).

[5] R.G. Frehlich, "Laser Scintillation Measurements of the Temperature Spectrum in the Atmospheric Surface Layer," submitted to J. Atmos. Phys.

Simulation of Wave Propagation
in
Three-Dimensional Random Media

Stanley M. Flatté and Charles Bracher
Physics Department and Institute of Tectonics
University of California at Santa Cruz
Santa Cruz, CA 95064 U.S.A.
Telephone: 408/459-2090
FAX: 408/459-2127
email: smf@pacific.ucsc.edu

(INVITED)

Waves traversing a random medium develop dramatic patterns of intensity fluctuations. The spatial patterns on an observing screen can be understood to only a limited extent from knowledge of their wavenumber spectrum; description of the complete pattern requires knowledge of all significant higher moments of intensity, which is very difficult to obtain either theoretically or experimentally.

Numerical simulation has offered a method for obtaining detailed information on the intensity behavior of single-frequency waves propagating through well-characterized media. Numerical simulations done at U.C. Santa Cruz over the last few years have provided insight into the spatial patterns, spatial spectra, and intensity variances (scintillation indices) for optical waves incident on media that have characteristics associated with fluid-dynamical turbulence[1,2]. The characteristics of the variations in index of refraction that have been used in these simulations are: Gaussian probability distributions; and spatial spectra that have a power-law form with inner and outer scales, and that have isotropic variations in the two directions transverse to the direction of propagation.

Plane-wave results[1] showed that images of intensity and phase at the observing plane for sufficiently strong medium fluctuations reveal dramatic patterns of caustic networks and interference fringes, whose description requires theoretical concepts beyond the power spectrum, although analytic results for the high and low wavenumber portions of the spectrum are well fit by the simulation results.

Point-source results[2] established that the known experimental measurements on images and scintillation indices for laser propagation through the atmosphere can be explained with homogeneous, isotropic turbulence having Kolmogorov power-law spectra and realistic values of the inner scale. In particular, intermittency and non-Gaussian probability density functions (PDF's) for the index of refraction variations are not required. Thus, in terms of quantitative comparison with experiment, as far as we know at this time the numerical simulations contain all the essential physics of laser propagation through atmospheric turbulence.

The probability density function (PDF) of intensity is one characteristic of the intensity pattern on the observing plane. The PDF is the probability of finding any particular value of intensity if one measures at one point and allows the medium to vary through its ensemble of possible realizations. The PDF contains all higher moments of intensity, and thus is not calculable from the second moment, unlike the scintillation index and the intensity spatial spectrum. The expectation for the PDF in the limit of weak fluctuations (and small intensity variance) is the log-normal distribution. The expectation for the PDF in the limit of strong fluctuations (and intensity variance near its asymptotic value of unity) is the exponential distribution. Many suggestions have been made for the PDF in the intermediate regime of fluctuation strength, for example: the K-distribution[3], the I-K distribution [4], the Generalized Gamma Distribution[5], and various convolutions of two of the above distributions, including the convolution of the log-normal and the exponential distributions[6].

In this paper we present numerical simulation results for the intensity PDF for plane waves incident on media characterized by homogeneous, isotropic Kolmogorov turbulence, with various values of the inner scale. We show that the PDFs of the simulation results, at least for negligible inner scale, agree well with the convolution of the log-normal and the exponential distribution. For significant inner scale, the distributions do not fit any of the previously suggested models.

The results for pure 1.7 power law (negligible inner scale) are shown in the accompanying figure. We show the results on a logarithmic scale in order to see both the high and low intensity regions with similar resolution. We scale lnI by its rms value so that all distributions that satisfy the lognormal distribution will lie on one curve
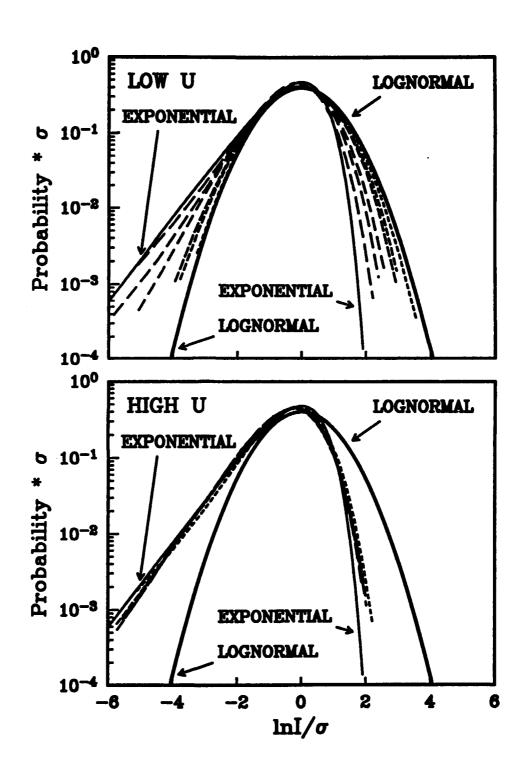
(labelled lognormal). The quantity U is the variance of intensity calculated under the weak-fluctuation assumption. The low-U section of the figure shows distributions for U=0.01, 0.06, 0.1, 0.3, 0.5, and 1.0. The high-U section shows U=1.0, 2.0, 4.0, 7.0, 12.0, and 15.0, and we see that the distribution is changing relatively slowly with U above U=1.0.

We also present a derivation of the underlying physics of the lognormal-exponential convolution in terms of the bundle of microrays that represent the propagation of energy from a point source to a point receiver. This derivation is appropriate in the saturated regime of propagation, but seems to be valid down to surprisingly low values of U.

References

1 **Martin, J M and Flatté, S M** 'Intensity images and statistics from numerical simulation of wave propagation in 3-D random media' *Applied Optics* 27 (1988) 2111–2126

2 **Martin, J M and Flatté, S M** 'Simulation of point-source scintillation through three-dimensional random media' *J. Opt. Soc. Am. A* 7 (1990) 838–847

3 **Jakeman, E and Pusey, P N** 'Significance of K distributions in scattering experiments' *Phys. Rev. Lett.* 40 (1978) 546–550

4 **Andrews, L C and Phillips, R L** 'I-K distribution as a universal propagation model of laser beams in atmospheric turbulence' *J. Opt. Soc. Am. A* 2 (1985) 160–163

5 **Ewart, T** 'A model of the intensity probability distribution for wave propagation in random media' *J. Acoust. Soc. Am.* 86 (1989) 1490–1498

6 **Churnside, J H, Hill, R J and Ochs, G R** 'Yet another probability distribution for intensity fluctuations in strong turbulence' *International Conference on Optical and Millimeter Wave Propagation and Scattering in the Atmosphere* Florence, Italy (May, 1986)

PROPAGATION OF WAVE FIELDS WITH INITIAL GAUSSIAN STATISTICS

THROUGH RANDOM MEDIA

Valery U. Zavorotny
Lebedev Physical Institute, Academy of Sciences of the USSR,
Leninskii pr., 53, Moscow, 117924, USSR;
NOAA/ERL/WPL, 325 Broadway, Boulder, CO 80303 U.S.A.; Tel: (303) 497-6616

Ivan G. Yakushkin
Institute of Atmospheric Physics, Academy of Sciences of the USSR,
Pyzhevskii per., 3, Moscow, 109017, USSR
(INVITED)

1. INTRODUCTION

Some times we deal with fields whose statistics are close to the Gaussian one over some parameters, but nevertheless have certain differences. Such a situation occurs, for instance, in the case of small-angle scattering of the coherent wave in sufficiently extended random media. In this case, on one hand, stochastic multipath propagation leads to the normalization of the field, but, on the other hand, large-scale inhomogeneities (larger then the field coherence length) produce additional random modulation which makes the measured field distribution deviate from the normal distribution [1-4]. The competition between the normalization and denormalization takes place also in the case of propagation of wave fields with the initial normal (Gaussian) distribution. Certain aspects of this problem were considered in papers [5-9]. This paper is devoted to a more complete study.

2. THE QUASI-GAUSSIAN MODEL FOR THE FIELD

Let us represent the observational field in the form

$$u(r) = L(r,\rho) \ v(\rho), \qquad (2.1)$$

where $v(\rho)$ is the incident Gaussian random field, for which

$$< v > = 0, \qquad < v(\rho_1) \ v*(\rho_1') > = \Gamma_2(\rho_1,\rho_1'), \qquad (2.2)$$

where L is the stochastic propagation operator. If L is a fully deterministic operator then the field $u(r)$ is normal (Gaussian). If L is a random operator then we should expect some deviation of the field probability distribution from the normal distribution.

It is known that the arbitrary order statistical moments of some field can be represented in the form of the cumulant expansion. We can divide the terms of the cumulant expansion to a group of the second order terms and a group of higher order moments. The first corresponds to the Gaussian distribution and the latter corresponds to a non-Gaussian remainder. In particular, for the moments of the field u for n > 1 we have

$$\Gamma_{2n} = < \prod_{i=1}^{n} u(r_i) \ u^*(r_i') > = \sum_{j=1}^{n!} P_j^0 + \Delta\Gamma, \qquad (2.3)$$

where

$$P_j^0 = \prod_{i=1}^{n} < u(r_{ij}) \ u^*(r_{ij}') > , \qquad (2.4)$$

are the Gaussian terms, $\Delta\Gamma$ is the non-Gaussian remainder, which contains

the cumulants of the order higher than second. The odd order terms equal to zero. Index j corresponds to the definite way by which we can split 2nth-order field moment into products of the second moments.

We will consider the small perturbations of the Gaussian shape of the initial field statistics. In this case the leading terms P_j^1 of the non-Gaussian remainder $\Delta\Gamma$ will contain only the fourth-order cumulants (not higher)

$$\Delta\Gamma_{2n} = \sum_{j=1}^{n!} P_j^1 \ , \quad P_j^1 = \sum_{k,l}^{n-2} \prod_{i\neq k,l} < u(r_{ij}) \ u^*(r'_{ij})> K_{jkl} \ . \qquad (2.5)$$

K is the fourth-order cumulant function connected with the joint probability distribution of the fields u and u^*. For instance, in the case $n = 2$ from Eqs.(2.3-2.5) we get

$$\Gamma_4(r_1,r'_1,r_2,r'_2) = \Gamma_2(r_1,r'_1) \ \Gamma_2(r_2,r'_2) + \Gamma_2(r_1,r_2) \ \Gamma_2(r'_1,r'_2) +$$

$$K(r_1,r'_1,r_2,r'_2) + K(r_1,r_2,r'_1,r'_2) \ . \qquad (2.6)$$

It is seen from this expression that the value K can be determined through the second and fourth moments of the receiving field. If we substitute Eqs.(2.1-2.3) into Eq.(2.6), we obtain the following formula for the function K

$$K = \left[<L_1 L_1^* L_2 L_2^*> - < L_1 L_1^*> < L_2 L_2^*> \right] \Gamma_{20}(\rho_1,\rho'_1) \ \Gamma_{20}(\rho_2,\rho'_2) \ . \qquad (2.7)$$

For the moments of intensity we get from Eq.(2.3) (assuming $<I(r_i)> = I = const.$)

$$< I^n> = n! \left[<I>^n + \frac{n(n-1)}{2} K <I>^{n-2} \right], \quad \left(K = K_{jkl}(\ r_k = r'_k = r_l = r'_l) \right). \qquad (2.8)$$

When $K = 0$, the probability distributions for the intensity I and for the field u are the Rayleigh and Gaussian (normal) distributions, respectively. When $K \neq 0$, the modulation of the initial field v due to the effect of L takes place and leads to the denormalization of the field statistics.

3. BEHAVIOR OF NON-GAUSSIAN FLUCTUATIONS BEHIND A PHASE SCREEN

Let us consider the behavior of the non-Gaussian term K behind the stochastic phase screen. The field u(r) at a distance z from the screen obeys Green's formula in small-angle approximation

$$u(r) = L(r,\rho) \ v(\rho) = \iint G_0(r,\rho) \ \exp(\ i\phi(\rho)) \ v(\rho) \ d^2\rho =$$

$$= \frac{ik}{2\pi z} \iint \exp \left[ik(r-\rho)^2/2z - i\phi(\rho) \right] v(\rho) \ d^2\rho \ , \qquad (3.1)$$

where ϕ is the Gaussian distributed phase, and we assume that

$$<\phi> = 0, \quad , \quad <[\phi(\rho) - \phi(\rho')]^2> = D_\phi(\rho - \rho') \ .$$

In the case of the weak fluctuating operator L ($<\phi^2> = \sigma_\phi^2 << 1$), and for a statistically homogeneous field we obtain from Eq.(2.7)

$$K = \frac{k^2}{(2\pi z)^2} \frac{1}{2} \iint \Gamma_{20}^2(\eta) \exp \ (ik\eta\varsigma/z)[D_\phi(\varsigma+\eta) + D_\phi(\varsigma-\eta) - 2D_\phi(\varsigma)]d\eta d\varsigma . \qquad (3.2)$$

It is clear from Eq.(3.2) that the non-Gaussian component of the field

vanishes for $\rho_0 \ll \sqrt{z/k}$, where ρ_0 is the transverse correlation length of the initial coherence function Γ_{20}. At the same time the scale of the region which is essential for propagation is estimated to be $s \sim z/k\rho_0 \gg \sqrt{z/k}$.

Let us now consider another limiting case of a strong fluctuating operator L. In this case Eq.(2.7) is suitable , but an expression for the value K has a different form. Let a be the scale of the phase correlation on the single-scale random phase screen and ρ_L is the correlation scale of the operator L. If $\rho_L < \rho_0, s/ka$ we obtain some kind of repeated normalization of the field, i.e. we have

$$K \sim < L_1 L_2^* > < L_2 L_1^* > \Gamma_{20}(\rho_1, \rho_1') \; \Gamma_{20}(\rho_2, \rho_2') \; \sim \rho_0^2 / s^2. \tag{3.3}$$

In the case of a single-scale screen s is estimated to be $s \sim z/k\rho_L$ and for $\rho^2 / s^2 \ll 1$ the value K can be neglected. As a result the field behind the screen can be considered Gaussian again, but with new coherence function Γ_2 which depends on phase screen properties

$$\Gamma_2 \sim \Gamma_{20} \exp \left[- \frac{1}{2} D_\phi(\rho_1, \rho_1') \right]. \tag{3.4}$$

4. THE QUASI-GAUSSIAN MODEL FOR THE FIELD IN EXTENDED RANDOM MEDIA

We will now apply the general idea of quasi-Gaussian field representation or the description of multi-point field statistics to the case of propagation of the Gaussian field $v(\rho)$ through extended random media. Here we also can represent the arbitrary order statistical moments for the received field in the form of Eqs.(2.3 -2.5) The value K can be determined through the solution for the fourth moment equation. One can do this using the asymptotic technique as in [2-4,10]. It is possible to apply this approach here since the non-Gaussian term K is supposed to be much smaller then the Gaussian one. The term K has been estimated for different regimes . Because of its complexity we present here only the qualitative description of its z dependence. It should be noted that the most important difference for our consideration between the case of a strong phase screen and extended media is the following. In the first case the field coherence length $\rho(z)$ may grow unlimitedly with the distance z in accordance with the van Cittert-Zernike theorem. In the second case $\rho(z)$, where z is a distance within the medium, may grow only to some limited distance z < Z where the weak effect of the medium can be assumed. On distance z > Z, where a random medium starts to damage the field coherence, $\rho(z)$ will decay.

Let us now consider the behavior of the value K for z << Z, supposing for simplicity's sake that the field v is statistically inhomogeneous, i.e. $\Gamma_{20} \sim \Gamma_{20}(v = \rho -\rho')$. For $z < k\rho^2(z)$ the value K has the same order as that for the case of a coherent incident radiance with an infinite ρ_0. For $z > k\rho^2(z)$ the region which is essential for propagation has the scale $s \sim z/k\rho(z)$. The estimations demonstrate that in this case K grows with the distance z << Z, but remains quite small. Thus, under the conditions considered above, the moderate denormalization of the propagating field takes place.

Now we will consider the behavior of K for z >> Z. Let us introduce the focal distance of the medium, f , which corresponds to the distance on which the intensity fluctuations of the initially coherent wave field reach the maximal value [10]. If the coherence length $\rho(z)$ grew to z < Z so fast

33

that for $z > Z$ we have $\rho(f) > \sqrt{f/k}$, then it means that our quasi-Gaussian approximation is not valid for the region $z \sim f$. In this case for the distance $z \gg f$ a strong denormalization occurs (which has a form of the repeated normalization of the field) that relates to the appearance of the stochastic multipathing. The repeated normalization makes a significant contribution to the value K on some propagation path ranges. However, with a further increase of the distance z this contribution becomes quite small, and the above-mentioned approximation is valid again. This situation takes place also in the case $\rho(z) \ll \sqrt{f/k}$. Indeed, if on distance $z < Z$ the coherence length $\rho(z)$ grew more slowly, then as a result for $z > Z$ we have $\rho(z) \ll \sqrt{f/k}$. Thus, in this case both for $z < Z$ and for $z > Z$ the non-Gaussian term is sufficiently small and we can use quasi-Gaussian approximation for all ranges of distances z.

5. CONCLUSION

As we see, the quasi-Gaussian approximation presented here gives us the uniform asymptotic representation for the 2nth order field moments in the extended random medium over distance z for the case $\rho(z) \ll \sqrt{f/k}$ and for the region of validity of the small-angle approximation. The obtained expressions describe the denormalization of the initially normal stochastic field, i.e. growth of the non-Gaussian part of the fluctuations up to some distance Z and then, its normalization, i.e. decrease of the non-Gaussian part of the fluctuation. Such behavior of the non-Gaussian term can be explained by a competition between two effects: "generation" of the non-Gaussian component when the wave is scattered by some layer of a random medium, and the process of normalization of the analogous components which appear because of the scattering of a wave in previous layers.

REFERENCES

1. V.U. Zavorotny, V.I. Klyatskin, and V.I. Tatarskii, Sov. Phys. JETP., 46(2), 252-260, (1977).
2. I.G. Yakushkin, Radiophys. Quantum Electron., 21, 835-840, (1978).
3. R. Dashen, J. Math. Phys., 20, 894-920, (1979).
4. K.S. Gochelashvili, and V.I. Shishov, Sov. Phys. JETP, 47, 1028-1030, (1978).
5. V.I. Shishov, and T.D. Shishova, Sov. Astron., 22, 235-239, (1978).
6. R.L. Fante, Optica Acta, 28, 1203-1207, (1981).
7. V.A. Banakh, V.M. Buldakov, and V.L. Mironov, Radiophys. Quantum Electron., 24, 482-484, (1981).
8. V.U. Zavorotny, Radiophys. Quantum Electron., 28, 1392-1399), (1985).
9. J.L. Codona, and R.G. Frehlich, Radio Sci., 22, 469-480, (1987).
10. I.G. Yakushkin, Radiophys. Quantum Electron.,28, 365-389, (1985).

Wave Propagation through the Random Media: the Most Significant Physical
Effects (1970 - 1990)

Yu. A.Kravtsov

General Physics Institute, GROT

Vavilov Str. 38 Moscow 117942 Russia

Tel. (095) 157 3845; FAX: (095) 135 0270

(INVITED)

The paper contains a microreview of the most significant and interestin?
wave phenomena in turbulent media revealed during last twenty years. These
phenomena are as follows:

1. Effects of intermittent turbulence on electromagnetic wave propagation
and scattering.

1.1. Enhancing of radio wave scattering in the turbulent atmosphere due to
intermittency (Gurvich, 1985; Tatarsky, Zavorotnyi, 1985).

1.2. Increasing of the transversal coherence radius in the intermittent
turbulence (Tatarsky, Zavorotnyi, 1985).

2. Effects of double passage through the turbulent medium on the phase va-
riance and related phenomena.

2.1. The phase variance of the retroreflected wave increases four times
over the variance of phase for single passage rather than twice as might be
expected from common sense consideration.

2.2. Corresponding increasing of variances for frequency shift, time delay
and angle of arrival.

3. Enhanced backscattering and related phenomena.

3.1. Enhanced backscatter from bodies immersed in a turbulent medium (Be-
len'kii, Mironov, Vinogradov, 1972; Kravtsov, Tatarskii, 1973; Gurvich,
Kashkarov, 1979).

3.2. Enhancing of the intensity fluctuations (Vinogradov, Kravtsov, Tatar-
skii, 1973; Belen'kii, Makarov, Mironov, Pokasov, 1978).

3.3. Partial reversal of the wave front in a turbulent media (Kravtsov,
Saichev, 1982).

3.4. The effect of long-distance correlations (Saichev, Krupnik, 1981).

3.5. Enhanced backscattering through a deep phase screen (Jakeman, 1988).

3.6. Enhanced backscattering from a particle randomly located near reflec-
ting layer or interface (Kravtsov, Namasov, 1979,1980; Lang, 1981; Akhunov,
Kravtsov, 1982).

3.7. Enhanced backscattering from a particle randomly placed within a wave
guide (Akhunov, Kravtsov, Kuzkin, 1984), from a system of two or several
randomly located scatterers or from randomly oriented bodies of intricate

geometry.

3.8. Enhanced backscattering from rough surfaces (different mecanisms of scattering are discussed by Kravtsov and Saichev, 1982; Zavorotny and Ostashev, 1982; Zavorotny, 1984; Nieto-Vesperinas and Soto-Crespo, 1987 and by others).

3.9. Giant scatter enhancement in laser sounding of the ocean (Vlasov,1985)

4. Weak localization of radiation backscattered by a half space filled bv scatterers (Barabanenkov, 1973, 1975; Kuga, Tsang, Ishimaru, 1984, 1985 and others).

5. Phenomena in the region of strong fluctuation under laser beam propagation.

5.1. Increasing of the coherence radius as compared with plane and spherical waves (Belen'kii, Kon, Mironov, 1977).

5.2. Variation of the mean curvature of the phase front and related phenomena: shift of the image plane, decreasing of resolution (Belen'kii, Boronoev,Gomboev, Moronov, Trubachev, 1980).

6. Statistical phenomena under retroreflection from phase conjugating mirrors (PSM), imbedded in a turbulent mediem.

6.1. Superfocusing of retroreflected waves due to effective increasing of PCM size in a turbulent medium (Polovinkin, Saichev, 1981; Saichev, 1982).

6.2. Magic cap effect making small scatterers placed near PCM invisible (Saichev, 1981, 1982).

6.3. Wind induced drift of the focal spot of the retroreflected wave (Akhunov, Bunkin, Vlasov, Kravtsov, 1985).

7. Phenomenon of residual scintillation due to fluctuation of primary wace propagated through the turbulent medium (Belen'kii, Mironov, 1974).

8. Increasing of the mean intensity in the shadow region of a random caustic (many authors).

9. Appearance of stochastic troposphere wave guides for UHF radio waves (Freilikher, Fuks, 1986).

10. Short time improving of the optical resolution through the turbulent media due to large turbulent lenses(Zavorotnyi, Myakinin, Chernotskii).

11. The effect of trancelucence of the turbid media with fluctuating parameters as compared with homogeneousturbid media of the same mean properties (Vardanyan, 1988; Kleorin et al, 1989).

12. Increased decaying of waves in waveguides due to scattering and mode conversion (many authors).

13. Observation of anisotropic turbulence at high altitudes (Gurvich et

al, 1988-1990).

14. Decreasing of the brightness temperature of media with random inhomo-geneities (Gurvich et al, 1974).

Many of the mentioned phenomena may be used for investigation of turbulence and are significant for applications.

ASYMPTOTIC ANALYSIS OF FLUX FLUCTUATIONS AVERAGING AND FINITE-SIZE SOURCE SCINTILLATIONS IN RANDOM MEDIA.

Michael.I.Charnotskii

RADIO-ASTRONOMICAL DEPARTMENT, PHYSICAL LEBEDEV INSTITUTE LENINSKY PROSPECT.53, MOSCOW,117924, UESR ,Tel 231-85-49.

1.Introduction. The purpose of this work is to obtain a complete set of exact asymptotes for the variance of the flux fluctuations in the Marcovian Stochastic Process Approximation [1]. and to determine the regions of applicability for these asymptotic formulae. Using Green function technique and reciprocity principle it can be shown that point source flux fluctuations through finite pupil coincide with finite-size source scintillation index provided that source brightness distribution and pupil transparency are similar.

It can be shown that as the sequence of the conservation of energy principle flux fluctuations decrease faster then a^{-2} when $a \to \infty$, where a is the pupil size. So here comes an idea of using a perturbation method for evaluating flux variance σ^2 for conditions when intensity fluctuations cannot be described by perturbation method.

We will limit ourselves by the case of turbulent medium when spectrum of medium fluctuations [1] is $\Phi_\varepsilon(x,p)=.033\ C_\varepsilon(x)p^{-11/3}$. It can be shown that σ depends on two dimensionless parameters. We choose them to be $\Omega = ka^2/L$ and $q = k\rho_0^2/L$, i.e. Fresnel numbers corresponding to the pupil size and spherical wave coherence radius. As a starting point we use a functional integral representation of σ^2 which can be derived from functional integral representation of the Green function [2], and Marcovian Stochastic Process Approximation [1],[3],[4]

$$\frac{\langle P^2 \rangle}{\langle P \rangle^2} = \sigma_p^2 +1 = \frac{4\pi^2 L^2}{k^2} \int d\mathbf{r}\ C_A(\mathbf{r}) \int D\mathbf{v}_1(\xi)D\mathbf{v}_2(\xi)\exp\left\{ik\int_0^L \mathbf{v}_1(\xi)\mathbf{v}_2(\xi)d\xi\right\}$$

$$\exp\left\{-\Phi[L,\mathbf{r}_1,\mathbf{r}_2]\right\}\delta\left(\int_0^L \mathbf{v}_1(\xi)d\xi\right)\delta\left(\int_0^L \mathbf{v}_2(\xi)d\xi\right), \qquad (1)$$

where $C_A(\mathbf{r})$ is the normalized pupil autocorrelation function,

$$\Phi[L,\mathbf{r}_1(\xi),\mathbf{r}_2(\xi)]= \frac{\pi k^2}{4} \int_0^L dx\left[2H(\mathbf{r}_1(x))+2H(\mathbf{r}_2(x))-H(\mathbf{r}_1(x)+\mathbf{r}_2(x))-H(\mathbf{r}_1(x)-\mathbf{r}_2(x))\right],$$

$$\mathbf{r}_1(x)= \int_x^L \mathbf{v}_1(\xi)d\xi,\quad \mathbf{r}_2(x)= \int_x^L \mathbf{v}_2(\xi)d\xi + \mathbf{r}(1-x/L) \ .$$

2. Weak/strong scintillations approach. We define 'weak scintillations' regime as a region of the (Ω,q) parameters space

where σ^2 is asymptotically close to the first term of series produced by the Taylor expansion of $\exp(-\Phi)$ in (1), i.e. the perturbation method, series. When $\Omega < 1$

$$\sigma_p^2 = .563 \ k^{7/6} L^{11/6} \int_0^1 C_\varepsilon^2(Lt) t^{5/6} (1-t)^{5/6} dt = O(q^{-5/6}). \tag{2}$$

In the opposite case $\Omega > 1$

$$\sigma_p^2 = .34 L^3 a^{-7/3} \int_0^1 C_\varepsilon^2(Lt) t^2 (1-t)^{-1/3} dt \tag{3}$$

A point of interest is the absence of wavelength dependence in (3). It is remarkable also that the rate of σ^2 diminishing $\propto a^{-7/3}$ is larger than a^{-2} as was pointed out . Formulae (2),(3)can easily be get from the results of [5].We evaluate applicability region of 'weak scintillations' expansion from condition of highest terms smallness with regard to the first in use and it appears to be $q > 1$ when $\Omega < 1$ and $q > \Omega^{-1}$ when $\Omega > 1$. It is remarkable that perturbation theory results in particular may be applied in the region $\Omega q > 1$ and $q < 1$ where intensity fluctuations are saturated.

We define 'strong scintillations' regime as a region of the (Ω,q) parameters space where 'weak scintillations' results are invalid and σ^2 is asymptotically close to the main terms of series produced in (1) by expansions

$$\exp\left\{-\Phi[L,r_1,r_2]\right\} = \exp\left\{-\frac{\pi k^2}{2} \int_0^L dx H(x,r_1(x))\right\}\left[1-Q_1[L,r_1,r_2]+..\right], \tag{4}$$

or

$$\exp\left\{-\Phi[L,r_1,r_2]\right\} = \exp\left\{-\frac{\pi k^2}{2} \int_0^L dx H(x,r_2(x))\right\}\left[1-Q_1[L,r_2,r_1]+..\right]. \tag{5}$$

We designate these series $M_1+M_2+..$ and $N_1+N_2+..$ correspondingly. The result is $\sigma^2 = N_1 = 1$ in the region $\Omega < q < 1$. In the region $q < \Omega < q^{2/3}$ the result is given by

$$\sigma^2 = N_1 = 1.10 \ a^{-2}\left[.73 \ k^2 \int_0^L dx C_\varepsilon^2(x)(1-x/L)^{5/3}\right]^{-3/5} = O(q \ \Omega^{-1}). \tag{6}$$

In the region $q^{2/3} < \Omega < q^{-1}$ the result is given by

$$\sigma^2 = M_2 = .27 L^{-11/5} k^{-7/15} \int_0^1 C_\varepsilon^2(Lt) t^2 (1-t)^2 \left[\int_0^1 C_\varepsilon^2(L\tau)\eta(t,\tau)d\tau\right]^{-7/5} dt = O(q^{1/3})$$

It can be seen that lower boundary of perturbation method coincides with the upper boundary of coherence channel expansion. Asymptotic values of σ^2 are in agreement in the neighborhood of this boundary. All these circumstances permit us to conclude that obtained set of asymptotes is a complete one.

3. Alternative approach to asymptotic analysis of quasi-plane wave flux fluctuations.

Here we will try to formulate a somewhat different approach to the problem. We suppose that coherence channel corresponding to expansion (4) is the main one. This means that we will use (4) throughout the plane (Ω, q). In some regions in (Ω, q) plane it is necessary to add a contribution from additional channel (5). The conditions of this necessity are

  (i) the actually restriction by the first exponent of contribution region for $M_i, i \geq 2$;

  (ii) the smallness of the first argument of Q_1 functions as compared with second one in the main contribution region.

Consider flux fluctuations for the source having initial field distribution $U(r) = \exp\{-ikr^2/2F\}$. This model describes a wave-front having constant amplitude and arbitrary curvature. In addition to dimensionless parameters q and Ω we introduce $\Delta = (1-L/F)$. This source model seems to be interesting as an object of application of main/additional coherence channel concept. Besides that case $\Delta=1$ (plane wave) is important for astronomical applications and permits us to compare our results with results of [6]. We may also verify the agreement with the results of previous section.

When $\Delta = 1$ asymptotic regions are qualitatively the same as in the case of point source. When $q > 1$ and $\Omega > 1$

$$\sigma^2 = M_2 = .563 \, k^{7/6} L^{11/6} \int_0^1 C_\varepsilon^2(Lt) t^{5/6} dt = O(q^{-5/6}), \quad (7)$$

and this is exactly the smooth perturbation method result [1] for plane wave intensity variance. When $\Omega > 1$ and $\Omega q > 1$

$$\sigma^2 = M_2 = .34 L^3 a^{-7/3} \int_0^1 C_\varepsilon^2(Lt) \, t^2 dt = O(q^{-5/6}\Omega^{-7/6}). \quad (8)$$

When $q < 1$ and $\Omega q < 1$ then

$$\sigma^2 = M_2 = .27 L^{-11/5} k^{-7/15} \int_0^1 C_\varepsilon^2(Lt) t^2 \left[\int_0^1 C_\varepsilon^2(L\tau) \min(t,\tau) d\tau \right]^{-7/5} dt = O(q^{1/3}), \quad (9)$$

and conditions (i) and (ii) are fulfilled. This means that it is necessary to take into account the additional coherence channel contribution.

In the region $q < 1$, $q > \Omega$, $N_1 = 1$, but when $q^{-1} > \Omega > q$,

$$N_1 = 1.10 \, a^{-2} \left[.73 \, k^2 \int_0^L dx C_\varepsilon(x) \right]^{-3/5} = O(q \, \Omega^{-1}). \quad (10)$$

Comparing values of M_2 and N_1 we conclude that if $1 > q > \Omega^{3/2}$ then $N_1 > M_2$ and $\sigma^2 \simeq N_1$ but if $q^{2/3} < \Omega < q^{-1}$ then $M_2 > N_1$ and $\sigma^2 \simeq M_2$. And so finally in the region $1 > q > \Omega$, $\sigma^2 = 1$. Under conditions $q < \Omega < q^{2/3}$ the result is given by (10) and σ^2

$= O(q/\Omega)$. Under conditions $q^{2/3} < \Omega < q^{-1}$ the result is given by (9) and $\sigma^2 = O(q^{1/3})$. All these asymptotic values and appropriate boundaries forms a complete set of asymptotes for the plane wave problem. For the case of inhomogeneities located near the pupil, i.e. if $X < L$ is the essential integration domain, point source results properly transforms to plane wave results.

Methodically the most interesting case is $\Delta < 1$ when under conditions $\Omega/\Delta < 1$ and $q\Delta < 1$

$$\sigma^2 = M_2 = .563 \ k^{7/6} L^{11/6} \Delta^{-5/6} \int_0^1 C_\varepsilon^2 (Lt) t^{5/3} dt = O\left[(q\Delta)^{-5/6}\right], (11)$$

under conditions $\Omega/\Delta > 1$ and $q\Omega > 1$

$$\sigma^2 = M_2 = .34 L^3 a^{-7/3} \Delta^{1/3} \int_0^1 C_\varepsilon^2 (Lt) t^{5/3} dt = O(q^{-5/6} \Omega^{-7/6} \Delta^{1/3}). \quad (12)$$

Under conditions $q\Delta < 1$ and $q\Omega < 1$

$$M_2 = .27 L^{-11/5} k^{-7/15} \Delta^{1/3} \left[\int_0^1 C_\varepsilon^2 (Lt) t^{5/3} dt\right]^{-2/5} = O\left[(q\Delta)^{1/3}\right], \quad (13)$$

and it is necessary to take into account the additional coherence channel contribution.

If $\Omega\Delta^{-2} < q < \Delta^{-1}$, $N_1 = 1$, but when $q^{-1} > \Omega > q\Delta^2$

$$N_1 = 1.10 \ a^{-2}\Delta^2 \left[.73 \ k^2 \int_0^L dx C_\varepsilon(x)(x/L)^{5/3}\right]^{-3/5} = O(q \ \Omega^{-1}\Delta^2). \quad (14)$$

Combining M_2 and N_1 values in the way similar to plane wave case we get in the region $1 > q > \Omega\Delta^{-2}$, $\sigma_P^2 = 1$, under conditions $q\Delta^2 < \Omega < q^{2/3}\Delta^{5/3}$ the result is given by (14) and $\sigma_P^2 = O(q \ \Omega^{-1}\Delta^2)$. Under conditions $q^{2/3}\Delta^{5/3} < \Omega < q^{-1}$ the result is given by (13) and $\sigma_P^2 = O\left[(q\Delta)^{1/3}\right]$.

Converging wave flux fluctuations seems us to be an interesting example of a problem where 'weak scintillations' regime realizes when point source intensity fluctuations are strong , but 'strong scintillations' regime realizes in opposite case.

[1] Rytov S M, Kravtsov Yu A and Tatarskii V I 1978 *Introduction to Statistical Radiophysics: Part 2* (Moscow:Nauka) (In Russian)
[2] Klyatskin V I 1975 *Statistical Description of Dynamical Systems with Fluctuating Parameters* (Moscow:Nauka) (In Russian)
[3] Codona J L and Frehlich R G 1987 *Rad. Sci.* 22 469-480
[4] Codona J L, Creamer D B, Flatte S M, Frehlich R G and Henyey 1986 *J. Math. Phys.* 27 171-177
[5] Tatarskii V I 1971 *The effect of the Turbulent Atmosphere on Wave Propagation* (NTIS, Springfield, Va)
[6] Shishov V I and Shishova T D 1978 *Sov. Astron.* 22 235-239

A Physical Model of Optical Scintillation

James H. Churnside
NOAA Wave Propagation Laboratory
325 Broadway
Boulder, CO 80303
USA
303-497-6744

(INVITED)

Wang and Strohbehn[1] introduced the log-normally modulated Rician model of optical scintillation in the turbulent atmosphere in 1974. This model is based on the fact that the atmosphere consists of turbulent eddies with a wide range of scale sizes.

Eddies that are much smaller than a Fresnel zone diffractively scatter a small portion of the incident radiation. If only small eddies were present, the optical field at a receiver would consist of the unscattered field plus the sum of the scattered fields from all of the eddies along the path. If we assume that many small eddies are positioned randomly along the path, we can invoke the central-limit theorem and claim that the sum of the scattered fields is a circular-Gaussian random variable. This implies that the received field amplitude will have a Rice-Nakagami probability-density function.[2]

Eddies that are much larger than a Fresnel zone act as weak refracting elements. Each perturbs the observed field by a multiplicative magnification factor that is near unity. The total magnification factor is the product of the factors from all of the eddies along the path. Therefore, if we assume that many such eddies exist, we can invoke the central-limit theorem to claim that the logarithm of the magnification factor is a Gaussian random variable.

From this model, we can derive the probability-density function of the irradiance. Normalizing the irradiance by the mean value, the density function is the log-normally modulated Rician[3]

$$p(I) = \int_0^\infty dz \; \frac{1+r}{z} \; \exp\left(-r - \frac{1+r}{z}I\right) I_0\left\{2\left[\frac{(1+r)\,r}{z}I\right]^{1/2}\right\}$$
$$\times \frac{1}{\sqrt{2\pi}\,\sigma_z z} \exp\left[-\frac{\left(\ln z + 0.5\sigma_z^2\right)^2}{2\sigma_z^2}\right] , \tag{1}$$

where r is a coherence parameter, σ_z^2 is the variance of the logarithm of the magnification factor, and I_0 is the zero-order modified Bessel function of the first kind. The moments of normalized irradiance are

$$\langle I^n \rangle = \frac{(n!)^2}{(1+r)^n} \exp\left[0.5\,n(n-1)\,\sigma_z^2\right] \sum_{m=0}^{n} \frac{r^m}{(n-m)!\,(m!)^2}. \tag{2}$$

The coherence parameter r is the ratio of the power that is not scattered by the small scale eddies to the power that is scattered by these eddies. In very weak path-integrated turbulence, the coherence parameter is very large. The result of large r is that the statistics of irradiance reduce to log normal.[4] There is a great deal of theoretical and experimental evidence to suggest that the statistics should be log normal in this regime.

In very strong path-integrated turbulence, the coherence parameter goes to zero. The resulting probability-density function of normalized irradiance is a log-normally modulated exponential:[5]

$$p(I) = \frac{1}{\sqrt{2\pi}\sigma_z} \int_0^{\infty} \frac{dz}{z^2} \exp\left[-\frac{I}{z} - \frac{\left(\ln z + 0.5\sigma_z^2\right)^2}{2\sigma_z^2}\right]. \tag{3}$$

This relationship has also been verified experimentally. In the extreme limit, it reduces to the negative exponential density function in agreement with available theory.

The two parameters, r and σ_z^2, can be found from the measured second and third moments of irradiance. Any other single-point statistics can then be found from the probability-density function. In experiments, we have found that r is generally small enough or large enough that either the formula for weak or that for strong path-integrated turbulence can be used.

It would also be nice to calculate the parameters from the propagation geometry and turbulence characteristics. We have been moderately successful at this. The coherence can be estimated from the mutual coherence function calculated using only scale sizes smaller than the Fresnel zone. The other parameter can be calculated numerically from the moment equation for the log-amplitude variance using only scale sizes larger than

a Fresnel zone. This has not yet been done. One can also calculate σ_z^2 using the heuristic saturation theory of Hill and Clifford.[6] This has been done, and reasonable agreement with measured irradiance variances was obtained.[3]

In the single-point model, we have assumed that the real and imaginary parts of the diffractively scattered field and the logarithm of the refractive modulation are each Gaussian random variables. We further assume that those same quantities, observed in two points in a plane perpendicular to the propagation direction, are jointly Gaussian random variables. This assumption leads to an expression for the joint probability-density function of the irradiance at two points in an observation plane.[7] The expression is too long to include here. In addition to the two parameters of the single-point case, it requires the correlation of the Rician fields and the correlation of the logarithm of the magnification factor. Reasonable agreement with experimental data has been obtained.[7]

The model is readily extended to provide the statistics of the optical power collected by a finite aperture.[8] In weak path-integrated turbulence, the statistics remain log normal, with a variance that is below the point detector variance by an amount that depends on the ratio of the aperture diameter to the larger of the Fresnel zone size $(L/k)^{1/2}$ and the turbulent inner scale. For small inner scale, the variance reduction is approximately

$$A = \left[1 + 0.214\left(\frac{kD^2}{4L}\right)^{7/6}\right]^{-1}, \qquad (4)$$

where D is the aperture diameter. This factor has been verified experimentally.

In strong path-integrated turbulence, two scale sizes become important: the transverse phase coherence length ρ_0 and the scattering disk size, which is the square of the Fresnel zone divided by ρ_0. The smaller scale, ρ_0, is due to the diffractive scattering. The irradiance variance in this scale is $(\sigma_I^2+1)/2$, where σ_I^2 is the total irradiance variance. The irradiance variance in the large scale is $(\sigma_I^2-1)/2$. The resulting variance reduction factor can be approximated by

$$A = \frac{\sigma_I^2 + 1}{2\sigma_I^2}\left[1 + 0.908\left(\frac{D}{2\rho_0}\right)^2\right]^{-1} + \frac{\sigma_I^2 - 1}{2\sigma_I^2}\left[1 + 0.613\left(\frac{kD\rho_0}{2L}\right)^{7/3}\right]^{-1}. \qquad (5)$$

If the aperture diameter is much larger than ρ_0, then the statistics of the power through the aperture will be nearly log normal. If the aperture is of the order of ρ_0, the probability-density function of power can be approximated by a lognormally modulated gamma

$$p(P) = \frac{m^m P^{m-1}}{\sqrt{2\pi}\,\sigma_z \Gamma(m)} \int_0^\infty dz\, z^{-m-1} \exp\left[-m\frac{P}{z} - \frac{(\ln z + 0.5\sigma_z^2)^2}{2\sigma_z^2}\right], \qquad (6)$$

where m is the number of ρ_0-size patches in the aperture.

References

1. T. Wang and J. W. Strohbehn, J. Opt. Soc. Am. **64**, 994 (1974).

2. J. W. Goodman, "Statistical Properties of Laser Speckle Patterns," in Laser Speckle, J. C. Dainty, ed. (Springer-Verlag, Berlin, 1975), Chap. 2.

3. J. H. Churnside and S. F. Clifford, J. Opt. Soc. Am. A **4**, 1923 (1987).

4. J. H. Churnside and R. G. Frehlich, J. Opt. Soc. Am. A **4**, 1760 (1989).

5. J. H. Churnside and R. J. Hill, J. Opt. Soc. Am. A **4**, 727 (1987).

6. R. J. Hill and S. F. Clifford, J. Opt. Soc. Am. **71**, 675 (1981).

7. J. H. Churnside, J. Opt. Soc. Am. A **4**, 1931 (1989).

8. J. H. Churnside, J. Opt. Soc. Am. A **6**, (1991) (accepted for publication).

Intensity Distributions for Two Scale Fluctuations

R. L. Phillips
University of Central Florida
Center for the Research in Electro Optics and Lasers (CREOL)
Depts of Electrical Engineering and Mathematics
Orlando, FL USA 32826
(407) 658-3908

Introduction

The propagation of waves through an irregular medium with a random index of refraction develops two scales of fluctuation. These two scales are due to the simultaneous mechanisms of diffractive and refractive scattering. The detected scattered wave appears to have a high frequency fluctuation modulated by low frequency fluctuations.

These two scales of fluctuation are most ubiquitous. Some years ago Prokorov [1] showed theoretically that two spatial scales develop on a wave propagating through an extended homogeneous random medium and random phase screens. This occurs for a medium with a Gaussian spectrum of refractive scatters or a power-law spectrum. Coles and Frelich [2] published results of a 1 Km atmospheric laser beam propagation experiment showing the presence of two spatial scales of fluctuation. Weeks and Phillips [3] reported results of phase screen experiments showing the two scale fluctuations. Rickett, Coles and Bourgois [4] analyzed intensity fluctuations of radio waves after passing through the interstellar medium and these also displayed the two scale characteristics.

Several probability density functions, PDF's, for the intensity have been proposed to account for this two scale fluctuation. The K-distribution is one of these and is based upon a compound spatial process or a random modulation of a random fluctuation. The K-distribution assumes the fine scale is due to a zero mean circular complex Gaussian statistic for the field and hence, the conditional PDF is negative exponential. The fluctuations of the intensity modulation are taken to be gamma distributed.

The K-distribution can be shown to be an approximation to an exact distribution based upon a Karhunen-Loéve expansion of the field. The expansion is used for each scale of fluctuation.

Theory

At any observation plane along the propagtion path, we decompose an isotropically scattered field, $U(r)$, displaying two distinct scales of spatial fluctuations, into two independent contributions

$$U(r) = 1 + U_a(r) + [U(r) - (1 + U_a(r))]$$

where $1 =$ normalized global mean value of the field; $U_a(r) =$ local average value about the mean and $[U(r) - (1 + U_a(r))] =$ local fluctuations. The term $U_a(r)$ accounts for large scale fluctuations and $[U(r) - (1 + U_a(r))]$ for small scale fluctuations. We compute the local average from the equation:

$$U_a(r) = \frac{1}{s_0} \int_{r-\frac{s_0}{2}}^{r+\frac{s_0}{2}} U(\alpha) \, d\alpha - 1 \qquad (1)$$

Hence $U_a(r)$ is a moving average at a point r centered in an interval $(-s_0/2, s_0/2)$. We take the interval to encompass the small scale structure. For spherical waves s_0 is defined by equating the phase structure to unity, i.e. $D_{sp}(s_0) = 1$. The large scale is approximately $\sqrt{z/k}/2s_0$. At any fixed distance z, as turbulence increases, s_0 decreases so one scale increases while the other decreases. Hence there appears to be less spatial modulation of the small scale fluctuations as s_0 decreases.

47

We write the total field in the form

$$U(r) = 1 + U_s(r) + \left\{ \frac{[U(r) - (1 + U_s(r))]}{[1 + U_s(r)]} \right\} [1 + U_s(r)] \tag{2}$$

We assume the denominator of the third term to be very slowly varying relative to the small scale fluctuations represented by the numerator term. For clarity we write

$$P_1(r) = U_s(r) \tag{3.a}$$

$$P_2(r) = \frac{U(r) - [1 + U_s(r)]}{[1 + U_s(r)]} = \frac{U(r) - [1 + U_s(r)]}{[1 + U_s(0)]} . \tag{3.b}$$

where we have assumed the denominator in $P_2(r)$ to be approximately constant relative to the numerator. The field can then be expressed as a product or modulation process

$$U(r) = 1 + P_1(r) + P_2[1 + P_1(r)] = [1 + P_1(r)][1 + P_2(r)] . \tag{4}$$

We can generalize this functional form as

$$U(\bar{r}, \bar{s}) = [A_1(\bar{r}) e^{i\psi_1(\bar{r})} + B_1(\bar{r}) e^{i\psi_1(\bar{r})}][A_2(\bar{s}) e^{i\psi_2(\bar{s})} + B_2(\bar{s}) e^{i\psi_2(\bar{s})}] \tag{5}$$

where $A_1 e^{i\psi_1}$ and $A_2 e^{i\psi_2}$ are the deterministic portions of the components; $B_1 e^{i\psi_1}$ and $B_2 e^{i\psi_2}$ are the fluctuating portions, each with zero mean. Further, we assume the random portions of the field are each circular complex Gaussian distributed. We then use a Karhunen-Loéve expansion of each component, independently, in a series over the area of the detector

$$U(\bar{r}, \bar{s}) = \sum_{n=1}^{\infty} (a_{1n} + b_{1n}) G_n(\bar{r}) \sum_{m=1}^{\infty} (a_{1m} + b_{1m}) W_m(\bar{s}) \tag{6}$$

The sets of functions $\{G_n()\}$ and $\{W_m()\}$ are taken to be orthonormal and eigenfunctions of the correlation functions of the large and small scale fluctuations, respectively. These sets can be considered spatial modes of the random field. The coefficients of the spatial modes a_1 and a_2 are the complex mean values of each mode, and b_1 and b_2 are zero mean, complex circularly Gaussian distributed random variables representing the fluctuating portions of the mode. The eigenvalues of the Karhunen-Loéve expansions are the variances of the random coefficients i.e. $\gamma_{1n} = \langle |b_{1n}|^2 \rangle$ and $\gamma_{2m} = \langle |b_{2m}|^2 \rangle$. The detected intensity is given by

$$I = \int_A \int_A |U(\bar{r}, \bar{s})|^2 \, d\bar{s} \, d\bar{r} = \sum_{n=1}^{N} \sum_{m=1}^{M} |a_{1n} + b_{1n}|^2 |a_{2m} + b_{2m}|^2 \tag{7}$$

where each component of the field is integrated over the area, A, of the detector and we have assumed that N and M are the number of significant values of γ_{1n} and γ_{2m}. We then compute the PDF, P(I), by first computing the PDF of each series and then use conditional probability, i.e.

$$P(I) = \int_0^{\infty} P(I \mid I_1) P(I_1) \, dI_1 . \tag{8}$$

We now take the deterministic portion of the modes to be zero, i.e. $a_{1n} = a_{2m} = 0$ so that the intensity is the product of the two series

$$I = \sum_{n=1}^{N} |b_{1n}|^2 \sum_{m=1}^{M} |b_{2m}|^2 . \qquad (9)$$

The characteristic function of each sum can be written as a product

$$C_1(j\omega) = \prod_{n=1}^{N} \frac{i}{1 - j\omega\gamma_{1n}} ; \quad C_2(j\omega) = \prod_{m=1}^{M} \frac{i}{1 - j\omega\gamma_{2m}} . \qquad (10)$$

We can write approximations to these products as

$$C_1(j\omega) = \frac{1}{(1 - j\omega\beta)^{\alpha+1}} ; \quad C_2(j\omega) = \frac{1}{(1 - j\omega\eta)^{\lambda+1}} \qquad (11)$$

where

$$\alpha + 1 = \frac{\left[\displaystyle\sum_{n=1}^{N} \gamma_{1n}\right]^2}{\displaystyle\sum_{n=1}^{N} (\gamma_{1n})^2} ; \qquad \beta = \frac{\displaystyle\sum_{n=1}^{N} (\gamma_{1n})^2}{\displaystyle\sum_{n=1}^{N} \gamma_{1n}} ; \qquad (12.a)$$

and

$$\lambda + 1 = \frac{\left[\displaystyle\sum_{m=1}^{M} \gamma_{2m}\right]^2}{\displaystyle\sum_{m=1}^{M} (\gamma_{2m})^2} ; \qquad \eta = \frac{\displaystyle\sum_{m=1}^{M} (\gamma_{2m})^2}{\displaystyle\sum_{m=1}^{M} \gamma_{2m}} . \qquad (12.b)$$

subject to the condition $\alpha \gg 1$ and $\lambda \gg 1$.[5]

Inverting these characteristic functions we have the gamma distributions. If we then use conditional probability, we can write

$$P(I \mid I_1) = \frac{(I)^\lambda e^{I_1/I_1\eta}}{I_1^{\lambda+1} \eta^{\lambda+1} \Gamma(\lambda+1)} \qquad (13)$$

and

$$P(I_1) = \frac{(I)^\alpha e^{I_1/\beta}}{\beta^{\alpha+1} \Gamma(\alpha+1)} \qquad (14)$$

We then substitute Equations (13) and (14), into Equation (8) to find

$$P(I) = 2 \; \frac{(I)^{\frac{\alpha+\lambda}{2}} \; K_{\alpha-\lambda}\left[2\sqrt{\dfrac{I}{\beta\eta}}\right]}{(\eta\beta)^{\frac{\alpha+\lambda}{2}+1} \; \Gamma(\alpha+1) \, \Gamma(\lambda+1)} \tag{15}$$

This is the generalized K-distribution, Ref. 6. If we let $\lambda = 0$ and substitute $\alpha - 1$ for α, we have what is known as the K-distribution.

Suppose we now assume $N = 2$, $M = 1$ and the eigenvalues $\gamma_{11} \neq \gamma_{12}$, γ_{21}. The characteristic functions $C_1(j\omega)$ and $C_2(j\omega)$ can be written as

$$C_1(j\omega) = \frac{1}{(1 - j\omega\gamma_{11})} \frac{1}{(1 - j\omega\gamma_{12})}; \quad C_2(j\omega) = \frac{1}{1 - j\omega\gamma_{21}} \tag{16}$$

The PDF from Equation (8) becomes

$$P(I) = \frac{2}{(\gamma_{11} - \gamma_{12})\gamma_{21}} K_0\left[2\sqrt{\dfrac{I}{\gamma_{11}\gamma_{21}}}\right] + \frac{2}{(\gamma_{12} - \gamma_{11})\gamma_{21}} K_0\left[\sqrt{\dfrac{I}{\gamma_{12}\gamma_{21}}}\right] \tag{17}$$

The PDF for the case $N = 3$, $M = 1$ when two of the eigenvalues are equal, i.e. $\gamma_{11} = \gamma_{12} = \gamma_0$, γ_{13}, γ_{21};

$$P(I) \;=\; \frac{2}{\gamma_{21}(\gamma_0 - \gamma_{13})} \left(\frac{I}{\gamma_0\gamma_{21}}\right)^{1/2} K_1\left[2\sqrt{\dfrac{I}{\gamma_0\gamma_{21}}}\right]$$

$$- \frac{2}{\gamma_{21}(\gamma_{13} - \gamma_0)^2} K_0\left[2\sqrt{\dfrac{I}{\gamma_0\gamma_{21}}}\right] + \frac{2\gamma_{13}}{\gamma_{21}(\gamma_{13} - \gamma_0)^2} K_0\left[2\sqrt{\dfrac{I}{\gamma_{13}\gamma_{21}}}\right] \tag{18}$$

Discussion

The K Bessel functional form of the PDF of the intensity fluctuations is due to the product form of the two scale Baussian fluctuations of the field. A Karhunen-Loéve expansion of each scale of the field gives a PDF that incorporates the spectrum of each scale. The well known K-distribution can be expressed as an approximation to the Karhunen-Loéve form.

References

1. A.M. Prokhorov, F.V. Bunkin, K.S. Gochelashvily, V.I. Shishov, "Laser Irradiance Propagation in Turbulent Media", Proc. IEEE, 63, 5, 790-811 (1975).
2. W.A. Coles, R.G. Frehlick, "Simultaneous Measurements of Angular Scattering and Intensity Scintillation in the Atmosphere", JOSA, Vol.22, No.8, Aug. 1982, pp.1042-1048.
3. A.R. Weeks, R.L. Phillips, "Experimental Verification of the K-distribution Family for Scattering", SPIE, Vol.1115, 38-48, (1989).
4. B.J. Rickett, W.A. Coles, G. Bourgois, "Slow Scintillation in the Interstellelar Medium", Astron. Astrophys., 134, 390-395 (1984).
5. A. Pupoules, The Fourier Integral and Its Applications, McGraw Hill 1962, New York, NY.
6. E. Jakeman, R.J.A. Lough, "Generalized K-distribution: A statisical model for weak scattering", J. Opt. Soc. Am: A. 4, 1764-1772 (1987).

ADAPTIVE OPTICS 1 & 2

A Method for the Investigations of the Spatio-Temporal Atmospherically Pertubed, wavefronts, at High Temporal Frequency

M. Abitbol

Optics and Optoelectronics Division
Bertin & Cie
Les Milles BP 22000, France
Tel. (33) 42604619

N. Subovitch and N. Ben-Yosef

Division of Applied Physics and Material Sciences
Graduate School of Applied Science and Technology
The Hebrew University of Jerusalem
Jerusalem 91904, Israel

1. Introduction

The investigation of an atmospherically pertubed wavefronts has been given considerable attention. The intensity fluctuations (scintillations) of such wavefronts were extensively studied as well. However, due to the complexity of the measurement, very few works investigate the spatio-temporal wavefronts structure [1]. These are based on interferometric techniques and are limited to low temporal frequencies. Those methods facilitate the measurement of the relative phase fluctuations between two wavefronts.

A novel method, based on the Hartman sensor principles, facilitating measurements at frequencies comparable to the turbulence temporal frequency content (a few KHz) is presented. It is shown that it is possible to perform measurements of a single wavefront, resolving the wavefront tilt from the higher spatial frequency contributions. The method is based on a geometrical measurement of the wavefront over the optical aperture.

The spatial structure of the phase front over the aperture can be described by a set of Zernike polynomials [2]. The second Zernike coefficient describes the inclination of the averaged (over the aperture) phase front, i.e. the tilt (or angle of arrival), the higher coefficients describe the fluctuations of the phase front relative to the tilt. In the present method it is possible to separate the second coefficient from the higher orders and study the temporal behaviour of each. It is shown that the tilt temporal behaviour is slower than the temporal variations of the higher order of fluctuations.

2. The Spatio-Temporal Wavefront Sensor

The present wavefront sensor is based on the Hartman wavefront sensing principles [3]. The Hartman sensor measures directly the phase front by spatially sampling it. This sampling is achieved by using a lenslet mosaic in an optical plane conjugate to the entrance pupil. The real images at the lenslet output are measured with the aid of a video camera. This classical arrangement, sampling the phase front slope in two dimensions, is limited in temporal resolution due to the frame rates of the video camera.

In the present case, one spatial direction is sacrified in order to obtain much higher rates. This aim is achieved by using a cylindrical lens utilized in conjunction with a linear CCD array, having line rates of a few KHz. The cylindrical lens forms the line spread function (while illuminated by a point source) due to the atmospheric effects (as opposed to the point spread in the case of spherical lens). The linear CCD samples it and facilites its measurement at high speeds.

The spatial resolution is defined by the diffraction of the optics and the CCD pixel size. For the present communication an resolution of 7 microns was obtained.In figure 1 512 successive (in time) CCD lines are shown. It is observed that the position and intensity of each line spread function is different . The position represents the wavefront slope (tilt), the width represents the higher order fluctuations while the intensity variations represents the scintillations. The fine structure of each line spread represent the higher order (higher than tilt) phase front fluctuations which are analyzed in details.

3. Experimental Results

Two main parameters are relevant for the present analysis. The position of the median of the line spread function (relative to the time averaged position) represents the measure of the tilt, the width (85% intensity points arround the median) represents the higher order fluctuations. The temporal autocorrelation and power spectrum of each was calculated for different optical apertures. The experimental results are compared to the theoretical prediction [4]. The complete analysis of the data processing procedures can be found in [3].

In figure 2 the autocorrelation function for the tilt and high order fluctuations are shown for an optical aperture of 20mm. It is clearly observed that the correlation time of the tilt is higher than the correlation time of the fluctuations. The same conclusion is drawn, more convincingly, from the temporal power spectrum of each phenomenon. In figures 3 and 4 the power spectra of each is shown for different optical apertures. It is observed that the slopes of the power spectra at high frequencies increases (in absolute values) with increasing optical diameter. This feature is clearly inderstood remenbering that aperture averaging acts as a filter.

However, a comparison with theoretical models [4] shown in figures 5 and 6, show deviations for the higher order fluctuations (a best fit with the theoretical model in this case is obtained only with an unrealistic wind velocity of 8 m/s). It was predicted that both tilt and higher order fluctuations will behave in a similar maner, results show that the tilt is more effectivelly filtered by the apperture than the high order fluctuations.

4. Conclusions

One can conclude that the Hartman sensor technique can be utilized for the study of the fast spatio-temporal fluctuations of an atmospherically degraded wavefronts. The experimental results indicate that the temporal behaviour of the various spatial components of the wavefront pertubations depend on the order of the pertubation.

5. Refrences

1. V.P. Lukin and U.V. Pokasov, "Optical Phase Fluctuations," Appl. Opt. 20, 121 (1981).

2.. R.J. Noll, "Zernike Polynomials and Atmospheric Turbulence," J.O.S.A. 66,207 (1976).

3. M. Abitbol, " Wavefront Sensing in Adaptive Optics System," Ph.d Thesis submited to the senat of the Hebrew University OCt. 1990.

4. S.F. Clifford et al., J.O.S.A. 61, 1279 (1971).

Fig. 1 The line spread function for 512 successive (in time) CCD line.
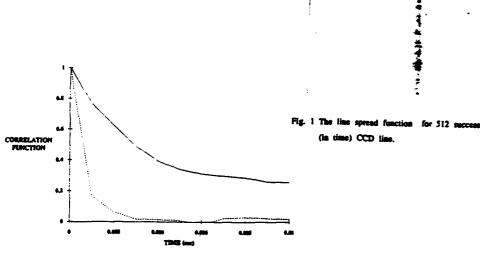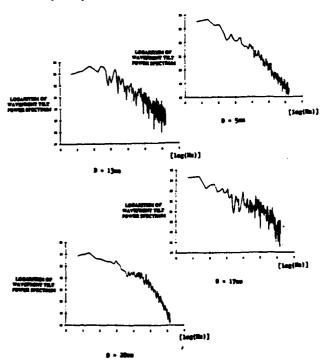
Fig. 2 Temporal correlations of the wavefronts tilt (solid line) and high order fluctuations (dots line) for an optical aperture of 20mm.

Fig. 3 Temporal power spectrum of the tilt fluctuations for differents optical diameter.

55
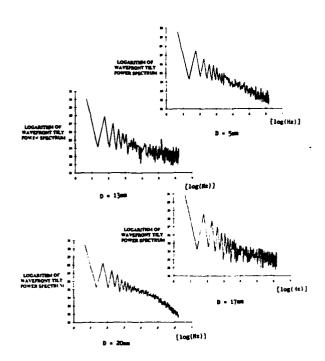
Fig. 4 Temporal power spectrum of the high order fluctuations for differents optical diameter.

Fig. 5 Comparison between theoretical behaviour of the temporal spectra of the tilt [4] and experimental results (the fit were performed for a measured wind velocity of 3m/s)
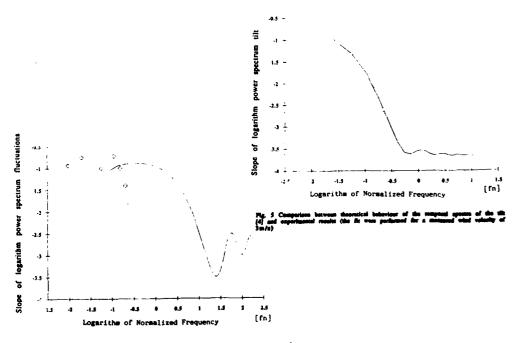
Fig. 6 Comparison between theoretical behaviour of the temporal spectra of the high order fluctuations [4] and experimental results (the fit were performed for a measured wind velocity of 3m/s, a more suitable fit can be obtained for an unrealistic wind velocity of 8m/s)

ATMOSPHERIC ADAPTIVE OPTICS

V.P. Lukin

Institute of Atmospheric Optics, Tomsk, 634055, USSR

(INVITED)

INTRODUCTION

The paper considers some aspects of application of adap-
tive optical systems (AOS) in the atmosphere. The main
problems have been emphasized using the above systems, namely,
transfer of optical contrast or image, conservation of initi-
al properties of optical radiation at propagation through the
atmosphere, and energy transfer in the atmosphere using la-
ser beams.

Modern optoelectron systems operating in the atmosphere
are not able to realize their potential efficiency. One of
the main ways for providing efficient work of optical sys-
tems in the atmosphere is the use of systems, algorithms and
elements of adaptive optics.

When describing the modern atmospheric adaptive optical
systems we should pay special attention to the following dis-
torting factors of the atmosphere, namely, refraction of op-
tical radiation along extended paths, atmospheric turbulence,
thermal self-action of radiation. As the compensation algo-
rithms of atmospheric effect the following factors will be
considered: optimization of initial parameters of radiation
(or initial system parameters at reception), a priori cont-
rol of parameters of amplitude-phase distribution of radia-
tion (profiled beams, "program" correction, refraction cor-
rection, etc.), phase correction of joint action of atmosphe-

ric turbulence and thermal self-action, amplitude-phase adaptive correction.

The goal of our analysis is the determination of limiting possibilities when applying adaptive optical systems. The relative increase of the Strehl parameter or energy criterion is calculated as a measure of correction quality.

The efficiency of AOS application in the atmosphere is analyzed on the basis of mathematical and physical modeling.

OPTIMIZATION OF INITIAL RADIATION PARAMETERS

The topic of discussion is either compensation of stationary distortions of the wavefront, for example, refraction and effects of thermal self-action or the effects connected with the turbulence action. In the latter case the following conditions for homogeneous optical path will be considered: a) optimal focusing of high-power radiation at thermal self-action, b) cylindrical focusing (in comparison with focusing by a spherical lens), c) program scanning using a high--power radiation beam.

The efficiency of a given optimization is estimated for the conditions of Gaussian beam focusing in the atmosphere. The possibilities for minimization of turbulent distortions of laser beams have been analyzed along horizontal and vertical atmospheric paths. Collimated, focused and diverging beams are compared.

A PRIORI CONTROL OF PARAMETERS OF AMPLITUDE-PHASE RADIATION
DISTRIBUTION

The paper deals with the method of program correction of laser radiation refraction along the ground path based

on the measurements of average temperature gradients. The use of this method has proved its efficiency along atmospheric paths of 500 to 2000 m length.

Transition from horizontal atmospheric paths to vertical ones varied essentially the nature of thermal self-action effects of high-power laser radiation. However, a qualitative analysis has shown that the propagation of a collimated Gaussian beam is accompanied by the same effects. As to the focused beams, the energy from the main maximum is distributed in the secondary maximums with the increase of the initial beam power. Transition from horizontal to vertical paths is accompanied by the increase of more than one order of maximum density power transmitted through the atmosphere both in collimated and in focused beams. The increase of transmitting aperture dimensions results in the growth of optimal power of laser transmitter as well. As the analysis has shown, the ring-shaped beams are the most efficient for vertical optical paths at propagation of high-power laser radiation.

The next stage for complication of an algorithm of phase control at emitting aperture is a priori correction of thermal distortions based on the introduction of phase predistortion. The eight-fold increase of maximum power density was observed experimentally. Optimal power of the transmitter increases greatly as well.

PHASE CORRECTION OF JOINT ACTION OF ATMOSPHERIC TURBULENCE AND THERMAL SELF-ACTION

The paper considers the possibility of phase-conjugate

system of adaptive correction based on the physical principle of reciprocity. The efficiency of "slow" and "quick" adaptive systems is investigated. The experiment has shown that "quick" adaptive systems do not only correct the structure of a focused beam but also increase the optimal mean power of the source.

AMPLITUDE-PHASE ADAPTIVE CONTROL

The possibilities of numerical simulation enable one to analyze the efficiency of a two-mirror adaptive system. Under definite conditions such a system provides the amplitude--phase control.

CONCLUSION

The conclusions presented in the paper are the result of mathematical modeling. Using these data one can determine the limiting possibilities of adaptive optical systems. The analysis carried out is needed at the stage of design of adaptive systems when it is necessary to define the efficiency of application of correction algorithms, to assess the limiting characteristics of the optical system and basic parameters of adaptive system.

The next stage of modeling requires the creation of realistic model of wave front detector, adaptive phase corrector (mirror) and also the entire set of noises occurring in optoelectronic system as a whole.

ADAPTIVE OPTICS AND ITS APPLICATION
IN ASTRONOMY

FRITZ MERKLE

European Southern Observatory

Karl-Schwarzschild-Str.2, 8046 Garching bei München

Federal Republic of Germany

Telephone: +-49-89-32006.341

(**INVITED**)

Introduction

The image quality degradation due to atmosheric turbulence is one of the main limitations for imaging. laser propagation, and communication through the atmosphere. In particular astronomical imaging suffers under this problem. Adaptive optics is a technology to overcome this by real-time phase compensation [1.2.3]. It is based on a measurement of the induced optical disturbances and their compensation by introducing corrections to the optical path which just cancel out the aberrations.

A perfect imaging system has a theoretical angular resolution of $\Delta\alpha = 1.22\frac{\lambda}{D}$ (λ: wavelength. D: aperture of the optical system), where $\Delta\alpha$ is the radius of the first dark ring of the diffraction pattern. However. in practice the image quality is degraded by constant and random spatially and temporally varying wavefront perturbations, originating directly from the aberrations of the optical system. and - to a much more serious extent - from the atmospheric turbulences and in the air path in front and inside the optical system.

All wavefront perturbations of an optical system together result in the complex phase aberration $\phi(\mathbf{r}.t) - iA(\mathbf{r}.t)$. The real part $\phi(\mathbf{r},t)$ represents the phase distortion of the wavefront. usually called "seeing". while the imaginary part $A(\mathbf{r},t)$ is a measure for the intensity fluctuations across the aperture plane. called "scintillation".

It is possible to correct these distortions with adaptive optics by measuring the aberrated wavefronts and applying this information to a phase shifting optical element in such a way that it just compensates all aberrations including the rapidly varying atmospheric phase distortions (see Figure 1). This adaptive optics system will then perform the correction $-\phi(\mathbf{r}.t) + \mu iA(\mathbf{r}.t)$ (where the factor μ takes care of the physical units). A correction of the scintillation would require a spatially and temporally controlable optical apodization element.

The Design Parameters for an Adaptive Optical System

As shown in Figure 1 an adaptive optical system contains three major components: a phase-shifting optical element. a wavefront sensor. and a servo-control system. The distortion of the

received wavefront is usually compensated by reflecting the light beam on a deformable mirror. The surface of this mirror is adjusted in real-time to compensate the path lengths aberrations. The information required to deform the mirror is obtained by analyzing the light with a wavefront sensor. A map of wavefront errors is then derived at each instant of time. Using this error map, the control system determines the signals required to drive the phase shifting optical element and to null the phase aberrations by closing the adaptive loop. The phase correction values can be obtained by expanding the phase-correction function $\phi(\mathbf{r}, t) = \sum_{n=1}^{N} a_n(t) f_n(\mathbf{r})$ in a spatially $(f_n(\mathbf{r}))$ and temporally $(a_n(t))$ dependent functions.
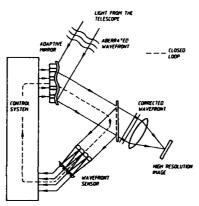
<u>Figure 1</u>: Generic view of an adaptive optics system as it can be applied to diffraction limited imaging in astronomy.

The complexity and design of an adaptive system depends on the atmospheric conditions [4,5] during its intended use, the aperture size of the optical system, and the direction of the optical path through the atmosphere. The atmospheric conditions are usually characterized by the Fried parameter r_0 and the correlation time τ_0. Typical values for night time seeing at astronomical observatory sites are given in the Table.

Table

λ	$0.5\mu m$	$2.2\mu m$	$5.0\mu m$	$10\mu m$
r_0	$10cm$	$60cm$	$160cm$	$360cm$
N	6400	180	12	4
τ_0	$6ms$	$35ms$	$95ms$	$220ms$
Θ	1.8"	10"	30"	70"

The sampling of the distorted wavefront or number of subapertures (N) (see Table), the correction rate ($\approx 1/\tau_0$), and the wavefront error amplitude range (Δz) are then the basic design parameters for an adaptive system. The number of subapertures can be approximated by $N \approx \left(\frac{D}{r_0}\right)^2$ and the coherence time by $\tau_0 \approx \frac{r_0}{v}$ where D is the aperture diameter and v the mean windspeed in the turbulent air layers. Typical values of these parameters for different wavelengths (assuming one of the future large astronomical telescope of the 8 meter class, of which several are currently

under design or construction) are also given in the Table with respect to an average seeing quality described by a correlation length r_0 of 10cm at 0.5μm wavelength.
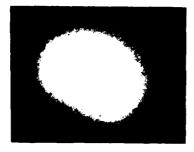
A perfect adaptive optical system will perform diffraction limited imaging only on the optical axis. Off-axis parts in the image have different viewing angles through the atmosphere. A limited angular range wherein the light suffers from quasi the same atmospheric disturbance is called isoplanatic angle Θ (see Table). An object within this angle could be used to measure the wavefront while the image of an on-axis object will be corrected. This angle is only a few arcseconds in the visible spectrum but grows to the range of arcminutes in the medium and far infrared. This parameter together with r_0 and τ_0 completely determines the optical propagation effects of the turbulent layers projected on the ground.

There are two ways to develop the phase-correction function, either by a modal or zonal (nodal) set of polynomials. In most cases the shape of an optical wavefront is represented by a set of orthogonal whole-aperture modal functions, like the Zernike polynomials, which correspond to the optical aberrations such as tilt, defocus, astigmatism, coma, etc. or vibration modes of the correcting element.

First Results from an Adaptive Optics System

In order to demonstrate the significant improvements which can be achieved with adaptive optics, results from a small scale system developed for the use at an astronomical telescope are presented. This adaptive optics prototype system [6,7] is based on a thin deformable mirror with 19 piezoelectric actuators and a Shack-Hartmann wavefront sensor with 5×5 subapertures.

Figure 2 displays the resulting image for real-time correction of a binary star observed with the European southern Observatory 3.6-Meter Telescope with this adaptive optics system at 3.8μm wavelength [8,9]. The corrected image shows clearly the diffraction limited nature with a diffraction pattern of 0.22 arcseconds FWHM.
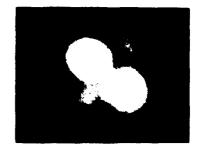
Figure 5: Image of the binary star HR6658 uncorrected (left) and corrected (right) in real-time by adaptive optics (r_0 = 13cm in the visible; 3.8μm wavelength). The separation of the two components is 0.38 arcseconds on the sky [8].

Limitations of Adaptive Optics

Any correction requires a measurement of the effect to be corrected. This is one of the major problems applying adaptive optics to astronomical imaging. Often the brightness of the object to be observed is not high enough for a wavefront sensing. A brighter nearby reference source within the same isoplanatic patch is rarely available. Only for infrared wavelengths the situation becomes more favorable because of the increase of the isoplanatic angle with the wavelength. The infrared/visible correlation of the atmospheric modulation transfer functions opens the possibility to measure for example the wavefront in the visible range and to get it compensated for infrared wavelengths (polychromatic adaptive correction). Recently, a new technique to overcome the reference source problem even in the visible range has been proposed by using an artificial laser guide star [10] generated by scattering laser light in high altitude atmospheric layers and first tests indicate its feasibility.

Outlook

Astronomical imaging is one possible application, in which adaptive optics proves its potentials. The technology seems to be much more adavanced for laser based defense systems. For other non-defense related areas, applications of adaptive optics are under development, like e.g. in ophthalmology or laser machining. More applications may come in the future, in which adaptive optics will bring the performance of the optical systems to their diffraction limits despite the disturbances of the atmosphere.

References

[1] Hardy J. W.. Proc. IEEE. **66**. 651 (1978).
[2] Pearson J. E.. Freeman R. H.. Reynolds H. C., in *Applied Optics and Optical Engineering*. **VII**. (Academic Press) (1979).
[3] Merkle. F.. "Adaptive Optics", in *International Trends in Optics*, Ed. J. Goodman, Academic Press Boston (1991).
[4] Roddier. F.. *"The Effect of Atmospheric Turbulence in Optical Astronomy"*, in Progress in Optics. E. Wolf Ed.. North Holland (1981).
[5] Tatarskii. V. I.. *Wave Propagation in a Turbulent Medium*, McGraw-Hill, New York (1961).
[6] Rousset G.. Fontanella J. C.. Kern P., Gigan P., Rigaut F., Léna P.. Boyer C.. Jagourel P., Gaffard J. P.. Merkle. F.. Astronomy and Astrophysics. **230**, L-29 (1989).
[7] Merkle. F.. Rousset. G.. Kern, P.. Gaffard, J.P., Proc. SPIE 1236, 193 (1990).
[8] Merkle. F.. Gehring G.. Rigaut F., Kern P.. Gigan P., Rousset G., Boyer C., The Messenger, **60**. 9 (1990).
[9] Rigaut F.. Rousset G.. Kern P., Fontanella J. C., Gaffard J. P., Merkle F., Léna P.. Astronomy and Astrophysics. submitted (1991).
[10] Welsh B. M.. J. Opt. Soc. Am. A, **8**, 69 (1991).

Wavefront curvature measurements:
application to atmospheric remote sensing and adaptive optics.

F. Roddier

Institute for Astronomy, University of Hawaii, 2680 Woodlawn Dr., Honolulu, HI 96822.
Phone: (808) 948 6157. Telex: 723 8459. Telefax: (808) 988 2790

(**INVITED**)

ABSTRACT

Adaptive optics systems currently use wave-front local slope measurements to sense and compensate atmospheric wave-front distortions. It is shown that the wave-front local curvature (Laplacian) can be advantageously used for the same purpose. The technique also applies to seeing measurements and remote sensing of atmospheric turbulence.

1. Introduction

Astronomical applications of adaptive optics require high performance wave-front sensors able to operate with broad-band light on faint, possibly extended, sources. Shack-Hartmann sensors are generally considered as providing the best performance. They measure local wave-front slopes. However image quality is only affected by differences in local slopes, that is by wave-front curvatures. A few years ago we proposed a new wave-front sensing technique based on local wave-front curvature measurements. It has the advantage of simplicity and high throughput, and avoids calibration difficulties [1]. Over a limited number of resolution elements it has the same sensitivity as a Hartmann sensor both on point and extended sources [2]. The technique which has already been adopted by several groups [3,4] consists of recording the illumination in two out-of-focus beam cross-sections symmetrically on each side of a focal plane. We first briefly review the theory and show that, at the geometrical approximation, the difference between the illuminations in the images provides a measure of the local wave-front total curvature (Laplacian) and of the wave-front radial slope at the edge of the telescope pupil. The wave front can be reconstructed by solving a Poisson equation with the edge slope as a Neumann boundary condition. A practical device is described to produce symmetrically defocused images on a detector without actually moving the detector. Next we review possible applications to atmospheric turbulence analysis as well as adaptive optics and describe results already obtained.

2. Theory

In the object space, the defocused images are conjugate to beam cross-sections taken symmetrically on each side of the telescope pupil. The problem is therefore to reconstruct the wave-front phase in the pupil plane knowing the illuminations I_1 and I_2 in two planes on each side of the pupil. A solution to this problem is given by the irradiance transport equation which describes the transport of irradiance along a propagating beam, at the paraxial approximation [5]. For a beam propagating along the z direction, this equation can be written

$$\frac{\partial I}{\partial z} = -\nabla I \cdot \nabla W - I \nabla^2 W \tag{1}$$

where $\nabla = \partial/\partial x, \partial/\partial y$ is the gradient operator in a plane (x,y) perpendicular to the direction of propagation, $I(x,y,z)$ is the irradiance distribution along the beam, and $W(x,y,z)$ is the wave-front surface as a function of the distance z on the propagation axis.

Let us apply Eq. (1) to the pupil plane. Assuming that the illumination is fairly uniform and equal to I_0 all over the pupil and zero outside, then $\nabla I = 0$ everywhere but at the pupil edge where

$$\nabla I = -I_0 \vec{n} \delta_c \tag{2}$$

Here δ_c is a linear Dirac distribution around the pupil edge and $\vec{n}$ is a unit vector perpendicular to the

edge and pointing outward. Putting (2) into the transport equation (1) yields

$$\frac{\partial I}{\partial z} = I_0 \frac{\partial W}{\partial n} \delta_c - I_0 P \ \nabla^2 W \tag{3}$$

where $P(x,y)$ is the pupil transmission function equal to one inside the pupil and equal to zero outside. $\partial W / \partial n = \vec{n} \cdot \nabla W$ is the wave-front derivative in the outward direction perpendicular to the pupil edge. If the illuminations I_1 and I_2 are recorded close enough to the pupil plane that is, in the image space, far enough from the telescope focal plane, the following approximation can be made also called the near-field or geometrical optics approximation:

$$I_1 = I_0 + \frac{1}{2} \frac{\partial I}{\partial z} \Delta z \qquad \text{and} \qquad I_2 = I_0 - \frac{1}{2} \frac{\partial I}{\partial z} \Delta z \tag{4}$$

where Δz is the distance between the two observed planes in the object space. One computes the following quantity called the sensor signal:

$$S = \frac{I_1 - I_2}{I_1 + I_2} = \frac{1}{2I_0} \frac{\partial I}{\partial z} \Delta z \tag{5}$$

Putting Eq. (3) into Eq. (5) gives

$$S = \frac{1}{2} \left[\frac{\partial W}{\partial n} \delta_c - P \ \nabla^2 W \right] \Delta z \tag{6}$$

Eq. (6) shows that the sensor signal is the sum of two signals, an edge signal $(\partial W / \partial n) \delta_c$ which in practice extends over a narrow band along the edges of the illuminated area, and an inner signal $P \ \nabla^2 W$ which covers the illuminated area. As long as the edge signal covers only a narrow area, the two signals can be distinguished providing both an estimate of the wave-front Laplacian $\nabla^2 W$ and an estimate of the wave-front slope $\partial W / \partial n$. It is therefore possible to reconstruct the wave-front surface W by solving a Poisson equation with Neumann-type boundary conditions. The solution with zero mean value is sought.

The method is well suited to test large optics because air turbulence or vibration effects are averaged out on long exposures. It has already been successfully used to test telescope optics using long exposure defocused stellar images [6]. Here we describe applications to atmospheric turbulence analysis and adaptive optics.

3. Implementation

Prism configurations have been proposed to record simultaneously defocused images on a detector [3,4,7]. However the defocus distance is set by the prism once for all and cannot be modified. Since the optimum defocus distance depends not only on the beam f/ratio but also on the magnitude of the aberrations (e.g. seeing conditions) and sets the sensitivity of the sensor and its linear operating range, it is quite important to be able to change the amount of defocus. At the University of Hawaii, we have developed a curvature sensor with a deformable membrane [8]. Light from the telescope is focused on an aluminized membrane stretched over a cavity. A converging lens or mirror collects the light reflected by the membrane and reimages the telescope entrance pupil on the detector. When changing the air pressure inside the cavity, the membrane becomes concave or convex and thus defocus the pupil image in either direction by an adjustable amount. Because the membrane is in a focal plane, the size of the pupil image is independent of the amount of defocus. At the resonance of the cavity, one can switch from one defocus position to the opposite a several KHz rate, producing a modulated light beam. The amplitude of the modulation is the difference between the two illuminations as given by Eq. 5. A lock-in amplifier can be used to detect and amplify the modulation producing feedback signals that can be directly used to actively control the wave front.

4. Application to atmospheric turbulence analysis

Image degradation by atmospheric turbulence is determined by the integral of the structure coefficient $C_N^2(z)$ over the propagation path z. It is generally expressed in terms of Fried's parameter

66

$$r_0 = \left[0.423 \, k^2 \int C_N^2(z) \, dz\right]^{-3/5} \tag{7}$$

where $k = 2\pi/\lambda$ is the wave number. Seeing monitors have been developed to measure r_0. The most successful ones are differential image motion monitors (DIMM) [9-11]. A DIMM is basically a Hartmann sensor reduced to two apertures. It measures the wave-front slope difference over the two apertures, which is directly related to the wave-front curvature in the direction of the two apertures. One can therefore advantageously replace a DIMM with a wave-front curvature sensor. Such a sensor will measure the total wave-front curvature or defocus aberration term induced by atmospheric turbulence over the seeing monitor aperture. The rms turbulence induced focus fluctuation is related to r_0 by

$$\sigma_f = 0.678 \lambda \, (f/D)^2 (D/r_0)^{5/6} \tag{8}$$

where D is the aperture diameter and f the focal length.

Such a seeing monitor has been built and successfully operated on Mauna Kea [12]. A single detector was used and a defocus signal was obtained by comparing the illumination on each side of the focal plane. This was done by switching very rapidly from one side of the focus to the other in a manner similar to that described in section 3. The illumination was estimated by measuring the total flux going through an aperture stop slightly smaller than the beam width. Compared to a DIMM, the monitor has two main advantages. First, most of the light from the telescope is used rather than being thrown away by a mask with two holes. Second, it has a much faster response due to the use of a single detector (rather than a CCD) which permits to better estimate the wave-front evolution time.

A very important advantage of measuring wave-front curvatures is that curvatures have a flat power spectrum. Assuming inertial turbulence, the spatial power spectrum of the wave-front phase error follows Kolmogorov's law and decreases as the -11/3 power of the spatial frequency f. Since in the Fourier domain derivation is equivalent to a multiplication by f, the Fourier transform of the wave-front Laplacian (sum of second order derivatives) is multiplied by f^2 and its power spectrum by f^4. It is therefore almost frequency independent. A consequence is that the spatial autocorrelation of the wave-front Laplacian is very narrow. Since the process is Gaussian, it means that local wave-front curvatures are almost statistically independent and are therefore the appropriate quantities to measure. Because the autocorrelation is narrow, one should easily detect wave-front motions induced by wind in the atmosphere, by correlating a map of the wave-front Laplacian at time t with the same map at time $t + \Delta t$. One could also correlate maps of the wave-front Laplacians produced by close binary stars revealing the distribution of turbulence with altitude. Such techniques have been developed to analyze shadow patterns produced by stellar scintillation [13,14] which is indeed produced by the wave-front local curvatures at higher altitude and has the same power spectrum. The sensitivity of this now called "SCIDAR" technique increases as the 5/6 power of the altitude which makes it insensitive to ground turbulence. The same technique applied directly to the wave-front curvature would produce similar results with an altitude-independent sensitivity. The determination of the speed and the altitude of turbulence layers is a first step towards dynamic [15] and multi-conjugate [16] wave-front compensation.

5. Application to adaptive optics

The University of Hawaii is currently building a wave-front curvature sensor for adaptive optics applications [8]. It consists of a vibrating membrane mirror as described in section 3, and 13 detectors with parallel read-out. The 7 inner detectors deliver signals associated with wave-front Laplacians whereas 6 detectors on the outer ring deliver signals associated with wave-front edge-slopes. Closed loop operation has already been demonstrated for wave-front tip/tilt compensation. High dynamic range is obtained by constantly matching the membrane stroke to the amplitude of the aberrations with an automatic gain control loop. Compared to a Hartmann sensor a similar resolution on the wave front can be obtained with a much smaller number of detector elements and no other pre-processing than simple lock-in detection. As a result a higher control speed can be obtained with a lower noise level.

Another interesting application of wave-front curvature sensing related to adaptive optics is the determination of the optimum control matrix. The control matrix is usually determined by inverting the mirror-sensor interaction matrix [17]. However this method does not take into account the statistics of the atmosphere. Wallner [18] has given an analytic expression for an optimum control matrix which

takes it into account but, for the method to be practically useful, it requires the determination of the average wave forms $<s_n \phi(x)>$ where s_n is the signal delivered by the nth sensor and $\phi(x)$ is the random atmospheric wave front. A simple way to determine this wave form is to build one-bit correlator that opens a shutter every time s_n is positive and records out-of-focus images. The statistical average is made by taking an exposure long enough to integrate atmospheric fluctuations. The wave form is reconstructed from the out-of-focus images by solving the Poisson equation.

6. Conclusion

Sensing wave-front local curvatures instead of local slopes offers many advantages especially when dealing with random atmospherically distorted wave fronts. It opens the way to new applications, most of them remain to be explored.

References

1. F. Roddier, "Curvature sensing and compensation: a new concept in adaptive optics," Appl. Opt. 27, 1223-1225 (1988).

2. F. Roddier, C. Roddier, N. Roddier, "Curvature sensing: a new wave-front sensing method," SPIE 976, 203-209 (1988).

3. F.F. Forbes, N. Roddier, "Curvature sensing adaptive optics system," SPIE 1542, paper 12 (1991).

4. M. Clampin, S.T. Durrance, D.A. Golimovski, "John Hopkins adaptive optics coronograph," SPIE 1542, paper 15 (1991).

5. F. Roddier, "Wavefront sensing and the irradiance transport equation," Appl. Opt. 29, 1402-1403 (1990).

6. C. Roddier et al., "Testing telescope optics: a new approach," SPIE 1236, 756-766 (1990).

7. L. Mertz, "Prism configurations for wave-front sensing," Appl. Opt. (in press).

8. F. Roddier, M. Northcott, J.E. Graves, "A simple low-order adaptive optics system for near-infrared applications," Pub. Astr. Soc. Pac. 103, 131-149 (1991).

9. F.F. Forbes, D.A. Morse, G.A. Poczulp, "Site survey instrumentation for the National New Technology Telescope (NNTT)," Opt. Eng. 27, 845-853 (1988)

10. F.D. Eaton et al., "Phase structure function measurements with multiple apertures," SPIE 1115 218-223 (1989).

11. M. Sarazin, F. Roddier, "The ESO Differential Image Motion Monitor," Astron. Astrophys. 227, 294-300 (1990).

12. F. Roddier, J.E. Graves, E. Limburg, "Seeing monitor based on wave-front curvature sensing," SPIE 1236 474-479 (1990).

13. A. Rocca, F. Roddier, and J. Vernin, "Detection of Atmospheric Turbulent Layers by Spatio-temporal and Spatio-angular Correlation Measurements of Stellar-light Scintillation," J. Opt. Soc. Am. 64, 1000-1004 (1974).

14. J.L. Caccia, M. Azouit, and J. Vernin, "Wind and C_N^2 profiling by single-star scintillation analysis," Appl. Opt. 26, 1288-1294 (1987).

15. R.J. Noll, "Dynamic Atmospheric Turbulence Corrections," SPIE 75, 39-42 (1976).

16. J.M. Beckers, "Increasing the size of the isoplanatic patch with multiconjugate adaptive optics," in Very Large Telescopes and their Instrumentation, M.H. Ulrich ed., ESO Proc. 30, 693-703 (1988).

17. J. Hermann, "Least-squares wave-front errors of minimum norm," J. Opt. Soc. Am. 70, 28-35 (1980).

18. E.P. Wallner, "Optimal wave-front correction using slope measurements," J. Opt. Soc. Am. 73, 1771-1776 (1983).

An Adaptive Optics System
for the Multiple Mirror Telescope

P. Wizinowich, J.R.P. Angel, B.A. McLeod, M. Lloyd-Hart, D.W. McCarthy
Steward Observatory
and
I.C. Scott-Fleming
Multiple Mirror Telescope Observatory

University of Arizona, Tucson, AZ 85721, U.S.A.
(602) 621-8353

Diffraction-limited imaging with ground-based telescopes can in principle be achieved through the methods of adaptive optics, in which the instantaneous wavefront shape is sensed and corrected in real-time by deformable optics which cancel the distortion. Array telescopes with adaptive optics offer the largest potential gain in resolution. However, traditional wavefront sensing techniques[1,2] either do not work, because of discontinuity across the wavefront, or require very complex implementations.

The imaging properties of an array of telescopes, in which the light is brought to a combined focus, are the same as for a single large telescope masked with apertures in the positions of the array elements. At infrared wavelengths the biggest seeing errors are the variations in pathlength and wavefront tilt between array elements. We have shown that these errors can be derived by an artificial neural network, given only a pair of simultaneous in-focus and out-of-focus images of a reference star formed at the combined focus of all the array elements.[3,4]

The degree to which the diffraction-limited image profile of an array can be restored by the piston and tilt correction of individual elements can be calculated from atmospheric turbulence theory. Fried[5] showed that removal of the best fit plane to a circular segment of Kolmogorov distorted wavefront resulted in a residual mean square phase error of

$$\Delta = 0.130 \left(\frac{D}{r_0} \right)^{\frac{5}{3}} , \tag{1}$$

where D is the segment diameter and r_0, a function of wavelength and seeing quality, is Fried's turbulence distance scale. If each array element is corrected with the tip, tilt and piston motion of a beam combining mirror, this error is also appropriate for the entire array.

A measure of the quality of a near diffraction-limited image is its Strehl ratio, the ratio of the peak intensity to that of the diffraction-limited image. For small phase errors, $\Delta < 1$ radian^2, the Strehl ratio can be approximated by

$$SR \approx e^{-\Delta} . \tag{2}$$

Strehl ratios less than unity correspond to loss of contrast rather than resolution, so most of the advantage for astronomical imaging and spectroscopy is maintained for SR > 0.5, corresponding to $D/r_0 < 2.7$.

At visible wavelengths ($\lambda = 0.5\mu m$), r_0 is typically 15 cm at good sites, and the element size satisfying the above condition is rather small. The situation is more attractive in the infrared since r_0 scales as $\lambda^{6/5}$. This also implies slower correction rates since the time scale for fluctuations is $\tau \approx r_0/v$, where v is the wind speed of the turbulent layers causing the seeing. At 2.2 μm wavelength, $r_0 \approx 1$ m and $\tau \approx 50$ ms, and array elements of 2 m diameter can be used.

Currently the largest imaging array and the largest baseline optical telescope in operation is the Multiple Mirror Telescope (MMT) in Arizona. The MMT consists of six 1.83 m diameter mirrors arranged hexagonally on a radius of 2.52 m, providing an overall baseline of 6.86 m when operated as a co-phased array.[6] At 2.2 μm the diffraction-limited angular resolution is 0.06 arcsec. A side view of two of the MMT telescopes and the beam combining system is shown in fig 1.

Our adaptive optics program is proceeding along four avenues: computer simulations, laboratory training of a net, telescope tests, and system development. Computer simulations of the MMT have shown the neural network approach to be extremely powerful for adaptive correction of array telescopes. The net and computer training and *performance simulations are* discussed in a paper at this conference by Lloyd-Hart et al.[7] This paper is primarily concerned with the development of a near-infrared adaptive optics system and some initial telescope tests of a neural network wavefront sensor.

A schematic represen-tation of a MMT adaptive beam combiner system is presented in fig. 2. The tilt and piston of each telescope beam will be controlled via three piezo-electric (PZT) actuators, in a
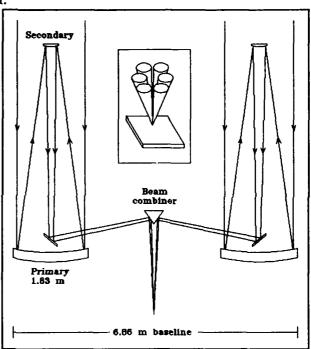
Figure 1 Two of the six MMT telescopes in cross section, showing the path of incoming starlight to the composite image plane. The expanded insert shows the six beams converging to a single image.

triangular pattern, on the back of each of the six beam combiner mirrors. The combined image of the reference star from all six telescopes is reimaged by a lens onto two infrared imaging detectors. The in- and out-of-focus image pair required by the net is produced by an optical device just before one of these detectors. These images are passed through a neural network on a transputer array, which has been trained to output a voltage for each of the 18 PZT actuators, to introduce the appropriate compensating tilts and pistons for the

six beams at the beam combiner. The voltages are converted from digital to analog (D/A) and amplified by a driver before being applied to the actuators. The second camera has a larger field and is used to integrate on the object of interest, within the isoplanatic patch around the reference star.

Initially the net will be trained on simulated data in the laboratory. Adaptive correction will then consist of passing pairs of images through the previously trained net. Measurements need to be completed in $\approx$ 20 ms, if the wavefront over 2 m elements is to remain effectively frozen until the correction is applied. We are currently using a 58×62 pixel InSb infrared array detector[8] designed for speckle interferometry as the detector for the neural net. Detector readout of two 20×20 images can be accomplished in 7 ms. The current six mirror net consists of 338 input nodes, 150 hidden nodes and 18 outputs. A single pass of two 13×13 images through this six mirror net represents some 150,000 floating point operations. Real-time processing can be accomplished in less than 10 ms by implementing the net on an array of 18 transputers. The transputers are parallel, rather than sequential, processors and can therefore take best advantage of the parallel structure of the net. The transputer array will also reduce our training and simulation times by a factor of 25 or more.
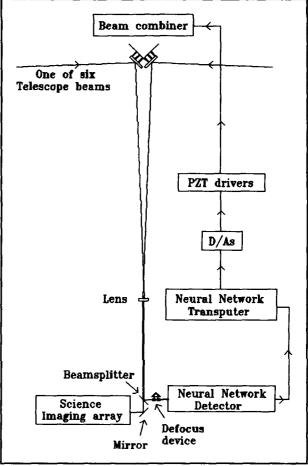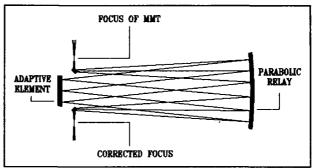
Figure 2 A schematic representation of an adaptive MMT beam combiner control system.

An alternative to making the existing MMT beam combiner adaptive is to make an adaptive instrument to mount at the Cassegrain focus of the MMT. This option is preferred since it makes the adaptive system self-contained and permits laboratory testing, independent of the telescope. Fig. 3 shows a possible optical path for such an instrument. A mirror just after the MMT focus folds the six beams to an off-axis portion of a parabola which collimates the beams. The pupil is reimaged onto the adaptive element consisting of six mirrors, each capable of tip, tilt and piston correction. A second reflection off the

parabola reconverges the beams at the same focal ratio. The beam can be folded either vertically or horizontally to feed the cameras. Image quality over a one arcminute field is better than the diffraction-limit and existing pupil stops within the IR cameras are unaffected.

Figure 3 Optical schematic for an adaptive MMT instrument.

Several tests are being made of the net's ability to deduce the correct tip, tilt and piston values from speckle images of bright stars recently recorded at the MMT. The first approach has been to try to reconstruct the real data in computer simulations by reimaging the net's derived wavefront. The simulated and recorded image pairs will match to the extent that the net derived wavefront corresponds to the actual wavefront.

The technique of speckle holography may also be applied, in which an independent estimate of the wavefront, the net output, is used to infer the spatial structure of the source.[9,10] In this case, since we know the source to be an unresolved star, the method is a test of the wavefront estimate.

In a more direct method at the telescope, a beamsplitter was used to send the visible light through optics which separated the six beams at a reimaged pupil location. The measured centroid motions of the separated visible images on a CCD video camera, corresponding to mean wavefront tilts across the individual apertures, are then expected to correlate with the net's tip and tilt outputs derived from infrared images taken simultaneously.

At the time of writing these observational tests are still being reduced, but they do indicate qualitative success. We hope to present these results and results of real-time MMT adaptive correction at this conference.

References
1. Hardy, J.W., SPIE Proc. 1114, 2-13 (1989).
2. Roddier, F., Appl. Opt. 27, 1223-1225 (1988).
3. Angel, J.R.P., Wizinowich, P., Lloyd-Hart M. & Sandler, D., Nature 348, 221-224 (1990).
4. Sandler, D., Barrett, T.K., Palmer, D.A., Fugate, R.Q. & Wild, W.J., submitted for publication (1990).
5. Fried, D.L., J. Opt. Soc. Am. 55, 1427-1435 (1965).
6. Hege, E.K., Beckers, J.M., Strittmatter, P.A. & McCarthy, D.W., Appl. Opt. 24, 2565-2576 (1985).
7. Lloyd-Hart, M., Wizinowich, P., Angel, J.R.P., this conference (1991).
8. McCarthy, D.W., McLeod, B.A. & Barlow, D., SPIE Proc. 1237, 496-507 (1990).
9. Hege, K., private communication (1990).
10. Primot, J., Rousset, G. & Fontanella, J.C., ESO Conf. on Very Large Telescopes and their Instrumentation, II, 683-692 (1988).

High-Resolution Astronomical Imaging through the Atmosphere

Gerd Weigelt

Max-Planck-Institut für Radioastronomie
Auf dem Hügel 69, D-5300 Bonn 1, Germany; Phone +49-228-525 243

(INVITED)

1. Introduction. The atmosphere of the earth restricts the angular resolution of large, ground-based telescopes to about 0.5 arcsec. Fortunately, it is possible to overcome atmospheric image degradation by various interferometric methods. The speckle interferometry method (Labeyrie 1970) can reconstruct the diffraction-limited autocorrelation. True images with diffraction-limited resolution (e.g., 0.02arcsec) can be reconstructed by the Knox-Thompson method (Knox and Thompson 1974), by the nonredundant mask technique (e.g., Baldwin et al. 1986; Readhead et al. 1988; Nakajima et al. 1989) and by the speckle masking method (Weigelt 1977; Weigelt and Wirnitzer 1983; Lohmann, Weigelt and Wirnitzer 1983). More references for image reconstruction methods can be found in the review articles on interferometric imaging by Dainty (1984), Roddier (1988), and Weigelt (1991). The nonredundant mask technique and speckle masking can measure the so-called 'closure phases' which are required for optical long-baseline interferometry. The great advantage of optical long-baseline interferometry with three or more telescopes is the fact that it can yield images and spectra with fantastic angular resolution. For example, with a baselines of 150m a resolution of 0.001arcsec can be obtained. Speckle spectroscopy methods have the advantage that they yield the spectrum of each resolution element of the object in addition to the high-resolution image. The raw data for the nonredundant mask technique are Michelson interferograms. Image reconstruction from the Michelson interferograms can be performed by various radio phase closure methods. The raw data for the Knox-Thompson and for the speckle masking method are speckle interferograms. The intensity distribution $i_n(x)$ of the n-th recorded speckle interferogram can be described by $i_n(x) = o(x) \otimes p_n(x)(n = 1, 2, 3, \ldots, N \sim 10^3 - 10^5)$,

where $o(x)$ is the object, $\otimes$ denotes convolution, $p_n(x)$ is the psf of the atmosphere/telescope, x is a 2-D space vector, and N is the total number of speckle interferograms. In the text below, the index n of the random functions i_n and p_n and of their Fourier transforms will be omitted.

2. Knox-Thompson Method (KTM). The first image processing step of the KTM is the calculation of the cross-spectrum

$$\langle I(u)I^*(u + \Delta u)\rangle = O(u)O^*(u + \Delta u)\langle P(u)P^*(u + \Delta u)\rangle,$$

where I, O, and P are the Fourier transforms of i, o, and p, respectively (from $i = o \otimes p$ follows $I = OP$). u is a 2-D coordinate vector, $*$ denotes complex conjugate, $\langle\ \rangle$ denotes ensemble average over all N speckle interferograms, and Δu is a small shift vector with $|\Delta u| \sim 0.2 r_o/\lambda$ (see Dainty 1984). r_o is the Fried parameter . If we divide by the KT transfer function (KTTF) $\langle P(u)P^*(u + \Delta u)\rangle$, we obtain $O(u)O^*(u + \Delta u) = \langle I(u)I^*(u + \Delta u)\rangle / \langle P(u)P^*(u + \Delta u)\rangle$. The KTTF can be derived from speckle interferograms of an unresolved star observed before or after the object. For the obtained KT spectrum $O(u)O^*(u + \Delta u)$ we can write

$$O(u)O^*(u + \Delta u) = |O(u)|\ exp[i\varphi(u)]\ |O(u + \Delta u)|\ exp[-i\varphi(u + \Delta u)],$$

where φ is the phase of $O(u)$. If we take only the phase terms, we see that we have measured

$$exp[i\varphi(u)]\ exp[-i\varphi(u+\Delta u)]\ =\ exp\{i[\varphi(u)-\varphi(u+\Delta u)]\}\ \text{or all}$$

phase differences $\Delta\varphi(u) = \varphi(u+\Delta u) - \varphi(u)$ between the coordinates $u+\Delta u$ and u. Therefore, we have a recursive equation for calculating the phase φ of $O(u)$: $\varphi(u+\Delta u) = \varphi(u) + \Delta\varphi(u)$. From the object Fourier phase measured by the Knox-Thompson method and the Fourier modulus measured by speckle interferometry a diffraction- limited image of the object can be reconstructed.

3. Speckle Masking Bispectrum Processing (SM). Speckle masking consists of the following image processing steps 1 to 3:

Image processing step 1: Calculation of the *ensemble average triple correlation*

$$\langle T(x,y)\rangle = \langle \int i(x')i(x'+x)i(x'+y)dx'\rangle, \text{ or calculation of the } \textit{ensemble average bispectrum}$$

$$\langle B(u,v)\rangle = \langle I(u)I(v)I^*(u+v)\rangle$$

of many interferograms $i(x)$. u and v are 2-D coordinate vectors. Since x, y, u, and v are 2-D vectors, the triple correlation $T(x,y)$ and the bispectrum $B(u,v)$ are *4-dimensional*.

Image processing step 2: Compensation of the speckle masking transfer function (SMTF). With $I = OP$ we get for the average bispectrum $\langle B(u,v)\rangle$:

$$\langle B(u,v)\rangle = O(u)O(v)O^*(u+v)\langle P(u)P(v)P^*(u+v)\rangle.$$

$\langle P(u)P(v)P^*(u+v)\rangle$ is called the SMTF. We can divided by the SMTF and obtain for the bispectrum $B_o(u,v)$ of the object $o(x)$,

$$B_o(u,v) \equiv O(u)O(v)O^*(u+v) = \langle I(u)I(v)I^*(u+v)\rangle / \langle P(u)P(v)P^*(u+v)\rangle.$$

Image processing step 3: Derivation of modulus and phase of $O(u)$ from $B_o(u,v)$. We denote the phase of the Fourier transform of the object by $\varphi(u)$ and the phase of the bispectrum of the object by $\beta(u,v)$, i.e., $O(u) = |O(u)|\ exp[i\varphi(u)]$, $B_o(u,v) = |B_o(u,v)|exp[i\beta(u,v)]$. Inserting yields

$$|B_o(u,v)|\ exp[i\beta(u,v)]\ =\ |O(u)|\ exp[i\varphi(u)]\ |O(v)|\ exp[i\varphi(v)]\ |O(u+v)|\ exp[-i\varphi(u+v)],$$

$$\Rightarrow exp[i\beta(u,v)] = exp[i\varphi(u)]\ exp[i\varphi(v)]\ exp[-i\varphi(u+v)] \quad \Rightarrow \varphi(u+v) = \varphi(u) + \varphi(v) - \beta(u,v).$$

This equation is a recursive equation for calculating the phase φ at coordinate $w \equiv u+v$ if φ is known at coordinates u and v. The above equation is called a "closure phase relation". Since SM can measure closure phases it can be applied to optical long-baseline interferometers. In this case the KT method cannot be applied. References for modifications or extensions of SM can be found in the review article (Weigelt 1991). Figs. 1 to 5 show SM observations of the double star Psi SGR (Fig. 1: one of 150 speckle interferograms; Fig.2: SM reconstruction; double star separation 0.18 arcsec; from Weigelt and Wirnitzer 1983), the variable object Eta Carinae (Fig. 3; reconstructed image; separation of the 3 close objects: 0.11 arcsec, 0.18 arcsec, and 0,21 arcsec; from Hofmann and Weigelt 1988), the central object in the HII region NGC 3603 (Fig. 4; reconstructed image; separation of the close double star at the bottom: 0.09 arcsec; from Baier et al. 1988), and of the Seyfert galaxy NGC 1068 (Fig. 5; reconstructed image; separation of the two off-axis objects: 0.5 arcsec; from Hofmann, Mauder and Weigelt 1990).

4. Speckle Spectroscopy. The two methods *objective prism speckle spectroscopy* (Weigelt 1981; Weigelt et al. 1986) and *projection speckle spectroscopy* (Grieger, Fleischmann and Weigelt 1988) can yield both high-resolution images and the spectrum of each resolution element. A first astronomical application was reported by Grieger and Weigelt (1990).

5. Optical Long-Baseline Interferometry and Aperture Synthesis. The great advantage of long-baseline interferometry is that it can yield images and spectra with fantastic angular resolution. Possible image reconstruction methods are the phase closure method (for the 'single-speckle' infrared case) (Jennison 1958; Rhodes and Goodman 1973; Baldwin et al. 1986; Readhead et al. 1988; Nakajima et al. 1989) and the speckle masking method (for the multi-speckle case; large telescopes at visible wavelengths). A complete computer simulation of optical long-baseline interferometry with the ESO VLT was reported by Reinheimer and Weigelt (1990).

Acknowledgements: We thank ESO for observing time. The results shown in Figs. 1 to 5 are based on data collected at the European Southern Observatory, La Silla, Chile.

Baier, G., K. Hofmann, W. Mauder, D. Schertl, H. Weghorn, G. Weigelt, 1988, Messenger 52, 11

Baldwin, J.E., C.A. Haniff, C.D. Mackay and P.J. Warner, 1986, Nature 320, 595

Dainty, J.C., 1984, Stellar Speckle Interferometry, in: Laser Speckle and Related Phenomena, Topics in Applied Physics, Vol. 9, ed. J.C. Dainty (Springer Verlag), ch. 7

Grieger, F., F. Fleischmann, G. Weigelt, 1988, Objective Prism Speckle Spectroscopy and Projection Speckle Spectroscopy, Proc. High-resolution Imaging by Interferometry (ESO), p. 225

Grieger, F., G. Weigelt, 1990, Projection Speckle Spectroscopy and Objective Prism Speckle Spectroscopy, in: Proc. 15th Congress of the ICO (SPIE Vol. 1319), p. 440

Hofmann, K.-H., and G. Weigelt, 1986, Astron. Astrophys. 167, L15

Hofmann, K.-H., and G. Weigelt, 1988, Astron. Astrophys. 203, L21

Hofmann, K.-H., W. Mauder and G. Weigelt, 1990, Photon-Counting Speckle Masking, in: Proc. 15th Congress of the ICO (SPIE Vol. 1319), p. 442

Knox, K.T., and B.J. Thompson, 1974, Astrophys. J. Lett. 193, L45

Labeyrie, A., 1970, Astron. Astrophys. 6, 85

Lohmann, A.W., G. Weigelt and B. Wirnitzer, 1983, Appl. Opt. 22, 4028

Nakajima, T., S.R. Kulkarni, P.W. Gorham, A.M. Ghez, G. Neugebauer, J.B. Oke, T.A. Prince and A.C.S. Readhead, 1989, Ap. J. 97, 1510

Readhead, A.C.S., T.S. Nakajima, T.J. Pearson, G. Neugebauer, J.B. Oke W. Sargent, 1988, Ap. J. 95, 1278

Reinheimer, T. and G. Weigelt, 1990, Optical Long-Baseline Interferometry in Astronomy, in: Proc. 15th Congress of the ICO (SPIE Vol. 1319), p. 678

Rhodes, W.T., and J.W. Goodman, 1973, J. Opt. Soc. Am. 63, 647

Roddier, F., 1988, Physics Reports 170, 97

Weigelt, G., 1977, Optics Commun. 21, 55
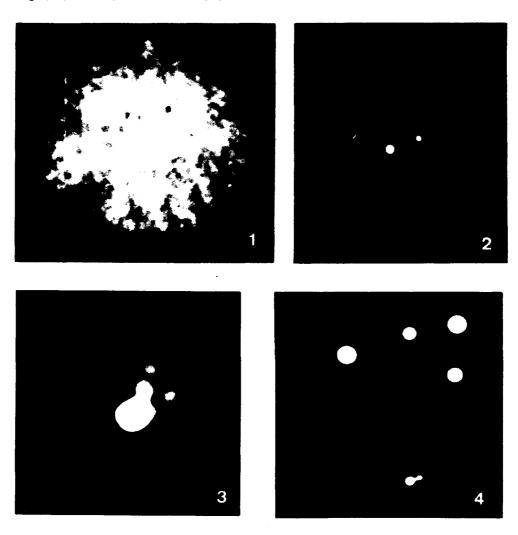
Weigelt, G., 1981, in: Conf. Proc. Scientific Importance of High-Angular Resolution at IR and Optical Wavelengths (ESO), p.95

Weigelt, G., G. Baier, J. Ebersberger, F. Fleischmann, K.-H. Hofmann, 1986, Opt. Eng. 25, 706

Weigelt, G., and B. Wirnitzer, 1983, Optics Lett. 8, 389

TEMPORAL ANALYSIS OF TURBULENT WAVEFRONTS SENSED BY ADAPTIVE OPTICS

G. Rousset and P.Y. Madec
Office National d'Etudes et de Recherches Aérospatiales
BP 72, 92322 Châtillon Cedex, France
Tel : 33.1.46.57.11.60

F. Rigaut
Observatoire de Meudon - 92195 Meudon Cedex, France
Tel : 33.1.45.07.75.44

In october 1989, first diffraction-limited infrared images were obtained by the so-called COME-ON adaptive optics prototype system on the 1.52 m telescope of the Observatoire de Haute Provence (France) [1]. For such a system, quantitative measurements of the turbulence parameters are of great importance to evaluate its performance. The two first parameters are the Fried diameter r_o and the atmospheric coherence time $\tau_o = r_o/\bar{V}$, where $\bar{V}$ is an average wind velocity [2]. Modal expansion and temporal spectrum of turbulence-induced wavefront fluctuations are more detailed information required when optimizing an adaptive optics system.

The measurements presented in this paper were made with the COME ON system in April 1990 on the ESO 3.6 m telescope at La Silla (Chili). The Hartmann-Shack wavefront sensor measures in real-time the turbulent distortions (sampling frequency 105 Hz) in a conjugated plane of the telescope pupil (for details see [3]). The integration time is 9.5 ms on the wavefront sensor camera. The sensor divides the telescope aperture in 20 subapertures and monitors the angle-of-arrival fluctuations in each subaperture. A wavefront computer processes the video signal and delivers the local wavefront slopes to the control computer [3]. These data are usually used to determine the error signal feeding the servo-loop. During this experiment, they are in addition stored in the control computer memory and saved after the end of acquisition on a floppy disk for later reduction.

Two cases were considered: without and with correction by both the 19 actuator deformable mirror and the tip-tilt mirror of the system. The recorded data are:
1) - the slopes of the turbulence-induced wavefront distortions without any correction,
2) - the slopes of the wavefront with the adaptive optics correction in order to monitor the residual error.

The data reduction lies in reconstructing the wavefront phase from its gradients and in calculating power spectral densities. The modal reconstruction method performs the calculation of the expansion of the phase in the set of the

Zernike polynomials [4]. The expansion of the phase φ over the Zernike polynomials (Z_i) takes the form:

$$\varphi(x,y) = \sum_{i=2}^{\infty} a_i \, Z_i(x,y)$$

where the a_i's are the expansion coefficients. Due to the finite number of subapertures, only the first 21 expansion coefficients are determined from the measurements.

Figure 1 shows: the measured Zernike coefficient variances from a set of 1000 successive records in the two cases above-mentioned, and the theoretical Kolmogorov variances derived by Noll [5] and computed for a ratio D/r_o of 33. D is the telescope diameter, therefore r_o is equal to 11 cm at the wavefront sensing wavelength: 0.5 μm. The ratio D/r_o is determined by the fit of the theoretical law to the measured variances, in the case without correction and for the polynomials 4 to 15. These polynomials correspond to the radial degrees 2, 3 and 4 [5].

The expansion of the uncorrected turbulent phase reveals a significant attenuation (40 %) of the variance of the two first Zernike polynomials. These polynomials are the two tilts and correspond to a radial degree equal to 1. This attenuation is due to the finite size of the outer scale L_o of the turbulence. On the other hand, the outer scale has a negligible effect on the higher order Zernike polynomials as it can be shown by the approach developed by Sasiela [6]. From the theoretical expression of the tilt variance attenuation [6], we deduce an outer scale of 50 m.
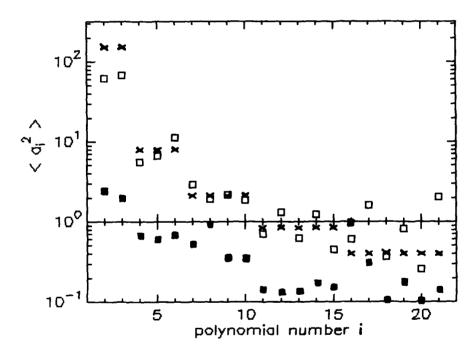
The comparison of the variances measured with and without correction reveals the reduction of the phase fluctuations obtained with adaptive optics. The reduction is about one order of magnitude. Even if the correction of the tilts is significant, the tilt residual fluctuation is still higher than anyone of the other polynomials. The residual error is due to the finite temporal bandwidth of the closed-loop control. In order to analyse this error for each polynomial, the power spectral density of each expansion coefficient has to be calculated.

The figure 2 presents the power spectral density of the 4th Zernike polynomial which is the defocus mode: 2a) of the turbulent wavefront and 2b) of the residual error after correction. The spectrum of figure 2a) has a cut-off frequency around 7 Hz and presents a sharp decrease for higher frequencies as a law close to $f^{-11/3}$. The spectrum of figure 2b) shows the filtering brought by the adaptive optics servo-loop. The correction is much more significant at low frequencies ($f \leq 1$ Hz) than at middle frequencies ($1 \leq f \leq 10$ Hz). After 10 Hz the correction is no more efficient, and the spectrum recovers the behavior of the spectrum of the figure 2a. The bandwidth, of the transfer function in open-loop at 0 dB point of the COME-ON system, is 10 Hz [3].
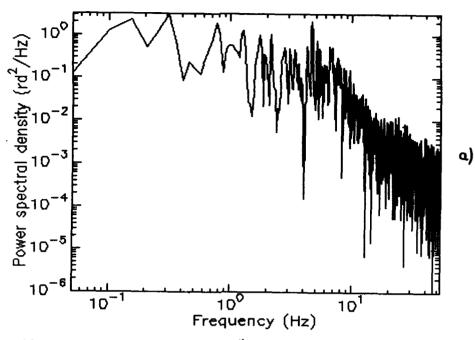
Detailed analyses will be given for different turbulence conditions and compared to the obtained image qualities. From the temporal correlation of the Zernike expansion coefficients, a coherence time will be evaluated in order to characterize the evolution time of the image.

REFERENCES
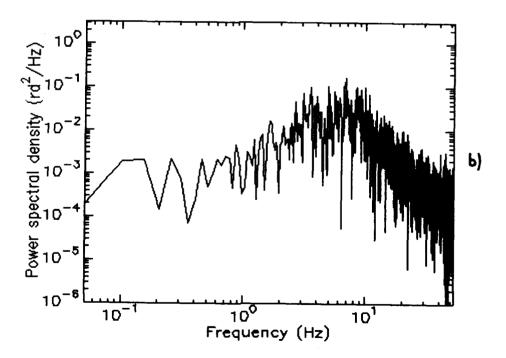
[1] - Rousset, G. et al: 1990, Astron. Astrophys. 230, L29.

[2] - Roddier, F.: 1981, in "Progress in Optics", (Wolf E. ed.) North Holland, Vol. 19, 281.

[3] - Rousset, G. et al: 1990, SPIE Proc., 1237, 336.

[4] - Primot, J. et al: 1990, J. Opt. Soc. Am. A, Vol. 7, 1598.

[5] - Noll, R.J.: 1976, J. Opt. Soc. Am, Vol. 66, 207.

[6] - Sasiela, R.J.: 1988, Technical Report 807, MIT Lincoln Laboratory (Lexington USA).

Figure 1: Variances of the Zernike polynomial expansion coefficients. The crosses: the theoretical Zernike representation of the Kolmogoroff spectrum for $D/r_0 = 33$. The squares are the experimental Zernike coefficients: white squares, for the expansion of the turbulent wavefront without correction, black squares, for the expansion of the residual error after correction by adaptive optics.

Figure 2: Power spectral densities of the 4th Zernike polynomial coefficient:
a) from the expansion of the turbulent wavefront without correction,
b) from the expansion of the residual error after correction by adaptive optics.

Considerations Effecting the Signal-to-Noise Ratio in
White-Light Speckle Astronomical Observations:
Dependence on Diameter, Spectral Bandwidth, and Use of Adaptive Optics

David L. Fried
and
David L. Hench

the Optical Sciences Company
Placentia, California 92670, USA

White-light speckle techniques in astronomical imaging offer the possibility of achieving nearly diffraction limited resolution despite the effects of atmospheric turbulence. A critical concern in making white-light speckle techniques work well is the signal-to-noise power ratio, $SNR(\kappa)$, that can be achieved for each spatial frequency, κ, of interest. In studying the dependence of the signal-to-noise ratio on the aperture diameter, D, we find that $SNR(\kappa)$ is a strictly monotonic increasing function of D. {It should be noted that this behavior is distinctly different from the behavior of the white-light speckle (or Labeyrie-Korff) transfer function, $\langle|\tau(\kappa)|^2\rangle$, evaluated by Korff [JOSA 63 971 (1973)] which is maximized when the diameter is a bit larger than $|\kappa|\lambda$.} In studying the dependence of the signal-to-noise ratio on the spectral bandwidth, $\Delta\lambda$, we find that $SNR(\kappa)$, is a *strictly monotonic increasing* function of $\Delta\lambda$, though for large enough values of $\Delta\lambda$ the continued increase is very slight and approaches an asymptotic value. For very small values of $\Delta\lambda$ we find that the signal-to-noise power ratio, $SNR(\kappa)$, is directly proportional to $\Delta\lambda$. [It should be noted that this behavior is distinctly different from that of the polychromatic version of the Labeyrie-Korff transfer function, $\langle|\tau(\kappa)|^2\rangle$, which is a strictly monotonic *decreasing* function of $\Delta\lambda$ — though decreasing only very slightly when $\Delta\lambda$ is sufficiently small.] We have defined an effective spectral bandwidth, $\Delta\lambda_{\text{eff}}$, as being equal to the asymptotic limit for $SNR(\kappa)$ when $\Delta\lambda$ is very large, divided by the rate at which $SNR(\kappa)$ increases with increasing $\Delta\lambda$ when $\Delta\lambda$ is very small. We find that for a midband wavelength $\overline{\lambda}$ we can write

$$\Delta\lambda_{\text{eff}} \approx \Delta\lambda \left\{ 1 + \left[\left(|\kappa|\overline{\lambda}/r_0 \right) \left(\tfrac{1}{2}\Delta\lambda/\overline{\lambda} \right)^{5/6} \right]^2 \right\}^{-1/2} .$$

Following the work of Nisenson and Barakat {JOSA 4-A 2249 (1987)} we have investigated the utility of low performance adaptive optics (i.e. adaptive optics with several radians of rms residual wavefront error) in the collection of white-light speckle data. We have investigated the utility of such adaptive optics in terms of both the Labeyrie-Korff transfer function, $\langle|\tau(\kappa)|^2\rangle$, and the signal-to-noise power ratio, $SNR(\kappa)$ — the latter for various spectral bandwidths. Extensive numerical results will be presented as we have not been able to capture the results in one (or even a few) expression(s). Our results indicate that the larger the aperture diameter, D, and the wider the spectral bandwidth, $\Delta\lambda$, the larger the mean-square adaptive optics residual wavefront error, σ_{AO}^2, can be and still provide a significant improvement in the signal-to-noise power ratio, $SNR(\kappa)$. We find that with $D/r_0 = 200$, for a narrow spectral band we go from an interesting improvement in $SNR(\kappa)$ (a multiplicative factor of about 30) to an almost negligible improvement (about 5) when the residual wavefront error goes from $\sigma_{AO}^2 = 4\text{rad}^2$ to $\sigma_{AO}^2 = 5\text{rad}^2$. For $\sigma_{AO}^2 = 3\text{rad}^2$ there is an even more substantial improvement (about 200). For $D/r_0 = 50$ the improvements are about equal to 2, 3, and 10 for $\sigma_{AO}^2 = 5\text{rad}^2$, 4rad^2, 3rad^2. But for wider spectral bands the improvement resulting from the use of such adaptive optics are more substantial. We find that the effective spectral bandwidth, $\Delta\lambda_{\text{eff}}$, can be nearly equal to the actual spectral bandwidth, $\Delta\lambda$, for $\Delta\lambda/\overline{\lambda}$ as large as 40%, with $\sigma_{AO}^2 = 5$ rad^2 for $D/r_0 = 200$, and with $\sigma_{AO}^2 = 3$ rad^2 for $D/r_0 = 100$.

Probability Imaging of Extended Astronomical Sources at Low Light Levels

Claude AIME, Eric ARISTIDI, Henri LANTERI, Gilbert RICORT

Département d'Astrophysique - U.R.A. 709 du CNRS
Université de Nice-Sophia Antipolis
Parc Valrose - 06034 Nice Cédex - FRANCE. tel. (33) 93 52 98 91

1 - Introduction.

Probability imaging belongs to the ensemble of techniques that make use of a statistical analysis to obtain high angular information in astronomical speckle interferometry, in spite of atmospheric turbulence and very low signal to noise ratio for each short exposure frame[1]. In many techniques, averaging processes currently used consist of the computation of moments of the intensity pattern, or of its Fourier transform[2-4]. Probability imaging is based upon the study of an alternative quantity, the probability density function (pdf) .

In the first proposal of the technique, it was shown that a second order analysis was sufficient to image a double star or a star cluster[5,6]. For a speckle pattern of intensity I(x) the second pdf $P_2 (\Omega_1, \Omega_2; \rho)$ is the quantity that describes the probability that I(x) has a value lying in the elementary interval $(\Omega_1, \Omega_1 + d\Omega_1)$ and simultaneously that I(x-ρ) has a value lying in the elementary interval $(\Omega_2, \Omega_2 + d\Omega_2)$.

For a point source speckle pattern obeying the classical negative exponential law for intensity, the double star second pdf $P_2 (\Omega_1, \Omega_2; \rho)$, represented for ρ = d (star separation), was theoretically found to appear as a strongly assymetrical figure, with a clear division of the image in two regions separated by a radial line whose angular direction gives immediately the magnitude difference and the orientation of the binary. The technique was successfully applied to the imaging of the double star ξ Aqr from one dimensional infrared speckle data[7] ; all the parameters of the double star, i.e. star separation, relative amplitude and position of components were derived from the analysis of the second pdf.

A generalization of the technique to the image reconstruction of any general extended astronomical object was recently proposed[8]. It involved the computation of the second order Characteristic Function (CF) $\Phi_{2s} (\omega_1, \omega_2; \rho)$, i.e. Fourier transform of $P_{2s} (\Omega_1, \Omega_2; \rho)$:

$$\Phi_{2s}(\omega_1, \omega_2; \rho) = \iint P_{2s}(\Omega_1, \Omega_2; \rho) \cdot \exp i(\omega_1 \Omega_1 + \omega_2 \Omega_2) \, d\Omega_1 \, d\Omega_2 \qquad (1)$$

The relevant role of the CF will be further developed in this note, namely in section 2 devoted to noise problems for low light level measurements. Particular attention is given to the photon counting case. The theoretical model leading to an analytical expression for the CF is presented in section 3 and possible reconstruction processes are proposed in section 4.

2 - Noisy measurements.

A - In the infrared case, the noise can be well represented as an additive, signal-independent contribution. As a consequence the signal pdfs are blurred by the noise pdfs.

$$P_{2Mesured} = P_{2Signal} * P_{2Noise}$$

A deconvolution operation is thus necessary to obtain P_{2s}. If we use the second order CF instead of the second order pdf, we have immediately :

$$\Phi_{2Mesured} = \Phi_{2Signal} \cdot \Phi_{2Noise}$$

and Φ_{2s} is easily obtained without deconvolution procedure.

B - At photon counting levels, the statistics must take into account the Poisson nature of photoelectron events. For a second order analysis the quantity that can be measured is the probability $p_{2s}(n_1, n_2; \rho)$ of registering n_1 photoelectrons at a point r and simultaneously n_2 photoelectrons at a point $r + \rho$. This quantity is related to the second pdf $P_{2s}(\Omega_1, \Omega_2; \rho)$ by the Poisson transform[6].

$$p_{2s}(n_1, n_2; \rho) = \iint \frac{(\alpha\Omega_1)^{n_1}}{n_1!} \cdot e^{-\alpha\Omega_1} \frac{(\alpha\Omega_2)^{n_2}}{n_2!} \cdot e^{-\alpha\Omega_2} \; P_{2s}(\Omega_1, \Omega_2; \rho) \cdot d\Omega_1 \, d\Omega_2 \qquad (2)$$
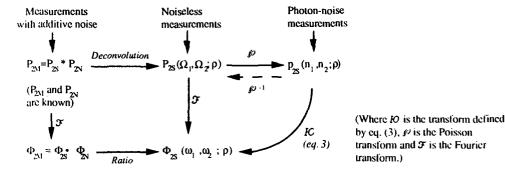
where α is the quantum efficiency of the detector, assumed constant for the whole detector in this analysis.

$P_{2s}(\Omega_1, \Omega_2; \rho)$ is obtained by inverting the previous relation ; this operation is not easy to implement. However, the second CF $\Phi_{2s}(\omega_1, \omega_2; \rho)$ is related to $p_{2s}(n_1, n_2; \rho)$ by the relation :

$$\Phi_{2s}(\omega_1, \omega_2; \rho) = \sum_{n_1=0}^{\infty} \sum_{n_2=0}^{\infty} \left(1 + \frac{i\omega_1}{\alpha}\right)^{n_1} \left(1 + \frac{i\omega_2}{\alpha}\right)^{n_2} p_{2s}(n_1, n_2; \rho) \qquad (3)$$

Therefore, an inverse Poisson transform becomes unnecessary. Note that eq. (3) resembles eq. (7.12) of ref. 9. It can be easily derived by writing $\Phi_{2s}(\omega_1, \omega_2; \rho)$ in the form :

$$\Phi_{2s}(\omega_1, \omega_2; \rho) = \iint \exp\left[\alpha\Omega_1\left(1 + \frac{i\omega_1}{\alpha}\right)\right] \exp\left[\alpha\Omega_2\left(1 + \frac{i\omega_2}{\alpha}\right)\right] \exp\left[-\alpha(\Omega_1 + \Omega_2)\right] P_{2s}(\Omega_1, \Omega_2; \rho) \, d\Omega_1 d\Omega_2 \quad (4)$$

and taking the Taylor expansion of the first two exponentials. The following scheme gives a summary of the previous developements.

Measurements with additive noise | Noiseless measurements | Photon-noise measurements

$P_{2M} = P_{2S} * P_{2N}$ $\xrightarrow{Deconvolution}$ $P_{2S}(\Omega_1, \Omega_2; \rho)$ $\xrightarrow{\mathcal{P}}$ $p_{2s}(n_1, n_2; \rho)$

(P_{2M} and P_{2N} are known)

$\Phi_{2M} = \Phi_{2S} \cdot \Phi_{2N}$ $\xrightarrow{Ratio}$ $\Phi_{2S}(\omega_1, \omega_2; \rho)$ $\xleftarrow{\substack{IC \\ (eq. 3)}}$

(Where IO is the transform defined by eq. (3), $\mathcal{P}$ is the Poisson transform and $\mathcal{F}$ is the Fourier transform.)

3 - Theoretical model.

We have seen that in all cases, the second CF of the intensity pattern is easier to obtain than P_{2s} and contains the same information ; moreover, the procedure used to extract imaging information from P_{2s} is very difficult to apply to an extended object sampled over N points described by :

$$O(x) = \sum_{n=1}^{N} \alpha_n \delta(x - d_n) \qquad (5)$$

mainly due to the fact that we do not have any theoretical expression for $P_{2s}(\Omega_1, \Omega_2; \rho)$; to overcome this problem a theoretical model was developped, giving an explicit relation between $\Phi_{2s}(\omega_1, \omega_2; \rho)$ and the unknowns α_n.

This model, presented elsewhere[8], is founded on the assumption that the complex amplitude of the wave at the focus of the telescope is a Gaussian. The method of obtaining an analytic form of the CF, consists of a generalized Karhunen-Loeve expansion of the wave at the focus of the telescope and is based on calculations performed in optics by Barakat and Blake[10]. The theoretical form of the CF appears as an infinite product, whose terms depends only on the eigenvalues of a generalized Fredholm type integral equation.

Using the expression (5) for the object, the second CF is expressed as the inverse of the determinant of a (2Nx2N) matrix :

$$\Phi_{2s}(\omega_1, \omega_2; \rho) = det^{-1} \begin{bmatrix} I - i\omega_1 \, R(0) \, D & - i\omega_2 \, R(\rho) \, D \\ - i\omega_1 \, R(\rho) \, D & I - i\omega_2 \, R(0) \, D \end{bmatrix} \qquad (6)$$

where I is the unit matrix (NxN), D is a diagonal matrix whose entries are the values of the astronomical object intensities :

$$D = \begin{bmatrix} \alpha_1 & & & \\ & \alpha_2 & & \\ & & \ddots & \\ & & & \alpha_N \end{bmatrix} \qquad (7)$$

and

$$R(\rho) = \{r_{m,n}\} = \{r \, (d_m - d_n + \rho) \} \qquad (8)$$

is the real, (NxN), symmetric covariance matrix; $r(.)$ is the covariance function of the complex amplitude of the point source speckle pattern. Thus the α_n appears explicitly in the expression of $\Phi_{2s}(\omega_1, \omega_2; \rho)$.

4 - Proposed reconstruction procedure

We can imagine a reconstruction procedure of the image founded on the comparison between the measured second CF $\tilde{\Phi}_{2s}$ and the theoretical one Φ_{2s}. The parameters α_n present in the expression of Φ_{2s} can be adjusted by a least-squares technique ; the aim of the proposed method is to minimise the distance

$$\left\| \Phi_{2s} - \tilde{\Phi}_{2s} \right\|$$

subject to a constraint on the spatial extent of the object, which constraint in obtained from the spatial extent of the experimental values of the autocorrelation. A possible procedure could be an iterative one :

i / Compute the autocorrelation to obtain the spatial extent constraint. So, the number N of components of the object (for a continuous object, N is the number of sampling pixels) and their relative positions are known.

ii / Compute from measurements $\tilde{\Phi}_{2s}(\omega_1, \omega_2; \rho)$ and $R(\rho)$.

iii / Start the iterative procedure with

$$D^{(0)} = \begin{bmatrix} \alpha_1^{(0)} & & & \\ & \alpha_2^{(0)} & & \\ & & \ddots & \\ & & & \alpha_N^{(0)} \end{bmatrix}$$

(with arbitrary $\alpha_n^{(0)}$).

iv / Compute Φ_{2s} by relation (6)

v / Compute $\left\| \Phi_{2s} - \tilde{\Phi}_{2s} \right\|$ — Iteration is terminated if $\left\| \Phi_{2s} - \tilde{\Phi}_{2s} \right\|^2 \leq \varepsilon$

vi / Compute Corrections $\Delta\alpha_n$ for all α_n.

vii / $D^{(k)}$ is updated

$$D^{(k+1)} = \begin{bmatrix} \alpha_1^{(k+1)} & & & \\ & \alpha_2^{(k+1)} & & \\ & & \ddots & \\ & & & \alpha_N^{(k+1)} \end{bmatrix} \qquad \alpha_i^{(k+1)} = \alpha_i^{(k)} + \Delta\alpha_i$$

viii / Repeat from step iv

Another procedure could be founded on the "building block" method proposed by Hoffman et al.[11] . In our case the basic function could be the second CF instead of the bispectrum. Anyway, this method will be tested on simulated and real data, firstly on double star. The goal is to implement a "black-box" algorithm whose input data are speckle patterns, and output is the diffraction-limited image of the object.

References

1. RODDIER F., *Physics Reports* (review section of Physics Letters), **170**, 2, 97-166, North Holland Pub. Co (1988)

2. LABEYRIE A., *Progress in Optics*, **XIV**, 49-87, North Holland Pub. Co (1976)

3. KNOX K.T., THOMPSON B.J., *Ap. J.*, **193**, L45-L48 (1974)

4. WEIGELT G., *Opt. Comm.*, **21**, 55-59 (1977)

5. AIME C., *J. Optic*, **18**, 101-110 (1987)

6. AIME C., *SPIE Proc.*, **808**, 14-18 (1987)

7. AIME C., RICORT G., PERRIER C., *Experimental Astronomy*, **1**, 267-284 (1990)

8. AIME C., ARISTIDI E., LANTERI H., RICORT G., *SPIE Proc.*, **1351** (1990)

9. MEHTA C.L., *Progress in Optics*, **VIII**, 373-440, North Holland Pub. Co (1970)

10. BARAKAT R., BLAKE J., *J. Opt. Soc. Am.*, **68**, 614-622 (1978)

11. HOFMANN K.H., HAUDER W., WEIGELT G., *SPIE Proc.*, **1351** (1990)

ROUGH SURFACE SCATTERING 1

BACKSCATTERING ENHANCEMENT FROM VERY ROUGH SURFACES AND RANDOM MEDIA

Akira Ishimaru
Department of Electrical Engineering
University of Washington
Seattle, Washington 98195 USA
(206) 543-2169

(INVITED)

This paper presents our recent studies on backscattering enhancement from rough surfaces and random media. Theoretical as well as numerical and experimental studies are included.

1. One-Dimensional Dirichlet and Neumann Very Rough Surfaces

Very rough surfaces are defined as those with the rms height of the order of a wavelength and the rms slope of the order of unity. We present a theory based on the first-order and second-order Kirchhoff approximations with shadowing. The analytical solutions show good agreement with the Monte Carlo simulations showing backscattering enhancement [1]-[5].

2. One-Dimensional Very Rough Penetrable Surfaces

We have extended the study to include dielectric and metallic rough surfaces [1]. For small roughness, the effects of surface waves appear as enhanced backscattering for p-polarization, as discussed by Maradudin and others. For very rough surfaces, our analytical theory is applicable and shows reasonable agreement with the Monte Carlo simulations.

3. Two-Dimensional Very Rough Surfaces

Our analytical theory is extended to include two-dimensional rough surfaces. Comparisons with millimeter wave experimental data are being made.

4. Effects of the Non Gaussian Roughness Spectrum

A study was made to determine whether the scattered wave was sensitive to different roughness spectrums. We compared the power-law with the Gaussian spectrum and found some differences in the scattering pattern [5].

5. Pulse Beam Wave Scattered From a Rough Surface

A pulsed beam wave with a finite beam width and finite duration is incident on a rough surface. The scattered wave is calculated using Kirchhoff approximations and the two-frequency coherence function. Numerical results are obtained showing the lateral spreading and the pulse broadening [5].

6. Millimeter Wave Experiments

Millimeter waves with 75 to 10 GHz are used for rough surface scattering experiments. The surfaces have a rms height of one wavelength and a correlation distance of one wavelength. Experimental data show enhanced backscattering and give good agreement with the Monte Carlo simulations. Two-dimensional rough surfaces are also being constructed [5].

7. Inverse Rough Surface Problem and the Use of Neural Network Technique

The scattered intensity at two wavelengths at the specular and backward directions can be used to determine the rms height and correlation distance of the rough surface. A neural network technique is applied to this inverse problem [6]. The neural network is trained with the data from the Monte Carlo simulations. It is found that the rms height and correlation distance can be obtained quickly from the observed scattered intensity by the trained neural network.

8. Backscattering From a Target in Turbulence

Because of multiple scattering, the radar cross section of a target becomes approximately twice the free space value. Furthermore, the scintillation index from the target becomes approximately 5. A theoretical study of this problem will be presented [7].

References

[1]   A. Ishimaru and J. S. Chen, "Scattering from very rough metallic and dielectric surfaces: a theory based on the modified Kirchhoff approximation," *Waves in Random Media,* 1:1, pp. 21-34, January 1991.

[2]   A. Ishimaru and J. S. Chen, "Scattering from very rough surfaces based on the modified second-order Kirchhoff approximation with angular and propagation shadowing," *Journal of the Acoustical Society of America,* 88:4, pp. 1877-1883, October 1990.

[3]   J. S. Chen and A. Ishimaru, "Numerical simulation of the second-order Kirchhoff approximation from very rough surfaces and a study of backscattering enhancement," *Journal of the Acoustical Society of America,* 88:4, pp. 1846-1850, October 1990.

[4]   J. S. Chen, "Wave Scattering From Very Rough Surfaces and a Study of Backscattering Enhancement," Ph.D. Dissertation, University of Washington, Seattle, Washington, 1990.

[5]   A. Ishimaru, J. S. Chen, P. Phu, and K. Yoshitomi, "Numerical, Analytical, and Experimental Studies of Scattering From Very Rough Surfaces and Backscattering Enhancement," *Waves in Random Media,* to be published.

[6]   A. Ishimaru, R. J. Marks II, L. Tsang, C. M. Lam, D. C. Park, and S. Kitamura, "Particle-size distribution determination using optical sensing and neural networks," *Optics Letters,* 15:21, pp. 1221-1223, October 1990.

[7]   E. J. Fremouw and A. Ishimaru, "Intensity scintillation index and mean apparent radar cross section on monostatic and bistatic paths," preprint.

Enhanced Backscattering of Light from Random Surfaces and Related Phenomena

Alexei A. Maradudin
Department of Physics
and Institute for Surface and Interface Science
University of California
Irvine, CA 92717, U.S.A.

(INVITED)

We begin by studying the scattering of a finite beam of p-or s-polarized light incident from the vacuum side onto a random grating whose grooves are perpendicular to the plane of incidence. The position of the surface is defined by the equation $x_3 = \zeta(x_1)$, where the surface profile function $\zeta(x_1)$ is initially assumed to be a stationary stochastic process with a well-defined surface height probability distribution function and surface height correlation function. The grating is ruled on the surface of a semi-infinite metal, dielectric, or perfect conductor. The angular distribution of the intensity of the incoherent component of the scattered light is obtained by the numerical solution of the integral equations satisfied by the source functions, and through the arithmetic averaging of the exact scattered intensity.

For large rms slope random metal gratings, a well-defined peak in this angular distribution is observed in the retroreflection direction, for both polarizations of the incident light. This peak is the manifestation of enhanced backscattering. We find that the details of the angular dependence of the intensity of the incoherent component of the light scattered from such surfaces depend on the form of the surface height correlation function, but not the existence of enhanced backscattering itself. We find that enhanced backscattering occurs from a one-dimensional, random surface whose surface profile is not a Gaussianly distributed random variable, as well as from one whose surface profile function is a Gaussianly distributed random variable. We also find that enhanced backscattering occurs from one-dimensional, random surfaces whose surface profile functions are not satationary stochastic processes. We do this by studying the scattering of p- and s-polarized light from a random grating of even or odd symmetry. On the basis of these and other results it is argued that, for a strongly rough metal surface, enhanced backscattering results primarily from the coherent

interference of each multiply-scattered optical path with its time-reversed partner.

Enhanced backscattering is also observed from weakly rough metal surfaces, but only for a p-polarized incident beam. In this case it is believed to be due to the multiple scattering of surface polaritons by the surface roughness. The surface roughness allows the excitation of surface polaritons by the incident beam, scatters them repeatedly, and induces their transformation back into propagating volume modes in the vacuum, above the surface. The coherent addition of such a path with its time-reversed partner again leads to an enhancement of the intensity of scattering into the retroreflection direction. To test this assumption we have carried out numerical simulations of the scattering of a p-polarized beam from a weakly rough random grating on the surface of an n-type semiconductor, along whose grooves a constant magnetic field is applied. In the presence of the magnetic field the dispersion curve for surface plasmon polaritons on the planar surface of the scattering medium becomes nonreciprocal, i.e. the wave number κ_+ (ω) for surface plasmon polaritons of frequency ω propagating in the $+x_1$- direction is different from the (magnitude) of the wave number κ_- (ω) for surface plasmon polaritons of the same frequency propagating in the $-x_1$- direction. For ω sufficiently large, the dispersion curve becomes completely nonreciprocal in the sense that only surface plasmon polaritons propagating in the $+x_1$- direction can exist. The scattering results display a shift of the enhanced backscattering peak to larger scattering angles, and a decrease in its amplitude and an increase in its width, when the magnetic field is increased from zero. This is interpreted as due to the breakdown of the coherency between a given light/surface plasmon polariton scattering sequence and its time-reversed partner described above, due to the nonreciprocal propagation of surface plasmon polaritons in a magnetic field, which in turn is due to the breakdown of time-reversal symmetry caused by the application of the field. When the frequency of the incident light is in the range in which surface polaritons propagate in only the $+x_1$- direction, enhanced backscattering is completely suppressed.

We have also studied the scattering of p-polarized light from a classical grating on a metal surface on which a random grating has been superimposed. In the absence of the random roughness the dispersion curve for surface plasmon polaritons propagating normal to the grooves of the classical grating displays a frequency gap in which no surface plasmon

polaritons exist. If the frequency of the incident light is in this gap region, and only the random grating is present, enhanced backscattering is observed, because in the absence of the underlying periodic structure surface plasmon polaritons with this frequency exist. When the periodic grating is superimposed on the random grating enhanced backscattering is strongly suppressed, because surface plasmon polaritons of this frequency no longer exist.

These two results testify to the essential role played by surface electromagnetic waves in the enhanced backscattering of light from small rms slope random surfaces.

We have carried out simulations of the scattering of light of both p- and s-polarizations from a rough transparent dielectric film on a plane, perfectly conducting substrate. It is found that for incident light of either polarization a strong enhanced backscattering occurs. The existence of enhanced backscattering of p-polarized light in the present geometry contrasts with its absence in the scattering of p-polarized light from a semi-infinite dielectric medium, characterized by the same roughness parameters and index of refraction. The enhanced backscattering of s-polarized light in the film geometry is much stronger than from a semi-infinite substrate. Similar, although weaker, enhanced backscattering is also observed in the scattering of light from a free-standing. transparent dielectric film whose illuminated surface is a random grating while its back surface is planar.

The differential transmission coefficient for a p-polarized finite beam, transmitted though a thin metal film, one or both of whose surfaces is a small rms slope randomly rough grating, is calculated by a numerical solution of the exact equations of electrodynamics. The mean differential transmission coefficient, as a function of the transmission angle, displays a peak in the antispecular direction.

We also present results for the scattering of p- and s-polarized light from small rms slope, two-dimensional, random surfaces on metals and transparent dielectric media. In this case, a random surface is generated within a square domain of the $x_1 x_2$-plane, which is then replicated periodically to cover the entire $x_1 x_2$-plane. The result is a bigrating, albeit with a very complicated period, and the methods of grating theory, based on the Reduced Rayleigh Equations, are used to solve the scattering problem. Enhanced backscattering is observed in cross-polarized, in-plane scattering from both kinds of surfaces, and is explained on the basis of the surface electromagnetic waves each type of surface can support.

We conclude by presenting some results concerning the enhanced backscattering of light from one-dimensional random surfaces on nonlinear substrates, which has some features not present in the scattering of light from random surfaces on linear substrates.

MULTIPLE SCATTERING EFFECTS IN ROUGH SURFACE SCATTERING AND PROPAGATION

By E Jakeman and D L Jordan
Defence Research Agency, RSRE Malvern, Worcestershire WR14 3PS, UK

(INVITED)

The scattering of electromagnetic and sound waves from rough surfaces is a problem of longstanding interest, relevant to remote sensing systems operating over a wide range of wavelengths. The single-scattering, tangent plane approximation, which is essentially a phase screen approximation, has been extensively investigated, although its range of validity is only now becoming clear with the implementation of numerical techniques of solution. To date these have been largely restricted to corrugated surfaces with simple, well defined statistical properties - typically situations in which the surface profile is well represented by a Gaussian process with a single scale spectrum. Unfortunately most real surfaces of interest are not corrugated but composite, typically non-Gaussian, non-stationary or intermittent with several scales, some larger and some smaller than the wavelength of the incident radiation. The application of numerical techniques to such complex scattering systems whether to effect solution or simulation would appear to be still some way off. On the other hand alternative analytical techniques to the tangent plane approximation also have limited ranges of applicability and suffer from various other shortcomings. Perturbation treatments would appear at first sight to be useful for surfaces which are relatively smooth by comparison with the wavelength but, to the author' knowledge robust features predicted by this approach such as polarisation ratios have not been satisfactorily verified and indeed experiments designed for this purpose appear to be extremely difficult, thereby casting doubt on the practical utility of the approximation. More recently, improvements of the tangent plane approximation have been sought by iteration of the integral equation for the boundary field so as to include multiple scattering events. The series generated in this way is generally not convergent and retention of only up to the double scattering term must be accompanied by somewhat ad-hoc correction factors to take account of shadowing in order to achieve agreement with full numerical solution of the problem. No presently available techniques appear to deal effectively with grazing angle geometries commonly employed by radar systems, for example, which are known to be particularly sensitive to surface characteristics.

In order to progress our understanding of observed robust features of low angle back-scattering by complex systems such as the sea surface we are investigating a composite particle-based model. Particle models have been particularly successful in modelling the fluctuation properties of non-Gaussian scattered wave fields but we believe they may also provide a useful means of calculating some features of the scattering cross-section itself in the case of complex surfaces. Specifically we assume that the surface consists of a dispersion of small inhomogeneities on a smoothly varying large scale structure. In the conducting case scattering by this composite surface can be treated approximately by Rayleigh's image method [1] as used by Twersky and others, replacing the continuous surface by incident fields satisfying the appropriate boundary

condition together with a set of symmetrised inhomogeneities or particles. In forward scattering directions the cross-section is dominated by the large scale structure and can be calculated using the tangent plane approximation. In back scattering directions, particularly at high incidence (low grazing) angles, the cross-section is determined by properties of the particle scattering system. We have investigated multiple scattering by this complex system using mean field and iterative techniques.

To complement the theoretical work outlined above we have constructed and carried out light scattering experiments from a wide range of surfaces designed to exhibit multiple scattering at high incident angles. Figure 1 shows the distribution of intensity in the neighbourhood of the back scattering direction obtained from a multi-scale metal foil surface illuminated at an incident angle of 82°. A backscattering enhancement of the order of 20% was observed in co-polar returns with an effect of the same order of magnitude in the weaker, noisier, cross-polar components. Similar results were obtained in the case of dielectric spheres deposited on a rough metal surface but with no cross-polar enhancement.
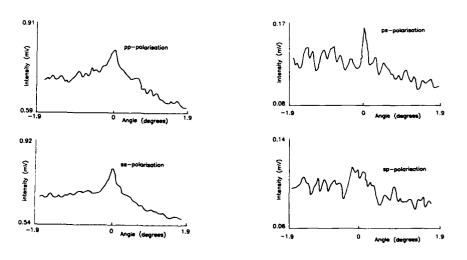
Fig 1: Back scattering from a multi-scale metal foil surface show enhancement peak. Angle of incidence 82°.

Perhaps the simplest wave-scattering geometry to show multiple scattering effects is the double passage configuration, in which a target illuminated by radiation incident through a scattering medium reflects radiation back along the same path. Extensive theoretical treatments of this problem are to be found, particularly in the Soviet literature [2], but relatively little experimental work has been reported and little has been published in the open literature on the implications for remote sensing and system performance. We find that some advantage is to be

had by active rather than passive imaging of incoherently scattering objects. The use of common transmit-receive optics also appears to improve the signal to noise ratio in detection and ranging systems operating over long atmospheric paths by taking advantage of the enhanced backscattering phenomenon. In an attempt to establish the robustness of this effect we have carried out indoor and outdoor experiments at visible and IR frequencies. From these it is clear that multiple scattering in folded path geometries is a common occurrence and should be taken into account in the design and performance analysis of remote sensing systems. Figure 2 shows a comparison of visible and IR returns from a smooth target over a 35m indoor path through turbulence generated by industrial heaters. The full lines are theoretical predictions based on a simple phase screen model. Enhancement factors of 1.7 above background were typically observed for visible frequencies but values in excess of 2 were commonly obtained in the IR using the same experimental geometry.
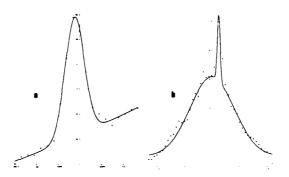
Fig 2: Enhanced backscattering of (a) visible and (b) infra red radiation observed in large scale laboratory propagation experiments.

References

1. Lord Rayleigh, 1907, Phil. Mag. Vol. 14, 350-359.
2. Yu A Kravtsov and A I Saichev, 1983, Sov. Phys. Usp Vol. 25, 494-508.

MULTIPLE LIGHT SCATTERING IN MAGNETO-OPTICALLY ACTIVE RANDOM MEDIA

Frank A. Erbacher and Georg Maret

Max-Planck-Institut für Festkörperforschung, Hochfeld-Magnetlabor, B.P.166

F-38042 Grenoble Cedex, France   Phone: (33) 76-88-10-01

Wave propagation in disordered media is of interest in many areas of physics. The extended investigations of quantum interference effects in electron transport in impure metals and semiconductors illustrate its importance in solid state physics. Studies on multiple scattering of *classical* waves such as light have attracted intention recently since they give direct insight into the coherent wave propagation over macroscopic length scales.[1] Laser sources provide almost arbitrarily good control over momentum and energy of the injected photons allowing, for example, the direct observation of coherent backscattering, the optical analog of weak localisation.

The particular influence of the *vector wave* nature of light has been discussed recently to some extend.[2-6] The light polarisation inside the diffusively scattering medium can be affected by a strong magnetic field (H) due to Faraday rotation. A theoretical model has been worked out to describe the resulting changes in the shape of the backscattering cone.[7]

We consider theoretically and experimentally the magnetic field induced changes of the multiple scattering speckle patterns as caused by Faraday rotation in transmission through a slab. The optical field cross correlation function C(H) between a reference speckle pattern at zero field and another one at field H can be calculated using diagrammatic expansion technics.[8] The underlying physical picture is resumed as follows: Multiple scattering is characterized by a transport mean free path l^*, the distance over which the memory of photon's direction is lossed. Depolarisation also occurs on a distance of order l^*.[2-6] In transmission through a slab of thickness L (L>>l^*) the photon propagation is described in the diffusion approximation, resulting in two independent speckle patterns of equal average intensity corresponding to two orthogonal output polarizations. The magnetic field induced rotation of the polarisation over the length l^* is of order $V l^* H$ for a step in direction l^*, V being the Faraday constant. The total Faraday rotation angle acquired along multiple scattering paths of length s is zero on average over all configurations. But it's mean square value $\langle \phi^2 \rangle$ is non zero and increases *linearly* with s. In this approximation C(H) is given by

$$C(H) = \int P(s) \, \exp^{-(\alpha V^2 H^2 l^* s)} \, ds \qquad (1)$$

where α is a numerical constant and $P(s)$ is the path length distribution function. With the well known expression for $P(s)$ in the diffusion approximation one obtains

$$C(H) = \frac{\gamma l^*}{L} \frac{\sinh(\gamma\sqrt{3\alpha}VHl^*)}{\sinh(\sqrt{3\alpha}VHL)} \qquad (2)$$

Since $P(s)$ has a maximum at path length comparable to L^2/l^* , $C(H)$ decays approximately as $\exp^{-\alpha V^2 L^2 H^2}$. So in first order, $C(H)$ does not explicitly depend on the scattering properties of the medium, which are expressed by l^*. In this model the effects of absorption can easily be incorporated.

We have determined $C(H)$ experimentally in transmission on turbid powders of rare earth doped glass microparticles using a monomode Ar^+ laser ($\lambda=514\mu m$). A digital video imaging
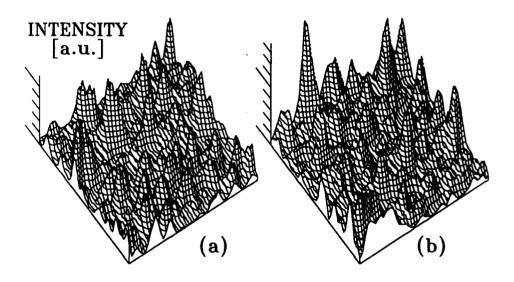
Fig.1: *Enlarged section of a transmission speckle pattern from a sample with L=860μm and linear output polarization. There is a large change in the pattern between (a) H=0 Tesla and (b) H=23 Tesla.*

technique was used to record about 600 independent speckle spots. Fig.1 shows the large change of the transmission speckle pattern as induced by a strong magnetic field. C(H) as calculated in the factorisation approximation is given in the inset of Fig.2 as a function of H. The loss of correlation becomes visible in fields above 2 Tesla and approaches zero at about 25 Tesla. C(H) is found to decay proportional to H^2 at small fields in agreement with eq.(2). In Fig.2 we also plot ln C(H) measured for various samples with different values of l^*, L and V versus the dimensionless quantity $V^2H^2L^2$. The data essentially fall on a single line revealing that $V^2H^2L^2$ is the appropriate scaling variable. We will provide a more detailed data analysis and comparison with theory.

These observations demonstrate that optical random interference patterns in the multiple scattering regime are sensitive to changes in the polarization states obtainable in strong magnetic fields. This provides a means to study experimentally optical weak localisation in time-reversal noninvariant media. This work also opens the possibility to measure Faraday constants in non transparent strongly scattering materials even without a detailed knowledge of the scattering properties of the sample.
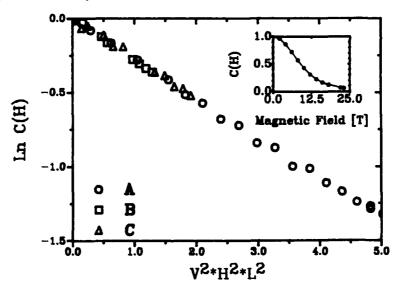
Fig.2: Magnetic field dependence of the correlation function C(H) of speckle patterns.
(a) L=1.215mm, V=137$m^{-1}T^{-1}$ (b) L=0.735mm, V=114$m^{-1}T^{-1}$ (c) L=0.760mm,V=114$m^{-1}T^{-1}$ The three samples have substantially different values of l^*, as varied in (c) by addition of strongly scattering TiO_2 microparticles. Inset: Sample with L=1.215mm, V=137$m^{-1}T^{-1}$.

[1] P.Sheng, Editor, Scattering and localization of classical waves in random media, World Scientific Publishing, London (1990)

[2] M.J.Stephen, G.Cwilich, Phys.Rev.B 34, 7564 (1986)

[3] M.P.van Albada, M.B. van der Mark, A.Lagendijk, Phys.Rev.Let. 58, 361 (1987)

M.P.van Albada, A.Lagendijk, Phys.Rev.B 36, 2353 (1987)

[4] E.Akkermans, P.E.Wolf, R.Maynard, G.Maret, J.Phys.France 49, 77 (1988)

P.E.Wolf, G.Maret, E.Akkermans, R.Maynard, J.Phys.France 49, 63 (1988)

[5] F.C.MacKintosh, J.X.Zuh, D.J.Pine, D.A.Weitz, Phys.Rev.B 40, 9342 (1989)

[6] I.Freund, M.Kaweh, R.Berkovits, M.Rosenblu, Phys.Rev.B 42, 2613 (1990)

[7] F.C.MacKintosh, S.John, Phys.Rev.B 37, 1884 (1988)

[8] E.Akkermans, unpublished

A Numerical Study of the Small Slope Approximation for Rough Surface Scattering

Shira Lynn Broschat
Electrical Engineering and Computer Science Department
Washington State University
Pullman, WA 99164-2752
(509) 335-5693

Eric I. Thorsos
Applied Physics Laboratory
College of Ocean and Fishery Sciences
University of Washington
Seattle, WA 98105
(206) 543-1369

I. Introduction

Wave scattering from rough surfaces is important in many diverse engineering and scientific applications [1]. Among these are integrated optics, microwave remote sensing, and underwater acoustics. The classical perturbation and Kirchhoff solutions to the rough surface scattering problem are limited in their regions of validity [2,3], and there is a clear need for a better model.

In recent years a number of rough surface scattering models have been introduced that attempt to "bridge the gap" between the perturbation and Kirchhoff approximations. Among these is the small slope approximation (SSA) developed by A.G. Voronovich [4]. In this paper, the first- and second-order small slope approximation reflection coefficients and bistatic scattering cross sections are derived for the Dirichlet problem. The second-order result is shown to reduce to those of the perturbation and Kirchhoff methods for the reflection coefficient and the first-order result to that of the perturbation method for the bistatic scattering cross section. Numerical results for the first-order SSA for one-dimensional, Dirichlet surfaces with a Gaussian spectrum are compared with exact numerical results obtained using a Monte Carlo technique.

II. Background

Consider a scalar plane wave incident on a one-dimensional surface described by the function $z = f(x)$ (see Fig. 1). The incident and scattered angles are given by θ_i and θ_s, respectively, and the incident wave vector $\mathbf{k}_i$ and the scattered wave vector $\mathbf{k}_s$ are parallel to the x-z plane. The total field on the surface vanishes everywhere (Dirichlet boundary condition), and a harmonic time dependence of $\exp(-i\omega t)$ is assumed.

The Helmholtz integral formulation of the extinction theorm [5] can be used to derive the following expression for the scattered field

$$\psi_s(\mathbf{r}) = \int dk_{sx} \exp[ik_{sx}x + ik_{sz}z] T(k_{sx}, k_{ix}) \tag{1}$$
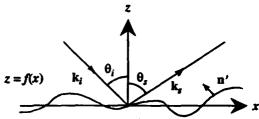
Figure 1. Scattering geometry.

where $\mathbf{r} = (x,z)$ is the observation point, k_{sx} and k_{sz} are the x- and z-components of the scattered wave vector $\mathbf{k}_s$ such that $\mathbf{k}_s \cdot \mathbf{r} = k_{sx}x + k_{sz}z$ and $k_{sz} = [k^2 - k_{sx}^2]^{1/2}$, and $\mathbf{k}_i = (k_{ix}, k_{iz} \equiv -\kappa_{iz})$. The square root is taken to be positive for $k^2 > k_{sx}^2$ and positive imaginary for $k^2 < k_{sx}^2$. The factor

$$T(k_{sx}, k_{ix}) = -i/(4\pi k_{sz}) \int dx' \exp[-ik_{sx}x' - ik_{sz}f(x')] \, \mathbf{n}' \cdot \nabla' \psi(\mathbf{r}') \qquad (2)$$

is known as the transition or T-matrix [6]. In (2), $\mathbf{r}' = (x', f(x'))$ is a point on the surface and $\mathbf{n}'$ is a vector normal to the surface. The quantity $\mathbf{n}' \cdot \nabla' \psi(\mathbf{r}')$ is the unknown surface source density excited on the surface by the incident plane wave. The equivalent expression used by Voronovich is given by

$$\mathbf{n}' \cdot \nabla' \psi(\mathbf{r}') = i \exp[ik_{ix}x' - i\kappa_{iz}f(x')]\Phi(k_{sx}, k_{ix}, [f(x')]) \qquad (3)$$

where the $[f(x')]$ indicates that Φ is a functional of $f(x')$. By explicitly extracting the exponential phase factor in (3), Φ does not depend on the zero wave vector components of $f(x')$. The phase factor accounts for the change in the T-matrix due to rigid translations of the surface $f(x')$ either horizontally or vertically. The unknown Φ is expanded in a functional Taylor series in the Fourier transform of $f(x')$:

$$\Phi(k_{sx}, k_{ix}, [f(x)]) = \phi_0(k_{sx}, k_{ix}) + \int dq \, \exp[iqx]F(q)\phi_1(k_{sx}, k_{ix}; q) +$$
$$\int dq_1 dq_2 \, \exp[i(q_1 + q_2)x]F(q_1)F(q_2)\phi_2(k_{sx}, k_{ix}; q_1, q_2) + \cdots \qquad (4)$$

where the primes have been suppressed for simplicity and where $F(q)$ is the Fourier transform of $f(x)$. The Taylor coefficients ϕ_n are found by expanding (2) with (3) and (4) in powers of $f(x)$ and comparing the results order by order in $f(x)$ with the perturbation expansion of (2) [2,7]. For the first two terms this yields

$$\phi_0 = -4\kappa_{iz}k_{sz}/v_z \qquad (5)$$

$$\phi_1 = (2i\kappa_{iz}k_{sz}/v_z) \{[k^2 - (q+k_{ix})^2]^{1/2} + [k^2 - (k_{sx}-q)^2]^{1/2} - v_z\} \qquad (6)$$

where $v_z = \kappa_{iz} + k_{sz}$.

III. Coherent Reflection Coefficient

The first-order SSA reflection coefficient is found using (3) in (2) with Φ approximated by (5) and taking the first moment of (2). The first-order result is given by

104

$$R_1 = -\exp[-2\kappa_{iz}^2 h^2] \qquad (7)$$

where h is the root mean square (rms) surface height. Note that (7) is precisely the reflection coefficient for the Kirchhoff approximation. The second-order SSA reflection coefficient is found using (5) and (6) in (4), (4) in (3), and (3) in (2) and taking the first moment. The second-order result is given by

$$R_2 = R_1 + 2\kappa_{iz}\exp[-2\kappa_{iz}^2 h^2] \int dK \, W(K)\{[k^2 - (K+k_{ix})^2]^{1/2} - \kappa_{iz}\} \qquad (8)$$

where $W(K)$ is the surface roughness spectrum. As we let $kh \to 0$, (8) reduces to

$$R_2 = -1 + 2\kappa_{iz} \int dK \, W(K)[k^2 - (K+k_{ix})^2]^{1/2} \qquad (9)$$

This is the perturbation result.

IV. Incoherent Bistatic Scattering Cross Section

The first- and second-order bistatic scattering cross sections [1] are found from the first and second moments of (2) using (3) and (4) with (5) and (6). They are given by

$$\sigma_1 = 4B/v_z^2 \int dx \, \exp[iv_x x]\{\exp[-v_z^2 h^2 C(x)] - 1\} \qquad (10)$$

$$\sigma_2 = \sigma_1 + (4B/v_z)\text{Re}\left\{ I^* \int dx \, \exp[iv_x x]\{1 - \exp[-v_z^2 h^2 C(x)]\} + \right.$$

$$\int dx \, \exp[iv_x x + v_z^2 h^2 C(x)] \int dK \, \exp[iKx]W(K)g^*(K)\right\} +$$

$$B\int dx \, \exp[iv_x x + v_z^2 h^2 C(x)]\left\{ 1/v_z^2 \int dK \, \exp[iKx]W(K)|g(K)|^2 - \right.$$

$$I\int dK \, \exp[iKx]W(K)g^*(K) + \int dK \, \exp[iKx]W(K)g(K)\int dK' \exp[iK'x]W(K')g^*(K') -$$

$$\left. I^* \int dK \, \exp[iKx]W(K)g(K)\right\} + B|I|^2 \int dx \, \exp[iv_x x]\{\exp[-v_z^2 h^2 C(x)] - 1\} \qquad (11)$$

where

$$B = k_{iz}^2 k_{sz}^2/(2\pi k) \, \exp[-v_z^2 h^2],$$

$$I = \int dK \, W(K)g(K),$$

$$g(K) = [k^2 - (K+k_{ix})^2]^{1/2} + [k^2 - (K-k_{sx})^2]^{1/2} - v_z \, ,$$
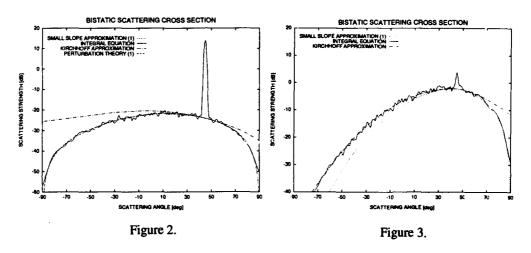
$v_x = k_{ix} - k_{sx}$, $C(x)$ = correlation function = $\langle f(x_0)f(x_0-x)\rangle/h^2$, and the asterisk denotes the complex conjugate. Equation (10) reduces to the Kirchhoff result in the specular direction. Also, in the limit as $kh \to 0$, (10) reduces to the first-order perturbation result.

V. Numerical Results

The numerical results given in this section are for the scattering strength defined by $SS = 10 \log [\sigma/2\pi]$. Figure 2 shows a comparison of the first-order SSA scattering strength as a function of the scattered angle θ_s with exact integral equation [3], first-order perturbation, and Kirchhoff approximation results for a Gaussian spectrum. In this example, $\theta_i = 45°$, $kh = 0.1$, $kl = 1.4$ (where l is the correlation length), and the rms surface slope angle $\gamma = 5.8°$.

The peak in the integral equation result here and in the next figure is due to the coherent part of the scattering strength and is not included in the approximate models. The fluctuations in the integral equation result are due to the finite number of realizations (50) used in the Monte Carlo average; as more surface realizations are added, the fluctuations decrease in magnitude. Because the first-order SSA cross section reduces to that of first-order perturbation theory, the scattering strengths of these two are coincident.

In Fig. 3, the first-order SSA, exact integral equation, and Kirchhoff approximation scattering strengths are compared. Here $\theta_i = 45°$, $kh = 1.33$, $kl = 7.46$, and $\gamma = 14.2°$. The Kirchhoff result is good away from low grazing angles while the SSA result is good in the specular region and at low forward grazing angles but underpredicts backscatter. Preliminary results indicate that the second-order SSA should significantly improve the accuracy of the small slope approximation for this example.

Figure 2.

Figure 3.

References

1. Ishimaru, A., *Wave Propagation and Scattering in Random Media*, Academic, New York, 1978.

2. Thorsos, E.I., and D.R. Jackson, "The validity of the perturbation approximation for rough surface scattering using a Gaussian roughness spectrum," J. *Acoust. Soc. Am.*, Vol. 86, 261-277, 1989.

3. Thorsos, E.I., "The validity of the Kirchhoff approximation for rough surface scattering using a Gaussian roughness spectrum," *J. Acoust. Soc. Am.*, Vol. 83, 78-92, 1988.

4. Voronovich, A.G., "Small-slope approximation in wave scattering by rough surfaces," *Sov. Phys. JETP*, Vol. 62, 65-70, 1985.

5. Waterman, P.C., "Scattering by periodic surfaces," *J. Acoust. Soc. Am.*, Vol. 57, 791-802, 1975.

6. Tsang, L., J.A. Kong, and R.T. Shin, *Theory of Microwave Remote Sensing*, John Wiley & Sons, New York, 1985.

7. Jackson, D.R., D.P. Winebrenner, and A. Ishimaru, "Comparison of perturbation theories for rough-surface scattering," *J. Acoust. Soc. Am.*, Vol. 83, 961-969, 1988.

The Relationship Between The Normalized First
Order Smoothing Method and Classical Rough
Surface Scattering Approximations

by

Gary S. Brown
Bradley Department of Electrical Engineering
Virginia Polytechnic Institute and State University
Blacksburg, Virginia 24061-0111, U.S.A.
Phone (703) 231-4467

Scattering by randomly rough surfaces comprises a topic of interest to all areas involving wave motion. Significant advancements have been accomplished recently through the numerical solution of the basic integral equations governing the scattering process. Among these are fundamental contributions to the understanding of the process known as enhanced backscattering wherein the scattering in the retro direction is larger than the scattering in any other direction. Unfortunately, a purely numerical approach to the scattering problem is presently limited to corduroy or one-dimensionally rough surfaces and it is not clear when this restriction can be overcome. Consequently, there is still a need for approximate scattering theories which enable consideration of the kinds of surfaces which cannot presently be addressed by purely numerical means.

There are a number of approximate scattering theories in the literature but only a relatively few are reasonably well understood in regard to their capabilities and limitations. In this catagory could be placed the Rice or boundary perturbation approximation, the physical optics or shadowed Kirchhoff method, the two-scale or composite surface roughness model, and a second order iteration of the integral equation describing the scattering process. It should be noted that it is only recently that the limitations of second order iteration are starting to be

107

understood. In addition to these classical approximate techniques, the method of smoothing has also been applied to the surface scattering problem. The most recent variant of the basic smoothing method has been called the normalized first order smoothing approximation or NFOS. The idea behind NFOS is to first normalize out the phase factor resulting from the evaluation of the incident field on the rough surface because it is this factor which limits first order smoothing to slightly rough surfaces even in the case of randomly elevated planar surfaces. That is, without the normalization first order smoothing will apply to the simple case of scattering by a randomly elevated planar surface only when the random elevation is small compared to the electromagnetic wavelength. In the NFOS method, first order smoothing is applied to the normalized integral equation.

The purpose of this paper is to compare NFOS with the classical approximations listed above. This will be done by showing how the general NFOS form simplifies under each set of corresponding surface simplifications. First, it will be shown that when the rough surface height and slopes are sufficiently small, NFOS yields the Rice perturbation result which, because of its dependence, is called a localized low frequency approximation. The term localized means that the current induced at a point on the rough surface by the incident field depends only on the surface and incident field at the single point. If, however, the surface slopes are not small then NFOS yields a nonlocalized low frequency approximation when the surface height is small. In this limit, the induced current at a point is determined by the current on other parts of the surface; hence, the change from localized to nonlocalized behavior.

Next, it is shown that if this small height roughness structure is superposed on a randomly elevated planar surface having arbitrary elevation, NFOS correctly recovers the fields scattered by this arrangement. If the randomly elevated planar surface is then permitted to be randomly tilted, NFOS works for this arrangement also. It is only when curvature is added to the

108

underlying tilted planar surface that NFOS starts to breakdown because of the possibility of multiple scattering on the large scale surface. Thus, NFOS not only recovers the classical composite surface scattering model but it also predicts when it fails and extends it into the realm of large surface slopes associated with the small scale surface height. It is shown that NFOS does not appear to lead to a shadowed Kirchhoff result. That is, one does not recover the physical optics approximation with NFOS.

A final demonstration of the relationship of NFOS to other classical approximations shows that it is similar to second order iteration with one important difference. NFOS gives rise to terms which are of zeroth and first order in the surface slopes while second order iteration includes zeroth, first, and second order terms in surface slopes. It is this inclusion of second order terms in slopes which leads to the divergence of a second order iterative solution when the slopes are large. NFOS, on the other hand, converges to the exact result when the height is small but the slopes are large.

Brewster's incidence and characterization
of dielectric rough surfaces

M. SAILLARD

Laboratoire d'Optique Electromagnétique, U.R.A. CNRS n°843,
Faculté des Sciences et Techniques de Saint-Jérôme, Case 262,
Avenue Escadrille Normandie-Niemen, 13397 Marseille Cedex 13, France

Phone : (33) 91 28 83 76
Fax : (33) 91 67 44 28

The basic question is : what is modified in the Brewster's phenomenon when a dielectric plane is randomly modulated ?

If a dielectric plane is illuminated by a TM polarized incident beam around Brewster's incidence, the specularly reflected beam is characterized by a zero of the intensity in the direction of Brewster's angle (Fig.1).
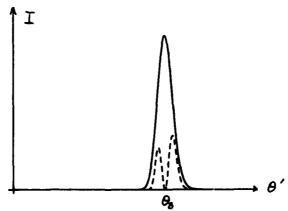
Fig.1 : _____ incident beam
- - - - - - - - - reflected beam.

Now, we are interested in the distribution of the specularly reflected intensity when the plane becomes modulated. Here, the surface has a gaussian correlation function

$$C(x) = \sigma^2 \exp(-x^2/\tau^2)$$

and is well-defined by the rms σ and the correlation length τ. A detailed study of the intensity as a function of σ and τ has been made. This study confirms the first results[1] and clearly shows that the "Brewster's angle" is shifted toward lower incidence angles.

The shift is an increasing function of the surface roughness, i.e., increases with σ and decreases with τ. But when the plane becomes modulated, the minimum of the intensity in the reflected beam is no longer rigorously zero. Its value increases with σ and finally it disappears. On the contrary, it has been possible to localize this minimum with very small correlation lengths and, thanks to homogenization techniques[2] we could test the results and get a limit value for a given σ.

A research of zeros of the reflexion coefficient in the complex plane of incidences for a random grating will also be achived.
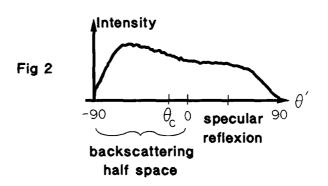
While we are still unable to give an explanation of this fact, the angle shift ($\gtrsim 1°$) can easily been detected by a modern apparatus and so may provide a very convenient way to characterize a dielectric rough surface.

About transmission, one can remark that the same phenomenon holds for the directly transmitted beam, except that the minimum is replaced by a maximum.

The second part is not directly related to the Brewster's phenomenon but is the natural complement of the first one.

When the roughness appears, the diffracted intensity is not restricted to the specularly reflected beam. Light is scattered in all directions and this speckle also contains information. So, we have also studied the total intensity scattered in the upper medium by a dielectric rough surface illuminated under Brewster's incidence. A similar study has been made for perfectly conducting surfaces in the laboratory[3]. Here, because of the transmission, the situation is much more complicated. The total scattered intensity can also provide a good mean for characterization. Of course, from a practical point of view, it is more convenient to localize a dark line in the reflected beam, but here the domain of application is not limited.

The influence of the statistical parameters has been studied and leads to simple laws, especially for low rms ($\gtrsim \lambda/10$). As the total intensity increases with σ, the shape of the angular distribution of the scattered intensity is also modified. For small rms, the intensity is localized around the direction of specular reflection. When the rms grows up, more and more light is scattered in what one could call the "backscattering half space" (Fig.2).

Fig 2

To measure the energy migration, one can define a center of energy by the direction θ_c which is separating the diffraction pattern in two regions containing the same energy

$$\int_{-\pi/2}^{\theta_c} I(\theta') \, d\theta' = \int_{\theta_c}^{\pi/2} I(\theta') \, d\theta'$$

For increasing roughness, θ_c is going toward the backscattering direction. Due to Brewster's phenomenon, the speed of the displacement is very high in the TM case of polarization for large incidence angles.

Thanks to these simple phenomena, Brewster's incidence seems to be very convenient in order to characterize a monodimensional dielectric surface roughness. And I think it will be much more interesting in the case of bidimensional rough surfaces with cross-polarization effects.

References.

1. M. Saillard and D. Maystre, "Scattering from metallic and dielectric rough surfaces", J. Opt. Soc. Am. A, Vol.7, n°6, 1990, p.982-990.
2. G. Bouchitté and R. Petit, "Homogenization techniques as applied in the electromagnetic theory of gratings", Electromagnetics, 5, 1985, p.17-36.

113

Perturbative model of the shift of the Brewster's angle on a rough surface

Jean-Jacques Greffet
Laboratoire d'Energétique Moléculaire, Macroscopique ; Combustion
Centre National de la Recherche Scientifique, Ecole Centrale Paris
92295 Châtenay Malabry Cedex

I Introduction

The Brewster's angle is the value of the angle of incidence for which the Fresnel reflection factor for p-polarized (Transverse Magnetic) light is null. If a plane wave illuminates a flat interface separating two lossless dielectrics, the light is entirely transmitted at the Brewster's angle. In the case of an illuminating bounded beam several angular components have to be used in order to describe it:

$$H(x,z) = \int A(k) \exp[ikx-i\alpha z]\, dk \quad \text{where} \quad \alpha = \left(\frac{\omega^2}{c^2} - k^2\right)^{1/2} \quad \text{and} \quad \text{Im}\,(\alpha) > 0$$

where k is the wave vector parallel to the interface, A(k) is the angular spectrum of the incident field and the angular spectrum of the reflected field is given by r(k) A(k), with r(k) the Fresnel reflection factor.

In a recent paper, Saillard and Maystre[1] have reported the observation of an angular shift of the Brewster's angle on a rough dielectric surface. This effect has been observed by means of MonteCarlo simulations of the scattering of p-polarized gaussian beams on a 1-D dielectric rough surface. For surfaces with a roughness of $\lambda/10$, a well developped speckle is observed as well as a specular peak which mainly reproduces the gaussian shape of the incident beam. For an angle of incidence close to the Brewster's angle θ_B, Saillard and Maystre have observed a clear minimum in the shape of the specular part of the reflected beam but at angles slightly lower than the Brewster's angle. Thus the effect of the roughness is not to suppress the null reflectivity but to shift the location of the minimum. The absolute value of this angular shift seems to increase with the roughness. However, when the roughness becomes larger than $\lambda/5$, the features of a flat interface, like the specular peak and the presence of a minimum of the reflectivity, tend to disappear.

Several questions are raised by these observations. The first is : what physical mechanism is responsible for this shift ? The second question is whether the minimum is a *true zero or a simple minimum*. It is very difficult to obtain the answer to this question from purely numerical results. An interesting point, regarding possible metrologic applications, is to study the behaviour of the angular shift versus the statistical parameters of the surface : roughness δ and length of correlation σ.

II Mechanism of the angular shift of the Brewster's angle on a rough interface

The Brewster's angle is a property of the Fresnel reflection factor. Thus we will study the specular (coherent) component of the reflected field on a rough surface. Let us first define the model used for the rough surface $z=S(x)$. Throughout this summary we will assume that the 1 D rough surface is a stationary random process characterized by the following assumptions :

$$<S(x)> = 0 \qquad (1)$$
$$<S(x) \, S(x')> \; = \; \delta^2 \exp(-|x-x'|^2/\sigma^2) \qquad (2)$$

The fact that the correlation function $\delta^2 \exp(-|x-x'|^2/\sigma^2)$ depends on x and x' only through their difference has the consequence that translational invariance is restored after an averaging process. Thus the average (coherent) reflected field has a specular component only. A commonly used expression for the reflectivity is given by $R(k)=r(k)\exp\{-2[(\omega/c)\delta \cos \theta]^2\}$, where r(k) is the Fresnel reflectivity. Clearly this expression does not produce any angular shift since it is null at the Brewster's angle. In order to obtain a more accurate expression for R(k), we need a better model of the scattered light.

Since we consider surfaces with roughnesses δ in the range $\lambda/10$- $\lambda/100$, the scattered light can be computed by perturbation techniques. Thus the amplitude of the magnetic field of the reflected light is of the form :

$$A = A^{(0)} + A^{(1)} + A^{(2)}+ ... \qquad (3)$$

The first term is simply given by the Fresnel reflection factor and corresponds to the reflected field by a flat interface. The following terms represent the contribution of the roughness to the reflected field to the first and second order. Averaging this equation leads to :

$$<A> = A^{(0)} + <A^{(2)}>+ ... \qquad (4)$$

The zero order term remains unchanged. The first order term varies linearly with S(x) and is null after averaging according with Eq.(1). The exact expression for $<A^{(2)}>$ is given in ref.2 ; it is derived from a perturbative treatment of scattering by a rough dielectric surface up to second order [3-4] and then averaged. Considering Eq. (4) it is seen that the reflected field is certainly not null at the Brewster's angle since there is no reason for $<A^{(2)}>$ to be null. The existence of a minimum is due to an interference effect between the two terms of Eq. (4).

In Fig.1, $A^{(0)}$, the real part of $<A^{(2)}>$ (noted $\mathcal{R}\{<A^{(2)}>\}$) and the modulus of the total field $|A^{(0)}+<A^{(2)}>|$ are displayed as a function of the incidence angle θ in the case of a reflection on a semi infinite glass substrate ($\varepsilon=2.25$, $\theta_B = 56.3°$). It is seen that for a value of θ lower than θ_B, the reflected field of order zero (i.e. the Fresnel reflection factor) has almost the same absolute value as the real part of the coherent scattered field, $\mathcal{R}\{<A^{(2)}>\}$, with a different sign.
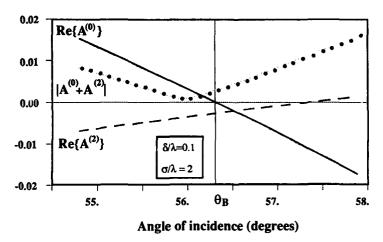
Figure1: Coherent reflected field

These two components interfere destructively producing a minimum in the modulus of the reflected field at an angle lower than the Brewster's angle. Since the coherent scattered field has an imaginary part, the interference between the zero order reflected field which is real, and the coherent scattered field, which is always complex (see ref. 2), cannot produce a zero value. Furthermore, it is seen that if the slope of $<A^{(2)}>$ versus the angle of incidence θ is modified, the location of the minimum may change considerably.

III Calculation of the angular shift of the Brewster's angle

In order to find the angular shift of the Brewster's angle, we search for the location of the minimum of the modulus of the coherent (specular) reflected field when the angle of incidence is varied. We assume that this shift is small in order to expand the formulas for the field around the Brewster's angle θ_B. Expanding the fields to the first order around k_B and neglecting second order terms leads to a closed form expression of the angular shift [2]. This formula gives explicitly the dependance of the shift upon δ and σ. In Fig. 2, the angular value of the shift $\delta\theta$ is given as a function of δ for different values of σ. It is seen that the angular shift varies like δ^2 and increases when σ decreases. In Fig. 3, $\delta\theta$ is displayed versus σ, it varies like σ^{-1} in the range $[0-\lambda]$.

In conclusion, let us note that although we have restricted our discussion to 1-D surfaces z=S(x) in order to allow a comparison between this approach and the numerical results, the basic mechanism proposed here should be valid for the more general case of a 2-D surface z=S(x,y). This problem remains to be examined in detail. Moreover, the predicted values of the shift should be verified by a suitable experiment.
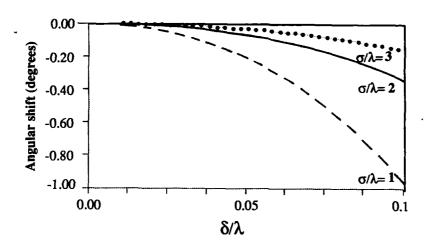
Figure 2: Angular shift vs the roughness δ/λ
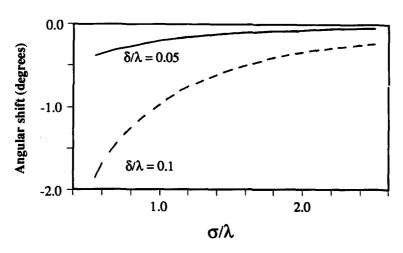
Figure 3 : Angular shift vs the correlation distance σ/λ

References

1. M. Saillard and D. Maystre, J.Opt.Soc.Am. **7**, pp982-990, 1990

2. J.-J. Greffet, submitted to Phys.Rev.Lett.

3 J.-J. Greffet, Phys.Rev.B**37**,pp6436-6441, 1988

4. A.A.Maradudin, J.Opt.Soc.Am. **6**, pp759-764, 1983

POSTER SESSION 1

POLARIZATION EFFECTS DURING SPATIAL STOCHASTIZATION OF OPTICAL FIELDS.

A.G.Ushenko and S.B.Yermolenko

Chernovtsy University, 2 Kotsyubinsky Street, 274012 Chernovtsy, U.S.S.R.   Tel. 44730.

Laser wave interaction with a rough surface is known to result in an object field with a complex amplitude, phase and polarization structure. The polarization structure, which has been studied less extensively, is analyzed here in the edge, Fresnel and Fraunhofer fields.

The edge field correlation zone associated with a randomly oriented rough surface site is found to be polarization modulated as a result of Fresnel and diffraction interactions of the radiation with the secondary microstructure. Besides, interference of the wave fronts and the polarization angles Ψ_M and $\Psi_m^{(i)}$ is observed. The resulting intensity of an edge field speckle can be written as

$$ I = M^2 + m_i^2 \cos^2\left(\Psi_M - \Psi_m^{(i)}\right) + 2M m_i \cos\left(\Psi_M - \Psi_m^{(i)}\right) \cos\Delta , \quad (1) $$

where M is the amplitude of the optical vibrations reflected by a site, m_i are the corresponding amplitudes of the field resulting from the radiation reflected by the secondary structure of the site, and Δ is the local phase shift. Since $m_i \ll M$, the resulting amplitude variation is insignificant. The corresponding value of the angle of polarization will be given by

$$ \Psi = \operatorname{arctg} \frac{M \sin\Psi_M + m_i \sin\Psi_m^{(i)}}{M \cos\Psi_M + m_i \cos\Psi_m^{(i)}} . \quad (2) $$

Speckle formation in the Fresnel field can be described by statistical interference of randomly phased wave fronts with different polarizations. The angle of polarization within a speckle in the Fresnel field will then be given by

$$ \Psi_s = \operatorname{arctg} \frac{\sum_{k=1}^{S} \sum_{j=1}^{S} A_k \sin\Psi_j}{\sum_{k=1}^{S} \sum_{j=1}^{S} A_k \cos\Psi_j} , \quad (3) $$

where A_κ are the arbitrary amplitudes of wave fronts forming an individual speckle, and S is the number of contributions.
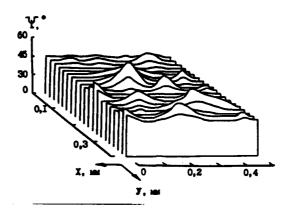
Fig.1. Distribution of angles of polarization in an edge field
       correlation zone obtained by line scanning of its image.

The resulting trajectory of the electric-field vector at each point of the speckle can be obtained from the equation

$$\frac{X^2}{\sum_\kappa \sum_s A_\kappa^2 \sin^2 \Psi_s} + \frac{Y^2}{\sum_\kappa \sum_s A_\kappa^2 \cos^2 \Psi_s} - \frac{2XY}{\sum_\kappa \sum_s A^2 \sin \Psi_s \cos \Psi_s} \cos\Delta = \sin^2\Delta . \tag{4}$$

At points where the resulting phase progression Δ =0°, linearly polarized optical vibrations

$$Y = \Psi' \cdot X \tag{5}$$

with randomly distributed angles of polarization

$$\Psi' = arctg \frac{\sum_\kappa \sum_s A_\kappa \sin \Psi_s}{\sum_\kappa \sum_s A_\kappa \cos \Psi_s} \tag{6}$$

will be observed.

As the phase progression increases, the linearly polarized parts of the speckle become elliptically polarized.

In the Fraunhofer field, speckles result from a large number of interfering plane wave fronts with phase progressions differing by not more than $\pi/4$. The angles of polarization are, however, modulated to a certain extent due to the diffraction superposition

of wave fronts resulting from inhomogeneities with like slopes.
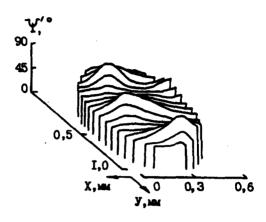
Fig.2. Polarization microstructure of a speckle in the Fresnel
field.
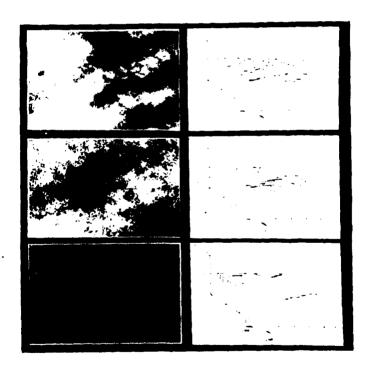
Fig.3. Polarization structure of a Fraunhofer field speckle at 50
cm, 100 cm and 300 cm from the surface.

123

The speckle structure is seen to remain practically unchanged with the distance, and changes in scale only are observed. However, when viewed through an analyzer, the structure reveals polarization modulation which can be described by a family of distributions $\widetilde{\Psi}$.

It is thus concluded that during spatial stochastization of coherent fields, polarization microstructure of speckles is observed in all diffraction fields.

Accurate determination of the Optical Properties of Biological Tissues using a Monte Carlo Inversion Technique

P2

P. van der Zee, M. Essenpreis, D.T. Delpy, M. Cope
Department of Medical Physics and Bio-Engineering
1st Floor Shropshire House
11-20 Capper Street
London WC1E 6JA
Tel 071-380-9700 Ex 8850

Introduction

There is an increasing use of optical methods in medicine, both for diagnostic and patient treatment purposes. For a better understanding of the measurements made for diagnostic purposes, and for a more accurate prediction of the therapeutic effect of optical forms of treatment, it is essential to have a knowledge of light transport in tissue, and to know the optical parameters of the tissue which govern this light transport. The near infrared (700-1100 nm) is a wavelength region of great clinical interest because of the relatively high transparency of most tissues at these wavelengths. In this wavelength range the parameters required for an accurate description of the light transport are the absorption coefficient μ_a, the scattering coefficient μ_s, and the single scattering phase function. The latter can be determined by measuring the angular distribution of the light scattered from an optically thin sample when illuminated by a well collimated beam. The coefficients μ_a and μ_s are determined from a measurement of the diffuse reflectance and transmittance of an optically thick sample for either diffuse or collimated illumination. In this paper we will present a new method to determine μ_a and μ_s based on a Monte Carlo inversion technique. We will compare the scattering and absorption spectra obtained with this method to those obtained with a conventional Kubelka Munk inversion.

Measurement of diffuse transmittance and reflectance

The system used for the measurement of diffuse reflectance and transmittance is shown in figure 1. A collimated light beam illuminates the tissue sample which is held between the two integrating spheres that are used to measure the diffusely reflected and transmitted light. For a monochromatic light source, the detectors employed can be photomultiplier tubes or photo diodes. When a broad band light source is used, the detector consists of a spectrograph or other monochromator. Figure 2 shows in more detail the sample and the sample holder. A slice of tissue is clamped between two thin glass slides, with a spacer of internal diameter A and thickness d fixing the dimensions of the sample.
Typical values are 5-20 mm for A and 1-2 mm for d.

Conventional methods of inversion

Some model for light transport in tissue is needed to give the relation between the absorption and scattering coefficients of the sample and the resulting diffuse reflectance and transmittance. By inverting this relation either analytically or numerically, values for μ_a and μ_s for the tissue can be determined from the measured values of diffuse reflectance and transmittance. In the past most authors have used the Kubelka Munk (KM) theory[1,2] for this purpose, since the simple analytical expression for diffuse transmittance and reflectance that it produces can be readily inverted[3,4,5]. More recently, 1D approximations of the diffusion theory have been used[6,7,8]. Both of these methods however are inexact, and this can lead to significant errors in the calculated optical parameters. Some of the reasons for this are:

1) Both the KM theory and the diffusion model assume an isotropic light distribution in the tissue.
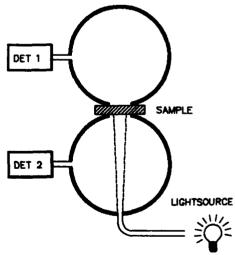
Figure 1 Integrating sphere system

This can lead to large errors because the sample is often only a few scattering lengths in thickness and therefore the light distribution is not in the multiple scattering regime. Also the absorption is not always much smaller than the scattering, which is another requirement for an isotropic distribution.

2) The scattering is assumed to be isotropic in the case of the KM model and at best linearly anisotropic in the case of the diffusion model. This is not realistic for biological tissues where the single scattering phase function is not isotropic but shows a strongly forward peaked distribution[9,10].

Figure 2 Detail of sample holder for integrating sphere

3) The KM and the diffusion model are both one dimensional models and are therefore strictly speaking only valid for an infinite slab geometry. The extent to which this can be approached with a real tissue sample is limited. The maximum diameter of the sample is limited by the largest size of the biological specimen that can be obtained as well as the size of the integrating sphere porthole. The sample thickness has to be considerably larger than the scattering length. In practice these constraints lead to a typical ratio between sample diameter and thickness of about five. The assumption of an infinite slab can therefore introduce sizeable errors.

4) Specular reflection and refraction of the light at the air-glass and the glass-tissue interfaces considerably alter both the light distribution inside the sample and the measured transmittance and reflectance. In particular the internal reflections at the glass-air boundaries can be as much as 60% for an isotropic light field. The specular reflection is highly dependant upon the angle of incidence of the light. Since neither the KM theory nor the diffusion theory give the angular distribution of the light field inside the sample, and because this distribution cannot be assumed to be isotropic, a proper correction for the specular reflection and refraction is impossible with these models.

5) Finally, the coefficients K and S which are produced by the KM theory are not true constants for the tissue but depend to some extent upon parameters such as the sample thickness. Furthermore they can only be related to the true μ_a and μ_s under certain simplifying assumptions.

Monte Carlo model

To avoid the problems of these former methods for the determination of μ_a and μ_s a Monte Carlo model for light transport in tissue was used. The model developed uses a measured single scattering phase function for the determination of the scattering angles and gives a full 3D description of light transport in tissue. It can also take into account the geometry of the tissue sample and the light beam, and the effect of specular refraction and reflection of the light at the boundaries as a function of the angle of incidence[11,12,13].

Monte Carlo inversion method

Given the tissue geometry, its single scattering phase function and a set of μ_a and μ_s values, the MC model will generate a set of transmittance and reflectance values. The problem is to invert this. An iterative method which would rerun the model for every set of μ_a and μ_s values in the iteration loop is impractical since it would consume a prohibitive amount of computer time. The MC model was therefore used to generate a lookup table of pairs of transmittance and reflectance values for a discrete set of μ_a and μ_s values. For each pair of measured transmittance and reflectance values, the inversion thus reduces to a search in the lookup table for the closest match of transmittance and reflectance values. This is followed by a linear interpolation between neighbouring values to increase precision and resolution.
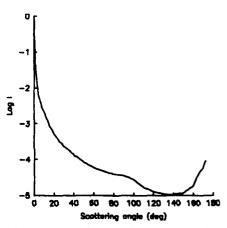
Figure 3 Phase function for adult rat brain

Results

To illustrate the results that are obtained with this technique, data from measurements on rat brain are presented. A quartz halogen light source and a CCD spectrograph detector[14] was used in the integrating sphere assembly of figure 1 to make measurements on samples of brain tissue from adult Wistar rats. The sample thickness d was 1.56 mm, the sample porthole p was 10 mm in diameter and the sample diameter A was 14.3 mm (figure 2). The blood content of the brain was minimised by ventilating the anaesthetized animal with 100% oxygen and exchanging the blood with physiological saline until death (Initial brain haematocrit 35% final haematocrit value of ~2%). The brain was then removed and stored in physiological saline at 4°C until needed. The single scattering phase functions for these samples were measured using a goniometer system with a collimated source and detector arrangement[11]. The angular resolution of this system was 0.5°. Figure 3 shows the average phase function for rat brain, determined from 7 different samples
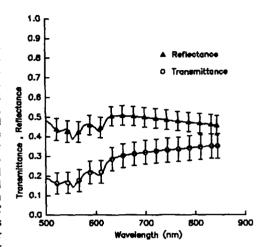
Figure 4 Average diffuse reflectance and transmittance for ratbrain.

from 4 rats. The average value for the cosine of the scattering angle, g was 0.82. With these phase functions and the geometric parameters of the integrating sphere system, the MC model was used to generate a lookup table. Figure 4 shows the average raw transmittance and reflectance spectra for a total of 19 samples from 4 different rats, while figure 5 gives the resulting spectra for μ_a and μ_s as produced by the Monte Carlo inversion method. The error bars in these spectra are the standard deviations. These result to a small extent from noise in the measurements, but largely from variation within the different samples.

For comparison, the same reflectance and transmittance data was analyzed using the KM theory. The external and internal specular reflection values were taken to be 4.4% and 53.9% respectively, where the latter is calculated for an isotropic light distribution in the tissue. These values are based on refractive indices for glass and tissue of 1.516 and 1.40 respectively. The transmittance and reflectance data were corrected for this using the expressions given by Kottler[15]. The K and S values produced by the KM equations were converted into μ_a and μ_s values using the expressions given by van Gemert[16] and the value for g. Figure 6 shows the results.

Discussion

The MC results for μ_a clearly show the absorption peaks of reduced cyt_{aa3} at 605 nm, cyt_b at 556 and 524 nm and cyt_c at 553 and 522 nm. For wavelengths above 650 nm the absorption spectrum is flat, as would be expected from the known absorption spectra for the cytochromes. There is no trace of the haemoglobin peak at 760 nm, confirming the low brain haematocrit. Results for μ_s show a marked decrease of scattering with wavelength. When comparing the MC and the KM results the following observations can be made: i) For μ_s, the KM values are between 5 and 100% higher than those for the MC result. Also, the peak to trough ratio for the spectrum between the peak at 553 and the minimum at 580 nm is 2.84 for the KM spectrum and 2.15 for the MC spectrum.
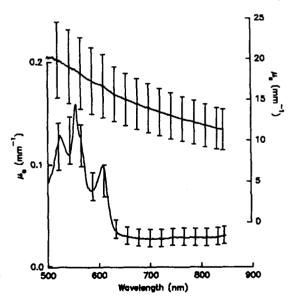
Figure 5 Absorption and scattering results obtained with the Monte Carlo method

Finally, there is a marked increase in the KM μ_a value with increasing wavelength above 650 nm. This seems to be a mirror image of the scattering spectrum. ii) For μ_s, the ratios between the KM values and the MC values are 0.68 at 500 nm and 0.48 at 850 nm, with the KM spectrum showing a markedly faster decrease with wavelength than the MC spectrum. More importantly however, the KM result shows marked fluctuations at the shorter wavelengths, coinciding with peaks in the absorption spectrum. This 'cross talk' between the μ_a and μ_s seems to be a general problem with data analyzed with the KM model. It can also be observed in μ_a and μ_s data obtained by using the 1D diffusion approximation[7,8].

Figure 6 Absorption and scattering results obtained with the KM theory.

Conclusion

Conventional methods of analyzing diffuse reflectance and transmittance tissue measurements using the KM or 1D diffusion model are very approximate in nature. Comparison of results obtained with the KM model with those of an exact MC model show that the KM model leads to considerable errors in both the μ_a and the μ_s spectra. Notably, the 'cross talk' between the absorption and the scattering spectrum is an artifact caused by the KM model. A similar observation can be made about μ_a and μ_s data published using the 1D diffusion model. The use of a more exact model for the analysis of diffuse reflectance and transmittance data is therefore very desirable.

References
1. Kubelka, P. and Munk, F. (1931) Zeitschrift Technischer Physik 12,593.
2. Kubelka, P. (1948) Journal of the Optical Society of America 38, 448-457
3. Wan S. et al (1981) Photochemistry and Photobiology, 34, 493-499.
4. Eggert, H.R. et al (1987) Neurosurgery, 21, 459-464.
5. Oraevsky, A.A. et al (1988) Lasers in the Life Sciences, 2, 275-288.
6. van Gemert, M.J.C. et al (1988) Lasers in the Life Sciences, 2, 1-18.
7. Karagiannes, J.L. (1989) Applied Optics, 28, 2311-2317.
8. Parsa, P. et al (1989) Applied Optics, 28, 2325-2330.
9. Flock, S.T.et al (1987) Medical Physics 14, 835-841.
10. Marchesini, R. et al (1989) Applied Optics 28, 2318-2324.
11. van der Zee, P. et al (1987) in: Adv. in Exp. Med. & Biol., 215, 179-192.
12. Delpy, D.T. et al (1988) Physics in Medicine and Biology 33:1433-1442
13. van der Zee, P. PhD thesis, University of London (In preparation).
14. Cope, M. et al (1989) Adv. in Exp. Med. & Biol., 247, 33-40
15. Kottler, F. (1980) Journal of the Optical Society of America, 50, 483-490.
16. van Gemert, M.J.C. et al (1987) Lasers in the Life Sciences, 1, 287-298.

Light scattering and speckle in folded path propagation problems

P3

E.R. Méndez, H.M. Escamilla,

División de Física Aplicada

Centro de Educación Científica y de Educación Superior de

Ensenada,

Apdo.Postal 2732

Ensenada, BC 22800, México.

Telephone: + 52-667-44501 to 06, ext.306

and

Z.H.Gu

Surface Optics Corporation

P.O.Box 261602

San Diego, CA 92126, U.S.A.

Telephone: + 619-578.8910

The phenomenon of enhanced backscattering has attracted a great deal of attention in recent years. This phenomenon has been observed in a variety of systems and situations. Of particular interest due to its relative simplicity and wide applicability is the problem of scattering in folded paths. This problem has been studied both, experimentally and theoretically.[1,2,3] However, to our knowledge, only the mean intensity and the spatial coherence function of the scattered light have been studied.

In this work we address scattering problems with the same

geometry as the one considered in Ref.2, and we make similar assumptions in formulating the problem. However, our analysis is based on an expression for the complex amplitude that can be obtained by manipulating the diffraction integrals appearing in the usual analysis. This expression has a simple physical interpretation, and also has some advantages over the techniques that have been reported so far, permitting analytical progress. For simplicity, we have only considered the one-dimensional or corrugated case, but the results can be easily generalized to two dimensions.

With this approach, we are able to derive exact (within the model) analytical expressions for the mean intensity and the amplitude correlation of the backscattered field. We find that the intensity exhibits backscattering enhancement, a fact that has already been observed and studied by several authors. However, we have also studied the motion of the speckle pattern, as one moves the angle of incidence. We find that the speckle pattern seems to track the backscattering direction, an effect that has been encountered and studied in volume scattering situations.[4] Another interesting result that can be seen by interpreting the calculated correlation is that under some circumstances, the speckle pattern produced in these geometries exhibits symmetries about the backscattering direction. This theoretical study is complemented by experiments that confirm our findings.

1.- Yu.A.Kravtsov and A.I.Saichev, "Effects of double passage of waves in randomly inhomogeneous media", Sov.Phys.Usp. **25**, 494-508 (1982).

2.- E.Jakeman, "Enhanced backscattering through a deep random phase screen", J.Opt.Soc.Am A **5**, 1638-1648 (1988).

3.- P.R.Tapster, A.R.Weeks, and E.Jakeman, "Observation of backscattering enhancement through atmospheric phase screens", J.Opt.Soc.Am. A **6**, 517-522 (1989).

4.- S.Feng, "Novel correlations and fluctuations in speckle patterns", in Scattering and Localization of Classical Waves in Random Media, P.Sheng,ed. (World Scientific, Singapore, 1990).

Time-Dependent Multiple Scattering of a Laser Beam   **P4**
Calculated by a Recursion Relation

Konrad Altmann

Messerschmitt–Bölkow–Blohm GmbH, ZTA 11 Optics Departement
P.O.Box 80 11 09, D–8000 München 80, Germany
Phone (089) 607 25696 Telefax (089) 607 25157

In Refs.1 and 2 a model for the recursive calculation of time-dependent multiple forward scattering was presented. In the mean time, the restriction to forward scattering could be dropped i.e. it was possible to generalize the model to scattering into the full solid angle.

The model uses an analytic-stochastic approach to transport theory, tracing the route of a collection of propagating photons, which are stochastically scattered and absorbed by the particles of the medium. Different from other recent work, the analytic-stochastic approach is used here in connection with a special coordinate system, which is particularly suited to derive a procedure for the recursive calculation of the contributions of the individual scattering orders to the total irradiance.

The concept of the model can be explained by the use of Fig.1. The photon starts at the transmitter T, is scattered at the points P_1 to P_n, and arrives with a certain probablity at the receiver R. The problem is to integrate this probability over all possible paths of the photon. To do this, the basic idea was to make up the path of the photon by triangles, which are obtained by drawing lines from each scattering point P_i to the receiver R. The triangles can rotate with respect to each other around said lines. Simultaneously the angles φ_i and χ_i can vary between zero and π. The recursion procedure consists in calculating the scattering irradiance for n^{th} order scattering from $(n-1)^{th}$ order scattering. Related to Fig.1 this means that the triangle TRP_1 is removed for the moment and the irradiance is calculated for a photon starting at point P_1. Then, point P_1 is thrug t to move along the line TP_1 radiating with an angular characteristic identical to the scattering phase f nction. In this way the irradiance of n-times scattering is obtained from (n-1)-times scattering.
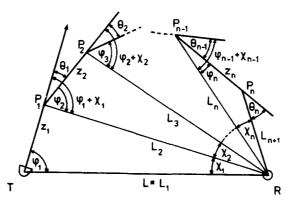
Fig. 1. Schematic representation of the n-fold scattering of a laser beam with vanishing divergence at the points P_1 to P_n through the angles θ_1 to θ_n, respectively.

Througthout the analytical description full mathematical accuracy is kept including spherical trigonometry for the angular relations between the scattering angles and the triangles.

133

Definitions and results of the analytical work can only be summarized here, details will be described in a publication being prepared presently[3].

The entire laser beam including transmitter and receiver is assumed to be embedded in a well mixed particulate medium, which can be completely described by the scattering coefficient σ_s, the extinction coefficient σ_e, and the single scattering phase function $P(\theta)$.

The dimensionless products of σ_s and σ_e with the distance L between laser and receiver, usually called optical depth, are designated by

$$\Delta_s = \sigma_s L, \tag{1}$$

$$\Delta_e = \sigma_e L. \tag{2}$$

In the present paper the scattering phase function is described by the following mathematical expression

$$P(\theta) = \frac{\tilde{\alpha}}{4\pi \sinh\tilde{\alpha}} \exp(\tilde{\alpha}\cos\theta), \tag{3}$$

where θ is the scattering angle. This equation holds in the full solid angle domain. For $\tilde{\alpha}=0$, $P(\theta)$ is a constant. With growing $\tilde{\alpha}$ however, it asymptotically approaches a Gaussian distribution with decreasing width. By the use of a sum of expressions of this type real phase functions can be approximated with high accuracy. The phase function can however be introduced also directly in digital form into the model[3].

The receiver is assumed to be open, that is, to register radiation incident from all directions with equal sensitivity.

Under these assumptions the multiple scattering irradiance $G^0(\varphi_1, t)$ initiated by a temporal δ-pulse of vanishing divergence can be expressed by the following series expansion with respect to the scattering order n

$$G^0(\varphi_1, t) = \exp\left[-\Delta_e\left(1 + \frac{\tilde{t}}{\tilde{\alpha}}\right)\right] \frac{\alpha^3 c}{\pi L^3 \sin\varphi_1} \sum_{n=1}^{\infty} \frac{\Delta_s^n}{\left[1 - \exp(-2\tilde{\alpha})\right]^n} A_n(\tilde{\varphi}_1, \tilde{t}), \tag{4}$$

where the zeroth order term, that means the unscattered contribution, is omitted. G^0 is rotationally symmetric with respect to the initial beam axis and is thus a function of the the angular offset φ_1 of the receiver with respect to this beam axis, and the time coordinate t. α is equal to $\sqrt{\tilde{\alpha}/2}$. $\tilde{\varphi}_1$ and $\tilde{t}$ are normalized coordinates with the normalization taken as follows

$$\tilde{\varphi}_1 = \alpha\varphi_1, \tag{5a}$$

$$\tilde{t} = \tilde{\alpha}ct/L. \tag{5b}$$

The series expansion is carried through with the help of the generalized functions $A_n(\tilde{\varphi}_1, \tilde{t})$ which only depend on the normalized coordinates $\tilde{\varphi}_1$, $\tilde{t}$, and the angular width $1/\alpha$ of the scattering phase function. Therefore, these functions have to be calculated just once for a given scattering phase function. Since the functions A_n describe the contributions of the individual scattering orders to the deformation of a temporal δ-pulse with vanishing divergence they represent in some sense Green's functions of time-dependent multiple scattering.

The first order function A_1 is given by

$$A_1(\tilde{\varphi}_1, \tilde{t}) = \frac{2u_1}{\alpha(u_1^2 + v^2)} \exp\left(-\tilde{\alpha}\frac{2v^2}{u_1^2 + v^2}\right). \tag{6}$$

Here and in the following

$$u_{1(2)} = \sin(\tilde{\varphi}_{1(2)}/\alpha), \tag{7}$$

$$v_{(1)} = 1 - \cos(\tilde{\varphi}_1/\alpha) + \tilde{t}_{(1)}/\tilde{\alpha}. \tag{8}$$

134

For n=2 and n=3 the functions A_n are given by the following recursion relation

$$A_n(\tilde{\varphi}_1,\tilde{t}) = 4u_1\alpha \int\limits_{1-\cos(\tilde{\varphi}_1/\alpha)}^{v} dv_1 \frac{\tau_1^{2-n}}{u_1^2+v_1^2} \int\limits_0^{\alpha\pi} d\tilde{\varphi}_2 I_0(\tilde{\alpha}\tau_1 u_1 u_2) \exp\left\{\tilde{\alpha}\left[\frac{u_1^2-v_1^2}{u_1^2+v_1^2}\cos(\tilde{\varphi}_2/\alpha)-1\right]\right\} A_{n-1}(\tilde{\varphi}_2,[v-v_1]\tau_1\tilde{\alpha}) \qquad (9)$$

where I_0 is the modified Bessel function of zeroth order, and

$$\tau_1 = 2v_1/(u_1^2+v_1^2). \qquad (10)$$

For n≥4 Eq.(9) does not work any longer, since for n≥4 the functions A_n diverge proportionally to $\tilde{t}^{\,n-3}$ for large $\tilde{t}$. Therefore, the functions A_n have been replaced by functions $\tilde{A}_n$ defined as follows

$$\tilde{A}_n(\tilde{\varphi}_1,\tilde{t}) = \tilde{t}^{2-n} A_n(\tilde{\varphi}_1,\tilde{t}) \text{ for } n≥3. \qquad (11)$$

For the functions $\tilde{A}_n$ a recursion relation similar to Eq.(9) can be derived in a straightforward manner by inserting Eq.(11) into Eq.(9). In this way, A_n can be calculated from A_{n-1} by the use of a 2-D numerical integration.

To check the accuracy of the numerical results obtained by the use of the recursion procedure the following relation can be derived analytically with the help of the renewal theorem[4]

$$\frac{1}{[1-\exp(-2\tilde{\alpha})]^n} \int\limits_0^{\alpha\pi} d\tilde{\varphi}_1 \int\limits_0^{\infty} d\tilde{t} \left(\frac{\tilde{\alpha}}{\tilde{\alpha}+\tilde{t}}\right)^{n+1} A_n(\tilde{\varphi}_1,\tilde{t}) = \frac{1}{n!}. \qquad (12)$$

Except fore some additional factors, the left hand side of this equation represents the integral of A_n over the domain of definition of the variables $\tilde{\varphi}_1$ and $\tilde{t}$. Eq.(12) is very important, since, in connection with the above equations, it allows for the first time control of the numerical accuracy of multiple scattering computations to a high degree.

Analogous to the forward scattering limit as described in Ref. 2, also in the general case three features can be directly concluded from the recursion relation given by Eq.(9). Since, according to this relation, the step from n-1 to n represents a procedure similar to a convolution, the functions A_n are smoothed from one step to the other. Simultaneously, since each increase in the number of scattering events causes an additional time delay, the centroid of the functions A_n is shifted towards increasing $\tilde{t}$. Most pronounced evidence of these features is found for small values of n. These more qualitative features correlate with the formal finding that, for n>1, at $\tilde{t}$=0 all functions A_n increase proportionally to $\tilde{t}^{\,n-1}$ for $\tilde{\varphi}_1$>0. Thus, they have a zero of (n-1)-th order at $\tilde{t}$=0. This third feature can be derived analytically from Eq.(9).

Numerical calculations have been carried through with the parameter $\tilde{\alpha}$ varying from 2 up to infinity. The last value represents the forward scattering limit, since, according to Eq.(3), for this $\tilde{\alpha}$ value $P(\theta)$ transforms into an infinitely small Gaussian distribution. Passing to this limit, the functions $A_n(\tilde{\varphi}_1,\tilde{t})$ change into the corresponding functions $S_n(\tilde{\varphi}_1,\tilde{t})$ as defined in Ref.1. Thus, it was possible to compare the results for the forward scattering limit, as presented in Ref.2, with those obtained for phase functions showing a relatively broad maximum as in the case $\tilde{\alpha}$=2. For low scattering orders i.e. n=1 to 3, this comparison revealed the very surprising result that, provided the normalization is chosen as in Eqs.(5), the shape of the functions A_n does not change essentially when $\tilde{\alpha}$ is increased from 2 to infinity. For n≥4 this similarity disappeared, instead, on the basis of the numerical results, a power law was found for the shape of the A_n which has been already quoted in Eq.(11). It was noticed that for large $\tilde{t}$ the A_n assume the following asymtotic form

$$A_n(\tilde{\varphi}_1,\tilde{t}) = C(\tilde{\alpha},n)\tilde{t}^{\,n-3}\sin\varphi_1 \qquad (13)$$

with the constant C depending on $\tilde{\alpha}$ and n only, and not on the angle $\tilde{\varphi}_1$. Since $\lim\limits_{\tilde{\alpha}\to\infty} C(\tilde{\alpha},n) = 0$, which can be proved

analytically, this power law does not appear in the forward scattering limit. This fact can already be observed for $n=3$. For this value of n the functions A_n converge to a constant greater than zero for $\tilde{\alpha}\geq 0$, whereas they vanish for $\tilde{\alpha}\to\infty$. For $n=4$, a linear increase of the A_n with $\tilde{t}$ was found numerically for $\tilde{\alpha}=2$ which leads to a considerable deviation between the cases $\tilde{\alpha}=2$ and $\tilde{\alpha}\to\infty$ for larger $\tilde{t}$. The case $n=7$ is shown in Fig. 2. To eliminate the dependence on $\sin\varphi_1$ the combination $A_7(\tilde{\varphi}_1,\tilde{t})/(\alpha\sin\varphi_1)$ is shown in the diagram. The graphs for $\tilde{\varphi}_1\leq 0.05$ are condensed into one line since they nearly coincide. Moreover, even the graph for $\tilde{\varphi}_1=0.5$ does not deviate very much from this line. In Fig. 2. the power law becomes clearly evident only for $\tilde{\varphi}_1=1.5$, but for values of $\tilde{t}$ larger than those shown in Fig. 2, the asymptotic increase being proportional to $\tilde{t}^4$ becomes dominant for much smaller values of $\tilde{\varphi}_1$ as well. The existence of this power law can in principle be explained analytically on the basis of the recursion relation for the functions A_n, but the details have not yet been understood sufficiently, and are thus subject of current research.
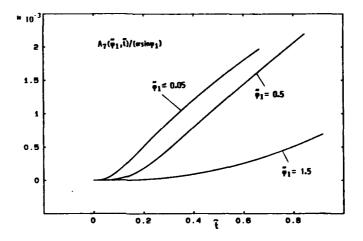
Fig. 2. Graphs of the function $A_7(\tilde{\varphi}_1,\tilde{t})/(\alpha\sin\varphi_1)$ for $\tilde{\alpha}=2$.

These findings show, that the recursion model may be useful to deduce general features of multiple scattering. Other advantages and capabilities of the model may be summarized as follows:

* High numerical accuracy which can be checked with the help of Eq.(12). By the use of this relation it could be shown that, up to high scattering orders, a numerical accuracy of few units per thousand was achieved. As a consequence of this high accuracy the model seems to be an ideal candidate to check the reliability of Monte-Carlo calculations as well as approximate models like Bissonnette's.
* Numerical check of the reliability of the small-angle approximations also for cw irradiation (e.g. the model of Tam and Zardecki)
* Exact computation of multiple scattering and pulse deformation in media of high particle density.

REFERENCES

1. K.Altmann, "Space-Time Distortion of Laser Pulses due to Multiple Scattering in Particulate Media", Appl.Opt., 27, 2451-2460(1988).

2. K.Altmann, "Recursive Calculation of Time-Dependent Multiple Forward Scattering", 3rd Int. workshop on Multiple Scattering Lidar Experiments, Oberpfaffenhofen F.R.G., Oct. 24-26, 1989, pp. 103-119.

3. K.Altmann, "Recursive Calculation of Time-Dependent Multiple Scattering: Exact Stochastic-Analytic Model for an Infinite Medium", in preparation.

4. U.G.Oppel, A.Findling, W.Krichbaumer, S.Krieglmeier, and M.Noormohammadian, "A Stochastic Model for the Calculation of Multiply Scattered Lidar Returns", German Aerospace Research Establishment (DLR), Oberpfaffenhofen F.R,G., DLR-FB 89-36, pp. 50-65.

Time correlation of far-field laser speckle produced by **P5**
a longitudinally moving diffuse object

Marek Kowalczyk

University of Warsaw, Faculty of Physics, Institute of Geophysics
Pasteura 7, 02-093 Warsaw, Poland; phone: (48-22) 235 281

We analyze the space-time and time autocorrelation functions of intensity fluctuation in the far-field laser speckle produced by a diffuse object that moves uniformly along the axis of illuminating Gaussian beam. Our analysis is aimed at the conditions under which intensity fluctuation detected by a point detector is stationary. We are interested in stationarity of dynamic-speckle fields because this feature plays a crucial role in laser-speckle velocimetry [1].

We consider two classes of deep transmitting diffusers: white -noise diffusers whose whose amplitude transmittance has the autocorrelation function of the form

$$R_w(\vec{x}_1, \vec{x}_2) = \langle \exp\{i[\phi(\vec{x}_1)\}\exp\{-i[\phi(\vec{x}_2)]\}\rangle = \Delta S \; \delta(\vec{x}_1 - \vec{x}_2),$$

where $\phi(\vec{x})$ is the phase shift introduced at the point $\vec{x}$, δ is a Dirac delta function and ΔS is the correlation area of $\exp[i\phi(\vec{x})]$ and Gaussian diffusers with Gaussian correlation of surface roughness. For such diffusers

$$R_w(\vec{x}_1, \vec{x}_2) = \exp\left[-|\vec{x}_1-\vec{x}_2|^2/\beta^2\right] .$$

where β stands for the effective correlation length defined as

$$\beta = r_\phi/\sigma_\phi ,$$

with r_ϕ and σ_ϕ being the correlation length and the standard deviation of the phase respectively. In our calculations the amplitude transmittance functions are multiplied by a window function, so that the finite size of practical diffusers is taken into account.

We have shown that the detected fluctuation of speckle intensity is a wide-sense stationary process if the following conditions are met:

(1) a source of illuminating Gaussian beam moves uniformly with respect to a diffuse object,

(2) the point detector remains immobile with respect to the diffuse object, and

(3) the width of the illuminating beam in the object plane is smaller than the diffuser size.

The corresponding time autocorrelation function has a Lorentzian shape and the correlation length $t' = 2\pi w_0^2/(\lambda|v|)$, where w_0 is the illuminating beam width at the beam waist plane, λ is the wave-length and v is the velocity at which varies the distance z between the beam waist and the diffuser.

Condition (3) means that stationarity of the speckle-intensity fluctuation is conditioned by simultaneous presence of two ef-

138

fects: variation in illuminating spot size (number of microscat-
terers) and variation in illuminating wavefront curvature.

The results we have obtained for the white-noise diffusers are
slightly different than those obtained for the Gaussian ones. For
the Gaussian diffuser the time autocorrelation functions of
speckle intensity depend on the angle at which the detecting
point is seen from the center of diffuser plane, whereas for the
white-noise diffuser do not. This concerns both stationary and
nonstationary cases. Moreover, if the diameter of Gaussian dif-
fuser fulfills inequalities $w^2 \gg D^2 > (2\pi|A|)^{-1}$, where w is the
illuminating beam width at the diffuser plane, D is the diameter
of diffuser and

$$A = \frac{1}{4\lambda}\left(\frac{1}{\rho(t_1)} - \frac{1}{\rho(t_2)}\right) ,$$

with ρ being the curvature of illuminating wavefront and the
distance z fulfills the far-field illumination condition, then
approximated form of the correlation coefficient of intensity
fluctuation depends only on time delay $t = t_1 - t_2$:

$$r_{\Delta I}(t;\vec{y}) = \frac{1}{1 + (t/t'')^2} \exp\left[-2\left(\frac{\pi\beta}{\lambda R_0}\right)^2 \frac{(t/t'')^2 |\vec{y}|^2}{1 + (t/t'')^2}\right] ,$$

where R_0 is the distance between diffuser and observation plane,
$\vec{y}$ is the coordinate of detecting point and

$$t'' = \frac{\pi\beta^2}{\lambda|v|} .$$

Thus, in this particular case the speckle intensity fluctuation is stationary irrespective of the fact that the condition (3) is not met. It is seen that $r_{\Delta I}(t;\vec{y})$ is Lorentzian and t'' has the meaning of correlation length only in the case of $|\vec{y}| = 0$.

From the above equation it results that by measurement of t'' (with a point photodetector placed at $|\vec{y}|=0$) we can determine the correlation length β, assuming that λ and v are known. With two measurements of t'' performed for two different wavelengths the correlation length r_ϕ and the standard deviation σ_ϕ can be measured.

Finally, we conclude that from the point of view of speckle velocimetry there is no essential difference between near-field [2] and far-field speckle fluctuation produced by a longitudinally moving diffuse objects.

References

1. T.Asakura and N.Takai, "Dynamic laser speckles and their application to velocity measurements of the diffuse object," Appl.Phys. 25, 179-194(1981) and references therein.

2. M.Kowalczyk and E.Bernabeu, "Space-time correlation properties of dynamic laser speckle in the near diffraction field of a longitudinally moving diffuse object," J.Opt.Soc.Am A, 6, 758(1989).

Jaroslav Holoubek

Institute of Macromolecular Chemistry, Czechoslovak Academy of Sciences,
162 06 Prague 6, Czechoslovakia
Phone: (422)360341

In this paper two problems are discussed. In section 1 the formalism of Mueller matrix is applied to the light scattering from a single anisotropic particle. In section 2 some application of the speckle effect caused by light scattering by multiparticle system are presented.

1. Small-angle light scattering by an anisotropic sphere

If the Stokes vector S is used to characterize the radiation, the transformation matrix, a 4x4 matrix called Mueller matrix[1] , is a characteristic of the medium and its determination is a necessary and major part of a complete optical description of a medium. We present the explicit form of the matrix which characterizes the small-angle light scattering from an anisotropic sphere when requirements of the Rayleigh-Gans-Debye (RGD) approximation are fulfilled[2]. We compare the angular dependences of single matrix elements for the Lorenz-Mie (LM) sphere (designation F_{ij}), with those of the appropriate form of the presented matrix (designated f_{ij}) for the case of a sphere without inherent anisotropy, i.e $\Delta n = n_r - n_t = 0$ (where n_r and n_t are the refractive indices in the direction of the radius and in the tangential direction). In the Figure 1 we present the comparison of the angular dependences of F_{11} and f_{11} elements for model parameters given in Table I.

Table I Optical parameters used in calculations of the corresponding matrix elements f_{ij} (the RGD approximation[2]) and F_{ij} (the LM theory, program BHMIE[1]); n_s is the refractive index of surrounding medium $\bar{n}$ is the relative refractive index. In the last column is the value of the phase shift.

Sample	Radius	Refractive indices			$2kR\,|\bar{n}-1|$
	R [μm]	n_s	$n_r = n_t$	$\bar{n}$	
1	1.00	1.49	1.514	1.0161	0.320
2	1.00	1.505	1.514	1.0060	0.119

The angular dependence of F_{11} is calculated according the LM theory using BHMIE program[1], f_{11} dependence is based on the presented approximation.
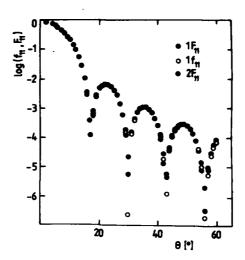
Fig.1 Angular dependences of matrix elements f_{11} for the sphere in the RGD approximation and F_{11} for the LM sphere. The optical parameters of models are summarized in Table I.

As can be inferred from Fig.1, the angular dependences of the F_{11} and f_{11} elements are in good accord. For f_{12} and f_{33} elements the RGD solution forms an envelope curve sui generis to the LM solution in accordance with the recent results[3]. The calculation of F_{34} elements for models in Table I confirms the necessity to include these elements into the theoretical description not restricted to the RGD approximation. The angular dependences of f_{ij} matrix elements for an anisotropic sphere are influenced by the magnitude and sign of the $(\bar{n}-1)/\Delta n$ parameter. Not surprisingly, the angular dependences for an anisotropic particle are more complex and are discussed in more detail elsewhere[2].

2. Light scattering and speckle effect

We restrict ourselves in this paper to the speckle patterns (SPs) created by propagation of the coherent light through an optically heterogeneous system (typically polymer film) in the arrangement usual for the small-angle light

scattering method (a single beam illumination and SP detection in the far-field). The methods in which the speckle effect is utilized can be generally characterized as techniques based on measurements of the intensity correlation of scattered light[4]. In the following we present methods of the spatial correlation measurements of two speckle patterns based on:

    a) statistical properties of SPs,

    b) subtraction and clipping.

a) A statistical analysis based on the measurement of the probability density function of addition of two correlated SPs provides the degree of correlation between them. By fitting the experimental data to the theoretical probability density function[5] the modulus of the normalized cross-correlation function of speckle amplitude $|\mu_A|$ can be obtained.

b) Subtraction and clipping of speckle patterns

The clipped representation is defined as

$$I_i' = \begin{cases} 1 & , \text{ if } I_i > c_i \\ 0 & , \text{ otherwise} \end{cases} \qquad (1)$$

The value of difference $< |I_1 - I_2|' >$ depends on the correlation between SPs and on the clipping threshold c_i. The explicit relation has the form:

$$(1/4 <I>) < |I_1 - I_2|' > = \exp \{-c / [<I> (1-|\mu_A|^2)^{1/2}] \} \qquad (2)$$

where $|\mu_A|$ is the modulus of the normalized cross-correlation function of speckle amplitudes. In the Fig.2 are presented results of correlation measurements based on this approach The sample used are polymer films with thickness 50 μm (P5), 160 μm (P0, P8) and 380 μmm (B2, B3) with different supermolecular structure. The determination of the correlation between SPs with different orientation of the polarization plane may provide a useful characterization of the light scattering from depolarizing media.

It can be concluded, that besides the measurement of surface roughness, deformation and displacement there is variety of other speckle-based methods. This paper presents a brief consideration of theoretical concepts and experimental methods with stress on application in material research.
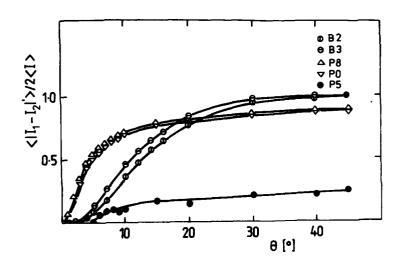
Fig.2 Dependence of $< |I_1 - I_2|'>$ on the difference of polarization plane orientation of subtracted SPs for samples B2,B3, P0, P8 and P5

References:
1.C.F.Bohren and D.R.Huffman, Absorption and Scattering by Small Particles (Wiley, New York; 1983)
2.J.Holoubek, Appl.Opt., in press
3.W.S.Bickel, A.J.Watkins and G.Videen, Am.J.Phys.55, 559(1987)
4.J.C.Dainty, Ed., Laser Speckle and Related Phenomena (Springer Verlag, Berlin-Heidelberg, 1975)
5.J.Holoubek, H.Krug, J.Křepelka, J.Peřina and Z.Hradil, J.Modern Opt.34, 633(1987)

THE BREWSTER'S LAW FOR REFLECTION FROM PERIODICALLY-INHOMOGENEOUS LAYER

S.M.Golynski, V.D.Gusev

Dept. Physics of the Atmosphere, Physics Faculty,

Moscow State University, Moscow 119899 GSP, USSR,

tel.:939-32-52

The artificial periodic inhomogeneities of the electron density in the ionosphere plasma can arise as result of powerful radiation influence. Such periodic formations have a strong hold over radiowaves propagation stimulating effective backscattering under certain conditions. Such a situation can take place in other problems of radiophysics, optics and acoustics.

We consider a one-dimensional periodic layer situated in the area $0 < z < L$. The dielectric constant of the layer's medium is $\mathcal{E}(z)=1+\mathcal{E}_1(z)$, $\mathcal{E}_1(z)= \mu \times \cos 2bz$, where μ and b are real positive quantities ($\mu < 1$). We assume that $\mathcal{E}(z)=1$ outside the layer. The problems of the oblique incidence of linear-polarized waves are investigated (θ_0 is the angle of incidence). We describe a wave with the electric vector E perpendicular to the incidence plane XZ as the TE-wave ($E_x=E_z=0$, $E_y \neq 0$), and a wave with the magnetic vector H perpendicular to the incidence plane as the TM-wave ($H_x=H_z=0$, $H_y \neq 0$).

Firstly we consider the reflection of the TE-wave $E_y(x,z)=E(z)e^{ik s_0 x}$ ($s_0 = \sin\theta_0$, $c_0=\cos\theta_0$), which satisfies the Helmholtz equation inside the medium

$$E'' + k^2 \left[\mathcal{E}(z) - s_0^2 \right] E = 0 \tag{1}$$

with the corresponding conditions of continuity on the both boundaries. Here k is a free-space wave number and the prime denotes the differentiation with respect to z. We assume that the incident wave has a unit amplitude, i.e. $E_0(z)=e^{i\tilde{\kappa}z}$ ($\tilde{k}=kc_0$). In the area $z>L$ we have the transparent wave $E_T(z)=T_\perp e^{i\tilde{\kappa}z}$ and in the area $z<0$ the reflected wave $E_R(z)=R_\perp e^{-i\tilde{\kappa}z}$. The unknown amplitudes T and R are complex transparency and reflection coefficients. The general solution of (1) can be represented in the form of two linear-independent waves, propagating in opposite directions

$$E = A\beta^{1/2}e^{i\tilde{\kappa}\Phi} + B\beta^{1/2}e^{-i\tilde{\kappa}\Phi}, \qquad \Phi = \int_z^z \beta^{-1}(z)\,dz .$$

Here A and B are integration constants defined by boundary conditions. The only unknown function $\beta(z)$ satisfies the nonlinear differential equation of the second order

$$2\beta\beta'' - (\beta')^2 + 4\tilde{\kappa}^2 \left[1 + c_0^{-2}\mathcal{E}_1 \right] \beta^2 - 4\tilde{\kappa}^2 = 0 \tag{2}$$

For initial conditions of (2) it is reasonable to use the result of geometrical optics approach (the WKB-method) $\beta(z)=c_0(\mathcal{E}-s_0^2)^{-1/2}$ [1], i.e.

$$\beta(z=0) = \beta_0 = \left[1 + \mu/c_0^2 \right]^{-1/2}, \quad \beta'(z=0) = 0 \tag{3}$$

In what follows we consider the simpliest case of very small inhomogeneities (for the ionosphere plasma – $\mu \sim 10^{-3}$)

$$\mu \ll c_0^2 \tag{4}$$

So for the initial conditions (3) we have approximately

$$\beta_0 \simeq 1, \quad \beta_0' = 0 . \tag{3'}$$

In this case the reflection and transparency coefficients, the general expressions for which can be derived by means of the boundary conditions, take the forms

$$R_\perp = -\frac{\beta_L' + 2i\tilde{\kappa}(1-\beta_L)}{\beta_L' - 2i\tilde{\kappa}(1+\beta_L)} e^{2i\tilde{\kappa}\Phi}, \qquad T_\perp = -\frac{4i\tilde{\kappa}\beta_L^{1/2}}{\beta_L' - 2i\tilde{\kappa}(1+\beta_L)} e^{-i\tilde{\kappa}(L-\Phi)} \tag{5}$$

Here the lower index L means the values of the corresponding functions on the upper boundary. The reflectability of the layer is defined by the reflection coefficient (5)

$$|R_\perp|^2 = \frac{\beta_L'^2 + 4\tilde{\kappa}^2(1-\beta_L)^2}{\beta_L'^2 + 4\tilde{\kappa}^2(1+\beta_L)^2} = 1 - |T_\perp|^2. \qquad (6)$$

To determine the unknown function β (z) we pass from (2) to the equivalent integral equation – the linear integral equation of the Volterra type, namely,

$$\beta(z) = 1 + \tilde{\kappa} \int_0^z \mathcal{H}(z,s)\,\beta(s)\,ds, \qquad (7)$$

where

$$\mathcal{H}(z,s) = -\frac{1}{2\tilde{\kappa}^2}\left\{\Omega_1(s)\sin 2\tilde{\kappa}(z-s) + \frac{1}{4\tilde{\kappa}}\Omega_1'(s)\left[1-\cos 2\tilde{\kappa}(z-s)\right]\right\},$$

$$\Omega_1(s) = 4\kappa^2\varepsilon_1 = 4\kappa^2\mu\cos 2bs.$$

To solve (7) we use the successive approximation method and conclude that the amplitudes of the progressive waves grow exponentially under the condition $\tilde{k}=nb$ ($n=1,2,\ldots$) [2] . Physically it means the increasing of reflection from the layer (the area of intransparency). The resonance values of $\tilde{k}$ lay in the domains of unstable solutions of the Mathieu equation, which is identical to the initial equation (1). For the most important in the practical applications case of the main resonance ($\tilde{k}=b$) we obtain the asymptotic solution ($\tilde{k}z \gg 1$) of (7)

$$\beta(z) \approx ch\, d_1 z - sh\, d_1 z \sin 2\tilde{\kappa}z, \qquad d_1 = \mu\kappa/2c_o. \qquad (8)$$

So the derivative of this function under condition (4) has a form

$$\beta'(z) \approx -2\tilde{\kappa}\,sh\,d_1 z\,\cos 2\tilde{\kappa}z. \qquad (9)$$

Substituting (8) and (9) into (6) we obtain the layer's reflectability for the case in question

$$|R_\perp|^2 \approx th^2\left(\frac{d_1 L}{2}\right) = th^2\left(\frac{\mu\kappa L}{2c_o}\right). \qquad (10)$$

To investigate the reflection of the TM-wave $H_y(x,y)=H(z)e^{i\kappa S_o x}$ it is reasonable to use the equation [1]

$$\varepsilon\left[\varepsilon^{-1}H'\right]' + \kappa^2\left(\varepsilon - S_o^2\right)H = 0 \qquad (11)$$

with the corresponding conditions of continuity for H and $\varepsilon^{-1}H'$ on the both boundaries.

The general solution of (11) can be represented in the form of the two progressive waves also

$$H = C(\varepsilon\gamma)^{1/2}e^{i\tilde{\kappa}\Psi} + D(\varepsilon\gamma)^{1/2}e^{-i\tilde{\kappa}\Psi}, \qquad \Psi = \int_0^z \gamma^{-1}(s)\,ds,$$

where C and D are integration constants and the unknown function γ (z) satisfies the equation

$$2\gamma\gamma'' - (\gamma')^2 + \gamma^2\left[4\kappa^2(\varepsilon - S_o^2) + 2\frac{\varepsilon''}{\varepsilon} - 3\left(\frac{\varepsilon'}{\varepsilon}\right)^2\right] - 4\tilde{\kappa}^2 = 0$$

with the initial conditions similar to (3). Under condition (4) we keep in this equation the terms of the first order of μ only, i.e. we consider the equation

$$2\gamma\gamma'' - (\gamma')^2 + \left(4\tilde{\kappa}^2 + \Omega_2\right)\gamma^2 - 4\tilde{\kappa}^2 = 0, \qquad (12)$$

$$\gamma_o = 1, \quad \gamma_o' = 0. \quad (\Omega_2 = 4\kappa^2\varepsilon_1 + 2\varepsilon_1'').$$

All the following calculations are analogous to the previous ones. Due to the condition (4) the formulas (5) and (6) are the same for the waves of the both types except the formal change of symbol β for γ . So the main difference for the TE- and TM-waves reflection in the case considered is connected with the difference of asymptotic solutions of (2) and (12).
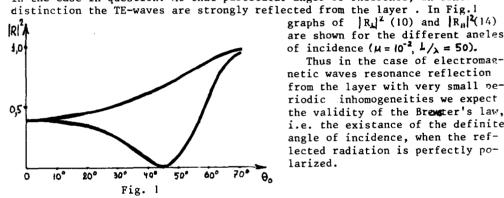
The nonlinear differential equation (12) can be transformed to the linear

integral equation analogous to (7), where we use the function $\Omega_2(z)$ instead of $\Omega_1(z)$. Analyzing the main resonance case ($\tilde{k}=b$), we obtain the asymptotic solution($\tilde{k}z \gg 1$)

$$\gamma(z) \approx ch\,\alpha_2 z - sh\,\alpha_2 z \sin 2\tilde{k}z \quad , \quad \alpha_2 = \frac{\mu K}{2C_0} \cos 2\theta_0 \qquad (13)$$

and the reflectability of the layer in the case of the TM-wave incidence

$$|R_{\shortparallel}|^2 = th^2\left(\frac{\alpha_2 L}{2}\right) = th^2\left(\frac{\mu K L}{4C_0} \cos 2\theta_0\right) \qquad (14)$$

Let us now discuss briefly the results obtained. The solutions (8) and (13) make it possible to calculate all the characteristics of the TE- and TM-waves both for the transparent radiation and reflected radia   1 in the case under consideration. So we have the full solution for the p blem of transparent and reflected radiation polarization. we conclude such a layer

Comparing the reflectabilities (10) and (14) of the layer, can play the role of the resonance polarizator. Really, when the angle of the incidence is equal to $\pi/4$, the TM-waves pass through the layer without reflection in the case in question. At that particular angle of incidence, in contradistinction the TE-waves are strongly reflected from the layer . In Fig.1 graphs of $|R_\perp|^2$ (10) and $|R_{\shortparallel}|^2$ (14) are shown for the different angles of incidence ($\mu = 10^{-2}, L/\lambda = 50$).

Fig. 1

Thus in the case of electromagnetic waves resonance reflection from the layer with very small periodic inhomogeneities we expect the validity of the Brewster's law, i.e. the existance of the definite angle of incidence, when the reflected radiation is perfectly polarized.

References:
1. V.L. Ginzburg, Propagation of Electromagnetic Waves in Plasma (Gordon & Breach, N.Y., 1961)
2. V.I. Klyatskin, Invariant Imbedding Method in the Theory of Wave Propagation (Nauka, Moscow, 1986)

Angular Correlations of Speckle Patterns

R Syratt and J C Dainty
Blackett Laboratory, Imperial College,
London SW7 2BZ, UK.
Telephone: +44 71 225 8847

Introduction

Following the experimental observation of enhanced backscattering from randomly rough surfaces by Mendez and O'Donnell[1,2], there has been a renewed interest in light scattering by very rough surfaces (whose rms roughness σ is greater than the optical wavelength λ). The experimental work to date has focussed on the average scattered intensity (scattering cross-section), where the average is actually over a solid angle, i.e. over many speckles; this solid angle is small compared to the structure expected in the average intensity and is therefore a good approximation to the ensemble average (the quantity that is found by numerical computations).

Enhanced backscattering was first observed for scattering from dense random media[3-5] and the basic mechanism for the volume and surface cases is the same: multiple scattering permits coherent co-operative effects that may result, in the backscatter direction, in an enhancement of intensity over the incoherent case of a factor of up to two. In the volume case, it has also been shown that the higher order statistics of the scattered intensity, in particular angular and wavelength correlations, contain interest information about the scattering medium[6]. The present work on surfaces is motivated by the results reported on dense volumes and aims to investigate the role of multiple scattering, if any, in angular correlations from random rough surfaces. The starting point is the experimental and theoretical work of Léger and Perrin[7,8] who, in a single scattering approximation showed that the angular correlation was a simple function of rms roughness σ of the surface (independent of the correlation length).

Experiments

Suppose that a collimated monochromatic beam of light is incident at angle θ_i ($-90° < \theta_i < 90°$) to the mean surface normal on an isotropic random surface. This beam defines a plane of incidence and in this paper we shall consider only scattering angles θ_s ($-90° < \theta_s < 90°$) in this plane; the angles θ_i and θ_s are defined in opposite senses, so that the specular direction is $\theta_s = \theta_i$ and backscatter is $\theta_s = -\theta_i$. Let $I(\theta_i, \theta_s)$ denote the scattered intensity at the scattering angle θ_s for an incident angle θ_i. We are interested in the normalised correlation between $I(\theta_i, \theta_s)$ and $I(\theta_i', \theta_s')$, where the primed and unprimed quantities are different angles:

$$C(\theta_i, \theta_s; \theta_i', \theta_s') \quad = \quad \frac{< I(\theta_i, \theta_s) \, I(\theta_i', \theta_s') >}{<I(\theta_i, \theta_s)><I(\theta_i', \theta_s')>} \quad - \quad 1.$$

Of particular interest in the initial experiments is the quantity $C(\theta_i, \theta_s=\theta_i; \theta_i', \theta_s'=\theta_i')$, which is the correlation of intensities in the specular directions for two different illumination angles.

In practice, the ensemble average has to be estimated by a finite angular average. In our experiments, we use a charge-coupled-device (CCD) camera to view around the specular direction with a total angular field of view of approx 10×13 mrad, the mean speckle diameter being on the order of 1 mrad. For each incidence angle, typically 25 frames viewed in the specular direction are averaged to reduce measurement noise, and the average frames are cross-correlated with each other to yield an estimate of the angular correlation $C(\theta_i, \theta_s=\theta_i; \theta_i', \theta_s'=\theta_i')$ for a set of pairs of incidence angles θ_i and θ_i'.

In our poster we shall show results for low- and high-sloped surfaces and comparisons with theoretical predictions.

References

1 E R Mendez and K A O'Donnell, Opt Commun, **61**, 91–95 (1987)
2 K A O'Donnell and E R Mendez, J Opt Soc Am A, **4**, 1194–1205 (1987)
3 Y Kuga and A Ishimaru, J Opt Soc Am A, **1**, 831–835 (1984)
4 M P van Albada and A Lagendijk, Phys Rev Lett, **55**, 2692–2695 (1985)
5 P-E Wolf and G Maret, Phys Rev Lett, **55**, 2696–2699 (1985)
6 S Feng, in *Scattering and Localisation of Classical Waves in Random Media*, edited by P Sheng, World Scientific Press, Singapore, 1990, pp179–206
7 D Léger, E Mathieu and J C Perrin, Appl Opt, **14**, 872–877 (1975)
8 D Léger and J C Perrin, J Opt Soc Am, **66**, 1210–1216 (1996)

A new method for measuring position-dependent volume reflection
Experimental setup and first results

R.A.Bolt and J.J.ten Bosch
Lab. for Materia Technica, Dental School, Groningen University
A. Deusinglaan 1, 9713 AV Groningen, The Netherlands
phone [31]50633140, fax [31]50633159

1 Introduction

Light transport in turbid media plays an important role in many applications, e.g. meteorology, medical applications, paint, and food industry.

Many studies have been done concerning transmission and absorption of radiation, some with angular dependence of reflection. Studies dealing with position dependent volume reflection are rare and usually focus on the diffusion area of the volume reflection pattern, i.e. the situation after many scattering events. (See for example [1], [2], [3])

The 'intermediate case' where neither the diffusion nor the single scattering approach is valid has hardly been studied. Our method is aimed at this part of the volume reflection pattern. We expect that this part of the reflection pattern is very sensitive to changes in g, and that it is possible to get information about g from of this part of the reflection pattern. More specific information can be derived by combining the 'intermediate case' with the diffusion case; one can determine a and s(1-g) from behaviour in the diffusion case. [1]

This paper describes the experimental setup, its properties and first results obtained with the equipment.

A sample is illuminated by a pencil-beam with normal incidence. The incident light is scattered by and absorbed in the sample. This results in a radiance profile at the surface of the sample. This profile is imaged by a lens onto a 2-dimensional detector, so that the radiance can be measured as a function of position. As a light source a HeNe laser is used.

2 Measuring method.

The measuring equipment is shown schematically in fig. 1.

The beam of a HeNe laser (4 mW at 632.8 nm) is directed onto a 10 μm pinhole. The pinhole is imaged onto the surface of the sample via a coated pellicle (reflection = transmission = 40%) using a microscope objective (4x, NA 0.12). The spot-size on the sample is approximately 100 μm, the beam divergence $\pm$ 10 mrad. The intensity profile on the sample surface, resulting from volume-reflection, is imaged onto a CCD-camera (EG&G-PAR, M 1430-P) using an enlarger lens (Rodenstock Apo-Rodagon 80 mm,
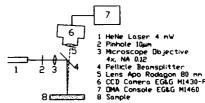
1 HeNe Laser 4 mW
2 Pinhole 10μm
3 Microscope Objective 4x, NA 0.12
4 Pellicle Beamsplitter
5 Lens Apo Rodagon 80 mm
6 CCD Camera EG&G MI430-P
7 OMA Console EG&G MI460
8 Sample

Fig. 1 The experimental setup.

F/4..F/22). The selected aperture is typically F/6.9. The surface of the sample is oriented horizontally. To eliminate the influence of specular reflection from the surface of the sample, the optical axis of the camera is tilted with respect to the optical axis of the illuminating system. The tilt is chosen such that the specular reflection falls just outside the aperture of the lens; in this way the specular reflection is not imaged onto the detector. A typical tilt angle is 75 mrad. To reduce thermal effects, like darkcurrent, the camera is cooled to -50°C. The quantity measured is counts/(pixel•sec), corresponding to $W•sr^{-1}•m^{-2}$, i.e. the radiance L. The image is transmitted to an OMA-console (EG&G-PAR, M 1460) for storage and simple calculations. For more complicated calculations a PC-386 is used.

The camera offers a 14 bit dynamic range, with a non linearity better than 1%. Field of view is variable from 8x12 mm to 80x120 mm. The spatial resolution is maximum 380*570 pixels. Integration time can be chosen from 20 msec upward. The readout-time varies, the typical value is 100 μs per pixel.

A regular, thick plate, beamsplitter would introduce ghost-images, displaced from the central beam by approx. 0.75x the thickness of the beamsplitter . Thus, the use of a pellicle beam-splitter is essential for measuring close to the illuminating beam.

3 Measuring procedure.
The radiance profile due to volume-reflection is measured and stored in the OMA-console, as described before.

To minimize noise, especially at low intensities, multiple pictures are added, typical 50. The integration time is chosen so that detector response is about 90% of saturation value. A typical value is 1 sec. The results are corrected for darkcurrent, offset and background signals. To reduce the influence of speckle, the sample is moved at 1 stroke per second in a horizontal plane, with a hub of 0.5 mm.

The illuminating flux is determined by measuring the reflection from a freshly prepared, diffusely reflecting, $BaSO_4$ tablet, according to DIN 5033 and CIE-standard [4].

4 Calibration of the equipment
The radiance pattern was determined for various samples, namely Teflon (PTFE), and suspensions of water-diluted latex paint.

In fig. 2 a cross section through the radiance profile of some of these samples is given on a log_{10} scale.

For a homogeneous and isotropic medium the radiance pattern must be circularly symmetric. In fig. 3 the radiance pattern determined using a diluted latex sample (2.26 ‰ latex paint in water) is plotted on a log_{10} scale. The dynamic range in these data is approximately 10 bits. The pattern is almost circularly symmetric. The method used to determine the centre is by determination of the centre of gravity for points with equal radiance. The centre-points determined in this way are randomly distributed around the actual centre.
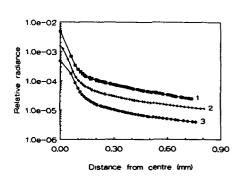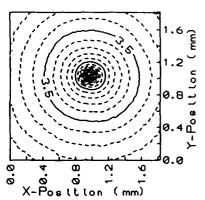
Fig 2. The relative radiance profile for 1) PTFE, 2) latex 2.26 % in water and 3) latex 0.82 % in water.

Fig 3. Equi-radiance pattern for a diluted latex sample (2.26 % latex paint in water).

From the measurements the integrated reflection in the normal direction was determined by calculating the integrated radiance (eq. 1). For large values of r this converges to the relative reflectance.

$$R_{CCD}(r) = \frac{\left[\int_0^r 2\pi r' L(r') \, dr'\right]_{Sample}}{\left[\int_0^\infty 2\pi r' L(r') \, dr'\right]_{BaSO_4}}$$

$$\triangleq \frac{\left[\sum_n^{(r_s-r)} r_n L(r_n) \Delta r\right]_{Sample}}{\left[\sum_n^\infty r_n L(r_n) \Delta r\right]_{BaSO_4}} \qquad (1)$$

Fig 4. Convergence of the integrated relative reflectance for a BaSO$_4$ tablet.

$L(r_n)$ is the radiance as determined at a distance r_n from the centre of the radiance pattern. The results of these calculations are plotted in fig. 4 for a BaSO$_4$ tablet. This tablet is used as a reference to determine the relative radiance, thus the integrated relative reflectance converges to 100%. From this graph we can determine the spot-size at the surface of this sample, this gives a spot-size at half height of approximately 100μm.

5 Comparison of the results with earlier work.

Volume reflection has been studied for the diffusion case, particularly by Groenhuis et al [1] and Bonner et al [2].

a) Comparison to Groenhuis et al.

Groenhuis et al [1] used diffusion theory to derive an approximating formula for the

153

relative radiance $L_r(r)$:

$$L_r(r) = \frac{C_1}{\sqrt{r}} e^{(-C_2 r)} \qquad (2)$$

This approximation is valid assuming large values of r.

Plotting $ln(L_r(r)*\sqrt{r})$ must give us a straight line. In figure 5 the radiance pattern determined using a 2.26 ‰ latex sample (also shown in fig. 2) is plotted in this way. The agreement is very good for large r. ($r > 0.3$ mm) C_2 amounts to 1.01 mm^{-1}
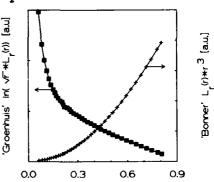
b) Comparison to Bonner et al.

Bonner et al [2] used random walk theory. In the absorbtion-free case their eq. 12 leads to :

$$L_r(r) * r^3 = Constant \qquad (3)$$
$$(for\ large\ r)$$

In figure 5 the radiance pattern determined using the same 2.26 ‰ latex sample is plotted in this way too. For the data as presented here eq. 3 does not describe the situation properly.

The approximation used is only valid for large values of r. The maximum value of r for the data presented here is 0.8 mm, which may not be large enough. Furthermore, Bonner assumes scatterers with $g=0$, located on a cubic grid. These assumptions are not valid for the materials under study.

Fig 5. Comparison of the results to Groenhuis and Bonner for the case of a 2.26‰ latex sample.

7 Conclusions.

With the setup as described in this paper it is possible to measure radiance profiles on samples illuminated by a pencil beam, down to a very short distance from the illuminating beam. Scanning of the pattern is not necessary. The spatial resolution and dynamics are good.

8 References

[1]   Groenhuis et al, Appl. Optics 22, 16, pp 2463..2467
[2]   Bonner et al, J. Opt. Soc. Am. A, 4, 3, pp 423..432
[3]   Schmidt et al, J. Opt. Soc. Am. A, 7, 11, pp 2141..2153
[4]   CIE publication nº 38, pp 123..124
[5]   Groenhuis et al, Appl. Optics 22, 16, pp 2456..2462

AND MEDIA

O.V.Angelsky and P.P.Maksimyak

Chernovtsy University, 2 Kotsyubinsky Street, 274012 Chernovtsy,
U.S.S.R.   Tel.44730.

Optical correlation methods are prospective for diagnostics
of phase-inhomogeneous objects and media since they ensure a
higher speed and precision of measurement/1-3/. Among the presen-
tly available optical correlation methods, the most promising
seems to be the one based on the measurement of the transverse
coherence function of the scattered field. Such measurements
have been made using a Mach-Zehnder interferometer arrangement,
and gave good results for slightly rough surfaces/4,5/. The me-
thod, however, has some limitations associated with the longitu-
dinal relative displacement of the interfering beams which accom-
panies the transverse relative displacement.

We propose here a new method for measuring the transverse
coherence function which allows to remove the above limitation.
The method utilizes a polarization displacement interferometer
arrangement which is shown in Figure 1.

Fig.1. Experimental setup for optical measurements: 1: laser, 2:
collimator, 3:sample, 4 and 7:polarizers, 5 and 6:biref-
ringent wedges, 8:objective lens, 9:field diaphragm, 10:
photodetector.

The displacement interferometer consists of two identical wedges cut from a birefringent crystalline material. The wedges form a plane-parallel plate. The principal axes of the wedges make a 90° angle with the beam propagation direction. The polarizers are crossed and make a 45° angle with the optical axes of the wedges. The beam exiting from one of the wedges is split into an ordinary and an extraordinary beams as a result of the difference in the refractive indices. After passing the other wedge, the rays propagate collinearly but with a relative displacement S given by

$$S = l\,(tg\,d_0 - tg\,d_e)\cos\varphi \qquad (1)$$

where l is the separation between the wedges, d_0, d_e are the angles of refraction of the ordinary and the extraordinary beams, respectively, and φ is the wedge angle. By moving the second wedge along the beam axis, one obtains alternating minimum and maximum intensities which can be used to calculate the transverse coherence function.

The above technique ensures much higher vibration resistance and resolution, and smaller longitudinal relative displacement of the split beam components as compared with the presently available interference techniques. The method was applied to measure polished plane-parallel plates cut from $LiNbO_3$, BaF_2 or GaP crystals with varying degrees of perfection.

Calculations were carried out using the random phase screen model/4/ which assumes an infinitely extended object, smooth surface inhomogeneity profile, and phase dispersion $6_s^2 < 1$.

The results of the phase correlation function $\psi_s(\rho)$ measurements obtained for various crystals are found to be in good agreement with X-ray topographs for these crystals.

The proposed method is also applicable to the studies of turbulence in liquids. For a special case of a plane wave propagating in a turbulent medium, one can employ the ray optics theory to obtain the following expressions for the transverse coherence function $\Gamma_\perp(\rho)$, phase dispersion $6_\perp^2$ and the structure function of the resulting field/4/

$$\Gamma_\perp(\rho) = \exp\left[-\tfrac{1}{2} D_\perp(\rho)\right],$$

$$D_\perp(\rho) = \begin{cases} 0{,}73\, C_\varepsilon^2 L\, k^2 \rho^{\frac{5}{3}}, & \rho \gg l_o \\ 0{,}82\, C_\varepsilon^2 L\, k^2 l_o^{-\frac{1}{3}} \rho^2, & \rho \ll l_o \end{cases} \qquad (2)$$

$$\sigma_\perp^2 = 0{,}1\, k^2 L\, C_\varepsilon^2 L_o^{\frac{5}{3}},$$

where C_ε^2 is the structure parameter of turbulence, l_o, L_o are the micro- and macroscales of turbulence, respectively, and L is the turbulent layer thickness. For $\rho = l_o$, the values of asymptotic expressions for $D_\perp(\rho)$ will be the same, and one can obtain l_o from the intersection of these curves. The values of C_ε^2 and L_o are also obtained from eq.(2).

Thus, by going over from the above quantities to the structure functions of the field, one can obtain the structure parameters C_ε^2 , L_o , l_o of a turbulent medium from the measured coherence function $\Gamma_\perp(\rho)$. Measurements were carried out on benzene, which confirmed the efficiency of the method.

The advantages of the proposed method for diagnostics of slightly rough surfaces are illustrated by Table 1, in which the results of the measurements on plane-parallel plates of fused quartz are given. The mean height deviation is seen to be about 25 Å.

Table 1. Surface roughness parameters of fused quartz samples. Profil.metric results are included for comparison.

Sample No.	1	2	3	4	5
Profilometric R_m measurement, μm	0.0833	0.0615	0.0437	0.0150	0.0112
Optical R_m measurement, μm.	0.0754	0.0586	0.0399	0.0131	0.0073

REFERENCES

/1/ H.Baltes et al., Inverse Source Problems in Optics, ed.by H.P.Baltes, Berlin: Springer, 1978, p.196.

/2/ V.M.Moiseyev, V.I.Mandrosov, Zarubezhnaya Radioelektr., 2, 3 (1982).

/3/ O.V.Angelsky and P.P.Maksimyak, Applied Optics, 5, (1990)

/4/ S.M.Rytov, Yu.A.Kravtsov, V.I.Tatarsky, Introduction to Sta-
    tistical Radiophysics. Part II. Random Fields (in Russian),
    Moscow: Nauka, 1978, p.464.

/5/ A.S.Monin and A.M.Yaglom, Statistical Hydromechanics. Part I.
    Moscow, 1965; Part II. Moscow, 1967 (in Russian).

SPATIAL STOCHASTIZATION OF OPTICAL FIELDS AND OPTICAL DIAGNOS- **P11**
TICS OF OBJECTS WITH LARGE PHASE INHOMOGENEITIES.

O.V.Angelsky, P.P.Maksimyak, I.I.Magun, and T.O.Perun

Chernovtsy University, 2 Kotsyubinsky Street, 274012 Chernovtsy,
U.S.S.R. Tel. 44730.

Laser wave interaction with a randomly phased object (RPO)
is known to result in a scattered field having a complex ampli-
tude and phase distribution called a speckle pattern. A unique
relationship between the RPO statistical structure parameters
and the correlation parameters of the field has been established
within the random phase screen model for RPOs with the phase dis-
persion $\sigma_{\varphi_0}^2 < 1$ /1/. This relationship has been used to develop se-
veral optical methods for measuring statistical field parame-
ters/2/.

However, for objects with large phase inhomogeneities, for
which $\sigma_{\varphi_0}^2 > 1$, the above relationship no longer exists. The pre-
sent paper deals with laser fields resulting from interaction
with such objects, with a view to investigate the possibilities
of their optical diagnostics by using the theory of stochastic
and chaotic vibrations/3/. The theory is shown to be applicable
to description of the RPO structure and the optical fields.
As the phase inhomogeneity increases, zero field amplitudes
appear, and interference fringe branching is observed, which is
interpreted as resulting from multiple changes of the spatial
frequency. The spatial stochastization of the field is represen-
ted as a sequence of bifurcations of the duplicating spatial pe-
riod.

The correlation dimension ν is used for numerical descrip-
tion of the stochastic optical field. The choice of this parame-
ter as a particular value of the generalized dimension of the
chaos was dictated by the fact that it lends itself to numeri-
cal procedures and is convenient for processing of experimental
results/3/. A well known procedure by Packard and Takens/4,5/ is
used to estimate the correlation dimension of the chaos in the

optical field, which makes possible to restrict the discussion to a single phase space coordinate, i.e. the object field intensity $I(\vec{r})$.

The objects were assumed to have the form of sinusoidal gratings. Plane wave diffraction by such a structure results in a superposition of plane waves whose propagation directions with respect to surface normal are given by

$$\sin\varphi_k = \pm k \frac{\lambda}{d}, \quad k = 0, 1, 2, \ldots \tag{1}$$

where λ is the wavelength, and d is the grating period. The amplitudes of the waves are given by $A_k \sim i^k J_k(h)$, J_k being the k-th order Bessel function of the first kind, h is the grating element height, and the number of waves k depends on the grating period.

The nature of the spatial distribution of intensity $I(\vec{r})$, i.e. the set of spatial frequencies, resulting from interference of all the waves diffracted by the grating, depends on the h value. The maximum spatial frequency in the intensity distribution increases with the grating element height h.

For a grating which is a superposition of m harmonic components with incommensurate periods d_m, the diffracted radiation will form a superposition of m sets of plane waves. For each set, the conditions of propagation will be given by expressions similar to eq.(1). Interference of all the diffracted waves will then result in a field $I(\vec{r})$.

The above results were compared to those of the measurements on complex diffraction gratings which were obtained holographically by multiple exposures using different number of beams, and good agreement was obtained.

The measurements of the correlation dimension of the object structure carried out on several rough surfaces indicated that it has a limit, $\vartheta \sim 4$, i.e. one can speak of a stochastic rather than random structure.

It is thus concluded that the correlation dimension of chaos in the object field depends on the height parameters of the diffraction structure, and shows a linear dependence on the number of such structures with incommensurate periods, i.e. on the corre-

lation dimension of the object structure. The correlation dimension of the actual phased objects is found to be limited, which means that the correlation dimension of chaos in the fields generated by such objects will be limited too.

The above findings make the prospects of structure diagnostics of RPOs with large phase inhomogeneities rather favourable, at least one can speak of a real possibility of making estimates of the anharmonicity of the object structure.

Our future work will be concerned with measurements of the correlation dimension of chaos in fields generated by actual two-dimensional phased objects, such as rough surfaces, liquid crystals, etc.

REFERENCES

/1/ S.M.Rytov, Yu.A.Kravtsov, and V.I.Tatarsky, Introduction to Statistical Radiophysics. Part II. Random Fields (in Russian) Nauka, Moscow, 1978, p.464.

/2/ O.V.Angelsky and P.P.Maksimyak, Appl.Optics 29, 2894 (1990).

/3/ Yu.I.Neymark and P.C.Landa, Stochastic and Chaotic Vibrations (in Russian), Nauka, Moscow, 1987, p.424.

/4/ N.H.Packard, J.P.Grutchfield, J.D.Farmer, and P.S.Shaw, Phys. Rev.Lett. 45, 712 (1980).

/5/ F.Takens, Lect.Notes in Math., 898, Berlin: Springer, 1981, p.366.

Statistical properties of Fraunhofer diffraction field **P12**
produced by random self-similar fractals

Jun Uozumi, Katsuhiro Uno and Toshimitsu Asakura

Research Institute of Applied Electricity, Hokkaido University
Sapporo, Hokkaido 060, Japan
Telephone: 011-716-2111 *ext.* 2646   *Fax:* 011-758-6098

1. INTRODUCTION

In order to investigate the fundamental properties of diffraction phenomena by self-similar fractals, we have studied the Fraunhofer diffraction patterns of generalized Koch curves in a recent paper[1]. It was shown in the paper that, if the object fractal is a regular one, the regular self-similar structure appears in its Fraunhofer diffraction pattern. However, when the object fractal is not completely regular with some degree of randomness, the regular self-similarity in its diffraction pattern is no more complete with some randomness. The randomness in the diffraction pattern increases with an increase of the randomness in the object fractal, and the diffraction pattern due to a highly random fractal object has an appearance of speckles. Randomization processes of the object fractal and its Fraunhofer diffraction pattern are shown experimentally in another paper[2].

The most dominant property of the Fraunhofer diffraction pattern due to random mass fractals is that the spatial distribution of the average intensity takes a form of the power-law[3]. However, other statistical properties concerning the diffraction field produced by fractal objects are not well understood, though some investigations have been carried out so far for phase objects having fractal properties[4-6]. In the present paper, some statistical properties of the optical field in the Fraunhofer diffraction region produced by fractal objects of real transmittance type (not phase screen type) are discussed mainly on the basis of the computer simulation technique.

2. FRACTAL OBJECTS AND SIMULATION PROCEDURE

In the present study, the randomized Koch fractals are employed as typical objects of the self-similar fractals. Fractals of this type modulate a real amplitude of the incident light, and do not act as phase screens. The most well-known type of Koch fractals may be a triadic Koch curve shown in Fig.1. This curve can be generated by a recur-
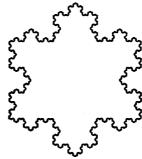
Fig. 1 Triadic Koch curve of level 5 generated on a triangular initiator.

sive operation of a generator in Fig.2(a) to an initiator in Fig.2(b).

In order to randomize this curve, we introduce random angles into two marginal segments of the generator as illustrated in Fig.2(c). A sequence of uncorrelated random numbers following a Gaussian probability density is generated in a computer and used for specifying the random angles of the generator. Figure 3 is an example of the random version of the triadic Koch fractal generated by using random numbers having a standard deviation of 15 degrees. It has been shown that the standard deviation larger than 10 degrees destroys completely the regular self-similarity in its diffraction pattern[2].

The simulation of the Fraunhofer diffraction field is carried out by calculating firstly the complex amplitude of every segments involved in the object by invoking the Fourier transform property of the diffraction and then summing up the contributions of all the segments.

Fig. 2 (a) Generator and (b) initiator for the triadic Koch curve in Fig.1, and (c) randomized generator.

3. RESULTS AND DISCUSSION

A simulated diffraction pattern of the curve in Fig.3 is shown in Fig.4(a) in a computer graphic image. It is noted that strong speckles are observed and that their statistics are not stationary because of radially decreasing trend of their average intensity. Performing an angular average operation shows that the intensity obeys a power law q^{-D} on average, where q and D are the spatial frequency and the fractal dimension of

Fig. 3 Random triadic Koch curve of level 5.

the object fractal, respectively. This fact indicates that the complex amplitude obeys the power-law of $q^{-D/2}$. The resemblance of this figure to the experimental results[2] is also noted.

*In order to evaluate the statistics of this speckle field, the nonstationarity is removed from the complex amplitude by compensating its power-law trend. The compensation is performed by multiplying simply the function $q^{D/2}$. The intensity distribution of the resultant field is shown in Fig.4(b). The probability density functions of the complex amplitude and
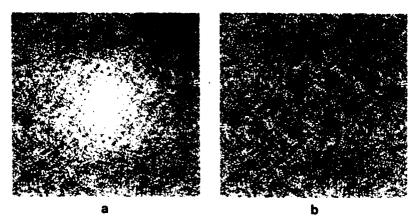
164

the intensity distribution of the compensated field are calculated and shown in Figs.5(a) and (b), respectively. These figures seem to imply that the compensated speckle field obeys approximately the zero-mean circular Gaussian statistics[7]. The speckle contrast[7] evaluated from the function of Fig.5(b) is 1.025, which also indicates that the speckle pattern is almost fully-developed.

However, there is another point to be noted in Figs.4(a) and (b). Namely, the speckles look like making clusters. The same phenomenon was also observed in experimental diffraction patterns[2]. This property seems to be associated with the individual feature of the object fractal. According-ing to fractality, the object has an arbitrary scale of structures as long as it is between outer and inner cutoffs of the self-similarity. The smaller structures contribute to create Gaussian speckles in the diffraction field.
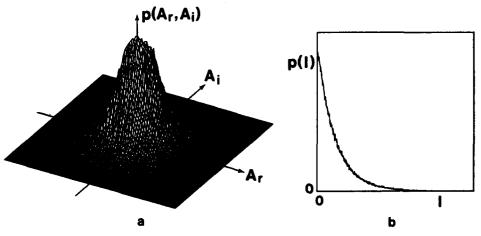
Fig. 5 (a) Joint probability density of the complex amplitude of the compensated dif-fraction field, and (b) probability density of the corresponding intensity distribution.

On the other hand, since the number of independent elements of relatively large structures is not sufficient to invoke the central limit theorem, such large structures act as adding to the diffraction field a non-Gaussian property, which may be observed as clustering of speckles. Therefore, the existence of the clustering of speckles may indicate that there is a slight deviation from the Gaussian statistics in the speckle field of Fig.4(a). A further study is required to clarify this point.

REFERENCES

1. J. Uozumi, H. Kimura and T. Asakura, *J. Mod. Opt.*, **37**, 1011 (1990)
2. J. Uozumi, H. Kimura and T. Asakura, *Waves in Random Media*, 1 (1991), to be published
3. J. Feder, *Fractals* (Plenum, New York, 1988)
4. M. V. Berry, *J. Phys. A: Math. Gen.*, **12**, 781 (1979)
5. E. Jakeman, *J. Opt. Soc. Am.*, **72**, 1034 (1982)
6. D. L. Jaggard and Y. Kim, *J. Opt. Soc. Am. A*, **4**, 1055 (1987)
7. J. W. Goodman, *Laser Speckles and Related Phenomena*, ed. by J. C. Dainty (Springer, Berlin, 1984)

Effects of Clipped Photon Detection in Speckle Interferometry   **P13**

Eric ARISTIDI, Gilbert RICORT, Henri LANTERI, Claude AIME
Département d'Astrophysique - URA 709 du CNRS - Université de Nice-Sophia Antipolis
Parc Valrose - 06034 NICE Cédex - FRANCE - Tel : (33) 93 52 98 98

1. Introduction.

Observation of weak sources in Speckle Interferometry requires the use of photon counting cameras. The photons can be detected one by one as they arrive, with their spatial coordinates and arrival time ; this is the case with for example the PAPA camera[1]. They can also be detected by frame, a single frame beeing the result of the integration of a few ms. Intensified CCDs like CP 40[2] belong to this last kind of device. Their advantages are the large number of pixels and the excellent stability of the CCDs.

Among the few problems that may affect the detection of the photon images[3] (geometrical problem, photon - centroiding...) we shall examine the effects of "clipping" photoevents. We denote by clipping the effects of saturation of the device that does not allow the detector to differentiate between a single photon and more than one photon. Clipping basically affects photon cameras of the integration type, but is also likely to influence the sequential ones if possible dead-time reactions of the photocathode are to be considered.

These effects are generally neglected owing to the very low probability of occurence of more than one photon per pixel for the weak astronomical sources of interest, giving generally less than one hundred photon per image. Moreover, these experimental considerations might appear to be well supported by the theoretical approach[4] that describes the photon noise limitation in speckle interferometry as a compound Poisson impulse process, which assumes that the probability of more than one photoevent is vanishingly small compared with the probability of one or zero photoevents. Then the detected signal is modelled as a sum of unit impulses located at different spatial locations[4].

It is necessary to emphasize that this representation assumes that the detector is continuous in space. Taking into account the finite dimensions of the pixels of the detectors, this ideal distribution is integrated and leads directly to Poisson statistics for the number of photons occuring in a fixed pixel size. So, the observed image is given by the number of photons received by the pixels. The effect of the clipping acts on the saturation of the Poisson law for each pixel.

We present in this communication the effects of the clipping in speckle interferometry, through a comparison between power spectra of clipped and non-clipped speckle patterns, making use of both an analytical approach and a numerical simulation.

2 - Clipping effects in Labeyrie's Speckle Interferometry technique

A - THEORY

The clipping problem can be approached in a theoretical way if one writes the autocorrelation function of the speckle pattern in the form[4,5] :

$$C(\rho) = \sum_{N=1}^{\infty} \sum_{Q=1}^{\infty} N.Q.p_2(N,Q;\rho) \tag{1}$$

where $p_2(N,Q;\rho)$ is the probability of joint occurence of N and Q photons at two spatial locations of the image separated by a distance ρ. In that expression, N and Q are likely to take all integer values between 0 and ∞. The clipping effect leads to modified speckle images, which are a succession of "0" and "1" ; "0" is written when no photon falls on the detector, whereas "1" is written when 1 or more photons arrive in the same integration time in a single pixel.

The second order statistics of clipped frames is described by the four values of $p_{2c}(n,q,\rho)$ for n,q=0 to 1, where $p_{2c}(n,q,\rho)$ is the second order probability to detect n and q photoevents at two points distant ρ[6]. In that case, the autocorrelation $C_c(\rho)$ of clipped images is expressed as :

$$C_c(\rho) = p_{2c}(1,1;\rho) = 1 - 2p_1(0) + p_2(0,0;\rho) \tag{2}$$

where we use the fact that the first pdf is a projection of the second pdf onto the axes.

Thus, the variations of $C_c(\rho)$ versus ρ are those of $p_2(0,0;\rho)$. One can see that the correlation measurements obtained with this type of camera gives the clipped probability $p_{2c}(1,1,\rho)$.

A theoretical model can be constructed if one supposes that the number of turbulent cells on the pupil is large; the central limit theorem shows that the complex amplitude of the wave at the focal plane of the telescope becomes a circular complex Gaussian random variable. The intensity of the speckles obeys the well known negative exponential law :

$$P(I) = \frac{1}{\langle I \rangle} \exp - \frac{I}{\langle I \rangle} \tag{3}$$

The second-order probability density function (pdf) $P_2(I_1, I_2, \rho)$ of finding two intensities I_1 and I_2 at two points separated by a distance ρ is given analytically for the Gaussian model[4] :

$$P_2(I_1, I_2; \rho) = \frac{\exp - \left(\frac{I_1 + I_2}{\langle I \rangle (1 - \mu^2)} \right)}{\langle I \rangle^2 (1 - \mu^2)} \cdot I_0 \left(\frac{2 \sqrt{I_1 I_2} \ \mu}{\langle I \rangle (1 - \mu^2)} \right) \tag{4}$$

where $\mu = \mu(\rho)$ is the complex coherence factor of the wave. In photon counting mode, the second order statistics are described by the probability $p_2(N, Q; \rho)$ of finding N and Q photons at two points distant ρ ; this function is given by a Poisson transform of $P_2(I_1, I_2, \rho)$[4] :

$$p_2(N, Q; \rho) = \iint \frac{(\alpha I_1)^N}{N!} e^{-\alpha I_1} \frac{(\alpha I_2)^Q}{Q!} e^{-\alpha I_2} P_2(I_1, I_2; \rho) \ dI_1 \ dI_2 \tag{5}$$

where α is the quantum efficiency of the detector. Making use of an expression given by Pedersen[7], it is possible to obtain $p_2(N, Q; \rho)$ in the form :

$$p_2(N, Q; \rho) = \sum_{n=0}^{\infty} \frac{1}{(n!)^2} \left(\langle I \rangle \mu \right)^{2n} \frac{\partial^{2n}}{\partial \langle I_1 \rangle^n \partial \langle I_2 \rangle^n} \left[\frac{(\alpha \langle I_1 \rangle)^N}{(1 + \alpha \langle I_1 \rangle)^{N+1}} \cdot \frac{(\alpha \langle I_2 \rangle)^Q}{(1 + \alpha \langle I_2 \rangle)^{Q+1}} \right] \tag{6}$$

where the expression in brackets, which appears as a product of Bose-Einstein laws, is the value of $p_2(N, Q; \rho)$ when I_1 and I_2 are uncorrelated. For $N=Q=0$, the 2n-order derivative is expressed as a geometrical series leading to a simple form for $p_2(0,0; \rho)$. Using relation (2), it is possible to obtain an analytical expression of $C_c(\rho)$, which can be written as :
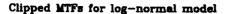
$$C_c(\rho) = \alpha^2 \langle I \rangle^2 (1 + \mu^2) \left\{ \frac{1 + \alpha \langle I \rangle \left(\frac{1 - \mu^2}{1 + \mu^2} \right)}{1 + \alpha \langle I \rangle \left[3 + \alpha \langle I \rangle (3 - \mu^2) + \alpha^2 \langle I \rangle^2 (1 - \mu^2) \right]} \right\} \tag{7}$$

This result is the same that was first obtained by Jakeman and Pike[8] and Barakat[9], making use of a different procedure. As a result, the effect of clipping on the autocorrelation is nonlinear. However when $\alpha \to 0$ $C_c(\rho)$ reduces to the unclipped autocorrelation $C(\rho) = \alpha^2 \langle I \rangle^2 (1 + \mu^2)$.

B - SIMULATION

The effects of photon clipping on the autocorrelation and power spectrum have been studied numerically on simulated speckle patterns. The interest of a simulative approach is double. First, it allows us to deal with realistic images and, what is more, makes it possible to check the clipping for the observation of extended objects.

The first results which are presented here are obtained making use of a set of $N=1000$ synthesized point-source speckle images of 64x64 pixels. The numerical speckle simulator assumes a log-normal hypothesis for the wave

Clipped MTFs for log–normal model

Clipping attenuation vs <N>

Spatial frequency

Mean number of photon/pixel <N>
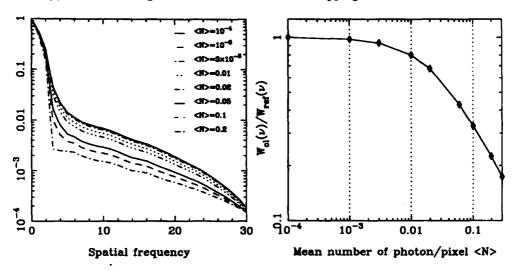
Fig 1 (left) : Result of a numerical simulation of the modulation transfer function, on a semi-logarithmic scale, for an average number of photon/pixel <N> varying from 10^{-4} to 0.2. The most visible effect is a global attenuation of the curve, mainly noticeable in the high frequencies of the power spectrum.

Fig 2 (right) : Representation on a log-log scale, as a function of the average number of photons per pixel <N>, of the attenuation factor $\gamma(v_c/2)$ defined by the ratio of the clipped to unclipped power spectra, at the spatial frequency $v=v_c/2$. The clipping effect appears already at <N>=10^{-3} and becomes more important at <N>=0.02 (80 photon per image of 64x64 pixels).

Clipping attenuation vs ν

Spatial Frequency (arbitrary scale)
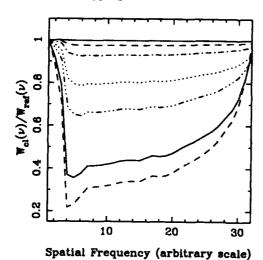
Fig 3 : Representation of the attenuation factor $\gamma(v)$ (ratio of the clipped to unclipped power spectra), as a function of the spatial frequency v. A global attenuation (visible in fig. 1) is observed, and this attenuation is reduced by a non-linear effect, as v approaches the cutoff frequency.
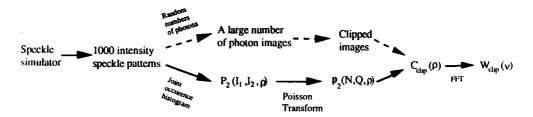
on the telescope aperture and a realistic phase structure function with a Kolmogoroff law[11]. It has been developed in our laboratory by Petrov and Borgnino[10].

The raw data-set represents continuous intensities. A step accounting for the photodetection process must be introduced. A possible procedure would be to obtain images of photoevents. A routine can be used to generate random numbers of events for each pixel of each image ; for that, the intensity of each pixel is taken as the expected value of a Poisson law, with a normalization factor proportionnal to $\mathfrak{N}$, the average number of photons per pixel. A clipping procedure may then be applied on each photoevent image for comparison of raw and clipped autocorrelation of power spectra.

When $\mathfrak{N}$ becomes very small, SNR problems are to be considered. In that case, it is well known[11] that the SNR varies as $\mathfrak{N}.T(f).N^{1/2}$, where $T(f)$ is the modulation transfer function at the spatial frequency f. The number of images can be increased if each intensity image gives rise to several (k) photon images. If we want the photodetected power spectra to have a SNR of the order of the raw intensity power spectrum, we have to make k at least of the order of $\mathfrak{N}^{-2}$. For $\mathfrak{N}=10^{-3}$, this means that we would have to compute at least one billion photoevent images.

We find it more interesting to use a different procedure, which is only partly simulative, and takes advantage of the theoretical approach developed here above. It consisted in computing first an estimate of the second pdf P_2 (I_1, I_2; ρ) from the original set of images. A Poisson transform (eq. 5) can then be applied to compute P_2 (0, 0; ρ) for different $\mathfrak{N}$ values ($\mathfrak{N}=\alpha<I>$ in eq. 5). The autocorrelation is obtained via eq. 2.

The two methods can be summarized by the following scheme.

The first results of the computation are given in Fig. 1 to 3. They appear to be in good agreement with the prediction of our theoretical model. As predicted, the clipping in Labeyrie speckle interferometry produces nonlinear effects on the energy transfer function. A more complete analysis of these effects on resolved speckle interferometry is currently under study[12]. We can already conjecture that these effects can produce artefacts on the visibility of sources that may lead to astrophysical misinterpretations, if overlooked.

References

1. PAPALIOLIOS C., NISENSON P., EBSTEIN S., *Appl. Opt.*, **24**, 287 (1985)
2. BLAZIT A., *Thèse de Doctorat* , Université de Nice (1985)
3. FOY R., *9th Santa Cruz Summer Workshop in Astronomy and Astrophysics*, July 13-24 (1987), L.B. Robinson - N.Y.: Springer (1987)
4. GOODMAN J.W., *Statistical Optics*, J. Wiley & Sons, N.Y. (1985)
5. STARK H., WOODS J.W, *Probability, Random processes and estimation theory for engineers*, Prentice Hall, New Jersey (1986)
6. AIME C., *J. Optics (Paris)*, **18**, 101 (1987)
7. PEDERSEN H.M., *J. Opt. Soc. Am. A*, **1**, 850, (1984)
8. JAKEMAN E., PIKE E.R., *J. Phys. A*, **2**, 411, (1969)
9. BARAKAT R.., *J. Opt. Soc. Am. A*, **5**, 1248, (1988)
10. PETROV R, BORGNINO J., *Private Communication*
11. RODDIER F., *Physics Reports* (review section of Physics Letters), **170**, 2, 97-166, North Holland Pub. Co (1988)
12. ARISTIDI E., AIME C., Paper in preparation

Volume Scattering and Absorption of Electromagnetic Waves in Polycrystalline Media

P14

P. Bussemer, K. Hehl and S. Kassam

Faculty of Physics, University of Jena, D-6900 Jena, Germany

M.J. Kaganov

Institute for Physical Problems, Academy of Sciences of USSR, 117 973 Moscow, USSR

The wave propagation in an inhomogeneous medium can formally be described by an equation of the type

$$\hat{L} u = \eta(\vec{r}) \hat{M} u \tag{1}$$

where $\hat{L}$ and $\hat{M}$ are non-fluctuating linear operators and $u(\vec{r})$ is a random function with the mean value $\bar{\eta} = 0$. For the wave field $u(\vec{r},t)$ we get with the ansatz

$$u = \bar{u} + u_1 \quad , \quad \bar{u}_1 = 0 \tag{2}$$

after averaging

$$\hat{L} \bar{u} = \overline{\eta \hat{M} u_1} \quad , \tag{3}$$

and by subtracting (3) from (1)

$$\hat{L} u_1 = \eta \hat{M} \bar{u} + \left\{ \eta \hat{M} u_1 - \overline{\eta \hat{M} u_1} \right\} \tag{4}$$

Unfortunately, the last two equations for $\bar{u}$ and u_1 are not closed, because higher correlations between η and u_1 appear in (4). For small field fluctuations we can take the approximation

$$\hat{L} u_1 \approx \eta \hat{M} \bar{u} \tag{5}$$

getting from (3) a closed equation for the mean field $\bar{u}$

$$\hat{L} \bar{u} = \overline{\eta \hat{M} \hat{L}^{-1} \eta \hat{M}} \; \bar{u} \tag{6}$$

which defines the wave propagation in an effective medium corresponding to the original fluctuating medium.

In our case we applicate this method to the propagation of electromagnetic waves in a medium which is made of anisotropic crystallites characterized by an intrinsic dielectric tensor $\mathcal{E}^{o}_{ik}$ with respect to the crystallite axes. The dielectric tensor $\mathcal{E}_{ik}(\vec{r})$ in the laboratory system is a random function because the orientations of the single crystallites are fluctuating from position to position:

$$\mathcal{E}_{ik}(\vec{r}) = \overline{\mathcal{E}}_{ik} + \Delta_{ik}(\vec{r}) \qquad . \qquad (7)$$

The fluctuating part Δ_{ik} denotes the deviation from the mean value $\overline{\mathcal{E}}_{ik}$ ($\overline{\Delta}_{ik} = 0$), where the average is over the orientation fluctuations of the crystallites. For an isotropic distribution of crystallites

$$\overline{\mathcal{E}}_{ik} = \mathcal{E}\, \delta_{ik} \qquad with \qquad \mathcal{E} = \frac{1}{3}\left(\mathcal{E}^{o}_{ii}\right) \qquad . \qquad (8)$$

Starting from Maxwell's equations for the microscopic electric field E_i and the constitutive relation $D_i = \mathcal{E}_{ik} E_k$ we construct a macroscopic dielectric tensor $\mathcal{E}^{*i}_{ik}$ for the fluctuating system in the sense of an effective medium approximation (EMA) in the following way: Splitting up E_i into a mean part $\overline{E}_i$ and a fluctuating part e_i ($\overline{e}_i = 0$)

$$E_i = \overline{E}_i + e_i \qquad (9)$$

we get from Maxwell's equations after averaging for a monochromatic wave with frequency ω

$$\frac{\partial^2 \overline{E}_k}{\partial x_i \partial x_k} - \frac{\partial^2 \overline{E}_i}{\partial x_k \partial x_k} - \frac{\omega^2}{c^2}\left(\overline{\mathcal{E}}_{ik}\overline{E}_k + \overline{\Delta_{ik}e_k}\right) = 0$$

$$\frac{\partial}{\partial x_i}\left(\overline{\mathcal{E}}_{ik}\overline{E}_k + \overline{\Delta_{ik}e_k}\right) = 0 \qquad (10)$$

if the deviation Δ_{ik} can be treated as a small perturbation $|\Delta_{ik}| \ll \mathcal{E}$. This equation defines the effective dielectric tensor $\mathcal{E}^{*}_{ik}$:

$$\mathcal{E}^{*}_{ik}\overline{E}_k = \mathcal{E}_{ik}\overline{E}_k + \overline{\Delta_{ik}e_k} \qquad (11)$$

172

The correlator between Δ_{ik} and e_i
wave equations using a subtraction procedure in
(1) and (3) yielding an inhomogeneous wave equation for
fluctuating field e_i

$$\frac{\partial^2 e_i}{\partial x_k \partial x_k} + \frac{\omega^2}{c^2} \varepsilon \, e_i = -\frac{\omega^2}{c^2} \Delta_{ik} \overline{E}_k - \frac{1}{\varepsilon} \frac{\partial^2}{\partial x_i \partial x_k} (\Delta_{kl} \overline{E}_l) \tag{12}$$

which can be solved with the help of Green's function taking
into account full retardation effects. For the effective ten-
sor ε_{ik}^* we get

$$\varepsilon_{ik}^* = \varepsilon \, \delta_{ik} + \gamma_{ik} \tag{13}$$

with

$$\gamma_{ik} = \frac{1}{4\pi\varepsilon} \left\{ \overline{\Delta_{il}\Delta_{km}} \int \frac{e^{ikr}}{r} \frac{\partial^2}{\partial x_i \partial x_m} \left[W(r) \, e^{i\vec{\varkappa}\vec{r}} \right] d\vec{r} \; + \right.$$

$$\left. + \, k^2 \, \overline{\Delta_{il}\Delta_{ik}} \int \frac{e^{ikr}}{r} W(r) \, e^{i\vec{\varkappa}\vec{r}} d\vec{r} \right\} \tag{14}$$

where $k = \frac{\omega}{c}\sqrt{\varepsilon}$ is the wave-number for the "unperturbed"
system and $W(r)$ is the analogue of the radial distribution
function for our system of misoriented crystallites. The assu-
med isotropic distribution of crystallites enables us to ex-
press the fourth-order tensor $\overline{\Delta_{il}\Delta_{mk}}$ by a single anisotro-
py parameter ν :

$$\nu = (\varepsilon_{ik}^o)^2 - \frac{1}{3}(\varepsilon_{ii}^o)^2 \tag{15}$$

The macroscopic tensor ε_{ik}^* exhibits a dynamic anisotro-
py

$$\varepsilon_{ik}^* = (\varepsilon + \gamma) \, \delta_{ik} + \delta \varkappa_i \varkappa_k \tag{16}$$
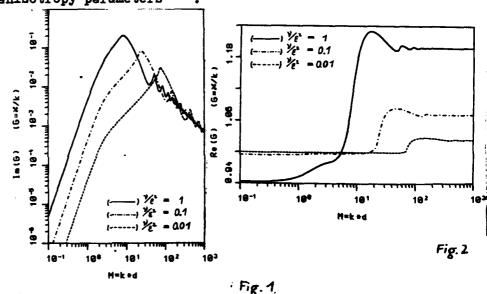
for a plane wave $\overline{E}_i = E_i^0 e^{i\vec{\varkappa}\vec{r}}$ with the wave vector $\vec{\varkappa}$.
The dispersion relation for transversal waves is

$$\varkappa^2 - \left(\frac{\omega}{c}\right)^2 (\varepsilon + \gamma(\varkappa)) = 0 \tag{17}$$

and for longitudinal waves

$$\varepsilon + \gamma(\varkappa) + \delta(\varkappa) \varkappa^2 = 0 \tag{18}$$

173

The tensor Γ_{ik} (14) depends on two phase factors, the wave-number $k = \frac{\omega}{c}\sqrt{\varepsilon}$ of the "host" medium with constant ε and the actual wave number $\varkappa$. In the sense of the distorted wave approximation in general scattering theory we treat the integrals in (14) as functions of $\varkappa$ and solve the dispersion relation (17) in a self-consistent manner. The numerical results for the imaginary and real part of the dimensionless wave number $G = \varkappa/k$ are shown in Fig.1 and Fig.2 as functions of the dimensionless wave-number of the incoming wave $M = kr_{max}$, where r_{max} characterizes the crystallite size, for different anisotropy parameters .

Fig. 1.

Fig. 2

The wave attenuation Im G exhibits four different ranges for increasing M . For small M we have usual Rayleigh scattering with Im $G \sim M^3$, but then a deviation from it. At $M \approx 2\pi\frac{\varepsilon}{\sqrt{v}}$ the attenuation reaches a resonance maximum and decreases for larger M . The oscillations for very large M can be explained as an interference effect between the waves in the effective medium and in the "host" medium with ε . Analoguous structures can be found in the real part Re G . For more details see /1/.

References:
/1/ P. Bussemer et al., Waves in Random Media,
    to be published (1991)

POLARIZATION-INDUCED PHASE IN IMAGERY AND IMAGE PROCESSING

P15

K.Bhattacharya, A.K.Chakraborty and Ajay Ghosh
Department of Applied Physics, University of Calcutta
92.Acharya Prafulla Chandra Road, Calcutta 700009, India

Introduction:

Use of various types of amplitude and phase coatings at the lens aperture has been of interest due to its inherent capability of modifying the PSF and the OTF of imaging systems (1-4). Similar modifications have also been achieved by the use of linear polarizers and retarders as masks at the lens aperture (5-9). The present paper attempts to show that by using suitable polarization masks, effects of all such phase and amplitude coatings can be achieved just by changing the polarization of the object beam. The fact that the magnitude of the effective phase and amplitude introduced can be continuously varied lends this technique a versatility unobtainable in conventional scalar techniques.

.Theory:

One method of studying the image characteristics of an imaging system is to study the image of a point source produced by the system. In what follows we consider the vector amplitude distribution in the image of a point source that sends out
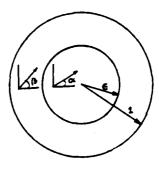
Fig-1

elliptically polarized light through a lens aperture masked by two polarizers — one at the central region and the other at the annular region (fig-1).

The amplitude distribution in the image of a point source due to the central circular region of the lens masked by the polarizer having transmission axis α with the x-axis may be represented by

$$\varepsilon'_a = \pi c^2 \left[J_1(2\pi c\rho)/2\pi c\rho \right] P(\alpha). \begin{vmatrix} a \\ b \exp(i\delta) \end{vmatrix} \tag{1}$$

where the column vector is the Jones vector of the input beam and $P(\alpha)$ is the Jones matrix of the polarizer used as mask in the central region.

Similarly, the vector amplitude distribution in the image of the point object produced by the outer annular portion of the lens is given by

$$\varepsilon'_a = \left[\{\pi \, J_1(2\pi\rho)/2\pi\rho\} - \{\pi c^2 \, J_1(2\pi c\rho)/2\pi c\rho\} \right].$$
$$P(\beta). \begin{vmatrix} a \\ b \exp(i\delta) \end{vmatrix} \tag{2}$$

Carrying out the matrix multiplication in (1) and (2), we obtain

$$\varepsilon_c = A \, R_1 . \exp(i\Delta_1) . \begin{vmatrix} \cos\alpha \\ \sin\alpha \end{vmatrix}, \tag{3}$$

$$\varepsilon_a = B \, R_2 . \exp(i\Delta_2) . \begin{vmatrix} \cos\beta \\ \sin\beta \end{vmatrix}, \tag{4}$$

where,

$A = \left[\pi \, J_1(2\pi\rho)/2\pi\rho \right] - \left[\pi c^2 \, J_1(2\pi c\rho)/2\pi c\rho \right]$

$B = \pi c^2 \, J_1(2\pi c\rho)/2\pi c\rho$

$R_1 = (a^2 \cos^2\alpha + b^2 \sin^2\alpha)^{1/2}$, $R_2 = (a^2 \cos^2\beta + b^2 \sin^2\beta)^{1/2}$

$$\Delta_1 = [b \sin 2\alpha \sin \delta] / [a \sin 2\alpha + b (1 - \cos 2\alpha) \cos \delta]$$

$$\Delta_2 = [b \sin 2\beta \sin \delta] / [a \sin 2\beta + b (1 - \cos 2\beta) \cos \delta]$$

It may be noted that the phase angles Δ_1 and Δ_2 depend on the amplitude of the two components of the input beam and on the orientation of the two polarizers used as masks.

Now, the vector amplitude in the image of the point object produced by the entire aparture along with the mask is given by

$$\mathbf{a}' = \begin{vmatrix} B\,R_1\,\exp(i\Delta_1)\,\cos\alpha + A\,R_2\,\exp(i\Delta_2)\,\cos\beta \\ B\,R_1\,\exp(i\Delta_1)\,\sin\alpha + A\,R_2\,\exp(i\Delta_2)\,\sin\beta \end{vmatrix}$$

Therefore, the vector intensity spread function is
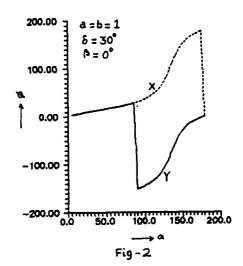
$$I_{PSF} = \begin{vmatrix} B^2 R_1^2 \cos^2\alpha + A^2 R_2^2 \cos^2\beta + 2ABR_1 R_2 \cos\phi \, \cos\alpha \, \cos\beta \\ B^2 R_1^2 \sin^2\alpha + A^2 R_2^2 \sin^2\beta + 2ABR_1 R_2 \cos\phi \, \sin\alpha \, \sin\beta \end{vmatrix}$$

where, $\phi = (\Delta_1 - \Delta_2)$

It is evident that the image intensity distribution is an incoherent superposition of two intensity distributions, one for each orthogonal components. By using an analyzer at the output side, the nature of the image can be continuously varied because the final intensity distribution is then determined by the interference of the components of both the orthogonal vibrations selected by the analyzer.

The two components of I_{PSF} also show that the intensity spread function is dependent on the phase difference ϕ whose value is determined by the state of polarization of the input beam. This implies that the imaging quality of the lens masked by polarizers can be continuously varied by varying the state of polarization of the input beam.

Results and discussions:

In order to show how the polarization induced phase ϕ can be varied we have computed Δ_1 and Δ_2 for different input polarization states. The phase ϕ, plotted as a function of the polarization angle α for both X and Y components of the output beam is shown in fig-2. Thus by chosing the orientations α and β of the polarization masks we can simulate the effects of different phase coatings on the imaging

Fig-2

characteristics of the lens system considered.

We have also studied the optical transfer function of the systems for different states'of polarization of the input beam. The study reveals that utilization of this technique lends an additional dimension to this system which adds to its versatility and application potentiality.

References:

1. H.Osterberg & J.E.Wilkins, J.Opt.Soc.Am.,39,553(1949)
2. J.E.Wilkins,Jr.,J.Opt.Soc.Am.,40,222(1950)
3. B.J.Thompson, J.Opt.Soc.Am.,55,145(1965)
4. T.Asakura et. al., Jap.J.Appl.Phys.,9,195(1970)
                                        10,879(1971)
5. A.K.Chakraborty & H.Mukherjee,J.Opt.(India)5,71(1976)
6. A.K.Chakraborty et.al., J.Opt.(Paris),9,251(1978)
7. A.Ghosh et.al., J.Mod.Opt.,34,281(1987)
8. A.Ghosh et.al., Optik,76,153(1987)
9. A.Ghosh et.al., J.Opt.Soc.Am.,A,5,227(1988)

MULLER MATRIX FOR LASER LIGHT
SCATTERED BY SURFACE WITH SMALL PERIODIC PROFILE

Yu. Avetisyan, V. Trifonov, V. Tuchin

Mechanical Engineering Institute
of USSR Academy of Sciences
Saratov Branch

As concerning the problems of surface roughness control by optical methods elaboration of simple and fast working calculation algorithms of laser scattering by different scatterers is necessary. Lately surface roughness contfol methods based on scattered light Muller matrix element measurement are developed intensively. In this paper the approximate method of Muller matrix element calculation for laser light scattered by the extended scatterer with small periodic profile of the scattering surface is discussed.

Let us discuss the plane monochromatic electromagnetic wave with electric intensity vector

$$\vec{E}_{\iota}(\vec{R},t) = \vec{E}_{\iota}\exp(-i\omega t + izk\mathrm{Cos}\,\theta_{\iota}) + c.c. \qquad (1)$$

making an angle of θ_{ι} with unlimited in transverse size spitter with the thickness of H, sides of which have the periodic profile of small depth of $h \ll \lambda$, where $\lambda = 2\pi/k$ is the wave length [Fig. 1]. Let us assume that the scattered field is formed by Rayleigh expansion

$$\vec{E} = \sum_{\vec{g}} \vec{E}_{\vec{g}} \exp(ik\vec{N}_{\vec{g}} \cdot \vec{R}) \qquad (2)$$

directions of propagation

$$\vec{N}_{\vec{g}} = (\mathrm{Sin}\,\theta_{\vec{g}}\,\mathrm{Cos}\,\varphi_{\vec{g}},\ \mathrm{Sin}\,\theta_{\vec{g}}\,\mathrm{Sin}\,\varphi_{\vec{g}},\ \mathrm{Cos}\,\theta_{\vec{g}}).\ (3)$$
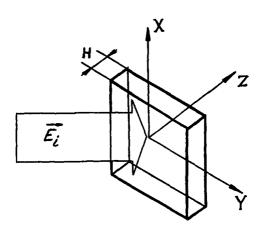
Fig 1.

It seems proper to present the connection of scattered wave complex amplitude Cartesian components $\vec{E}_{\vec{g}} = (E_{\vec{g}}x,\ E_{\vec{g}}y,\ E_{\vec{g}}z)^{T}$

with inciding wave complex amplitude independent components $\vec{E}_{i} = (E_{i_1},\ E_{i_2})^{T}$ by rectangular matrices $\hat{\beta}_{\vec{g}}$ of 3×2 dimensionality, mentioned in [1],

$$\vec{E}_{\vec{g}} = \hat{\beta}_{\vec{g}}\,\vec{E}_{i}.\tag{4}$$

It should be noted that formulae (2) – (4) can be assumed not only for reflected light (region Z < –H/2 in Fig.1) but for transiting light also (region Z > H/2).

Let us assume that the radiating laser beam can be

Let us assume that the radiating laser beam can be approximated to modulated wave with complex amplitude

$$\vec{E}_i(\vec{R}') = f(\vec{R}') \vec{E}_i(0). \qquad (5)$$

Setting our attention upon rather wide beams with complex amplitude distribution profile described by smooth function $f(\vec{R}')$ we assume that in this case formulae (2) – (4) will stay approximately valid but will acquire local nature what corresponds to substitution $\vec{E}_i(\vec{R}')$ for $\vec{E}_i$ according to (5). Thus applying Green function method for scattered in far region of diffraction field we obtain

$$(\vec{E}_\theta , \vec{E}_\rho)^T = (1/-ikR)\exp(ikR)(\pm\sum_{\vec{g}} \Psi_{\vec{g}} \,\hat{\alpha}_{\vec{g}} \,\hat{\beta}_{\vec{g}})\vec{E}_i(0) \qquad (6)$$

Here $R = |\vec{R}|$ is the point radius-vector module of observation in the direction of $\vec{R}_o = (\mathrm{Sin}\,\theta\,\mathrm{Cos}\,\varphi,\,\mathrm{Sin}\,\theta\,\mathrm{Sin}\,\varphi,\,\mathrm{Cos}\,\theta);$

$$\Psi_{\vec{g}} = (k^2/4\pi)\int d^2\vec{r}'\,\exp\,[-ik(\vec{r}_o - \vec{n}_g)\,\vec{r}'\,]f(\vec{r}')\qquad (7)$$

is the diffraction integral; $\vec{r}'$, $\vec{r}_o$, $\vec{n}_g$ are two dimensional components of $\vec{R}$, $\vec{R}_o$, $\vec{N}_g$ vectors correspondingly in plane $Z = Z_o$. Choice of the sign $+$ ($-$) answers calculation for transiting (reflected) light. Rectangular matrices $\hat{\alpha}_g$ of 2×3 dimensionality have the elements:

$$\alpha_{\vec{g}}\,(1,1) = -\mathrm{Cos}\varphi\,(1 + \mathrm{Cos}\theta\,\mathrm{Cos}\theta_{\vec{g}}\,);$$

$$\alpha_{\vec{g}}\,(1,2) = -\mathrm{Sin}\varphi\,(1 + \mathrm{Cos}\theta\,\mathrm{Cos}\theta_{\vec{g}}\,);$$

$$\alpha_{\vec{g}}\,(1,3) = \mathrm{Cos}(\varphi_{\vec{g}} - \varphi)\,\mathrm{Cos}\theta\,\mathrm{Sin}\theta_{\vec{g}}\,;$$

$$(8)$$

$$\alpha_{\vec{g}}(2,1) = \text{Sin}\varphi \ (\text{Cos}\theta + \text{Cos}\theta_{\vec{g}});$$

$$\alpha_{\vec{g}}(2,2) = -\text{Cos}\varphi \ (\text{Cos}\theta + \text{Cos}\theta_{\vec{g}});$$

$$\alpha_{\vec{g}}(2,3) = \text{Sin}(\varphi_{\vec{g}} - \varphi) \ \text{Sin}\theta_{\vec{g}};$$

The sought for Muller matrix can be defined, as it is well known [2], through the scattering amplitude matrix of 2×2 dimensionality

$$\hat{S} = \begin{pmatrix} S_2 & S_3 \\ & \\ S_4 & S_1 \end{pmatrix} = \pm \sum_{\vec{g}} \psi_{\vec{g}} \ \hat{\alpha}_{\vec{g}} \ \hat{\beta}_{\vec{g}} \quad (9)$$

which is determined by the formulae (6) – (8).

Thus, we got simple approximate formulae for scattering indicatrix and Muller matrix elements that are true for wide beams scattering on samples with small periodic profile surfaces. For calculation of parameters mentioned above widely known algorithms for plane electromagnetic wave diffraction on unlimitedly extended scatterer of the same structure are used.

R E F E R E N C E S

[1] Ahmanov S., Seminogov V., Sokolov V. // Journal of Experimental and Theoretical Physics. 1987. V.93 p.1654 (in Russian)

[2] van de Hulst H.C. Light scattering by small particles. Wiley, New York, 1957.

A Neural Network Wavefront Sensor
for Array Telescopes

M. Lloyd-Hart, P.L. Wizinowich & J.R.P. Angel

Steward Observatory,
University of Arizona,
Tucson, Arizona 85721, U.S.A.
(602) 621-1514

1. Introduction

Images formed by ground-based telescopes are degraded by atmospheric 'seeing'. Diffraction-limited performance can be recovered with the techniques of adaptive optics, in which the instantaneous wavefront shape is sensed and corrected. The greatest advances in ground-based optical resolving power will be achieved by long-baseline arrays of telescopes under adaptive control. Traditional methods of measuring wavefront errors are unfortunately not applicable for an array. A new method was suggested by the work of Sandler et al.[1] who trained an artificial neural network to recognize low order aberrations from far-field images for a single circular aperture. The method derives from the fact that a wavefront can be reconstructed entirely from the information contained in an in-focus and out-of-focus pair of images, taken simultaneously. Since far-field images result from the interference of photons from every point in the pupil, the method should not be limited to continuous apertures.

Wizinowich et al.[2] describe work proceeding at the Steward Observatory on the design and implementation of a novel near-infrared adaptive optical system for the Multiple Mirror Telescope (MMT), on Mt. Hopkins in Arizona,[3] currently the largest optical array in operation. The MMT has six 1.83 m diameter mirrors, arranged hexagonally on a radius of 2.52 m, providing a baseline of 6.86 m. The system is designed to operate at a wavelength of around 2.2 μm, where the resolution of the MMT is 0.06 arcseconds. At these wavelengths Fried's length[4] r_0 is typically 0.8 m to 1 m and it is sufficient to correct variations in pathlength and wavefront tilt between array elements, without correcting the wavefront distortion across individual elements.

In this paper, we concentrate on the the crucial component of the system, the wavefront sensor, which is a trained artificial neural network.[5] Computer simulations, modelling the effects of turbulence at the MMT, have shown this approach to be extremely powerful for adaptive correction of array telescopes.

2. The Neural Network Wavefront Sensor - Computer Simulations

Atmospheric turbulence is well described by the Kolmogorov structure function.[6] For the purpose of modelling, Kolmogorov turbulence with $r_0 = 1$ m is assumed at 2.2 μm, typical of good MMT seeing. A Fraunhöfer diffraction calculation is used to trace the wavefront from the six mirrors to detector arrays at the in- and out-of-focus image planes. The plate scale is set to 0.05 arseconds/pixel, closely matching the resolution scale. Before being shown to the neural net, the images are recentred on the energy centroid of the in-

focus image, to reduce the detector format.

We have trained a perceptron class of supervised neural net[7] to examine the image at the combined focus of all six telescopes. Figure 1 is a schematic representation of the net, as part of the complete system. The in- and out-of-focus images are superposed on two detector arrays, where each pixel represents an input node of the net. The input values are the normalized image intensities, I_i, at each pixel. A single layer of hidden nodes is used. At each hidden node a weighted sum over all the input pixel values is formed, and then passed through a sigmoid function to form the node output,
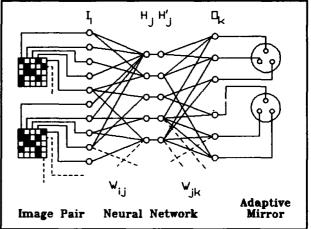
Figure 1 A schematic representation of a neural network for MMT adaptive correction.

$$H_j' = \frac{1}{1+e^{-(\sum_i W_{ij} I_i - \theta_j)}} \quad , \tag{1}$$

which "turns on" when the sum reaches a certain threshold, θ_j. The indices i, j, and k refer to the input, hidden, and output nodes respectively, and the Ws are the connecting weights. There are 18 output nodes, whose signals are weighted sums over the hidden node outputs. These outputs,

$$O_k = \sum_j W_{jk} H_j' \quad , \tag{2}$$

are the x tilt, y tilt and piston for each of the six MMT mirrors.

The goal of net training is to determine optimum values for the weights connecting the input, hidden and output layers, and the sigmoid offsets. Initially all are set to small random values. The net is then shown a large set of image pairs generated from random Kolmogorov-distorted wavefronts. For each image pair the net outputs are compared to the known wavefront tilts and pistons, and the net weights and offsets are adjusted to bring the outputs into better agreement. The formal back propagation algorithm, based on the least squares method, was derived by Rumelhart et al.[8]

The network for images at 2.2 μm wavelength consists of 338 input nodes (two 13×13 arrays) and 150 hidden nodes. Training was accomplished with 250,000 simulated image pairs. The image that would result from continuous on-line correction was modelled by adding together 500 individual images corrected by the neural net. A measure of the quality of a near-diffraction-limited image is its Strehl ratio,[9] the ratio of the peak intensity to that of the undistorted image. The integrated uncorrected image is seeing-limited with a full width half maximum of ≈0.5 arcseconds and a Strehl ratio of only ≈0.045. The corrected

result is a nearly diffraction-limited integrated image, figure 2 (top), with a Strehl ratio of 0.66. A comparison with the theoretical point spread function of the co-phased MMT, shown in figure 2 (bottom), dramatically illustrates the success of this neural net wavefront sensor.

3. Internal Structure of the Neural Net

Training for the present six mirror net required some 200 hours on the fastest computer then available to us. Any understanding of the net's internal functioning which might allow that time to be shortened is therefore highly desirable.

An image pair may be thought of as occupying a point in an 18-dimensional space, whose axes are the tips, tilts, and pistons of the six mirrors. The point's position vector is the set of values corresponding to the best fit of the six mirrors to the wavefront. The origin represents the undistorted diffraction pattern; moving away from the origin, the images become progressively degraded. A given value of r_0 defines a volume $V(r_0)$ centred on the origin, containing images of wavefronts characterised by a Fried length $\geq r_0$. The smaller r_0, the larger is V. In the process of net training at a particular r_0, say R, images are drawn from a volume V(R). The net outputs correspond one-to-one to the spatial axes, so each hidden node j of the net may also be thought of as a point in the space, specified by the weights W_{jk} connecting it to the outputs. It is then apparent that the job of training is to distribute the hidden nodes throughout the space such that the mean wavefront fitting error over all images in V(R) is minimized.

Figure 3 is a plot of the input weights for four hidden nodes, each weight plotted in the position of the pixel to which it connects. A large positive weight (white) will tend to turn the node on when energy is present at that pixel (see equation (1)). Energy at a pixel with a negative weight (dark) will tend to switch the node off. By this means, each hidden node picks out certain features of any image presented to the net.

As a limiting case, the features to which each hidden node responds may be precisely those of the images associated with the same point as the node. In that case, when such an
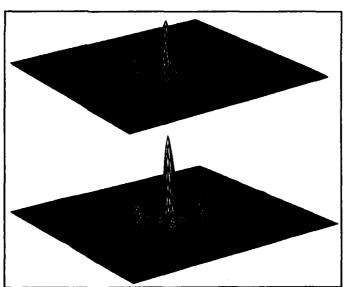
Figure 2 Top) A net-corrected long exposure image, Strehl ratio = 0.66, at 2.2 μm. Bottom) The theoretical unaberrated image profile of the cophased MMT. The scale is 1.3 arcseconds along each side.

185

image pair is shown to the net, the corresponding node will turn hard on (output = 1), while the other hidden nodes will, if the images are chosen to be orthogonal to each other, remain essentially off (output = 0). The output weights W_{jk} for node j are then the 18 best fit parameters for the image pair associated with the same point as node j. The sigmoid thresholds, θ_j, are to be adjusted such that, on moving away from node j, its output switches off just as its nearest neighbour's output begins to switch on. It is thus feasible to construct a net which
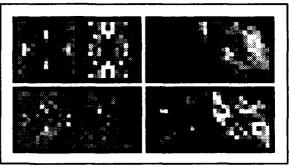
Figure 3 The features encoded in input weights of four hidden nodes. The left half of each pair corresponds to the in-focus image, the right half to the out-of-focus image.

requires little or no training to achieve its aim, by specifying the position vectors of the hidden nodes and determining the corresponding images. This exercise has been successfully carried out for the simple case of a much smaller net controlling just two mirrors.

4. Conclusion

We have presented a novel approach to wavefront sensing which, incorporated as part of an adaptive optical system, will provide astronomers with a dramatic improvement in the quality of ground-based imaging. Wider applications of this neural net approach, even beyond atmospheric compensation, can be envisioned. In particular, the method would be well suited to the sensing of the alignment errors of the telescope arrays being planned for high resolution imaging in space.

5. References

1. Sandler, D., Barrett, T.K., Palmer, D.A., Fugate, R.Q. & Wild, W.J., submitted for publication (1990).
2. Wizinowich, P.L., Angel, J.R.P., McLeod, B.A., Lloyd-Hart, M., McCarthy, D.W. & Scott-Fleming, I.C., this conference.
3. Carleton, N.P. & Hoffmann, W.F., Physics Today **31**, 30-37 (1978).
4. Fried, D.L., J. Opt. Soc. Am. **55**, 1427-1435 (1965).
5. Angel, J.R.P., Wizinowich, P., Lloyd-Hart M. & Sandler, D., Nature **348**, 221-224 (1990).
6. Kolmogorov, A., Turbulence, ed. S.K. Friedlander & L. Topper, 151-155 (Interscience, New York, 1961).
7. Lippmann, R.P., IEEE ASSP Magazine, 4-22 (April, 1987).
8. Rumelhart, D.E., Hinton, G.E. & Williams, R.J., Parallel Distributed Processing: Explorations in the Microstructure of Cognition, Vol. 1: Foundations, ed. D.E. Rumelhart & J.L. McClelland, 318-362 (MIT Press, 1986).
9. O'Neill, E.L., Introduction to Statistical Optics, 87-88 (Addison-Wesley, Reading, Mass., 1963).

AN ANALYSIS OF THE FAR-FIELD PROPERTIES OF THE DIFFRACTION FIELD PRODUCED BY A MOVING ROUGH SURFACE   **P18**

WU JIAN
Institute of Applied Physics,
University of Electronic Science and Technology of China
610054 Chengdu,Sichuan ,CHINA
(028)33.3312-2474

WANG LIMING
Avionics division,
Chengdu Aircraft Industrial Corporation
P.O.Box 800--604,610000,Chengdu,Sichuan ,CHINA
(028)66.9461-2808

1. INTRODUCTION

In recent years,the intensity distribution ,spatial coherence and the propagation properties of the diffraction field produced by rotating diffusers have been experimentally investigated [1] [2] [3] .It is shown that properties of the diffraction field are very similar to which of partially coherent wavefield produced by a planar gaussian Schell-model source .In this paper,the relation between the statistical properties of a rough surface and the parameaters of a planar gaussian Schell-model source produced by a rough surface when it's moving is theoretically considered.By comparing the far-field intensity distribution of the gaussian Schell-model beam with the experimental results,and its coherence length with size of the speckles produced by a rough surface ,it is obtained that a moving rough surface illuminated by a fully coherent gaussian beam, approximately produces a planar gaussian Schell-Model source.

2. GAUSSIAN SCHELL-MODEL(GSM) LIGHT BEANS

Let us consider a planar source whose intensity correlation function (cross-spectral density function),at some particular frequency ω,is of the form

$$W(r_1,r_2) = \sqrt{I(r_1)} \cdot \sqrt{I(r_2)} \cdot g(r_1 - r_2) \tag{2.1}$$

(Here r_1 and r_2 are the position vectors of two typical points in the source plane ,I(r) is the intensity at point r in the plane and $g(r') = g(r_1 - r_2)$ is the complex degree of the spatial coherence of the light across the source).The so-called Schell-model source is first considered by A.C.Schell [4] .If the intensity distribution and spatial coherence are both gaussian,i.e.

$$I(r) = A \cdot \exp(-r^2 / 2\sigma_1^2), \tag{2.2}$$

$$g(r') = \exp(r'^2 / 2\sigma_g^2) \tag{2.3}$$

(here A, σ_I and σ_g being positive constants), it is also called a planar Gaussian Schell-Model (GSM) source.It has been shown [5] that such sort of source generates the wavefield whose radiant intensity ,in a direction specified by a unit vector s that makes an angle θ with the direction normal to the source plane ,is given by

$$J_{(\theta)} = J_{(0)} \cos^2\theta \cdot \exp(-\sin^2\theta / 2\triangle^2), \tag{2.4}$$

187

$$\triangle = (1 / k\sigma_g)[1 + (\sigma_g / 2\sigma_I)]^{1/2} \qquad (2.5)$$

with $k = w / c$, c the speed of light and $J(0)$ the radiant intensity in the direction normal to the source plane.

The correlation function of GSM wavefield is ,given by A.T.Friberg and R.J.Sudal [6],

$$W(\rho_1, z_1; \rho_2, z_2) = (\frac{k}{2\pi})^2 \frac{1}{z_1, z_2} \iiiint_{-\infty}^{\infty} W(r_1, r_2)$$

$$\exp\{-ik[(\rho_1 - r_1)^2 / 2z_1 - (\rho_2 - r_2)^2 / 2z_2]\}d^2r_1 d^2r_2 \qquad (2.6)$$

(Ref.Fig. 1)here (ρ_1, z_1) and (ρ_2, z_2) are two points in the field ,with $\rho_1 = (x_1, y_1)$ and $\rho_2 = (x_2, y_2)$, respectively. Furthermore,it is shown that this sort of source has several interesting properties ,

(1)The transverse coherence length $lg(z)$ is simpley expresed by

$$l_g(z) = \sqrt{2}\,\sigma_g \triangle(z). \qquad (2.7)$$

where

$$\triangle(z) = [1 + (z / k\sigma_I \sigma_t)^2]^{1/2} \qquad (2.8)$$

with

$$\frac{1}{\sigma_t^2} = \frac{1}{4\sigma_I^2} + \frac{1}{\sigma_g^2}. \qquad (2.9)$$

$\triangle(z)$ is called the beam expansion coefficient.

(2) $l_g(z)$ is propertional to $l_I(z)$,the beamwidth in a plane $z = $ constant > 0.It is expressed by

$$l_g(z) / l_I(z) = \sigma_g / \sigma_I \qquad (2.10)$$

3. FAR–FIELD PROPERTIES OF MOVING ROUGH SURFACES

3.1 rough surface model

Let us consider a rough surface illuminated by a fully coherent laser.Assuming that the structure of the indident amplitude $P(x,y)$ is coarse compared with the structure of the phase angle $\theta(x,y)$,the surface height fluctuation is a gaussian random process and the normalized correlation function of the surface height is also gaussian [7] i.e.

$$\rho_h(r') = \exp[-r' / r_c)^2], \text{here} \quad r' = r_1 - r_2 \qquad (2.11)$$

,then(see Fig.1)the complex coherence factor of the field in the exit–plane(the nearest plane out off the surface) is given by

$$\alpha(r') = \exp\{-\sigma_\theta^2[1 - \exp[-(r' / r_c)^2]]\} \qquad (2.12)$$

Here

$$\sigma_\theta^2 = [\frac{2\pi}{\lambda}(1 + \cos\beta)]^2 \cdot \sigma_h^2 \qquad (2.13)$$

is the variance of phase angle $\theta(x,y)$ with β representing the incident angle and σ_h representing the variance of height function $h(x,y)$.

If a rough surface is vertically illuminated by a perfectly coherent gaussian beam ,a

GSM source will be produced in the exit–plane when the surface rotates in the surface plane . [1] [2] [3] If a rough surface moves in the surface plane ,it is assumed that the diffraction field at the exit–plane is alse a planar GSM source. It can be expressed that at the exit–plane,

(1) the Schell–Model (eq.(2.1)) is correct;

(2) the averaged intensity distribution of the diffraction field remains ganssian;

(3) the amplitude remains spatial coherence.The paramater σ_g in eq.(2.3), the spatial coherence length of the diffraction field, could be defined as the value of r' in eq.(2.12) when the complex coherence factor decreases to e^{-1} It is easy to show

$$\sigma_g = r_c[-ln(1-\sigma_\theta^{-2})]^{1/2} \tag{2.14}$$

3.2 far–field intensity distribution

This subject has been experimentally investigated by N.Takai [8] et.al. Fig.2(a),(b) and (c) obviously show that the theoretical prediction of the far–field intensity distribution from (2.4) and (2.14) is approach to the experimental data measured by N. Takai .If the surface is rough enough, the prediction is very good .

3.3 transverse coherence length

In many cases,the coherence properties of wavefield are interesting.Relation between the statistical paramaters of a rough surface(σ_h and r_c)and the coherence length of the GSM source is shown in Fig.3. When the detecting point is far enough ,eq.(2.7) becomes

$$l_g(z) = \frac{\sqrt{2} \cdot z \cdot \sigma_g}{k\sigma_I\sigma_t} \tag{3.1}$$

If the surface is rough enough,σ_g is usually much less than σ_I (ref.Fig.3).From eq.(2.9),σ_t is approach to σ_g So the far–field coherent length becomes a relative constant

$$l_g(z) = \frac{\lambda}{\sqrt{2} \pi\sigma_I} \cdot z$$

It is equal to the scale of speckes produced by the diffuser when it is not moving [9] .

4. CONCLUSIONS

It is concluded that the gaussian Schell partial coherence model is a good approximation to the diffraction field produced by a moving rough surface illuminated by gaussian light beams Its far–field intensity distribution is gaussian and the transverse coherence length is equal to the scale of speckles produced by the surface.

5. REFERENCES

(1) Q.He, A.T.Friberg, Opt. Commun. 67(1988), 4, 245.

(2) J.D.Farina, L.M.Narducci, E.Collett, Opt. Commun. 32(1980), 2, 203.

(3) P.DeSantis, F.Gori, G.Guattari, C.Palma, Opt.Commun. 29(1979),256.

(4) A.C.Schell, Doctoral Dissertation, M.I.T. (1961).

(5) E.Wolf, E.Collett, Opt. Commun. 25(1978), 3, 292.

(6) A.T.Friberg, R.J.Sudol, OPTICA ACTA, 30(1983), 8, 1075.

(7) J.W.Goodman, in *Laser Speckle And Related Phenomena*, ed. by J.C.Dainty, Spring–Verlag, 1975.

(8) N.Takai, Jap. Jour. of Appl. Phy., 13(1974), 12, 2025.

(9) J.Y.Wang, Appl. Opt., 23, 15, 2559.
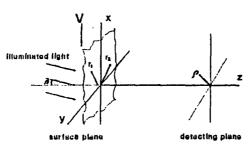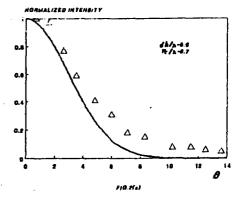
FIG.1 Illustration of the coordinate system

FIG.2(a)

FIG.2(b)

FIG.2(c)
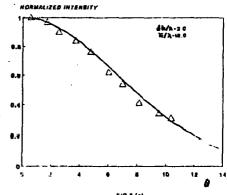
FIG.2 Theoritical data compared with experimental data
Solid line represents theoritical data
Points represent N.TAKAI's experimental data
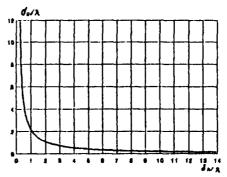
FIG.3 Relation between the degree of surface roughness
and coherence length of the GSM source

190

by Cao Long Van and Le Quan
Vietnam National Atomic Energy Commission

Stimulated Raman scattering (SRS) is the well-known phenomenon
and is explained theoretically since a long time. Standard theoretical
models of SRS have been builded by means of semiclassical theory of
radiation [1,2]. In this model it is assumed that two waves propagate
in the medium: the pump wave and the Stokes wave. The Stokes wave
satisfies a wave equation with the source being the polarization of
the medium, which is created by two above-mentioned waves. Such self-
consistent models describe very well the amplification of the Stokes
wave, however they can not describe correctly the spontaneous Stokes
generation.

Sometimes ago the quantum theory of Stokes generation 3,5 , which
treats spontaneous scattering and spatial propagation in a unified way,
has been proposed. In this model atoms of the medium and the Stokes
field are treated as one quantum system. For simplicity we consider
only one-dimensional problem, when the interaction volume is taken to
be a cylinder with a cross-sectional area A and length L, giving a
Fresnel number $F = A/\lambda_s L$ near unity. The Heisenberg equations for dyna-
mical quantities involved in the problem have the following form:

$$\left(\frac{\partial}{\partial z} + \frac{1}{c}\frac{\partial}{\partial t}\right) E_S(z, t) = -i k_2 Q^+(z, t) E_L(z, t) \qquad (1a)$$

$$\frac{\partial}{\partial t} Q^+(z, t) = i k_1 E_L^* E_S(z, t) - \Gamma_0 Q^+(z, t) + F^-(z, t) \quad (1b)$$

where $Q(z)$ is the atomic-transition operator and E is the slowly
varying Stokes field operator. The Γ_0 and F^+ terms described collision-
induced damping and fluctuations, respectively.

General solutions of Eq.(1) have been obtained in the case of
copropagating waves, when the waves E_L and E_S travel with equal velo-
city. In this case the pump-laser field E_L depends only on the local
time variable $\tau = t - z/c$. Assuming that in the initial state all atoms
stay in their ground states and no Stokes photons are present we
obtain the following Stokes intensity

$$I_S(z, \tau) = |k_2 E_L(\tau)|^2 = \left\{ e^{-2\Gamma_0 \tau} \left[I_0^2(\sqrt{4 k_1 k_2 z p(\tau)}) - I_1^2(\sqrt{4 k_1 k_2 z p(\tau)}) \right] \right.$$
$$\left. + 2\Gamma_0 \int_0^\tau d\tau' e^{-2\Gamma_0(\tau-\tau')} \left[I_0^2(\sqrt{4 k_1 k_2 z(p(\tau)-p(\tau'))}) - I_1^2(\sqrt{4 k_1 k_2 z(p(\tau)-p(\tau'))}) \right] \right\}$$

where $p(t) = \int_0^t |E_L(\tau)|^2 d\tau$. This result shows that the Stokes intensity is

independent of any fluctuations in the phase of the pump field E_L .
Although this fact gives insight into the nature of the quantum
generation of Stokes light, it does not correspond to the usual
experimental situation in which the light from pump sources exhibits
both amplitude and phase fluctuations.

A well-known model that can account for both amplitude and phase
fluctuations in the pump is that of colored chaotic light (CF).
Using this model authors of papers [6,7] considered the mean Stokes
intensity and correlation functions of higher order. It was pointed
out in [6] that the average intensity of Stokes generation is enhanced
over that resulting from a coherent pump in both transient and steady-
state limits.

Recently the concept of a pre-gaussian (PG) stochastic process
has been introduced in order to model noises in strong laser-atom
interactions [12-14] . The PG stochastic process is a special Markov
chain composed of n independent two-state jump processes (telegraphs).
It has been shown in [8, 12-14] that many dyanmical equations involving
the PG noise can be solved exactly. Multimode lasers are commonly
described by a Gaussian statistics. That does not diminish our
treatment because PG process buided of only a few telegraphs can
approximate the Orstein-Uhlenbeck (chaotic) process very well [8].

The purpose of this paper is to extend the quantum theory of
forward Stokes generation to the case that the pump wave is described
as pregaussian process. Again as in the case of the chaotic light,
a strong dependence on pump bandwidth is found. Moreover the calcula-
tions manifest the fast convergence of PG model to the chaotic light.
model as it was pointed out above, and in some context they are
simpler in comparison with CF (for example the simpler analytical
property of a function involved in the problem).

The mean Stokes intensity $\langle I(t)\rangle$ is calculated in [15] , and calcu-
lations of correlation functions of higher order is the subject of
the paper [16] .

References

1 Wang, C.S.: Phys. Rev. 182, 482(1969)

2 Carman, R.L., Shimizu F., Wang, C.S., Bloembergen, N.:Phys.
   Rev. A2, 60(1970)

3. Raymer, M.G., Walmsley, I.A., Mostowski, J., Sobolewska, B.:
   Phys. Rev. A32, 332(1985)

4. Raymer, M.G., Mostowski, J.: Phys. Rev. 124, 1980(1981)

5. Mostowski, J., Raymer, M.G.:Opt. Commun. $\underline{36}$, 237(1981)

6. Trippenbach, M., Rzążewski, K., Raymer, M.G.,J. Opt.Soc.Am.$\underline{B1}$, 671(1984)

7. Trippenbach, M., Cao Long Van: J.Opt.Soc.Am.$\underline{B3}$, 879(1986)

8. Cao Long Van, Wódkiewicz, K.,J. Phys.$\underline{B19}$, 1925(1986)

9. Gradshtein, I.S., Ryzik, I.M.: Table of integrals, series, and products, 4th Edn. Eqs.(6.615), (6.621-4), (8.486), and (6.681.3). New York: Academic Press 1965

10. Abramowicz, M., Stegun, I. (eds.): Handbook of Mathematical Functions (U.S. Goverment Printing Office, Washington, D.C.,1964), Eqs. (9.6.16) and (11.3.12)

11. Krylov, V.I., Skoblya, N.S.: Handbook of Numerical Inversion of Laplace transforms (Israel Program for Scientific Translations, Jerusalem, 1969)

12. Wódkiewicz, K., Shore, B.W., Eberly, J.H.: J.Opt.Soc.Am.$\underline{B1}$, 398 (1984)

13. Wódkiewicz, K., Shore, B.W., Eberly, J.H.: Phys.Rev. $\underline{A30}$, 2390 (1984)

14. Eberly, J.H., Wódkiewicz, K. Shore, B.W.:Phys.Rev. $\underline{A30}$, 2381(1984)

15. Cao Long Van, Z.Phys. $\underline{B65}$, 535(1987)

16. Cao Long Van, Le Quan: in preparation.

Electromagnetic Wave Propagation in Inhomogeneous Media **P20**

John B. Smyth
Smyth Research Associates
3555 Aero Court
San Diego, CA 92123

Maxwell's equations represent a single relationship between an electrical conduction current and an associated electromagnetic field, two elements never directly observed and defined only by that which is implicit in the relationship. The equations are assumed to be valid throughout the universe, which, by and large is a vacuum called "free space" with electromagnetic properties: dielectric constant $\varepsilon_o = 8.85 \times 10^{-12}$ farad per meter; permeability constant $\mu_o = 4\Pi \times 10^{-7}$ henry per meter; and electric conductivity $\sigma = 0$. As far as field theory is concerned the infintessimally small bits of substance called matter may be considered regions of "free space" with different electromagnetic properties together with sources (sinks) of the electrical conduction current. The electrical conduction current is that jinni involved in transforming energy between the corporeal state represented by inertial mass and the incorporeal state represented by electromagnetic fields in an amount given by Einstein's famous equation $E = mc^2$. Our investigation does not involve the electrical conduction current . We deal only with the "polarization currents" which redistribute energy already in the electromagnetic field, but contribute no energy to the field.

In the vacuum universe the "polarization currents" reduce to the electrical displacement current $\partial D / \partial t$, and the magnetic displacement current $\partial B / \partial t$ where $D = \varepsilon_o E$ and $B = \mu_o H$. Let us consider a small region of the vacuum universe occupied by a substance with electromagnetic properties ε, μ, σ. Assuming this region source free, Maxwell's equations become

$$V \times E = -i\omega\mu H \quad \text{and} \quad V \times H = (\sigma + i\omega\varepsilon) E. \tag{1}$$

We can rewrite equations (1) in the form

$$V \times E = -i\omega\mu_o H - i\omega(\mu - \mu_o) H \quad \text{and} \quad V \times H = i\omega\varepsilon_o E + \sigma E + i\omega(\varepsilon - \varepsilon_o) E \tag{2}$$

where $\sigma E + i\omega(\varepsilon - \varepsilon_o) E$ is the electrical polarization current and . $i\omega(\mu - \mu_o) H$ is the magnetic polarization current. We may assume that the electromagnetic constants of the region occupied by the substance are those of "free space" and that the fields external to the substance have induced the above polarization currents which now account for all electromagnetic phenomena associated with the presence of the substance. Unfortunately, these polarization currents depend on the unknown field intensities. In the event the electromagnetic constants of the substance differ little from the vacuum, the differences may be ignored in the first approximation. The "free space" fields are used to compute polarization currents which are placed in Maxwell's

equations to yield electromagnetic fields which are superimposed on the external field providing a first order approximation of the effect of the inhomogeneity.

This scheme has been basic to many attempts to describe the effects of atmospheric inhomogeneities on the propagation of electromagnetic waves. In the troposphere, the electrical conductivity is taken to be zero and the permeability equal to that of "free space". Only the dielectric constant varies in space and time. A popular description of this variation has been the use of G.I. Taylor's "autocorrelation" function. The fourier transformation of the autocorrelation function is the power spectrum of sinusoidals making up its structure. Since the phase relationship between the different sinusoidals is missing, we are not able to identify any member of the ensemble represented by the autocorrelation function. Therefore, we are not certain of how to compare the theoretical predictions with the experimental observations.

Implicit in this consideration is the fact that we have ignored the phase relationships of the polarization currents. There are cases where the phase variation is dominant. For example: consider an optical lens coated with a film transforming the wave impedance of the incident monochromatic light field into the wave impedance of the field within the glass. Experience teaches us that the spatial distribution of intensity of light emerging from the lens is small, whereas the phase variation over the same plane is large. A superposition of the fields from this source distribution of displacement currents yield enhanced field intensities in the focal plane. At distances large compared to the diameter of the lens, the perturbation of the intensity of the light field is no longer measurable.

Another approach widely used which enjoys great reputation in the field of quantum mechanics is known as WKB (Wentzel-Kramers- Brillouin).[1,2] This method keeps track of the phase of waves propagating in inhomogeneous media. In regions where there are no discontinuities of the index of refraction or its first derivative the wave impedance is continually transformed to match the local value of the intrinsic impedance of the medium. This results in a constant flow of energy along with the propagating disturbance. Reflections do not occur unless a discontinuity of the medium's index of refraction or it's first derivative occurs. This result peculiar to the WKB approximation has induced a number of investigators to falsely conclude that at least one of these discontinuities must be present if reflection is to take place. An application[3] of this method to the propagation of radio waves in the ionosphere demonstrates[4] how a discontinuity in the first derivative of the index of refraction is solely responsible for the derived reflection coefficient.

The use of Huygens' principle in optics has enjoyed a great deal of success in describing many observed wave phenomena. In describing diffraction through apertures large compared to the wavelength of the radiation, Kirchoff's formula has been quite useful. With the development of microwaves it has been observed

that Kirchoff's formula does not describe adequately electromagnetic radiation from horns . This raised several questions[5] concerning Huygens' basic concept which remain unanswered.

References

1. Brenner, H. Communication on Pure and Applied
     Mathematics 4; 105-115,1951.

2. Schelkunoff, S.A. ibid 4; 117-128, 1951.

3. Gibbons, J. and R.J. Nertney, J. Geophys. Res. 57; 355-
     371,1951.

4. Smyth, J.B. J. Geophys. Res. 57; 423-426, 1952.

5. Schelkunoff, S.A. ibid 4; 43-59, 1951.

"Imaging" by Partial Phase Conjugation of Doubly Scattered Wave Fields **P21**

William T. Rhodes

University of Colorado at Boulder
Optoelectronic Computing Systems Center
Boulder, Colorado 80309-0425
(303) 492-4863

Gisele Welch

Georgia Institute of Technology
School of Electrical Engineering
Atlanta, Georgia 30332
(404) 894-3151

Let a quasimonochromatic, spatially coherent wave field be incident on a moving diffuser as shown in Fig. 1. If the scattered light is reflected back through the diffuser, it is possible to determine the form of the incident wave field by making coherence measurements on the doubly scattered light. At time t, the complex amplitude of the doubly scattered wave field, $U_{ds}(x,t)$ is given by

$$U_{ds}(x,t) = \phi(x-t) \int_{-\infty}^{\infty} U_{inc}(\xi) \, \phi(\xi-t) \, \exp[i\alpha(x-\xi)^2] \, d\xi, \tag{1}$$

where $\phi(x)$ denotes the complex amplitude transmittance of the diffuser and $\alpha=\pi/\lambda 2d$. The mutual intensity J_{12} associated with this wave field is given by
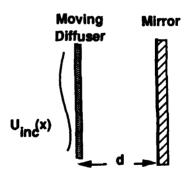
Fig. 1. Model Geometry.

$$J_{12} = <U_{ds}(x_1) \ U_{ds}^*(x_2)>_t$$

$$= \int_{-\infty}^{\infty} \int_{-\infty}^{\infty} U_{inc}(\xi) \ U_{inc}^*(\eta) < \phi(x_1\text{-}t) \ \phi^*(x_2\text{-}t) \ \phi(\xi\text{-}t) \ \phi^*(\eta\text{-}t)>_t$$

$$\times \ \exp[i\alpha(x_1\text{-}\xi)^2] \ \exp[\text{-}i\alpha(x_2\text{-}\eta)^2] \ d\xi \ d\eta, \tag{2}$$

where $<.>_t$ denotes time average. Assuming ergodicity and an essentially white noise power spectrum for the diffuser, we can write

$$<\phi(x_1) \ \phi^*(x_2) \ \phi(\xi) \ \phi^*(\eta)>_t = \Gamma(x_1\text{-}x_2) \ \Gamma(\xi\text{-}\eta) + \Gamma(x_1\text{-}\eta) \ \Gamma(\xi\text{-}x_2), \tag{3}$$

where $\Gamma(x)$ is the correlation function of the diffuser. Assuming the diffuser is sufficiently good, we can write $\Gamma(\zeta) = \kappa\delta(\zeta)$ in the integrals, with the result

$$J_{12} = \kappa \ \Gamma(x_1\text{-}x_2) \ \exp[j\alpha(x_1^2\text{-} x_2^2)] \int_{-\infty}^{\infty} |U_{inc}(\eta)|^2 \ \exp[i2\alpha(x_2\text{-}x_1)\eta] \ d\eta$$

$$+ \ \kappa^2 \ U_{inc}(x_2) \ U_{inc}^*(x_1), \tag{5}$$

where

$$\kappa = \int_{-\infty}^{\infty} \Gamma(\zeta) \ d\zeta. \tag{6}$$

The first term in the expression for J_{12}, being characterized by a small spatial correlation distance, represents the spatially incoherent part of the wave field. The second term represents the spatially coherent contribution to that wave field. Since it has the coherence properties of the incident wave field, it must propagate exactly as that wave field itself would. This term represents the enhanced backscatter, typically observed in the far field. For example, if $U_{inc}(x)$ represents a plane wave, the coherent contribution to the doubly scattered wave field will be focused to a diffraction-limited spot by a lens. The incoherent contribution, on the other hand, will not be focused, producing only a broad background distribution in the far field.

Associated with the mutual intensity J_{12} is the complex coherence factor

$$\mu_{12} = \mu(x_1,x_2) = \frac{J_{12}}{\sqrt{J_{11}J_{22}}}. \tag{7}$$

Assuming that $|x_1 - x_2|$ is sufficiently large compared to the coherence length for the diffuser and that

$$\Gamma(0) \int_{-\infty}^{\infty} |U_{inc}(\eta)|^2 d\eta \gg \kappa |U_{inc}(x)|^2, \qquad (8)$$

we can write

$$\mu(x_1, x_2) = \frac{1}{\Gamma(0)} \frac{\int_{-\infty}^{\infty} \Gamma(x)dx}{\int_{-\infty}^{\infty} |U_{inc}(x)|^2 dx} U_{inc}(x_2)U_{inc}^*(x_1), \qquad (9)$$

or, generalizing to two dimensions,

$$\mu(x_1,y_1; x_2,y_2) = \kappa_2 U_{inc}(x_2,y_2)U_{inc}^*(x_1,y_1) \qquad (10)$$

where the constant κ_2 is given by

$$\kappa_2 = \frac{1}{\Gamma(0,0)} \frac{\int_{-\infty}^{\infty}\int_{-\infty}^{\infty} \Gamma(x,y)\, dxdy}{\int_{-\infty}^{\infty}\int_{-\infty}^{\infty} |U_{inc}(x,y)|^2\, dxdy}. \qquad (11)$$

As discussed in Sec. 5.2 of Ref. 1, μ_{12} can be determined by measuring light intensities and the classical visibility and spatial phase of a set of sinusoidal intensity fringes in the output of a Young's two-pinhole interferometer. Since μ_{12} is proportional to the product $U_{inc}(x_2,y_2)U_{inc}^*(x_1,y_1)$ we reach the important conclusion that $U_{inc}(x,y)$ can be determined, to within a complex proportionality factor, by coherence measurements made immediately following the second passage through the diffuser. In most cases κ_2 is quite small, making such measurements difficult.

References

1.   Joseph W. Goodman, **Statistical Optics** (John Wiley, New York, 1985).

ROUGH SURFACE SCATTERING 2 & 3

Optical Scattering from Moderately Rough Surfaces

Theodore V. Vorburger, Egon Marx, and Thomas R. Lettieri
National Institute of Standards and Technology
Bldg. 220, Room A117
Gaithersburg, MD   20899   USA
Ph. (301) 975-3493

(INVITED)

Introduction

Light-scattering techniques have become important tools for the study of surface finish, and several such techniques have been developed [1]. The choice depends, among other factors, upon the degree of roughness: for very smooth surfaces a technique such as total integrated scatter can be used, while for rougher surfaces angle-resolved light scattering should be applicable [1]. In this paper, we discuss some of the work being conducted at the National Institute of Standards and Technology which applies laser light scattering to the measurement and understanding of the topographic properties of moderately rough surfaces (about 0.01λ to 1λ rms roughness, where λ is the wavelength of the incident light).

Angle-Resolved Light Scattering

For all of the work summarized here, angle-resolved light scattering (ARLS) was the optical technique used to determine the surface parameters [1]. The ARLS measurements (scattered intensity versus angle) were made using the Detector Array for Laser Light Angular Scattering instrument, described elsewhere [2]. To determine the roughness parameters, the experimental ARLS patterns are compared to calculated patterns based on electromagnetic scattering theory. Our work has indicated that the particular roughness parameter that can be measured this way depends upon the degree of roughness (Fig. 1).

Measurement of Autocorrelation Length

For smooth surfaces (less than 0.14λ rms roughness), Leridon, et al. at NIST [3] have used a Fraunhofer diffraction model developed by Chandley [4] to demonstrate that ARLS can be used to determine the surface autocorrelation length, T. The optical measurements of T compare favorably with values obtained from stylus profilometry, as shown in Fig. 2.

Measurement of RMS Surface Height

For surfaces with rms roughness less than about 0.3λ, it has been shown that if a specular beam is present in the scattered light, then its intensity can be used to determine the rms roughness of the surface [5]. Figure 3 shows a comparison between

experimental and calculated ARLS patterns for light scattered from a hand-lapped stainless steel specimen. Measurements of the surface using a stylus profilometer gave an rms roughness, σ_m, of 0.08 μm, while the optical measurements gave a value of $\sigma_o = 0.064$ μm. The discrepancy is ascribed to bandwidth (i.e., surface spatial frequency) differences between optical measurements and mechanical measurements [1]. Nevertheless, the ratio between σ_o and σ_m was constant within experimental error for all of the rms roughness measurements between 0.1λ and 0.8λ [5].

Measurement of RMS Surface Slope

For the roughest surfaces we have studied optically (up to about 1λ rms roughness), only the rms surface slope Δ_q can be determined accurately. Several theoretical studies have shown that the width (second moment) of a light scattering pattern is linearly related to Δ_q [6]. This linearity was experimentally verified at NIST by Cao, et al., and others, for both sinusoidal and random rough surfaces with lay [7]. The linearity holds for a wide range of surface slopes, as indicated in Fig. 4.

Conclusions

For moderately rough surfaces (about 0.1λ to 1λ rms roughness), angle-resolved light scattering can give surface-finish parameters that compare well with mechanical stylus measurements, if allowances are made for the fact that, in general, each technique is sensitive to different spatial wavelengths. This range of moderate roughness occurs, for example, in the machining and processing of metal parts, which is our primary interest at NIST. However, we have also used light scattering to measure the roughness properties of glossy coatings on paper [8], since the models we are using are independent of surface material properties.

References

[1] See for example: J. Bennett and L. Mattsson, "Surface Roughness and Scattering," (OSA, Washington, DC, 1989).
[2] T. Vorburger, et al. **J. Res. MBS 89**, 3-16 (1984).
[3] B. Leridon, E. Marx, T. Lettieri, J. Song, and T. Vorburger (preprint).
[4] P. Chandley, **Opt. Quan. Electr. 8**, 329-33 (1976).
[5] E. Marx and T. Vorburger, **Appl. Opt. 29**, 3613-26 (1990).
[6] See for example: J. Rakels, **Proc. SPIE 1009**, 119-25 (1988).
[7] L.-X. Cao, T. Vorburger, A. Lieberman, and T. Lettieri, **Appl. Opt.** (in press).
[8] T. Lettieri, E. Marx, and T. Vorburger, **Appl. Opt.** (in press).
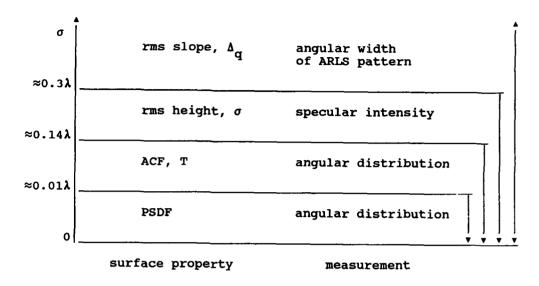
Fig. 1   Roughness-parameter ranges of the ARLS technique.
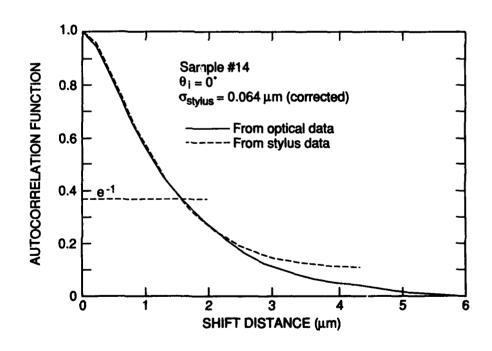
Fig. 2   Autocorrelation functions for surface with σ=0.064 μm.
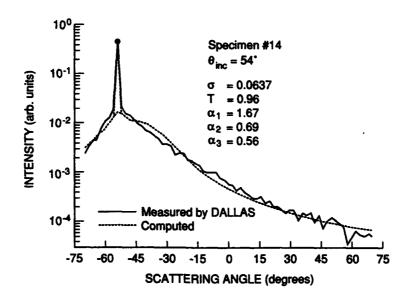
Fig. 3 Experimental and calculated ARLS patterns for hand-lapped
stainless steel surface with σ=0.064 μm.
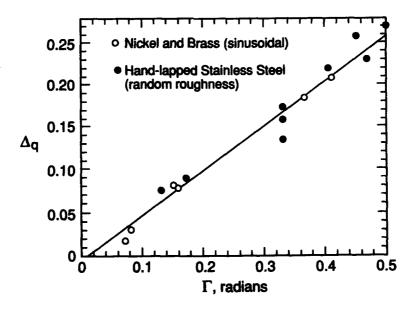
Fig. 4 Plot of ARLS pattern width (Γ) vs. rms surface slope (Δ_q).

SIMPLISTIC MODELS FOR SURFACE, INTERFACE AND VOLUME SCATTERING

Ad Lagendijk[*]

Natuurkundig Laboratorium
Universiteit van Amsterdam
Valckenierstraat 65
1018 XE Amsterdam
The Netherlands

and

FOM-Institute for
Atomic and Molecular physics
Kruislaan 407
1098 SJ Amsterdam
The Netherlands

[*]work performed in collaboration with Meint P. van Albada,
Peter A. Molenaar, Theo M. Nieuwenhuizen, Bart A. van
Tiggelen, and Adriaan Tip.

(INVITED)

INTRODUCTION

The field of multiple light scattering has seen a tremendous
revival. The main reason for this comeback is the realiza-
tion that interference effects can be found even after many
multiple-scattering events. One of these interference ef-
fects is enhanced backscattering. Right after its dis-
covery[1-3] two directions were pursued: volume scattering
and surface scattering[4]. Groups working in either of these
fields do their best to minimise the influence of the other
type of scattering. Multiple volume scattering can be opti-
mised by minimising scattering at interfaces and by minimi-
sing absorption. Surface scattering can be optimised at the
cost of volume scattering by inducing as much scattering as
possible at the interface. As a consequence much work on
surface scattering is performed with metal surfaces whereas
volume scattering is regularly studied by using dielectric
systems. It is however obvious that in many cases a clear
distinction can not be made and both effects will occur.

Some general remarks pointing to important differences
between the two areas are in order here. A surface is
usually a very complicated object. Perturbation theories and
Kirchhoff's approximations are commonly not valid for many
interesting situations. For rough surfaces higher than
first-order scattering is important but the influence of
higher-order bounces is often limited to the lowest higher-
order events: inclusion of only two bounces is already al-
most sufficient. The complication with this situation is
that it implies that these few bounces should be treated in

great detail in order to obtain agreement with experiment. As a result details of the surface structure have to be taken into account carefully and in many cases only numerical work (Monte Carlo and/or large diagonalization of matrices) will bring about valuable results, often limited to one-dimensional systems.

This condition is in great contrast to volume scattering where in many cases real multiple scattering (up to extremely high order) can occur. As a matter of fact many of the new interference effect, like localization of light, only come about at very high order (in principle even infinite order) of scattering. The building block of the theory of volume scattering is the t-matrix of one scatterer. In many cases this t-matrix is known in detail but when many orders of scattering are present the details of a single-scattering event can not be that important. All the details will be washed out and simple, even simplistic, models for single scattering can be used to obtain realistic predictions and descriptions of multiple scattering. In contrast to the case of surface scattering one can even often neglect the vector character of light fur multiple volume scattering. If the scattering is so strong that no small parameter can be identified, the single-scattering t-matrices are still useful because, with the help of techniques borrowed from many-body theory and field theory, resummation to infinite order can be performed.

FINITE SIZE SYSTEMS
The serious handicap with theory of bulk scattering is that on the one hand conservation laws are extremely important and on the other hand in developing a theory it is extremely difficult to "enforce" these conservation laws and extremely simple to violate them. The difficulty lies in the fact that in a calculation of scattering the computation is usually decoupled into a part relating to the amplitude of the waves and into a part relating to the intensity of the waves, whereas energy conservation in a diagrammatic theory is the result of a very subtle interplay between amplitude and intensity properties. Exact energy conservation is absolutely necessary to describe diffusive transport and breakdown of diffusive transport due to interference properly. The combination of energy conservation and multiple-scattering interference effects is really a very difficult one. To illustrate this we would like to point out a serious defect of the theory of enhanced backscattering in the bulk. This effect is now considered to be well-understood and well-documented, but nobody knows, or has demonstrated, where the energy for the enhancement is coming from. We all believe (!) that it is borrowed from the incoherent background but no theory exists yet explaining this energy balance.

Theoreticians working on volume scattering have a passion for infinite systems. Such systems have (statistical) translational symmetry and the theory, and especially inclusion

of energy conservation, becomes much simpler. As many of the experimental observations are done under scattering conditions, inhomogeneity and finite-size effects have to be included right from the outset. Localization of light in an infinite system can simply be considered to be associated with the vanishing of the diffusion constant. The observation of such an effect is performed by studying a finite system. Localization of light will come about as a peculiar and unexpected dependence on the size of the system (in official jargon called "the scaling behaviour"). This brings immediately the importance of the interface into play (in official jargon called "the boundary conditions").

In mesoscopic solid-state physics one studies the multiple scattering of electrons off impurities in a solid. In the study of (the scaling behaviour of) localization of these electrons it was soon realized that also in this case the boundary conditions are very important. Intense discussions can be found in the literature on this point[5] and very recently even the influence of interface scattering has been explored.

The conclusion is that when scaling behaviour or finite-size effects are being studied one should be very careful because by definition interfaces are present and they should be taken into account properly. In our opinion the influence of these effects have been overlooked up to now to a great extent. We would like to discuss several of these interface and surface effects when studying volume scattering.

AMPLITUDE AT AN INTERFACE

When one wants to investigate wave propagation near an interface an great number of problems appear immediately. The single-scattering properties of a scatterer near an interface become very different from the bulk value. What is the relevant length scale here, the wavelength or the mean-free path?

When resonant scatterers are used the impedance mismatch due to scattering at the interface can be very important. This effect is well-known for alkali vapours ("selective reflection") near their internal resonance (like sodium on the D-lines), but the effect is also very important for dielectric resonant scattering. We will show some of our results using simplistic theories for resonant scattering.

In a strongly scattering medium there is not much left of a coherent wave. However we know, or feel, that properties like "the average dielectric constant" or the "average index of refraction" must still have some meaning. How else do we know how much light is reflected from an interface separating a homogeneous medium from an strongly scattering medium. Is it still possible to measure Brewster's angle? We will describe in our presentation some of our measurements of the Brewster angle of a strongly scattering medium.

INTENSITY AT AN INTERFACE

If one uses some approximate description of the amplitude of a wave near an interface one still has to cope with the problem of the scattered light near an interface. How is the diffusion affected by the presence of an interface? Even if one would have an exact theory of the amplitude-Green's functions for all positions in the sample, including positions in the proximity of the interface, one would have serious problems in calculating the intensity with them. It would be extremely difficult to use such an amplitude function as a building block in a theory for the intensity in a multiple scattering situation. We have in the past developed a simplistic model to account for the modification of the diffusion of light near an interface. We will discuss some of its features.

SURFACE SCATTERING

When a new physical effect is discovered for the volume case a question that comes to mind almost instantaneously is: Is this effect still present at a surface? I already pointed out that for multiple scattering in the bulk predictions made on the basis of simplistic theories can be trusted. This approach has proven to be very fruitful for the phenomena of enhanced backscattering, localization and long-range speckles[6]. Is it possible to find simplistic surface models that could be used to estimate the order-of-magnitude of the new effects for surfaces? We will describe such a model which is simple enough that some predictions become possible without too much calculation.

REFERENCES

1 L. Tsang and A. Ishimaru, JOSA 1, 836 (1984)
2 M.P. van Albada and A. Lagendijk, Phys. Rev. Lett. 55, 2692 (1985).
3 P.E Wolf and G. Maret, Phys. Rev. Lett. 55, 2696 (1985).
4 E. R. Mendez and K. A. O'Donnell Optics Commun. 61, 91 (1987).
5 S. Feng, C. Kane, P.A. Lee, and A.D. Stone, Phys. Rev. Lett. 61, 834 (1988).
6 R. Landauer in " Analogies in optics and micro-electronics", edited by van W. van Haeringen and D. Lenstra (Kluwer, Dordrecht 1990).

Speed of Light in Strongly Scattering Media

Bart A. van Tiggelen[a], Ad Lagendijk[a,b],
Meint P. van Albada[b] and Adriaan Tip[a]

[a] *FOM-Institute for Atomic and Molecular Physics, Kruislaan 407, 1098 SJ Amsterdam, The Netherlands.*

[b] *Natuurkundig Laboratorium, Universiteit van Amsterdam, Valckenierstraat 65, 1018 XE Amsterdam, The Netherlands.*

In recent localisation theories [1], the energy flux carried by electrons or classical waves such as light, is investigated under circumstances where multiple scattering is dominant. It refers to situations where one could use a diffusion theory as a starting point. Both the diffusion coefficient and the transport mean free path play a crucial role. For this reason many experiments have been undertaken to measure them under varying experimental conditions. In a dynamic transport measurement the diffusion coefficient is obtained, whereas in steady state experiments the outcome is determined by by the transport mean free path only. The relation between the diffusion constant, D, and the transport mean free path, ℓ, is given by the classical formula:

$$D = \frac{1}{3} v_E \ell. \tag{1}$$

We want to point out here that the significance of the velocity v_E has been overlooked up to now in the multiple scattering of waves. Usually one uses the phase velocity as a good estimate for v_E, which can be obtained from a primitive volume fraction argument, but also comes out of sophisticated Coherent Potential Approximations (CPA) [2] [3]. For electrons it is given by the velocity at the Fermi level, k_F/m. As it appears in our new theory, this last result remains valid, but modifications arise for classical waves. The reason for this special property of classical waves is a well-known difference in the nature of the interaction of classical waves with matter as illustrated in the underlying wave equations. Electrons satisfy the Schrödinger wave equation, from which the *additive* nature of the interaction appears,

$$\left(-\frac{\hbar^2}{2m} \frac{\partial^2}{\partial x^2} + V \right) \Psi = i\hbar \frac{\partial \Psi}{\partial t}, \tag{2}$$

whereas electromagnetic waves obey the equation:

$$\left[\frac{\partial^2}{\partial t^2} - \frac{\partial}{\partial x} . \varepsilon^{-1} \frac{\partial}{\partial x} \right] \Psi = 0, \tag{3}$$

in which the interaction is given by the dielectric constant $\varepsilon = 1/c^2$, and is seen to be *multiplicative*. Polarization effects have been ignored in eq.(3), but can easily be taken into account. The similarity of eqs. (2) and (3), especially in the Slowly Varying Envelope Approximation (SVEA) [4], has been pointed out by many workers [5]. In the limit of multiple scattering in a random medium, the space-space, time-time correlation function $\langle \Psi(x_1, t_1) \Psi^*(x_2, t_2) \rangle$, where $\langle \cdots \rangle$ denotes ensemble averaging, turns out to obey in both cases the following generalised Boltzmann equation [6]

$$\left[\frac{-2E\omega}{c_o^2} + 2\mathbf{q}\cdot\mathbf{p} + \Sigma(E^+,\mathbf{p}^+) - \Sigma(E^-,\mathbf{p}^-)\right]\Phi_{\mathbf{p}}(\mathbf{q},\omega|E) =$$

$$= \Delta G(\mathbf{q},\omega|E,\mathbf{p})\left[1 + \sum_{\mathbf{p}'}U_{\mathbf{p}\mathbf{p}'}(\mathbf{q},\omega|E)\Phi_{\mathbf{p}'}(\mathbf{q},\omega|E,)\right]. \tag{4}$$

Here $\Phi_{\mathbf{p}}(\mathbf{q},\omega|E)$ represents the upper correlation function, Laplace transformed (variable ω) with respect to time and Fourier transformed (variable $\mathbf{q}$) with respect to position; E and $\mathbf{p}$ are the internal oscillations of the wavepacket. Furthermore Σ is the mass operator, U the irreducible vertex [7], ΔG the difference between retarded and advanced amplitude Green function $G(E^+,\mathbf{p}^+) - G(E^-,\mathbf{p}^-)$, and $E^\pm \equiv E \pm i\epsilon \pm \frac{1}{2}\omega$, $\mathbf{p}^\pm \equiv \mathbf{p} \pm \frac{1}{2}\mathbf{q}$.

In modern theories [8] [6], eq. (4) is used as a starting point to obtain weak localisation corrections to the diffusion constant, with final goal to find the location of the mobility edge where diffusion (or conduction) vanishes, along with the critical exponents. In this work we will limit ourselves to simple Boltzmann diffusion, for which ΔG is approximated by a delta function. This means that the scattered wave is always taken to obey the dispersion relation ("on-shell"). In addition we approximate Σ and U by their lowest order in density:

$$\Sigma(E^\pm,\mathbf{p}) = n\, t_{\mathbf{p}\mathbf{p}}(E^\pm),$$

$$U_{\mathbf{p}\mathbf{p}'}(\mathbf{q},\omega|E) = n\, t_{\mathbf{p}+\mathbf{p}'+}(E^+)\, t_{\mathbf{p}'-\mathbf{p}-}(E^-), \tag{5}$$

with n the density and t the T-matrix of one scatterer. We will use standard methods to obtain the diffusion coefficient [8]. However, a careful expansion for Σ and U in terms of ω and $\mathbf{q}$ is employed. The outcome is eq. (1) with

$$v_E = \frac{c_o^2}{c_p}\left[1 - n\,\frac{d}{dp^2}\,\mathrm{Re}\,t_{\mathbf{p}\mathbf{p}}(p) + n\,\langle I(\Omega)\frac{d\phi(\Omega)}{dp}\rangle_\Omega\right]^{-1}. \tag{6}$$

$$\ell = \frac{\ell_{sc}}{1 - \langle\cos\theta\rangle}. \tag{7}$$

$I(\Omega)$ and $\phi(\Omega)$ denote the scattered intensity and the phase shift in the direction Ω, ℓ_{sc} is the scattering mean free path, describing the exponential attenuation of the coherent wave, and $\langle\cos\theta\rangle$ is the average cosine of the scattering angle. Eq. (6) agrees completely with the final result of Loudon [9], although obtained in a different way. It is very important to note that the second and third term in eq. (6) cancel in the electron case, due to a Ward-Takahaski identity [7], but *not* for classical waves. Obviously the nature of the interaction must play a part here. Apart from the second term the v_E can be shown to equal the group velocity, $v_g = dE(p)/dp$, which is often taken to represent the speed of propagation of the *coherent* wave. It is known to be anomalous near a resonance, which fact is compensated for by the third term. Insertion of the on-shell T-matrix of a Mie scatterer [10] and application of the orthogonality property of the different partial waves yields:

$$\frac{v_E}{c_o} = \frac{c_o^2}{c_p^2}\left[1 + \frac{3}{4}\frac{f}{x^2}\sum_{n=1}^\infty (2n+1)\{\frac{d\alpha_n}{dx} + \frac{d\beta_n}{dx}\}\right]^{-1}, \tag{8}$$

where f is the volume fraction of the Mie spheres, $x = aE/c_o$ the size parameter, and α_n and β_n represent the (Van de Hulst) phase shifts of the individual partial waves.

214
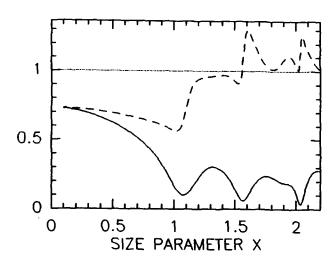
Figure 1. The transport velocity (solid) and the phase velocity (dashed) for Mie spheres with refractive index $n = 2.73$ and volume fraction $f = 0.36$. For details see [12]. Unit is c_0.

We compare these results with our experiments. The latter [11] involve $220\,nm$ TiO_2 particles at a packing fraction of 36%, and with refractive index 2.7. The first Mie resonance is probed at size parameter $ka = 1.1$, which corresponds to a wavelength of $633\,nm$. Various independent measurements of both the mean free path and the diffusion coefficient resulted in $D = 11.7 \pm 1\,m^2s^{-1}$ and $\ell = 0.57 \pm 0.05\,\mu m$, which implies, by eq. (1), $v_E = 5 \pm 1 \cdot 10^7\,ms^{-1}$, thus $v_E/c_0 \approx 0.16$. Insertion of the appropriate values in eq. (8) gives the numerical value $v_E/c_o \approx 0.14$. Thus experiment and theory agree very well. As illustrated in Figure 1, the phase velocity is roughly a factor 5 larger.

References.

[1]. For reviews see for instance P. Sheng (ed.) *Scattering and Localization of Classical in Random Media*, 1990, World Scientific, Singapore.

[2]. E.N. Economou, C.M. Soukoulis and A.D. Zdetsis, 1984, *Phys. Rev. B.* **30** , 1687.

[3]. P. Sheng, Z.Q. Zang, 1986, *Phys. Rev. Letters* **57** , 1879.

[4]. D. Lenstra, W. van Haeringen, 1990, in: *Analogies in Optics and Micro Electronics*, eds. D. Lenstra and W. van Haeringen, Kluwer.

[5]. M. Kaveh, 1990, in: *Analogies in Optics and Micro Electronics*, eds. D. Lenstra and W. van Haeringen, Kluwer.

[6]. T.R. Kirkpatrick, 1985, *Phys. Rev. B.* **31** , 5746.

[7]. G.D. Mahan, *Many-Particle Physics*, 1981, Plenum Press, New York.

[8]. D. Vollhardt and P. Wölfe, 1980, *Phys. Rev. B.* **22** , 4666.

[9]. R. Loudon, 1973, *The Quantum Theory of Light*, Clarendon, Oxford, first edition.

[10]. H.C. van de Hulst, 1981, *Light Scattering by Small Particles*, Dover, New York.

[11]. J.F. de Boer, M.P. van Albada, A. Lagendijk, 1991, to be published.

[12]. M.P. van Albada, B.A. van Tiggelen, A. Lagendijk, A. Tip, 1991, to be published.

ANGULAR CORRELATIONS OF LIGHT SCATTERED FROM RANDOM ROUGH SURFACES

M. Nieto-Vesperinas and J.A. Sánchez-Gil

Instituto de Optica, C.S.I.C.
Serrano 121
Madrid 28006. Spain

When light is scattered from a random rough surface, the resulting speckle pattern varies with the angle of incidence. However, even in the presence of multiple scattering, as the incident beam moves, there remains a degree of correlation between the successive speckle patterns. This fact, coined as the "memory effect" in light scattering from dense volume media (1,2), also exists in reflection and transmission from random rough interfaces separating two different media. It is shown in this communication that, with respect to this effect, the main difference between volume and surface scattering lies on the much slower decrease of the degree of correlation in the latter case as the angle of incidence varies. This is because the number of scattering events of the wave is smaller on a surface than in a volume.

By applying a Monte Carlo technique previously developed (3,4), we calculate the angular correlation function of the intensities obtained under two different angles of incidence. The maximum of these functions has an envelope that characterizes the memory effect. This is studied about the specular, backscattering, and other directions of observation.

The influence of the surface parameters is studied; namely, the refractive index (whether metal or dielectric), root mean square and correlation length of the surface profile. In this respect, it is important to carry out an analysis in regimes either lower or higher than the wavelength. Also, comparisons with situations of single scattering, described by the Kirchhoff approximation, and with very long angular correlation distance, are performed.

REFERENCES

1. S. Feng, C. Kane, P.A. Lee and D. Stone, Phys. Rev. Lett. 61, 459 (1988).

2. I. Freund, M. Rosenbluh and S. Feng, Phys. Rev. Lett. 61, 2328 (1988).

3. M. Nieto-Vesperinas and J.M. Soto-Crespo, Opt. Lett. 12, 979 (1987); J. Opt. Soc. Am. A 6, 3367 (1989).

4. A.A. Maradudin, E.R. Mendez and T. Michel, Opt. Lett. 14, 151 (1989); (with A. Mc Gurn), Ann. Phys. 203, 255 (1990).

Radiative transfer in stochastically bounded densely packed particulate media

Jouni I. Peltoniemi and Kari Lumme

Observatory and Astrophysics Laboratory, University of Helsinki

Tähtitorninmäki, 00130 Helsinki, Finland

tel. (int.): +358-0-191 2943, fax: 191 2952, Email: PELTONIEMI@FINUH

Introduction

A generalization of radiative transfer theory for stochastic surfaces was presented by Lumme et al. [1,2]. Recently Peltoniemi [3] has made simulations with densely packed particulate media. Here we enlighten and extend the ideas behind these works and study what happens when they are combined to represent a densely packed particulate medium bounded by a stochastically rough interface. We operate mainly in the geometric optics regime and assume Fresnelian reflections from the surfaces of the particles. We present explicitly only first order scattering, but the effects of multiple scattering are also briefly discussed.

Theory

We describe the statistics of the surface ζ with a Gaussian probability density $n_k(\zeta)$ for heights $\zeta = [\zeta(x_1, y_1), \ldots, \zeta(x_k, y_k)]^T$ at k arbitrary points $\{x_i, y_i\}$ with mean $\bar{\zeta}$ and covariance matrix $\Sigma_{ij} = \sigma^2 C(d_{ij})$, where σ is the standard deviation, C the autocorrelation function and d_{ij} the distance between the two points i, j. We denote the cumulative distribution by $N_k(\zeta)$.

If multiple scattering between different surface elements can be neglected and the scale of roughness is much larger than the penetration depth of light, the reflection coefficient can be written in the form [1]

$$
\begin{aligned}
R_1(\mu, \mu_0, \alpha) &= \int \mathcal{D}\zeta[x, y] n_\infty(\zeta[x, y]) V(\zeta[x, y], \mu, \mu_0) \frac{\mu' \mu_0'}{\mu \mu_0} \sqrt{1 + t_1^2 + t_2^2}\, R'(\mu', \mu_0', \alpha) \\
&= \int \mathrm{d}\zeta_0\, \mathrm{d}t_1\, \mathrm{d}t_2\, n_1(\zeta_0; \sigma)\, n_1(t_1; \rho)\, n_1(t_2; \rho)\, \langle V(\mu, \mu_0; \zeta_0, t_1, t_2) \rangle \\
&\quad \times \frac{\mu' \mu_0'}{\mu \mu_0} \sqrt{1 + t_1^2 + t_2^2}\, R'(\mu', \mu_0', \alpha),
\end{aligned}
\tag{1}
$$

where $\mathcal{D}\zeta$ means functional integration over the realizations of the surface ζ, V is the propagation operator ($V = 1$, if the surface element is visible and illuminated and 0 otherwise), R' is the reflection coefficient of the inclined surface element, $t_1 = \partial \zeta_0 / \partial x$ and $t_2 = \partial \zeta_0 / \partial y$ are the slopes, $\rho = \sqrt{-\sigma^2 C''(0)/d^2}$ (second derivative) their standard deviation, μ' and μ_0' are the cosines of the angles of incidence and emergence with respect to the normal and μ and μ_0 with respect to the mean normal.

The propagation probability can be approximated as [1,2,4,5]

$$
\langle V \rangle = \lim_{k \to \infty, \Delta \to 0} N_k(z(\Delta), z(2\Delta), \ldots, z(k\Delta)|\zeta_0, t_1, t_2)
\tag{2}
$$

$$
\approx \exp\left\{ -\int \mathrm{d}s \langle \beta(s) \rangle - \frac{1}{2} \int \mathrm{d}s_1 \mathrm{d}s_2 \left[\langle \beta(s_1) \rangle \langle \beta(s_2) \rangle - \langle \beta(s_1) \beta(s_2) \rangle \right] - \ldots \right\},
\tag{3}
$$

where $\int ds$ is an integration over the ray path, $z(s) = \zeta_0 + \mu s$ and

$$\langle \beta(s) \rangle = \lim_{\Delta \to 0} \frac{N_2(z(s), -z(s+\Delta)|\zeta_0, t_1, t_2)}{\Delta \ N_1(s|\zeta_0, t_1, t_2)}$$

$$\langle \beta(s_1)\beta(s_2) \rangle = \lim_{\Delta \to 0} \frac{N_4(z(s_1), -z(s_1+\Delta), z(s_2), -z(s_2+\Delta)|\zeta_0, t_1, t_2)}{\Delta^2 \ N_2(z(s_1), z(s_2)|\zeta_0, t_1, t_2)} \quad , \text{etc.}.$$

We have calculated both Eq.2 with a finite number of points and the Smith-approximation, i.e. the first order of Eq.3. Sample results are presented below. A third approach [6] to rough surfaces, especially suitable for multiple scattering simulations, is obtained by a Fourier transform of the surface.

For the particulate medium one can use similar approach. Assuming a single localized reflection from the surface of a particle, the reflection coefficient is

$$R'_1(\mu', \mu'_0, \alpha) = \int_{-\infty}^{\infty} dz_0 f_1(\mathbf{r}_0) \int d^2\mathbf{a} \frac{\mu'' \mu''_0}{\mu' \mu'_0} R''(\mathbf{a}) \int d^{3K}\mathbf{r} \, f^K(\mathbf{r}_1, \ldots, \mathbf{r}_K | \mathbf{r}_0) \prod_i^K V_i \qquad (4)$$

$$\approx \int_{-\infty}^{\infty} dz_0 f_1(\mathbf{r}_0) \int d^2\mathbf{a} \frac{\mu'' \mu''_0}{\mu' \mu'_0} R''(\mu''(\mathbf{a}), \mu''_0(\mathbf{a}), \alpha)$$

$$\times \exp\left\{ -\sum_i \langle U_i \rangle - \frac{1}{2}\sum_{ij}[\langle U_i U_j \rangle - \langle U_i \rangle \langle U_j \rangle] - \frac{1}{3!}\sum_{ijk}[\cdots] - \cdots \right\}, \quad (5)$$

$$\langle U_i \cdots U_j \rangle \equiv \int d\mathbf{r}_i \cdots d\mathbf{r}_j \, U_i \cdots U_j f(\mathbf{r}_i, \ldots, \mathbf{r}_j | \mathbf{r}_0),$$

where f is the reduced particle distribution function, $U_i = 1 - V_i$ the single particle shadowing operator, R'' the reflection function of the surface of the particle and the integration $\int d^2\mathbf{a}$ extends over the surface of the particle. If also the shape is allowed to vary, one must average over all shapes, as in [3,7].

The short range roughness of the boundary can be accounted for in Eq. 5 by including the surface distribution $(N_k(\{\mathbf{z}\}))$ to the particle distribution function f. On the other hand we need not necessarily define the particles at all to get a porous medium but we can extend the rough surface. The trick is to add some z-dependence on the expressions of the autocorrelation function and the 'mean height'. The interpretation would now be a three dimensional cross-section of a four dimensional surface. Depending on these two functions one can model media from a slightly rough surface to a porous foam-like or sparse quasi-particulate medium.

The generalization of the above formulae to multiple scattering using successive order method is straightforward only in principle. We have done very time consuming Monte-Carlo simulations by randomly generating a limited number of media and tracing the rays. Neglecting the second and higher cumulants in Eq.5 leads to the common radiative transfer equation or in Eq.3 to the generalized equation by Lumme et al. [2]. While these have the advantage that there exist some proven methods to solve them, the disadvantage is their inaccuracy in the cases where the correlations are large. One can partially avoid this problem by treating the first order with better approximations, but as the results by Peltoniemi [3] indicate, even this will not always work.

Discussion of results

Some sample results are presented in Figure 1. The already well known effects that arise from making the surface rougher are the general isotropization and darkening near grazing emergencies where shadowing is intense. If multiple scattering between surface elements were allowed, the surface would be brightened at higher emergencies.

The increase of volume density widens the opposition effect and brightens the medium at large angles of incidence and emergence, due to the fact that on the average the tops of the particles are much more illuminated and visible than the other parts, contrary to the case of low density, where all parts of the illuminated or visible profile are almost equally shadowed. Our simulations also showed that the less absorption and thus the more multiple scattering, the less the density affects the reflected flux. The light transmitted through a finite layer is always sensitive to density.

Combining these two cases produces the expected net effect, though the density brightening is stronger than the roughness darkening.

Further steps

Because nature is even more complicated than assumed here, there are several things to do before one can accurately apply these results to real problems:

1. Include wave optics effects like diffraction and coherent backscattering [8,9]
2. Account for the possibility of very complex internal structure of the particles
3. Develop an effective but still accurate code for multiple scattering

References

[1] K. Lumme, J. I. Peltoniemi, and W. M. Irvine. *Adv. in Space Res.* **10**, 1, 187–193, (1990)

[2] K. Lumme, J. I. Peltoniemi, and W. M. Irvine. *Transp. Theory Stat. Phys.*, **19** (3–5), 317–332 (1990)

[3] J. I. Peltoniemi and K. Lumme. Light scattering by closely packed particulate media. to be submitted to *J.Opt.Soc.Am.* (1991)

[4] B. G. Smith. *IEEE Trans. Antennas and Propag.* **AP-14**, 668–671 (1967)

[5] F. G. Bass and I. M. Fuks. *Wave scattering from statistically rough surfaces*, (Pergamon. New York, 1979)

[6] K. Muinonen, K. Lumme, B. Zhukov, J. I. Peltoniemi, M. Kaasalainen, and W. M. Irvine. Statistical photoclinometric methods for the analysis of surface topography. Space Research Institute, Academy of Sciences, USSR, Preprint 1631,1–16, (1990)

[7] J. I. Peltoniemi, K. Lumme, K. Muinonen, and W. M. Irvine. *Appl. Opt.*, **28**, 4088–4095 (1989)

[8] K. Muinonen, Ph.D. Thesis. University of Helsinki, (1990)

[9] K. Muinonen and K. Lumme. subm. to Proc. 126th IAU Colloquim, Kyoto, (1990)

roughness=0.0, density=0.1%   roughness=1.0, density=0.1%

roughness=0.0, density=30%   roughness=1.0, density=30%
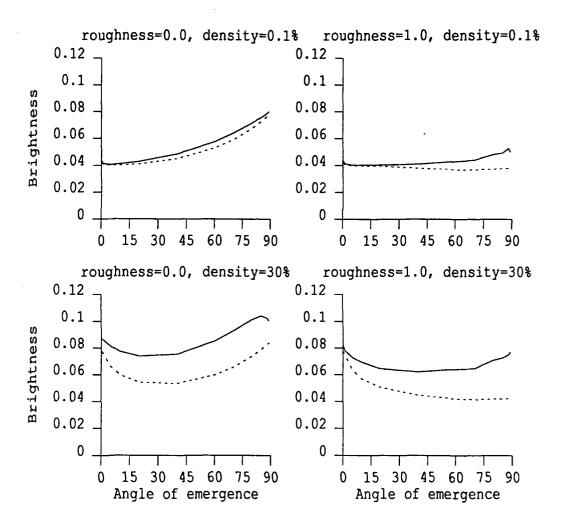
FIGURE 1.   The bidirectional reflection function $R_1(\mu, 1, \alpha)$ for first order reflection from stochastically bounded media of hard totally reflecting spheres at normal incidence. The roughness (ρ), defined as the standard deviation of the slope, varies from 0 to 1 and the volume density (fractional volume occupied by the particles) from 0.1% to 30%.

The solid line is calculated using Eqs. 1 and 2 with 61 points for the large scale surface roughness, third order cumulant expansion (Eq. 5) for the mutual shadowing between particles and assuming total specular reflection from the surface of a spherical particle. The dashed line is based on the somewhat simpler model by Lumme et al. [1], i.e. the approximate first order of Eqs. 3 and 5 with point-like scattering.

Note the clear brightening after compression and darkening after roughening. It is obvious that the use of the presented higher order formulation is necessary for dense media.

IMAGING A COHERENTLY ILLUMINATED OBJECT AFTER DOUBLE PASSAGE THROUGH A RANDOM SCREEN

C.J. Solomon, J.C. Dainty, R.G. Lane and T. Mavroidis
Blackett Laboratory, Imperial College, London SW7 2BZ, U.K.

ABSTRACT

The possibility of performing diffraction-limited imaging after two-way propagation through a random screen is examined. We demonstrate that the average intensity spectrum for a deterministic object which is coherently illuminated and viewed through the same random screen contains diffraction-limited information on the Fourier modulus of the object. Further, the retrieval of this information is shown to be trivial if a suitable non-redundant aperture is employed. Computer reconstructions of simple objects are presented. The problem of imaging a statistically varying object is also discussed.

THEORY AND PHYSICAL EXPLANATION

By considering the special case of a deterministic object situated in the far-field and a random screen described by complex-gaussian statistics, it can be shown[1] that diffraction-limited information is present in the time-averaged image when the object is coherently illuminated and viewed through the same screen. This is because a fraction of the light forming the image always interferes constructively irrespective of the severity of the phase and amplitude fluctuations induced by the screen. Physically, this effect is closely related to the back-scatter enhancement of light scattered by dense random media and rough surfaces[2,3], the critical feature being the constructive interference in the back-scatter direction which can result from multiple scattering.

In Fig. 1, we depict a deterministic object in the far-field of a random screen which is situated in the pupil plane of the illumination and viewing system. A uniform beam of monochromatic laser light of unit amplitude is transmitted through the combined system of lens and random screen.

Analysis of this model, assuming a complex-gaussian model for the atmospheric statistics, yields a general expression for the time-averaged image spectrum,

$$\langle I(\eta) \rangle = \int_{-\infty}^{\infty} \int_{-\infty}^{\infty} \int_{-\infty}^{\infty} [C(\eta)C(\xi'' - \xi') + C(\xi'' - \xi)C(\eta + \xi - \xi')] \ h_0(\xi)h_0^*(\xi + \eta)$$
$$h_0(\xi')h_0^*(\xi'')l(\xi')l^*(\xi'') \ \tilde{O_C}(\xi + \xi')\tilde{O_C}^*(\xi + \xi'' + \eta) \ d\xi d\xi' d\xi''$$

(1)

where $C(\xi)$ is the atmospheric coherence function, $h_0(\xi)$ is the aperture function and $\tilde{O_C}(\xi + \xi')$ is the Fourier transform of the object reflectivity, $o(x)$.

Eq. 1 can be shown to contain diffraction-limited information on the object Fourier modulus[1]. However, the existence of diffraction-limited information can be most easily demonstrated by considering a point source imaged through a simple Michelson-Fizeau or two-pinhole aperture,

$$h_o(\xi) = \delta(\xi - \xi_0) + \delta(\xi + \xi_0) \tag{2}$$

Substitution of Eq. 2 into Eq.1 and integration gives,

$$\begin{aligned}
\langle i_b(\eta) \rangle = &\left[6 + 4C(-2\xi_0) + 4C(2\xi_0) + 2| C(2\xi_0) |^2 \right] \delta(\eta) \\
&+ \left[1 + 4C(-2\xi_0) + 2C^2(-2\xi_0) + | C(-2\xi_0) |^2 \right] \delta(\eta + 2\xi_0) \\
&+ \left[1 + 4C(2\xi_0) + 2C^2(2\xi_0) + | C(2\xi_0) |^2 \right] \delta(\eta - 2\xi_0)
\end{aligned} \tag{3}$$

If the separation of the two pinholes is greater than the correlation length of the atmosphere we can see from Eq. 3 that the relative magnitudes of the image frequencies at $2\xi_0$ and $-2\xi_0$ to the zeroth frequency are in the ratio of 1 to 6. We therefore see that even when the field at the two pinholes is totally uncorrelated there is a quite definite, non-zero transmission of the spatial frequency defined by the pinhole separation. A similar result can be obtained for a phase screen obeying the Kolmogoroff power spectrum for phase fluctuations. In this case the ratio is 1 : 4.

A simple physical interpretation of this exists. In fig. 2, there are four different optical paths which contribute to the image. These are A-O-A, B-O-B, A-O-B and B-O-A. Of these paths, the latter two will always give rise to constructive interference in the image plane as the total phase error picked up on either path is $\theta_1 + \theta_2$ irrespective of the absolute magnitude of the perturbations. These two paths give rise to a steady fringe pattern in the image plane. Other combinations of these 4 paths also give rise to instantaneous fringes but because of the time-varying nature of the atmospheric phase perturbations, the fringes randomly translate in the image plane and, in the limit of infinite time averaging, will wash-out to form a uniform background. Computer simulations have confirmed this prediction accurately.

It is this effect which lies at the physical basis of the double passage effect. The approach can be extended to a general non-redundant aperture described by,

$$h_0(\xi) = \sum_{j=1}^{N} \delta(\xi - \xi_j) \tag{4}$$

By demanding that the vector separation of any two of the N sub-apertures is greater than the correlation length of the atmosphere, we obtain a remarkably simple result,

$$\langle I(\xi_F - \xi_B) \rangle = | \tilde{O}(\xi_F + \xi_B) |^2 \tag{5}$$

224

where $\xi_F - \xi_B \neq 0$. Eq. 5 shows that an image frequency given by the vector separation of two pinholes in the non-redundant aperture corresponds to an object frequency given by the sum of the pinhole vectors. *Thus the time-averaged image spectrum provides direct knowledge of the Fourier modulus of the object spectrum.* Fig. 3 shows the result of double passage imaging of a two point object, performing the mapping described by eq. 5 to estimate the Fourier modulus of the object and executing a phase recovery routine. This satisfactorily demonstrates the validity of Eq. 5.

DISCUSSION

Double passage imaging of a deterministic object in the far-field has been shown to yield diffraction-limited information on the object Fourier modulus irrespective of the severity of the amplitude and phase fluctuations induced by the screen. The recovery of this information has been easily accomplished when imaging takes place through a non-redundant aperture which excludes spatial frequencies less than $\frac{r_0}{\lambda R}$, where r_0 is the correlation length of the screen.

In our analyses, we have made certain simplifying assumptions. In particular, the use of complex gaussian statistics to describe the atmosphere and we have restricted the location of the random screen to the pupil plane. The importance of these assumptions will be discussed together with the prospects of imaging a statistically varying object.

REFERENCES

1. T. Mavroidis and J.C. Dainty, " Imaging after double passage through a random screen ", Opt Lett, August 1st (1990)

2. K.A. O'Donnell and E. Mendez, " Experimental study of scattering from characterised random surfaces ", J. Opt. Soc. Am. A 4, 1194 - 1205, (1987)

3. M.J. Kim, J.C. Dainty, A.T. Friberg and A.J. Sant, " Experimental study of enhanced backscattering from one and two dimensional random rough surfaces ", J. Opt. Soc. Am. A 7, 569–577 (1990)
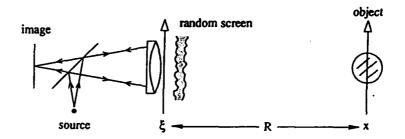
FIGURE 1
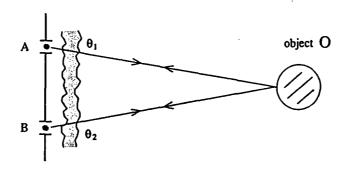
FIGURE 2

FIGURE 3

Iterative Methods for Scattering from Rough Surfaces
Varying in either One or Two Dimensions

C. Macaskill, School of Mathematics and Statistics, University of Sydney, N.S.W. 2006, Australia,

and

B.J. Kachoyan, Combat Systems Division, DSTO (Sydney), P.O. Box 44, Pyrmont, N.S.W. 2009, Australia.

(INVITED)

This paper is a numerical investigation of iterative techniques as applied to the integral equation formulation for scattering from rough surfaces, see e.g. Axline and Fung (1978), Kachoyan and Macaskill (1987), Macaskill and Kachoyan (1988), Soto-Crespo and Nieto-Vesperinas (1989), Nieto-Vesperinas and Soto-Crespo (1987), Thorsos(1988), Fung and Chen (1985), Maradudin, Méndez and Michel (1989). Only the scalar case, with a Dirichlet boundary condition, is treated here, but it is felt that the conclusions have general validity. Surfaces varying in both one and two dimensions are treated.

Formulation

It is assumed that a plane wave is incident from above on a rough surface. The mean location of the surface is at $z = 0$ and cartesian coordinates (x, y, z) are chosen with the x- and y-axis parallel to the mean level of the surface and the z-axis normal to it. The rough surface is given by $z = \zeta(x, y)$, where $\zeta(x, y)$ has Gaussian statistics and has a Gaussian correlation function with correlation length L. The rms surface height is h. The wavefield $\phi(x, y)$ at the surface $z = \zeta(x, y)$ satisfies the integral equation

$$\frac{1}{2} \frac{\partial \phi(x, y)}{\partial \nu} = \frac{\partial \phi_{inc}(x, y)}{\partial \nu} + \int\int_S \frac{\partial G(r)}{\partial \nu} \frac{\partial \phi(x', y')}{\partial \nu'} \, dS, \tag{1}$$

where the Green's function $G(r) = \frac{1}{4\pi r} \exp(ikr)$, $r = |\mathbf{x} - \mathbf{x}'|$, $\mathbf{x} = (x, y, \zeta(x, y))$, $\mathbf{x}' = (x', y', \zeta(x', y'))$ and the notation $\frac{\partial}{\partial \nu}$ represents the normal derivative. This form is appropriate for the Dirichlet boundary condition, where $\phi = 0$ on the surface. The initial condition is

$$\phi_{inc}(\mathbf{x}) = \exp(i\mathbf{k} \cdot \mathbf{x}) = \exp ik[x \sin\theta - \zeta(x, y) \cos\theta], \tag{2}$$

where θ is the angle the normal to the incident wavefront makes with the z-axis. Here the initial wave vector is in the x-z plane, without loss of generality as the surface is assumed statistically isotropic (but see later). By setting

$$\psi(x, y) = \frac{\frac{\partial \phi}{\partial \nu}}{\sqrt{1 + \left(\frac{\partial \zeta}{\partial x}\right)^2 + \left(\frac{\partial \zeta}{\partial y}\right)^2}}$$

we obtain

$$\frac{1}{2} \psi(x, y) = \psi_{inc}(x, y) + \int\int_S K(r) \psi(x', y') \, dx' dy'. \tag{3}$$

with $K(r) = \frac{\partial G(r)}{\partial \nu}$. This equation can be solved using a straightforward generalization of the methods described in the papers referenced in the first paragraph. We use a two-dimensional extension of the one-dimensional approach of Kachoyan and Macaskill (1987). We generate a set of 2-d periodic surfaces with appropriate statistics and correlation function. For each such surface, (2) is discretized using a trapezoidal rule for the integral, leading to a set of linear equations of the form

$$(I + A)\, \Psi = 2\Psi_{inc}, \tag{4}$$

where I is the identity matrix and A corresponds to the discrete form of the integral operator and $\Psi = [\psi_1, \psi_2, \ldots \psi_{N-1}]^T$ and similarly for Ψ_{inc}. This is a 2-d surface problem and so there are $\sqrt{N}$ equally spaced mesh-points in each of the x- and y- coordinate directions. Here $A_{ij} = -2K(r_{ij}) \Delta x \Delta y$, and $r_{ij} = |\mathbf{x}_i - \mathbf{x}'_j|$, $i, j = 1, \ldots N - 1$. By contrast with the integral equation for the 1-d case, the kernel has a singularity, which must be explicitly allowed for when calculating the elements A_{ij}. This is done here by a process of 'subtracting out' the singularity.

The system (4) must be inverted to find Ψ on the surface. This is the major part of the numerical procedure; once Ψ is known the scattered field can then be calculated analogously to the 1-d case (see Kachoyan

and Macaskill, 1987). Finally an ensemble average over all surface realisations gives the average scattered intensity as a function of angle.

The present work was carried out on an Apollo 10000 computer with 40 Mbytes of store. Some changes in approach are possible if significantly more store or faster cpu's are available. The 1-d version of (4) can be solved directly using elimination for up to about 1024 unknowns (Linpack routines take about 10 minutes cpu for each realization on the Apollo for this case). However for a larger number of unknowns the cost in cpu and storage is prohibitive. The 64 x 64 surfaces treated here generate systems of dimension 4096 : it is estimated that inversion of such a system would take over 11 hours on our system. Thus iterative techniques must be used to solve (4). For the cases described here each realisation was completed in less than 2 hours cpu.

Iterative methods

Following Boyd (1989), Chapter 12, write (4) as

$$\frac{d}{dt}\Psi + (I + A)\Psi = 2\Psi_{inc},\tag{5}$$

and look for a steady state solution. If (5) is approximated using the Euler method, with timestep τ, we find

$$\Psi^{n+1} = \Psi^n - \tau(I + A)\Psi^n + 2\tau\Psi_{inc},\tag{6}$$

with $\Psi^0 = 2\Psi_{inc}$ which is known as Richardson iteration for the iterations $n = 0, 1, \ldots$. The relaxation parameter is τ; the simplest choice is $\tau = 1$. This scheme applied to (4) proved to be successful, but with the number of iterations required generally increasing as h/L, the scaled rms height, was increased. In addition, when extensive tests were performed on 1-d problems where direct inversion was possible, convergence was always to the correct result. (Note that the initial approximation $\Psi^0 = 2\Psi_{inc}$ corresponds to the Kirchhoff approximation.) This scheme is implemented for 2-d problems with A being recalculated at each iteration due to storage limitations; this is then the major cost of the computation. An improvement on (6) is obtained by using minimum residual relaxation (see Boyd, 1989) which gives an optimal choice for τ for *symmetric* systems for each iteration and involves very little extra calculation. Although the system (4) is not symmetric, improved convergence rates were obtained using this method (see the discussion of S.C. Eisenstat, H.C. Elman and M.H. Schultz, 1983). A further improvement on (6) can be obtained by writing

$$\Psi^{n+1} = \Psi^n - \tau(I + B)^{-1}(I + A)\Psi^n + 2\tau(I + B)^{-1}\Psi_{inc},\tag{7}$$

where B is a preconditioner matrix. In the present context this was chosen to be the kernel matrix A on a coarser grid. This was conveniently calculated in the Fourier transform domain and involved a neglect of high frequency components for Ψ. For the Apollo system the matrix B corresponding to a 32 x 32 surface could be stored in memory; $(I + B)^{-1}$ was in all cases accurately and quickly approximated using several terms (say 5) in the series $(I + B) \approx I - B + B^2 - \ldots$. The use of a preconditioner matrix was found to give significantly improved convergence rates so that no more than 15 iterations were required to obtain all the results shown here. These numerical techniques have also been used for 1-d systems that can in general be solved directly; the advantages for such systems are that accurate solutions can be obtained much faster using iteration and that extremely long surfaces can be treated.

Several other possibilities have not been explored. The generalized conjugate residual method appears to be the most effect method for improving speed of convergence in non-symmetric systems (see Rohklin, 1983 and S.C. Eisenstat, H.C. Elman and M.H. Schultz, 1983). However, as adequate convergence rates were obtained without this degree of sophistication, the extra storage and complexity involved was deemed to be not worthwhile for the very large systems treated here. Another possibility is to use the first kind integral equation equivalent to (2) (see e.g. Thorsos, 1988), thus giving rise to a symmetric system, for which iterative solvers are far better understood. However, the condition number of such a system is not asymptotically limited, by contrast with the second kind integral equation used here (see Rohklin, 1983) and so it is not clear if this approach would necessarily be better.

Results

The methods described above have been used to generate intensity distributions in the parameter regime where enhanced backscatter is expected (see O'Donnell and Méndez, 1987, Kim et al, 1990). In figure 1(a),

using 30 realizations of a 64 x 64 surface, we show the intensity distribution as a function of the scattering angles θ_s, ϕ_s, measured from the z-axis, in the x-z and y-z planes respectively. These results correspond to the experimental case treated by O'Donnell and Méndez for $kL = 9.9$, $h/L = .7$ and incident angle $\theta = 40°$ (their surface #83). The results, on a regular 201 x 201 grid in θ_s, ϕ_s have been obtained by bivariate linear interpolation on the reflection coefficients which are equally spaced in the *cosines* of the scattering angles. In addition results are shown (fig. 1(b)) for the cut $\phi_s = 0°$. Polarization effects are *not* included in this scalar treatment, so the simulations are compared with the component in the experiments that experiences no change in polarization. Both curves are normalized so that the integral with respect to radian angle is unity; this will probably tend to overestimate the experimental curve as no account has been taken of the component that has undergone a change in polarization. The general agreement is good except in the forward direction where the peak intensity from simulations is much greater than the corresponding measurement. It is unclear what the source of this discrepancy is. In figure 2 we present normal incidence results; the 2-d distribution of intensity is to be compared with figure 12 of O'Donnell and Méndez. As there is no polarization in the simulations these are expected to give axially symmetric results, by contrast with the experiments, and this seems to be confirmed. In figure 2(b), where again both curves have been normalized to integral one the scattering peak is well predicted, but the side lobes do not appear in the simulations.

References

R.M. Axline and A.K. Fung, "Numerical computation of scattering from a perfectly conducting random surface", IEEE Trans. Antennas Propag. **AP - 26**, pp 482 - 488, (1978).

J.P. Boyd, *Chebyshev and Fourier Spectral Methods*, Springer-Verlag, Berlin, Heidelberg (1989).

S.C. Eisenstat, H.C. Elman and M.H. Schultz, "Variational iterative methods for nonsymmetric systems of linear equations", SIAM J. Numer. Anal., **20**, pp 345 - 357, (1983).

A.K. Fung and M.F. Chen, "Numerical simulation of scattering from simple and composite random surfaces", J. Opt. Soc. Am., **A2**, pp 2274 - 2284, (1985).

B.J. Kachoyan and C. Macaskill, "Acoustic scattering from an arbitrarily rough surface", J. Acoust. Soc. Am., **82**, pp 1720 - 1726, (1987).

M.-J. Kim, J.C. Dainty, A.T. Friberg and A.J. Sant, "Experimental study of enhanced backscattering from one and two dimensional random rough surfaces", J. Opt. Soc. Am., **A7**, pp 569 - 579, (1990).

C. Macaskill and B.J. Kachoyan, "Numerical evaluation of the statistics of acoustic scattering from a rough surface", J. Acoust. Soc. Am. **84**, pp 1826-1835, (1988).

A.A. Maradudin, E.R. Méndez and T. Michel, "Backscattering effects in the elastic scattering of p-polarized light from a large amplitude random grating", in *Light Scattering from Surfaces and Volumes*, eds. M. Nieto-Vesperinas and J.C. Dainty, (Elsevier), 1989.

M. Nieto-Vesperinas and J.M. Soto-Crespo, "Monte Carlo simulations for scattering of electromagnetic waves from perfectly conducting random rough surfaces", Optics Lett. **12** pp 979-981, (1987).

K.A. O'Donnell and E.R. Méndez, "Experimental study of scattering from characterized random surfaces", J. Opt. Soc. Am. A, **4**, pp 1194-1205, (1987).

J.M. Soto-Crespo and N. Nieto-Vesperinas, "Electromagnetic scattering from very rough random surfaces and deep reflection gratings", J. Opt. Soc. Am., **A 6**, pp 367-384, (1989).

V. Rokhlin, "Solution of acoustic scattering problems by means of second kind integral equations", Wave Motion, **5**, pp 257 - 272, (1983).

E.I. Thorsos, "The validity of the Kirchhoff approximation for rough surface scattering using a Gaussian roughness spectrum", J. Acoust. Soc. Am., **83**, pp 78-92, (1988).
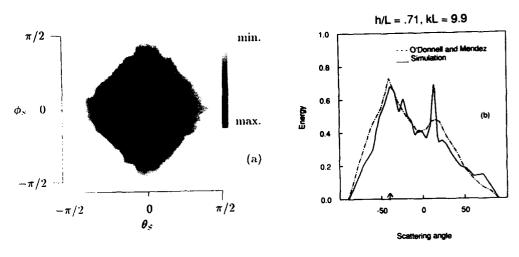
Figure 1. Comparison of simulation results with those of O'Donnell and Méndez (1987) (their diffuser #83). The incident angle is 40° and the wavenumber corresponds to a wavelength of .633μm. The experimental curve in figure 1(b) corresponds to the ss data of figure 11 in their paper. (Note that darker regions correspond to *higher* intensities.)
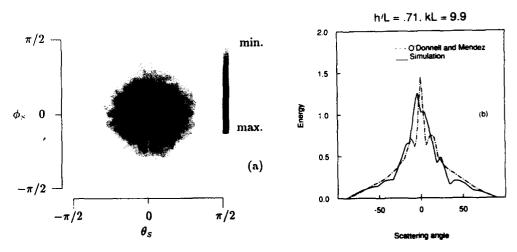
Figure 2. As in figure 1, but now with a normally incident wave. This corresponds to the case described in figures 9 and 12 of O'Donnell and Méndez (1987). In figure 2(b) the ss data taken from their figure 9 is shown.

The Role of Polarization in Enhanced Backscattering from Rough Surfaces

K.A. O'Donnell and M.E. Knotts
The School of Physics
Georgia Institute of Technology
Atlanta, Georgia 30332
USA

(**INVITED**)

The consequences of multiple scattering have recently been of considerable interest in the scattering of light waves from randomly rough surfaces. For surfaces that have strong slopes and correlation scale comparable to the incident wavelength, enhanced backscattering has been observed for surfaces rough in one and two dimensions[1, 2], and considerable theoretical work has been applied to the one-dimensional case[3-5]. It has perhaps been less appreciated that polarization plays a very significant role in scattering from both one and two-dimensional surfaces, and as is discussed below, it is not at all unusual for the scattered field to be found in a polarization state that is very different from the incident field.

In particular, second-order moments of the scattered field are normally of principal interest, where averages are taken over the ensemble of surface realizations. A natural formulation of these scattering problems is thus in terms of the Stokes vectors of the incident and scattered fields[6]. These Stokes vectors are generally related by a 4 x 4 matrix characteristic of the scatterer, which we will refer to as the Stokes scattering matrix. The form of the Stokes matrix clearly dictates what quantities are of theoretical interest and what experimental procedures should be followed.

One particularly simple example of a Stokes matrix is that of a one-dimensionally rough surface. It is well-known that a one-dimensional scatterer will not depolarized the light if the incident field has amplitude E_{1i} orthogonal to the corrugation direction, or else has amplitude E_{2i} that is along the corrugation direction [3-5] ; these polarization states are commonly referred to as p and s polarization, respectively. It may be derived directly from these considerations that the Stokes vectors of the incident and scattered field are related by a simplified Stokes matrix as in[7, 8]

$$\begin{bmatrix} I \\ Q \\ U \\ V \end{bmatrix} = \begin{bmatrix} s_{11} & s_{12} & 0 & 0 \\ s_{12} & s_{11} & 0 & 0 \\ 0 & 0 & s_{33} & s_{34} \\ 0 & 0 & -s_{34} & s_{33} \end{bmatrix} \begin{bmatrix} I_i \\ Q_i \\ U_i \\ V_i \end{bmatrix} \quad , \tag{2}$$

$$\text{or} \quad V = S \, V_i \quad , \tag{3}$$

where the elements of the Stokes vector of the scattered field V are given in the usual way by

$$I = \, <|E_1|^2> + <|E_2|^2> \; ,$$
$$Q = \, <|E_1|^2> - <|E_2|^2> \; ,$$
$$U = 2 \, \text{Re} \, [\, <E_1 E_2^*>] \; ,$$
$$\text{and} \quad V = 2 \, \text{Im} \, [\, <E_1 E_2^*>] \; , \tag{4}$$
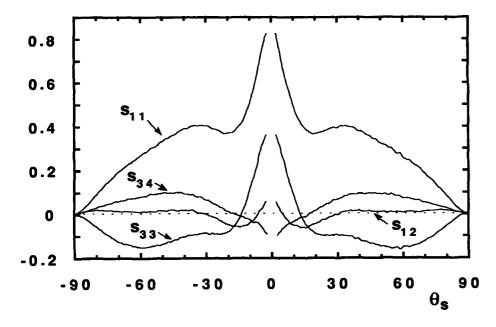
where E_1 and E_2 are the scattered wave amplitudes, and the Stokes parameters of the incident field are analogously defined in terms of E_{1i} and E_{2i}. Angle brackets represent averages over the ensemble of surfaces.

The Stokes matrix S contains only four unique elements, each of which appears in two places. The quantities s_{11} and s_{12} may be shown to be sums and differences of the p and s scattering cross-sections, respectively; these cross-sections have been investigated in considerable previous work[2-5]. However, it is clear that they comprise only two of the four quantities necessary to describe the properties of the scatterer. The other two matrix elements may be readily measured with a polarization state that is either a circular or ±45° linear state. For example, if the incident field is linearly polarized at +45° and thus has Stokes vector $V_+ = \{1, 0, 1, 0\}$, it is readily shown from Eq.(2) that the scattered Stokes vector is $\{s_{11}, s_{12}, s_{33}, -s_{34}\}$.

Experiments have been carried out to measure the four unique Stokes matrix elements of a one-dimensional random surface that produces enhanced backscattering. This surface was fabricated in photoresist using speckle exposing techniques[1,2], and the surface was then vacuum coated with a layer of gold. Data obtained with a Talystep surface profilometer estimated the standard deviation of the surface heights to be 1.95 µm and the correlation function to be an excellent approximation to a gaussian with $1/e$ width 3.57 µm. The histogram of surface heights

also provided a close fit of the desired gaussian form (coefficient of skewness = .062, kurtosis = 2.79).

The scattering properties of this surface were studied at wavelength 3.392 μm using a Jodon HN-20 He-Ne laser as a source. An incident beam was prepared in a linear state at +45°, and the four Stokes parameters of the scattered field were measured with standard techniques[9] from the powers passed by polarization components in the scattered field.

The plots above are experimental data for the four unique Stokes matrix elements as a function of the scattering angle θ_s and for $\theta_i = 0°$. First, s_{11} is the total scattered intensity for the +45° incident state V_+; it clearly shows the enhanced backscattering surrounding $\theta_s = 0°$. The element s_{12} depends on the difference between the s and p cross sections, and remains fairly small but also presents a maximum near $\theta_s = 0°$. The curve for s_{33} is clearly very significant; its positive regions represent angles where the scattered field is more strongly polarized at 45°, while at higher angles the curve is negative and the scattered field contains more power at −45°. The positive parts of s_{34} are regions where V_+ is scattered to left-elliptical states, though in the backscattering region s_{34} is

negative and V_+ is scattered to right-elliptical states. Hence, although a one-dimensional surface may not depolarize a p or s incident wave, the incident state V_+ produces a wide variety of scattered states at various field angles, and perhaps more importantly, all of the four unique Stokes matrix elements are implicit in the properties of the scattered field.

For surfaces that are rough in two dimensions, the Stokes matrix also takes on a simplified form if the surface is isotropic in the statistical sense. Though investigation of the full matrix is quite tedious in this case, we discuss some special cases of scattering from such a surface following gaussian height statistics. In particular, for a linearly polarized incident state, we show experimentally that the scattered field is composed of both pure polarized and randomly polarized components that are functions of position in the scattering hemisphere. The polarized component contains linear, elliptical, and even nearly circularly polarizations at various field angles. These observations are shown to be strongly dependent on the ratio of the incident wavelength and the surface correlation length.

References:

1) K.A. O'Donnell and E.R. Méndez, J. Opt. Soc. Am. A 4, 1194-1205 (1987).
2) M.J. Kim, J.C. Dainty, A.T. Friberg, and A.J. Sant, J. Opt. Soc. Am. A 7, 569-577 (1990).
3) J.M. Soto-Crespo and M. Nieto-Vesperinas, J. Opt. Soc. Am. A 6, 367-384 (1989).
4) T. Michel, A.A. Maradudin, and E.R. Méndez, J. Opt. Soc. Am. B 6, 2438-2446 (1989).
5) M. Saillard and D. Maystre, J. Opt. Soc Am. A 7, 982-990 (1990).
6) A. Ishimaru, *Wave Propagation and Scattering in Random Media*, Vol. 1 (Academic Press, New York, 1978).
7) K.A. O'Donnell and M.E. Knotts, J. Opt. Soc. Am. A (in press).
8). T.R. Michel, M.E. Knotts, and K.A. O'Donnell , J. Opt. Soc. Am. A (submitted).
9) M. Born and E. Wolf, *Principles of Optics* (Pergamon, Oxford, 1975).

Space-frequency coupling in scattering
from rough surfaces

Daniel Maystre and Marc Saillard

Laboratoire d'Optique Electromagnétique,
Unité de recherches associée au CNRS n° 843,
Faculté des Sciences et Techniques de Saint Jérôme,
Case 262,
Avenue Escadrille Normandie Niemen,
13397 MARSEILLE Cédex 13
                                        France

Phone : (33) 91288374

The aim of the communication is to describe the phenomena of scattering of a beam of wavelength λ illuminating a quasi-grating the shape of which is given by the equation

$$y = h_1 \cos(\alpha x) + h_2 \cos(\beta x + \phi)$$

with

$$\alpha = \frac{\lambda}{d_1}$$

$$\beta = \frac{\lambda}{d_2}$$

d_1 and d_2 being the periods of the two sine functions and ϕ the phase shift.

When the wavelength λ and the incidence angle θ have been fixed ($\lambda = 1\mu m$ and $\theta = 30°$ in our first calculations), as well as h_1/d_1 and h_2/d_2 (these two parameters are taken equal to each other in our first calculations), and if one is measuring the scattered intensity in a given direction (the backscattering direction in our first calculations), the scattering phenomena can be described by a 3D graph giving the intensity versus α and β, provided ϕ has been fixed (0 in our first calculations). Such a surface is sometimes called quasi grating. Indeed, it must be noticed that it identifies to an actual grating when α/β is rational. Otherwise, the periodicity of the surface does not hold any longer. This limit between periodic and non periodic surfaces is in fact too mathematical in nature and it comes out that the actual separation between periodic and non periodic surfaces depend on the width of the incident beam : the periodicity of the surface has not any influence on the scattered field when the incident beam does not illuminates at least 5 periods of the grating. Furthermore, it must be noticed that even when the surface may be considered as a grating in that sense, the considered direction of scattering does not always coincide with a direction of *scattering of the grating. The direction of observation coincides with an order of* the grating when the following relation, called "equation of privileged directions" is satisfied

$$n\alpha + m\beta = c$$

where c is a constant depending on the incident and scattering angles θ and θ'

$$c = \sin(\theta') - \sin(\theta)$$

, and n, m is a couple of positive integers. As a consequence, the location of the gratings in the 3D dgraph is a set of straight lines.

The first conclusion of our calculations was that the notion of intensity is not well adapted to this study. Indeed, when the surface is a grating illuminated on more than 5 periods, the "efficiency" of the grating (viz. the energy going into

a given order of the grating) is the ratio of the integral of the scattered intensity in that direction on the integral of the incident intensity . We have defined the notion of "efficiency of an arbitrary rough surface in a given direction", which identifies with the classical efficiency of the grating when the direction of scattering which is observed identifies with the direction of a grating order, provided that the width of the incident beam is large enough.

Using this new notion, we have drawn the 3D graph of the scattering efficiency of the quasi grating. The perturbation theory shows that when h_1 and h_2 are very small compared with λ, the 3D graph identifies with very short ridges concentrated around the lines where the equation of privileged directions is satisfied with $n=0$ and $m=1$ or $n=1$ and $m=0$. Then, when the height of the grooves is increased, new ridges appear since all the priviledged directions receive progressively some efficiency while the width of the ridges increases.

One of the fundamental results deals with the coupling range : The coupling strongly decreases when the two periods become very different to each other.

We shall present these results and other ones, showing that it exists a phenomenon of space frequency coupling, which means that the scattering by a quasi grating cannot be deduced simply from the scattering of the two components of the profile, except for very small heights. A good knowledge of these coupling phenomena should bring us valuable informations on the phenomena of scattering from random rough surfaces or more complicated structures like scale invariant surfaces.

Optical properties of porous pigment coatings; dependent vs. independent scattering

Timo Hyvärinen and Juha Sumen
Technical Research Centre of Finland, Electronics Laboratory
P.O.Box 200, SF-90571 Oulu, Finland

Introduction

In pigment coatings the scatterers usually occupy an appreciable fractional volume. E.g., in paper coatings which are applied on printing papers to improve their optical and printing properties, 50-75 % of the volume is occupied by the pigments, 35-20 % by the pores and the rest by the binder. These figures indicate that even if the pores are considered as scatterers, paper coatings are dense random distributions of scatterers for which the assumption of independent scattering is not valid. In these cases the materials' scattering and absorption coefficients per unit volume are nonlinear functions of the scatterers' concentration. This phenomenon is often called dependent scattering.

The optical properties of pigment coatings, and dense scattering materials in general, have been the object of experimental and theoretical studies for more than three decades. Semi-empirical models, e.g. /1/, as well as more physical models based on heuristic modifications of Mie theory /2,3/ have been proposed. Recently various approximate solutions of the multiple scattering equations have been developed to treat the dependent scattering problem /4,5/. We have considered a hybrid theory approach in which we first characterize the dense medium by calculating the dependent extinction and scattering properties per one scatterer using the multiple scattering theory with the quasicrystalline approximation (QCA) and the distorted Born approximation (DBA), and then apply these results in the conventional radiative transfer theory (RTT). In this paper the dependent scattering theory is used for studying the optical properties of paper coatings, and the results are also compared to independent scattering calculations (based on Mie and radiative transfer theories). The pores in the coating are considered as scatterers because their volume fraction is smaller than that of the pigments, and also their form factor (shape deviation from a sphere) is usually smaller. The interesting pore size range in paper coatings is from 0.05 to 1 μm.

Theory

The theoretical approach for dependent scattering is based on the configurational averaring (over the scatterer positions) of the multiple scattering equations. This leads to a hierarchy of equations which is truncated by using the QCA, resulting in the consideration of pair correlation between the scatterers, only. By assuming spherical scatterers of one species embedded in a medium with a propagation constant k, a plane normally incident wave and a plane wave solution for the coherent field, and by using the T-matrix formalism for the scatterers, the following generalized Evald Oseen and Lorentz-Lorenz equations for the dependent (effective) propagation constant K can be derived /4/:

$$K-k = - (\pi i n_o/k^2)\sum_n(2n+1)(T_n{}^M X_{1n}{}^M + T_n{}^N X_{1n}{}^N), \text{ and} \tag{1}$$

$$X_{1v}{}^M = - 2\pi n_o\sum_n\sum_p(2n+1)\{L_p(k,K|b)+M_p(k,K|b)\}\{T_n{}^M X_{1n}{}^M a(1,n|-1,v|p)A(n,v,p) \\ +T_n{}^N X_{1n}{}^N a(1,n|-1,v|p,p-1)B(n,v,p)\}, \tag{2a}$$

$$X_{1v}{}^N = - 2\pi n_o\sum_n\sum_p(2n+1)\{L_p(k,K|b)+M_p(k,K|b)\}\{T_n{}^M X_{1n}{}^M a(1,n|-1,v|p,p-1)B(n,v,p) \\ +T_n{}^N X_{1n}{}^N a(1,n|-1,v|p)A(n,v,p)\}, \tag{2b}$$

where

$$L_p(k,K|b) = \{-b^2/(K^2-k^2)\}\{kh_p{}'(kb)j_p(Kb)-Kh_p(kb)j_p{}'(Kb)\} \tag{3}$$

$$M_p(k,K|b) = \int_b^\infty r^2\{g(r)-1\}h_p(kr)j_p(Kr)dr, \tag{4}$$

and A, B and a are coefficients depending on the harmonic indices n and p. $T_n{}^N$ and $T_n{}^M$ are T-matrix elements for a sphere, b is the diameter of the sphere, n_o is the number of scatterers per unit volume, h_p is Hankel and j_p spherical Bessel function, and g(r) is the pair distribution function for which the Percus Yevick solution is used. K and the unknown field coefficients $X_{1n}{}^M$ and $X_{1n}{}^N$ can be numerically solved from Eqs. 1 and 2. The real and the imaginary parts of K are proportional to the dependent refractive index n_e and extinction coefficient β_{te} of the dense medium,

respectively, $n_e = \lambda Re(K)/2\pi$ and $\beta_{te} = 2Im(K)$. The dependent extinction coefficient β_{ee} and cross section C_{ee} for the spherical scatterers in the dense medium can now be calculated, $\beta_{ee} = 2Im(K-k)$ and $C_{ee} = 2Im(K-k)/n_o$.

As a second step, the single scattering of the coherent field is calculated by applying the DBA /4/. By assuming a randomly polarized incident wave, the following equation for the dependent scattering cross section C_{se} of a sperical scatterer can be derived:

$$C_{se} = (\pi/|k|^2)\int_0^\pi \{ \, |\, \Sigma_n\{(2n+1)/n(n+1)\}\{T_n{}^M X_{1n}{}^M \pi_n(\cos\theta_s) + T_n{}^N X_{1n}{}^N \tau_n(\cos\theta_s)\}\, |^2$$
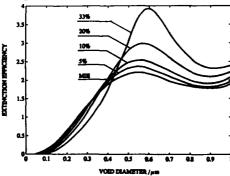
$$+ |\, \Sigma_n\{(2n+1)/n(n+1)\}\{T_n{}^M X_{1n}{}^M \tau_n(\cos\theta_s) + T_n{}^N X_{1n}{}^N \pi_n(\cos\theta_s)\}\, |^2\} W(\theta_s,\phi_s)\sin\theta_s d\theta_s, \qquad (5)$$

where

$$W(\theta_s,\phi_s) = 1 + n_o Re\{\int_{-\infty}^\infty \{g(r)-1\}\exp\{i(ReK-k_s)\bullet r\}dr, \qquad (6)$$

and π_n and τ_n are the angle function notations used in Mie theory /6/. (θ_s,ϕ_s) is the scattering angle. The vector K goes downward and the vector k_s in the scattered direction. The effective asymmetry parameter g_e is calculated according to its definition, by multiplying the integrand in Eq. 5 by $\cos\theta_s$ and then dividing the result by C_{se}. It is interesting to compare (5) with the classical Mie theory. In Mie theory the coefficients X and W are absent. For a sparse concentration of scatterers the values of X and W approach 1, and the two cases reduce to each other.

A dependent scattering computer code has been generated. In its present form it can be used for size parameters up to about 20. Some discrepancies have been found with larger size parameters between the calculated values of C_{ee} and C_{se} for nonabsorbing scatterers although the values should be the same. It is not yet clear whether the discrepancies are due to theoretical or numerical inaccuracies. Fig. 1 shows the extinction efficiency and asymmetry parameter for a pore in a polystyrene matrix as calculated from Mie and the dependent scattering theories. Pore size ranges from 0.05 to 1 μm corresponding to a size parameter from 0.74 to 10.9 at 460 nm wavelength. For pores smaller than 0.35 μm the dependent extinction efficiency is smaller than the independent value, the relative difference increasing with smaller pore sizes. For pores larger than 0.4 μm the dependent extinction efficiency exceeds the independent value, the first maximum having a strong amplification with an increasing concentration. The dependent asymmetry parameter is smaller than the Mie value for all pore sizes. In Fig. 2 the calculated dependent and independent extinction coefficients for pores in polystyrene are compared as a function of concentration (porosity).

To calculate the optical properties of a coating layer the dependent single scattering parameters C_{ee} and g_e are used in the conventional RTT. The radiative transfer eqution (RTE) for a parallel plane geometry is used because usually the dimension of the area under measurement is much larger than the thickness of the coating. A further simplification is achieved by using the so called Eddington and Delta-Eddington approximations to solve the RTE /7/. These approximations are well suited for cases where parameters averaged over the angle distribution (such as the hemispherically integrated reflectance) are determined. This is the usual practice in paper measurements. Reflections at the coating boundaries are calculated assuming smooth boundaries and using the dependent refractive index for the coating.
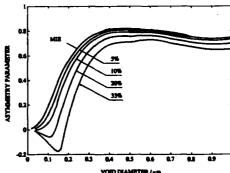
Fig. 1. Calculated independent and dependent (for 5, 10, 20 and 33 % porosities) extinction efficiency and asymmetry parameter for a pore in a polystyrene matrix as a function of the pore size. $\lambda = 460$ nm.
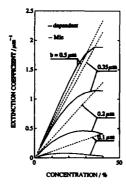
Fig. 2. Calculated extinction coefficient for pores in a polystyrene matrix as a function of porosity. b is pore diameter. $\lambda = 540$ nm

Table 1. Measured (R_m) /10/ and calculated (R_{dep}, R_{ind}) reflectances of suspension layers of polystyrene spheres in water. b is sphere diameter, f is sphere concentration and l is layer thickness. $\lambda = 436$ nm.

b = 0.102 μm					b = 0.530 μm				
f(%)	l(mm)	R_m	R_{dep}	R_{ind}	f(%)	l(mm)	R_m	R_{dep}	R_{ind}
					0.5	1.47	60.0	60.4	59.8
2.8	1.01	79.3	77.6	77.4	2.8	1.47	86.3	85.9	85.2
9.1	0.61	82.3	81.8	84.9	9.4	0.51	87.1	87.4	86.5
13.6	0.61	84.0	83.9	88.1	12.7	0.56	89.7	89.8	89.2
18.1	0.61	84.6	84.3	89.8	15.0	0.61	91.5	91.0	90.6
18.1	1.01	89.3	88.4	92.0	15.0	1.07	93.0	93.0	92.7
22.0	1.01	88.8	88.2	92.7	21.7	1.01	93.8	93.6	93.4
28.9	1.01	86.6	86.7	93.4	29.5	1.01	94.2	93.9	94.0

Comparison with experiments

Two kinds of experimental results have been used to verify the theoretical calculations. First, experiments with water suspensions of well defined polystyrene spheres have been used. There are two published papers presenting coherent wave attenuation measurements for dense polystyrene sphere suspensions, and comparisons to dependent scattering calculations /8,9/. We have extended the measurements to the near infrared region (1.0-2.5 μm) where strong absorption effects by water are present. The measurement set-up consisted of a sample cuvette illuminated by a collimated beam from a FTIR-spectrometer, and a narrow field of view (0.3°) detector system. The coherent wave attenuation was measured as a function of wavelength over a range of concentrations up to about 50%, and, so far, for three sphere sizes, 0.14, 0.26 and 0.39 μm. Fig. 3 shows the measured and calculated transmission spectra of nine suspension layers, related to the transmission of pure water. The transmission peaks at the water absorption bands (1.45 and 1.93 μm) are due to the fact that in the suspensions strongly absorbing water is substituted by less absorbing polystyrene. The calculated spectra are based on the dependent scattering theory. Correspondence between theory and experiment is very good. Fig. 3d depicts the results in another form; the extinction coefficients 2Im(K-k) for three ka values as a function of sphere concentration.

Vasalos has measured transmission and reflection as a function of angle for similar suspensions /10/. Table 1 shows the hemispherically integrated reflectance values determined from the measurements and corresponding calculated values. Again, there is an excellent agreement between experiments and dependent scattering calculations.
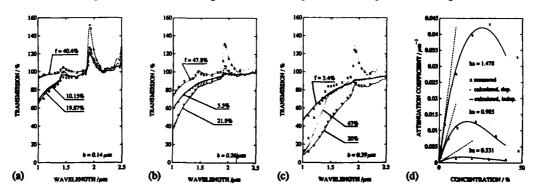
Fig. 3. (a ,b and c) The measured (lines) and calculated (symbols) transmission spectra of nine suspension layers consisting of polystyrene spheres in water. Layer thickness is 52 μm. f is sphere concentration and b is sphere diameter. (d) The extinction coefficient of the spheres as a function of the sphere concentration. λ=1.1 μm.

241

Secondly, reflection measurements made by Alince and Lepoutre /11/ and by Lindblad et al /12/ with dry binderless coatings formed of polystyrene spheres have been used for verifications. They have measured the reflectance of the coatings over black and white backings, and determined the Kubelka-Munk scattering coefficient S in relation to basis weight (kg/m²). Fig. 4 shows the measured and correspondingly calculated scattering coefficients as a function of the coating pore size. Assuming the uniformly sized pigments ideally packed, an equivalent spherical pore diameter was estimated based on the hydraulic diameter concept /12/. For 33% porosity the pore size is 0.33b when b is the pigment diameter. The independent scattering results seem to fit well to the measurements by Alince and Lepoutre, but due to the discrepancies in the experimental results, a question remains how coincidential this is. The investigation of the electron micrographs of the coating surfaces reveals that, infact, the spheres are not ideally packed, and the coatings have some void size distribution above the ideal values. Fig. 4 (c and d) shows preliminary results obtained by the scattering theories after enhancement for multiple species of scatterers. Pore size distribution from 0.33b to 0.55b was used in the calculations. Now the agreement between the dependent scattering theory and experiment is fairly good. However, more measurements of porous structures over larger pore size and porosity ranges are needed.
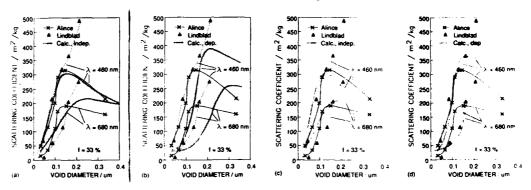
Fig. 4. The measured and calculated scattering coefficients of polystyrene sphere coatings as a function of pore size, (a and b) assuming uniform pore size, and (c and d) pore size distribution from 0.33b to 0.55b, b is sphere diameter.

References

1. H.C. Hottel, A.F. Sarofim, W.H. Dalzell and I.A. Vasalos, "Optical properties of coatings. Effect of pigment concentration", AIAA Journal, Vol 9, 1895-1898, 1971.

2. L.F. Gate, "Light-scattering cross sections in dense colloidal suspensions of spherical particles", J. Opt. Soc. Am., Vol 63, 312-317, 1973.

3. S. Fitzwater and J.W. Hook, "Dependent scattering theory: A new approach to predicting scattering in paints", J. Coatings. Tech., Vol. 57, 39-47, 1985.

4. L. Tsang, J.A. Kong, and R.T. Shin, Theory of microwave remote sensing, Wiley-Interscience, New York, 1985.

5. L. Tsang and A. Ishimaru, "Radiative wave and cyclical transfer equations for dense nontenuous media", J. Opt. Soc. Am. A, Vol. 2, 2187-2193, 1985.

6. H.C. van de Hulst, Light scattering by small particles, Wiley, New York, 1957.

7. J.H. Joseph, W.J. Wiscombe and J.A. Weinman, "The delta-Eddington-approximation for radiative flux transfer", J. Atmos. Sci., Vol. 33, 2452-2459, 1976.

8. V.K. Varadan, V.N. Bringi, V.V. Varadan and A. Ishimaru, "Multiple scattering theory for waves in disdrete random media and comparisons with experiments", Radio Sci., Vol. 18, 321-327, 1983.

9. V.V. Varadan, Y. Ma and V.K. Varadan, "Propagator model including multipole fields for discrete random media", J. Opt. Soc. Am. A, Vol. 2, 2195-2201, 1985.

10. I.A. Vasalos, Effect of separation distance on the optical properties of dense dielectric particle suspensions, Doctoral Dissertation, Massachusetts Institute of Technology, 1969.

11. B. Alince, and P. Lepoutre, "Light-scattering of coatings formed from polystyrene pigment particles", J. Colloid & Interface Sci., Vol. 76, 182-187, 1980.

12. G. Lindblad, T. Iversen, H. Bergenblad and M. Rigdahl, "Light scattering ability of coatings as a tool to protect paper and board against photo-oxidation", Nordic Pulp and Paper Res. J., No. 4, 253-257, 1989.

RANDOM ROUGHNESS CHARACTERIZATION OF CaF2/Ag AND Ag/CaF2 SYSTEMS

L.E. REGALADO[+] , R. MACHORRO, J.M.SIQUEIROS
Instituto de Física, Universidad Nacional Autónoma de México
Apdo. Postal 2681, 22800 Ensenada, B.C. MEXICO

S U M M A R Y

The optical properties of thin-film materials may be revisited by considering both interference and scattering effects due to surface roughness and inhomogeneities. There are many techniques for measuring random roughness surfaces, however, in a multilayer system the interfaces may be buried and inaccessible to some surface probes. Optical techniques, such as the one we describe here are capable of reaching inner interfaces and have the advantage of not requiring controlled ambient for the measurements.

The use of light as a probe for surface and interface *roughness* characterization is aimed in this case, to the excitation and detection of surface plasma waves (SEW). A typical experimental set up is the Attenuated Total Reflection configuration (ATR) shown in Fig. 1 /1/, where p-polarized light
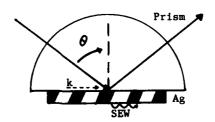
Fig.1   Typical set up for RTA characterization

enters through a prism into the sample. The existence of evanescent waves at the glass-film interface allows the coupling of

light to the normal collective modes of the electrons at the film-air interface, exciting SEW. An evanescent EM wave and a longitudinal plasma wave will propagate along the film surface and couple to light through the random roughness /2/ reradiating onto the air space, where light is detected.

The statistical reflected distribution is to be treated by using the linear theory of dispersion /3/ and compared to previous results on Ag/CaF2 system reported by Ames et al. /4/ and the corresponding results of N. Mayani et al /5/ using a replication technique.
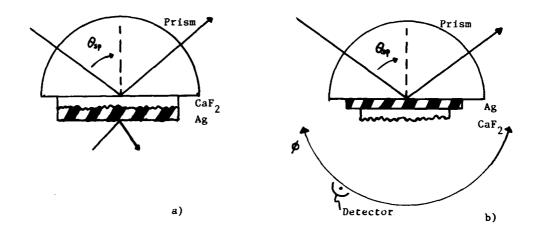
Fig.2   Configurations under study a) CaF$_2$/Ag,   b) Ag/CaF$_2$

The systems under study are shown in Fig. 2. The CaF2/Ag system is chosen because our previous work /6/ has shown that this configuration is more sensitive than the one where the Ag surface is artificially roughened through the CaF2 underlayer. Some preliminary results on the kind of radiation distribution emitted by the rough surface are shown in Fig. 3.

Enhancement phenomena on the scattered light may be conveniently approached with this technique and a comparison of this method of surface roughness characterization with other techniques will allow us to evaluate its sensitivity.
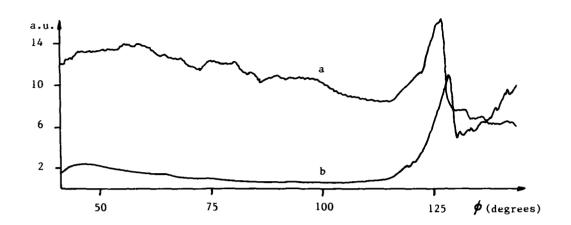
Fig. 3   Surface plasmon decay into light due
to rough surfaces in systems a) and b) from Fig.2

REFERENCES

† On sabbatical leave from Universidad de Sonora, CIFUS
Permanent Address: A.P. 5-088, 83191, Hermosillo, Sonora, México

/1/ E. Kretschmann, H. Raether, Z. Naturforsch 23a, 2135
(1968).

/2/ E. Kretschmann, Opt. Comm. 10, 356 (1974).

/3/ H. Raether, Surface Plasmons on smooth and rough surfaces
and on gratings, Springer tracts in Modern Physics, Vol. III,
Berlin (1988).

/4/ G.H. Ames, D.G. Hall, A.J. Braundemeir Jr., Opt. Comm. 43,
247 (1982).

/5/ N. Mayani, F. Varnier, G. Rasigni, J.Opt.Soc.Am.A 7, 191
(1990).

/6/ L.E.Regalado, R. Machorro, T. Yamaguchi (in press)

SCATTERING

MULTIPLE SCATTERING, FLUCTUATIONS AND LOCALIZATION OF LIGHT

R. MAYNARD
CRTBT and Université Joseph Fourier
BP 166X, 38042 Grenoble Cedex, France

(INVITED)

Multiple scattering of light in disordered media has been a subject of intensive study the last years. It may be noted that stimulations for these studies came partly from the analogies between the optical problem and the transport properties in impure metals where have emerged the concepts of weak and strong localization. This led to the discovery of the coherent backscattering peak in random substances built up by constructive interferences between direct and time reserved multiply-scattered waves. The specific law of time variation of the correlation function of intensity at very short time for Brownian motion of scatterers, long range correlation analogous to the "Universal conductance fluctuations" in the speckle patterns, and the problem of the Anderson Localization transition are presently actively studied.

Today, the present state of art can be summarized around the following principles :

– The concept of light mean free path l or better, of the transport mean free path l* (defined from standart mean free path by dividing l by <1-cosθ>) is the relevant parameter for separating the regime of weak localization (kl*>>1) from strong localization regime (kl*<1) (k : wave vector),

– Strong multiple scattering regime (where the size of the sample is much larger than l*) can be described in terms of a simple diffusion theory of parameter D = cl*/3 (c : light velocity). The validity of this analysis is surprisingly broad : high concentration of scatterers or even, proximity of the Anderson Localization where D is reduced and vanishes continuously when the characteristic size of the system diverges,

– Contrasting with electrons, the vector nature of the electromagnetic fields introduces new degrees of freedom. Beyond the concept of depolarization of light by multiple scattering, new effects have been proposed and observed : polarization memory effect, and distribution of the stokes parameters through a microstatistics of optical waves. Most of these results have been obtained by the BAR-ILAN group.

– The research of the Anderson Localization is a stimulating challenge in the field of multiple scattering. The most advanced studies of this transition have been made recently by the GENACK and coworkers by using microwaves.

The main references about these topics up to 1990 can be found in the reference 1.

INTENSITY FLUCTUATIONS

Consider a slab of thickness L, of transverse dimension W, and an incident plane waves parallel to the slab. The transmitted intensity fluctuations, I(ω), measured for instance, normally to the slab of a "frozen" sample varies with ω. For an ensemble of random samples a correlation function is built up :

$$C(\Delta\omega) = \frac{<I(\omega)I(\omega+\Delta\omega)> - <I(\omega)><I(\omega+\Delta\omega)>}{<I(\omega)><I(\omega+\Delta\omega)>}$$

This corresponds to the situation where two incoming beams, therefore 4 fields E(ω), E*(ω), E(ω+Δω) and E*(ω+Δω) of frequency ω and ω +Δω are present in the slab. The waves are supposed scalar for simplicity. The values of the emerging fields result from distinct sequences of scattering or Feynmann trajectories. But the ensemble average forces the paths of the direct and conjugate fields to be identical : this is the approximation of "Ladder-diagrams" and only two distinct paths, one with E(ω) and E*(ω) and the other with E'(ω+Δω) and E'*(ω) can subsist after this average in C(Δω). Three categories must be considered : the independant trajectories, the one-crossing trajectories, the double crossings.

$$C(\Delta\omega) = C^{(1)} + C^{(2)} + C^{(3)}$$

1) The independent trajectories (or the factorization) approximation :

Within this approximation $C^{(1)}(\Delta\omega)$ is proportional to $<E(\omega)E^*(\omega + \Delta\omega)>^2$. For a given sequence of scatterings, the frequency shift introduces a phase change proportional to the length s of the trajectory : $\Delta\phi(s) = \Delta\omega s/c$. Let us call $P(\vec{r} - \vec{r}' ; s)$ the probability to travel in a slab by random walk from $\vec{r}$ to $\vec{r}'$ on path of length s. Hence the correlation function of the field is nothing else than the Fourier transform of $P(\vec{r} - \vec{r}' ; s)$: $\int P(\vec{r} - \vec{r}' ; s) e^{i \Delta\omega s/c} ds$ 　　　　　(1)

This function introduces a new length : $\xi(\Delta\omega) = (D/\Delta\omega)^{1/2}$ the diffusion or attenuation length and the integral in (1) varies as $\exp(-/\vec{r} - \vec{r}'//\xi)$. For the slab geometry, one finds easily

$$C^{(1)}(\Delta\omega) \simeq <T_{ab}>^2 e^{-L/\xi}$$
　　　　　(2)

when $l^* << \xi << L$. (Alternatively one can write $L/\xi(\omega) = (\Delta\omega/\omega_c)^{1/2}$ where $\omega_c = D/L^2$). The average transmission factor $<T_{ab}>$ from one - channel of incoming wave a to one channel of outgoing wave b is equal to ℓ/NL where N is the number of incoming channels (for instance $(W/\lambda)^2$ in a wave guide of transverse dimension W).This exponential decay is well established theoretically [2][4] numerically [3] and experimentally [5] [6].

Another consequence of this correlation arises when the incident waves vectors differ by $\Delta\vec{k_a}$ and the emergent vectors by $\Delta\vec{k_b}$ in a slab of infinite transverse direction. This configuration maintains the translationnal invariance parallel to the slab in average which produces the selection rule $\Delta\vec{k_a} = \Delta\vec{k_b}$. This "memory effect", despite the random multiple scattering of the light, has been observed [7] as an entire move of the speckle pattern following any small change in the incident wave vector. In reflection [8], as for the coherent backscattering, the time reversed sequence of scattering or crossed-diagrams are responsible for another "selection rule" leading to a second peak in $\Delta\vec{k_a}$.

2) Long-range correlations

The next term which contributes to the intensities fluctuations originates in the possible crossing between any two Feynmann trajectories. For an infinite slab this occurence is rather rare. But for a wave guide or strip geometry which confines the trajectories in the transverse dimension, this event becomes sizeable.

It is not difficult [9] [10] to estimate the probability of crossing two trajectories : the typical number of elementary steps in a diffusive path is $(L/l^*)^2$. This number must be compared to the total number N_T of elementary coherent volume $\lambda^2 l^*$ in the total volume of the sample $W^2 L$: $N_T = W^2 L/\lambda^2 l^*$. The probability for an elementary volume to belong to a Feynmann path in $(\lambda/W)^2 L/l^* = g^{-1}$. If $1-\Pi$ is the probability of zero crossing, one can write : $(1-\Pi) = (1-g^{-2})^{N_T}$ which gives $\Pi \simeq L^2/gl^{*2}$ in the weak-disorder limit. Therefore the amplitude of the correlation function $C^{(2)}$ related to the crossing of Feynmann trajectories is reduced by a factor of $1/g$ as compared to the previous correlation function $C^{(1)}$.

Another important property of the crossing Feynmann trajectories is the multiplicity of configurations generated by interchanging the fields. For instance the pairs of path represented in figure 1 do not carry any phase difference in the left part between O and z but only in the right part of the figure.

The plane z of the crossing points can be considered as a source and it is uniformly distributed between O and R. The portion of space where dephasing occurs, through independent trajectories is located between z and L and produces an exponential decreases of precedent type : $\exp(-(L-z)/\xi)$. By summing over z from O to L one gets a correlation function decreasing slowly as :

$$C^{(2)} \simeq \frac{<T_{ab}>^2}{g} \frac{\xi}{L} \simeq (\frac{\omega_c}{\Delta\omega})^{1/2}$$
　　　　　(3)

This is the long range fluctuation regime predicted theoretically [2] [11] [12] and observed with visible light [6] and microwave radiation [13].

3) Universal "conductance" fluctuations [2] [14] [15]

The occurence of double crossings for two Feynmann paths introduces still a longer range of correlation. The probability of occurence is proportionnal to $1/g^2$, while the dephasing part of the trajectories is delimited by two planes z_1 and z_2 within the slab (see figure 2). The resulting correlation is independent of L and depends only weakly of ξ/l^*. The amplitude is weak : $C^{(3)} \simeq <T_{ab}>^2/g^2$ which is just N^{-4}, but $C^{(3)}$ acts between all the channels. Hence the sum over all the input and output channels is of order of unity : they are precisely the giant fluctuations of the conductance of impure metals in units of

$(e^2/h)^2$ observed in mesoscopic conductor. A recent attempt for measuring $C^{(3)}$ is reported in reference (13).

§ 2 Diffuse wave spectroscopy [17]

Consider the temporal intensity fluctuations for scatterers undergoing random (Brownian) or deterministic (flow) motion. Now the one of the two fields running in the same sequence of scattering is delayed by time t. For independent trajectories the dephasing is due to the change of position of the γth scatterer $\Delta \vec{r}_\gamma (t)$ $(\vec{k}_\gamma - \vec{k}_{\gamma-1})$ where $\vec{k}_\gamma$ are the successive scattered wave vectors. In average this change of phase is zero since $\Delta \vec{r}_\gamma(t)$ is randomly distributed by the brownian motion of scatterers, but the second moment of the phase change is non zero and equal to :

$$\overline{\Delta \phi^2}(s) = t/\tau_B \ s/l^* \qquad (4)$$

where τ_B is the characteristic time for dephasing $\tau_B^{-1} = D_B k^2$ where D_B is diffusion constant for the Brownian motion. Mathematically the situation is identical to the previous case where $\Delta \omega$ probed the length of trajectories : here $\xi(t) = l^*(\tau_B/3t)^{1/2}$ represents the attenuation length due to delay between the field and its conjugate. For transmission this temporal correlation varies as $e^{-L/\xi(t)}$ but for reflection for thick slab, ξ is less than L and one finds [18] that $\ln C_1^{(t)}$ decrease as $-\alpha(t/\tau_B)^{1/2}$ where α is a factor of order 1.This strong decrease of C_1 for short time originates from the multiple scatterings : altough at short times the Brownian motion of the scatterers is only a small fraction of the wavelength, the cumulative displacement of a great number of scatterers for large path operates efficiently.

The long range correlation could also be present for dynamical fluctuations if the geometry of wave guide is used. From the previous calculation of $C^{(2)}$, a long time behavior is predicted in transmission as ξ/L or $(l^*/L) (\tau_B/3t)^{1/2}$ or even nearly constant from $C^{(3)}$. While these special regimes have not been observed so far, the "square-root" decrease of the time correlation has been tested experimentally[19][20]. Moreover a detailed analysis of the short-time self-diffusion constant of spheres in hydrodynamic interaction validates the diffusion approximation of light in correlated dispersions[21].
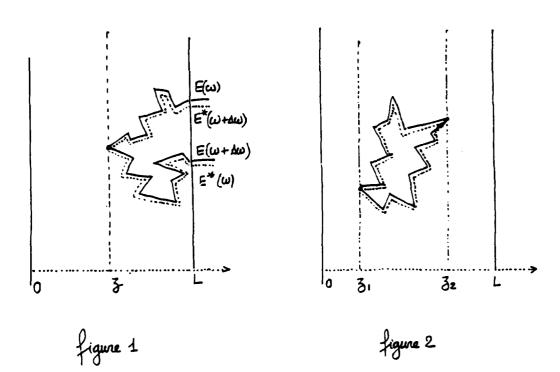
For laminar flow dragging the scatterers the displacement of the scatterers at time t is now linear in t. Actually it is the r m s of the gradient of the velocity field which must be averaged over a typical trajectory of light diffusion. A new characteristic time of the laminar flow occurs τ_l^{-1} α kl r m s $(\partial V_z/\partial_x)$ where z is orientated perpendicular to the plane slab. A new decorrelation length ξ appears $l^*(\tau_l/3t)$ which leads in reflection to a decreasing linear regime[17] in t (instead of $\sqrt{t}$) for shear flow. The previous law has been generalized[22] to Poiseuille flow and plug flow.

I would like to thank Drs G. Maret and E. Wolf for valuable suggestions and comments.

Bibliography

(1)   Scattering and localization in classical waves in random media, P. Sheng, Editor World Scientific (1990).
(2)   S. Feng, C. Kane, P.A Lee and A.D. Stone, Phys. Rev. Lett. 61, 834 (1988)
(3)   I. Edrei and M. Kaveh, Phys. Rev. B40, 9419 (1989)
(4)   I. Edrei and K. Kaveh, Phys. Rev. B38 950 (1988)
(5)   A.Z. Genack and J.M. Drake, Europhysics Letters, 11, 331 (1990)
(6)   M.P. Von Albada, J.F. De Boer and A. Lagendijk, Phys. Rev. Lett. 64, 2787 (1990)
(7)   I. Freund, M. Rosenbluh and S. Feng, Phys. Rev. Letters 61, 2328 (1988)
(8)   R. Berkovits and M. Kaveh, Phys. Rev. B 43, 1279 (1991)
(9)   A.Z Genack, Europhysics Letters 11 (8) 733
(10)   N. Shemb and M. Kaveh, Phys. Rev B 43, 1279 (1991)
(11)   M.J. Stephen and G. Cwilich, Phys. Rev. Lett. 59, 285 (1988)
(12)   R. Pnini and B. Shapiro, Phys. Rev. B 39, 6986 (1989)
(13)   A.Z. Genack, N. Garcia and W. Polkosnik, Phys. Rev. Lett. 65, 2129 (1990)
(14)   P.A. Lee and A.D. Stone, Phys. Rev. Lett. 55, 1622 (1985)
(15)   B.L. Al'tshuler, JETP Lett. 41, 648 (1985)
(16)   See for a review : S. Feng and P. Lee, Science Magazine
(17)   D.J. Pine, D.A. Weitz, G. Maret, P.E. Wolf, E. Herbolzheimer and P.M. Chaikin in Scattering and Localization of classical waves in random media, P. Sheng Editor, World Scientific, (1990)
(18)   M.J. Stephen, Phys. Rev. B 37, 1 (1988)

251

(19) G. Maret and P.E. Wolf, Z. Phys. B **65**, 409 (1987)
(20) M. Rosenbluh, M. Hoshen, I. Freund and M. Kareh, Phys. Rev. Lett. **58**, 2754 (1987)
(21) S. Fraden and G. Maret, Phys. Rev. Lett. **65**, 512 (1990)
(22) D. Bicout, E. Akkermans and R. Maynard, J. Phys. I **1**, 471, (1991)

figure 1

figure 2

Diffusing-wave Spectroscopy:
Dynamic Light Scattering in the Multiple Scattering Limit

D.J. Pine, D.J. Durian, D.A. Weitz, and J. Zhu

Exxon Research and Engineering Co., Annandale, New Jersey 08801

Telephone: 908-730-2968

(INVITED)

I. INTRODUCTION

Since the advent of the laser, dynamic light scattering (DLS) has been the principal tool for studying particle motion in colloidal systems. In a typical DLS experiment, one measures the motion of particles which scatter light by analyzing the temporal fluctuations of the scattered intensity. Until very recently, such an analysis was practical only for singly-scattered light. However, renewed interest in the study of multiply-scattered light, and in particular the search for photon localization, stimulated research on the possibility of extending DLS to systems which very strongly multiply scatter light.[1] As a result, a new class of dynamic light scattering experiment, applicable to multiply-scattered light, has been developed.[1-4] This new technique is known as diffusing-wave spectroscopy (DWS).

The development of DWS greatly expands the range of systems which can be studied with dynamic light scattering. For example, with DWS, particle motion in systems which *multiply* scatter light, such as *dense* colloids, emulsions, and foams, can be studied. Thus, DWS has great potential for investigating the structure and dynamics of materials of practical interest including paints, blood, biological tissues, milk, and other complex fluids. In addition, DWS greatly extends the range of length and time scales that can be studied with dynamic light scattering. Conventional DLS probes particle motion on length scales comparable to the wavelength of light, λ. By contrast, DWS probes motion over length scales $\lambda/\sqrt{N} \ll \lambda$, where $N \sim 10$ to 10^7 is the degree of multiple scattering. Thus, it is possible to probe motion over Ångstrom length scales with DWS.

II. DYNAMIC LIGHT SCATTERING

To appreciate DWS, we first consider a conventional DLS experiment from a monodisperse aqueous suspension of colloidal spheres.[5] Laser light illuminates the sample and is singly scattered from the suspended particles. The light scattered through an angle θ is collected by a photomultiplier tube which is sensitive to the intensity, that is, to the square of the scattered electric field. The scattered intensity fluctuates in time because the phase of the field scattered from each particle changes relative to the field scattered by other particles as the particles move. For particles diffusing by Brownian motion, the time scale of these fluctuations is approximately $1/Dq^2$, where D is the diffusion coefficient of the colloidal particles and $q = (2\pi n/\lambda)\sin(\theta/2)$ is the scattering wavevector, with λ/n the wavelength in water of the incident light. The intensity fluctuations are typically characterized by their

253

temporal autocorrelation function, which is defined as

$$g_2(t) \equiv \frac{\langle I(0)I(t)\rangle}{\langle I\rangle^2} - 1 = \left(\frac{\langle E(0)E(t)\rangle}{\langle |E|^2\rangle}\right)^2 \equiv |g_1(t)|^2. \tag{1}$$

The second equality, known as the Siegert relation, is valid in most cases of experimental interest and implies that the intensity autocorrelation function, $g_2(t)$, is simply the square of the electric field autocorrelation function, $g_1(t)$. For diffusing Brownian particles, $g_1(t) = \exp(-Dq^2 t)$.

III. DIFFUSING-WAVE SPECTROSCOPY

To understand the extension of DLS to the multiple scattering regime, we first consider a single light path, consisting of N scattering events, through an optically thick (opaque) colloidal suspension. Each scattering event contributes a factor of $\exp(-Dq^2 t)$ to the decay of $g_1(t)$. Thus the total *average* decay due to N successive scattering events is $g_1^s(t) \simeq \exp(-D\langle q^2\rangle t N)$. For $N \gg 1$,

$$\langle q^2\rangle = 4k_0^2\langle \sin^2(\theta/2)\rangle = 2k_0^2\langle 1 - \cos\theta\rangle = 2k_0^2\frac{\ell}{\ell^*}. \tag{2}$$

where $k_0 = 2\pi n/\lambda$, ℓ is the mean free path between scattering events, and ℓ^* is the transport mean free path. Physically, ℓ^* is the average length scale over which the direction of the scattered light is randomized. Rewriting the autocorrelation function due to a single path in terms of the total path length, $s = N\ell$, we obtain,

$$g_1^s(t) \simeq e^{-2Dk_0^2 t(s/\ell^*)}. \tag{3}$$

To obtain the full autocorrelation function, we incoherently sum the contributions of paths of all lengths over the distribution of path lengths, $P(s)$:

$$g_1(t) \simeq \int P(s)g_1^s(t)\,ds = \int P(s)e^{-2Dk_0^2 t(s/\ell^*)}\,ds. \tag{4}$$

The distribution of path lengths, $P(s)$, can be calculated within the diffusion approximation for light. Thus, we assume that the light executes a random walk through the sample with a photon diffusion coefficient of $c\ell^*/3$ (to be distinguished from the much smaller diffusion coefficient, D, for the Brownian motion of the colloidal particles). In general, the distribution of path lengths depends on the geometry of the sample. Thus, $P(s)$ must be determined for each experimental geometry. For transmission of light through a slab of thickness L, the autocorrelation function is

$$g_1(t) \simeq \frac{x}{\sinh x}. \tag{5}$$

where $x = (L/\ell^*)\sqrt{6Dk_0^2 t}$. In the multiple scattering regime, $L \gg \ell^*$. In order obtain quantitative information from a transmission experiment, i.e., to determine D, ℓ^* must be known. Typically, ℓ^* is determined experimentally by measuring the light transmission

coefficient, $T \propto \ell^*/L$. In special cases, ℓ^* can be calculated from Maxwell's equations. For backscattering from a semi-infinite sample with broad illumination, the autocorrelation function is

$$g_1(t) \approx e^{-\gamma\sqrt{6Dk_0^2 t}},\tag{6}$$

where γ is a numerical constant which depends on the distribution of the short non-diffusive paths; typically, $\gamma \sim 2$. Experimental data for the transmission and backscattering geometries agree with Eqs. 5 and 6 and demonstrate the basic validity of this approach. This suggests that DWS may be used to quantitatively study the dynamics of colloids. [4]

IV. NON-DIFFUSIVE BROWNIAN MOTION AT SHORT TIMES

One of the chief advantages of DWS compared to conventional DLS is its ability to probe particle motion over very short length and time scales. This feature of DWS has been exploited recently to probe the Brownian motion of colloidal particles before the motion is fully diffusive. [6] For non-diffusive particle motion, the quantity $6Dt$ appearing in the preceding expressions for $g_1(t)$ must be replaced by the mean square displacement of a Brownian particle, $\langle r^2(t)\rangle$. At sufficiently long times, $\langle r^2(t)\rangle \simeq 6Dt$. However, at very short times, this relation must break down if the particle velocity and acceleration are to remain finite. In general, it is expected that at short times, the particle motion is ballistic, $\langle r^2(t)\rangle \propto t^2$. In the simplest Langevin theories of Brownian motion, one assumes that the force on a Brownian particle can be separated into two parts: a slowly varying friction force, ζv, and a rapidly varying random thermal force, $f(t)$:

$$m\dot{v} = \zeta v + f(t),\tag{7}$$

where m is the particle mass and v is the velocity. The basis for this decoupling is that the time scales for the two forces are vastly separated: the time scale for the friction force, $T = m/\zeta$, is typically 10^{-8} s for colloidal particles, whereas the time scale for the thermal fluctuations is 10^{-12} s. The mean square particle displacement obtained from Eq. 7 is

$$\langle r^2(t)\rangle = 6D[t + T(e^{-t/T} - 1)].\tag{8}$$

The separation of time scales is most evident in this result if we consider the time-dependent "diffusion coefficient", $D(t) \equiv \frac{1}{6}\frac{d}{dt}\langle r^2(t)\rangle$: for $t \gg T$, $D(t) \to D$ and for $t \ll T$, $D(t) \simeq Dt/2T = (k_B T/m)t$. The transition between these two regimes occurs exponentially with time constant T. However, this simple theory is flawed in that it fails to take into account the inertia of the fluid and the resulting time-dependence of the frictional force. The frictional drag coefficient, ζ, is usually taken to be the Stokes drag, $6\pi\eta a$, which is valid only in the steady-state, or for times much greater than T. When the full time dependence of the drag is taken into account, the transition is no longer exponential but has an asymptotic power-law time-dependence. Furthermore, apart from a very rapid transient due to acoustic damping, the effective mass of the particle at early times is increased to $\frac{3}{2}m$ for neutrally buoyant particles; that is, some extra mass of fluid is dragged along with the particle.

These predictions are confirmed by DWS measurements of $D(t)$ on colloidal suspensions at low volume fraction, $\phi < 0.05$. At early times, we find that $D(t)$ rises more slowly than predicted by the simple Langevin theory; this is consistent with an increased effective mass. At longer times we find that $D(t)$ approaches the asymptotic value of D much more slowly than predicted by the simple theory; this illustrates the effect of the time-dependent friction.

At higher particle volume fractions, ϕ, the asymptotic value of $D(t,\phi)$ becomes smaller and the overall shape of $D(t,\phi)$ appears to change. However, our data exhibit a remarkable scaling behavior when plotted as $D(t)/D(t = \infty, \phi)$ vs $t/\alpha(\phi)$, where $\alpha(\phi)$ is a dimensionless parameter adjusted so that the data collapse onto a single master curve ($\alpha(0) \equiv 1$).[7] To within experimental uncertainty, we find that the scaling factor, $\alpha(\phi)$, exhibits exactly the same ϕ-dependence as the bulk viscosity of the suspension. This suggests that for times greater than τ_H, a single Brownian particle "sees" the rest of the suspension as an effective medium which has the viscosity of the suspension as a whole.

V. CONCLUSIONS

These experiments demonstrate the utility of DWS for studying the dynamics of concentrated colloidal suspensions. Compared to conventional dynamic light scattering, DWS has the advantages of being able to probe dynamics on much shorter time scales and being able to study opaque systems. The only significant requirements for a system to be studied with DWS are that it be optically thick (opaque) and that it not be too strongly absorbing. If the system to be studied is white in appearance, then DWS can be used to study the system dynamics. One important example of how DWS can be used to study novel systems is the recent application of DWS to study foam coarsening and dynamics.[8] In that study, DWS was used to follow how bubbles coarsen and how they rearrange themselves during the coarsening process. We expect that there will be many other novel applications of DWS as this new technique develops.

REFERENCES

[1] G. Maret and P.E. Wolf, Z. Phys. B **65**, 409 (1987).

[2] D.J. Pine, D.A. Weitz, P.M. Chaikin, and E. Herbolzheimer, Phys. Rev. Lett. **60**, 1134 (1988).

[3] D.J. Pine, D.A. Weitz, G. Maret, P.E. Wolf, E. Herbolzheimer, and P.M. Chaikin, *Scattering and Localization of Classical Waves in Random Media*, ed. P. Sheng (World Scientific, Singapore, 1990).

[4] D.J. Pine, D.A. Weitz, J.X. Zhu, and E. Herbolzheimer, J. Phys. France **51**, 2101 (1990).

[5] N.A. Clark, J.H. Lunacek, and G.B. Benedek, Am. J. Phys. **38**, 1134 (1970).

[6] D.A. Weitz, D.J. Pine, P.N. Pusey, R.J.A. Tough, Phys. Rev. Lett. **63**, 1747 (1989).

[7] We note that this scaling cannot be expected to hold for time scales less than the time it takes hydrodynamic interactions to propagate between colloidal particles. This time is determined by the momentum diffusion time between particles, τ_H; for our samples, τ_H is on the order of 10 to 50 ns.

[8] D.J. Durian, D.A. Weitz, and D.J. Pine, Science **252**, 686 (1991).

Depolarization of radiation due to multiple scattering.

P.Bruscaglioni, G.Zaccanti.
Department of Physics University of Florence. Italy.

(INVITED)

Natural turbid media, such as clouds, fogs, sea water are often modelled as random suspensions of particulate (liquid or ̦olid) in a homogeneous fluid (gaseous or liquid).

The simplest model assumes that suspended particles (pure scatterers or also absorbers) are of spherical shape. For fogs or clouds this can be a sufficient approximation, when one is interested in evaluating transmission and backscattering of power theoretically. In these cases some models of radii distribution of the particles are assumed.

For spherical particulate one of the effects caused by multiple scattering in dense media is the change of polarization state of radiation transmitted or backscattered.

However, even single scattering can cause a change of polarization when particles are of non spherical shape.

Investigating the possible different features of the two polarization effects can be interesting. A distinction between them in practical situations could be made easier by the knowledge of their characteristics.

In our paper we shall report on our recent studies on depolarization due to multiple scattering by spherical particles. Results of numerical calculations and laboratory measurements will be shown.

During the same I.C.O. meeting other researchers will present their results concerning non spherical particles.

Calculations were carried out by using a previously developed Monte Carlo code, modified in order to allow us to deal with Stokes vectors, rotation and scattering matrixes.

The code uses statistical laws to determine single tract lengths of photon trajectories, as well as the couples of angles defining their changes of direction in space.(In general no rotational symmetry around photon directions is assumed to determine their directions after the scattering events).

The series of measurements were carried out in the laboratory by using scattering cells with suspensions of latex spheres in water. In our laboratory we measured the transmission of a continuous wave beam (He Ne 10 mw), while the facilities of LENS (European Laboratory for Non Linear Spectroscopy) were used to study the transmission and backscattering of picosecond pulsed laser beams.

In backscattering some difficulties arose for some types of latex spheres, due to their apparent non perfect sphericity, which was evidenced by the presence of a small depolarization for single scattering in the backward direction.

Figures 1, 2, 3 show examples of numerical and

laboratory experimental results.

Fig 1 refers to the results of transmission of a collimated continuous laser (He Ne) beam through different suspensions in water of latex spheres. Pn/Pp represents the ratio between transmitted power polarized perpendicularly to the polarization direction of the (linearly polarized) beam and parallel polarized transmitted power. On the abscissa axis one has the quantity TAUD which is the product of the optical depth TAU of the investigated suspension time 1-g, where g is the asymmetry factor of the relevant phase function. For the different suspensions g varies between 0.67 and 0.92. One can however note that for not small values of TAUD the ratio Pn/Pp depends on this quantity. This result can be considered as an extension to a vector case of the prediction of the diffusion theory, which is generally used in the framework of a scalar treatment of propagation through thick turbid media.

Figures 2 and 3 refer to a geometry typical of a Lidar apparatus sounding a cloud or a fog bank. Fig.2 shows the results of numerical (Monte Carlo) calculations relative to a homogeneous cloud, with a radii distribution equal to the Deirmendjian model C1. The extinction (assumed pure scattering) coefficient of the cloud medium is 0.02 m^{-1}, and the assumed wavelength is 1.064 μm.
The Laser source-cloud base distance is 1000 m and the Lidar receiver F.O.V. is 5 mrad or 0.5 mrad for the two curves of the figure.
The ratio Pn/Pp of the two polarization components of the returns is plotted versus the depth of the sounded part of the cloud (actually p on the abscissa axis is depth corresponding to time for single scattering Lidar return and is now indicated as "apparent depth").

Figure 3a shows results of a laboratory experiment. Here the geometry of the situation pertaining to Fig.2 is scaled down by a factor 3000, and a suspension of latex spheres of average radius 0.1 μm (λ = 0.7665 μm) in a water cell constitutes the turbid medium. Laser pulses of 4 ps are used to sound the medium and the returns are received and analyzed by means of a streak camera. This type of experiment was performed at LENS.
As in Fig.2 the ratio Pn/Pp is plotted in Fig.3 versus the apparent depth of the sounded part of the medium.
Fig.3b shows calculated ratio Pn/Pp for the case of Fig.3a. p on the abscissa axis is the apparent depth for a corresponding cloud at a distance of 1000 m.
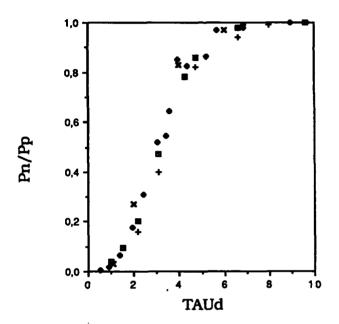
Fig.1. Results of measurements and calculations of
polarization of an initially linearly polarized
continuous laser (He Ne) beam after the passage through
suspensions of latex spheres of average diameter D in
water.
Pn/Pp = ratio between cross polarized and parallel
polarized transmitted power. The ratio is plotted versus
= TAUD = TAU(1-g).
TAU = optical depth of the suspension, g = asymmetry
factor of the phase function of the medium.
 ▣ :   spheres with D = 0.3 μm (measurements) , ✦ :
spheres with D = 0.3 μm (Monte Carlo).
 ◊ :   spheres with D = 0.99 μ m (measurements). ✗ :
spheres with D = 0.99 μm (Monte Carlo).
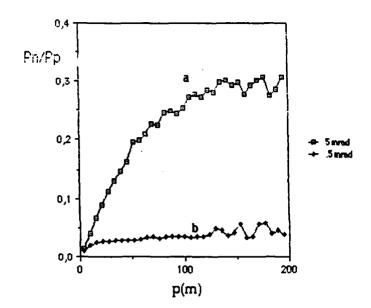
Fig.2. Calculated (Monte Carlo) ratio Pn/Pp of the Lidar
return from a homogeneous C1 cloud. Wavelength 1.064 μm.
a : receiver F.O.V. = 5 mrad, b : F.O.V. = 0.5 mrad
p = sounded (apparent) depth inside the cloud.
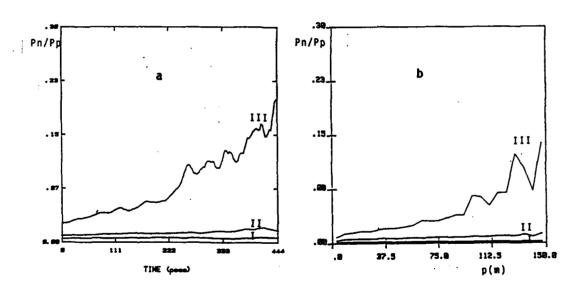
Fig.3. a: Results of laboratory measurements of
polarization of returns in a scaled down geometry of a
Lidar experiment of sounding a cloud. 10 cm cell
containing suspensions in water of latex spheres with
average diameter = 0.09 μm. I : optical depth of the
cell TAU = 1 , II : TAU = 3, III : TAU = 6.7.
b : Results of Monte Carlo calculations relative to the
laboratory experiment of Fig. 3a. p on the abscissa axis
is the apparent sounded (single scattering) depth for a
cloud at a distance of 1000 m corresponding to the scaled
down geometry of the laboratory simulation.

260

Some effects of partial coherence in propagation and scattering

F.Gori

Department of Physics. University "La Sapienza". P.le A.Moro, 2.- 00185 Rome, Italy

1) Introduction and preliminaries

Most of the light fields that we can use are neither completely coherent nor completely incoherent. They are instead partially coherent from both the spatial and the temporal standpoint and their coherence properties affect the propagation and scattering phenomena in which they are involved. In this contribution we shall discuss a few manifestations of this influence of the coherence state of the field under the hypothesis of stationarity.

The basic function describing the coherence properties of radiation is the mutual coherence function [1]. For most problems, its Fourier transform with respect to the temporal variable, i. e. the cross spectral density [2] is usefully employed. It is denoted by $W(P_1, P_2, \nu)$ for two typical points P_1, P_2 and at the temporal frequency ν. It has been proved [3] that W can be thought of as the result of the following average

$$W(P_1,P_2,\nu)=\left\langle V(P_1,\nu)V^*(P_2,\nu)\right\rangle, \tag{1.1}$$

over an ensemble of suitable monochromatic fields $V(P, \nu)$. In particular, for $P_1=P_2=P$, the function W coincides with the ordinary spectral density or power spectrum $G(P, \nu)$. The normalized version of the cross spectral density is known as the spectral degree of coherence and is defined as follows

$$\mu(P_1,P_2,\nu)=W(P_1,P_2,\nu)/\left[G(P_1,\nu)G(P_2,\nu)\right]^{1/2}. \tag{1.2}$$

It will be noted that , at any frequency, μ expresses the spatial coherence of the field. The cross spectral density obeys two Helmholtz equations and the corresponding propagation law can be given the form

$$W_z(r_1,r_2,\nu)=\int\int W_o(\rho_1,\rho_2,\nu)K(r_1,\rho_1,\nu)K^*(r_2,\rho_2,\nu)d^2\rho_1 d^2\rho_2, \tag{1.3}$$

where $W_z(r_1,r_2,\nu)$ and $W_o(\rho_1,\rho_2,\nu)$ are the cross spectral densities across the planes $z=0$ and $z=const>0$ respectively, at frequency ν, for typical points with position vectors r_j and ρ_j (j=1,2). The kernel K describes the propagation. It can be either a free space propagator or the coherent impulse response of a general linear system.

2) Spatial distribution of the optical intensity

We note that when the temporal frequency is fixed the power spectrum $G(P,\nu)$ gives information about the spatial distribution of the power of the radiation field. For this reason, it is often said that $G(P,\nu)$ is the optical intensity at frequency ν and the symbol $I(P)$ is

used, dropping the explicit dependence on ν. In the present section we conform to this usage.

We shall focus our attention on certain effects of coherence in free propagation. For simplicity, we refer to paraxial propagation. Equation (1.3) then becomes

$$W_z(r_1, r_2) = \frac{1}{\lambda^2 z^2} \int \int W_o(\rho_1, \rho_2) \exp\left\{\frac{ik}{2z}\left[(r_1 - \rho_1)^2 - (r_2 - \rho_2)^2\right]\right\} d^2\rho_1 \, d^2\rho_2, \qquad (2.1)$$

where the dependence of W on ν has been omitted. Here, $k = 2\pi/\lambda$ is the wavenumber associated to the fixed temporal frequency. Let us refer to the optical intensity across the plane $z = \text{const} > 0$. Making use of the spectral degree of coherence, such an intensity can be written

$$I_z(r) = \frac{1}{\lambda^2 z^2} \int \int \left[I_o(\rho_1) I_o(\rho_2)\right]^{1/2} \mu_o(\rho_1, \rho_2) \exp\left\{\frac{ik}{2z}\left[\rho_1^2 - \rho_2^2 - 2r \cdot (\rho_1 - \rho_2)\right]\right\} d^2\rho_1 \, d^2\rho_2. \quad (2.2)$$

Let us think of the plane $z = 0$ as the plane of a primary or secondary source. Equation (2.2) evidentiates that the intensity of the propagated field depends on both the intensity and the spectral degree of coherence across the source. This does not mean that sources with different coherence properties cannot produce the same intensity pattern across a given plane. For example, it is well known that certain sources with poor global coherence can give in the far zone the same intensity as a coherent, lowest order laser beam [4].This is obtained by a suitable balance of the effects produced by the two source functions entering eq. (2.2), namely I_o and μ_o. The resulting sources are known as Collett-Wolf sources. Alternatively, the characteristics of a Collett-Wolf source can be adjusted so as to give the same pattern as a laser across a plane at a finite distance [5]. On the other hand, partially coherent fields can exhibit interesting features not shared by coherent ones. As an example, we can build up a partially coherent field that propagates in the form of a blade of light [6] maintaining a thin cross section with the same shape at any plane orthogonal to the direction of propagation. This would be impossible with coherent light where a beam of light squeezed, say in the x direction would progressively change into a beam squeezed in the y direction during propagation.

Therefore, partially coherent fields can imitate the intensity produced by coherent ones at certain planes or they can give completely different propagation phenomena. It is interesting to ask whether two fields with different coherence properties can produce the same intensity pattern across any plane. Two such fields could not be distinguished on an intensity basis only. At least in some cases, fields of this type exist as we shall now show. To this aim, let us consider the following coherent field distributions across the plane $z = 0$

$$V_0^{(\pm)}(\rho, \varphi) = F_o(\rho)\exp(\pm in\varphi), \qquad (2.3)$$

where ρ and φ are polar coordinates, n is an integer and either the plus or the minus sign is chosen on both sides. It is easily proved that the field at any plane $z = \text{const}$ is given by

$$V_z^{(\pm)}(r, \vartheta) = F_z(r)\exp(\pm in\vartheta), \qquad (2.4)$$

where $F_z(r)$ is a suitable integral transform of $F_0(\rho)$. Clearly, the intensity distribution across any plane is independent from the choice of the sign in front of the angular part of the field. Let us superimpose $V^{(+)}$ and $V^{(-)}$ in an uncorrelated manner with equal weights. It is easy to evaluate the spectral degree of coherence of the resulting partially coherent field. It turns out that, at any plane z=const, μ has a modulus

$$\left|\mu(\vartheta_1,\vartheta_2)\right| = \left|\cos\left[n(\vartheta_1-\vartheta_2)\right]\right|, \tag{2.5}$$

that depends only on the angular distance between the two points.

In the general case, some simple parameter can give information about the difference between coherent and partially coherent propagation. For example, let us define the following quantities

$$\Delta x_z^2 = \int x^2 I_z(x)dx \Big/ \int I_0(x)dx, \qquad \Delta p^2 = \int p^2 \tilde{W}_z(p,-p)dp \Big/ \int I_0(x)dx, \tag{2.6}$$

where the tilde denotes Fourier transformation and a one-dimensional notation is used. Under suitable hypotheses, the quantity Δx_z is a measure of the transverse width of the field at a typical plane z=const, whereas Δp measures the angular width. Using eq. (2.2) it can be proved [7] that the width Δx_z changes according to the law

$$\Delta x_z^2 = \Delta x_\zeta^2 + M^4 \frac{\lambda(z-\zeta)^2}{16\pi^2 \Delta x_\zeta^2}, \tag{2.7}$$

where ζ is the coordinate of the plane in which Δx_z has a minimum value Δx_ζ and the so-called M^2-factor [8] is defined as $M^2=4\pi\Delta x_\zeta\Delta p$. Equation (2.7) holds for any state of coherence of the field and the M^2-factor is given by the formula

$$M^2 = \left\{\Delta x_\zeta \int \left[\partial^2 W_\zeta(x_1,x_2)\big/\partial x_1\partial x_2\right]_{x_1=x_2=x} dx \Big/ \int I_\zeta(x)dx\right\}^{1/2}. \tag{2.9}$$

The state of spatial coherence also influences scattering phenomena [9]. This can be easily illustrated in the simple case of a plane scatterer. If $C(\rho_1, \rho_2)$ is the correlation function of the scatterer transparency, it can be shown [10] that the far zone expression for the scattered intensity is given by

$$I_z(r) = \frac{1}{\lambda^2 z^2} \int\int W_0(\rho_1,\rho_2) C(\rho_1,\rho_2)\exp\left[-\frac{ik}{z}r\cdot(\rho_1-\rho_2)\right]d^2\rho_1\, d^2\rho_2, \tag{2.10}$$

where W_0 is the cross spectral density of the illuminating field. Then, we see that the same scatterer can give rise to different patterns in the far zone depending on the coherence properties of the illuminating field. This has been confirmed by experiment. It is interesting to observe that this could be used, in principle, to distinguish between coherent and partially coherent light [9].

3) Spatial distribution of the power spectrum

In the previous section, we thought of the temporal frequency ν as a fixed parameter. We can instead inquire about the ν-dependence of the function $G(P, \nu)$ at different points in space. This can be done again using eq. (1.3) and letting $r_1=r_2$. More precisely, it is interesting to see whether $G(P, \nu)$, as a function of ν, has the same shape at different points. To enucleate the shape of that curve, one divides $G(P, \nu)$ by the total power at point P making reference to the normalized power spectrum [11].

Generally speaking, the normalized spectrum varies in space [11,12]. As a simple example, we consider a laser beam oscillating with a certain bandwidth. Inasmuch as the spot size in a laser cavity is an increasing function of the wavelength, the normalized spectrum in the outer part of the beam is red-shifted with respect to the inner part.[12]. This phenomenon is mainly due to the basic laws of diffraction. More precisely, it can be traced back to the ν-dependence of the kernel K describing the propagation within the laser cavity (see eq. (1.3)). As a consequence, it holds true even for spatially coherent fields. A richer class of phenomena arises when the spatial correlations across the source are taken into account.As was shown by Wolf [11], for quasi-homogeneous sources [13] the far zone normalized spectrum can be independent from the observation point if the degree of specral coherence satisfies a certain scaling law. For other sources, different conditions can ensure spectrum invariance [14, 15]. In the general case, however, the spatial source correlations change the spectrum with respect to the case of an uncorrelated source. In particular, red- and blue-shifts can arise [16, 17]. Most of these predictions have been confirmed by experiments [18-20]. Similar phenomena occur in scattering processes, where the scattered light can exhibit red- and blue-shifts with respect to the illuminating light [21].

References

1. M.Born and E.Wolf, Principles of Optics (6th Ed., Pergamon Press, New York 1980)
2. L.Mandel and E.Wolf, J.Opt.Soc.Am. 66 (1976) 529
3. E. Wolf, J.Opt.Soc.Am. 72 (1982) 343
4. E.Collett and E.Wolf, Opt.Lett. 2 (1978) 27
5. B.E.A. Saleh, Opt.Comm. 30 (1979) 135
6. F.Gori and G.Guattari, Opt.Comm. 48 (1983) 7
7. F.Gori, M. Santarsiero and A. Sona, Opt. Comm. 82 (1991) 197
8. A.E.Siegman, at Conference on Laser Resonators SPIE/OE LASE '90, Los Angeles, January 1990
9. J. Jannson, T. Jannson and E. Wolf, Optics Lett. 13 (1988) 1060
10. F. Gori, C. Palma and M. Santarsiero, 74 (1990) 353
11. E. Wolf, Phys. Rev. Lett. 56 (1986) 1370
12. F.Gori and R.Grella, Opt.Comm. 49 (1984) 173
13. W.H. Carter and E. Wolf, J. Opt. Soc. Am. 67 (1977) 785
14. F. Gori, G. Guattari, C. Palma and C. Padovani, Opt. Comm. 66 (1988) 1
15. F. Gori, G.L.Marcopoli and M. Santarsiero, Opt. Comm. 81 (1991) 123
16. E. Wolf, Nature 326 (1987) 363
17. E. Wolf, Opt. Comm. 62 (1987) 12
18. G.M. Morris and D. Faklis, Optics Comm. 62 (1987) 5
19. F. Gori, G. Guattari, C. Palma and C. Padovani, Opt. Comm. 67 (1988) 1
20. H.C. Kandpal, J.S. Vaishya and K. Joshi, Opt. Comm. 73 (1989) 169
21. E. Wolf, J. T. Foley, F. Gori, J. Opt. Soc. Am. A, 6 (1989) 1142

Spectral Changes Generated by Static and by Dynamic Scattering

Emil Wolf[1]
Department of Physics and Astronomy, University of Rochester, Rochester, New York 14627, U. S. A.
Phone: (716) 275-4397

(INVITED)

It has been conclusively demonstrated in recent years, both theoretically and experimentally that spatial correlations of source fluctuations throughout the source region will, in general, give rise to changes in the spectrum of the emitted radiation[2]. The changes may be of many different kinds, e.g. they may result in narrowing, broadening or shifting of spectral lines, splitting of the lines into several components etc. Subsequently it was shown that similar changes may arise on scattering from media whose response functions (e.g. the refractive index or the dielectric susceptibility) are suitably correlated random functions of position and possibly also of time[3,4]. In particular it was demonstrated that under appropriate conditions spectral changes produced by dynamic scattering may completely immitate the Doppler effect, even though the source, the scatterer and the observer are all at rest with respect to each other[5-7].

In this talk we will present a review of a recently developed theory of scattering of electromagnetic waves of any state of coherence and polarization by a weak, linear, non-magnetic, medium, whose dielectric susceptibility is a random function of position and time, characterized by a statistical ensemble which is stationary, homogeneous and isotropic[8]. We will illustrate the theory by considering spectral changes that can be produced by scattering from some model media, both static and dynamic. Some potential applications of the theory will be briefly mentioned.

1. Also at the Institute of Optics, University of Rochester.

2. For a brief review of these researches see E. Wolf, "Influence of Source-correlations on Spectra of Radiated Fields", in *International Trends in Optics*, J. W. Goodman ed. (Academic Press, New York, 1990), pp. 221-232.

3. J. T. Foley, F. Gori and E. Wolf, "Frequency Shifts of Spectral Lines Produced by Scattering from Spatially Random Media," *J. Opt. Soc. Amer.* A **6**, 1142 -1149 (1989).

4. J. T. Foley and E. Wolf, "Frequency Shifts of Spectral Lines Generated by Scattering from Space-time Fluctuation," *Phys. Rev.* A. **40**, 588 - 598 (1989).

5. E. Wolf, "Correlation-induced Doppler-like Frequency Shifts of Spectral Lines", *Phys. Rev. Lett.* **63**, 2220-2223 (1989).

6. D. F. V. James, M. Savedoff and E. Wolf, "Shifts of Spectral Lines Caused by Scattering From Fluctuating Random Media," *Astrophys. J,* **359**, 67-71 (1990).

7. D. F. V. James and E. Wolf, "Doppler-like Frequency Shifts Generated by Dynamic Scattering," *Phys. Letts.* A **146**, 167-171 (1990).

8. E. Wolf and J. T. Foley, "Scattering of Electromagnetic Fields of any State of Coherence from Space-time Fluctuations," *Phys. Rev.* A. **40**, 579 -587 (1989).

Effects of Multiple Scattering on the Spectrum of Light Propagating in a Spatially Random Medium

Brian Cairns
Institute of Optics, University of Rochester, Rochester, N.Y. 14627, U.S.A.
Phone: (716) 275 7879

Emil Wolf[1]
Department of Physics, University of Rochester, Rochester, N.Y. 14627, U.S.A.
Phone: (716) 275 4397

In a recent investigation the changes in the spectrum of light produced by scattering on spatially random media have been studied[2]. In particular it was shown that the interaction of an incident field with such a medium may give rise to shifts of spectral lines, either towards the longer or towards the shorter wavelengths, depending on the correlation properties of the medium. The results were found to be somewhat analogous to those that were previously found in connection with effects of source correlations on spectra of radiated fields[3].

The analysis presented in ref.2 was based on the first-order Born approximation. Very recently Lagendijk[4] showed that correlation-induced spectral changes may also be produced in enhanced backscattering from disordered media. However, since the phenomenon of enhanced backscattering can only be understood within the framework of the theory of multiple scattering, it is desirable to extend the previous analysis relating to spectral changes beyond the first-order. In this paper we consider a related problem within the accuracy of the multiple-scattering, paraxial, Markov approximation; namely the changes which are produced by scattering of light on a turbulent medium which is statistically stationary, homogeneous and isotropic.

We first derive an expression for the changes in the spectrum of light propagating a distance x from a planar, secondary source of any state of coherence. We then show that if absorption is negligible and if certain other approximations are made, the spectrum of the light

transmitted beyond a certain distance is entirely determined by the source-integrated spectrum, i.e. it is not affected by the physical properties of the medium.

Next we consider propagation through the turbulent medium from the source plane to a small reflector and its subsequent propagation back to the source plane. A somewhat similar problem was recently considered by other authors[5], but we address a different question. Our analysis shows that as a consequence of correlations which exist between the refractive index fluctuations along the forward and the backward paths, the spectral density of the reflected light is enhanced; and that under certain circumstances the enhancement may be appreciably greater than is produced in backscattering from discrete media.

We also address the inverse problem of determining the structure function of the refractive index fluctuations from measurements of the spectrum of the reflected light.

We illustrate the analysis by some analytic and computer-simulated examples.

1.   Also at the Institute of Optics, University of Rochester.

2.   E. Wolf, J. T. Foley and F. Gori, "Frequency shifts of spectral lines produced by scattering from spatially random media," *J.Opt.Soc.Am.* A6, 1142-1149 (1989).

3.   A review of these investigations is given in E. Wolf, "Influence of source correlations on spectra of radiated fields," in *International Trends in Optics,* J.W. Goodman, ed. (Academic Press, New York, 1991), pp. 221-232.

4.   A. Lagendijk, "Terrestrial redshift from a diffuse light source," *Phys.Letts.* A147, 389-392 (1990).

5.   Yu. N. Barabenkov, Yu. A. Kravtsov, V. D. Ozrin and A. I. Saichev, "Enhanced backscattering in optics," in *Progress in Optics,* vol. 29, E.Wolf, ed. (North Holland, Amsterdam, 1991), in press.

POSTER SESSION 2

Zhengfang Song and Yixin Zhang
Anhui Institute of Optics and Fine Mechanics, Academia Sinica
P. O. Box 25, Heifei, Anhui, 230031 P. R. China
Tel. 0551-291004

The research of the statistical characteristics of beam's parameter when a beam passes through a random media twice has been increasing concerned for the purpose of laser ranging and lidar atmospheric probing. Previous theory[1-8] and experiments[2] show in same turbulent atmosphere, the statistical characteristics of reflected wave's parameters are different from the wave passed directly through same path. The statistical characteristics of reflected wave's parameters are depended on reflector's geometric form, some reflectors (such as plane mirrior) can amplify distortion, others (such as corner reflector) can compensate some distortions. Therefore, studying the reflective effect of all kinds of reflector in detail is very usefull to make use of reflective effect to increase or decrease atmospheric turbulent effect and to increase signal-noise-ratio of measuring atmospheric parameters.

Based on Markov process approxmation and complex wave amplitude normal distribution approximation, the statistical characteristics of beam wander and arrival angle fluctuation of reflected wave beam propagating through turbulent atmosphere in both regions of weak and strong fluctuation are discussed in this paper.

1. Beam wander

When a beam propagates in a folded path while the area of plane reflector is much larger than the beam's cross-section, the complex wave amplitude u can be discribed with following parabolic equations[7]

$$\frac{\partial u}{\partial x} = (i/2k) \Delta_R u + i k N_1(x, R) u,$$

$$u(\rho, R) = u_0(r) \tag{1}$$

where $N_1(x, R) = \begin{cases} n_1(x, R), & x < L \\ n_1(2L-x, R), & L < x < 2L \end{cases}$

n_1 is the fluctuation of refraction index, R is the position vector, $k = 2\pi/\lambda$ is wave number, Δ_R is Laplacian operator, $u_0(R)$ is complex amplitude of light wave.

In the range of $L < x < 2L$, the complex amplitude of reflected wave u_r fits following equations

$$\frac{\partial u}{\partial x} = (i/2k) \Delta_R u_r + i k n_1(2L-x, R) u_r,$$

$$u_r(L, R) = u_i(L, R) \tag{2}$$

where $u_i(L, R)$ is the complex amplitude of incident beam at reflective plane.

It is assumed that the center of transmitting beam overlaps nearly the center of reflective beam. Let $\xi = x$, in the range of $0 < \xi < L$, according to the theory of beam wander, the victor of beam's centroid coordinate is[8]

$$\rho_c = (1/P_0) \int_0^L (L-\xi) d\xi \iint_\infty d^2 R I(\xi, R) \nabla_R n_1(\xi, R) \tag{3}$$

While in the range of $L < \xi < 2L$, the vector of beam's centroid coordinate is

$$\rho_{er} = (1/P_o') \int_L^{2L} (2L-\xi) d\xi \iint_{-\infty}^{\infty} d^2R I_r (2L-\xi, R) \nabla_R n_1 (2L-\xi, R) \tag{4}$$

Ignoring the effect of atmospheric absorption and back scattering, from the principle that the beam's entire flux is constant, we have $P_o' = P_o^{[2]}$, let $\xi' = \xi - L$, Eq. (4) becomes

$$\rho_{er} = (1/P_o) \int_0^L (L-\xi) d\xi \iint_{-\infty}^{\infty} I_r (L-\xi, R) \nabla_R n_1 (L-\xi, R) d^2R \tag{5}$$

Using the characteristic of delta correlation[7], the variance of wander angle fluctuation reflected by a mirror reflector is

$$\sigma_{cA}^2 (2L) = <\rho_{cA}^2>/L^2 = <\rho_c^2>/L^2 + <\rho_{er}^2>/L^2$$

$$= (2\pi L/P_o^2) \int_0^1 (1-\xi)^2 d\xi \iint d^2K K^2 \Phi_n (K) \int_{-\infty}^{\infty} d^2R_1 d^2R_2 \exp[iK \cdot (R_1 - R_2)]$$

$$\cdot <I(1-\xi, R_1) I(1-\xi, R_2)> + \sigma_{cr}^2 (L) + 2\sigma_{ce}^2 (L), \tag{6}$$

where the first term is the often-used variance of single-path wander angle fluctuation $\sigma_c^2(L)$, $\sigma_{cr}^2(L)$ is the variance of reflective wander angle fluctuation after the beam passes through path L, $2\sigma_{ce}^2(L)$ is the contribution of phase fluctuation to beam wander which results from the coherence of incident and reflected beams, their expressions are followings, respectively

$$\sigma_{cr}^2 (L) = (2\pi L/P_o^2) \int_0^1 (1-\xi)^2 d\xi \int_{-\infty}^{\infty} d^2R_1 d^2R_2 K^2 \Phi_n (K)$$

$$\cdot <I_r (1-\xi, R_1) I_r (1-\xi, R_2)> \exp[iK \cdot (R_1 - R_2)], \tag{7}$$

$$\sigma_{ce}^2 (L) = (2\pi L/P_o^2) \int_0^1 (1-\xi) \xi d\xi \int_{-\infty}^{\infty} d^2R_1 d^2R_2 K^2 \Phi_n (K)$$

$$\cdot <I(\xi, R_1) I_r (\xi, R_2)> \exp[iK \cdot (R_1 - R_2)], \tag{8}$$

Obviously, $\sigma_{cA}^2 (2L) > \sigma_c^2 (2L)$, where $\sigma_c^2 (2L)$ is the variance of wander angle fluctuation when beam passes through the turbulent path of 2L directly.

In the region of weak turbulence, for collimating or focusing beam's propagation, we can assume $I(\xi, R) \approx I(0, R) \approx I_r (L-\xi, R)$ [9]. According to this, we can get $\sigma_{cr}^2 (L) = 2\sigma_{ce} (L) = \sigma_c^2 (L) = [0.099 \pi^2 \Gamma (1/6) C_n^2/2\sqrt{2}] L (2\alpha_o)^{-1/3} = (1/2) \sigma_c (2L)$ from Eq. (8) and Eq. (9). Substituting it in Eq. (6), following equation is obtained:

$$\sigma_{cA}^2 (2L) = (3/2) \sigma_c^2 (2L) \tag{9}$$

This conclusion agrees with that of Kopilevich and Sochilin[11] for the case of limited plane wave. However, our result is also valid for focusing beam's propagation.

Now we discuss the amplification effect of beam wander in the region of strong turbulence using wave mutual coherence function $\Gamma_{2L} (\rho, R)$. According to the reciprocity principle, the mutual coherence function of reflected wave propagated in the range of $x \in (0, L)$ is discribed by following equation after the beam is reflected by a plane reflector at the point of $x = L$ [8].

$$\Gamma_{2L} (\rho, R) = <u_{2L} (R + \rho/2) \cdot u_{2L}^* (R - \rho/2)> = \int_{-\infty}^{\infty} u (R_0 + \rho_o/2) u^* (R_0 - \rho_o/2)$$

$$\cdot <G (R_0 + \rho_o/2; L, R' + \rho'/2) \cdot G^* (0, R_0 - \rho_o/2; L, R' - \rho'/2) G (0, R + \rho/2; L, R' + \rho'/2)$$

$$\cdot G^* (0, R - \rho'/2; L, R' - \rho'/2) > d^2R_0 d^2\rho_o d^2R' d^2\rho' \tag{10}$$

where $u(\rho)$ is the complex amplitude of incident wave at the turbulent layer of $x=0$, $u_{2L}(\rho)$ is the complex amplitude of reflected wave at the point of $x=2L$, $G(0, \rho_o; x, \rho)$ is the complex amlitude of spheric wave in turbulent media, it fits following equation

$$2ik \frac{\partial G}{\partial x} + \Delta_R G = 2k^2 n_1 (x, \rho) G, \quad G(0, \rho_o, x, \rho) = \delta (\rho_o - \rho).$$

Assuming turbulent fluctuation is strong enough and the complex amplitude of spheric wave is normal distribution statistically, we can derive following equation from the characteristic of normal distribution:

$$\Gamma_{2L}(\rho,R) = \Gamma_{1r}(L,\rho,R) + \Gamma_{2r}(L,\rho,R),$$

$$\Gamma_{1r}(L,\rho,R) = (k/2\pi L)^2 \int_{-\infty}^{\infty} d^2R_0 d^2\rho' u(R_0+\rho'-\rho/2) u^*[R_0-(\rho'-\rho/2)]$$

$$\cdot \exp[(ik/L)(\rho-\rho')(R-R_0) - D_a(\rho',\rho) - D_a(\rho', 2\rho'-\rho)],$$

$$\Gamma_{2r}(L,\rho,R) = (k/2\pi L)^2 \int_{-\infty}^{\infty} d^2R_0 d^2\rho' u(R_0+\rho'-\rho/2) u^*[R_0-(\rho'-\rho/2)]$$

$$\cdot \exp[(ik/L)(\rho-\rho')(R-R_0) - D_a(\rho', R_0-R+\rho') - D_a(\rho', R-R_0+\rho)],$$

where D_a is the phase structure function of spheric wave, Γ_{1r} is the mutual coherence function when the wave passes through the distance of 2L directly, Γ_{2r} is the long distance mutual coherence function of reflected field. Γ_{2r} relates with the beam before and after it passes through the same inhomogenous media. When turbulence is so strong that turbulent expansion is much larger than diffraction, we can get $<I_{2r}(L,R)> << <I_{1r}(L,R)>$, i. e. $<I_{2L}(L,R)> \approx <I_{1r}(L,R)>^{[8]}$, where $<I_{1r,2r}(L,R)> = \Gamma_{1r,2r}(L,0,R)$.

The discussion here indicates the reflective effect of plane reflector Γ_{2r} is rather weak when turbulent expansion is much lager than diffraction. Corresponding with this, the contribution of $2\sigma_{cA}^2(L)$ to $\sigma_{cA}^2(2L)$ can be ignored. Then, we derive $\sigma_{cr}^2(2L) = \sigma_c^2(2L)$. This indicates the amplification effect of beam wander reflected by a plane reflector decreases when popagating distance becomes longer or turbulence becomes stronger to make the ratio of turbulent expansion to diffraction increase.

The expression of beam wander reflected by a corner reflector is discussed with the same method and the same process as plane reflector's, the result is same as that of plane reflector except there is a minus in the last term of Eq. (6). So the result in the region of weak fluctuation is

$$\sigma_{cA}^2(2L) = (1/2) \sigma_c^2(2L) \qquad\qquad (11)$$

In the region of strong fluctuation, $<I_1 I_2> \approx <I_1><I_2> + |\Gamma_2|^2 \approx <I_1><I_2>$. According to Krupnik et. al's discussion about the mutual coherence function for reflective path, we have $<I_r(L)> = <I_d(2L)>$ when beam's radius $a_0 >> \rho_0$ (ρ_0 is coherence length of spheric wave), so the result is $\sigma_{cA}^2(2L) \approx \sigma_c^2(2L)$. This indicates the reflector's special effect disappears with the longer propagating distance or stronger turbulence, same as the plane reflector.

2. arrival angle fluctuation

Previous experiments show both of the root mean square of beam wander angle and arrival angle are less than $10^{\circ [9, 10]}$, so we can discuss arrival angle using near-axis-optics approximation method. Under this condition, the beam's random arrival angle α_0 at receiving plane is[3]

$$\alpha_a = \frac{d\rho_a}{dx} = P_0^{-1} \int_0^\infty d\xi \int_{-\infty}^{\infty} \nabla_R n_1 I_r(\xi,R) t(R) d^2R \qquad\qquad (12)$$

where $t(R) = t_0 \exp(-R^2/a_t^2)$[11], t_0 is transmittance, a_t is radius of receiving aperture.

Previous discussions show the random arrival angle fluctuation at receiving plane of

273

wave front reflected by a plane reflector at the middle point of light path is

$$\frac{d\rho_{ar}}{dx} = \frac{d\rho_{a1}}{dx} + \frac{d\rho_{a2}}{dx} \tag{13}$$

where $d\rho_{a1}/dx$ and $d\rho_{a2}/dx$ are wave front fluctuation in the range of $0 < \xi < L$ and $L < \xi < 2L$, respectively.

Using the method derived previously, we can obtain the reflected beam's variance of arrival angle fluctuation from Eq. (12) and Eq. (13) as followings:

$$\langle \alpha_a^2 \rangle = \langle \frac{d\rho_{ar1}}{dx} \cdot \frac{d\rho_{ar2}}{dx} \rangle = \langle \alpha_a^2(2L) \rangle + 2\langle \frac{d\rho_{a1}}{dx} \frac{d\rho_{a2}}{dx} \rangle \tag{14}$$

where $\langle \alpha_a^2(2L) \rangle$ is the variance of arrival angle fluctuation which passes through the turbulent path of $2L$. The second term of Eq. (14) is the contribution to arrival angle fluctuation resulted from the coherence between the beams before and after it is reflected, the expression is

$$\langle \frac{d\rho_{ar1}}{dx} \cdot \frac{d\rho_{ar2}}{dx} \rangle = (2\pi/P_0)^2 \int_0^L d\xi \int_0^\infty dK K^3 \Phi_n(K) \int_{-\infty}^{\infty} d^2R_1 d^2R_2 \exp[iK \cdot (R_1 - R_2)]$$

$$\cdot \langle I(\xi, R) I_r(1-\xi, R_2) \rangle t(R_1) t(R_2) \tag{15}$$

In the region of weak fluctuation, we can make the approximation that $I(\xi, R) = I_r(\xi, R) \approx I(0, R)$ when the light source is collimating or focusing, then $\langle \frac{d\rho_{ar1}}{dx} \frac{d\rho_{ar2}}{dx} \rangle \approx \langle \alpha_a^2(L) \rangle = (1/2) \langle \alpha_a^2(2L) \rangle$. Thus we can get

$$\langle \alpha_{aA}^2(2L) \rangle = 2\langle \alpha_a^2(2L) \rangle \tag{16}$$

The result agrees with the results derived from other methods in references [1] and [11], $\langle \alpha_{ar}^2(2L) \rangle$ becomes $\langle \alpha_a^2(2L) \rangle$ when turbulent expansion is much larger than diffraction same as the discussion of last section. This indicates not only beam wander amplification effect reflected by a plane reflector decreases when the propagating distance increases, but the amplification effect of arrival angle fluctuation of reflected beam also decreases when turbulent intensity C_n^2 is stronger to make the turbulent expansion much more than diffraction.

If the nuclear function of reflected wave is introduced, it is not difficult to get the expressions of arrival angle fluctuation of reflected beam at the region of weak fluctuation. The term $\langle \frac{d\rho_{ar1}}{dx} \cdot \frac{d\rho_{ar2}}{dx} \rangle \to 0$ in the region of weak fluctuation, so the conclusion is $\langle \alpha_{aA}^2(2L) \rangle = 2\langle \alpha_a^2(2L) \rangle$. The arrival angle fluctuation of reflective field in the region of strong fluctuation is same as that of the beam propagates directly through the distance of $2L$.

References

[1]. Yu. I. Kopilevich, G. B. Sochilin, *Soviet J. Quant. Electron.*, 1984, 44, No. 2, 217.

[2]. V. P. Lukin, V. M. Sazanovrch, *Radiophys. Quant. Electron.*, 1980, 23, No. 6, 484.

[3]. R. J. Cook, *J. Opt. Soc. Am.*, 1975, 65, No. 8, 942.

[4]. T. Chiba, *Appl. Opt.*, 1971, 10, No. 10, 2456.

[5]. M. S. Molenkii, V. L. Mironov, *Soviet J. Quant. Electron.*, 1982, 12, No. 1, 3.

[6]. V. I. Klyatskin et al., *Ж. Э. Т. Ф.*, 1973, 65, No. 1, 54.

[7]. V. L. Mironov, V. V. Nosov, *J. Opt. Soc. Am.* 1977, 67, No. 8, 1073.

[8]. A. B. Krupnik, A. I. Saichev, *Radiophys. Quant. Electron.*, 1982, 24, No. 10, 840.

[9]. V. E. Zuev, *Laser Beam in the atmosphere*, Interscience, New Yourk, 1982, Charpt 4.

[10]. Zhengfang Song, *Chinese J. Infrared Res.*, 1986, A5, No. 1, 43 (in Chinese)

[11]. V. L. Mironov, V. V. Nosov, *Izv. Vuz. SSSR, Ser. radiofiaka*, 1977, 20 No. 10, 1530.

Spatial/Temporal Spectral Density and Flux Comparison **P23**
for Water Vapor Observed by Raman Lidar

W. Porch, D. Cooper, L. Auer, W. Eichinger, D.
Holtkamp, and F. Barnes

Los Alamos National Laboratory
Los Alamos,NM 87544
Telephone 505-667-0971

L. Hipps
Utah State University
Logan, Utah 84322

W. Dugas
Blackland Research Center
Temple, Texas 76502

An experiment was conducted over an instrumented
alfalfa field in June, 1990 at Maricopa, Arizona. The
focus of this experiment was the comparison of remotely
sensed water vapor using a Raman lidar and an array of
point water vapor and vapor flux instrumentation.
Vertical water vapor profile measurements were also
made at the upwind and downwind sides of the field. The
lidar during this experiment could resolve water vapor
to 1.5 m over about 400 m range. In order to compare
rapidly varying water vapor measurements, the data
range was limited to 130 m for this aspect of the
experiment. The sampling rates varied from 0.8 to 2.9
seconds per pulse average. This allows the averaging of
numerous spatial variability spectra with time. These
average spectra can be related to point variability and
flux measurements. Likewise, temporal spectra at a
single 1.5 m range bin can be averaged over space.
These data provide a unique opportunity to compare
spatial and temporal water vapor spectra with standard
water vapor flux measurements over a well documented
and instrumented agricultural field. High water vapor
mixing ratios were assured as the field had been
irrigated just prior to this study and record daytime
temperatures were observed ranging from 48 to 50 $^\circ$C.

The Raman lidar system used in this study was
developed at Los Alamos National Laboratory. The system
is solar blind and, therefore, can measure water vapor
variation both day and night. The laser beam is
propagated coaxially to the 41 cm diameter receiving
telescope. The laser is a 0.5 J/pulse, ultraviolet (248
nm), KrF system. The detection system measures both the
Raman-shifted light due to H_2O at 273 nm and due to
atmospheric nitrogen at 263 nm. The nitrogen return is
used to normalize the water signal to remove optical

train, atmospheric transmission and $1/range^2$ signal losses. To interpret the return signal in water vapor units, one measurement of water vapor must be made along the laser path with a precision hygrometer.

The spatial power spectra were calculated for each laser shot over the alfalfa field at a height of about 3 m. These spectra were averaged over the shots in a time series which varied from 100 to about 500 seconds. As the number of spectra averaged increased, the average spectra began to take a form showing the -5/3 slope of the inertial subrange. The spectral averaging technique was suggested by R. Hill of NOAA/WPL. The spatial wavelength range exhibiting this slope varied from about 10 to 40 m. For wavelengths shorter than about 5 m, the spectral density decreased rapidly as the Nyquist wavelength of 3 m is approached. The spectral density for wavelengths longer than 40 m was more variable due in part to the low statistical significance of spectra at wavelengths approaching the range of the data set (130 m). Also, many of the data showed a significant linear trend usually with the wetter air regions closer to the lidar. When the linear trend is removed to calculate the spectra, less energy remains at long spatial wavelengths. Figure 1 shows the evolution of the spatial spectral density averaged for each sample time throughout the day on 28 June 1990. Low spectral energy in the night and evening are shown with the largest values in the early afternoon.

Time spectra of the water vapor values measured with the lidar indicate that for ranges greater than about 60 m the water vapor variations had more high frequency variations than in the first 60 m. This may be instrument noise or a real feature of turbulence over the field. It is important to point out that lidar was at the edge of the field and the start of the lidar data was 22.5 m away from the lidar into the field. This reduces but does not eliminate the effect of the field boundaries on the measured spectra.

The spatial spectral densities were compared to water vapor fluxes measured with micrometeorological systems mounted on towers in the field. The momentum flux was also measured at these towers. The square root of the spatial power spectral density within the inertial subrange is proportional to q_* the turbulent specific humidity scaling parameter. q_* multiplied by the square root of the momentum flux (u_*) should be proportional to the water vapor flux. This relationship between the spatial spectral densities and the micrometeorologically estimated water vapor fluxes was tested with this data set and the results were encouraging. The relationship between the spatial spectral densities at a wavelength of 10 m and water

276

vapor fluxes were within about +/- 20% of a linear relation to the measured water vapor flux values (Table 1 and Figure 2). The spatial wavelength of 10 m was chosen as a representative scale of the inertial subrange in the data (close to -5/3 slope). The R squared analysis of variance for this comparison was 0.92. This is in part fortuitous because the measured values consisted of 15 minute averages while the lidar data were only collected for 1 to 5 minutes. Also there was considerable spatial variability in the water vapor fluxes over the field. These effects probably cause the constant of proportionality to be more site and sampling specific than under more ideal conditions. The constant of proportionality between the square root of the spatial spectral density at spatial wavelengths of about 10 m multiplied by u_* was about 0.18.

The temporal spectra of water vapor at each 1.5 m range were averaged in space over the 130 m range. These spectra also took the form of a -5/3 slope as spectra were averaged. For periods shorter than about 10 seconds the slope began to approach a flat slope indicative of white noise. The temporal spectra showed a tendency to increase between morning and early afternoon, however this tendency was not as closely related to water vapor flux as shown by the spatial spectra.

Table 1 Comparison of Micrometeorologically Measured Water Vapor Fluxes with Spatial Spectral Power from Raman Lidar Showing a Linear Relationship with a Proportionality Constant of About 0.18.

Time LST (Hr:Min)	Power(P) at 10 m $(g/m^3)^2$	u_* (m/s)	$(P^{.5})u_*$ $(g/m^2 \cdot s)$	Micro Met H_2O Flux $(g/m^2 \cdot s)$
01:10	0.38	0.15	0.09	0.00
02:10	0.14	0.26	0.09	0.01
05:00	0.70	0.15	0.13	0.01
05:10	0.22	0.18	0.09	0.01
07:51	1.30	0.30	0.34	0.02
08:50	1.00	0.50	0.50	0.08
10:10	0.90	0.45	0.43	0.11
10:30	1.30	0.55	0.63	0.13
13:00	2.35	0.53	0.81	0.18
14:30	3.70	1.24	2.38	0.34
19:10	0.44	1.15	0.76	0.15
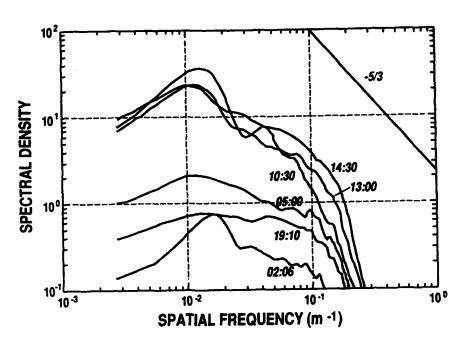
Fig. 1 Average spatial spectral densities over beginning sampling times shown six times during the day, and the -5/3 inertial subrange slope.
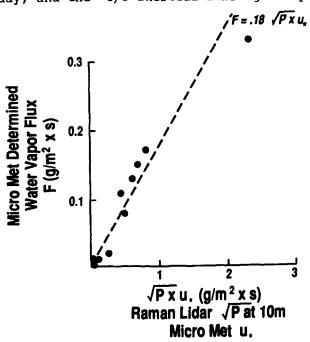
Fig. 2 Comparison of micrometeorologically determined water vapor fluxes with Raman lidar spectral density.

Structure of turbulence and irradiance scintillations in the **P24** convective tank

Zeng Zongyong, Xu Xeidong, Zhang Jun, Wong Lingqang
Anhui Institute of Optics and Fine Mechanics , Acadamia Scinica China
230031, P. O. Box 25, Hefei Anhui, China , Tel. 0551-291012

Abstract

The space-time structure of turbulence in convective tank was analysed. The probability density of irradiance was measured and compared with numerical modeling results.

1. Introduction

Many propagation experiments in convective tank have been down , but the relation between space fluctuations and temporal variance in the turbulence medium appeares to be not clear because average velocity equals zero . The space-time structure function of refractivity will be developed and compared with measurement. The probability density of irradiance scintillations was measured and compared with numerical modeling results.

2. The space-time structure function of refractivity

Suppose turbulent diffusivity $K_h \gg K$ (molecular) and the turbulence is stationary and homogeneous , it can be proved that space-time structure function

$$D(r,\tau) = \begin{cases} D(|r - v_{or}\tau| + \sigma_v \tau) & |\tau < R_\tau| \\ D(|r - v_{or}\tau| + \sqrt{K_h \tau}) & |\tau > R_\tau| \end{cases}$$

where r the distance between two observation points.

  v_{or} the average velocity of organic convective circulatian.

  σ_v^2 vaniance of velocity fluctuations.

  R_τ Lagrangian time scale.

  τ time delay.

In Fig 1. structure function measured at two point $D(r)$ and time structure function $D(\tau)$ measured at one point by Dantec thermol film sensor in the convective tank which like Bessonnitte' s tank [1], but length is 2.0 m.

When $r > 10$ mm , σ_v was replased by $\sqrt{K_h \tau}$, therefore $D(\tau) < D(r)$. previous formula was demonstrated.

3. Space-time feature of Scintillation

When the weighted means of transvers convective velocity in the tank , is 0.0 , temporal correlation equal zero . This result has been demostrated by experiment. The spatial correlation is given in Fig 2.

In Fig 3. temporal probability density of log-normal was obtained . Correct results of spatial irradiance fluctuations have not been obtained due to the resolution of CCD camera is lower (about 0.5mm).
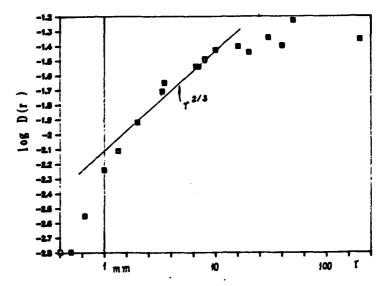
Fig 1. Spatial and temporal structure function
(■) D (r) , (□) D (τ)
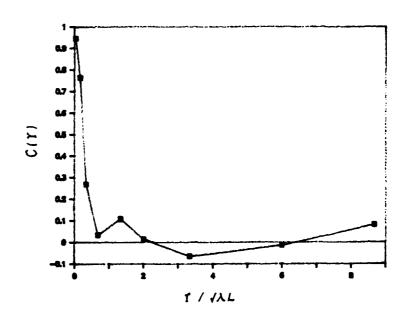
Fig 2. Spatial coherence function $\sigma_i^2 = 1.8$

280
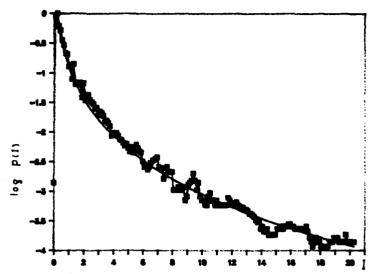
Fig 3. Probability density of irradiance scintillation
$\sigma_1^2 = 5.6$, detecter size 0.18 mm, L= 4.0 m
(□) data , (—) log-normal.
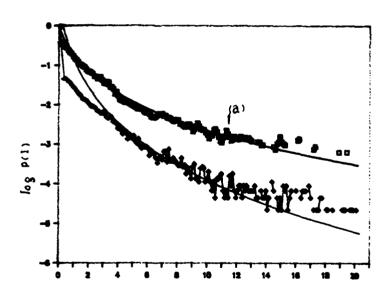
Fig 4. Probability density of irradiance scintillation
numerical result, using von Karman spectrum,
$\sigma_1^2 = 2.4$, resolution 0.1 mm,
inner scale 1 mm, outer scale 10 mm ,
(a) dark region was deleted. (—) log-normal.

Fig 5. represents numerical result calculating by phase screen
method. Both weak and strong irradiance have departured from log-normal.
From Fig 5. we can see that the light pattern was broken and some dark
region appeared .But the light pattern passed through the tank was not .

a   b
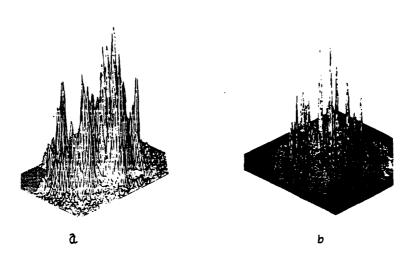
Fig 5.   Spatial distribution of irradiance intensity
a: experiment   b: theoritical numerical calculation

4. Conclusion

There is not much difference between spatial and temporal
temperture structure in the convective tank . The probability density
of irradiance scintillations seems to depend the characters of
turbulence. In our convective tank the range of turbulent sperta is
very narrow . The pattern of light would not break under the strong
turbulence condition . It is different from scintillations in the
atmosphere .The different between spatial and temporal structure of
turbulence is probably not the reason of PDF departure from log-normal.

References

(1). L . R . Bissonett , Appled Optics , Vol 16, PP 2242 2251, 1977.

(2). R . Elliot , J . Kerr and P . Pincus , Appled optics , Vol 18,
PP 3315- 3323 1979.

R. L Phillips

University of Central Florida
Department of Electrical Engineering, Orlando FL, USA 32816
Tel (407) 658 3908

and

L. C. Andrews

University of Central Florida
Department of Mathematics, Orlando FL, USA 32816
Tel (407) 823-6284

1. INTRODUCTION

For heterodyne monostatic laser radar, the fluctuations of the phase of the return signal can be very deleterious to the detection process. To understand this, let us consider the case of an optical plane wave traveling a distance L through an extended random medium after which it is reflected back through the same inhomogeneities as the incident wave. The wave has thus traveled a distance 2L, but has fluctuation properties quite distinct from a wave traveling a single path of length 2L. For example, it is known that double passage of a wave through a random medium leads to enhancement in both the average intensity of the wave and its phase variance.[1,2] In particular, the geometric optics approximation leads to a doubling of the phase variance while the log-amplitude variance increases by a factor of six.

2. ENHANCEMENT OF PHASE VARIANCE

The enhancement of phase fluctuations of the reflected wave passing through the same turbulence as the incident wave is defined by [1]

$$N_\phi = \frac{2 \int_0^\infty \cos^2\left[\frac{\kappa^2 L}{2k}\right] F_\phi(\kappa,0) \kappa \, d\kappa}{\int_0^\infty F_\phi(\kappa,0) \kappa \, d\kappa}, \tag{1}$$

where

$$F_\phi(\kappa,0) = \pi k^2 L \left[1 + \frac{k}{\kappa^2 L} \sin \frac{\kappa^2 L}{k}\right] \phi_n(\kappa) \tag{2}$$

is the two-dimensional spectral density of phase fluctuations of a plane optical wave. The quantity $\phi_n(\kappa)$ is the three-dimensional power spectral density of the refractive index which, according to Tatarski, assumes the form

$$\phi_n(\kappa) = 0.033 \, C_n^2 \, \kappa^{-11/3} \exp(-\kappa^2/\kappa_m^2). \tag{3}$$

where $\kappa_m = 5.92/\ell_0$ and C_n^2 is the structure parameter of the refractive index. Here ℓ_0 denotes the inner scale of the turbulence. To account for a characteristic bump in the spectrum that appears in experimental data at high wave numbers, Andrews [3] has suggested that

$$\phi_n(\kappa) = 0.033 \, C_n^2 \left[1 + B_1 \left[\frac{\kappa}{\kappa_\ell} \right]^\mu - B_2 \left[\frac{\kappa}{\kappa_\ell} \right]^{\mu-\alpha} \right] \kappa^{-11/3} \exp(-\kappa^2/\kappa_m^2). \quad (4)$$

where $\mu = 0.25$, $\alpha = 0.1$, $\kappa_\ell = 4.08/\ell_0$, $B_1 = 2.6$ and $B_2 = 1.76$.

By writing (1) as

$$N_\phi = 1 + \frac{I_2 + I_3}{1 + I_1} \quad (5)$$

and using the Tatarski spectral model (3), we find that

$$I_1 = \frac{6}{11} \left[\frac{\kappa_m^2 L}{k} \right]^{5/6} \left[1 + \frac{k^2}{\kappa_m^4 L^2} \right]^{11/12} \sin \left[\frac{11}{6} \tan^{-1} \left[\frac{\kappa_m^2 L}{k} \right] \right]. \quad (6)$$

$$I_2 = \left[\frac{\kappa_m^2 L}{k} \right]^{5/6} \left[1 + \frac{k^2}{\kappa_m^4 L^2} \right]^{5/12} \cos \left[\frac{5}{6} \tan^{-1} \left[\frac{\kappa_m^2 L}{k} \right] \right]. \quad (7)$$

and

$$I_3 = \frac{6}{11} \left[\frac{2\kappa_m^2 L}{k} \right]^{5/6} \left[1 + \frac{k^2}{4\kappa_m^4 L^2} \right]^{11/12} \sin \left[\frac{11}{6} \tan^{-1} \left[\frac{2\kappa_m^2 L}{k} \right] \right]. \quad (8)$$

On the other hand, the bump spectral model (4) gives us

$$I_1 = \frac{6}{11} [P_1(b)]^{5/6} [P_3(b)]^{11/12} \sin \left[\frac{11}{6} P_2(b) \right]$$
$$+ 0.963 [P_1(b)]^{0.708} [P_3(b)]^{0.854} \sin[1.708 P_2(b)]$$
$$- 0.709 [P_1(b)]^{0.758} [P_3(b)]^{0.879} \sin[1.758 P_2(b)], \quad (9)$$

$$I_2 = [P_1(b)]^{5/6} [P_3(b)]^{5/12} \cos \left[\frac{5}{6} P_2(b) \right]$$
$$+ 1.625 [P_1(b)]^{0.708} [P_3(b)]^{0.354} \cos[0.708 P_2(b)]$$
$$- 1.233 [P_1(b)]^{0.758} [P_3(b)]^{0.379} \cos[0.758 P_2(b)], \quad (10)$$

and

$$I_3 = \frac{6}{11} [2P_1(b)]^{5/6} [P_5(b)]^{11/12} \sin \left[\frac{11}{6} P_4(b) \right]$$
$$+ 0.963 [2P_1(b)]^{0.708} [P_5(b)]^{0.854} \sin[1.708 P_4(b)]$$
$$- 0.709 [2P_1(b)]^{0.758} [P_5(b)]^{0.879} \sin[1.758 P_4(b)]. \quad (11)$$

In (9)–(11), $b = \sqrt{\lambda L}/\ell_0$, $P_1(b) = 2.65 \, b^2$, $P_2(b) = \tan^{-1}[P_1(b)]$, $P_3(b) = 1 + 1/[P_1(b)]^2$, $P_4(b) = \tan^{-1}[2P_1(b)]$, and $P_5(b) = 1 + 1/[2P_1(b)]^2$.

For both spectral models Eq. (5) leads to $N_\phi \cong 2$ in the geometric optics approximation and $N_\phi \cong 4.62$ in the limit $\sqrt{\lambda L}/\ell_0 \to \infty$. We have plotted N_ϕ as a function of $\sqrt{\lambda L}/\ell_0$ in Fig. 1 for both spectral models.

3. ENHANCEMENT OF LOG-AMPLITUDE VARIANCE

The enhancement in the variance of log-amplitude χ of a plane wave is defined by

$$N_\chi = \frac{2 \int_0^\infty \sin^2\left[\frac{\kappa^2 L}{2k}\right] F_\phi(\kappa,0)\kappa \ d\kappa}{\int_0^\infty F_\chi(\kappa,0)\kappa \ d\kappa}, \tag{12}$$

where

$$F_\chi(\kappa,0) = \pi k^2 L\left[1 - \frac{k}{\kappa^2 L} \sin\frac{\kappa^2 L}{k}\right]\phi_n(\kappa) \tag{13}$$

is the two-dimensional spectral density of log-amplitude fluctuations. We can also write (12) in the form

$$N_\chi = \frac{1 + I_1 - I_2 - I_3}{1 - I_1}, \tag{14}$$

where I_1, I_2, and I_3 are defined above using both spectral models. In the geometric optics approximation these expressions lead to the enhancement factor $N_\chi \cong 6$, while in the limit $\sqrt{\lambda L}/\ell_0 \to \infty$ both models predict that $N_\chi \cong 2.62$ (see Fig. 1).

4. DISCUSSION

A plane wave passing twice through the same inhomogeneities in a random medium shows an enhancement of the phase fluctuations at each point on the phase front. As shown in Fig. 1, this enhancement factor in the diffraction regime increases over that in the geometric optics regime and is dependent on the spatial spectrum model of the refractive index fluctuations. Diffraction decreases the enhancement factor for the variance of log-amplitude and there appears to be only a weak dependence on the particular spectrum model. The distinction that arises from the two spectrum models seems to suggest that the dominance of any particular scale size, like those in the bump spectrum, diminishes both the phase and log-amplitude variances for large $\sqrt{\lambda L}/\ell_0$ values.

References

[1] Y. A. Kravtsov and A. I. Saichev, "Effects of double passage of waves in randomly inhomogeneous media," Sov. Phys. Usp. 25(7), 494 (1982).

[2] G. Welsh and R. L. Phillips, "Simulation of enhanced backscatter by a phase screen," JOSA A 7, 578 (1990).

[3] L. C. Andrews, "New analytic scalar spectra models and their application to optical propagation through the atmosphere," (submitted).
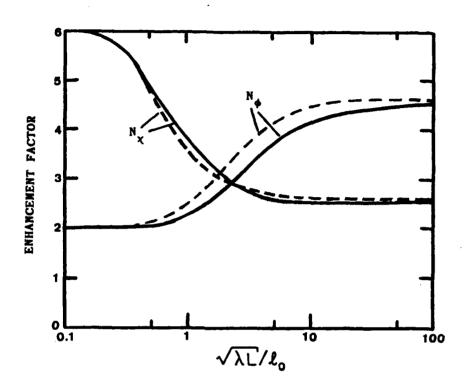
Figure 1 *Enhancement factor for phase and log-amplitude variances. The solid curve is based on the Andrews spectrum (4) while the dashed curve is based on the Tatarski spectrum (3).*

L. C. Andrews

University of Central Florida
Department of Mathematics, Orlando FL, USA 32816
Tel (407) 823-6284

1. INTRODUCTION

Several optical methods for measuring the path-averaged value of inner scale ℓ_0 have been proposed. Two such methods utilize two optical waves differing in wavelength but propagating in overlapping paths. In one case the log-amplitude variance of each optical wave at propagation distance L is simultaneously measured [1]. In the absence of dispersion in the refractive index structure parameter C_n^2, the ratio of these variances is then a function of only wavelengths λ_1 and λ_2, propagation distance L, and the unknown inner scale ℓ_0. In the other case it is the bichromatic correlation coefficient of the two optical waves that is of interest for determining ℓ_0 [2]. Both methods, however, are dependent upon the model assumed for the spatial power spectrum of refractive index fluctuations. In this paper we compare inner scale predictions based on the standard Tatarski spectrum

$$\phi_n(\kappa) = 0.033 \, C_n^2 \, \kappa^{-11/3} \, \exp(-\kappa^2/\kappa_m^2), \tag{1}$$

where $\kappa_m = 5.92/\ell_0$, and the newly developed Andrews spectrum [3] which exhibits the characteristic bump at high wave numbers, viz.,

$$\phi_n(\kappa) = 0.033 \, C_n^2 \left[1 + B_1 \left[\frac{\kappa}{\kappa_\ell}\right]^\mu - B_2 \left[\frac{\kappa}{\kappa_\ell}\right]^{\mu-\alpha} \right] \kappa^{-11/3} \, \exp(-\kappa^2/\kappa_\ell^2), \tag{2}$$

where $\mu = 0.25$, $\alpha = 0.1$, $\kappa_\ell = 4.08/\ell_0$, $B_1 = 2.6$ and $B_2 = 1.76$.

2. RATIO OF VARIANCES METHOD

Neglecting dispersion effects in C_n^2, the *ratio of log-amplitude variances* of two optical waves with wavelengths λ_1 and λ_2 leads to the expression

$$\frac{\sigma_\chi^2(\lambda_1)}{\sigma_\chi^2(\lambda_2)} = \left[\frac{\lambda_2}{\lambda_1}\right]^{7/6} \frac{f(\beta_1)}{f(\beta_2)}. \tag{3}$$

where $f(\beta_1)$ and $f(\beta_2)$ denote the normalized variances of each optical wave, and $\beta_1 = \ell_0/\sqrt{\lambda_1 L}$ and $\beta_2 = \ell_0/\sqrt{\lambda_2 L}$. For plane waves we write

$P_1(\beta) = A_p/\beta^2$, where $A_p \approx 5.58$ (Tatarski spectrum) or $A_p = 2.65$ (Andrews spectrum). $P_2(\beta) = \tan^{-1}[P_1(\beta)]$, and $P_3(\beta) = 1 + 1/[P_1(\beta)]^2$. Then, using the Tatarski spectrum (1) we find

$$f(\beta) = 3.86[P_3(\beta)]^{11/12}\sin\left[\frac{11}{6}P_2(\beta)\right] - 7.08/[P_1(\beta)]^{5/6} \qquad (4)$$

whereas using the Andrews spectrum (2)

$$f(\beta) = 3.86[P_3(\beta)]^{11/12}\sin\left[\frac{11}{6}P_2(\beta)\right] - 9.82/[P_1(\beta)]^{5/6}$$

$$+ 7.02\frac{[P_3(\beta)]^{0.854}}{[P_1(\beta)]^{0.125}}\sin[1.71P_2(\beta)] - 5.26\frac{[P_3(\beta)]^{0.879}}{[P_1(\beta)]^{0.075}}\sin[1.76P_2(\beta)]. \qquad (5)$$

For spherical waves we define $S_1(\beta) = A_s/\beta^2$, $S_2(\beta) = \tan^{-1}[S_1(\beta)]$, and $S_3(\beta) = 1 + 1/[S_1(\beta)]^2$, where $A_s = 1.394$ (Tatarski spectrum) or $A_s = 0.662$ (Andrews spectrum). In this case the Tatarski and Andrews spectra models lead to, respectively,

$$f(\beta) = 5.54[S_3(\beta)]^{5/12}\cos[5S_2(\beta)/6] - 5.54/[S_1(\beta)]^{5/6}$$

$$- 1.54[S_3(\beta)]^{-1/12}\sin[S_2(\beta)/6] \qquad (6)$$

and

$$f(\beta) = 5.54[S_3(\beta)]^{5/12}\cos[5S_2(\beta)/6] + 9.38\frac{[S_3(\beta)]^{0.354}}{[S_1(\beta)]^{0.125}}\cos[0.708\,S_2(\beta)]$$

$$- 7.24\frac{[S_3(\beta)]^{0.379}}{[S_1(\beta)]^{0.075}}\cos[0.758\,S_2(\beta)] - 7.68/[S_1(\beta)]^{5/6}$$

$$- 1.54\frac{\sin[S_2(\beta)/6]}{[S_3(\beta)]^{1/12}} - 2.22\frac{\sin[0.292\,S_2(\beta)]}{[S_1(\beta)]^{0.125}[S_3(\beta)]^{0.146}}$$

$$+ 1.83\frac{\sin[0.242\,S_2(\beta)]}{[S_1(\beta)]^{0.075}[S_3(\beta)]^{0.121}}. \qquad (7)$$

In Fig. 1 we show the ratio of variances as a function of inner scale ℓ_0 for plane and spherical waves as predicted by both the Tatarski and Andrews spectra models. The results are for a path length $L = 150$ m and a Nd:YAG ($\lambda_1 = 1.064$ μm) and He-Ne ($\lambda_2 = 0.6328$ μm) laser pair. Similar results can be obtained for other path lengths and laser beam pairs. Here we see that for a given ratio of variances, the Tatarski spectrum model generally predicts a larger value of inner scale ℓ_0 than does the Andrews spectrum model.

3. BICHROMATIC CORRELATION METHOD

Another measure of inner scale ℓ_0 involves the *bichromatic correlation coefficient* defined by

$$\rho(\lambda_1,\lambda_2) = \frac{1}{(1-\Omega^2)^{5/12}} \frac{f(\ell_0/\sqrt{\lambda L}) - \Omega^{5/6} f(\ell_0/\sqrt{\lambda L\Omega})}{[f(\beta_1)f(\beta_2)]^{1/2}}. \tag{8}$$

where $\lambda = (\lambda_1 + \lambda_2)/2$ and $\Omega = (\lambda_1 - \lambda_2)/2\lambda$. In Fig. 2 we show the bichromatic coefficient as a function of inner scale for the same case considered in Fig. 1 using the ratio of variances method. Here again we find the Tatarski spectrum model predicting larger inner scale values than those predicted by the Andrews spectrum. Finally, in Fig. 3 we show the measured path-averaged correlation coefficient versus point measurements of ℓ_0 taken from the data in Fig. 4 of Ref. 4 along with both theoretical curves from the two spectra models. Here the path length was 120 m (two meters above the ground) with $\lambda_1 = 10.59$ μm and $\lambda_2 = 0.6328$ μm. Clearly, the Andrews spectrum model more closely fits the experimental data.

4. DISCUSSION

The dependence of an optical technique for measuring inner scale on the chosen spectra model is clearly evident in Figs. 1-3. Since the inner scale measurement also affects any optical measurement of C_n^2, the error in calculating the refractive index structure parameter is compounded by any error in ℓ_0. Finally, based on the experimental data in Fig. 3, it is also clear that the Andrews bump spectra model gives closer agreement to point measurements of ℓ_0 than the standard Tatarski model.

REFERENCES

[1] L. C. Andrews and R. L. Phillips, "Proposed method of measuring inner scale of atmospheric turbulence and C_n^2," OSA 1988 Annual Meet., Santa Clara, CA, Oct. (1988).

[2] E. Azoulay, V. Thiermann, A. Jetter, A Kohnle and Z. Azart, "Optical measurement of the inner scale of turbulence," J. Phys. D: Appl. Phys. 21 (1988).

[3] L. C. Andrews, "New analytic scalar spectra models and their application to optical propagation through the atmosphere," (submitted).

[4] V. Thiermann and E. Azoulay, "Modeling of structure constant and inner scale of refractive index fluctuations — an experimental investigation," Proc. SPIE Technical Symposia on Aerospace Sensing, Orlando, FL, March (1989).

Figure 1 *Ratio of variances as a function of ℓ_0 for a Nd:YAG/He-Ne pair and propagation distance 150 m. The solid curves correspond to the Andrews spectrum and the dashed curves to the Tatarski spectrum.*
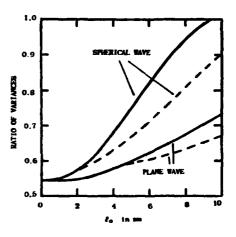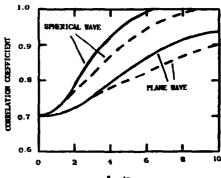
Figure 2 *The bichromatic correlation coefficient as a function of ℓ_0 for a Nd:YAG/He-Ne pair and propagation distance 150 m. The solid curves correspond to the Andrews spectrum and the dashed curves to the Tatarski spectrum.*
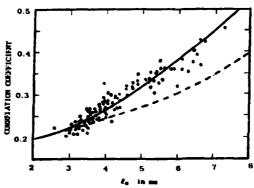
Figure 3 *Dependence of the measured bichromatic correlation coefficient on the inner scale ℓ_0 derived from point measurements. The theoretical curves are based on the spectra of Andrews (solid) and Tatarski (dashed).*

290

MULTISCALE SOLUTIONS FOR HIGH-FREQUENCY PROPAGATORS WITH APPLICATIONS TO THE ANALYSIS OF RANDOM **P27** PROPAGATION AND DOUBLE-PASSAGE PROBLEMS

Reuven Mazar, Alexander Bronshtein and Mark Rozental

Department of Electrical and Computer Engineering,

Ben-Gurion University of the Negev, P.O.Box 653,

Beer-Sheva, Israel 84105

Tel: 972-57-461-513 Fax: 972-57-31340

1. Introduction

For the treatment of random high-frequency phenomena it is convenient to deal with a field solution which contains random information about the refractive index variation along the propagation path in an explicit functional form. From that solution the statistical measures of the field can be constructed if the distribution function of the random part of the refractive index is known.Such an approach was adopted in the recently formulated Stochastic Geometrical Theory of Diffraction in the form of a paired field measure called the two-point random function (TPRF)[1-7]. Its propagation is described in the coordinate system $\{r,\sigma\}$ centered on a properly chosen deterministic ray of the background medium, where the range along that ray is measured by the coordinate σ, and the transverse variation in the normal plane at σ is described by the two-dimensional vector r. The scalar high-frequency field

$$U(r,\sigma) = u(r,\sigma) \exp\left\{ ik\int_{\sigma_0}^{\sigma} d\zeta\, n(0,\zeta) \right\} \tag{1}$$

is presented here as a product of parabolic wave function $u(r,\sigma)$ and the exponential term which accounts for the dominant phase variation along the reference ray, where k is the radiation wavenumber, and the refractive index of the medium is given by the function $N(r,\sigma) = n(r,\sigma) + \tilde{n}(r,\sigma)$. Here $n(r,\sigma)$ describes the deterministic background variation, and $\tilde{n}(r,\sigma)$ is the random part. The TPRF is defined in the range plane σ as a paired product of the parabolic amplitude and its complex conjugate:

$$\Gamma(p, s,\sigma) = u\left(p + \frac{s}{2},\sigma\right)u^*\left(p - \frac{s}{2},\sigma\right), \tag{2}$$

where $p = (r_1 + r_2)/2$, and $s = r_1 - r_2$ are transverse sum and difference coordinates.

The TPRF at the initial plane σ_0 can be related to its value at the range plane σ via the propagation relation

$$\Gamma(\mathbf{p},\,\mathbf{s},\sigma) = \int\!\!\!\int_{-\infty}^{\infty} d^2p_0 d^2s_0 \; g(\mathbf{p},\,\mathbf{s},\sigma \mid \mathbf{p}_0,\,\mathbf{s}_0,\sigma_0)\Gamma(\mathbf{p}_0,\,\mathbf{s}_0,\sigma_0), \qquad (3)$$

where, $g(\mathbf{p},\mathbf{s},\sigma \mid \mathbf{p}_0,\mathbf{s}_0,\sigma_0)$ is the TPRF propagator corresponding to the point source (delta-function) inputs.

In order to bring these propagation relations to a workable form, we applied the multiscale expansion procedure to solve the parabolic equation governing the propagation of the TPRF in an inhomogeneous background random medium. We have shown that the resulting solution has the necessary spectral content to reproduce the uniformized intensity distribution in the transitional regions as predicted by the uniform ray asymptotics, together with the information about the random refractive index variation along the propagation path to give the solutions for the multifrequency intensity statistical moments of an arbitrary order.

In some cases there is a need to relate the TPRF at the observation plane σ to the source with a given angular intensity distribution. Such a source can be described by the so called Wigner distribution defined as a spectral transform of $\Gamma(\mathbf{p},\mathbf{s},\sigma)$ in the s - variable [5-8]:

$$\hat{\Gamma}(\mathbf{p},\boldsymbol{\rho},\sigma) = \int\!\!\!\int_{-\infty}^{\infty} d^2s \; \Gamma(\mathbf{p},\,\mathbf{s},\sigma) \; \exp(-ik\boldsymbol{\rho}\cdot\mathbf{s}), \qquad (4)$$

with the corresponding propagation relation connecting $\Gamma(\mathbf{p},\mathbf{s},\sigma)$ at the observation plane with the source distribution $\hat{\Gamma}(\mathbf{p}_0,\boldsymbol{\rho}_0,\sigma_0)$.

For a homogeneous background random medium, the deterministic ray trajectories are straight lines, and the corresponding solutions for the high-frequency propagators obtain more simple analytic form [5-7]. Here, we demonstrate application of these solutions to several random propagation problems.

2. Finite Aperture Effects on Intensity Fluctuations

The first of the problems is related to finite aperture effects on the intensity fluctuations characteristics. The two-scale solutions provided results for the normalized intensity variance and intensity correlation functions for plane and spherical wave excitations[9-11]. However the treatment of finite aperture sources and the numerical evaluation of the expressions was difficult because of the large number of integrations involved. In order to reduce the number of integrals, we adopt here a physical approximation considering a point source with a given Gaussian angular intensity distribution:

$$\hat{\Gamma}(\mathbf{p}_0,\boldsymbol{\rho}_0,\sigma_0) = 2\sqrt{\pi}\,b \; \delta(\mathbf{p}_0) \exp(-\rho_0^2 \, k^2 b^2) \,. \qquad (4)$$

Such a source is not physically realisable. However in the farfield region it approximates, for example, the main radiation pattern of a directional antenna. Also in the farfield region, this spectral distribution creates the same TPRF with the same beam divergence as a regular

laser beam with source width b. The described approach allows us to present a computable algorithm for the intensity correlation characteristics of a finite aperture source [5,6]. The numerical evalution of the algorithm shows a different behavior of these characteristics compared with those of plane and spherical waves.

3. Two-Frequency Correlation

Analysis of the random propagation shows that refractive index fluctuations give rise to dispersive effects in propagation phenomena. Using the solutions for the high-frequency propagators, we constructed the two-frequency intensity correlation function

$$B_{12}(k_1, k_2) \equiv \frac{<[I(k_1)-<I(k_1)>][I(k_2)-<I(k_2)>]>}{\sqrt{<[I(k_1)-<I(k_1)>]^2><[I(k_2)-<I(k_2)>]^2>}} . \tag{5}$$

We investigated the two-frequency correlation for plane and spherical wave excitations and for various refractive index correlation spectra. Numerical results are presented.

4. Backscattering Analysis in Random Media

The presence of random refractive index fluctuations in location and remote sensing experiments and double passage of the propagating radiation through the same random inhomogeneities as the incident one, results in new statistical effects not observed along unidirectional paths [12]. Theoretical analysis of the double-passage problem is rather complicated. The usual average moment approach common in the theory of wave propagation in random media along isolated paths is inapplicable here because there is a requirement to correlate the forward-backward propagating events. The fact that the TPRF contains the information about the random refractive index variation along the propagation path makes it suitable for the analysis of the double-passage effects[5,7]. To account for the correlation of such events, we transformed the propagator g to a symmetrical form represented by the propagator g^r_2 satisfying the reciprocity condition:

$$g^r_2(r_1, r_2, \sigma \mid r_{10}, r_{20}, \sigma_0) = g^r_2(r_{10}, r_{20}, \sigma_0 \mid r_1, r_2, \sigma)^*, \tag{6}$$

Observing the retroreflected radiation at the source plane σ_0 we obtain for the retroreflected TPRF at that plane:

$$\Gamma_{ref}(\mathbf{r}_{1b},\mathbf{r}_{2b},\sigma_0,\sigma) = \int\!\dots\!\int d^2r_{10}\, d^2r_{20}\, d^2r_1\, d^2r_2\, \Gamma(\mathbf{r}_{10},\mathbf{r}_{20},\sigma_0)$$

$$\times\ K(\mathbf{r}_1)\, K^*(\mathbf{r}_2)\, g_2^r(\mathbf{r}_1,\mathbf{r}_2,\sigma \mid \mathbf{r}_{10},\mathbf{r}_{20},\sigma_0)\, g_2^r(\mathbf{r}_1,\mathbf{r}_2,\sigma \mid \mathbf{r}_{1b},\mathbf{r}_{2b},\sigma_0). \qquad (7)$$

where $\Gamma^r(\mathbf{r}_1,\mathbf{r}_2,\sigma)$ is the TPRF in the configurational domain, and $K(\mathbf{r})$ is the local plane wave reflection (or diffraction) coefficient. The average intensity distribution is obtained by applying ensemble averaging to (7), and setting $\mathbf{r}_{1b} = \mathbf{r}_{2b} = \mathbf{r}_b$. In this work, we consider intensity enhancement effects for several source - reflector configurations.

References

1. R.Mazar and L.B.Felsen , "Stochastic geometrical theory of diffraction", J.Acoust.Soc.Am.,**86**(6), 2292-2308, (1989).

2. R.Mazar and L.B.Felsen, ""Geometrical theory of diffraction of high - frequency coherence functions in a weakly random medium", Optics Letters,**12**(3),146-148, (1987).

3. R.Mazar and L.B.Felsen,"Stochastic geometrical diffraction theory in a random medium with inhomogeneous background",Optics Letters,**12**(5), 301-303,(1987).

4. R.Mazar, "High-frequency propagators for diffraction and backscattering in random media", J.Opt.Soc.Am.,**A7**, 34-46, (1990).

5. R.Mazar, and A.Bronshtein, "Finite aperture effects on intensity fluctuations in random media", Optics Comm., **75**,365-369, (1990).

6. R.Mazar, and A.Bronshtein, and M.Rozental, "Analysis of random propagation problems using multiscale random propagators", to be published in Waves in Random Media.

7. R.Mazar, and A.Bronshtein, "Coherence properties of retroreflected radiation in a power-law random medium", Optics Letters, **15**(14),766-768,(1990).

8. M.J.Bastians, "Application of the Wigner distribution function to partially coherent light", J.Opt.Soc.Am.,**A8**(3), 1227-1238, (1986).

9. S.Frankenthal, A.M.Whitman, and M.J.Beran,"Two-scale solutions for the intensity fluctuations in strong scattering", J.Opt.Soc.Am.,**A1**(6),585-597, (1984).

10. A.M.Whitman and M.J.Beran,"Two-scale solution for atmospheric scintillation", J.Opt.Soc.Am.,**A2** 2133-2143,(1985).

11. R.Mazar, J.Gozani and M.Tur, "Two-scale solution for the intensity fluctuations of two-frequency wave propagation in a random medium"J.Opt.Soc.Am.,**A2**,2152-2160, (1985).

12. Y.A.Kravtsov and A.I.Saichev, "Effects of double passage of waves in randomly inhomogeneous media",Sov.Phys.Uspekhi, **25**(7) , 494-508, (1982).

H. M. Loebenstein and Z. Azar
Soreq Nuclear Research Center
Department of Atmospheric Optics
Yavne, ISRAEL 70600

I. INTRODUCTION

Optical methods for the remote-sensing of atmospheric parameters are usually performed by measuring intensity light fluctuations by dual station laser/receiver systems[1-2]. In order to facilitate the experimental set-up, many authors[3-5] used a single-ended system that transmits a·laser beam from the same location of the receiver toward a mirror/retro-reflector or diffuse target. This folded beam method has the disadvantage of having contributions from both paths (from the transmitter to the reflector and backward) and the possible interdependence between them[6-7].

In this paper we propose a new measurement scheme for the single-ended configuration that significantly reduces the backward contribution. We measure the reflected beam by two uncorrelated receivers. Measuring the time delayed correlation between the two receivers reflects the beam fluctuations falling on the reflector, and the backward path contribution is averaged out by the two uncorrelated detectors.

II. THEORY

Let us consider the experimental set-up given in Fig. 1.
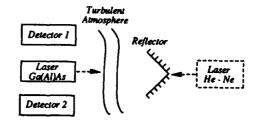
Figure 1: Experimental configuration

The power falling on the reflector can be written symbolically as:

$$P_R(t) = P_L K_0 R_0(t) \tag{1}$$

where P_L is the laser power, K_0 represents all the constant factors (geometric and atmospheric), and R_0 represents the random part of the fluctuating power. Neglecting interference effects, one can write the power received by each of the two detectors as:

$$P_I(t) = P_R(t) K_I R_I = P_L K_0 k_I R_0(t) R_I(t) \qquad I=1,2 \tag{2}$$

where K_I represents the constant factors on the way back, and R_I is the random part of the fluctuating power on the way from the reflector toward the receiver I (I=1,2).

The time delayed correlation function between the two receivers is defined by:

$$\beta(\tau) = \frac{<(P_1(t) - <P_1(t)>)(P_2(t+\tau) - <P_2(t)>)>}{\sigma_1 \sigma_2} \tag{3}$$

where σ_I is the variance of $P_I(t)$, and $<>$ represents time average. Assuming that the random parts $R_I(t)$ (I=0,1,2) are uncorrelated, the expression for the correlation function reduces to:

$$\beta(\tau) = \frac{[<P_1(t)><P_2(t)>][<R_0(t)R_0(t+\tau)> - <R_0(t)>^2]}{\sigma_1 \sigma_2 <R_0(t)>^2} \tag{4}$$
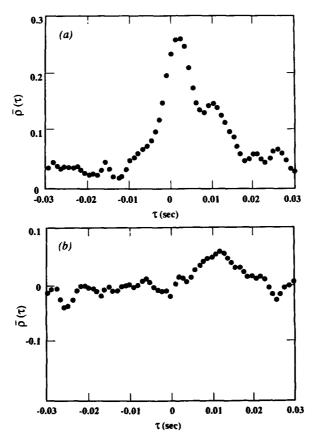
The normalized auto-correlation function of the power falling on the reflector becomes:

$$\frac{<P_R(t)P_R(t+\tau)>}{<P_R(t)>^2} = \frac{\beta(\tau)\sigma_1 \sigma_2}{<P_1(t)><P_2(t)>} + 1 \tag{5}$$

Setting $\tau=0$, one obtains the normalized variance of the power falling on the <u>reflector</u>.

III. EXPERIMENTAL RESULTS AND DISCUSSION

In the experimental set-up depicted in Fig. 1, we used a 2mW Ga(Al)As CW diode laser, emitting 0.83μm radiation with a divergence angle of 0.1 mrad. A retro-reflector having 68mm diameter was placed 1300m from the transmitter. The two detectors had receiving apertures with diameters 45mm and 80mm respectively and were placed apart (in order to reduce their correlation) at a distance of 250mm from each other. The outputs of the detectors, proportional to the instantaneous power of the reflected beam, were sampled every 0.2msec (5KHz) by an 8 bit ADC under the control of a micro-computer which also stored the data on a diskette for later processing. The length of each signal record was 4096 points (0.82sec) for each detector, and the time delayed correlation function was computed by using 3600 data points.

Figure 2: Average of twelve time-delayed correlation functions. (a) Folded path. (b) Direct He-Ne beam.

A typical time delayed correlation function as measured by the two uncorrelated receivers is shown in Fig. 2(a) We obtained this correlation function by averaging 12 runs taken during 15 minutes. As expected, the time delayed correlation function has a clear peak near $\tau=0$, and it is nearly symmetric because it represents an auto-correlation of $R_0(I)$. The slightly unsymmetric structure may be caused due to the extent that some correlation remains in the atmospheric factors $R_I(t)$ from the region near the retro-reflector.
The smaller peaks to the right of the central peak agrees with the prevailing wind direction during the experiment. For comparison, we placed a He-Ne laser with 1mrad divergence at the location of the retro-reflector and measured the direct beam correlation function with the same two detectors and obtained the smoothed correlation function of 12 runs shown in Fig. 2(b). It is obvious from figure 2(b) that the direct beam correlation function does not have any typical structure and exhibits only a random correlation.

In summary, at the expense of longer measuring time, the proposed remote-sensing method eases the experimental set-up by having an experimental system that couples the source and the detector at the same location. The proposed single-ended system reduces significantly the atmospheric turbulence effects on the way back from the reflector. Moreover, one can easily change the experimental conditions by having several reflectors placed around a central measuring station.

IV. REFERENCES

1. R.J. Hill and G.R. Ochs, Appl. Opt. 17, 3608 (1978).
2. Z. Azar, E. Azoulay and M. Tur, CLEO'87, paper number MA4.
3. D. Bensimon, A. Englander, S. Shtrikman, M. Slatkine and D. Treves, Appl. Opt. 20, 947 (1981).
4. P.A. Pincus, M.E. Fossey, J.F. Holmes and J.R. Kerr, J. Opt. Soc. Am. 68, 760 (1978).
5. J.F. Holmes, M.H. Lee and J.R. Kerr, J. Opt. Soc. Am. 70, 355 (1980).
6. V.P. Aksenov, V.A. Banakh and V.L. Mironov, J. Opt. Soc. Am. 1, 263 (1984).
7. V.P. Aksenov and V.L. Mironov, J. Opt. Soc. Am. 69, 1609 (1979).

Laser scintillation, C_n^2, and ℓ_0 measurements in evolving atmospheric turbulence. **P29**

Anna Consortini, Fausto Cochetti, James H. Churnside[*] and Reginald Hill[*]

Physics Department University of Florence, via S. Marta 3, 50139 Florence, Italy

Results of simultaneous measurements of laser scintillation, structure constant and inner scale made during continuously evolving atmospheric turbulence comprising low, moderate, and high levels are presented.

1 - Introduction

Measurements of intensity fluctuations of a diverged laser beam were made at NOAA's Table Mountain Field site near Boulder, CO, USA, where turbulence homogeneity is excellent. The horizontal propagation path was 1.2 m above ground and 1200 m long. Refractive index structure "constant" C_n^2 and inner scale ℓ_0 were measured simultaneously. Measurements were also made with the laser shuttered to obtain background and noise values to be removed from the signal.

Figure 1 shows a scheme of the experimental setup. The radiation from an argon ion continuous laser was diverged by a lens behind which was a shutter. After traveling the atmospheric path, the light passed through a pinhole and a filter and was collected by a photomultiplier. The filter and pinhole were on the front side of a black tube having a number of internal diaphragms, and the photomultiplier was on the back side. The pinhole diameter was 0.25 mm. This value was chosen on the basis of a previous work [1] to simulate a point receiver. The diaphragms were used to reduce background light from lateral directions, although they do not intercept direct laser and background radiation. Reducing the background allows us to efficiently use the dynamic range of the instrumentation. Recall that the parameter, α, describing the quality of a system to measure intensity fluctuations, is given by [2]

$$\alpha = I_{sat}/<I> .$$

where I_{sat} is the saturation value of the electronic of the system and $<I>$ is the mean value of the fluctuating signal to be measured. Large values of α are needed to mitigate the effects of detector saturation on the high-order moments of irradiance [3]. In our case the value of α

----

[*]NOAA/ERL/WPL, Boulder, CO, USA

was usually larger than 80.

The instrument for measuring C_n^2[4] operated on a 600-m path parallel to the laser propagation path. The apparatus for measuring the inner scale, built [5] to measure ℓ_0 according Obukov's definition, operated on a 150-m path near the receiver. They have a time constant of ~1 s. The transverse wind was also measured on the 600-m path.

2 - Measurement procedure

Data were collected during August and September 1987 from early morning to mid day. On some days, the data were collected at sunset. The elementary measurement was a cycle of about 70 s. During a cycle 64000 intensity data values were collected by the acquisition system at a rate of 1000 data/s and stored on a disk. Then the system recorded the C_n^2, ℓ_0, and cross wind (in less than 1 s). Due to the large value of the time constant of the corresponding instruments, these values represent spatially average values at the end of the cycle. Finally, the computer sent a signal to the shutter and 3200 data were collected in 3.2 s with the laser shuttered.

A data run consisted of many subsequent cycles. Every five consecutive cycles data collection paused to check laser alignment and saturation level. A maximum of up to 70 sequential cycles were collected in a file. A complete measurement consisted of a number of files, with an interruption of several minutes between one file and the following one. The data were transferred to a magnetic high-density tape suitable for analysis in Florence, Italy.

The first step of the analysis was to produce histograms for both the "total" signal and the signal with the laser shuttered. As discussed in Ref.1, the noise of the acquisition system was independent of the laser signal and was very low. Hereafter the signal with laser shuttered is denoted by "background". The histograms as well as the meteorological data were finally stored on diskettes suitable for analysis with a personal computer.

From the histograms, some low order moments of both intensity signal and background were obtained. The moments of the laser intensity of each cycle were obtained by a background subtraction procedure. Last, the moments were normalized by the corresponding power of the mean intensity.

3 - Scintillation index

From the normalized second moment m_2 the laser intensity

scintillation index $\sigma_I^2 = m_2 - 1$ was obtained. A typical result is shown in Fig. 2, where σ_I^2 measured on August 15 (files 11 to 14) is plotted versus local time from early morning to midday. Analogous curves were obtained for C_n^2 and ℓ_0. A comparison among the different curves allows one to follow the evolution of σ_I^2. The high initial value (presumably not saturated) of σ_I^2 in Fig.2 is justified both by a high value of C_n^2 and by a high ℓ_0 value, typically in the range $\ell_0 = 10$ to 20 mm in early morning. In general there is a trend of all the quantities with some fluctuations superposed. In Fig.2, σ_I^2 reaches very low values in the minimum, where C_n^2 reaches values of order $10^{-15}\,m^{-2/3}$ then σ_I^2 increases, reaches a maximum and finally decreases reaching values clearly in the "supersaturation region". In this region both large values of C_n^2 ($>10^{-13}\,m^{-2/3}$) and small ℓ_0 values are present. On different days values were reached deeply in the supersaturation region.

Plots of σ_I^2 versus C_n^2, for selected ranges of ℓ_0, confirm a role of the inner scale, as expected from existing theories.

References

1 - J.H. Churnside, R.J. Hill, G. Conforti and A. Consortini: "Aperture size and bandwidth requirements for measuring strong scintillation in the atmosphere" - Applied Optics 28, 4126-4132 October 1989

2 - A. Consortini, G. Conforti: "Detector Saturation Effect on Higher-Order Moments of Intensity Fluctuations in Atmospheric Laser Propagation Measurement" - J. Opt. Soc. Am. A1, n.11, 1075 Nov. 1984

3 - A. Consortini, E. Briccolani, G. Conforti: "Strong-Scintillation Statistics-Deterioration Due to Detector Saturation" - J. Opt. Soc. Am. A3, 101-107, 1986

4 - G.R.Ochs, W.D. Cartwright, and D.D. Russel: "Optical C_n^2 Instrument Model II", NOAA Tech. Memo. ERL WPL-51 (available from National Technical Information Service, 5285 Port Royal Rd., Springfield, VA. 22161; order number WPL51: PB 80-209000), 1979

5 - G.R. Ochs and R.J. Hill: "Optical-Scintillation Method of Measuring Turbulence Inner Scale", Appl. Opt. 24, 2430-2432, 1979
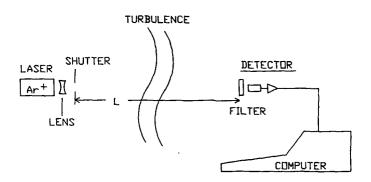
Fig.1 Experimental set up
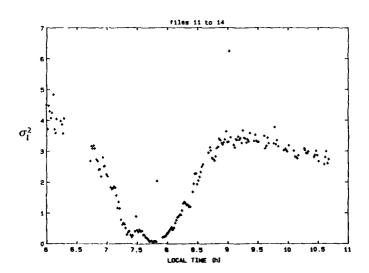
Fig.2 Experimental results

Atmospheric Intensity Scintillation of Stars   **P30**
on Milli- and Microsecond Time Scales
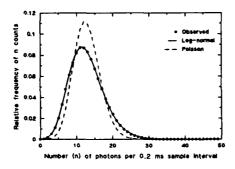
D. Dravins,   L. Lindegren,   E. Mezey

Lund Observatory, Box 43, S-22100 Lund, Sweden

A detailed understanding of stellar atmospheric scintillation is required to understand the physics of atmospheric turbulence, and to test theories of light propagation in random media. It is needed for the design of adaptive optical systems, and is required in searches for rapid astrophysical variability, where the sources must be observed through the turbulent atmosphere.

Observations, instrumentation, and data reduction

Extensive and systematic observations of stellar intensity scintillation on short and very short time scales ($\simeq 100\,\mathrm{ms}$ – $100\,\mathrm{ns}$) have been made using a 60 cm optical telescope at the astronomical observatory on La Palma (Canary Islands), at 2400 m altitude. Photon counting photomultipliers and real-time signal processors were used to study atmospheric scintillation as function of telescope aperture size and shape, degree of apodization, for single and double apertures, for single and binary stars, in different optical colors, using different optical passbands, at different zenith distances, at different times of night, and different times of year. Scintillation properties were recorded as temporal auto- and cross correlation functions, and intensity probability distributions, sometimes supplemented by simultaneous video recordings of the stellar speckle images, as well as seeing disk measurements in an adjacent telescope.

The stellar photometer attached to the telescope uses two photon counting photomultiplier tubes. The signals from these are fed to a digital photon correlator. The correlator measures temporal auto-correlation (ACO), cross correlation (CCO) and photon count distribution (probability density, PDE) with time resolutions (sample time) from 20 ns to 1 s. It has 64 registers for data storage, i.e. correlation measurements are made with 64 different delays simultaneously. In PDE mode, the number of occasions when $0, 1, \ldots, 63$ photons are recorded during one sample interval, is measured. Rapidly changeable mechanical aperture masks in front of the telescope provide different entrance apertures.
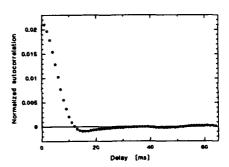
Figure 1. To the left a typical observed photon count distribution is shown. A log-normal distribution is fitted to the data. The Poisson distribution corresponding to zero atmospheric intensity fluctuation is also shown. To the right is a typical normalized autocorrelation of the starlight intensity, measured at time delays 1, 2, 3, etc. milliseconds, integrated for 100 s.

The ACO is a measure of the time scale of the intensity fluctuations. It is normalized to $ACO(0) = \sigma_I^2$ and $ACO(\infty) = 0$, where σ_I is the RMS value of $\Delta I/<I>$. The Fourier transform of the ACO yields the scintillation power spectrum.

The PDE is a measure of the statistics of the intensity fluctuations. The observed distribution is a convolution of the atmospheric fluctuations with the Poisson distribution of the photon counts. We have fitted log-normal distributions to all our data (several hundred measurements under different conditions), and found it to be an adequate distribution for $\sigma_I^2 < 0.4$, a range that covers all our measurements.

Elementary theory predicts a functional dependence of σ_I^2 on aperture size D, wavelength λ, and zenith distance z, with the limiting forms for large and small apertures:

$$\sigma_I^2 = \begin{cases} \text{const} \cdot D^{-7/3} \ (sec\,z)^3 \int_0^\infty h^2 C_N^2(h)\,dh, & D >> r_0 \quad\quad (1a) \\[2em] \text{const} \cdot \lambda^{-7/6} \ (sec\,z)^{11/6} \int_0^\infty h^{5/6} C_N^2(h)\,dh, & D < r_0 \quad\quad (1b) \end{cases}$$

(e.g. Roddier, 1981), where r_0 is Fried's parameter and $C_N^2(h)$ the refractive index structure coefficient as a function of height above the telescope.

Several properties of the observed fluctuations can be qualitatively understood in terms of the illumination pattern caused by diffraction in inhomogeneities at high atmospheric layers. These structures are carried by winds, resulting i.. 'flying shadows' on the ground (e.g. Young, 1971).

Zenith distance dependence

As seen in Figure 2, there is a linear relationship between $log(\sigma_I^2)$ and $log(sec\,z)$ with slope 2.7, in rather close agreement with the theoretical value of 3 in Eqn (1a), although our aperture cannot be much larger than r_0.

Both the amplitudes and the widths of the autocorrelations increase with z. The increasing half widths (13 ms to 27 ms) may be interpreted as a geometrical effect. The time for a disturbance, carried by a horizontal wind, to traverse the telescope entrance beam, increases as $sec\,z$. The power spectra show that only fluctuations $\lesssim 30$ Hz are significantly affected.
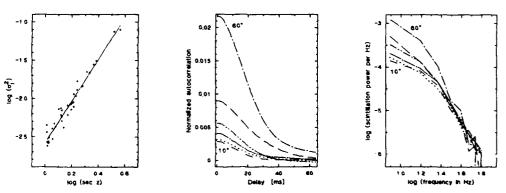
Figure 2. Zenith distance dependence measured with a 22 cm aperture. Left, the observed increase of σ_I^2 with increasing zenith distance, and a linear fit to the data. Representative normalized autocorrelation functions and power spectra are shown at $10°$ intervals in z at center and right.

Aperture dependence

Figure 3 shows how the fluctuations decrease with aperture size, and for larger apertures approach the slope $-7/3$ in Eqn (1a). Both the fluctuation amplitudes and the autocorrelation half widths become essentially independent of the aperture for $D < 5$ cm, where the spatial structures in the 'flying shadows' on the ground appear to be resolved. Different shapes of the autocorrelation functions are observed at different times, exemplified in Figures 4a and 4b. However, for all observations the half widths increase with aperture size.
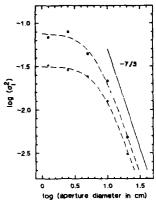
Figure 3. Aperture dependence of σ_I^2 measured at different times.
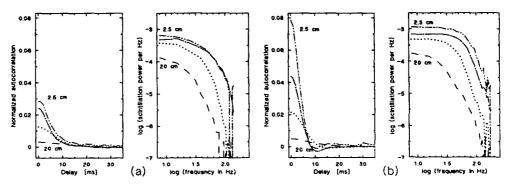
Figure 4. Aperture dependence of autocorrelation functions and power spectra measured at different times during the same night. (a) shows measurements early in the evening at moderate zenith angles, (b) shows measurements closer to midnight at small zenith angles. Aperture diameters are 2.5, 5, 10, and 20 cm.
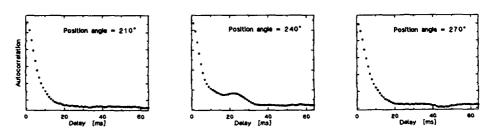
Figure 5. Autocorrelation with a double aperture. Intensity fluctuations are measured through a mask with two holes. If the same 'flying shadows' pass both holes, a secondary peak will appear in the autocorrelation. From the spacing and orientation of the holes, the speed and direction of the 'flying shadows' can be determined. For hole sizes of 10 cm, and a spacing of 30 cm, reproducible secondary peaks appear within an interval of $\approx 30°$. Typical delays of 20 ms indicate a 'flying shadow' speed of ≈ 15 m/s, apparently the windspeed in the high atmosphere.

305

Wavelength dependence

This was observed on several occasions with different broadband filters and different aperture sizes. For apertures smaller than $\simeq 10$ cm there was a measurable difference for different colors. For a 2.5 cm aperture, our data agree well with the theoretical slope $-7/6$ in Eqn (1b), but the wavelength dependence rapidly diminishes for larger apertures. The correlation halfwidth increases with wavelength, but the power of the fluctuations decreases at all frequencies.
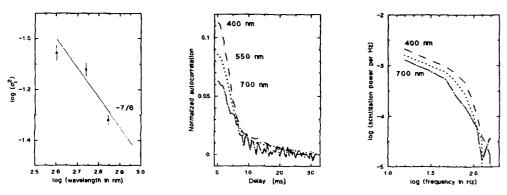
Figure 6. Wavelength dependence measured with a 2.5 cm aperture at λ 400, 550, and 700 nm. The dependence of σ_I^2 is shown to the left. In the middle are the measured autocorrelations, and the power spectra are to the right.

The cross correlation between different wavelengths was also measured. Near zenith the fluctuations are essentially simultaneous, but with increasing zenith distance a time delay gradually develops between different wavelengths. This is apparently due to atmospheric chromatic dispersion, which causes relative displacements of the 'flying shadows' in different colors.
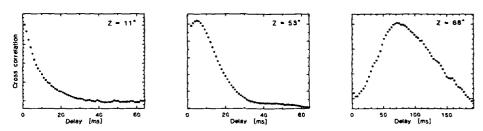
Figure 7. Cross correlation between intensity fluctuations at λ 400 and 700 nm, as function of zenith angle.

The analysis and interpretation of these and other data is in progress with an aim of better understanding the physics of stellar scintillation (e.g. Jakeman et al., 1978), and for comparing the La Palma conditions to those at other observatories, such as Mauna Kea on Hawaii (Dainty et al., 1982).

References

Dainty, J.C., Levine, B.M., Brames, B.J., O'Donell, K.A.: 1982, *Appl. Opt.* **21**, 1196
Jakeman, E., Parry, G., Pike, E.R., Pusey, P.N.: 1978, *Contemp. Phys.* **19**, 127
Roddier, F.: 1981, *Progress in Optics* **19**, 281
Young, A.T.: 1971, *Sky and Telescope*, **42**, 139

Inner Scale, C_n^2, and Surface Fluxes Obtained in the Atmospheric Surface Layer Using Scintillation

Reginald J. Hill
NOAA/ERL, Wave Propagation Laboratory
325 Broadway
Boulder, CO 80303 U.S.A.

Optical scintillation can be used to measure the turbulence inner scale, l_o, and refractive structure parameter, C_n^2. These quantities, in turn, determine the surface fluxes of heat and momentum. An experiment combining scintillation and micrometeorological measurements demonstrated that the two types of measurement are in good agreement. Deriving l_o from optical scintillation requires an accurate model of the refractive index spectrum. The results verify the model spectrum of Ref. [1].

Let σ^2 be the variance of log-intensity obtained using a diverged laser source (effective spherical wave) that has an optical wavenumber $k = 2\pi/\lambda$, λ being the radiation wavelength, propagating over a path of length L to a small-aperture receiver (effective point receiver). This variance depends on L, k, C_n^2, and l_o ; outer scale effects are negligible. However, for the case of weak scintillation the scaled variance, $\tilde{\sigma}^2$, defined by

$$\tilde{\sigma}^2 = \sigma^2/0.5\, k^{7/6}\, L^{11/6}\, C_{n(\lambda)}^2 \; , \tag{1}$$

is a function of only $l_o/\sqrt{L/k}$. Theoretical curves for $\tilde{\sigma}^2$ are in Ref. [2].

Let σ_{LA}^2 be the variance of the logarithm of the signal from a large-aperture circular receiver of diameter D for light propagating on a path of length L from a uniformly illuminated, phase-incoherent, circular transmitter also of diameter D. Suppose that D exceeds $2\sqrt{\lambda_{LA} L}$, where λ_{LA} is the transmitted wavelength; then σ_{LA}^2 is independent of λ_{LA} to excellent approximation [3]. This variance, σ_{LA}^2 , is a function of L, D, C_n^2, and l_o; it is insensitive to the outer scale provided that D is much less than the outer scale. However, for weak scintillation, the scaled variance, $\tilde{\sigma}_{LA}^2$, defined by

$$\tilde{\sigma}_{LA}^2 = \sigma_{LA}^2/0.9\, L^3 D^{-7/3} C_{n(\lambda_{LA})}^2 \tag{2}$$

depends only on l_o/D. Theoretical curves for $\tilde{\sigma}_{LA}^2$ are in Ref. [3].

The ratio of the two scaled variances,

$$y(x,d) \equiv \tilde{\sigma}^2/\tilde{\sigma}_{LA}^2 \; , \tag{3}$$

can be taken to be a function of $l_o/\sqrt{L/k}$ and $\sqrt{L/k}/D$, as well as proportional to r_n, where

$$r_n \equiv \frac{C_{n(\lambda)}^2}{C_{n(\lambda_{LA})}^2} = \left[\frac{n(\lambda)-1}{n(\lambda_{LA})-1}\right]^2 . \tag{4}$$

Our inner-scale scintillometer uses $\lambda = 0.6328$ μm and $\lambda_{LA} = 0.938$ μm for which $r_n = 1.016$ for dry air. As $l_o \rightarrow 0$, y tends to r_n. Ochs and Hill [4] showed good agreement between theory and measured values of y/r_n as a function of l_o. Hill [5] shows y/r_n as a function of $l_o/\sqrt{L/k}$ for two values of $\sqrt{L/k}/D$, as well as $\bar{\sigma}^2$ as a function of $l_o/\sqrt{L/k}$ and $\bar{\sigma}_{LA}^2$ as a function of l_o/D.

The inner scale is related to the kinematic viscosity, v, and the dissipation rate of turbulent kinetic energy, ϵ, by [2]

$$l_o = 7.4(v^3/\epsilon)^{1/4} . \tag{5}$$

We measured mean temperature, T, pressure, P, and the height above ground, z, of the measurements. Mean wind speed, V, was obtained using a propeller-vane anemometer. Using a three-axis sonic anemometer and a resistance-wire thermometer, we measured the correlations $<u'w'>$, $<T'w'>$, and $<w'^2>$, where w' and u' are fluctuations of the vertical and the streamwise velocity components, T' is the fluctuation of temperature, and the angle brackets denote averaging. From these data we determined the surface roughness length z_o. All of our measurements were performed at a height of $z = 4$ m. The parameters for the optical scintillation are $L = 150$ m, $\lambda = 0.6328$ μm, $\lambda_{LA} = 0.938$ μm, and $D = 4.4$ cm. The two propagation paths are separated by 14 cm at their ends, and they cross in the middle. The micrometeorological instrumentation is described in Ref. [6].

Monin-Obukhov similarity theory (MOST) relates many turbulence statistics for the horizontally homogeneous atmospheric surface layer. This layer is the lowest few tens of meters of the atmosphere. Several micrometeorological experiments have determined the MOST empirical relationships between turbulence statistics [7]. There are four ways to obtain l_o from our micrometeorological data. We have values of T, P, and z. Given these, the values of $<u'w'>$ and $<T'w'>$ are sufficient to determine ϵ and therefore l_o. Likewise, either $<w'^2>$ and $<T'w'>$ or V, $<T'w'>$, and z_o are sufficient to determine l_o. It is also possible to determine l_o from the level of the inertial range of the temporal power spectrum of the time series of w'.
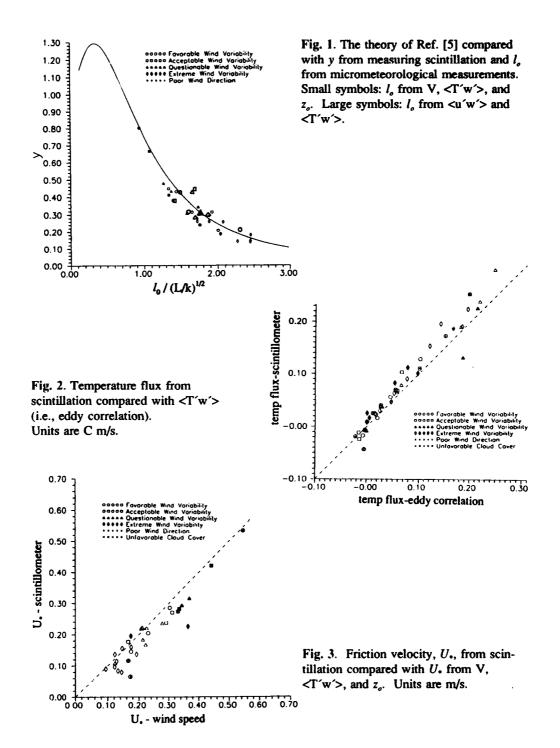
Figure 1 shows our measured value of y as a function of l_o; l_o is scaled by the Fresnel zone size $\sqrt{L/k} = 3.9mm$. The solid curve in Fig. 1 is the theory by Hill [5]. That the data lie on the decreasing part of the theory curve beyond the maximum shows that the laser variance, σ^2, is dominated by the dissipation range of temperature fluctuations, not by the inertial range. There is very good agreement of experiment and theory. For most of the data points in Fig. 1, we used V, $<T'w'>$, and z_o to determine l_o. However, for the nine larger symbols, l_o was determined using $<u'w'>$ and $<T'w'>$; that only nine data points are given

308

for this method of measuring l_o reflects the requirement of steady wind direction and speed to obtain a reliable value of $<u'w'>$. The symbols in Fig. 1 denote the wind direction variability during each data run as well as those runs having wind from the direction of poorest homogeneity (see Ref. [6] for details). There is agreement of theory and experiment even for nonideal micrometeorological conditions.

Using $<w'^2>$ and $<T'w'>$ to determine l_o also gave agreement with theory, but the data are more scattered [6]. Using the inertial-range level of the power spectrum of w' to determine l_o gave data points deviating systematically from the theory for reasons given in Ref. [6].

The measured value of y and the theoretical relationship depicted in Fig. 1 are sufficient to yield l_o. Given this l_o, either the measured value of σ^2 or that of σ_{LA}^2 suffices to yield C_n^2. One obtains C_n^2 using (1) or (2) and the theoretical curves in Refs. [2] and [3], which give the scaled variances as functions of $l_o/\sqrt{L/k}$ and l_o/D. Knowing l_o and C_n^2, the MOST relationships can be used to obtain the surface heat and momentum fluxes. Heat flux is proportional to the temperature flux, $<T'w'>$. Momentum flux is proportional to $<u'w'>$; the friction velocity U_* is defined by $U_* = \sqrt{-<u'w'>}$. In Fig. 2, the temperature flux obtained from scintillation-derived l_o and C_n^2 is compared with that obtained by the correlation $<T'w'>$ measured by the resistance wire and three-axis sonic anemometer. In Fig. 3, data for U_* from scintillation are compared with U_* deduced from V, $<T'w'>$, and z_o using MOST. Scintillation-derived U_* also agrees with U_* from $<u'w'>$ [6]. The scintillation method agrees very well with the standard micrometeorological method. In particular, very nonideal micrometeorological conditions are included in Figs. 2 and 3, yet the agreement remains good.

References

[1] Hill, R.J., 1978. Models of the scalar spectrum for turbulent advection. *J. Fluid Mech.* 88:541-562.
[2] Hill, R.J., and S.F. Clifford, 1978. Modified spectrum of atmospheric temperature fluctuations and its application to optical propagation. *J. Opt. Soc. Am.* 68:892-899.
[3] Hill, R.J., and G.R. Ochs, 1978. Fine calibration of large-aperture optical scintillometers and an optical estimate of inner scale of turbulence. *Appl. Opt.* 17:3608-3612.
[4] Ochs, G.R., and R.J. Hill, 1985. Optical-scintillation method of measuring turbulence inner scale. *Appl. Opt.* 24:2430-2432.
[5] Hill, R.J., 1988. Comparison of scintillation methods for measuring the inner scale of turbulence. *Appl. Opt.* 27:2187-2193.
[6] Hill, R.J., G.R. Ochs, J.J. Wilson, D.A. Furtney, and J.J. Priestley, 1991. Results of the 1988 fluxes-from-scintillation experiment, NOAA Technical Memorandum, NOAA Environmental Research Laboratories, Boulder, CO (in press).
[7] Kaimal, J.C., and J.C. Wyngaard, 1990. The Kansas and Minnesota experiments. *Boundary-Layer Meteorol.* 50:31-47.

Fig. 1. The theory of Ref. [5] compared with y from measuring scintillation and l_o from micrometeorological measurements. Small symbols: l_o from V, $<T'w'>$, and z_o. Large symbols: l_o from $<u'w'>$ and $<T'w'>$.

Fig. 2. Temperature flux from scintillation compared with $<T'w'>$ (i.e., eddy correlation). Units are C m/s.

Fig. 3. Friction velocity, U_*, from scintillation compared with U_* from V, $<T'w'>$, and z_o. Units are m/s.

310

Removing noise from histograms of probability density in laser scintillation P32

A. Consortini, F. Cochetti
Physics Department University of Florence, Via S. Marta 3, 50139
Florence - Italy

A procedure is described to remove a large uncorrelated noise from probability density
histograms of intensity fluctuations of a laser beam propagated through atmospheric
turbulence

A procedure is described to remove a large uncorrelated noise from
probability density histograms of intensity fluctuations of a laser beam
propagated through atmospheric turbulence.

The data were collected by very small apertures (0.04 mm^2 areas)
during an experiment at NOAA/ERL/WPL Boulder, USA, in conditions of
homogeneous and isotropic turbulence. The apertures belong to an array
of five sensors of different small areas ranging from about 20 mm^2
(circle of radius 2.5 mm) down to 0.04 mm^2 (square of 0.2 mm on a
side) that collected laser radiation that had propagated along a 1200 m
path in the atmosphere. The aim of that experiment did not require
noise resolved measurements at small irradiance [1]. During each
measurement (cycle) each aperture collected 32,000 data (at a rate of
500 samples/s) of laser radiation followed by 1600 samples with the
laser screened off. These last samples were collected in order to
subtract the contribution due to background and noise from the signal.
Generally the background in a cycle was a constant additive signal. The
dominant noise source was thermal noise of the large feedback resistor
in the transimpedance preamplifier and therefore it was independent of
the original signal. For simplicity the data taken with the laser screened
off are here referred to as "noise".

The data from both signal and noise in one cycle were subsequently
grouped in histograms. In general for the largest apertures the noise
histograms were simple lines and their subtraction from the signal
histograms allowed one to obtain the noise free laser histograms.

The noise was large in the smallest two apertures which interest us
here. An example is given in Fig. 1 where the probability histograms of

"total" signal and noise of a square aperture, of 0.2 mm on a side, are represented.

The lower and larger histogram was obtained with 32000 data from a 64 sec measurement of total signal. The higher and thinner histogram was obtained with the 1600 data taken with the laser shuttered off in the subsequent 3.2 sec. The histograms were obtained by grouping the original data from the acquisition system in steps of two bins each, to remove an effect due to the sampling system.

As can be seen from the measurements the noise is "large".

Let us denote by s the "total" signal. One has

1) $s = i + b$

where i denotes the signal from the laser, b denotes "noise" and as already stated b includes both background signal and noise from the amplifier.

As is well known, the (measured) probability density of the total signal, P(s) is the convolution of the probability densities of signal, P(i), and noise, P(b),

2) $P(s) = P(b) \otimes P(i)$

where $\otimes$ denotes convolution. In order to remove P(b) from P(s) one is therefore faced with a deconvolution problem.

Deconvolution belongs to the so called ill-posed problems [2] where a small error on the data has a great influence on the solution or, equivalently, small variations of the error give rise to very different solutions (instability).

In our measured histograms, the errors are due to statistical uncertainty.

In order to apply a deconvolution procedure, the probability distribution of noise is assumed to be gaussian. A check between the measured noise histogram and the theoretical histogram obtained by a gaussian distribution having the same mean value and variance showed that the assumption is correct.

In our case it was useful to express the data in matrix form.

To obtain an approximate solution a regularization is required. Here we have used the iterative procedure of deconvolution described by Schafer

in Ref.3, where a rather broad class of iterative restauration techniques were presented. This technique allows one to obtain regularization and to include "a priori" knowledge of the solution properties in terms of a constraint operator. In our case a suitable condition is that the solution be positive.

The procedure was developed for a small computer and the deconvoluted histogram evaluated. The first step was to apply the procedure without any constraint. Fig. 2 represents the results of the restoration of the data of Fig. 1 after 10 iterations. It appears that the deconvolution procedure introduces not only negative values of P(. but also negative values of the intensity I. After 100 iterations the result was practically the same and it appeared that it is not worthwile to go much further than 100 iterations. Including the positivity condition in the algorithm leads to a physically acceptable distribution that is not very different from the unconditioned one in the region $I \geq 0$ and practically vanishes for $I < 0$.

A test of the quality of the results was made by comparing the moments obtained by the deconvoluted histogram with those obtained by directly removing noise moments from signal moments as described in Ref.1. The comparison was made by using the first five moments. After a small number of iterations, of the order of ten, a good agreement was found.

REFERENCES

1- J.H. Churnside, R.J. Hill, G. Conforti and A. Consortini: "Aperture size and bandwidth requirements for measuring strong scintillation in the atmosphere" Applied Optics 28, 4126-4132, 1989.

2- See e.g. M. Bertero: "Linear inverse and ill-posed problems" in Advances in Electronics and Electron Physics, vol.75, Ed. P.W. Hawkes. Academic Press, 1989, p. 1-120.

3- R.W. Schafer, R.M. Mersereau and M. Richards: "Iterative Restoration Algoritms" Proc. IEEE 69, 432-450, April 1981.
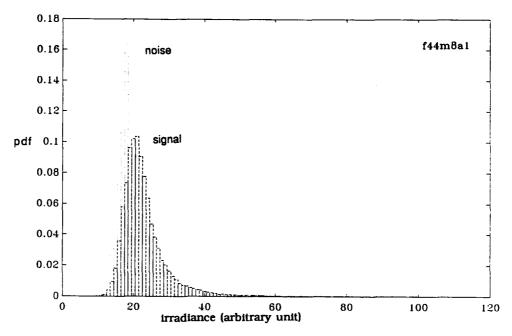
Fig. 1 Probability density histograms of total signal (lower and larger distribution) and noise (thinner and higher distribution).
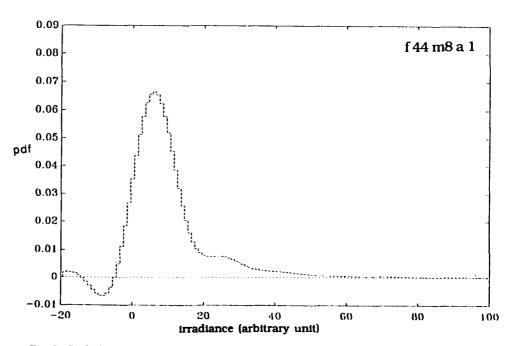
Fig. 2 Probability density histogram of deconvoluted signal after 10 iterations with no constraint.

CHARACTERIZATION OF TURBULENCE EFFECTS ON INFRARED IMAGERY **P33**

Wendell R. Watkins
U.S. Army Atmospheric Sciences Laboratory
Attn: SLCAS-AR-I
WSMR, NM 88002-5501
ph:(505) 678-4313

Jay B. Jordan
New Mexico State University, Dept. 3-0
Box 30001
Las Cruces, New Mexico 88003
ph:(505) 646-3115

INTRODUCTION

Modern infrared (IR) imagers are now producing digital images of scenes with increased spatial resolution and therefore are more susceptible to degradation due to atmospheric effects. Detailed characterization of the degradation caused by phenomena such as atmospheric turbulence, spatial nonuniformity, smoke, dust, aerosols, and other effects is being investigated using the Mobile Imaging Spectroscopy Laboratory (MISL) with its Target Contrast Characterizer (TCC)[1]. In the past, efforts to isolate the degradation of image quality due to the atmospheric propagation of the radiation field constituting the zero-range image have been largely model driven with little if any supporting field measurements to validate the models. What is needed to further this work are simultaneously collected close-up or near-field (NF) imagery together with optically matched distant or far-field (FF) imagery.

OVERVIEW OF INSTRUMENTATION

The TCC is a mobile IR instrumentation system built around two Inframetrics model 610 dual channel, high resolution, IR imagers and a unique Recognition Concepts, Inc. real-time image processor. The optics and the electronics of the instrumentation system are designed for simultaneous acquisition of close-up and distant IR signatures of various objects under typical field conditions. For characterizing atmospheric propagation phenomena, a large (1.78m x 1.78m effective surface area) black body source and a removable 3.5 cycle vertical notched bar pattern were used. The black body source surface was tilted back to eliminate the vertical temperature gradient typical of large sources. This together with the separation of the notched bar pattern from the source gives a nearly perfect transition horizontally between the hot and cold portions of the bar pattern.

DESCRIPTION OF EXPERIMENT

For this experiment, the TCC was specifically configured to obtain data useful in characterizing the IR image degradation caused by atmospheric turbulence and spatial nonuniformity. For the measurements presented here, only the 8-14 micron imagery was used. Characterization of this scene degradation or atmospheric modulation transfer function (AMTF) should prove useful in predicting and improving imager performance under varying atmospheric and field conditions.

The close-up imager (NF) was placed 0.1 km (96m) from the large area black body source with the vertical bar pattern in place. The distant imager (FF) was placed 1.6 km (1,637 m) from the black body source, giving an atmospheric path difference of 1.5 km. The FF imager was optically matched to the NF imager using a 17 power telescope. The imagers were co-aligned on the black body source through real-time registration by using a fiber optic imager control and data link and the TCC image processing system.

In theory, characterization of the AMTF is straight forward. If the imagers are noiseless with identical transfer functions, $h_i(x,y)$, and the degradation (the AMTF) is a deterministic point spread function $h_d(x,y)$, then the zero-range or "truth" image, $f(x,y)$, as observed by the close-up imager is $f_{NF}(x,y) = f(x,y) * h_i(x,y)$. Where * denotes two dimensional spatial convolution. The image, $f(x,y)$ as observed by the distant imager is $f_{FF}(x,y) = f(x,y) * h_i(x,y) * h_d(x,y)$. The AMTF (degradation transfer function) is given by the inverse Fourier transform of the quotient of the Fourier Transforms of the long and short range images.

$$hd(x,y) = F^{-1} \frac{F(x,y) \times Hi(x,y) \times Hd(x,y)}{F(x,y) \times Hi(x,y)} \tag{1}$$

In practice, however, several difficulties arise. The imagers are not identical and each has an

associated noise process that must be characterized. Each imager exhibits a different line to line scan anomaly and the imagers are neither line to line nor frame synchronized. The AMTF is not a deterministic point spread function, but rather a complicated non-stationary random process. The quality and usefulness of the AMTF obtained from the TCC data depend largely on how well these difficulties are characterized and resolved. Because the imagery data obtained using the TCC have only been available for analysis since the beginning of December, 1990, all the data reduction techniques have not been perfected and the results presented are preliminary.

CHARACTERIZING AND REMOVING THE CAMERA SCAN ANOMALY

Each of the 8-14 micron imagers used has a single mechanically deflected scanning detector that introduces a phasing problem. The imager acquires data while scanning in both directions, left to right and right to left. A phasing adjustment is required to align vertical edges in the scene, such as the vertical bar pattern, fig. 1. To minimize the effects of this phasing error, only scan lines for the same direction of scan and in the same image field are considered for analysis. These lines are approximately 0.25 ms apart. Because of the short duration between scan lines, the "frozen" atmospheric degradation effects can be averaged over several scan lines if indeed the short exposure time used in astronomy[2] of 1 ms to 10 ms holds for horizontal path turbulence in the infrared region.

CHARACTERIZING THE CAMERA NOISE PROCESS

Because of the large amount of a priori knowledge about the black body target board and the manner in which the data were collected, several options are available for noise reduction in the TCC imagery. First, the NF camera has an instantaneous field of view (IFOV) of 2.0 mrad x 2.0 mrad which represents a 19 cm x 19 cm square on the black body 96 m away. The optically matched FF imager with its 17 power lens also has a 19 cm x 19 cm square at 1,637 m for its IFOV of 0.12 mrad x 0.12 mrad. The vertical bars were 25 cm wide; and hence, with a corresponding slit response of approximately 0.7 for 2.5 mrad, the camera should be able to resolve 40% of the unobstructed black body ΔT in the target pattern open vertical slits. The single detector imager can be adjusted to scan a smaller field of view (FOV). To observe the target pattern distortions better, the camera FOV was reduced by a factor of 4 in both vertical and horizontal scans. This resulted in an image pixel size of approximately 0.14 mrad x 0.14 mrad which corresponds to a factor of 15 oversampling in the horizontal scans. This oversampling can be used to eliminate a significant portion of the high frequency noise common to single detector imaging systems through appropriate filtering. Also scan line and/or field and frame averaging can be used to reduce the camera noise.

CHARACTERIZING THE AMTF

Fig. 1 shows a NF 256 x 256 pixel portion of the target board scene where the individual vertical bars are 15.5 pixels wide or a 31 pixel bar cycle. Fig. 2 shows an afternoon FF scene of the target board with significant turbulence induced (C_n^2 on the order of 10^{-13} to 10^{-12} range) degradation of the bar pattern. In addition, approximately a 40% reduction in the bar pattern ΔT is present due to atmospheric absorption of the 1.5 km path difference. The average of ten same field, same direction line scans across the target board bar pattern are shown in fig. 3 for the NF and FF images. The corresponding Discrete Fourier Transforms (DFTs) are shown in fig. 4. With a bar cycle of 31 pixels, the NF DFT (top curve) has a strong, broad DFT at index at 8 (corresponding to a 32 pixel period) with smaller peaks at indices 3 and 5. These are harmonics of the large fundamental frequency (index 1) caused by the overall "square-wave" nature of the signal. The DFT of the FF target board image (bottom curve) shows a significant reduction in the characteristic DFT index 8 peak due to the turbulence induced degradation of the bar target pattern. Now the AMTF can be derived using eq. 1 from the DFTs in fig. 4 and assuming the hi(x,y) is the same for NF and FF. This represents a short exposure or "frozen" AMTF and is not useful in correcting the long exposure or average turbulent degradation present for partial image restoration for imaging systems. What the "frozen" AMTF does show is the dynamics of the turbulence induced degradation. Three 10 row average AMTFs for three images separated in time by approximately 10s each are given in fig. 5. These graphs exhibit some interesting characteristics for the comparable high level of afternoon turbulence. First, plots of right-to-left and left-to-right estimated AMTFs from the same field

316

(not shown) are nearly identical, indicating very little change in the AMTF over time spans of the order of 0.25ms. The AMTFs changed dramatically, however, between the 10s intervals although the overall decrease of the characteristic DFT index 8 was nearly the same. The interesting phenomena for this experiment influence DFT peaks on either side of this characteristic index 8 approximately from index 5 to index 10. The turbulence appears to have a characteristic stretch and compression associated with perhaps the dominant turbule size. This would result in the 32 pixel or point bar cycle being compressed or widened. The FF2 curve, taken approximately 10s after FF1, shows a peak at DFT index 6 which corresponds to a cycle width between 42 and 43 or a stretch of 11 or 12 pixels. FF3 shows a peak at index 7. Note that above index 10, the signals are so weak in both the NF and FF that the AMTF is not meaningful, being determined mainly by path radiance noise and camera noise.

With such dynamics occurring in the "frozen" AMTF, the question of how many rows of images must be averaged needs to be addressed since the long exposure AMTF is of most interest in image restoration. Fig. 6 shows the result of averaging the 30 rows shown as 10 row averages in fig. 5; and, fortunately, the AMTF dynamics are significantly reduced although several more images and rows will be needed to eliminate the dips at 2 and 4. There is very little energy in these frequencies in the target bar pattern and their value in the estimated AMTF is consequently influenced more by noise than by the effect of atmospheric turbulence. For the strong bar pattern component, index 8, the magnitude of the AMTF resolution loss is close to 70% for all of the estimated AMTFs shown in figures 5 and 6. The overall low pass nature of the long exposure AMTF is evident by picturing the curve formed using only the high energy frequencies and ignoring the low energy components represented by indices 2,4,6, and above 10.

CONCLUSIONS

A measurement technique has been devised and fielded to measure the image degradation or Atmospheric Modulation Transfer Function (AMTF) due to turbulence in the infrared. The technique utilizes real-time registration of optically matched close-up and distant images of a large area uniform temperature thermal bar target. The short exposure or "frozen" AMTF exhibits the dynamics of the atmosphere as a complicated, non-stationary random process. The "frozen" AMTF does, however, exhibit some characteristic stretching and compression of the characteristic frequencies of the bar pattern. The optimum number of image fields and time interval needed to extract the long exposure AMTF is a solvable problem utilizing the data collected, but remains unanswered at this time. Averaging scan line Discrete Fourier Transforms (DFTs) worked better in reducing system noise than averaging digitized frames before taking the DFT.
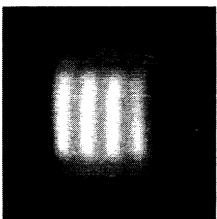
Fig. 1   Bar Target Image
from 96m (NF 14:42:58:456)
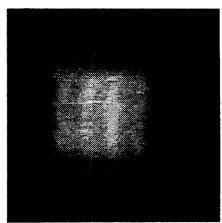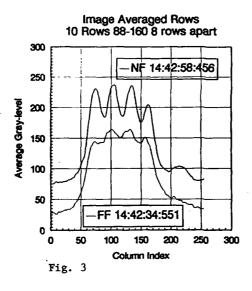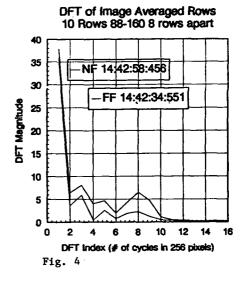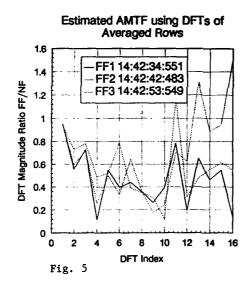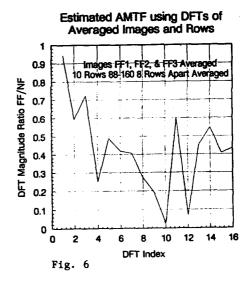
Fig. 2 Bar Target Image from
1,637m (FF 14:42:34:551)

Image Averaged Rows
10 Rows 88-160 8 rows apart

Fig. 3

DFT of Image Averaged Rows
10 Rows 88-160 8 rows apart

Fig. 4

Estimated AMTF using DFTs of
Averaged Rows

Fig. 5

Estimated AMTF using DFTs of
Averaged Images and Rows

Fig. 6

REFERENCES

1. Watkins, W.R., et. al. "Transmission Measurements with the Target Contrast Characterizer," _Proceedings of the SPIE International Symposium on Propagation Engineering_, Vol. 115, Orlando, FL 1988.

2. Goodman, Joseph W., _Statistical Optics_, p. 402, John Wiley & Sons, Inc., 1985.

Experimental evaluation of amplification-factor of fold-path
of optical scintillation in laboratory-generated turbulence

P34

Zhang Jun, Zeng Zongyong, Wong Lingqang
Anhui Institute of Optics and Fine Mechanics, Academia Sinica, China
230031, P.O.Box.25, Hefei Anhui, China, Tel.0551-291012

Abstract

The measuring amplification-factor of experiment is performed in
laboratory- generated turbulence . The results are compared with
theoritical prediction of weak scintillation .

1. Introduction

In some previous paper , the problem of fluctuation of the laser
radiation field retroreflected from a target in a turbulent atmosphere
were discussed (Ref. 1. 2.). These results are formulated based on the
equations of statistical moments of the Location Green function . For
the fold-path of the normalized variance of the intensity fluctuations,
the major conclusions are : the statistical intensity characteristics
are present a sum of two terms, one of which corresponds to the double
-length path; the second is caused by the correlation between direct
and reflected waves.

$$6\vec{\mathcal{R}}_{.1}(\vec{R}) = 6\vec{\mathcal{I}}_{.b}(2L) + 2B_{1.b}(\vec{R}) \qquad (1)$$

where $\vec{R} \gg \sqrt{L/k}$ ($k=2\pi/\lambda$) , the correlation between direct and
reflected waves vanishes.

In this paper, a propagation experiment of artificial turbulent
-tank is performed with a 1.5 mW He-Ne laser transmitted over fold-path
. The amplification-factor of intensity fluctuation is obtained. The
results are proved the effect of the intensity fluctuation
amplification. otherwhile, we use Rytov method for deriving the
intensity fluctuation of fold-path.

2. Experiment

The method for measuring the reflection of a plane wave of the
amplification factor is sketched in figure 1.
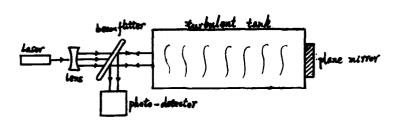
Fig 1. Schematic diagram of the equipment used in measuring
amplification factor
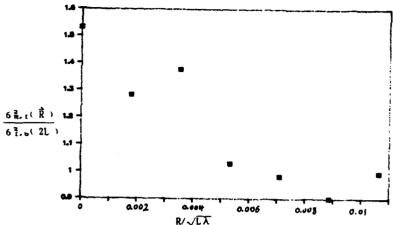
Fig 2. Measured (■), amplification-factor of fold-path weak scintillation, $C_n^2 = 1.0 \times 10^{-10}$ m$^{-2/3}$, L = 2.0 m.
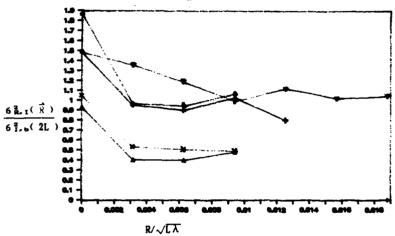
Fig 3. Measured points, amplification-factor of fold-path.
($\blacktriangledown$) $C_n^2 = 1.0 \times 10^{-10}$ m$^{-2/3}$, (+) $C_n^2 = 5.4 \times 10^{-10}$ m$^{-2/3}$
($\blacklozenge$) $C_n^2 = 2.3 \times 10^{-9}$ m$^{-2/3}$, ($\times$) $C_n^2 = 9.6 \times 10^{-9}$ m$^{-2/3}$
($\blacktriangle$) $C_n^2 = 1.3 \times 10^{-9}$ m$^{-2/3}$, L = 2.0m.

The receiving aperture is 0.18 mm, the scintillation signal is separated by two ways. One of that is mean-intensity. The other is the variance. The analysis of values of $\sigma_{R,r}^2$ show that, in the strictly backward direction, the fold-path of the intensity fluctuation amplification for a plane wave is stronger that for one way. The experiment of results of different turbulent level, different $\bar{R}$ are showed in fig(2),(3). In Fi 2. points are the experiment results,

can be accounted for a larger overlapping to the correlation between direct and reflected wave.

In the case of laboratory generated turbulence, this theoritical prediction is proved. But saturation of scintillation of amplification factor makes inaccurate. Fig 3. points ($\Diamond$), ($\times$), ($\triangle$).

3. Theoritical approach

We shall consider weak scintillation and reflector is an infinite mirror.

The amplitude perturbation produced in the wave by the reflective index variance has been determined by Tatarski using the Rytov method (Ref 3.). The result obtained for the variance induced in the logarithm of the amplitude by a component of the refractive field over a one-way path of length L is given by

$$dX = -k \int_0^L \sin\left[\frac{K^2 z(L-z)}{2kL} \right] \exp(i\vec{K} \cdot \hat{\rho} z/L) \, dn(\vec{K}, z) dz \qquad (2)$$

where X represents the log-amplitued perturbation. $k=2\pi/\lambda$ is the wave-number in free space. $\rho = |\vec{\rho}| = (x^2 + y^2)^{1/2}$ is the modules of the radius vector in a plane perpendicular to the direction of propagation OZ. $n(\vec{\rho}, z)$ is the fluctuations of the refractive index, the refractive index is assumed to be real. Its variance with x and y can be analyzed by the Furier-Stieltjes formula:

$$n(\vec{\rho}, z) = \int_{-\infty}^{+\infty} e^{i\vec{K} \cdot \vec{\rho}} \, dn(\vec{K}, z) \qquad (3)$$

Under the hypothesis of homogeneity and isotropy turnulence, using Markovian approximation, the spectral amplitudes of refractive index $dn(\vec{K}, z)$ are described by

$$\langle dn(\vec{K_1}, z_1) dn(\vec{K}, z_1) \rangle = 2\pi \delta(\vec{K_1} + \vec{K_2}) \delta(z_1 - z_2) \Phi_n(\vec{K}) d\vec{K_1} d\vec{K_2} dz_1 dz_2 \qquad (4)$$

where $\Phi_n(\vec{K})$ is the three-dimensional spectral density of the fluctuations.

Now, we shall assume a reflecting plane is located at a distance $z=L$ from a source. Then, the path is equivalent, in respect of the conditions of propagation, to a double(of length 2L) line in which fluctuations of the refractive index $n(\vec{\rho}, z)$ satify the condition

$$n(\vec{\rho}, z) = n(\vec{\rho}, 2L-z) \qquad (5)$$

Equation (1) can be extend to cover the fold-path situation.

$$dx = -k \int_0^L \sin\left[\frac{K^2 z(2L-z)}{4kL} \right] (\exp(i\vec{K} \cdot \vec{\rho} z/2L)$$
$$+ \exp(i\vec{K} \cdot \vec{\rho}(2L-z)/2L)) \, dn(\vec{K}, z) dz \qquad (6)$$

Thus, the amplitude variance for the fold-path given by

$$dX = dX_l + dX_r \qquad (7)$$

where dX_l is the amplitude variance for one-way path of length L, Eq(1) is given. dX_r is the amplitude vaniance for reflected-path.

Supposing $d = |\vec{\rho_1} - \vec{\rho_2}|$, we discuss the variance of the log amplitude.

If $\vec{\rho_1}$ and $\vec{\rho_2}$ are the modulus of the radius vector in a plane perpendicular to the direction of propagation OZ.

So $\quad \langle X^2 \rangle = \langle X_1^2 \rangle + \langle X_r^2 \rangle + \langle X_{1r}^2 \rangle \qquad (8)$

where $\langle X_1^2 \rangle + \langle X_r^2 \rangle$ corresponds to the direct double-length path; $\langle X_{1r}^2 \rangle$ is caused by the correlation between direct and reflected waves.

$$\langle X^2 \rangle > \langle X_1^2(2L) \rangle \qquad (9)$$

Then we find that, under the reflection of a spherical wave, the amplification coefficient of log amplitude fluctuation is more than unit.

Further calculations will be made for a turbulent spectrum corresponding to the Kolmogorov law.

$$\Phi_n(K) = 0.033 \, C_n^2 K^{-11/8} \qquad (10)$$

where C_n^2 is the structure characteristic of the refractive index fluctuations.

Therefore, we determine that, under the reflection of a spherical waves, the amplification factor $6_{\text{a},l}^2(\vec{R}) / 6_{\text{i}}^2(2L)$ is close to 2.0, and under the reflection of a plane wave is about 1.5.

4. Conclustions

The experiment of correlation between direct and reflected waves is very easy in simulation- tank than in atmosphere, For the weak scintillation, amplification factor is accurate for prediction. in the case of saturated scintillation, ti makes inaccurate. We have derived the fluctuation of fold-path using Rytov method for weak scintillation. Meanwhile, using this method, we also can derived other fluctuations.

References

(1). V . P . Aksenov   Vol. 1 No. 3/March, 1984, Opt. Soc. Am. (A).

(2). G . Ya . Patrushev   Sov. J. Quantum. Electron 8(11),Nov. 1978.

(3). V . I . Tatarski   Wave Propagation In Turbulent Medium.
                        McGraw - Hill, New York (1961).

SIMULATION OF THE RADAR ECHO OF AN IONIZED ATMOSPHERIC TURBULENT WAKE

N. SUAUD * , F. CHRISTOPHE * , M. PYEE **

* O.N.E.R.A./C.E.R.T./D.E.R.M.O.   ** Université Paris VI   L.D.I.R.M.
  2, av. Edouard Belin   4, place Jussieu   Tour 12 2e Etage
  31055   TOULOUSE FRANCE   75005   PARIS   FRANCE
  Phone number: 61 55 71 11

Introduction:

This article presents a simulation of the scattering of electromagnetic waves by an ionized atmospheric turbulent wake. The electronic density inside the turbulent wake is supposed to be a 3D stochastic inhomogeneous process with known first and second moments as well as the spectral power density.

As the fluctuations of the refractive index due to the electronic density are weak, the interaction between the simulated medium and an incident electromagnetic beam is calculated by a Born approximation.

Simulation of the turbulent medium[2]:

An atmospheric ionized wake model is intended to be implemented only in order to analyse its radar echo, so a simplified model of turbulence is enough. The electronic density $N_e(\bar{r})$ is separated into a mean and a fluctuating electronic densities ($N_a(\bar{r})$ and $N_f(r)$)[1]. The fluctuating electronic density is modelled as a Gaussian , zero-mean, inhomogeneous, time invariant (frozen turbulence), 3D random function. The spectral power density is supposed to be isotropic and given by the Von Karman's spectrum: $\Phi(\bar{K}) = A (K^2 + L_0^{-2})^{-11/6} \exp(K^2/K_m^2)$

$K_m = 5,92/l_0$

L_0, l_0 : external and internal scales of turbulence

A : amplitude factor dependant on local variance of $N_f(\bar{r})$

$\bar{K}$: wave vector associated with the spatial vector $\bar{r}$

The mean value of the electronic density $N_a(\rho,z)$ and the variance of the fluctuating electronic density $\sigma^2(\rho,z)$, in cylindrical coordinates, are known.

Firstly, a random function $N_{f0}(\bar{r})$ is generated. At each point $\bar{r}-\bar{r}_0$, $N_{f0}(\bar{r}-\bar{r}_0)$ is a Gaussian random process of standard deviation $\sigma(\bar{r}-\bar{r}_0)$ and mean value zero. All these processes are independant. This function is then filtered so that its spectral power density $\Gamma_{Nf}(\bar{K})$ equals the Von Karman's spectrum. As $N_{f0}(\bar{r})$ is an inhomogeneous white noise, its autocorrelation function $C_{Nf0}(\bar{r}_1,\bar{r}_2)$ can be written :

$$C_{Nf0}(\bar{r}_1,\bar{r}_2) = \sigma^2(\bar{r}_1) \; \delta(\bar{r}_1 - \bar{r}_2) = \sigma^2(\bar{r}_1) \delta(\bar{r}) \qquad \text{for } \bar{r} = \bar{r}_1 - \bar{r}_2$$

If $\bar{r}_1$ is considered as a fixed vector, the local spectral power density of the inhomogeneous process $N_{f0}(\bar{r}_1)$ may be defined as : $\Gamma_{N_{f0}}(\bar{r}_1,\bar{K}) = \sigma^2(\bar{r}_1)$ by taking the Fourier transform over $\bar{r} = \bar{r}_1 - \bar{r}_2$ of $C_{N_{f0}}(\bar{r}_1,\bar{r})$.

Let $h(\bar{r})$ be the response of the filter to a Dirac impulse.

$$N_f(\bar{r}_1) = h(\bar{r}_1) * N_{f0}(\bar{r}1) \quad\text{so}\quad C_{N_f}(\bar{r}_1,\bar{r}) = \iiint \sigma^2(\bar{r}_1-\bar{u})\ h(\bar{u})\ h^*(\bar{u}-\bar{r})\ d^3\bar{u}$$

If $N_{f0}(\bar{r}_1)$ can be considered as homogeneous inside the response of the filter (that is $\sigma^2(\bar{r}_1-\bar{u})$ not too different of $\sigma^2(\bar{r}_1)$ when $\bar{u}$ is varying), then the local spectral power density of $N_f(\bar{r}_1)$ is : $\Gamma_{N_f}(\bar{r}_1,\bar{K}) = \sigma^2(\bar{r}_1)\ |H(\bar{K})|^2$

There are no particular conditions for the filter and it is no use to make it causal. But its energy must equals the unity.
So in the spectral domain:

$$H(\bar{K}) = \frac{(K^2 + L_0^{-2})^{-11/12}\ \exp(-K^2/2\ K_m^2)}{\iiint (K^2 + L_0^{-2})^{-11/6}\ \exp(-K^2/K_m^2)\ d^3K}$$

Wave-Medium interaction [4]:

The Born approximation is a perturbation method that can be used in case of weak fluctuations of the refractive index n or, as $\varepsilon = n^2$, of weak fluctuations of the permittivity ot the medium. An ionized wake is, in fact, a cold plasma. Its permittivity can be related to its electronic density by the formula [3]:

$$\varepsilon(\bar{r}) = 1 - \frac{0,806\ 10^8\ N_e(\bar{r})}{f_0^2(1 + j\ v(\bar{r})/f_0)}$$

f_0 : analysing frequency (centimetric wavelengths)
$v(\bar{r})$: electron-neutral collision frequency (around 6 MHz)
As $v(\bar{r}) \ll f_0$ and $N_e(\bar{r}) = N_a(\bar{r}) + N_f(\bar{r})$ one can deduce: $\varepsilon_a(\bar{r}) \# 1$

$$\varepsilon_f(\bar{r}) \# - 0,806\ 10^8\ N_f(\bar{r}) / f_0^2$$

In the first order Born approximation, the field scattered by a finite volume at the point r is given by :

$$\bar{E}_s(\bar{r}) = - k_0^2 \iiint_V \varepsilon_f(\bar{r}')\ \widetilde{G}_a(\bar{r},\bar{r}')\ \bar{E}_0(\bar{r}')\ d^3\bar{r}'$$

with $\widetilde{G}_a(\bar{r},\bar{r}') = [\widetilde{I} + \nabla\nabla/k_a^2]\exp(j\ k_a\ |\bar{r}-\bar{r}'|)/(4\pi\ |\bar{r}-\bar{r}'|)$
   $k_a = k_0 \sqrt{\varepsilon_a(\bar{r}')}$
$\bar{E}_0(\bar{r}')$: zeroth order field inside the scattering volume
       as $\varepsilon_a \# 1$ $\bar{E}_0(\bar{r}')$ is supposed to be the incident field

The scattering volume is considered as the intersection of 3 cylinders: the wake enveloppe, the transmitted and the received beams in case of bistatic geometry

(these are simulated by Gaussian beams troncated at 20 dB beyond the maximum)(see Fig 1).

The first order approximation is enough to calculate the scattered field only if the second order field is much smaller than the first order one. For the worst conditions of simulation, largest possible value of $\sigma^2(r)$, the second order field was negligible in front of the first order field.

The curves 2 and 3 show the simulated Radar Cross Section of two homogeneous wakes. The first one is generated with a constant standard deviation of the fluctuating electronic density of 10^{10} electrons cm^{-3}. For the second one the standard deviation is 10^8 electrons cm^{-3}. The wake which turbulence is frozen travels in front of the radar antennas at a constant speed. The incident and scattered angles of the beams are $\pi/4$.

A statistical study verifies that the scattered field modulus follows nearly a Rayleigh law (Fig 4).

Numerical remarks:

The numerical code has been tested for different sizes of mesh. The $\lambda/5$ mesh was found to be well suited. On Fig 5, one can compare the R.C.S. computed with a $\lambda/10$ and a $\lambda/5$ frames for the same simulated wake.

The simulation is separated in 3 parts:
- wake's simulation (nearly 1 ms for 1 frame node)
- spatial filtering (nearly 0,5 ms for 1 frame node)
- R.C.S. computation (nearly 200 ms for 1 frame node)

In most cases, the whole simulation is less than 5 mn Cray 1 XMP computer time.

Conclusion:
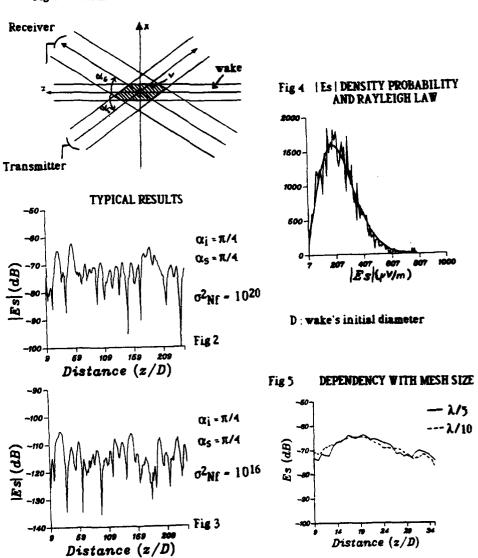
This study shows the efficiency of Born method for microwaves with a $\lambda/5$ frame. The numerical code describes completely an experiment (simulation of the wake, of the radar beams and of the interaction) with moderate CPU requirements. Coupled with experiments, it is an inverse scattering tool for analysing the parameters of the turbulence.

References:
[1]   V.I. TATARSKI
      Wave Propagation in a Turbulent Medium
      Dover Publications, Inc   New-York   1967
[2]   C. MACASKILL, T.E. EWART
      Computer Simulation of Two Dimensional Random Wave Propagation
      I.M.A. Journal of Applied Mathematics (1984), 33, 1-15
[3]   A. ISHIMARU
      Wave Propagation and Scattering in Random Media
      Vols 1 and 2   Academic   New York   1978

[4] A.H. NAYFEH
Perturbation Methods
John Wiley & Sons, Inc   1973

Fig 1   GEOMETRICAL CONFIGURATION

Fig 2

TYPICAL RESULTS

$\alpha_i = \pi/4$

$\alpha_s = \pi/4$

$\sigma^2 Nf = 10^{20}$

Fig 4 | Es | DENSITY PROBABILITY AND RAYLEIGH LAW

D : wake's initial diameter

$\alpha_i = \pi/4$

$\alpha_s = \pi/4$

$\sigma^2 Nf = 10^{16}$

Fig 3

Fig 5   DEPENDENCY WITH MESH SIZE

— $\lambda/5$

--- $\lambda/10$

326

TRANSMISSION OF A PULSED THIN LIGHT BEAM THROUGH THICK MEDIA: P36
EXPERIMENTAL RESULTS

G. Zaccanti*, P. Bruscaglioni*, A. Ismaelli*, L. Carraresi* , M. Gurioli**, and Q.N.Wei ****

* Dipartimento di Fisica Università di Firenze

Via S. Marta 3, 50139 Firenze Italy (Tel 39-55-4796330)

** European Laboratory for Non-Linear Spectroscopy

Largo E. Fermi 2, 50125 Firenze Italy

***Anhui Institute of Optics and Fine Mechanics

P.O. Box 25, 230031 Hefei P.R. China

INTRODUCTION

Experimental results on light pulse transmission through thick turbid media are presented. Measurements were carried out on polystyrene latex spheres by using a picosecond thin laser beam and a streak camera system. The results showed that the shape of the received pulse mostly depend on the transport mean free path and on the absorption coefficient of the medium, indicating that both the absorption coefficient and the asymmetry factor of the scattering function can be obtained from the pulse shape. The results also showed that a detectable amount of received photons follows trajectories near to the source-receiver line even for large values of optical depth, indicating the potentiality of a time gated scanning imaging system to detect absorbing structures inside thick turbid media

EXPERIMENTAL SETUP

The experimental setup used is the picosecond system of the European Laboratory for Non-Linear Spectroscopy (LENS) at the Physics Department in Florence. The system is summarized in Fig.1. The laser system generates pulses of about 4 ps with a frequency of 77 MHz. The wavelength is tunable from visible to near infrared. The streak camera system is a detector capable of a time resolution of a few picoseconds.

The scattering cell was 4 cm long with a diameter of 8 cm. A beam splitter and a delay line were used to take a sample of the emitted pulse directly on the streak camera in order to obtain a reference for measuring the time delay of the broadened pulse.

EXPERIMENTAL RESULTS

Figure 2 shows one example of the results pertaining to the shape of a pulse propagated throughout the scattering cell . The wavelength was 0.758 μm. In the figure t = 0 is taken as the time corresponding to the arrival of the unscattered beam. The results refer to water suspensions of polystyrene spheres with diameter ϕ = 0.99μm at optical depths (due to the spheres) ranging from 0 (clear water) to 207. The results show that both the time corresponding to the maximum of the received pulse and the width of the pulse increase

proportionally with the optical depth τ, when the values of τ are sufficiently large.

To analyze the experimental results it is necessary to take into account that, though the polystyrene spheres are purely scattering media, the albedo of the overall medium is rather smaller than one, due to the absorbing coefficient of water ($\sigma_a \approx 2.5\mathrm{m}^{-1}$ at the used wavelength). Though the value of σ_a is very small with respect to the scattering coefficient σ_s, the small absorbing effect can strongly affect both the pulse shape and the overall transmitted power when the pulse length becomes large.

Figure 3 shows a comparison between pulse shapes obtained for spheres of different sizes. The curves of each group refer to spheres with different sizes and different optical depths, but they are almost indistinguishable. An analysis of these results showed that the pulse shapes are practically equal when the value of the quantity $\tau_d = \tau(1-g)$ (with g asymmetry factor of the phase function) is the same for different diffusers. This result agrees with the one obtained with the diffusion approximation. Results like those presented in Fig.3 clearly show that measurements of pulse shape can be used to obtain reliable values for important optical parameters like g and σ_a the ones that strongly affect light propagation in dense turbid media.

CONCLUSIONS

Measurements of pulse broadening in the pulse transmission show the potentiality of modern electrooptical apparatuses both for the study of light propagation in dense turbid media and for obtaining reliable measurements of fundamental optical parameters.

Figure 1 - Schematic diagram of the experimental set-up.
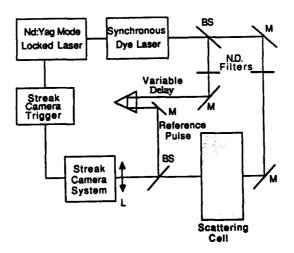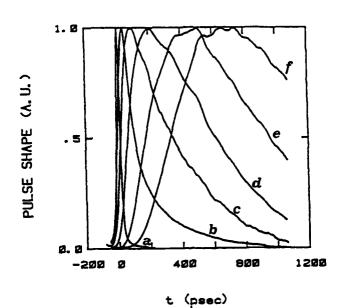
Figure 2 - Example of pulse transmission: the pulse shapes measured for several values of τ are reported for $\phi = 0.99\mu m$ spheres. Curves a-f pertain to $\tau = 0, 37, 59, 85, 137, 207$ respectively.
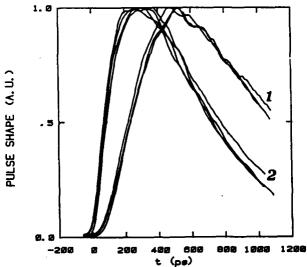
Figure 3 - Comparison between pulse shapes pertaining to different sizes of spheres. Results show curves practically indistinguishable when the product $\tau(1- g)$ has the same value: curves 1 pertain to $\phi =0.305$, 0.99, 5.7 and 15.8μm at $\tau = 20.7$, 99.4, 105, 108 respectively. The corresponding values of $\tau (1- g)$ are encompassed between 9.5 to 10 Curves 2 pertain to $\phi = 0.305$, 0.99 and 5.7 μm at $\tau =32.8$, 161 and 166 respectively. The corresponding values of $\tau (1- g)$ are from 15.7 to 16.1

329

NUMERICAL PROCEDURE OF CALCULATION AND EXPERIMENTAL VALIDATION FOR THE EFFECT OF A TURBID MEDIUM ON THE SPREAD FUNCTION OF AN OPTICAL SYSTEM **P37**

P.Bruscaglioni, P. Donelli, A. Ismaelli, G. Zaccanti
Department of Physics. University of Florence. Italy

ABSTRACT.
A Monte Carlo procedure was used to calculate the effect of a turbid medium on the spread function of an optical system. Comparisons of results with measurements will be shown.

The effect of a turbid medium on the spread function of an optical system is evaluated by means of a Monte Carlo procedure.

The numerical method calculates the distribution of the irradiance in the image plane of a point source when a turbid medium is considered (hence MTF is obtained by Fourier transform).

The basis of the numerical calculation is that particles causing radiation arriving from a point source to be scattered are considered as secondary point sources which have defocused images on the image plane of the source A Monte Carlo code is used to calculate the positions of the scattering points in the medium,

Each scattering point is the source of a spherical wave whose intensity in the different directions depends on the considered phase function. The resulting distribution of irradiance on the image plane is calculated by using simple laws of geometrical optics, i.e. by following ray trajectories of the photons. A code "SEMIM" was developed to implement the procedure(1).

An initial confirmation of the validity of the code came from the comparison with experimental data published by Kuga and Ishimaru(2,3). It showed that the calculated MTF compared well with the experimental data, even for situations where the small angle approximation scheme (SAA) proved to be inadequate (See Fig.s 1, 2).

Multiple scattering effects in the propagation of radiation depend largely on the geometry of the situations. Thus, to extend the

examination of the validity of SEMIM code, a series of laboratory experiments with an arrangement rather different from that of Kuga and Ishimaru were performed.

The aim of the experiment was to compare measured and calculated irradiance distribution on the image plane of a point source. The actual configuration of the source emission was not the important point, since we mainly wished to check the validity of a calculation procedure. So we did not need the emission to be strictly similar to that of a real source (e.g. a Lambertian source).

The experimental set-up included a scattering cell illuminated by a conical light beam whose vertex represented a point source of radiation. β was the semiaperture angle of the beam. The laser source used was a 10 mW He-Ne CW-laser (λ = 0.6328 μm in air). The scattering cell was filled with a suspension of polystyrene microspheres in water representing the diffusing turbid medium. A thin lens L was the image-forming optics. A common PIN photodiode constituted the detector. A variable diameter diaphragm was placed in the image plane of the point source in front of the detector, in order to perform power measurements referring to different values of the receiver radius. Thus we obtained the power distribution (i.e. the spread function) on the image plane of the system, integrated over circles of different radii.

The scattering cell was cylindrical (radius 7 cm) with a length of 10.8 cm. Its distance from the source was 5 cm (input window) and from the lens was 30 cm (output window).

Fig.s 3,4 give examples of comparison between calculated irradiance (integrated over the circle of radius r: continuous lines) and the results of measurements (bars).

(1) P. Bruscaglioni, P. Donelli, A. Ismaelli and G. Zaccanti : J. Mod. Optics, 38, 129, 1991

(2) Y. Kuga and A. Ishimaru : J. Opt. Soc. Am. A, 2, 2330, 1985

(3) Y. Kuga and A. Ishimaru : Appl. Opt., 25, 4382, 1986
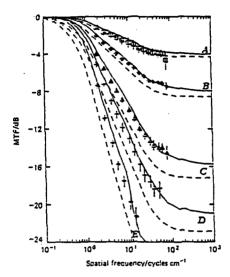
Fig.1. Comparison of calculated data (continuous lines) with experimental
data of Kuga and Ishimaru. Dashed lines : theoretical (SAA) results of
K. and I. Latex spheres with diameter 11.9 microns. He Ne wavelength.
A: Optical depth τ = 0.85. B: τ= 1.71. C: τ= 3.41. D: τ= 4.55. E: τ= 6.82.

SPATIAL FREQUENCY   (cycles/cm)
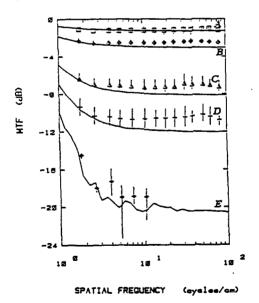
Fig.2. Same as Fig.1. Spheres with diameter 0.109 microns. A: τ= 0.85.
B: τ= 1.7. C: τ= 3.4. D: τ= 4.5. E: τ= 6.8.
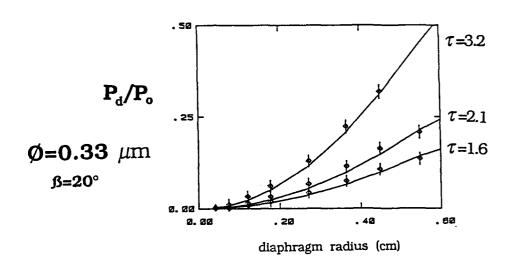
Fig.3. P_d/P_0 : Contribution of scattered power to the spread function integrated over circles of different radii and divided by total received unscattered power. Continuous curves: calculated values (SEMIM). Marks: measured values. Spheres: diameters = 0.33 microns. Optical depths are indicated.
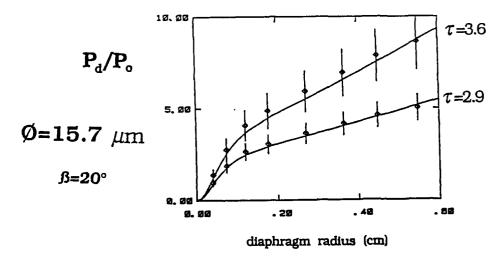
Fig.4. Same as Fig.3. Spheres with diameter = 15.7 microns.

Control of Spatial Coherence Using a Source Filter **P38**

Tomohiro Shirai and Toshimitsu Asakura

*Research Institute of Applied Electricity, Hokkaido University,
Sapporo, Hokkaido 060, Japan*
Telephone: 011-716-2111 *ext.* 2648 *Fax:* 011-758-6098

1. INTRODUCTION

There are various optical fields in which the properties of spatial coherence have an important role. For example, the decrease of spatial coherence is required to reduce the effect of speckles and, then, the imaging properties of an optical system are also changed. On the other hand, the imaging properties of holographic instruments require the high spatial coherence. The properties of spatial coherence desired in various fields are usually different for their own purposes.

In the present paper, a source filter is proposed to control the spatial coherence of light generated from a partially coherent source. The source filter is a kind of the spatial filter which is placed just behind the source to change the intensity distribution across the source. Usually, aperture filtering is utilized to change the properties of an optical system. However there are some cases that the spatial filtering over the aperture has no effect on the properties of the system. For instance, the small filtering region does not give the desired properties in the synthetic-aperture optical processing. In the following, the source filter is studied to control the spatial coherence in various cases.

2. THEORY

As a source model for analysis, we consider a Gaussian-correlated quasi-monochromatic partially-coherent circular source with an uniform intensity distribution on the source plane. The partially coherent source may be a realistic model for the present analysis because the complete coherent and incoherent lights do not exist. Since the quasi-homogeneity [1], which means that the degree of coherence across the source changes more rapidly than the variation of the intensity distribution on the source, is not assumed for the partially coherent source, the ratio of the correlation interval to the varying intensity distribution across the source may be selected arbitrarily.

The partially coherent source used in the analysis is realized by using the far-field propagation of light from an incoherent source and by applying van Cittert-Zernike theorem. However, when the correlation interval on the source is set to be relatively large compared with the size of the source, this model can also be regarded as a statistically-averaged multi-mode laser.

For the present analysis, the appropriate quantity to be considered is the mutual intensity. Assuming that the intensity distribution across the source is uniform and that the correlation coefficient on the source takes a Gaussian form and depends on position vectors u_{s1} and u_{s2} only through the difference $u_{s1} - u_{s2}$, we obtain the mutual intensity on the source filter plane,

$$J_s(u_{s1}, u_{s2}) = I_0 S(u_{s1}) S(u_{s2}) \exp(-|u_{s1} - u_{s2}|^2 / 2\sigma_g^2) \qquad (1)$$

where $S(u_{si})$ (i=1,2) indicates the amplitude transmittance of the source filter and I_o is constant.

The mutual intensity at the observation plane placed in arbitrary free space is determined with the help of propagation law [2] of the mutual intensity defined by

$$J_o(u_{o1},u_{o2})= \iiint J_s(u_{s1},u_{s2})K(u_{s1},u_{o1})K^*(u_{s2},u_{o2})du_{s1}du_{s2}. \qquad (2)$$

When the observation plane is located in Fresnel and Fraunhofer diffraction fields, the propagation function $K(u_s,u_o)$ in Eq.(2) is given by

$$K(u_s,u_o)= \begin{cases} \exp(i\pi|u_s-u_o|^2/\lambda Z) & : \text{Fresnel diffraction} \\ \exp(-i2\pi u_s u_o/\lambda Z) & : \text{Fraunhofer diffraction.} \end{cases} \qquad (3)$$

Numerical analysis by means of a computer is required to evaluate Eq.(2). The degree of spatial coherence for two points situated symmetrically about the optical axis at the observation plane and the intensity distribution across the observation plane are calculated from Eq.(2). The degree of spatial coherence is defined as

$$\gamma_{12}=J(u_1,u_2)/[J(u_1,u_1)^{1/2}J(u_2,u_2)^{1/2}], \qquad (4)$$

where $J(u_i,u_i)$ (i=1,2) stands for the intensity at each point u_i (i=1,2). Thus intensity distribution at the observation plane can be derived by setting $u_{o1}=u_{o2}$ in Eq.(2).

3. RESULTS AND DISCUSSION

3-1 Spatial coherence of partially coherent radiation

First, we show some resultant properties of partially coherent radiation without a source filter. For the sake of simplicity, our discussion is restricted in an one-dimensional case.

Figures 1 and 2 show the intensity distributions and the degrees of coherence at the observation plane in the Fraunhofer field. The parameter σ normalized by the source radius a means the coherence interval on the source. The curves in Fig.1 indicate that the intensity distribution becomes more and more peaked around the vertical axis with an increase of σ. It is also clear especially from Fig.2 that the degree of coherence approaches unity as the values of σ are increasing.

The negative values in the graphs of coherence mean that the phase of the mutual intensity changes with π. Since the
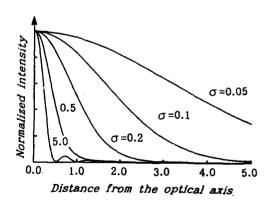
Fig. 1 Intensity distribution at the observation plane in the Fraunhofer region for various values of σ

336

symmetric source and the realizable intensity distribution across the source are assumed, the phase difference of two points situated symmetrically about the optical axis is either zero or π without having intermediate values.

The distances between two points corresponding to the minima of coherence curves tend to coincide for larger values of σ than unity. In this case, the two points are located on the dark rings of an Airy disk-like intensity distribution.
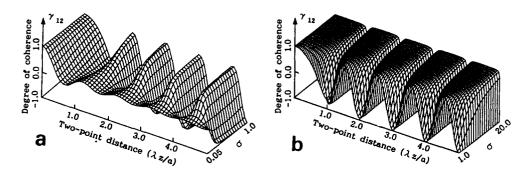
Fig. 2 Degree of spatial coherence at the observation plane in Fraunhofer region for (a) small values of σ and (b) large values of σ

3-2 Effects of the source filter on spatial coherence

In this section, some effects of a source filter on the spatial coherence in the Fraunhofer region are discussed. Two types of the source filter are taken into consideration as simple examples. Transmittances of the source filters and the corresponding degrees of coherence at the observation plane are shown in Fig.3 and 4, respectively.
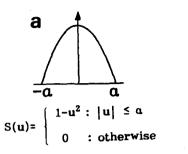
For small values of σ, Figs.4(a) and (b) are extremely distinguished from Fig.2(a) in performance of the coherence function. There is a tendency for Fig.4(a) not to fluctuate, but Fig.4(b) is conversely disposed to fluctuate. With an increase of σ, each curve turns gradually to be similar to the curves in Fig.2(a). Performance of the coherence function having an intermediate value of σ are very interesting.

In general, only the coherence interval may be treated at the observation plane in order to estimate the properties of spatial coherence. However, it is very important in some practical problems to investigate the shape of the coherence function as well as the coherence interval. Even though the coherence interval takes the same value, there are some cases that the difference in the shape of coherence function causes some effects, for example, in the case of partially coherent imaging.

In view of the above discussion, a source filter is considered to have the ability of controlling the spatial coherence of partially coherent light.

4. CONCLUSION

In the present paper, the new concept of a source filter, which is placed at the source plane and changes the intensity distribution across the

$$S(u) = \begin{cases} 1-u^2 : |u| \leq a \\ 0 \quad : \text{otherwise} \end{cases}$$

$$S(u) = \begin{cases} u^2 : |u| \leq a \\ 0 \quad : \text{otherwise} \end{cases}$$
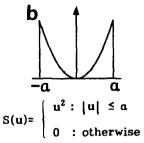
Fig. 3 Two types of transmittance of the source filter
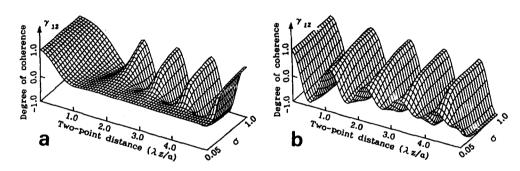
Fig. 4 Degree of spatial coherence corresponding to Figs.3(a) and (b)

source, has been proposed. It is important to control the spatial coherence of radiation because the spatial coherence desired in various areas of optics is different from each other. The source filter is very useful for controlling the spatial coherence of light due to its easy realization. By an appropriate selection of the transmittance of the source filter, an arbitrary state of spatial coherence can be realized.

REFERENCES

[1] E. Wolf: J. Opt. Soc. Am. **68**, 6-17 (1978).
[2] M. Born and E. Wolf: Principles of Optics, 6th ed. Pergamon Press (1980).

H.C.Kandpal , J.S.Vaishya and K.C.Joshi

Standards Division
National Physical Laboratory
New Delhi-110012, INDIA

It has been established that correlations in the
fluctuations of a source distribution influence the spectrum
of radiation when it propagates through free space. In parti-
cular,it has been shown theoretically [1-3] and subsequently
confirmed by experiments [4-9] that suitable spatial correla-
tions within the source or developed between field points on
propagation can affect the distribution of energy in the
spectrum of radiated fields resulting in a shift in its fre-
quency.Recently it has been predicted theoretically [10-13]
that similar changes may also occur on scattering of radiation
by a medium whose physical parameters (e.g. the dielectric
susceptibility) are random function of its position but have
an appropriate correlation property. Such spectral changes may
imitate the Doppler effect,even though the source of radiation,
the scattering medium and the observer are at rest with respect
to each other.

This communication reports the experimental verification
of the theoretical prediction [12-13] that frequency shift can
be produced by scattering of radiation by spatially random
medium like a dynamical scatterer formed by p-methoxy benzylidene
p-n-butyl aniline(MBBA) liquid crystal film.

Wolf et al [10] have analysed the spectrum of the poly-
chromatic radiation scattered by a statistically homogenous
medium . Their analysis shows that the spectrum of the scatt-
ered field is modified by (1)dipole contribution which is
proportional to the fourth power of frequency and (2)Fourier
trasform of dielectric susceptibility spatial correlations
Therefore scattering can give rise to Doppler like freque-
ncy shift. James and Wolf [13] has shown that if temporal
fluctuations of dielectric susceptibility are also present
then the magnitude of frequency shift could be very large.
Therefore,scattering of polychromatic partially coherent
light by a medium whose dielectric susceptibility varies
randomly both in space and time but suitably correlated has
been studied with MBBA type liquid crystal film sandwitched
between two conducting glass plates. The experimental setup
consists of a tungsten halogen lamp kept at the centre of an
integrating sphere(0.5 m diameter and coated with $BaSO_4$ paint).
Light from a 2 mm diameter opening on the surface of the
integrating sphere is passed through an aperture (size 1mm)
followed by interference filter so that a narrow band of poly-
chromatic partially coherent light is obtained.This light
is focussed on the dynamic scatterer. Since the degree of
coherence produced at the focal plane of the lens depends
on the aperture size and the focal length of the lens, it can
be varied. The transmitted/scattered radiation is focussed
at the entrance slit of a Spex double grating monochromator
equipped with data acquisition and processing system.A
schematic diagram of the experimental setup is shown in fig.1.
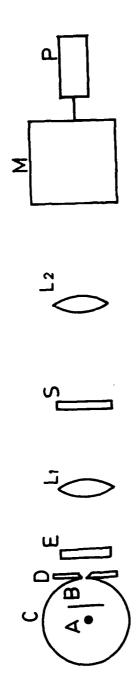
Curve A in FIG.2 shows the transmitted spectrum of the
interference filter in the absence of the liquid crystal
sample placed in the optical path.Curve B shows the spectrum
when the liquid crystal film is put at the focal plan of lens.
It is noted that curve B is red shifted compared to curve A
by about 0.05 nm.This frequency shift in curve B is essen-
tially the effect of scattering by a medium whose phys-ical

properties are characterised by random functions of position
of its constituents while temporal fluctuations are slow enough
to be ignored. Under such circumstances the process of scattering
is influenced by the response of dipole oscillators of the
scatterer and their correlation. The different frequencycompo-
nents of the incident light are scattered in a particular direc-
tion with varying strengths. Also the polarisation induced
in the scattering medium by the incident wave may be correlated
over finite distances of the medium. As a result,the spectrum
of the scattered light differs from that of the incident -light
Curve C in fig.2 shows the spectrum when electric field of fre-
quency 1 KHz is applied across the liquid crystal film. Curve
C is red shifted by about 0.2 nm compared to curve A.Similar
results are obtained when a field of varying frequency from 10 Hz
to 1 KHz is applied. On applying the electric field dipoles of
the liquid crystal orient themselves in the direction of the
applied field. But due to the oscillating nature of the field
the dipoles also vibrate. Interaction of the molecular dipole
moment of the liquid crystal and the electric field of the incident
light causes scattering of the light and a shift is observed. The
results are consistent with the theoretical prediction of James
and Wolf . Due to limitation in the selection of the dynamic
scatterer and also its limited ability to get influenced by the
varying electric field due to large molecular dimension of the
liquid crystal desired frequency shift could not be obtained as
predicted by James and Wolf . Further work in this direction
is in progress.

R E F E R E N C E

1.   E Wolf, Phys Rev Lett 56, 1370, (1986).

2.   E Wolf, Nature 326, 363, (1987).

3.   E Wolf, Opt Commun 62, 12, (1987).

4.   G M Morris and D Faklis, Opt Commun 62, 5, (1987).

5.   D Faklis and G M Morris, Opt Lett, 13, 4, (1988).

6.   H C   Kandpal, J S Vaishya and K C Joshi, Phys Rev A 41, 4541, (1990).

7.   H C Kandpal, J S Vaishya and K C Joshi, Opt Commun, 73, 169 (1989).

8.   F   Gori, G Guattari, C Palma and G Padovani, Opt Commun 67, 1 (1988).

9.   G Indebetouw, J Mod Opt 36, 251, (1989).

10. E Wolf, J T Foley and F Gori, J Opt Soc Am.A, 6, 1142 (1989).

11. E Wolf, Phys Rev Lett, 63, 2220, (1989).

12. J T Foley and E Wolf, Phys Rev A, 40, 588, (1989).

13. David F V, James and Emil Wolf, Phys Lett A, 146, 167, (1990).

- F I G. 1 -

A – LIGHT SOURCE,   B- LIGHT STOP,   C – INTEGRATING SPHERE
D   1.5mm PRIMARY APERTURE,   E – INTERFERENCE FILTER,
L₁   FOCUSING LENS, L₂ – COLLECTING LENSE, M – MONOCHROMATOR,
P   DATA PROCESSING UNIT   S – SCATTERER

Schematics of experimental set up

- F I G . 2 -

WAVELENGTH (nm)

NORMALISED INTENSITY

Spectrum of the light transmitted by the interference filter (A). In absence of sample S (B) when MBBA liquid crystal film embeded between glass plate is introduced at the focal plane of lens L_1 (C) when electric field of varying frequency is applied across MBBA liquid crystal film.

Multichannel acoustooptic device
for measurements of light scattering in atmosphere

Ivanov A.N.

Moscow State Technical University, Moscow, 107005,

2 Baumanskaya, 5a, 263-66-56.

Efimenko I.M.

Joint counsil "Optics" Academy of Science, Moscow, Pyatnitskaya,

48, TEL 231-06-69, TLX 411576 ASCON SU, FAX 7.095.230.20.81

Knoledge of the single-scattering parameters of the light
in random media needed for the understanding of the transfer of
solar and IR radiation in planetary atmospheres. We consider an
optical device to measure light scattered from different elements
of media. In classical phase or distance-finders information is
inferred from the time delay or phase shift of signals. A disad-
vantage of this measurement technique lies in a complicated and
sometimes long-lasting processing of results. The measurement
depends on plenty reasons such us signal-to-noise ratio and con-
struction of optical system.

The basic idea of the acoustooptic device is illustrated in
Fig. 1.
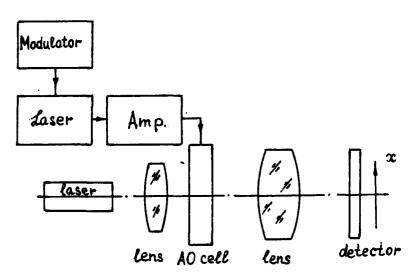
Fig.1 Simplified schematic of an acoustooptic device

The media being investigated is illuminated by a laser beam S with modulated intensity.

$$S(t) = S_0 \left\{ \cos(\omega t + \varphi_o) + \cos\left[(\omega + \Delta\omega)t + \varphi_o\right] + \ldots + \right.$$
$$\left. + \cos\left[(\omega + N\Delta\omega)t + \varphi_o\right] \right\}$$

where φ_0 is initial phase of harmonics and

ω and $\Delta\omega$ are main frequensy and frequensy step respectively. On passage through the atmosphere time phase shift increases and each spectral components save it in the backskattered light. All phases may be expressed in form

$$\varphi_{i+1} = \varphi_i + \Delta\varphi(D)$$

where D is distance to elementary volume and φ_i is a phase shift connected with i-th harmonic. The photodetector is photomultiplier. The signal from its output passes through bandpath amplifier which is turned to the frequency range F1 — FN. The output of amplifier is connected with acoustooptic cell. An acoustic wave is generated in the crystal that forms N moving 1-D diffraction gratings.

A collimated light sourse illuminates the cell. With the assumption that acoustooptic cell is operated in the Bragg regime only one diffraction order resclts. Then N rays are focused by lens at the detector plane where they interferes. The light distribution at the detector plane is periodic. The more harmonics are used the more distribution shrinks in point. According to /1/ intensity in detector plane is given by

$$I\left(f, \frac{x}{x_m}\right) = I_o(f) \, \text{sinc}\left(\frac{x}{x_m} \frac{w}{\ell}\right) \frac{\sin^2\left[\pi N\left(\frac{x}{x_m} + d\right)\right]}{\sin^2\left[\pi\left(\frac{x}{x_m} + d\right)\right]}$$

where $\text{Sinc}(z) = \sin\pi z / \pi z$

w,l — parameters of AO cell, d — parameter of elementary volume, $\frac{x}{x_m}$ — coordinate of point at the detector plane.

A detailed analysis which includes calculations with diffe-
rent quantity of harmonics shows that N=6 is optimal value. The
results for N=6 and N=3 are represented by the curves in Fig.2.
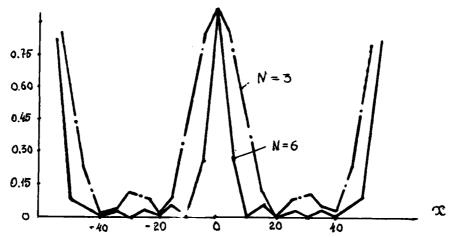
Fig.2 Distribution of intensity at the charge-coupled

device detector plane

Evidently all process is completely characterized by single point
of maximum intensity. The position of the latter at charge-coupled
device detector is defined by distance to the scattering volume.
As a result the range of scattered on the trajectory light is spread
vertically as shown in Fig.1. Signal calibration consist of determina-
tion of the koefficient which depends on optic geometry and pro-
perties of media. Accuracy of system is mainly defined by angular
resolution of acousooptic unit. For phase stabilization in recei-
ved signal the field of vision of optical system is 1 grade. F1=
160 MHz and F=10 MHz.

Using 16-channel acoustooptic cell it is easely to built de-
vice with linear aperture and parallel signal processing.

Reference

Lambert L.B., Arm M., Aimette A. Electro-optical processor for
phased array antennas. Optical and information processing.
Mass. Inst. of Techn. Press., 1965, p.715-748.

L.I.Podkamen and A.D.Arkhelyuk

Chernovtsy University, 2 Kotsyubinsky Street, 274012 Chernovtsy, U.S.S.R.   Tel.44730.

When using polarized radiation to obtain estimates of the shape and orientation degree of aerosol or hydrosol particles, situations often arise when this radiation passes through a scattering layer of a certain thickness.

We investigated this situation using a polarized, $\lambda = 0.63 \mu m$ laser beam passing first through an optically thin ($\tau \approx 1$) layer containing oriented $\gamma - Fe_2O_3$ particles, and then through a clouded optical glass plate with optical thickness τ varying between 0.1 and 8. In the following, these are referred to as layer 1 and layer 2, respectively. To obtain estimates of the parameters of the radiation transmitted by the layers, one can then use a product of the known scattering matrices $|F_{ik}|$ for each of the layers,

$$\{S'\} = |F_{ik}^{(2)}| \times |F_{ik}^{(1)}| \times \{S^0\} = |F_{ik}^{(3)}| \times \{S^0\} \tag{1}$$

where $\{S^0\}$ and $\{S'\}$ are the Stokes vectors of the incident and the scattered light beams, respectively, and $|F_{ik}^{(3)}|$ is the resulting scattering matrix of the two layers. For a layer 2 with $\tau < 1$, the $|F_{ik}^{(3)}|$ matrix is still a characteristic of an elementary scattering volume, thus one can easily separate the information concerning layer 1. As layer 2 thickness increases, the angular behaviour of the normalized $f_{ik}^{(3)}$ components of the resulting $|F_{ik}^{(3)}|$ matrix will become different, and so will the polarization characteristics of the scattered radiation.

It has been shown that for arbitrary orientations Θ and scattering angles α, the only zero components of a 16-component scattering matrix of layer 1 are the f_{41} and f_{14} components. The scattering matrix of layer 2 is characteristic for isotropically scattering media, and has nonzero components $f_{12}=-f_{21}$, f_{22}, f_{33}, $f_{34}=-f_{43}$, and $f_{44}/1/$.

Measurements carried out for a particle orientation $\Theta = 45°$ and different scattering angles indicated the dependence of the polarization characteristics of the scattered radiation on layer 2 optical thickness to be the most pronounced in the range of small scattering angles, $\alpha < 15°$. The reason seems to be that for the particle orientation $\Theta = 45°$ in layer 1, the maximum values of non-zero components $f_{13}(f_{31})$, $f_{24}(f_{42})$, f_{22}, f_{33} and f_{44} will be observed for $\alpha \approx 0°$, decreasing very little with α increasing up to $15°$. Thus, in this range of scattering angles, large values of $f_{13}^{(3)}$, $f_{23}^{(3)}$, $f_{24}^{(3)}$ and $f_{42}^{(3)}$ components of the resulting matrix will be observed, which determine the ellipticity q and the angle of rotation of the plane of polarization Ψ of the radiation scattered by the two layers for a linearly polarized incident beam /2/,

$$q = \left(f_{41}^{(3)} \pm f_{42}^{(3)} \right) \Big/ \left(1 \pm f_{42}^{(3)} \right), \quad \Psi = \frac{1}{2} \, \mathrm{arctg} \left(\frac{f_{31}^{(3)} + f_{32}^{(3)}}{f_{21}^{(3)} + f_{22}^{(3)}} \right) \quad (2)$$

$$(3)$$

Thus, for small scattering angles, well defined polarization effects are observed. With layer 2 optical thickness increasing, the number of scattering events also increases, and the transmitted radiation becomes depolarized causing changes in the quantities defined by eq.(2) and (3). For scattering angles ranging from $15°$ to $70°$, only f_{22} component of layer 1 changes its value slightly (from 0.96 at $\alpha = 15°$ to 0.85 at $\alpha = 70°$). The other components decrease dramatically, thus causing decrease of the nonzero components of the resulting matrix f_{ik}. Therefore, the polarization effects described by eq.(2) and (3) are small in this range of α, and layer 2 optical thickness affects very little the polarization characteristics of the transmitted radiation.

The values of the diagonal components $f_{22}^{(3)}$, $f_{33}^{(3)}$, and $f_{44}^{(3)}$ of the resulting matrix were found to be practically independent of layer 2 optical thickness for thickness values ranging from 0.1 to 8. These components are transitional between the identical Stokes parameters of the transmitted and the incident beams. Their weak τ dependence indicates that the polarization type and angle of the incident beam are well preserved, which fact can be utilized

in the actual measurements. A circularly polarized incident beam
seems to be preferable here, since its intensity along the beam
axis decreases by a factor of 1.1 as layer 2 thickness increases
from 0.1 to 8, while for a linearly polarized beam this decrease
is by a factor of 1.6 .

The increase in layer 2 thickness causes a decrease in the
value of $f_{31}^{(3)}$ component along the beam axis ($\alpha = 0^\circ$) and its incre-
ase beyond the direct beam zone (see Fig.1a). The reason for this
is that an increasing number of light quanta,which experienced
only a small number of scattering events and preserved the polari-
zation of the radiation exiting from layer 1, leaves the direct
beam zone as layer 2 thickness increases. The increase of the $f_{31}^{(3)}$
component is also associated with the τ dependence of the angu-
lar distributions of the intensities scattered by layer 1 for pola-
rizations parallel and perpendicular to particle orientation (see
curves 1-4, Fig.1a).
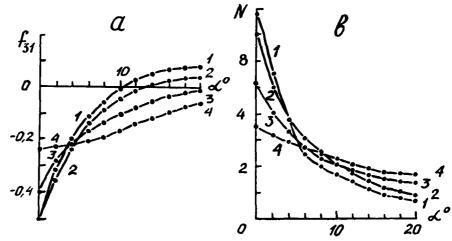
Fig.1. Angular dependences of $f_{31}^{(3)}$ (a) and N (b) for different
layer 2 thicknesses: 1: τ =0.01, 2: τ =0.69, 3: τ =6.2,
and 4: τ =8.

There is, however, a range of scattering angles ($\alpha \sim 5 - 7^\circ$) where
the $f_{31}^{(3)}$ components is less sensitive to layer 2 thickness varia-
tions.

The $f_{42}^{(3)}$ component of the resulting scattering matrix was found to have a similar $f_{31}^{(3)}$ dependence, although with a smaller range of variation.

The most sensitive to changes in the scattering angle and layer 2 thickness was found to be the $N = (I_{135,135})/(I_{45,45})$ ratio whose angular dependence is shown in Fig.1b. Here, $I_{135,135}$ and $I_{45,45}$ refer to the scattered intensities with polarization angles 135 and 45°, which are the same as in the incident intensities. The above ratio is stringly dependent on τ along the beam axis $(\alpha \sim 0^{o})$, while for $\alpha > 15^{o}$ it remains practically unchanged with increasing α and τ.

REFERENCES

/1/ L.I.Podkamen, S.G.Huminetsky, and A.D.Arkhelyuk, Izvestiya
    Akad Nauk SSSR. FAO, 22, 1287 (1986).

/2/ S.Ye.Kondrashev, in: Optics of the Ocean and Atmosphere (in
    Russian), Leningrad: Nauka, 1972, p.136.

Zege E.P., Katsev I.L., Polonsky I.N.

Institute of Physics, Byelorussian Academy of Sciences
Leninski Prospect 70, Minsk, 220602 USSR
Phone (0172)394729, Telex 252277 NAUKA SU

A new synthetic multicomponent approach to calculation of light field characteristics in aerosol atmosphere, clouds, mists and other real scattering media is represented here. Being as simple and illustrative as the known approximate methods of the transfer theory (small-angle, small-angle diffusion, diffusion ones) [1], it essentially increases the calculation accuracy and extends their applicability.

The idea of this approach was given in [2,3]. The scattering indicatrix $\chi(\beta)$ is introduced in the form

$$\chi(\beta) = \sum_{i=1}^{N} a_i \chi_i(\beta), \qquad \sum_{i=1}^{N} a_i = 1, \qquad (1)$$

where $\chi_i(\beta)$ are the functions which satisfy the requirements to optical indicatrices and have a more simple form than $\chi(\beta)$. In accordance with representation (1) the total scattering radiance in r point in n direction will also be sought as the sum

$$I_s(r,n) = \sum_{i=1}^{N} I_i(r,n), \qquad (2)$$

where the components $I_i(r,n)$ satisfy the system of radiative transfer equations, each of them having its own effective parameters. For clouds and atmospherical aerosol the number $N = 3$ in eq. (1,2) is enough in many cases.

Let a medium is illuminated by monodirectional light beam normal to the boundary. Then an expression for a nonscattered light field component is of the form

$$I_0(r,n) = \exp(-\varepsilon z) \, \delta(r_\perp) \, \delta(n_\perp), \qquad (3)$$

where $r_\perp$ and $n_\perp$ are the projections of the r and n vectors onto the z = const plane.

We have obtained the following approximate solution $I_k(r,n)$ at k = 1,2 [3]

$$I_k(r,n) = \frac{S_k}{4\pi(D_{\theta k}D_{rk}-A_k^2)} \exp\left\{-\frac{r_k^2}{2D_r} - \frac{(n_\perp - A_k r_\perp/D_{rk})^2}{2(D_{\theta k}-A_k^2/D_{rk})}\right\}, \qquad (4)$$

where S_k is the total flux of the kth radiation component through the z = const plane, $D_{\theta k}$ and D_{rk} are variances of angu-

lar and spatial radiance distributions at depth z and A_k describes the correlation of angular and space coordinates for kth component. Here

$$S_k = T_k \exp[-(\varepsilon_k - \sigma_k)z] / \mathrm{ch}\, \zeta_k$$

$$D_{\vartheta k} = \frac{s_k}{\varepsilon_k - \sigma_k}\, \mathrm{th}\, \zeta_k / T_k$$

$$D_{rk} = \frac{z}{\varepsilon_k - \sigma_k} [\, 1 - (\mathrm{sh}\, \zeta_k)/\zeta_k\,] / T_k\ , \qquad (5)$$

$$A_k = \frac{1}{\varepsilon_k - \sigma_k} (\, 1 - 1 / \mathrm{ch}\, \zeta_k) / T_k\ ,$$

$$T_k = 1 - \exp(-\varepsilon_k z)\, \mathrm{ch}\, \zeta_k\ ,$$

$$\zeta_k = s_k z\ , \qquad s_k = \sqrt{(\varepsilon_k - \sigma_k)(1 - g_k)\sigma_k}\ .$$

$$\varepsilon_k = \varepsilon - \sum_{i=1}^{k-1} \sigma_i\ , \quad \sigma_k = \sigma\, \alpha_k\ .$$

The diffusion approximation can be used to take solution for $I_3(r, n)$, when optical thickness $\tau \gg 1$ [1]   .

$$I_3(r, n) = S_3\, u_0(\mu)\, \exp\left\{-\frac{r_1^2}{2D_{r3}}\right\} / 2\pi D_{r3}\ , \qquad (6)$$

where

$$S_3 = \frac{\mathrm{sh}\, 5\gamma q - \exp(-\varepsilon_3 z)\, \mathrm{sh}\, \gamma(\varepsilon z + 5q)}{\pi\, \mathrm{sh}\, \gamma(\varepsilon z + 4q)}\ ,$$

$$D_{r3} = \frac{z}{\gamma \varepsilon_3} \left\{ \mathrm{cth}\, \gamma(\varepsilon z + 4q) - \frac{1}{\gamma(\varepsilon z + 4q)} \right\}\ ,$$

$\gamma = \sqrt{(1-\Lambda)/q}$, $q = 1/[3(1-g)]$, $u_0(\mu) = 3(1+2\mu)/7$, $\mu = \cos\vartheta$.

Illustration of the feasibilities of our approach are given for light field characteristics in cloud model C.1 at $\lambda = 0.7\ \mu m$. The scattering indicatrix was of form (1) at $\alpha_1 = .404$, $\alpha_2 = .512$, $\alpha_3 = .084$, $g_1 = .9995$, $g_2 = .879$, $g_3 = 0$.

Fig.1 gives the components of the irradiance $E_k(z, r_1=0)$ and total irradiance $E_s(z, r_1=0)$ induced by a scattered light on the beam axis plotted as function of optical thickness τ. You see that for thin layers small-angle components $(E_1 + E_2)$ play a decisive part in light field formation close to the beam axis. At layer thickness $\tau = 8 \div 16$ the irradiance is determinated by a compatible contribution of all the components

and at $\tau \geq 16$ the main contribution is made by E_3, or diffusion component.

Emphasize that the proposed approach allows simple description of oblique incidence. A joint using of two our methods (multicomponent technique and local reference system [4]) offers detailed description of a complex angular field structure in aerosol atmosphere and clouds. The local reference system with the z-axis directed to maximum $I_k(r,n)$ is introduced for each component. Comparison of our approach data with the Monte-Carlo simulation is given on Fig.2 and shows excellent agreement of the results.

The solution of the nonstationary problem (pulse beam propagation, lidar return) based on this approach is represented in [5].

All our results demonstrate the substantial opportunities of the proposed approach for solving varios problem. Our solutions include simple analytical formulas, which allow convinient and effective estimation and physical analysis of light field characteristics. Comparision with different types of calculations shows that this technique provides the accuracy which is acceptable for solution of many practical problem.

REFERENCES

1. Zege E P, Ivanov A P & Katsev I L 1990. Image Transfer through a scattering medium. - Heidelberg, Springer-Verlag, 395p.

2. Zege E P, Katsev I L & Polonsky I N 1988. On one approach to solving the radiative transfer equation with an arbitrary scattering indicatrix. Proc 4th All-Union Conf Laser Beam Propagation in a Scattering Media, Obninsk-Barnaul, USSR, 172-174.

3. Zege E P, Polonsky I N & Chaikovskaja L I 1985, Peculiarity propagation of the radiance with oblique incidence light on the absorbing media with strongly anisotropic scattering, Izv AN SSSR, Fiz Atm Okeana, 23, N5, 486-492.

4. Zege E P, Katsev I L & Polonsky I N 1988. Modification of the small-angle diffusion approximation with regard to peculiarity form of the indicatrix into small angle. Atmospheric optic, 1, N11, 19-27.

5. Zege E P, Katsev I L, Polonsky I N 1990. New approximate approaches to laser beam propagation and laser return in cloud and mists. Proc Workshop MUSCLE 3, Florence, Italy.
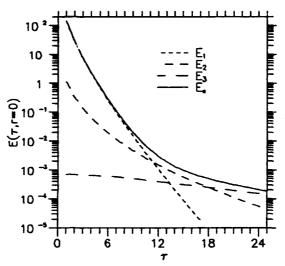
Figure 1 - Irradiance $E_s(z, r_\perp=0)$ and its components $E_k(z, r_\perp=0)$ (dashed lines) vs optical thickness τ.
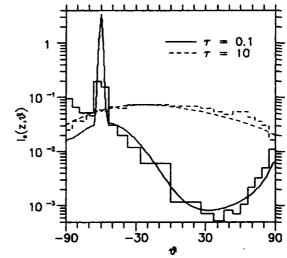
Figure 2 - Transmitted radiance for incident angle $\vartheta_0=60°$ vs polar angle ϑ. Histograms are the Monte-Carlo simulation data.

356

MODELING OF THE VISIBLE AND UV RADIATIVE TRANSFER P43
IN ATMOSPHERE. CONCEPT, MODELS AND PROGRAMS

Zege E.P., Prikhach A.S.

Inst. of Phys., BSSR Ac. of Sc.
70, Leninsky pr., 220602, Minsk, USSR
Phone (0172)394729, Telex 252277 NAUKA SU

A great number of scientific and applied problems require calculation of radiative characteristic including spectral-polarization ones in atmosphere and in atmosphere-underlying surface system. In particular optical satellite problems including the atmospheric correction in satellite researches, estimation of characteristics and optimization of vision, location and communication systems, optimizations of ozonometry methods, inverse problems of atmosphere optics fall into that class of problem.

Nowadays, such problems may and should be solved using special PC programs, which operate in an efficient interactive mode. This tool is deadly required for researches and engineers of the field. We have recently developed such a tool. It is the ATMOTOOLS package implemented for IBM PC which synthesizes up-to-date optical atmosphere models and special radiation calculation procedures.

ATMOTOOLS includes:
- Data banks on optical models of atmosphere incorporating the aerosol model, molecular scattering and absorption of water vapour, ozone and other trace gases, of ocean, ocean surface, earth surface;
- Atmospheric model creation procedures regarding for the input current experimental information using data banks on optical characteristics of atmospheric aerosols;
- Data banks on optical characteristics of atmospheric aerosols and calculation procedures for optical characteristics of composite aerosols;
- Special calculation procedures for radiative transfer in the atmosphere-underlying surface system.

An atmosphere model is a plane or spherical stratified scattering medium incorporating the aerosol and molecular atmospheric models. The full optical atmosphere model includes extinction coefficient, single scattering albedo and angular dependence of the scattering matrix elements as function of the altitude and wave length in visible, near UV and IR. Different standard molecular models are used regarding for the Rayleigh scattering and absorption by ozone, water vapour and other trace gases. For instance, the data banks of ozone contains the regional and seasonal profile of ozone concentration and detail data of spectral absorption of ozone. Data bank for water vapour and other trace gases are organized

in the similar way. In aerosol models each layer contains a definite type of aerosol, whose concentration may change with the height. The law of concentration variation may be included as a table or as an analytical function.

These data banks of atmospheric models include standard atmospheric aerosol models approved by the Radiation Commission of International Association for Meteorology and Atmospheric Physics (World Climate Research Program) and regional models developed using experimental measurements. Among them are also aerosol models based on the lidar data. The bank of atmospheric models is supplied with the procedures, which offer novel models in accordance with the input experimental information.

We pay a deal of attention to atmospheric aerosols. The optical characteristics of aerosols from data banks include: extinction coefficient $\varepsilon^{aer}(\lambda)$ per unit volume concentration, single-scattering albedo and scattering matrix with a scattering indicatrix as a first element. All parameters are given for wavelength λ ranged from 0.25 to 1.2 μm. The λ grid provides a high accuracy of determining optical parameters of aerosols by linear interpolation.

The data banks contain, first of all, optical parameters of simple aerosols such as *DUST*, *WATER-SOLUBLE* [1] are defined by a complex refractive index of aerosol particles and their size distribution function. A simple aerosol fraction is quasi-monodisperse simple aerosol having equal number of particles within the range between ρ and $\rho +\Delta\rho$ ($\rho = 2\pi a/\lambda$ is the dimensionless diffraction parameter, a is the particle diameter). The parameter $\Delta\rho$ is larger than the Mie solution oscillation period but smaller than the characteristic variation scale of the oscillation-average function $\varepsilon^{aer}(\lambda)$.

Optical parameters of simple aerosols and their fractions were preliminary computed by the Mie formulas on large computer. The results of a great deal of these computations are summed up by data banks. The optical characteristics of simple aerosols with any distribution function are found through simple weighted addition.

Optical parameters of composite aerosols such as *MARITIME* and *CONTINENTAL* [1] consisting of simple aerosols with different concentrations are also formed by weighed addition.

Data banks contain optical characteristics of the majority of the known atmospheric aerosols. The available procedures allow formation of optical characteristics of new multicomponent aerosols of a second. Such an arrangement of data banks on optical aerosol characteristics proved to be very useful. Also the computation speed ,as well as realization of effective interactive mode is ensured in many respects.

The calculation procedures of radiation transfer are developed with regard of atmosphere stratification.

polarization of light, multiple scattering, reflection direct and scattered sunlight by rough sea surface or the earth one. The procedures are based on special multicomponent methods of solution of radiation transfer equation included vector-parametric one, developed by authors recently [2-4]. They incorporate the approach based on the special representation of the real scattering indicatrix (or matrix elements) as a sum of more simple functions. Then, as we have showed, we obtain the set of transfer equations. At definite conditions the problem may be represented as a sum of solutions of the separate equations with comparatively simple kernels.

We checked the accuracy of our computation procedures carefully by comparison with the results of calculation for simplified optical models on large computers using Monte-Carlo simulation, doubling and characteristics methods. The error of multiple scattering estimations in our programs does not exceed 5%. Our method provides a compromise between the computation accuracy and calculation time.

The effective interactive mode for personal IBM computers is provided by this special radiative transfer calculation procedures as well as above mentioned special organization of data banks.

The calculations of spectral-polarization characteristics are carried out at different wavelength and parameters of experimental geometry.

Up to now, several ATMOTOOLS versions have been realized, among them calculation of visible and UV radiative transfer in the atmosphere-ocean system (version 1), optimization and study of the ozonometry technique, including satellite technique (version 2), estimation and optimization of the systems of optical vision and communication in the atmosphere ocean system (version 3) and so on. Now, the version for effective atmospheric correction to determine biological productivity of ocean is under development as well as the version for solving inverse problems of atmospheric optics with passive and active remote sensing using spectral satellite data. We continue up-dating these versions as well as developing new ones. The generality of the concept and module-type program allow simple expansion of their feasibilities. All ATMOTOOLS versions run in an effective interactive mode and show ease of service (minimum requirements for the user skill, error diagnostics, etc.). These packages offer ample scope for methodological studies. In fact, ATMOTOOLS is a bench to test the accuracy of methods and instruments, applicabilities of simplified models, optimization and development of new approaches.

REFERENCES

1. Lenoble J & Broquez C 1984, A Comparative Review of Radiation Aerosol Models, *Contribution to Atmospheric Physics*, 57, 1, 1-20.

2. Zege E P, Ivanov A P & Katsev I L 1990, *Image Transfer Through Scattering Medium*, Springer-Verlag, Berlin, 395p.

3. Zege E P, Katsev I L & Polonsky I N 1988, On one approach to solving the radiative transfer equation with an arbitrary scattering indicatrix, *Proc 4th All-Union Conf Laser Beam Propagation in a Scattering Media*, Obninsk-Barnaul, USSR, 172-174.

4. Zege E P & Chaikovskaja L I 1985, Approximate equations of polarized radiative transfer in media with strongly anisotropic scattering, *Izv AN SSSR, Fiz Atm Okeana*, 21, 10, 1043-1049.

SCINTILLATION 3

Dynamic properties of time-varying speckles produced by a series of moving phase screens

Takashi Okamoto and Toshimitsu Asakura

Research Institute of Applied Electricity, Hokkaido University,
Kita-ku, Sapporo, Hokkaido 060, Japan
Telephone: 011-716-2111 *ex.* 2646   *FAX:* 011-758-6098

1. INTRODUCTION

Speckle patterns are observed when the coherent light is reflected by an optically rough surface, or when it propagates through a dense scattering medium. Different treatments must be adopted to analyze rigorously these two types of scattering phenomena. In some cases, however, the scattering from extended media can be approximated as successive scatterings from a large number of rough surfaces by introducing a set of random phase screens[1-7].

We investigate the dynamic properties of speckle patterns produced by deep random-phase screens being spaced some distance apart from each other and moving at constant velocities. The space-time correlation functions of the time-varying speckle intensity are evaluated to examine the relationship between the velocities of the screens and the time-correlation length of intensity fluctuations arising from them.

2. THEORETICAL RESULTS

Figure 1 shows the optical arrangement used for evaluating the space-time correlation function of multiply-scattered speckle patterns. Random phase screens spaced in parallel with each other move at constant velocities in their own planes. By illuminating these diffusers with a coherent Gaussian beam, a dynamic speckle pattern resulting from the multiple scattering is produced at the observation plane located in the Fresnel diffraction region. For simplicity, the scalar wave approximation is used.
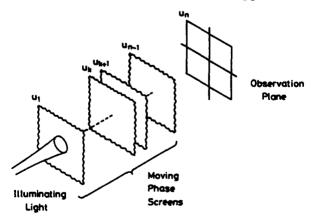
Fig. 1 Schematic diagram used for the analysis

The space-time correlation function of speckle intensity fluctuations observed at the plane u_n is given by
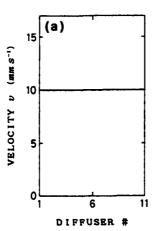
$$\langle \Delta I_n(u_n, t) \Delta I_n(u_n', t+\tau) \rangle$$

$$= \exp[-2 \sum_{l=0}^{n-1} \sum_{m=0}^{n-1} A_n(l,m) v_l v_m \tau^2 + 2 \sum_{l=0}^{n-1} B_n(l)(u_n'-u_n) v_l \tau]$$

$$\times \exp(- \frac{|u_n'+u_n|^2}{q_n^2}) \exp(- \frac{|u_n'-u_n|^2}{\zeta_n^2}), \tag{1}$$

where v_l and v_m are the velocities of the lth and mth phase screens, respectively, q_n is the extent of the illuminating field, and ζ_n represents the average speckle radius. The parameters $A_n(l,m)$, $B_n(l)$, q_n and ζ_n are given by the recursion formulas which are useful for numerical computations. By using Eq. (1), we examine whether the velocity of a multiple scattering object can be measured by using the time-correlation length defined as the width of the autocorrelation function of intensity fluctuations at a single point.

Two velocity profiles are considered; one is the homogeneous velocity distribution and the other has a velocity gradient following the parabolic profile. These profiles are shown in Figs. 2 (a) and (b), respectively, where eleven phase screens are assumed to be placed 1 mm apart from each other and to move in the same direction. The average velocity of all the phase screens is the same value of 10 mm s^{-1} for the two velocity profiles. Furthermore, some random variations are added to the velocity of each phase screen. The extent of the random distribution of the velocities is estimated statistically by the standard deviation σ_v which is expressed as the ratio to the average velocity.
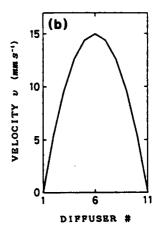
Fig. 2 (a) Homogeneous and (b) parabolic velocity profiles of a series of phase screens

Figures 3 (a) and (b) show the reciprocal of the time-correlation length as a function of the average velocity for the homogeneous velocity distribution and the velocities with parabolic profile, respectively. The curves A in the figure are obtained when there is no variation in the velocity of each diffuser. In this case, the reciprocal of the time-correlation length has a proportional relationship with the average velocity of all the phase screens as long as the velocity profile of those screens remains the same. Hence, the time-correlation length becomes a measure for determining the velocity of a multiple-scattering object whose velocity profile does not change with time.
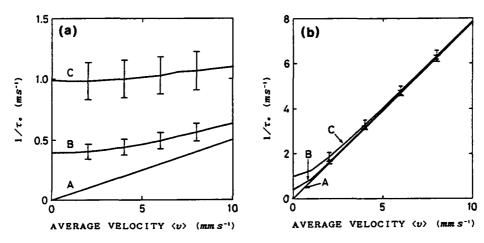
Fig. 3 Dependence of the reciprocal of the time-correlation length on the average velocity obtained for the velocity profiles shown in Figs. 2 (a) and (b).

The curves B and C are obtained by allowing the velocity of each phase screen to be distributed randomly to the extents of 2 % and 5 % of the average velocity, respectively. When the average velocity of each phase screen has the same value (namely, no velocity gradient exists), the linearity observed in the curve A in Fig. 3 (a) has disappeared if the velocity variations become more than 2 % of the average velocity. On the contrary, for the parabolic velocity profile shown in Fig. 3 (b), the variations in the velocity have little effect on the time-correlation length. Therefore, it can be said that, when we measure the average velocity of a multiple scattering object using the time-correlation length, more reliable values are expected to obtain for objects in which steeper velocity gradients of the fixed shape exist in the scattering volume.

3. CONCLUSION

The statistical properties of a dynamic speckle pattern produced by a series of random phase screens moving across their own planes have been investigated theoretically. The space-time correlation function for the intensity fluctuations in the Fresnel diffraction region has been evaluated to give a statistical description of multiply-scattered speckle patterns.

It has been shown that the time-correlation length measures the velocity of a multiple scattering object containing scatterers whose velocity distribution is fixed. Even if there are some random variations in the velocity of each diffuser, the velocity gradient in the scattering volume prevents the velocity variations from affecting the motion of resulting speckles and the information on the average velocity can be extracted from the intensity fluctuations detected at a single point.

REFERENCES

1. R.W.Lee and J.C.Harp,"Weak scattering in random media, with applications to remote probing," Proc.IEEE 57, 375-406(1969).
2. F.Roddier, J.M.Gilli, and G.Lund,"On the origin of speckle boiling and its effects in stellar speckle interferometry," J.Opt.(Paris) 13, 263-271(1982).
3. D.L.Knepp,"Multiple phase-screen calculation of the temporal behavior of stochastic waves," Proc.IEEE 71, 722-737(1983).
4. B.J.Uscinski,"Analytical solution of the fourth-moment equation and interpretation as a set of phase screens," J.Opt.Soc.Am.A 2, 2077-2091 (1985).
5. J.F.Goldenberg and T.S. McKechnie,"Diffraction analysis of bulk diffusers for projection-screen applications," J.Opt.Soc.Am.A 2, 2337-2348(1985).
6. Y.Kim and D.L.Jaggard,"Optical beam propagation in a band-limited fractal medium," J.Opt.Soc.Am.A 5, 1419-1426(1988).
7. T.Okamoto and T.Asakura,"Velocity measurements of two moving diffusers using a temporal correlation length of doubly-scattered speckle," J.Mod. Opt. 37, 389-408(1990).

Spacecraft Observations of Star Scintillations through Atmosphere

A.S.Gurvich

Institute of Atmospheric Physics, USSR Academy of Sciences
Pyzhevsky 3, Moscow 109017, USSR
tel.231-21-68
(INVITED)

The analysis of distortions of visible image of the Sun during
its observation from space through atmosphere has shown that in-
homogeneities of air refractive index n at altitudes more than
12-15 km are strongly stretched along the surface of the Earth
[1]. According to this factor in order to describe fluctuation
phenomena appearing during observations of stars occultations be-
hind the Earth's atmosphere the paper [2] suggests a model of
turbulent inhomogeneities statistically locally isotropic upon
the sphere and locally homogeneous by height. In this model the
structure function

$$D_\nu = <(\nu(\mathbf{r}_1)-\nu(\mathbf{r}_2))^2>, \qquad \nu = \delta n / (\bar{n}(r)-1) \qquad (1)$$

of fluctuations of air refractive index δn normalized by $\bar{n}(r)-1$
depends only on the angular distance θ between the vectors $\mathbf{r}_1$ and
$\mathbf{r}_2$ and on the differences of altitudes r_1 and r_2, where $\bar{n}(r)$ is
the average value of n at the distance r from the center of the
Earth. Practically it is more convenient to use the distance $a_e\theta$
where a_e is the radius of the Earth instead the value of angle θ.

A two-dimensional spectrum of star scintillations was calcu-
lated for this model in [3] to be used by an observer who is far
away from the atmosphere aboard a spacecraft.The atmospheric in-
fluence was described as usual by an equivalent phase screen.
Earlier a theory of fluctuations phenomena was developed in [4]
for occultation experiments for the inhomogeneities which are
statistically locally isotropic on the horizontal plane (not upon
the sphere!) and locally homogeneous along the height. The dif-
ference in results of [3] and [4] becomes relevant in case when
the horizontal scale of inhomogeneities exceeds the vertical one
by many times. The big parameter $(a_e/H_o)^{1/2}$ where H_o is the
height of homogeneous atmosphere is the criterion for the value

of anisotropy η, which is equal to the ratio between the horizontal and vertical scales of inhomogeneities. Fig.1 displays qualitatively the peculiarities of model [2] for $\eta^2 \gg a/H_0$ and for $1 \leqslant \eta^2 < a_e/H_0$. In first case the turn of inhomogeneities to the angle $(a_e/H_0)^{-1/2}$ with respect to the beam results in decrease of their turbulent action. In the second case such a decrease does not occur.

For anisotropic inhomogeneities it is shown in [5] that the reconstruction of two dimensional spectrum of scintillations by set of one-dimensional spectra may be done by means of computing tomography methods. It was shown in [6] that a three-dimensional spatial spectrum of locally isotropic inhomogeneities of refractive index can be reconstructed by measurements of one-dimensional spectrum of scintillations. In case of inhomogeneities strongly stretched along the Earth's surface $\eta^2 \gg a_e/H_0$, this problem is simplified [5] and one can reconstruct relatively easily from one dimensional scintillations spectra a vertical spectrum of inhomogeneities $V_\nu(\mathit{æ}_1)$

$$V_\nu(\mathit{æ}_1) = 2\pi \int_0^\infty \mathit{æ}\, d\mathit{æ}\, \Phi_\nu(\mathit{æ}_1, \mathit{æ}) \qquad (2)$$

where Φ_ν is a three-dimensional spectrum of inhomogeneities $\delta\nu$, $\mathit{æ}^2 = \mathit{æ}_2^2 + \mathit{æ}_3^2$, $\mathit{æ}_1$ – is a vertical wave number.

The first spacecraft observations of star scintillations [7] revealed that the spectrum of inhomogeneities of refractive index evidently greatly differs from Kolmogorov's one. By now we have results of more than 20 observations of scintillations for the range of ray perigee heights from 20 to 45 km. The analysis of calculated scintillations spectra revealed that the anisotropy $\eta \approx 150$ [8]. This made it possible to calculate vertical spectra V_ν by these measurements in the scale range 1 km $\leqslant 2\pi/\mathit{æ}_1 \leqslant 20$ m.
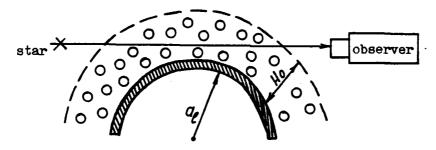
In the height range of 25-38 km the obtained spectra $V(\mathit{æ}_1)$ have a similar form with the typical vertical scale about $l_* = 40\text{-}60$ m. At low frequencies $\mathit{æ}_1 < 2\pi/l_*$ the spectra decrease

approximately as $æ_1^{-3}$, at high frequencies $æ_1 > 2\pi/l_*$ the spectral density decreases more rapidly – approximately as $æ_1^{-5}$. Up to the scales $2\pi/æ_1 \cong 15$ m we never observed in the atmosphere at these altitudes an area which would correspond to Kolmogorov's spectrum of inhomogeneities. The corresponding estimates lead to the fact that the structural characteristic C_n^2 present in "the law of 2/3" for the refractive index at altitude of 25 km is small $C_n^2 < 2*10^{-22}$ $m^{-2/3}$.
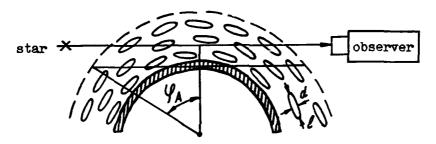
Fig.2 represents the agreement between vertical temperature spectra obtained from direct measurements taken from high-altitude balloons [9] and calculated from observations of scintillations.

References

1. Gurvich A.S., S.V.Zagoruyko, L.I.Popov, V.V.Ryumin, S.A.Savchenko and P.A.Chochia. Dokl .Academy of Sciences, USSR, 1980, V.256, N 6, p.1330 (in Russian).
2. Gurvich A.S. Radiophysics and Quantum Electronics, 1984, V.27, 8, p.665.
3. Gurvich A.S. Atmospheric Optics, 1989, V.2, N 3, p.188.
4. Woo R., A.Ishimaru, F.-Ch.Yang. Radio Sci. 1980, V.15, N 3, p.695.
5. Gurvich A.S., Kan V. Atmospheric Optics. 1989, V.2, N 4, p.277.
6. Gurvich A.S., N.S.Time, L.S. Turovtzeva and V.F.Turchin. Izvestiya Academy of Sciences, USSR. Atmospheric and Oceanic Physics. 1974, V.10, N 5, p.292.
7. Grechko G.M., A.S.Gurvich and Yu.V.Romanenko. Izvestiya Academy of Sciences. Atmospheric and Oceanic Physics. 1980, V.16, N 4, p.227.
8. Alexandrov A.P., Grechko G.M., Gurvich A.S., Kan V., Savchenko S.A. Atmospheric Optics. 1990, V.3, N 8, p.879 (in Russian).
9. Cot Ch., J.Barat. Geophys Res.Lett. 1990, V.17, N 10, p.1577.

isotropic inhomogeneities

anisotropic inhomogeneities, $\eta=d/l$.

Fig.1. Diagram of scintillation observations, $\varphi \simeq \sqrt{2H_0/a}$.
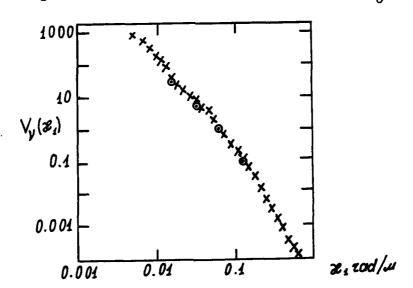
Fig.2. Spectra of $V_\nu(\varkappa)$: ✗ — estimated from scintillations measurements, ⊚ — direct measurements from balloon [9].

THE SPECTRUM OF VELOCITY AND REFRACTIVE TURBULENCE
IN THE VISCOUS AND VISCOUS-DIFFUSIVE RANGE

V.I. Tatarskii,

Lebedev Physical Institute, Moscow, USSR,

and

NOAA/ERL/WPL, Boulder, CO, USA. Tel. (303) 497-3668

& M.M. DUBOVIKOV

Lebedev Physical Institute, Moscow, USSR, (INVITED)

Knowing the form of the temperature spectrum in the viscous-diffusive range is essential to the understanding of several optical propagation phenomena. One is its relationship to the structure parameter C_n^2 and the Kolmogorov microscale η which allows us to calculate them from simultaneous intensity and beam displacement measurements or from measurements of other properties sensitive to these parameters. Another is the level of fluctuations in the region of saturated intensity scintillations which is also sensitive to the structure of the temperature spectrum in the viscous-diffusive region.

It is well known that for very large Reynolds numbers there exists a universal structure for spectra of velocity and passive scalar fields in the turbulent flow. This is the so-called equilibrium interval of spectra.

The general expression for the one-dimensional spatial temperature spectrum $V_T(k)$ due to dimensional analysis is given by the formula [1]

$$V_T(k) = N\ \varepsilon^{-1/3}\ k^{-5/3}\ \varphi_T(k\eta, Pr)\ \ldots\text{for } kL \gg 1.$$

Here k is the wavenumber, ε is the rate of energy dissipation per unit of mass, N is the rate of dissipation of temperature inhomogeneities, ν and χ are the molecular viscosity and heat conductivity coefficients, $Pr = \nu/\chi$ is the Prandtl number, $\varphi_T(x,y)$ is the universal dimensionless function depending on dimensionless arguments, $\eta = (\nu^3/\varepsilon)^{1/4}$ is the Kolmogorov scale of turbulence, and L is the outer scale of turbulence.

For the inertial-convective interval the parameters ν and χ are not essential and for this case the well-known formula is

valid:

$$V_{\tau}(r) = M \, C_{\tau}^{2} \, k^{-3/3}, \quad C_{\tau}^{2} = a^{2} \, N \, \varepsilon^{-1/3}.$$

Here M, a^{2} are dimensionless constants.

In the present paper we obtain the theoretical expression for the temperature fluctuation spectrum for a Prandtl number of the order of unity (for air it is approximately 0.72) and for $k\eta$ >> 1. Asymptotic theory for the refractive index spectrum in the turbulent atmosphere is developed. It is valid in the region where both viscosity and molecular heat conductivity are essential.

The assumption of smallness of the dimensionless quantity

$$\gamma(r) = \frac{<v_{p}(1)v_{q}(2)(\partial T_{1}/\partial x_{p1})(\partial T_{2}/\partial x_{q2})>}{<v_{p}(1)v_{q}(2)><(\partial T_{1}/\partial x_{p1})(\partial T_{2}/\partial x_{q2})>} - 1,$$

which is proportional to the correlation coefficient between the product of velocities in two points and the corresponding product of temperature (refractive index) gradients is made. This assumption received confirmation in recent experiments [3] in a wind tunnel. In Fig. 1 the value of γ as a function of the distance r between two points 1 and 2 is presented. It is obvious that γ decreases together with r and is small even for r of the order of 10η.

For the longitudinal spectrum of the velocity field, $E_{LL}(k)$, the viscous range asymptote obtained in Ref. [2] is used:

$$E_{LL}(k) =$$

$$60\left[k\eta + (4/13\xi)\right]\exp\{-\xi k\eta\} + \ldots, \quad \xi \approx 10.85$$

In Fig.2 this function and the corresponded experimental data are presented.

In general we can represent the

Fig. 1. The results of measurements of $\gamma(r)$.

temperature spectrum in the form

$$V_{\tau}(r) = M \, C_{\tau}^2 \, k^{-5/3} \phi_{\scriptscriptstyle 1}(k\eta, Pr).$$ Our theory [4] leads to the following expression for the function $\phi_{\scriptscriptstyle 1}$:
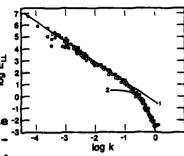
$$\phi_{\scriptscriptstyle 1}(k\eta) = \theta(\kappa - k\eta) +$$
$$+\theta(k\eta - \kappa) \, D \, \exp(-k\eta\xi)(k\eta)^{\mu - 1 + 5/3} \times$$
$$(1 + \mu(9 - 2\mu)(13\xi)^{-1}(k\eta)^{-1} + \ldots).$$

Here κ, D, are dimensionless numbers, the roots of the system of algebraic equations, depending on the Prandtl number, and the constant a^2, $\theta(x)$ is the step function, $\mu = (1/2)\{[1 + 120(Pr)^2]^{1/2} - 3\}$.

Fig. 2. Comparison of the results of the calculation and the results of measurements of the longitudinal turbulence spectrum.

The theory leads to the appearance of the bump between the inertial-convective and viscous-diffusive ranges of the spectrum, which was observed in many experiments (see [5]). The dependence of this bump position on the wavenumber axis is in qualitative agreement with experimental results. The height of the bump in this theory depends on the value of the dimensionless constant in the 2/3 law and there is agreement between these values. In Fig. 3 the function $\phi_{\scriptscriptstyle 1}(k\eta)$, which shows the deviation of the spectrum on power law, and corresponding experimental values are presented. The theory developed has no free parameters thus making it possible to obtain the coincidence of the maximum position of the theoretical curve with the corresponding experimental dependence. The displacement obtained must be the object of additional consideration.

Fig. 3. The function $\phi_{\scriptscriptstyle 1}(k)$ for the parameters: $\xi = 10.85$, $\mu = 2.55$, $a^2 = 2.3$, $D = 1323$, $\kappa = 0.1715$. The data points are experimental values

373

REFERENCES

1. Monin, A.S. and Yaglom, A.M. 1975 *Statistical Hydrodynamics*, vol. 2, M.I.T. Press, Cambridge, MA.

2. Dubovikov, M.M.and Tatarskii V.I. Calculation of the asymptotic form of the spectrum of locally isotropic turbulence in the viscous range. Sov. Phys. JETP vol. 66(6), Dec. 1987, pp 1136-1141.

3. Tatarskii, V.I., Praskovsky A.A, and Karyukin, M.Yu. Experimental Verification of a Hypothesis on the Mixed Fourth Moment for Temperature and Velocity Fields in Turbulent Flow. Submitted to J. of Fluid Mech.

4. Tatarskii, V.I. and Dubovikov, M.M. Temperature Fluctuation Spectrum in the Dissipation Range for Statistically Isotropic Turbulent Flow. Submitted to J. of Fluid Mech.

5. Hill, R.J. Models of the scalar spectrum for turbulent advection. J. Fluid Mech. 88, 541-562.

Turbulent Surface Layer Fluxes Derived from C_n^2

Volker Thiermann

FGAN-Forschungsinstitut für Optik (Doc. 1991/11),
Schloss Kressbach, D-7400 Tübingen 1, Germany, Tel. (0)7071 709-0

Introduction

Optical scintillation measurements can be used to determine the structure constant C_n^2 and the inner scale ℓ_0 of refractive index fluctuations.[1] Neglecting the humidity contribution to refractive index, C_n^2 is a measure of the structure constant of temperature fluctuations C_T^2.[2] ℓ_0 can be related to the dissipation rate ϵ of turbulent kinetic energy by $\epsilon = \nu^3 (7.4/\ell_0)^4$, where ν is the kinematic viscositiy of air.[3]

If one assumes that C_T^2 and ϵ obey Monin-Obukhov similarity, scintillation measurements can be used to infer the turbulent fluxes of heat Q_0 and momentum u_*^2.[4] Compared to classical, local flux measurement methods, the optical technique has the advantage to average over the propagation path and to provide a stable statistics in a relatively short time. However only few experimental data of optically derived heat and momentum fluxes exist until today.[5]

A known optical technique to measure C_n^2 and ℓ_0 is based on bichromatic scintillation.[6] In 1988, a bichromatic scintillometer was operated over a 120 m long and 2 m high propagation path for several days. The path was situated above a stubble field near Meppen in northern Germany.[2] The scintillometer was based on a HeNe ($0.63\mu m$) and a CO_2 ($10.6\mu m$) laser. The humidity contribution to the laser scintillation was eliminated through its wavelength dispersion. The measurements have now been used to derive the turbulent fluxes of heat and momentum. Here examples of time series will be given and compared to conventional micrometerological data.

Flux derivation method

The derivation of the turbulent fluxes is based on a set of hypothetical Monin-Obukhov scaling expressions. These expressions are quite similar to others found in the literature and are discussed in a forthcoming paper.[7] The equations are:

$$C_T^2 \, (k \, z)^{2/3} \, Q_0^{-2} \, u_*^2 = 4 \, \beta_1 \, [1-7z/L+75(z/L)^2]^{-1/3} \quad \text{for } z/L < 0,$$
$$= 4 \, \beta_1 \, [1+7z/L+20(z/L)^2]^{1/3} \quad \text{for } z/L > 0,$$

$$\epsilon \, k \, z \, u_*^{-3} = (1-3z/L)^{-1}-z/L \quad \text{for } z/L < 0,$$
$$= [1+4z/L+16(z/L)^2]^{1/2} \quad \text{for } z/L > 0,$$

where z is the height above ground, k is the von Kármán constant (0.4), β_1 is the one-dimensional Obukhov-Corrsin constant (0.86), and L stands for the Monin-Obukhov length: $L=-Tu_*^3/(kgQ_0)$, with the air temperature T in K and the gravitational acceleration g (9.8 m/s^2).

If T and the sign (direction) of Q_0 are known, the above equations can be solved to give Q_0 and u_*^2 from values of C_T^2 and ϵ which are derived from measurements of C_n^2 and ℓ_0.

Results

Fig. 1 shows time series for one afternoon. In Fig. 1a, 10 minute averages of the net radiation are

given. The visible short term variations were caused by the passage of cumulus clouds. In Fig. 1b, the scintillometrically measured heat flux is plotted with 1 minute resolution. At times when the net radiation was quite constant, also the measured heat fluxes did not show much scatter. At other times, sudden changes of the net radiation, not resolved in Fig. 1a, caused stronger temporal variations. Heat fluxes computed from 10 minute averages of the optical data are plotted in Fig. 1c (solid line). This curve correlates well with the net radiation. In Fig. 1c also results of a conventional heat flux measurement are drawn in (dashed line). Here the eddy-correlation method was applied to ultrasonic anemometer thermometer data taken near the centre of the propagation path (2 m height, 10 minute averages). The agreement with the 10 minute averaged optical data is quite good. Small values have to be considered carefully due to signal-to-noise limitations.

Friction velocities u_* ($=\sqrt{u_*^2}$) derived from 1 minute averages of the optical data are plotted in Fig. 1d. The scatter is due to the natural variability of wind speed and to the statistical uncertainty of the data samples. The latter can be estimated to cause several percent error for both Q_0 and u_*.[7] The smoother curve for u_* in Fig. 1e (solid line, left scale) is computed from 10 minute averages of the optical data. As expected close to the ground for an unchanging surface roughness, u_* correlates well with the wind velocity u (dashed line, right scale). The data imply a roughness length of $z_0 = 1.5$ cm if a logarithmic wind profile, $u = (u_*/k) \ln(z/z_0)$, is assumed. A value of z_0 = 1±0.5 cm was derived from a nearby measured wind profile.

Fig. 2 shows time series for some hours during a clear night. Again u_* correlates well with the wind speed. Since the wind direction was different from that in Fig. 1, the respective effective surface roughness lengths cannot be compared. The optically and conventionally derived heat fluxes have about the same magnitude. From the energetics of turbulence it is known that under conditions of a (nocturnal) stable densitiy stratification, the vertical turbulent heat flux is driven against the buoyancy forces exclusively by turbulent friction and is (partly) balanced by the net radiation. Hence, for periods of a quite constant net radiation as it is visible in Fig. 2a, a strong correlation between the heat and momentum fluxes should exist. This correlation, in fact, is observed for the optical data. The conventional data, however, do not clearly exhibit such a behaviour, which demonstrates that they must be affected by errors. The known inherent errors of the eddy correlation technique result from a weak statistics even for 10 minute averages and from flow distortions in the vicinity of the instrument.

Conclusion

It was demonstrated that the turbulent surface layer fluxes of heat and momentum can be accurately measured by use of optical scintillation. Beside others, a major advantage of the optical method is that it provides a very high temporal resolution. Even averaging periods as small as 1 minute do not cause more than several percent scatter.

References

[1] A. Consortini, in *Scattering in Volumes and Surfaces*, M. Nieto-Vesperinas and J. C. Dainty eds., North-Holland, Amsterdam (1990).
[2] V. Thiermann and E. Azoulay, SPIE Proc. 1115, 124-135 (1989).
[3] R. J. Hill and S. F. Clifford, J. Opt. Soc. Am. 68, 892-899 (1978).
[4] J. C. Wyngaard and S. F. Clifford, J. Atmos. Sci. 35, 1204-1211 (1978).
[5] R. J. Hill and G. R. Ochs, Conference on Optical Remote Sensing of the Atmosphere (Opt. Soc. Am.), paper WD18 (1990).
[6] E. Azoulay, V. Thiermann, A. Jetter, A. Kohnle and Z. Azar, J. Phys. D: Appl. Phys. 21 S41-S44 (1988).
[7] V. Thiermann and H. Grassl, submitted to Boundary-Layer Meteorol. (1991).
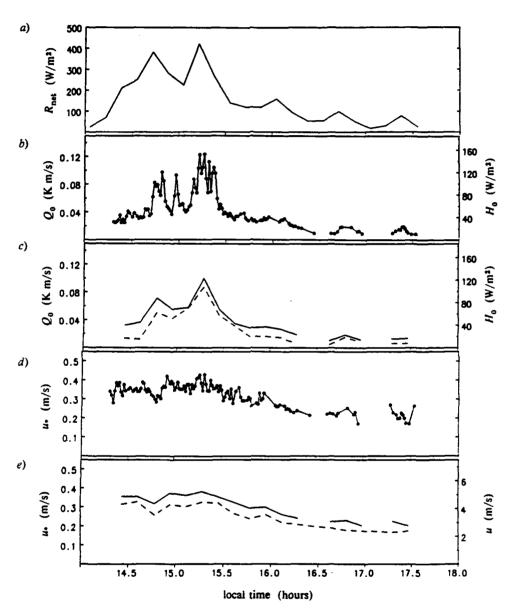
Fig. 1. Time series for one afternoon, 2 pm to 6 pm local time. *a*) net radiation R_{net} (10 minute averages). *b*) heat flux Q_0 derived from optical data with 1 minute resolution; left scale: Q_0 in K m/s; right scale: converted into unit W/m^2 for mean temperature and pressure. *c*) solid line: same as *b*) but for 10 minute averages; dashed line: 10 minute averages of heat flux from local measurements. *d*) friction velocity u_* derived from optical data with 1 minute resolution. *e*) solid line, left scale: same as *d*) but for 10 minute averages; dashed line, right scale: 10 minute averages of wind velocity u.

377
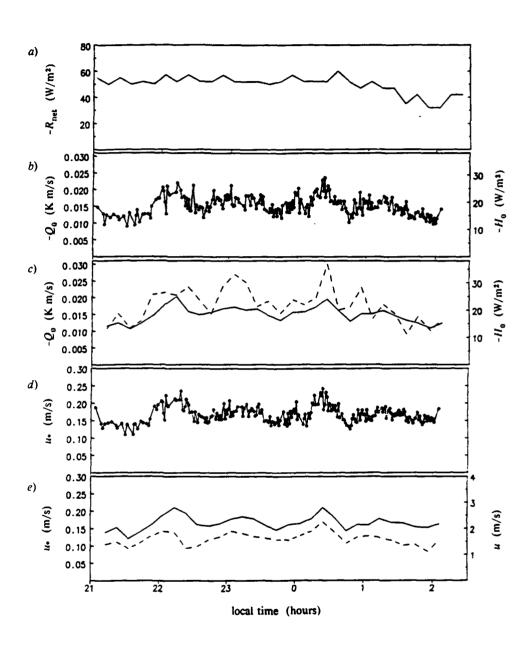
Fig. 2. Same as Fig. 1 but for a clear night, 9 pm to 2^{30} am.

EFFECT OF INTERMITTENT TURBULENCE ON THE REFRACTIVITY STRUCTURE CONSTANT IN CLEAR AIR

G. d'Auria, F.S. Marzano, U. Merlo

Dipartimento di Elettronica, Università di Roma "La Sapienza"
Via Eudossiana 18, 00184 Roma - Italia

1. INTRODUCTION

Clear air scintillations are usually estimated by means of the refractive-index structure constant C_n^2. In many cases, e.m. measurements of C_n^2 derived from radars, satellite links or scintillometers appear to be appreciably lower than those predicted by using contemporary radiosonde data. This may happen because the turbulence of the atmosphere along the e.m. path is intermittent and the regions that are in stable conditions do not contribute to the value of C_n^2.

In this work, the effect of the turbulence intermittency on C_n^2 has been statistically considered. Estimation of the mean value of C_n^2 has been performed and applications to radio and optical cases have been discussed.

2. ESTIMATION OF C_n^2 IN NON HOMOGENEOUS TURBULENCE

The local instability of the atmosphere is characterized by the Richardson number $R_i=B/S$, where $B=gdln\theta/dz$ is the local buoyancy, θ the potential temperature, g the acceleration of gravity, z the altitude and $S=t^2=|d\underline{v}/dz|^2$ is the square of the local shear t, being $\underline{v}$ the horizontal wind velocity vector. If $R_i \leq R_{ic} \approx 0.25$ the atmosphere may become turbulent, while values of $R_i > R_{ic}$ correspond to stable conditions. In volumes where $R_i \leq R_{ic}$ and the turbulence is constant following the Kolmogorov's law, C_n^2 is given by the Tatarskii's equation /1/:

$$C_n^2 = a \, L_o^{4/3} \, M^2 \qquad (1)$$

where a=2.8, L_o is the outer scale of turbulence and M is the vertical gradient of mean refractive-index, expressed by:

$$M=[-77.6*10^{-6}p_o(gT_o)^{-1}(1+15500q_oT_o^{-1})]B_o-0.605p_oT_o^{-2}H_o=\xi_oB_o+\zeta_oH_o \qquad (2)$$

being p_o the local mean pressure (mb), T_o the local mean temperature, B_o the local mean bouyancy and $H_o=dq_o/dz$ the mean vertical gradient of local mean specific humidity q_o. Eq.(2) is derived from the continuous term of the real refractivity for radiowaves /2/, but it may be extended to optical frequencies omitting the "wet" terms q_o and H_o.

Due to the extreme variability of meteorological quantities in Eq.(2), the common estimation tecnique for C_n^2 is to divide the path into layers in which C_n^2 may be considered as constant. Considering a plane wave incident on a point receiver, for m subsequent layers the variance of the log-amplitude χ (dB) of scintillations is /3/:

$$\sigma_\chi^2 = 23.2 \, k_0^{7/6} \, (\sin\alpha)^{11/6} \sum_{i=1}^{m} (z_i^{11/6}-z_{i-1}^{11/6}) \, C_n^2(i) \qquad (3)$$

where k_o is the wavenumber, α the elevation angle and i refers to i-th layer. The Eq.(3) holds for weak scintillations and when $l_o \leq (2\pi L/k_o)^{1/2} \leq L_o$, being l_o the inner scale of turbulence and L the turbulent path lenght. Direct application of Eq.(1) into Eq.(3) can be performed only by selecting the events and the slabs where meteorological data make sure of well developed turbulence with $R_i \ll R_{ic}$. Only by using this procedure a satisfactory agreement has been found in space-earth links. An example is reported in Fig.1 that shows the regression lines of the variance measured from SIRIO satellite microwave link and of the corresponding variance calculated by Eq.(3) from radiosonde data. From these lines it can be also derived an interesting dependance of the outer scale L_o on the ambient (ground level) temperature T (°C), expressed by:

$$L_o = \exp(3.042-0.021T) \qquad (4)$$

Applying Eq.(1) also where $R_i \geq R_{ic}$, i.e. in stable layers, the values of σ^2_χ estimated by Eq.(3) result well in excess of the corresponding e.m. measurements of σ^2_χ. Similar overestimation has been already found using radar measurements of C_n^2 /4/. Radar measurements give also evidence of local "intermittent" or "patched" turbulence at different heights /5/, suggesting to take into account the finite probability that $R_i \leq R_{ic}$ /6/.

3. EFFECT OF INTERMITTENT TUURBULENCE ON C_n^2

The intermittency of turbulence is associated to the random fluctuations of R_i across the critical value $R_{ic} \approx 0.25$. We may approach the problem of evaluating C_n^2 in these conditions by noting that the local shear variability is the most significant factor in the intermittency /6/. Therefore, if the fluctuations B' are small in respect to the local mean value B_o, Ri can be written as $R_i = B_o/S$. In general, all of the local mean quantities involved in Eq.(2) may vary randomly during the measurements, but we note that p_o, T_o and q_o do not vary appreciably to affect the value of C_n^2. From Eq.(3), the quantity M results a function only of the random variables B_o and H_o. There is also experimental evidence that Lo may be a random variable.

The use of the model in Eq.(1) should be carefully limited only where $R_i \leq R_{ic}$ and elsewhere, i.e. when $R_i > R_{ic}$, it may be assumed $C_n^2 = 0$. This corresponds to consider the structure constant C_n^2 as a random function of L_o, S, B_o and H_o, expressed by:

$$C_n^2(L_o, S, B_o, H_o) = a\, L_o^{4/3}\, (\xi_o B_o + \zeta_o H_o)^2\, u(S - S_c) \tag{5}$$

where $u(S - S_c)$ is the step function centered on the "critical square shear" $S_c = B_o/R_{ic}$. In locally homogeneous atmosphere, the first characteristic of interest is the mean value $<C_n^2>$ of C_n^2, given by:

$$<C_n^2> = \int_0^\infty C_n^2 p(C_n^2) dC_n^2 = \int_\infty^\infty \int_\infty^\infty \int_0^\infty \int_0^\infty C_n^2\!\left(L_o, S, B_o H_o\right) p\!\left(L_o, S, B_o, H_o\right) dL_o dS dB_o dH_o \tag{6}$$

where $p(C_n^2)$ and $p(L_o, S, B_o, H_o)$ are the probability density of C_n^2 and the joint probability density of (L_o, S, B_o, H_o). The calculus of Eq.(6) may be simplified assuming (B_o, H_o) as statistically independent from (Lo, S), i.e.: $p(L_o, S, B_o, H_o) = p(L_o, S) p(B_o, H_o)$. Besides, when the relative variations of B_o are small in respect to those of S, the value of S_c may be considered as constant and, by use of Eq.(5), we may rewrite Eq.(6) as:

$$<C_n^2> = a\, (<M>^2 + \delta_M^2) \int_{S_c}^\infty \int_{l_o}^{l_{max}} p(L_o, S) L_o^{4/3}\, dL_o dS \tag{7}$$

where L_{max} is the maximum value of Lo and:

$$<M>^2 = (\xi_o <B_o> + \zeta_o <H_o>)^2 \tag{8}$$

$$\delta^2_M = \xi_o^2\, \sigma_{Bo}^2 + \zeta_o^2 \sigma_{Ho}^2 + 2\xi_o^2 \zeta_o^2 \sigma_{Ho} \sigma_{Bo} r_{BoHo} \tag{9}$$

where $<M>$ is the mean of M and $<B_o>$, $<H_o>$, σ_{Bo}^2, σ_{Ho}^2 are the means and variances of B_o and H_o, while r_{BoHo} is the B_o-H_o correlation coefficient.

Further simplification of Eq.(7) is possible remembering that the coherence between humidity and temperature is often high, positive or negative. Assuming a T_o-q_o correlation coefficient equal to ± 1 [2] [6], for small relative variations both of T_o and q_o, it follows that $r_{BoHo} = \pm 1$. Besides, supposing L_o as statistically dependent on S, i.e.: $p(L_o, S) = p(L_o|s) p(S)$, we obtain:

$$<C_n^2> = a\, (<M>^2 + \sigma_M^2) \int_{S_c}^\infty p(S) \int_{l_o}^{l_{max}} p(L_o|S) L_o^{4/3}\, dL_o dS \tag{10}$$

where σ_M^2 is the variance of M given by:

$$\sigma_M^2 = (\xi_o\, \sigma_{Bo} \pm \zeta_o\, \sigma_{Ho})^2 \tag{11}$$

with the sign of the term $\zeta_o \sigma_{Ho}$ equal to the sign of r_{BoHo}.

4. EVALUATION OF MEAN C_n^2 FOR RADIO AND OPTICAL CASES

If the turbulent path is within troposphere and both the term $\xi_o<B_o>$ and $\zeta_o<H_o>$ of Eq.(8) are relevant, it can be shown that from Eqs.(8) and (11) it results $<M>^2>>\sigma_M^2$ /7/ and for $H_o/\sigma_{Bo}=B_o/\sigma_{Ho}$, we have:

$$\sigma_M/<M> = [(\xi_o<B_o>\pm\zeta_o<H_o>))/(\xi_o<B_o>+\zeta_o<H_o>)]\sigma_{Ho}/H_o \qquad (12)$$

For $r_{BoHo}=+1$ and $r_{BoHo}=-1$, Eq.(12) gives respectively the upper bound and the lower bound of $\sigma_M/<M>$.

At optical frequencies or in upper atmosphere, the "wet" terms q_o and H_o in Eq.(2) are negligible and Eqs.(8) and (11) become:

$$<M>^2_{dry} = (-77.6*10^{-6}p_o(gT_o)^{-1}<B_o>)^2 \qquad (13)$$

$$\sigma_M^2{}_{dry} = (-77.6*10^{-6}p_o(gT_o)^{-1}\sigma_{Bo})^2 \qquad (14)$$

As an example, using a typical daytime spring radiosounding in Rome, in Fig.2 they are shown, at various heights and for a given constant ratio σ_{Bo}/B_o, the values of Eqs.(13) and (14), resulting that $<M>^2_{dry}>>\sigma_M^2{}_{dry}$.

In microwave earth-satellite links, it has been shown that scintillations are primarily due to the humidity gradient term within the first 3 Km above the ground /3/, that is $(\zeta_o<H_o>)>>(\xi_o<B_o>)$. In this cases, Eqs.(8) and (11) may be reduced to the following expressions:

$$<M>^2_{wet} = (\zeta_o<H_o>)^2 \qquad (15)$$

$$\sigma_M^2{}_{wet} = (\zeta_o \sigma_{Ho})^2 \qquad (16)$$

The Fig.3 shows, for the same radiosounding of Fig.2 and for a given σ_{Ho}/H_o, the values of Eqs.(14) and (15), resulting that $<M>^2_{wet}>>\sigma_M^2{}_{wet}$. From Fig.2 and Fig.3, it is confirmed that $(\zeta_o<H_o>)>>(\xi_o<B_o>)$.

With $<M>^2>>\sigma_M^2$ and if L_o is constant, the Eq.(10) may be approximated by:

$$<C_n^2> \cong a \ F \ L_o^{4/3} <M>^2 \qquad (17)$$

where

$$F = \int_{Sc}^{\infty} p(S)dS \qquad (18)$$

The quantity $F\leq 1$ may be intended as an empirical reduction factor for C_n^2, similar to that proposed in /4/.

In Fig.4 it is shown an evaluation of the reduction factor F in function of the mean shear t_o, normalized to the "critical shear" t_c. The instantaneous shear t varies during the measurements following a normal (dashed line) and log-normal (continuous line) distribution with mean value t_o and standard deviation σ_t. It is clear how, even for $t_o/t_c\leq 1$, some turbulence is present and $F\neq 0$. Appreciable reduction may be found also when $t_o>t_c$ and the reduction is stronger assuming the log-normal distribution. If $\sigma_t=0$, no shear fluctuation is present and F corresponds to the step function $u(t_o/t_c-1)$. Values of 0.1 in troposhere and 0.01 in stratosphere have been supposed for the parameter similar to F /4/, while in the upper troposphere mean values of F equals to 0.15 have been calculated /7/.

It is worth noting that, when $p(S)=0$ for $S\leq Sc$, the Eq.(17) reduces to the Tatarskii's model given in Eq.(1).

In conclusion, the intermittency of turbulence suggests to estimate the mean value $<C_n^2>$ through the models given in Eqs. (7), (10) or (17). As a consequence, from Eq.(17), the scintillation power for e.m. links given by Eq.(3) may be more generally estimated by:

$$\sigma_\chi^2 = a \ 23.2k_0^{7/6}(\sin\alpha)^{11/6}\sum_{i=1}^{m}(z_i^{11/6}-z_{i-1}^{11/6}) \ F(i) \ L_0^{4/3} <M^2(i)> \qquad (19)$$

The reduction factor $F\leq 1$ is independent of frequency and it could be estimated from wind shear measurements or by comparing meteorological data with measurements at radio or optical frequencies. By use of the proposed models, a better agreement between meteorological and e.m. estimates of C_n^2 is to be expected also for long terrestrial and slanth paths.

REFERENCES

/1/ Tatarskii,V.I., 1971, "The effects of turbulent atmosphere on wave propagation", NTIS, Springfield, VA.

/2/ Hill, R.J., Clifford, S.F., and Lawrence, R.S., 1980, J. Opt. Soc. Am., 70, 1192-1205.

/3/ Merlo,U., Fionda E. and Wang,J., 1987, Applied Optics, 27, 2247-2252.

/4/ Van Zandt, T.E., J.L. Green, K.S. Gage, and Clark, W.L., 1978, Radio Science, 13, 919-829.

/5/ Gossard,E.E., Gaynor,J.E., Zamora,R.J, and Neff,W.D., 1985, J. Atmos. Science, 42, 2156-2169

/6/ Desaubies, Y, and Smith, W.K., 1982, Amer.Meteo.Soc., 12, 1245-1259.

/7/ d'Auria,G., Marzano,F.S. and Merlo,U., 1991, Proceedings of 7th I.C.A.P., York (U.K.).
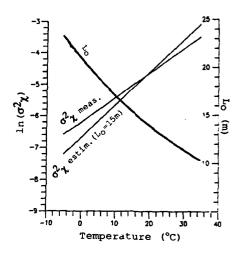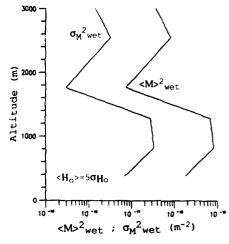
Fig.1 Measured and estimated variance σ^2_χ together with derived L_o in function of the ground level temperature (Rome, 1984).

Fig.2 Profile of the quantities $<M>^2_{dry}$ and $\sigma_M^2{}_{dry}$ for a typical spring daytime radiosounding in Rome.
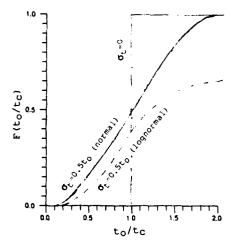
Fig.3 Profile of the quantities $<M>^2_{wet}$ and $\sigma_M^2{}_{wet}$ for the same radiosounding used in figure n.2.

Fig.4 Factor F in function of the mean shear t_o normalized to t_c for normal and lognormal distribution of local shear t.

CLOUD SCATTERING
(GNFAO Session)

On The Variability in Atmospheric Light Scattering Properties with Altitude

Frank W. Gibson
Geophysics Laboratory
Hanscom AFB, MA 01731-5000
(617)377-3092

Angular scattering characteristics of the atmosphere in the visible spectral range reflect optical properties and size distribution of suspended aerosol particles. The altitudinal variability in such properties is germane to investigations involving remote optical probes using inversion techniques. For example, most LIDAR techniques are based on a priori assumptions with respect to the relation between backscatter and extinction, but little in situ data exits on the altitude/range dependence of the scattering phase function.

Because of the dearth of such data a comprehensive analysis of observations with a balloon-borne polar nephelometer was under taken. The flights were conducted in the very clear atmosphere over New Mexico, to 26 km altitude. The instrument configuration facilitated measuring the change in the phase function with altitude along with spectral dispersion characteristics of the volume scattering function. In turn inferences related to aerosol particle size could be made and compared with particle counting observations of other researchers.

The balloon-borne experimental pay-load has been described in previous publications[.] The primary components of the nephelometer were a 150-watt Xenon light source and five stationary photometers, all mounted on a rigid frame so as to measure the scattered light at 15°, 30°, 50°, 100° and 150° from a defined volume (about 250 cm³) of atmosphere. Spectral filters at 0.475, 0.515, 0.660 and 0.745μm in each photometer were used to observe atmospheric scattering in the visible region. The original data demonstrated the vertical distribution of optical properties such as angular volume scattering function, turbidity and polarization. Of particular emphasis in this paper is an investigation of the dissymmetry in angular scattering as a measure of aerosol particle phase function, which together with turbidity, leads to estimates of particle size and concentration. In this connection, the dissymmetry parameter is simply the ratio of observed scattering intensities at 30° and 150°. That is, at a designated altitude,

$$R = \frac{\beta(30°)}{\beta(150°)} = \frac{\sigma_r P_r(30°) + \sigma_a P_a(30°)}{\sigma_r P_r(150°) + \sigma_a P_a(150°)} \tag{1}$$

where β = volume scattering function [cm^{-1}]
σ_r = Rayleigh scattering coeff. [cm^{-1}]
σ_a = Aerosol particle scattering coeff. [cm^{-1}]
P_r = Rayleigh/molecular phase function [sr^{-1}]
P_a = Aerosol phase function [sr^{-1}] .

The Rayleigh phase function is given by

$$P_r(\varphi) = \frac{3}{16\pi}(1 + \cos^2\varphi) \tag{2}$$

and since $P_r(30°) = P_r(150°)$ it renders the scattering from air molecules symmetric with respect to $90°$. Thus, $R > 1$ indicates forward enhanced scattering due to aerosols. The turbidity parameter, the optical analog to the aerosol particle mixing ratio, is defined by the quotient of the aerosol and molecular scattering coefficients,

$$\tau = \sigma_a / \sigma_r \tag{3}$$

A reasonable estimate for this quantity can be determined from the volume scattering function at $50°$, because in very clear air $P_a(50°) \approx P_r(50°)$. Therefore, at $\varphi = 50°$

$$\left(\frac{\beta_t}{\beta_r}\right) -1 = \frac{\beta_a}{\beta_r} = \frac{\sigma_a P_a(50°)}{\sigma_r P_r(50°)} \approx \left(\frac{\sigma_a}{\sigma_r}\right) \tag{4}$$

where $\beta_t = \beta_a(50°) + \beta_r(50°)$ is the measured intensity due to both aerosols and air molecules. Now τ depends upon wavelength, but is independent of scattering angle, because it refers to the scattering in all directions; therefore, equivalent to extinction when absorption is negligible .

Equation (1) can then be exppressed in terms of τ. Moreover, for simultaneous measurements at $\lambda_1 = 0.660$ μm and $\lambda_2 = 0.475$ μm, and if it is assumed that the aerosol phase function is approximately the same at both wavelengths, the respective measurements of R_1 and R_2 at λ_1 and λ_2 can be used to characterize P_a. From Eq. (1)

$$P_a(30°) = 1.3\left(\frac{R-1}{\tau}\right) + R\, P_a(150°) \tag{5}$$

and

$$P_a(150°) = \frac{1.3}{(R_1-R_2)} \left[\left(\frac{R_2-1}{\tau_2}\right)\right] - \left[\left(\frac{R_1-1}{\tau_1}\right)\right] \tag{6}$$

where $P_r(30°) = P_r(150°) = 1.3$, when Eq. (2) is normalized to 4π for convenience. $P_a(150°)$ and, in turn $P_a(30°)$ at either wavelength, can be determined from observable parameters.

The turbidity-wavelength dependence contains information on the particle size distribution. This follows from the Angström empirical formula

$$\beta_a \sim \lambda^{-(\nu-2)} \tag{7}$$

where ν is the exponent in a power-law size distribution, such as, Junge's for natural aerosol in the size range (0.1 $\mu m < \nu < 2\mu m$),

$$\frac{dn}{d(\log \nu)} = Cr^{-\nu} \tag{8}$$

Since $\beta_r \sim \lambda^{-4}$ we get $\tau \sim \lambda^{+(6-\nu)}$ \qquad (9)

and thus

$$v = 6 - \left[\frac{\log(\tau 1/\tau 2)}{\log(\lambda 1/\lambda 2)} \right] \quad . \tag{10}$$

With the exponent v extracted, the number density of particles with radius greater than r can be determined from an expression deduced by Bullrich, et. al[2].

$$N \simeq \frac{\beta_a(\varphi)}{P_a(\varphi)} \; \frac{1}{v} \left(\frac{\lambda}{2\pi r} \right)^v \cdot \left(\frac{2\pi}{\lambda} \right)^2 [cm^{-3}] \quad . \tag{11}$$

Also

$$\frac{\beta_a(\varphi)}{P_a(\varphi)} = \sigma_a = \frac{\tau \, \beta_r(\varphi)}{P_r(\varphi)}$$

is independent of φ, and at a given altitude, is obtained from τ and Rayleigh quantities from the Standard Atmosphere. In order to make comparisons with particle counter measurements of Hofmann and Rosen[3] the number of particles with radius greater than 0.15 μm were converted to aerosol mixing ratio or the number of particles per milligram of air.

Table (1) lists some of the observations for a flight is June 1976, a period approximately two years after the Fuego volcanic eruption.

The principal conclusion is the absence of uniqueness in the relationship between angular scattering and particle size distribution or turbidity, despite the apparent correlation between such parameters and the variability in forward scattering. It is thus difficult to establish a predictable vertical profile for the phase functions even in very "clear" air.

References

1. F.W. Gibson, Appl. Opt 15, 2520 (1976)

2. K. Bullrich, E. de Barry, K. Danger, R. Eiden, G. Hanel, "Research on Atmospheric Optical Radiation Transmission, Report AFCRL-66-212, Hanscom AFB, (1966).

3. D.F. Hofmann and J.M. Rosen, J. Atmos.Sci 38, 168 (1981)

TABLE 1. Scattering Parameters and Particle Number Densities (June 1976)

Altitude (Km)	R_1	τ_1	R_2	τ_2	$P_a(30°)$	$P_a(150°)$	υ	N>15µ (cm⁻³)	N/mg air
4	9.07	4.09	7.05	2.18	7.25	0.518	4.0	5.6	7.1
5	5.5	2.8	4.74	1.87	5.77	0.668	4.7	2.3	2.9
6	2.0	0.81	1.39	0.29	2.08	0.231	2.8	1.9	2.9
7	3.0	3.29	2.4	1.88	1.68	0.297	3.7	3.8	6.6
8	2.2	0.69	1.5	0.24	3.6	0.634	2.8	1.4	2.7
9	1.8	0.3	1.3	0.10	5.03	0.867	2.6	0.6	1.3
10	2.0	0.4	1.4	0.14	4.88	0.833	2.8	0.6	1.5
11	3.3	3.6	2.2	1.20	2.22	0.422	2.6	5.6	14.9
12	2.2	0.9	1.3	0.20	2.26	0.24	2.0	2.0	6.1
13	2.2	1.0	1.3	0.25	2.04	0.37	2.0	1.9	6.3
14	2.1	1.11	1.5	0.37	2.92	0.78	2.6	1.1	4.1
15	2.5	1.47	1.5	0.43	1.79	0.185	2.3	1.5	6.7
16	3.2	2.1	1.7	0.50	2.34	0.305	2.0	2.4	12.2
17	4.0	3.8	2.1	1.0	1.87	0.212	2.0	3.7	19.1
18	4.2	3.5	2.2	1.01	1.94	0.182	2.2	2.4	18.0
19	4.7	3.7	2.3	1.10	1.76	0.098	2.3	2.1	17.8
20	4.4	3.2	2.6	1.20	2.24	0.196	3.0	0.9	9.3
21	3.2	3.8	2.0	1.30	1.41	0.206	2.7	1.1	14.2
22	3.05	3.2	2.2	1.50	1.55	0.234	3.7	0.4	6.1
23	4.4	5.0	3.0	1.60	3.21	0.519	2.5	1.3	22.6
24	2.5	2.8	2.1	1.80	1.31	0.245	4.6	0.2	3.2
25	3.5	5.3	2.5	2.0	1.88	0.367	3.0	0.7	16.4
26	2.6	4.9	1.8	2.0	0.729	0.119	3.2	0.5	14.7

A Total-Direct-Diffuse-Radiometer to Measure the Optical Properties of Aerosols and Clouds

Francisco P. J. Valero, NASA Ames Research Center, Atmospheric Physics Branch
Moffett Field, CA 94035, (415) 604-5510

Peter Pilewskie, NASA Ames Research Center, Atmospheric Physics Branch
Moffett Field, CA 94035, (415) 604-5231

Warren J. Gore, NASA Ames Research Center, Atmospheric Physics Branch
Moffett Field, CA 94035, (415) 604-5533

Standard methods of sun-photometry rely on tracking the sun, a difficult task when faced with long, unattended observations from aircraft or balloon platforms, when payload restrictions apply, and when cloudy conditions may be encountered. We describe here a robust and high precision state-of-the-art radiometer that uses an optical system capable of separating the contribution of the direct (parallel) solar beam from the total hemispherical radiative flux, thereby rendering sun-tracking unnecessary. These measurements are subsequently used to derive aerosol and cloud properties such as optical depth and particle size.

The total-direct-diffuse radiometer (TDDR) has seven narrow-band (10 nm) channels in the visible and near-infrared, centered in regions free from gaseous absorption: 380, 412, 500, 675, 778, 862, and 1064 nm. A shadow-arm occludes the solar disk twice every cycle of oscillation, allowing only the diffusely scattered (F_d) of the total radiation field to reach the optical aperture. On the other hand, when the shadow ring is out of the radiometric field-of-view, the total hemispherical radiation field (F_t) is measured. From the values of F_d and F_t, the direct solar flux, F_s, is obtained.

As with any photometric system, errors arise due to molecular and aerosol forward scattering. However, the manner in which the direct flux is obtained from TDDR measurements permits the forward scattered diffuse component (F_f) to be interpolated; this value is then used to correct the direct solar flux, F_s. Measurements made from several flight levels are used to derive the optical thickness of intervening atmospheric layers. When the TDDR is operated at the ground, the exoatmospheric constants, acquired from Langley method calibrations, are used to determine total

389

atmospheric optical depths.

Because of the continuous shadow arm motion, details in the angular features of the diffusely scattered field can be inferred, giving important information on particle size, shape, and composition. Optical measurements from the TDDR under hazy conditions during the Arctic Gas and Aerosol Sampling Project (AGASP) were inverted to infer particle sizes and results agreed well with *in-situ* measurements. Another result from the TDDR data acquired during AGASP implies that this radiometer might be used to detect "invisible cirrus", a frequent nuisance in sun photometry.

Infrared Backscattering of Pacific Basin Free Tropospheric Aerosols

R.F.Pueschel, G.V.Ferry, and K.G.Snetsinger, Mail Stop 245-4, NASA Ames
Research Center, Moffett Field, CA 94035-1000, Phone: (415) 604 5254.

J.M.Livingston, SRI International, Menlo Park, CA 94025.

During NASA's Global Backscatter Experiment (GLOBE) mission flights in
November 1989, a DC-8 aircraft probed the Pacific Basin free troposphere for
about 90 hours between +72 and -62 degrees latitude, +130 and -120 degrees
longitude, and 8000 and 35000 feet altitude. Aerosols were sampled continuously
in situ by optical particle counters (Particle Measurement System FSSP300 and
ASASP100X) to measure concentration and particle size, and during fourty-eight
10-minute intervals by wire impactors for concentration, size, composition, phase
and shape analyses. The optical particle counters cover the radii range $0.1 < r < 20$
μm; wire impactors extend the range downward to 0.03 μm. The two sampling
methods give identical counting and sizing results in the overlap region $r > 0.1$
μm. Log-normal curves fitted through the data points yield parameters 0.05
μm$< r_g < 0.6$ μm; $12 < N < 64$ cm^{-3}; $1.23 < \sigma < 1.30$.

We analyzed individual particles sampled by wire impactors also for elemental
composition using X-ray energy-dispersive analysis (responsive to elements with
atomic number $A > 10$). Results indicate that about 50% (by number) of particles
contain S, followed by Cl (31%), Si (15%), Na (7%), and Mg (5%). The distribution
of S-containing particles is fairly uniform throughout the free troposphere,
indicating a spatially homogeneous generation process. In contrast, Cl- and Na-
containing particles decrease strongly with altitude, suggesting that they are
generated at or near the earth's surface. The fraction of particles emitting S only,
indicative of $(NH_4)_2SO_4$ and/or H_2SO_4 aerosol, is <20% throughout the free
troposphere, and <5% in the boundary layer.

The measurements of particle number, size, and shape were utilized together
with the assumption of a refractive index corresponding to $(NH_4)_2SO_4$ (to account
for the prevalence of sulfur) in a Mie scattering algorithm to calculate aerosol
extinction and backscatter properties for a range of wavelengths between 0.385
μm and 10.64 μm. Calculations for 29 randomly selected samples yield volume
backscatter coefficients in the visible ($\lambda = 0.525$ μm) between 6×10^{-6} and 1.3×10^{-3}
km^{-1} sr^{-1}. The modal value is about 8.0×10^{-6} km^{-1} sr^{-1}, and the distribution is
skewed toward smaller values. In the infrared ($\lambda = 9.25$ μm), the calculated
backscatter coefficients vary between 5.0×10^{-10} and 5.0×10^{-7} km^{-1} sr^{-1}. The
modal value is 2.0×10^{-8} km^{-1} sr^{-1}.

The calculations indicate that large particles (radii >0.3 μm) contribute more
than 50% to the total backscatter and extinction in the visible ($\lambda = 0.525$ μm), and
almost 100% in the infrared ($\lambda = 9.25$ μm). These results suggest that continuous

measurements of particles with radii > 0.3 μm with an optical particle counter, such as performed during GLOBE with a resolution of 10 sec (2 km) can provide the information necessary to define an optical aerosol climatology of the Pacific Basin free troposphere. The results also suggest that the free troposphere is optically homogeneous over distances between tens and hundreds of kilometers. Figure 1 shows the frequency distribution of backscatter coefficients of 31 background conditions, characterized by homogeneous aerosol concentrations, in the Pacific Basin free troposphere.
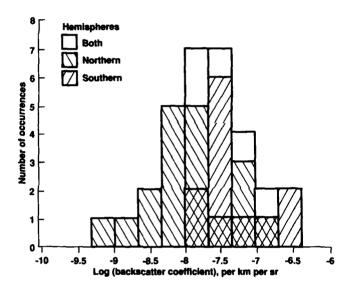
Figure 1: Frequency distribution of infrared (λ=9.25 μm) backscattering coefficients of the Pacific Basin free troposphere in November 1989.

Spectral variability of light scattering by hexagonal ice crystals

A. MACKE and E. RASCHKE
GKSS Forschungszentrum, Institut für Physik
Postfach 1160
D - 2054 Geesthacht
Phone: (04152) 87-1881

1   Introduction

Due to the hexagonal molecular structure of atmospheric ice, cirrus clouds predominantly consist of hexagonal crystals (Hobbs, 1974). These clouds play an important role in the climate system of our planet (e.g. Stephens (1990). Opposite to water droplet and aerosols, the scattering behaviour of ice crystals depends not only on size and wavelength but additionaly on their form and orientation. Even if these particles are randomly oriented in space, the assumption of a spherical shape (Mie-theory) leads to serious differences in the scattering phase function (Wendling et al. 1979). The comparison of different methods for single scattering calculations leads to the conclusion, that using geometrical optics is the best way to consider both shape and orientation of atmospheric ice. Many works present scattering properties for randomly orientation in space or in a horizontal plane (e.g. Coleman and Liou, 1981; Cai and Liou, 1982; Takano and Liou, 1988), but the influence of absorption on the scattering behaviour has always been excluded. The present paper, based on a work from Rockwitz (1989), shows that the classical formula for refraction (Snells law) undergoes some changes, when absorption is included.

The major goal of this work was to provide a tool for radiative transfer and remote sensing works which deal with cirrus clouds.

2   Ray tracing technique

The basic idea of a ray tracing technique is to trace the reflection and transmission procedures of a sufficiently dense beam of rays at a predefined particle. The energy of each individual outgoing ray will be sampled in that solid angle interval which corresponds to the direction of that ray. The subsequent analysis of the entire intervals yields a quantitative image of the particle scattering behaviour. The present technique differs from previous ones mainly due to it's general applicability to any convex crystal shape. The latter is defined by it's corner coordinates in a three-dimensional cartesian coordinate system. Each crystal plane is described by one plane equation, resulting from the plane-belonging corner coordinates. Each ray is described by the intersection of two plane equations, where their normal vectors corresponds to the oscillating-plane of the electric field vectors. The intersection of these three planes is the point, where the ray hits the crystal surface. Once this point and the angle of the incoming ray is known, the direction of the transmitted and reflected ray and its intensity can be calculated by means of Snells Law and Fresnels formulas. The path of the transmitted ray inside the crystal will be traced as long as the number of internal reflections decrease the remaining intensity below a predefined minimum value. Finally, this procedure will be repeated for a large number of equidistant rays, which together overlapp the geometrical crystal-cross-section.

3   Wave propagation in absorbing media

The Maxwell equations for a homogeneous, isotropic, and absorbing media leads to the following formula for the electric field vector:

$$\mathbf{E}(\mathbf{r},t) = \mathbf{E}_0 e^{-\frac{\omega}{c} n\kappa \mathbf{r} \cdot \mathbf{s}} e^{i\omega[\frac{n}{c}\mathbf{r}\cdot\mathbf{s}-t]} \tag{1}$$

The first exponential term describes the wave attenuation along the ray path $l = \mathbf{r}\cdot\mathbf{s}$, the latter one describes the field oscillation. The intensity ω_e of the electric field is proportional to $\mathbf{E}\cdot\mathbf{E}^*$:

$$\omega_e = \omega_{l0} e^{-\chi l}, \qquad \chi = \frac{2\omega}{c} n\kappa = \frac{4\pi}{\lambda}\kappa \tag{2},$$

393

where n and κ describe the complex index of refraction $\hat{n} = n(1 + i\kappa)$ and χ is the absorption coefficient of the media.

To obtain the angle of refraction, Snells law, $\sin\theta_t = \frac{1}{\hat{n}}\sin\theta_i$ must be modified, since θ_t is now complex. The actual direction of refraction is equal to the planes of constant phase in the absorbing media (Born and Wolf, 1970). This leads to a modified law of refraction

$$\frac{\sin\theta_i}{\sin\theta_t} = n^* = n^*(\theta_i),\qquad(3)$$

where the 'refractive index' n^* is no longer a material constant but a function of the direction of the incoming light.

The polarisation state of a light beam is described by two complex field amplitudes $E^t_{0\perp}$ and $E^t_{0\parallel}$ perpendicular and parallel to the plane of incidence, respectively. Since $\hat{n}$ is complex, so are the Fresnel coefficients T and R for reflection and transmission, respectively.

$$T_\perp = |T_\perp|e^{i\tau_\perp}, \quad R_\perp = |R_\perp|e^{i\rho_\perp}, \quad T_\parallel = |T_\parallel|e^{i\tau_\parallel}, \quad R_\parallel = |R_\parallel|e^{i\rho_\parallel}\qquad(4)$$

Amplitude changes and phase shift of the transmitted and reflected components are as follows:

$$E^t_{0\perp} = |T_\perp|E_{0\perp}, \quad E^t_{0\parallel} = |T_\parallel|E_{0\parallel}, \quad \tau = \tau_\parallel - \tau_\perp\qquad(5a)$$

$$E^r_{0\perp} = |R_\perp|E_{0\perp}, \quad E^r_{0\parallel} = |R_\parallel|E_{0\parallel}, \quad \rho = \rho_\parallel - \rho_\perp\qquad(5b)$$

To obtain the scattering phase function it is neccesary to calculate the (real) projection of the Poynting vector onto the actual surface:

$$P^r = \Re(\hat{n})\frac{c}{4\pi}|E^r_0|^2\cos\theta_i, \quad P^t = \Re(\hat{n})\frac{c}{4\pi}|E^t_0|^2\cos\theta_t\qquad(6)$$

The total intensity of the outgoing rays will be normalized to satisfy $\int_0^{2\pi}\int_0^\pi P(\eta,\phi)\sin\eta d\eta d\phi = 4\pi$.

Finally, the phase function due to diffraction (Rockwitz, 1989)

$$P_{diff}(\theta,\epsilon) = \frac{(1+\cos\theta)^2}{8\pi^3}k^2a^2R\int_0^{2\pi}D(kr\sin\theta\sin\Phi)D(krv(\epsilon,\Phi))\sin\theta\cos\Phi d\Phi, \quad D(x) = \frac{\sin(x)^2}{x^2}\qquad(7)$$

has also be included. In this case, r represents the radius of a cylinder comprising the crystal. R is given by the ratio of it's length to radius, k represents the wavenumber, and θ is the scattering angle. Ψ is the integration parameter and denotes the azimuth angle around the forward direction. v is a correction function to account for different projected areas of the crystal.

4 The spectrum of ice

The spectral variation of refraction and absorption of ice can be expressed by the complex index of refraction (Fig. 1a) The tremendous changes in the absorption strength is caused by the different kinds of initiation mechanism. These are electronic transitions in the UV region, vibrational modes between 3 and $6\mu m$, a rotational oscillation at $12\mu m$, lattice vibrations in the far IR and overtones of all these mechanisms in the VIS and near IR. To estimate the most important spectral regions for modelling the single scattering behaviour, the absorption strength was multiplied with the intensity of the downwelling solar and upwelling terrestrial intensity (Fig. 1a) and subsequently discretised (Fig. 1b).
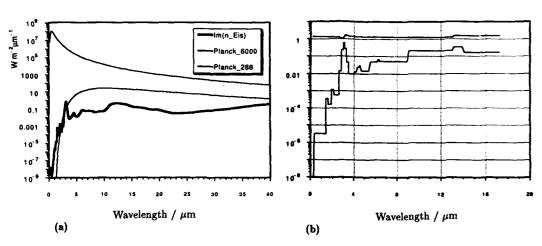
Fig. 1 a) The imaginary part of the refractive index of ice, in comparison with the thermal radiation at 6000K (sun) and 288K (earth). b) The discretised complex refraction index of ice.

5 Results

Fig. 2 shows the three-dimensional scattering phase function (polar diagram) for a horizontal oriented crystal with aspect ratio $L/2a = 120\mu m, \; ?0\mu m$ illuminated from 45°with respect to the horizontal plane. The wavelength of the incoming light is $\lambda = 1.504\mu m$. The corresponding index of refraction is $\hat{n} = 1.291 + i0.00059$.

Sun elevation: 45°(nadir)   Sun elevation: 45°(zenith)
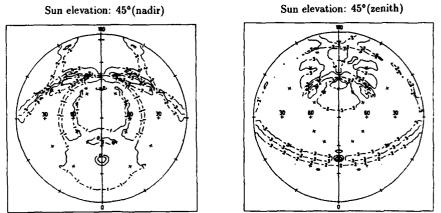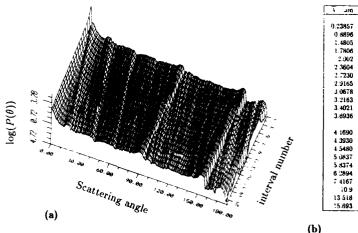
Fig. 2 Scattering phase function $log(P(\eta, \phi))$ for downward scattered (nadir) and upward scattered (zenith) radiation. The light source is located at (45 °,180 °).

The main feature of the polar diagrams above is the azimuthal variability of the scattering behaviour. The nadir-plot shows the expected maximum in forward direction (45°,180°). and the 22°-halo surrounding this peak. Additionaly, the subsuns can be identified as halo-indentations at the same zenithal distance. The circumzenithal arc is formed above the forward scattering direction. Outgoing from the subsuns, the horizontal arc can be recognized.

Fig. 3 shows the spectral variation of the more common two-dimensional phase function $P(\theta)$ for the same type of crystal and illumination as described above.

395

λ μm	$\bar{n}_R$	$\bar{n}_I$	interval
0.23857	1.3665	$1.3083 \cdot 10^{-8}$	1
0.8896	1.3041	$3.1351 \cdot 10^{-6}$	2
1.4805	1.2919	$0.14986 \cdot 10^{-3}$	3
1.7806	1.2892	$0.15618 \cdot 10^{-3}$	4
2.002	1.2736	0.0011619	5
2.3604	1.2423	$0.56473 \cdot 10^{-3}$	6
2.7230	1.1384	0.014138	7
2.9165	1.002	0.22639	8
3.0678	1.2777	0.56933	9
3.2163	1.6094	0.26822	10
3.4021	1.5062	0.0436	11
3.6936	1.408	0.0094987	12
4.1690	1.3495	0.0128	13
4.3930	1.3383	0.023	14
4.5480	1.3422	0.0292	15
5.0837	1.342	0.014229	16
5.8374	1.292	0.048111	17
6.2894	1.3187	0.065333	18
7.4167	1.312	0.05087	19
10.9	1.2136	0.208	20
13.518	1.5314	0.3344	21
15.693	1.5525	0.16109	22

Fig. 3 a) Phase function $\log(P(\theta))$ versus the discretised wavelengths of the incoming light. b) Table of the mean values for wavelength, and real and imaginary part of the refractive index.

The forward scattering intensity is decreasing with increasing wavelength due to diffraction. Since the law of reflection does not allow for any change, each phasefunction shows a reflection maximum at 90°(horizontal crystal surface) and 150°(tilted crystal surfaces). With increasing wavelengths, the halo-peaks move to higher scattering angles (higher refraction) and their intensity becomes less pronounced (higher absorption).

6   Conclusions

Fig. 2 reflects the typical scattering features of hexagonal crystals. The intensity of this submaxima may change due to different crystal types (different aspect ratio), but their location should remain fixed. The above explained discretisation should be regarded as a simple approximation for estimating the spectral variation of the ice crystal scattering behaviour. There are of course many other user-dependent wavelength selections, in particular the spectral sensitivity of satellite- and airborne radiometers or the spectral location of lidar systems. With regard to this applications, the model presented here provides a tool for analyzing active or passive remote sensing measurements.

Finally, the azimuthal variation of the scattering behaviour emphasises the need for a three-dimensional radiative transfer model, particulary if cirrus clouds with horizontal oriented ice crystals are to be considered.

References

Born, M., E. Wolf , 1970 : Principles of Optics, Pergamon Press

Cai, Q., K.N. Liou , 1982 : Polarized light scattering by hexagonal ice crystals: theory, Appl. Optics,21, 3569 - 3580

Coleman, R.F., K.N. Liou , 1981 : Light scattering by hexagonal ice crystals, J. Atmos. Sci.,38, 1260 - 1271

Hobbs, P. , 1974 : Ice Physics, Clarendon Press - Oxford

Rockwitz, K.-D., 1989 : Scattering properties of horizontally oriented ice crystal columms in cirrus clouds, Part 1, Appl. Optics,28, 4103 - 4110

Stephens, G.L., Si-Chee Tsay, P.W. Stackhouse, P.J. Flatau , 1990 : The relevance of the microphysikal and radiative properties of cirrus clouds to climate and climatic feedback, J. Atmos. Sci.,47, 1742 - 1753

Takano, Y., K.N. Liou , 1988 : Solar radiative transfer in cirrus clouds, part I: Single-scattering and optical properties of hexagonal ice crystals, J. Atmos. Sci.,46, 3 - 18

Wendling, P., R. Wendling, H.K. Weickmann , 1979 : Scattering of solar radiation by hexagonal ice crystals, Appl. Optics,18, 2663 - 2671

Measurements of Scattering Matrices of Water Droplets and Ice Crystals

F. Kuik, P. Stammes, M.L. Streekstra and J.W. Hovenier

Free University, Department of Physics and Astronomy, de Boelelaan 1081, NL-1081 HV Amsterdam, The Netherlands, tel. 020-5484114.

1 Introduction

In atmospheric sciences single and multiple scattering of light are important processes. To investigate these processes knowledge about single scattering properties of the particles in the atmosphere is required. For some special types of particles these properties can be computed, but for complex and irregularly shaped particles this is not possible and only experimental determination remains.

Although various types of light scattering experiments have been reported [references are given e.g. by Van de Hulst, 1957, Kerker, 1969, and Bohren and Huffman, 1983], until now only few experimental results for the complete scattering matrix of nonspherical and irregular particles have been published.

Therefore, we designed and built an experimental setup, based on polarization-modulation, for measuring scattering matrices of various types of solid and liquid particles [Stammes, 1989, Kuik et al., 1990]. In this paper a description of the experimental setup is given, some test results for water droplets and preliminary results for water ice crystals are presented, and some of our plans for future work are revealed.

2 Theory of the experiment

The intensity and state of polarization of a beam of light can be completely specified by its so-called Stokes vector $\mathbf{I} = \{I, Q, U, V\}$ [cf. Van de Hulst, 1957, sect. 5.12]. Here I represents the total intensity, Q and U are related to the linear polarization, and V to the circular polarization. The scattering process can now be described by a transformation of the Stokes vector of the incident beam into the Stokes vector of the scattered light, which depends on the scattering angle θ. Here we assumed azimuthal symmetry. The scattering plane is the reference plane for the Stokes vectors.

The Stokes vector of the scattered light is obtained by multiplying that of the incident beam by the (4×4) *scattering matrix* $\mathbf{F}(\theta)$, the elements of which contain all the optical information about the scatterers. For randomly oriented particles having a plane of symmetry the scattering matrix has the form

$$\mathbf{F}(\theta) = \begin{pmatrix} F_{11}(\theta) & F_{12}(\theta) & 0 & 0 \\ F_{21}(\theta) & F_{22}(\theta) & 0 & 0 \\ 0 & 0 & F_{33}(\theta) & F_{34}(\theta) \\ 0 & 0 & F_{43}(\theta) & F_{44}(\theta) \end{pmatrix} \tag{1}$$

where $F_{12}(\theta) = F_{21}(\theta)$ and $F_{34}(\theta) = -F_{43}(\theta)$ [cf. Van de Hulst, 1957, sect. 5.22]. For various kinds of particles we want to determine experimentally the six independent scattering matrix elements occurring in Eq. (1).

In the experimental setup several optical components are used, such as linear polarizers, quarter-wave plates and an electro-optic modulator. They all influence the state of polarization of a beam of light as it crosses the component. Mathematically, this can be described by multiplying the Stokes vector of the incident beam by a so-called (4×4) *Mueller matrix* [Shurcliff, 1962], to obtain the Stokes vector of the transmitted beam. The Mueller matrix of an optical component depends on its orientation relative to some reference plane. This orientation is given by the angle γ, defined as the angle between the scattering plane (here the horizontal plane) and the principal axis of the component. When a Mueller matrix is known for $\gamma = 0°$ it can be computed for any other γ [Shurcliff, 1962].

In the experimental setup we used an electro-optic modulator to modulate the polarization of the incident beam. When the voltage over the crystal in the modulator is varied sinusoidally in time with an angular

frequency ω, the intensity component of the scattered light will consist of parts varying in time as $\sin \omega t$, $\cos 2\omega t$, etc. [see e.g. Hunt and Huffman, 1973]. By using lock-in detection these components can be separated. In our setup the $\sin \omega t$ and $\cos 2\omega t$ components plus a constant part in the detected signal are sufficient to determine all relevant elements of the scattering matrix.

Let the Stokes vector of the beam leaving the light source be $\mathbf{I}_L$ and that of the scattered light reaching the detector $\mathbf{I}_D(\theta)$. Then $\mathbf{I}_D(\theta)$ is obtained by multiplying $\mathbf{I}_L$ by all Mueller matrices of the components in the optical train, including the scattering matrix,

$$\mathbf{I}_D(\theta) = \mathbf{A}_{\gamma_A} \mathbf{Q}_{\gamma_Q} \mathbf{F}(\theta) \mathbf{M}_{\gamma_M} \mathbf{P}_{\gamma_P} \mathbf{I}_L \qquad (2)$$

where $\mathbf{A}$, $\mathbf{Q}$, $\mathbf{M}$, and $\mathbf{P}$, are the Mueller matrices of the analyzer, quarter-wave plate, modulator and polarizer, respectively, $\mathbf{F}(\theta)$ is the scattering matrix, and γ_A, γ_Q, γ_M, and γ_P are the orientation angles of the corresponding components. In our experiment we use four different combinations for the orientation angles $\gamma_A, \gamma_Q, \gamma_M$, and γ_P, which suffices to determine all relevant scattering matrix elements from four measurements of I_D, i.e. the intensity reaching the detectors. In Table 1 these four combinations for the orientation angles are given, along with the corresponding expressions for I_D, following from Eq. (2).

Table 1 Detected intensity I_D for four different combinations of orientation angles of the polarizing components of the setup. In combinations 1, 2 and 3 the quarter-wave plate is not used.

combination	γ_P	γ_M	γ_Q	γ_A	$I_D = $ constant $\times$
1	$0°$	$-45°$	–	$45°$	$F_{11} - F_{34} \sin \phi + F_{12} \cos \phi$
2	$0°$	$-45°$	–	$0°$	$F_{11} + F_{21} + (F_{12} + F_{22}) \cos \phi$
3	$45°$	$0°$	–	$45°$	$F_{11} - F_{34} \sin \phi + F_{33} \cos \phi$
4	$45°$	$0°$	$0°$	$45°$	$F_{11} - F_{44} \sin \phi + F_{43} \cos \phi$

3   The experimental setup

A schematic diagram of the experimental setup of the light scattering experiment is shown in Figure 1. The light source is a He-Ne laser producing a linearly polarized beam with wavelength $\lambda = 632.8$ nm.
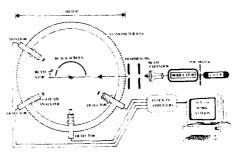
Figure 1   Schematic diagram of the experimental setup as seen from above.

The laser beam passes a linear polarizer, a modulator (Pockels cell, Gsänger GmbH, model LM 0202), a beam expander (optionally) and two iris diaphragms. The light is then scattered by a vertical jet of aerosol particles at the scattering centre, and subsequently reaches the detectors after it has passed a quarter-wave plate (optionally) and an analyzer. One detector is used to monitor the intensity of the scattered light at a fixed angle. If fluctuations in the intensity occur during the measurement (caused by fluctuations in the jet of aerosol particles, or for any other reason), they can be corrected for using the signal measured by the monitor detector. Three detectors are used for measuring the scattered light as a function of the

scattering angle. The detectors are mounted on trollies that run over a goniometer ring. On the goniometer ring we can read the scattering angles at which the measurements are performed. The detected signals are led to lock-in amplifiers where they are separated as mentioned in sect. 2, and then stored in a computer. The raw data are reduced employing a SUN 3/60 workstation and the results are two or three scattering matrix elements, depending on which combination of Table 1 is used. Opposite all detectors is a black screen to avoid measuring background light. A detailed description of the experimental setup has been given by Stammes (1989).

4 Results

4.1 Test measurements for water droplets

The experimental setup was tested using measurements for several kinds of spherical particles [Stammes, 1989]. Here we will only show test results for six measured scattering matrix elements for an ensemble of water droplets produced by a nebulizer (TSI Inc. atomizer model 9302A). The experimental results were compared with Mie computations for water spheres ($m = 1.332$) having a log-normal size distribution with an effective radius $r_{eff} = 0.75$ μm and an effective standard deviation $\sigma_{eff} = 0.45$ [Hansen and Travis, 1974]. The results are depicted in Figure 2. From this figure it can be seen that the experimental results for water
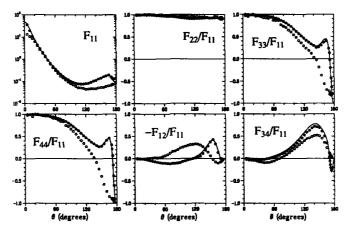
Figure 2 Scattering matrices of ensembles of water droplets and ice crystals. The measured data for the water droplets are denoted by ● and those for the ice crystals by o. The solid curves are computations for a log-normal size distribution of water spheres.

droplets agree well with the computed results, although there is a slight discrepancy for the ratio F_{22}/F_{11}, especially at backward scattering angles, since for spheres F_{22}/F_{11} should be equal to 1 for all θ. We do not know the exact reason for this deviation, but some preliminary calculations [Wauben, 1990] showed that it could be due to multiple scattering effects.

4.2 Measurements for ice crystals

An ice crystal generator was designed and built to produce a jet of ice crystals. The principle is very simple (see Figure 3). In a Dewar liquid nitrogen is boiling. The nitrogen vapour rises and water vapour is added just below the scattering centre. On travelling the last 30 cm to the scattering centre the water vapour turns into micrometer sized ice crystals. Some preliminary experimental results for ice crystals are also shown in Fig. 2. We looked at other experimental results for water ice crystals [references given by Stammes, 1989] and found little agreement. The reason for this is that probably the size distribution and shapes of the crystals we used differ from those in the other experiments. However, for our measurements we checked
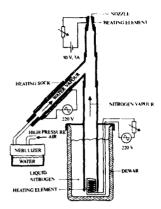
Figure 3 Schematic picture of the ice crystal generator.

certain inequalities which theoretically hold for the type of scattering matrix we use [Hovenier et al., 1986] and found complete agreement.

5 Conclusions and future work

Our experimental setup is suitable for measuring *all* relevant scattering matrix elements of jets of solid and liquid aerosol particles. This is very important, as six scattering matrix elements provide much more information about the scatterers than just the F_{11} and F_{12} elements.

In many planetary atmospheres (including our own) ice crystals are present. However, very few experimental data on scattering matrices of ice crystals are available, and therefore a start has been made to fill this gap. First results were presented, but many improvements are needed before we can really control the sizes and shapes of the crystals. We are planning to extend our research to NH_3 ice crystals.

Exact theoretical computations to obtain scattering matrices of irregularly shaped particles are very difficult or in many cases even impossible. However, we can compare measured data with computed results for size distributions of spheres, spheroids, finite and infinite cylinders. These computations are usually very expensive, and to do them properly we need accurate information on the sizes and shapes of the particles. At this moment we are investigating several techniques for determining the particle sizes and shapes (e.g. digital image processing and diffraction techniques) to find out which method is best for our setup.

References

Bohren, C.F., Huffman, D.R., *Absorption and Scattering of Light by Small Particles*, Wiley & Sons, New York, 1983

Hansen, J.E., Travis, L.D., "Light Scattering in Planetary Atmospheres", Space Sci. Rev. **16**, p.527, 1974

Hovenier, J.W., van de Hulst, H., van der Mee, C.V.M., "Conditions for the Elements of the Scattering Matrix", Astron. Astrophys. **157**, p.301, 1986

Hulst, H.C. van de, *Light Scattering by Small Particles*, Wiley & Sons, New York, 1957 (also Dover, 1981)

Hunt, A.J., Huffman, D.R., "A New Polarization-modulated Light Scattering Kerker, C.F., *The Scattering of Light and other Eletromagnetic Radiation*, Academic Press, New York, 1969

Kuik, F., Stammes, P., Hovenier, J.W., "Experimental Determination of Scattering Matrices of Water Droplets and Quartz Particles", submitted to Appl. Opt. 1990

Shurcliff, W.A., *Polarized Light, Production and Use*, Harvard Univ. Press, Cambridge, Mass./Oxford Univ. Press, London, 1962

Stammes, P., *Light Scattering Properties of Aerosols and the Radiation inside a Planetary Atmosphere*, Ph.D. Thesis, Free University, Amsterdam, 1989

Wauben, W.M.F., Private communication, 1990

Optical Properties of Hexagonal Ice Crystals: Model Calculations

Michael Hess and Matthias Wiegner
Meteorologisches Institut der Universität München
Theresienstraße 37, D-8000 München 2

Introduction

Because of their significance to climate, cirrus clouds and contrails are important topics of actual meteorological research. However, the dependence of radiative properties of cirrus clouds on their microphysical parameters is not yet understood completely. The radiative properties of ice crystals are required for radiative transfer calculations to study the impact of ice clouds, and for interpretations of lidar and radiometer measurements.

In this paper, we briefly describe our model for calculating optical properties of ice crystals and the extent of our data library containing these properties. Finally, we show an example of our results.

We consider two crystal shapes (hexagonal plates and columns), six crystal sizes with varying aspect ratios, and 14 wavelengths between $\lambda = 0.355$ μm and $\lambda = 3.7$ μm. Our results, including extinction-, scattering-, and absorption coefficients σ_e, σ_s, and σ_a respectively, single scattering albedo ω_o, phase function $p(\theta, \phi)$, asymmetry parameter g, and lidar ratio S, constitute a comprehensive base for climate modeling and remote sensing. Furthermore, they can be used to find new approaches to infer microphysical properties from remote sensed data.

Model

We use a geometrical optics model to calculate the Stokes-vector of singly scattered radiation. The model is based on Wendling et al. (1979) with the following extensions:

- the ice crystals may be oriented randomly in a horizontal plane (Strauss, 1989).

- diffraction is exactly calculated for hexagonal particle cross sections after Takano et al. (1983).

- absorption of radiation inside the crystal is determined by means of an approximation taking into account the absorption along the photon paths. The effects of the imaginary part of the refractive index on Fresnel's formulae, Snell's law, and the absorption coefficient are neglected.

- the state of polarization of the scattered radiation is calculated.

Hexagonal columns and plates are used as particle shapes. The incident radiation can be unpolarized to simulate solar radiation, or linearly polarized for lidar applications. The wavelengths, zenith angle ϑ_o of incident radiation, and the calculated parameters for both applications are listed in Table 1. Information on the state of polarization is given as 'depolarization of backscattered radiation', defined as

$$\delta = \frac{I_s}{I_p}$$

or as 'degree of linear polarization'

$$P(\theta, \phi) = \frac{(I_s - I_p)}{(I_s + I_p)}$$

respectively, where I_s and I_p are scattered intensities polarized perpendicular (s) and parallel (p) to the reference plane.

Table 1: *List of Model Input and Output Parameters*

incident radiation	laser	sun
wavelength in [nm]	355, 532, 694, 1064	423, 535, 630, 780, 850, 873, 1015, 1555, 1680, 3700
particle orientation	random and horizontal	random and horizontal
zenith angle of incident radiation for horizontal orientation	0°	$0° < \vartheta_o < 90°$ $\Delta\vartheta = 5°$
calculated optical properties	$\sigma_e, \sigma_s, \sigma_a, \omega_o, g,$ S, δ	$\sigma_e, \sigma_s, \sigma_a, \omega_o, g, p(\theta, \phi),$ $P(\theta, \phi)$

Table 2 contains the particle sizes in μm where a is the crystal radius and b the crystal length. The aspect ratios are chosen after Auer and Veal (1970).
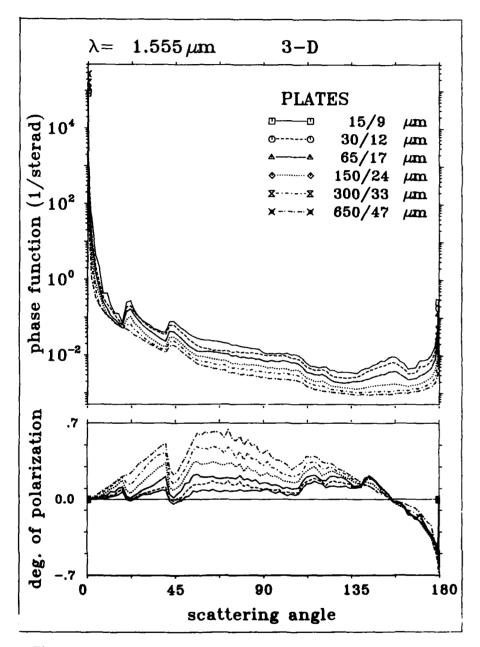
Figure 1: *Phase function and degree of polarization for plates at different sizes and aspect ratios*

403

Table 2: *Sizes and Aspect Ratios of Hexagonal Crystals Used for Calculation*

		1	2	3	4	5	6
columns	a	10	22	41	60	80	110
	b	30	60	130	300	600	1300
	b/2a	1.5	1.4	1.6	2.5	3.8	5.9
plates	a	15	30	65	150	300	650
	b	9	12	17	24	33	47
	b/2a	0.3	0.2	0.13	0.08	0.055	0.036

Results

Only one example of our results can be presented here. Fig. 1 shows the phase function and the degree of linear polarization at $\lambda = 1.555$ μm for six platelike crystals (according to Table 2) in random orientation. The smaller particles show all of the well-known features of the phase function of hexagonal particles, i.e. the 22°- and 46°-halo and the enhanced backscatter near $\theta = 150°$ which is due to multiple internal reflections. Additionally, the smallest plate exhibits the relative extrema of a broad diffraction pattern. With increasing particle size, absorption effects become significant. They smooth out all parts of the phase function which are related to long photon path lengths inside the crystal, in particular the 22° halo and the relative maximum near $\theta = 150°$. Similarly, the point of neutral polarization corresponding to the double refraction of the 22° halo, vanishes.

The single scattering albedo at $\lambda = 1.555$ μm varies between 0.85 and 0.97 for plates and between 0.72 and 0.97 for columns. Absorption is significant for all wavelengths larger than 1 μm.

The asymmetry parameters generally increase with wavelength. In the visible region, this effect is attributable to the change of the halo position. In the IR region, the reason is the reduced sideward scattering due to relatively strong absorption.
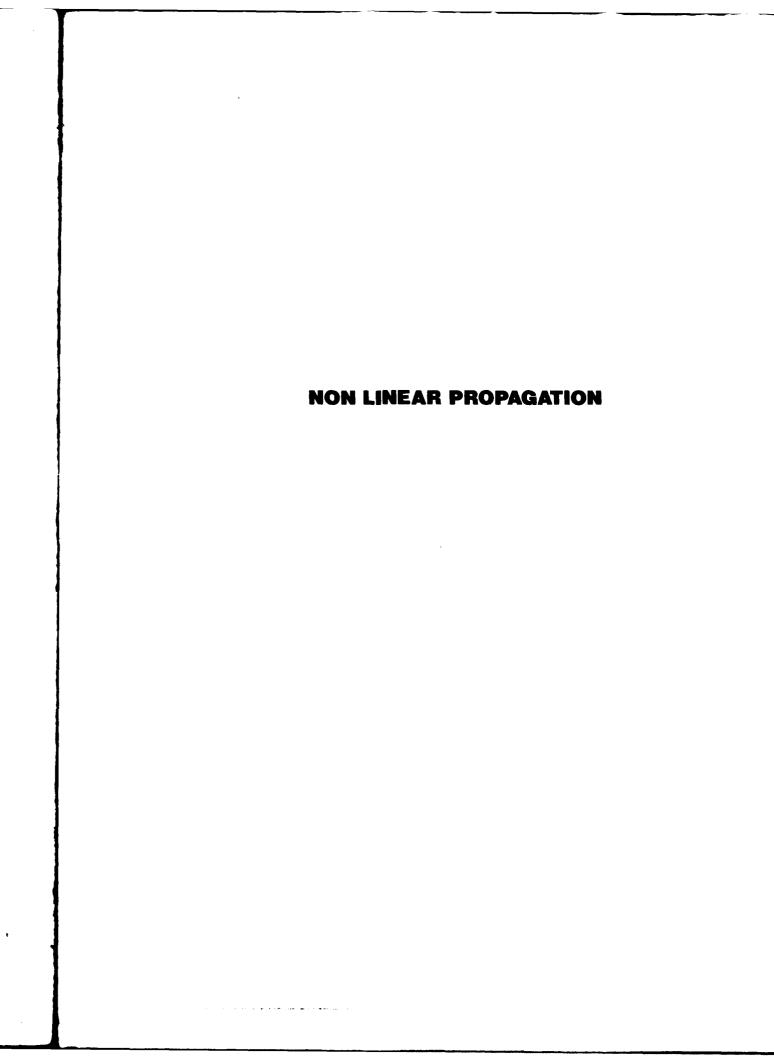
References

Auer, H.A. and D.L. Veal (1970): *The dimensions of Ice Crystals in Natural Clouds*, J. Atm. Sci., 27, 919-926

Strauss, B. (1989): *Modellierung der Einfachstreuung an hexagonalen Eiskristallen - mit besonderer Berücksichtigung der horizontalen Ausrichtung der Eiskristalle*, Diplomarbeit für Meteorologie, Universität München, 79 pp

Takano, Y. and S. Asano (1983): *Fraunhofer Diffraction by Ice Crystals Suspended in the Atmosphere*, J. Met. Soc. Jap., 61, 289-300

Wendling, P., R. Wendling and H.K. Weickmann (1979): *Scattering of solar radiation by hexagonal ice crystals*, Appl. Opt., 18, 2663-2671

NON LINEAR PROPAGATION

THERMAL NONLINEAR OPTICS OF WATER AEROSOLS

V.E. Zuev,Yu.E. Geints, A.A. Zemlyanov, A.M. Kabanov,
V.A. Pogodaev

Institute of Atmospheric Optics SB USSR Acad. Sci.,
1, Akademicheskii avenue, Tomsk, 634055 USSR
(INVITED)

The paper presents the investigation results of interaction of the intensive laser radiation with the absorbing water aerosol and the optical aftereffects of the interaction. The analysis of regularities of the intensive laser radiation propagation at the atmospheric paths containing water aerosols (fog, drizzle, rain, wet haze) /1/ is carried out in the paper.

A large set of kinetic and dynamic processes occurring during an interaction between the high-power light field and the water aerosol absorbing particles with 1 to 10^3 μm particle-size range, pulsed and continuous operation regime of the laser sources with intensity from 10^4 to 10^9 W/cm^2 in the interaction region is studied. The experiments are carried out and the physical models of interaction are constructed. Matematical statements of the problems and their numerical solutions are realized on the basis of these models providing the data obtained on the more essential process characteristics (metastable superheating, boiling kinetic, gas dynamics of two-phase mixture explosive broadening, supercritical state, vaporization of small-size particles with high temperature, heterogeneous condensation, light-induced deformations, droplet relaxation oscillation).

The model of the droplet explosion under the radiation effect with $\lambda = 10.6$ μm wavelength is developed. For homogeneously absorbing particles the model determines quantitative relationships between the main explosive vaporization characteristics (time of explosion, explosive vaporization degree, fragmentation degree) and the laser radiation parameters. Appropriate models for the average-size droplet and large-size drop.

let aerosols (Fig.1) indicate the relationship between the energy being absorbed and distortion dynamics.

The models of polydispersed extinction coefficients at the wavelength λ =10.6 μm are constructed for the conditions of the nonlinearity processes of the droplet spectrum tuning during their explosive and regular vaporization and fragmentation as well. Strong dependence is determined for the early after-explosion stage of the extinction coefficient temporal evolution on the laser radiation energetic and time parameters as well as the initial aerosol microstructure. It is shown that under the long-term energy release at the late stage of the process the extinction coefficient level is weakly susceptible to the type of the initial particle spectrum and it is close to the value being determined by the water vaporization stationary regime. In the case of the small-size droplet and average -size droplet aerosols the decrease of the extinction coefficient is observed. The extinction coefficient increases in the case of large-size droplet aerosol.

For the visible range wavelengths in conditions of the droplet distortion under the radiation effect with λ = 10.6 μm and with the heating rate more than $10^9 K \ s^{-1}$ the small-size droplet fog effect is observed for the whole time interval of the process.

The paper determines the dependences of the laser sounding beam scattering signals in the region of interaction between the high-power laser pulse and aerosol (Fig,2) and the parameters of the acoustic pulses generated with this region on the initiating beam energy density in the medium local region.

For the purpose of interpretation of a large set of the experimental data of the CO_2-laser pulsed radiation transmission at the natural surface paths (Fig.3) the model of the focused beam propagation in the aerosol medium and in the different optical weather conditions is constructed. High efficiency of the use of the pulse-frequency radiation beams at the surface paths is shown for conditions of the manifestation of the thermal nonlinear effects in aerosol and an optical breakdown in the large-size fraction of the background aerosol. The role of humidity for the laser flash formation in hazes is shown.
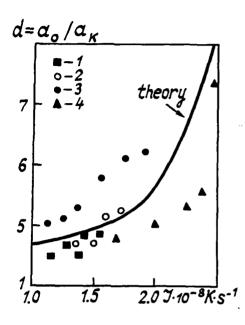
Fig.1. Comparison of the experimental data /2/ with the theoretical dependence of the fragmentation degree of water droplet $d = a_0/a_K$ (a_K is the average size of fragments being formed) with the different initial radius a_0 =10(1); 20(3) and 25 μm (4) on their heating rate with the laser radiation.
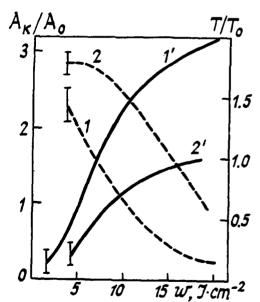
Fig.2. The dependence of transparency T/T_0 (solid line) and the signals of scattering A_K/A_0 (dashed line) on the energy density W of the CO_2-laser initiating pulse λ =10.6 μm. Measurements have been carried out at the sounding beam wavelength in the visible range in 3 μs after the beginning of the CO_2-laser pulse effect. Aerosol medium – monodispersed aerosol $\bar{a}_0$=2.7 μm (1,1'); polydispersed aerosol (2,2').

409
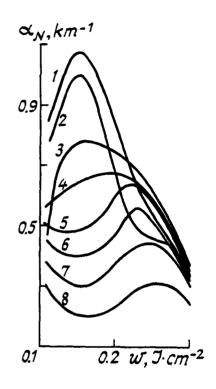
Fig. 3. The dependence of the radiation nonlinear extinction
coefficient α_N on the radiation energy density w
in the beginning of the paths. The curves represent
different meteorological conditions: 1,2 - rain, aero-
sol extinction coefficient of the unperturbed atmos-
phere α_0 =0.8 and 0.73 km^{-1}, respectively; 3,4 - snow-
fall (α_0 =0.61 and 0.53 km^{-}); 5,6 - winter haze(α_0=
=0.42 and 0.32 km^{-1}); 7,8 - fog haze (α_0=0.22 and
0.12 km^{-1}).

References

1. Zuev V.E., Zemlyanov A.A., Kopytin Yu.D. Nonlinear Atmosphe-
ric Optics. - L. Gidrometeoizdat, 1989. - 253 p.

2. Dennis R.A., Armstrong J.G. Explosive vaporization of aero-
sol drops under irradiation by CO_2-laser beam. - Appl. Opt.,
1987, v.26, N 23, p. 533-536.

THE TRANSFORMATION OF EFFECTIVE PARAMETERS
OF INTENSE LASER BEAMS ON ATMOSPHERIC PATHS

V. E. Zuev, A. A. Zemlyanov, A. V. Martynko, S. N. Sinev

Institute of Atmospheric Optics SB USSR Acad. Sci.

Tomsk, 634055, U. S. S. R.

This paper investigates the regularities of transformation of laser beams effective parameters (effective radius, vector of beam center, effective radius of phase front curvature and effective radius of coherence) on inhomogeneous atmospheric paths. The refractive effects in transparent atmosphere are investigated. The nonlinear effects in aerosols were described in / 1 /.

The equations connecting the laser beams effective parameters with integral characteristics of nonlinear medium are formulated. The cases of realization of equation exact solutions are presented. The paper shows that nonlinear refractive channel transforms the effective parameters like an abberation optical system.

The correlations connecting the laser beam effective parameters in nonlinear medium with the characteristics of inhomogeneous path and the initial beam parameters were obtained.

The formulas for the limiting angular divergence and the limiting diviation of laser beam center were also obtained. In case of strong defocusing nonlinearity the effect of similarity for the self-action of collimated laser beams with different spatial structure and media with different mechanisms of nonlinearity was determined. The results are presented in Fig. 1 for the nonlinear medium with stationary wind flow and the laser beams with initial distribution of intensity $I(x, y, 0) = I_0(m)\exp(-(x/R_0)^m - (y/R_0)^m)$, where parameter $m = 2, 4, 6 \ldots$, R_0 is the initial radius of Gaussian beam on e^{-1} level, $I(m)$ is the maximum intensity, which is selected to obtain an equal power for the beams with different structure.

For the problem of partially coherent beams self-action it was shown that weak initial fluctuations of intensity and multimode structure of laser beam don't contribute greatly in nonlinear divergence. The law of transformation of spatial coherence effective radius along the distance was obtained.

As is stated in the paper, the relationship of spatial coherence effective radius to the effective radius of radial tube around the "diffractive" ray is statistically invariant. In weak defocusing nonlinear medium with turbulent fluctuation of dielectric constant increase of coherence radius near the beam axis as compared with the coherence radius in linear random inhomogeneous medium was defined.

In the case of long pulse thermal defocusing along vertical atmospheric path the asymptotic regimes of directivity diagram formation were established. The results are presented in Fig.2. The limiting angular divergence in regime of strong nonlinear distortions is determined by season and initial characteristics of laser beam. In case of weak and moderate nonlinear distortions it also depends on coherent properties of the beam and the parameter which characterizes the inhomogeneity of the atmospheric path.

The transformation of the effective parameters of partially coherent beams in the presence of kinetic cooling was investigated. The worsening of spatial coherence is able to change the typical for kinetic cooling self-focusing to defocusing.

References

1. V. V. Zuev, A. A. Zemlyanov, Yu. D. Kopytin and A. V. Kuzikovskii , High Power Laser Radiation in Atmospheric Aerosols, D. Reidel Publ. Comp. Holland, 1985.
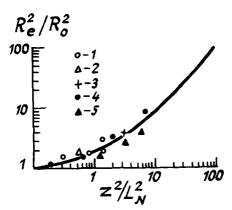
Fig.1. The similarity effect for relative
effective radius of the beams: $m = 2$ (1,4),
$m = 4$ (2,5), $m = 6$ (3) ; L_n - self-action

length / 1 /, Z - distance. Points are based
on numerical results of different authors.
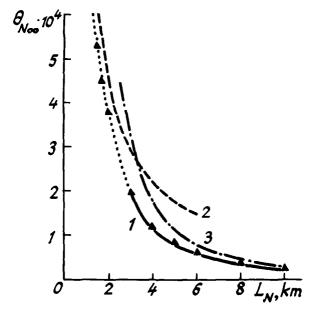
Fig.2. The dependence of nonlinear part $\theta_{n\infty}$ of

limiting angular divergence of coherent laser
beam (initial angular divergence $\theta = 2.08 \ 10^{-6}$):
calculation by transfer equation method (solid)
and extrapolation (dotted) curve (1);asymptotics
of strong (2) and weak (3) nonlinear distortions;
Δ-approximation dependence;

413

Superheating Phenomena in Pulsed Laser-Irradiated Micron-Sized Droplets*

R. L. Armstrong
Physics Department, New Mexico State University
Las Cruces, NM U.S.A. (505) 646-3832

Atmospheric laser propagation is influenced by interactions with molecular and aerosol constituents; however, aerosol interactions often dominate. In this presentation we describe recent studies of absorbing micron-sized droplets (e.g., water droplets) interacting with intense pulsed laser radiation.

When a laser beam irradiates an absorbing droplet, localized heating occurs within regions of high internal field intensity. Conductive heat transfer may not efficiently remove this heat; moreover, in the absence of heterogeneous nucleation conventional boiling is suppressed. Under these conditions portions of the droplet may become highly superheated.

Laser-irradiated droplet superheating exhibits several noteworthy features.[1-5] Source function inhomogeneities generate characteristic droplet explosion patterns. Droplet disruption occurs only if the laser fluence exceeds a well-defined threshold. Finally, delays which may occur in the initiation of superheating explosions are predicted by homogeneous nucleation theory.

Previous superheating measurements using a short-pulse ($0.4\mu s$) CO_2 laser revealed the complex temporal behavior of droplet disruption. These measurements have been extended using short-pulse and long-pulse (effective width $10\mu s$) CO_2 lasers, to times following laser excitation > the longest period surface oscillation.[3] As a result, we have demonstrated the existence of a second superheating threshold. Disruption of superheated droplets occurs in two distinctive modes depending on laser fluence: a low-fluence deformation mode characterized by subsequent droplet oscillations and minimal mass loss; and, a high-fluence disintegration mode where the droplet fragments into numerous microparticles and vapor.

A second noteworthy finding is the first observation of a droplet surface instability following high-irradiance, short-pulse (10nsec) Nd:YAG laser excitation.[4] The instability is conjectured to occur when the laser irradiance exceeds a well-defined threshold. Additional evidence for this follows from the fact that superheating fluence thresholds are similar for both CO_2 and Nd:YAG excitation ($\sim1-5$ J/cm^2); however instability is not seen following CO_2 excitation whose irradiance ~50 times smaller than the Nd:YAG laser.

Initiation of the instability $\sim$ 50 nsec after termination of the Nd:YAG pulse results in the appearance of large amplitude,

small scale roughening of all or part of the droplet surface and in the swelling of the droplet volume by as much as 50%. The surface appears rough down to the smallest resolvable scale. At longer times (~ a few μsec) the instability disappears. The fate of the droplet depends both on fluence and droplet absorption (see Fig. 1). For weakly absorbing droplets (absorption index <10^{-4}) the instability threshold lies below both deformation and disintegration thresholds. Here, the droplet exhibits the unique behavior of initially becoming unstable and completely recovering at later times. As absorption is increased, the instability threshold first exceeds the deformation threshold, and for the highest absorption studied, coincides with the disintegration threshold. Thus, following initiation and decay of the instability, the droplet undergoes long-term oscillations (instability threshold greater than deformation threshold) or violently explodes (instability threshold coincident with disintegration threshold).

The experimental arrangement, described in Ref. 1, is summarized here. A stream of ~ 30μm radius droplets ejected from a vibrating-orifice generator is irradiated by a pulsed CO_2 or Nd:YAG laser. Following a selectable delay time the irradiated droplets, back-illuminated by an air-plasma (duration ~20 μsec) produced by another Nd:YAG laser, are viewed or photographed through an optical microscope.

Figure 1 illustrates the behavior of 24μm radius ethanol droplets 40 μsec after irradiation by a long-pulse CO_2 laser. No instability is seen following excitation by this laser. The oscillatory behavior is clearly visible for a fluence exceeding the deformation threshold and droplet explosion occurs when the fluence coincides within the disintegration threshold. Deformation and disintegration thresholds may be unambiguously distinguished only for delay times > the longest period surface oscillation.[5] A delay time of 40 μsec satisfies this criterion for the photographs in Fig. 1. Figure 2 plots the threshold for 24 μm radius droplets of several liquids. A qualitative explanation of these curves can be given in terms of thermal conductivity, surface tension, and thermally-induced optical inhomogeneities.

Figure 3 exhibits photographs of Nigrosin-dye doped water droplets irradiated by a Nd:YAG laser. The photographs, taken ~1 μsec after laser excitation, show the fully developed instability (Fig. 3b) and, for lower irradiance, a number of homogeneously nucleated vapor bubbles but no instability (Fig. 3d). Bubbles appear promptly within ~20 nsec, near the end of the exciting laser pulse (Figs. 3a, 3c). Below the instability threshold the bubble growth rate is in agreement with classical bubble theory.[7] Above this threshold the instability develops rapidly within the next 40 nsec. Figure 4 shows the various thresholds as a function of absorption index. A qualitative understanding of the instability may be based on the work of Landau.[8]

1. R. G. Pinnick, A. Biswas, R. L. Armstrong, S. G. Jennings, J. D. Pendleton, and G. Fernandez, Appl. Opt. 29, 918 (1990).
2. B.-S. Park, A. Biswas, R. L. Armstrong, and R. G. Pinnick, Opt. Lett. 15, 206 (1990).
3. H. Latifi, J.-G. Xie, T. E. Ruekgauer, R. L. Armstrong, and R. G. Pinnick, submitted.
4. J.-G. Xie, T. E. Ruekgauer, R. L. Armstrong, and R. G. Pinnick, submitted.
5. C. F. Wood, D. H. Leach, J.-Z. Zhang, R. K. Chang, and P. W. Barber, Appl. Opt. 27, 279 (1988).
6. H. M. Lai, P. T. Leung, K. L. Poon, and K. Young, J. Opt. Soc. Am. B6, 2430 (1989).
7. A. Prosperetti and M. S. Plesset, J. Fluid Mech. 85, 349 (1978).
8. L. D. Landau and E. M. Lifshitz, Fluid Mechanics (Pergammon Press, New York, 1959), p. 479; D. L. Frost and B. Sturtevant, J. Heat Transfer 108, 418 (1986).

Fig. 1. Time-resolved photographs of 24 μm radius ethanol droplets irradiated by a pulsed CO_2 laser. Energy sequence for droplets irradiated by a long pulse laser (effective pulse duration ~10μsec) at long time (40 μsec after droplet leaves the beam) showing deformation and disintegration thresholds.

Fig. 2. Deformation and disintegration thresholds, F_{def} and F_{dis}, of micron-sized droplets irradiated by pulsed CO_2 lasers plotted versus imaginary refractive index: a) F_{dis} for long-pulse, b) F_{dis} for short-pulse laser, c) F_{def} for long-pulse laser, d) F_{def} for short-pulse laser.

Fig. 3.   Photographs of 52 μm radius absorptive dye-doped water droplets (absorption index ~10^{-4}) irradiated by a pulsed frequency-doubled Nd:YAG laser showing time evolution of droplet instability and nucleation: at a laser fluence slightly above the instability threshold, microbubbles form at early time (50 ns) after initiation of the heating laser pulse (a); the droplet swells by ~50% of its initial volume when the instability is fully developed at 1 μs (b); at a laser fluence below the instability threshold but above the nucleation threshold, numerous microbubbles again form at early time (~50 ns) (c); at a later time (~0.7 μs), most bubbles are quenched or coalesce into a small number of larger bubbles (d).

Figure 4. Measurements of laser fluence thresholds for initiation of vapor bubble nucleation, evaporative instability, deformation, disintegration, and plasma in ~30 μm radius absorptive dye-doped water droplets irradiated by a pulsed frequency-doubled Nd:YAG laser versus droplet absorption index. The clean-air breakdown threshold is also shown.

Fig. 1
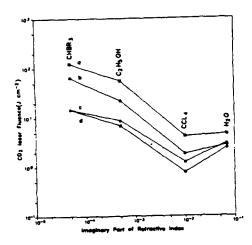
Fig. 2
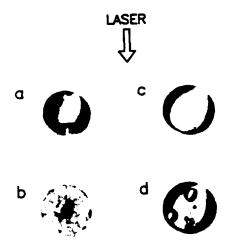
Fig. 3
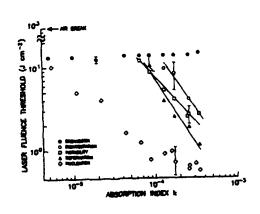
Fig. 4

WAVEGUIDES AS RANDOM MEDIA

WAVEGUIDING PROPERTIES OF RANDOMLY LAYERED MEDIA

V.D. Freilikher, S.A. Gredeskul
Department of Physics, Bar-Ilan University, Ramat-Gan, 52100 Israel
(INVITED)

The prediction of electromagnetic field strengths at large distances from a transmitter is of highest importance to designers and users of telecommunication systems. Although considerable progress has been realized in the study of UHF radiowaves propagation in atmosphere, neither of the theories currently in wide use seems to be capable of explaining the anomalously high signal levels at the ranges greatly beyond the horizon (~500 km and more), which has been observed in many of the experiments involving radio waves propagations over the sea surfaces. This shortcoming serves as the motivation for search for new mechanism of wave channeling in the atmosphere.   .

There exists a considerable body of experimental evidence obtained mostly by means of the remote sensing of the atmosphere from satellites, indicating the presence of strongly-stretched fluctuations of the troposphere refractive index at the altitudes of order 0.5 + 3 km, which may be approximately treated as a horizontally homogeneous random layer. The effect of such "one-dimensional" layered structure is the least studied for two reasons. Firstly, in this case it is necessary to make allowances for the interference of multiply scattered waves, especially backscattered. Therefore, the conventional forward-scattered methods (parabolic approximation, geometrical optics, WKB, etc.) as well as the methods based on the use of radiation transfer equation, appear to be useless. Secondly, in one-dimensional media many of radiophysical quantities, e.g., the intensity of a plane wave, are not self averaging, but strongly fluctuating ones, and so their average values, which are usually calculated, do not carry any information on their behavior of individual tylpical realizations.

It is shown in this paper that horizontally stretched fluctuations of refractive index lead, in contradistinction to isopropic ones, to field increasing far beyond the line-of-sight range. Randomly stratified medium, that is homogeneous on the average, represents in certain cases a

fluctuation waveguide arising with the high probability at typical realizations as result of interference of multiply scattered fields.

The starting point of the analysis is the Helmholtz equation

$$\Delta\Psi(R) + \frac{\omega^2}{C^2}\varepsilon(z)\Psi(R) = F(R); \quad (R) = \{x,y,z\} \qquad (1)$$

where $\Psi(R)$ is the wave field created by the sources distribution $F(R)$ in the z-stratified medium with permittivity.

$$\varepsilon(z) = \begin{cases} \varepsilon_0 + \delta\varepsilon(z), & 0 \le z \le L \\ \varepsilon_0; & z > L \end{cases} \qquad (2)$$

The function $\delta\varepsilon(z)$ is taken to be the statistically homogeneous random function with zero average $<\delta\varepsilon(z)> = 0$ and the correlations decreasing at infinity. A time factor $e^{-i\omega t}$ (ω is the frequency, $\omega/C = k$) common to both the source and the wave function, has been dropped. The boundary conditions are

$$\frac{\partial\Psi(z=0)}{\partial z} + a\Psi(z=0) = 0 \qquad (3)$$

and a condition of outgoing radiation at infinity.

If $F(R) = \delta(0)$, that corresponds to a plane source placed at the point $z = 0$, the flux density emitted from the layer

$$J = 2Img'(L)g^*(L) \qquad (4)$$

is nonselfaveraging quantity, moreover its relative fluctuations increase with the system size L. None the less the average value $<J> = 2/k$ (when a in (3) is equal to zero) does not depend on the fluctuations and coincides with the flux density in the homogeneous space $\delta\varepsilon = 0$. This means that $<J>$ does not contain any information about flux behavior at individual realizations. It may be shown that at the typical ones, that is to say, with probability $p \sim 1 - \exp(-\frac{L}{l})$ the energy radiated out of layer is exponentially small if the size L is large enough

$$J(L) = \frac{2}{k}\exp(-\frac{L}{l}) \qquad (L \gg l).$$

Here l is the localization length, which for the δ-correlated fluctuations $<\delta\varepsilon(0)\delta\varepsilon(z)> = 2D\delta(z)$ is equal to

$$l \equiv (k) = \frac{2k^2}{D} \qquad (4)$$

In the case of a point source $F(R) = \delta(R - R_o)$, the wave field $\Psi(R - R_o)$ can be represented as

$$Y(R - R_o) = \sum_n \Psi_n(z) \Psi_n'(z_o) \exp(ik_n\rho) \qquad (5)$$

Here ρ is the longitudinal vector $r = \{x-x_o, y - y_o\}$; $\Psi_n(z)$ are the eigenfunctions of the equation $\Psi'' + k^2\epsilon(z)\Psi = 0$ with boundary conditions (3), $k_n = \sqrt{k^2 - q_n^2}$. The eigenvalues q_n obey a fundamental-mode equation which can be expressed in terms of plane-wave reflection coefficient as follows: $(a = 0$ in Eq. (3))

$$1 - R(q_n) = 0 \qquad (6)$$

Here $R(q_n)$ represents the plane-wave reflection coefficient from the layer $[0,L]$ with vacuum below $z = 0$.

If the layer is thick enough $(L \gg l)$ there exists (with probability $p \sim 1 - \exp(-L/l)$ the real-valued solutions of Eq. (6). The corresponding terms in (5) describe the normal modes propagating along the layer without attenuation. In this respect the disordered system under consideration is equivalent to a dielectric layer that is optically denser than the environment. However, in our case the energy canalization is purely a fluctuation effect vanishing when $\delta\epsilon = 0$.

The energy flux density of a point source in a randomly layered medium behaves like a dielectric waveguide — away from the source it decreases as ρ^{-1}. However the z-distribution of normal waves field has some pecularities. The moduli of wave functions $\Psi_j(z)$ are essentially different from zero by a size of approximately l (q_n) near random localization centers z_j and exponentially decrease with increasing distance from the centers. This means that the energy is channelized along the layer in a narrow strip of size $\sim l$ near the point source position z_o.

There is also a set of complex-valued roots q_n of Eq. (6) with the imaginary parts being exponentially small with respect to large ratio $L/l \gg 1$. Such states correspond to quasi-homogeneous waves attenuating at exponentially large distances D_n from the source

$$D \sim \frac{1}{\text{Im}q_n} \sim L\exp(\frac{L}{l})$$

This attenuation is due not to dissipation but to upward ($z > L$) emergence of the field. However, when $\rho < D_n$ quasi-homogeneous waves are localized within the layer.

Thus a randomly layered medium, being homogeneous on average, represents a fluctuation waveguide, caused not by regular refraction but by interference of multiply scattered waves.

Such waveguides could play a noticeable role in UHF waves propagation far beyond the radio-horizon. For effective trapping of the wave by a fluctuation waveguide the localization length $l(q_n) \cong l(k \sin \varphi_n)$ (φ_n being a grazing angle) should not exceed the fluctuation la εr width L. For characteristic near-water tropospheric parameters values, $\sigma_\varepsilon \sim 3.10^{-7} \cong 0.3$ N units and correlation radius $r_c \sim 10^3$cm, for the wavelength k = 3 cm and grasing angle $\lambda \sim 10^{-3}$, the localization length appears to be $l \sim 50$ m. If allowance is made for the fact that inhomogeneities of the dielectric permittivity with the gradient $|d\varepsilon/dz| \sim 10^{-1}$N units per metre are observed in atmosphere up to the heights of 1 km and more, the fluctuation waveguide can be expected to channel the energy even more effectively than the waveguide related to regular refraction, which captures angles φ that hardly exceed the values of $\sim 10^{-4}$.

Although the goal-directed radiophysics and meteorological measurements have not been carried out in search for the fluctuation waveguide, a series of indirect data favor its possible existence. Thus the signal decay depth increase for large distances from the source was noticed as its average level and the distance increases. Such behavior of the signal amplitude is not typical for regular tropospheric waveguides. As an indication of fluctuation waveguide existence, one can consider a frequently observed noticeable correlation between the field level far beyond the horizon and the dispersion of fluctuations of refraction index σ_ε^2 in the troposphere: the signal intensity increase with σ_ε even if the average gradient $|d\varepsilon/dz|$ is small enough, so there is no regular waveguide.

RAYS AND MODES IN A RANDOM MEDIUM WAVEGUIDE

by

R.Mazar , B.Katz

Department of Electrical and Computer Engineering

Ben Gurion University of the Negev, P.O.Box 653

Beer Sheva 84105, Israel,

Tel: 972-57-461-513, Fax: 972-57-31340

and

L.B.Felsen

Department of Electrical Engineering and Computer Science,

Polytechnic University, Farmingdale,N.Y. 11735, U.S.A.

Waveguiding channels existing in various geophysical environments may be pereturbed by random fluctuations of their parameters. In the present work, we consider a plane parallel waveguide filled with a weakly fluctuating statistically isotropic random medium with the squared refractive index

$$N^2(\mathbf{r},z) \approx n^2[1 + 2\tilde{n}(\mathbf{r},z)], \quad <\tilde{n}> = 0, \quad |\tilde{n}| << 1, \tag{1}$$

which has been separated into a homogeneous background portion n and a normalized random portion n, with <> denoting ensemble average. When these refractive index fluctuations have correlation scales $l_n >> \lambda = 2\pi/k$, where λ is the wavelength and k the wavenumber in the homogeneous background, it is possible to adapt ray-optical techniques to the calculation of the average field and intensity distributions[1]. Because of multiple reflections between the waveguide walls, the ray fields are more effectively reorganized into guided modes by recourse to Poisson summation [2,3]. The result is a guided mode expansion that contains coherent and noncoherent parts.

For the simplest illustration, the planar waveguide boundaries, separated by a distance $a >> l_n$, are assumed to be perfectly reflecting. With coordinates and dimensions chosen as in Fig.1, the field U(r,z), r = (x,y), observed at M(x,0,z) due to a unit strength monochromatic point source at S(xs,0,0) can be expressed as a contribution from an actual source at S(xs,0,0) and image sources located in the unbounded medium at y = z = 0, x = 2ma ± xs, m = ±1,±2,..., with polarizations such as to satisfy the boundary conditions U(x=0,z)=0, and U(x=a,z)=0.
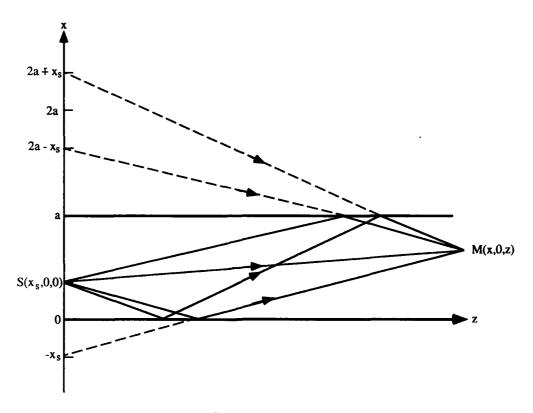
Fig.1

As in the deterministic case [2,3], this is done by extending the waveguide region into the infinite domain. In this extension, constraints on the fluctuations imposed by the reflection symmetry for imaging are ignored; the important ray fields traverse the medium at oblique angles where these effects are minimized. The average intensity at M can be expressed as

$$I(x,0,z) = < \left(\sum_{m=-\infty}^{\infty} [U(x,0,z|x_{ms}^+) - U(x,0,z|x_{ms}^-)] \right)$$

$$\times \left(\sum_{m=-\infty}^{\infty} [U^*(x,0,z|x_{ms}^+)\cos\alpha_m^+ - U^*(x,0,z|x_{ms}^-)\cos\alpha_m^-] \right) > \qquad (2)$$

where $U^\pm(r,z|x_{ms}\pm)$ are the fields created by the various sources in the unbounded medium. Invoking the parabolic approximation and introducing individual ray-centered coordinates [1], one finds

426

$$U^{\pm}(\mathbf{r}, z| x_{ms}^{\pm}) = U_m^{\pm}(0, \sigma_m^{\pm}), \tag{3a}$$

$$U_m^{\pm}(\mathbf{r}, \sigma_m^{\pm}) = u(0, \sigma_m^{\pm}) \exp(ik\sigma_m^{\pm}), \tag{3b}$$

where transverse location with respect to each ray is measured by the coordinate $r_m^{\pm}$, and distance from the source along the ray to the observation point M by the coordinate

$$\sigma_m^{\pm} = [z^2 + (x + x_{ms}^{\pm})^2]^{1/2}. \tag{4a}$$

The cosine of the angle α between the reference ray "m" and the waveguide axis z is

$$\cos\alpha_m^{\pm} = \frac{z}{\sigma_m^{\pm}}. \tag{4b}$$

The $\pm$ sign in Eqs.(2)-(4) distinguishes sources with positive and negative polarity. If the source S and the observer M are far apart axially ($z>a$) and located far (compared to l_n) from the waveguide walls, ray field contributions from different image sources are well separated, and their fields may be taken as uncorrelated. An exception occurs for contributions from distant image locations, but these are strongly attenuated and can be neglected. Thus, paired products arising from different rays in (2) can be averaged separately. Collective averaging is necessary only for the field products pertaining to the same reference ray.

The average parabolically approximated field at σ_m on the axis of the reference ray is [4]

$$<u(0, \sigma_m)> = \frac{k}{2\pi i \sigma_m} \exp\left[-\frac{1}{2} k^2 A_n(0)\sigma_m\right], \tag{5}$$

where the refractive index fluctuations are assumed to be delta correlated along the reference ray, and described by the correlation function $B(r_1 - r_2, \sigma_1 - \sigma_2) = A_n(r_1 - r_2)\delta(\sigma_1 - \sigma_2)$. The average intensity of a spherical wave on the reference ray can be obtained from the solution for the two-point coherence function[4]:

$$<I_m(0, \sigma_m)> = \left(\frac{k}{2\pi\sigma_m}\right)^2. \tag{6}$$

Then, based on the assumed independence of the fields along different rays, the total average intensity I(M) at M can be represented as a sum of a noncoherent and coherent portions.

To transform the possibly slowly convergent ray series into modal form, we apply the Poisson sum formula [2,3]

$$\sum_{m=-\infty}^{\infty} f(2\pi m) = \frac{1}{2\pi} \sum_{q=-\infty}^{\infty} \int_{-\infty}^{\infty} f(\xi) \exp(-iq\xi)\, d\xi. \tag{8}$$

Situation when either the source or the observer are near the waveguide wall can be treated in a similar way.

References

1. R.Mazar and L.B.Felsen , "Stochastic geometrical theory of diffraction", J.Acoust.Soc. Am.,**86**(6), 2292-2308, (1989).

2. D.S.Ahluwalia and J.B.Keller , in "Wave propagation and underwater acoustics", Ed. by J.B.Keller and J.S.Papadakis, Lecture Notes in Physics, vol.**20**, (Springer, Berlin 1977).

3. L.M.Brekhovskikh, "Waves in layered media", Ch.5, (Academic Press, New York 1960)

4. V.I.Tatarskii and V.U.Zavorotnyi, "Strong fluctuations in light propagation in randomly inhomogeneous media", Progress in Optics, vol. **XVIII**, edited by E.Wolf, (North-Holland, Amsterdam 1980).

STATISTICAL THEORY OF RADIATIVE TRANSFER IN LAYERED RANDOM MEDIA (STATIONARY PROBLEMS)

V.I. Klyatskin

Pacific Oceanological Institute
Far Eastern Branch USSR Academy of Sciences
7 Radio , Vladivostok, 630032, USSR, Telex: 213121 SVT SU POI

At present , the spreading of different origin waves in natural media is intensively studying (ocean acoustics, atmosphere optics, ionosphere and plasma physics and so on...). In general , parameters of these media undergo large disturbances in space and time. Such problems are described mathematically by the boundary-value problem for the wave equation with nonstationary in time and nonuniform in space refraction factor. Parameters variation being statistical, the boundary-value character of the problem gives difficulties of principal. We shall examine below the formation of main problems of waves in layered media, technique of their solution, based on the imbedding method and main fundamental peculiarities of statistical problems solution connected with the property of statistical energy localization.

Here are considered formulations of statistical waves problems described by the boundary-value problem for the equation of Helmholtz.

1. Wave incidence on the medium layer (L_o, L):

$$\frac{d^2}{dx^2} U(x) + k^2[1 + \epsilon(x) + i\gamma]U(x) = 0 \quad ,$$

$$U(x) + \frac{i}{k}\frac{d}{dx} U(x)\Big|_{x=L} = 2 \quad , \quad U(x) - \frac{i}{k}\frac{d}{dx} U(x)\Big|_{x=L_o} = 0 \quad .$$

2. Wave source inside the medium layer (L_o, L):

$$\frac{d^2}{dx^2} G(x,x_o) + k^2[1 + \epsilon(x) + i\gamma]G(x,x_o) = 2ik\delta(x - x_o) \quad ,$$

$$G(x,x_o) + \frac{i}{k}\frac{d}{dx} G(x,x_o)\Big|_{x=L} = 0, G(x,x_o) - \frac{i}{k}\frac{d}{dx} G(x,x_o)\Big|_{x=L_o} = 0.$$

3. Wave source inside the medium layer having the reflective boundary:

$$\frac{d^2}{dx^2} G(x,x_o) + k^2[1 + \epsilon(x) + i\gamma]G(x,x_o) = 2ik\delta(x - x_o) \quad ,$$

$$\frac{i}{k}\frac{d}{dx} G(x,x_o)\Big|_{x=L} = 0, G(x,x_o) - \frac{i}{k}\frac{d}{dx} G(x,x_o)\Big|_{x=L_o} = 0 \quad ,$$

where $\epsilon(x)$ is a random real function, and the quantity $\gamma \ll 1$

describes the absorption of the wave in the layer.

The statistical problem is formulated in the following way: it requires to calculate statistical characteristics of the wave field intensity, the statistics of the medium characteristic $\varepsilon(x)$ being given.

Solutions of these three different boundary-value problems have the same space structure for the fixed realization of the function $\varepsilon(x)$. They are distinguished only by numerical factors, various for different realizations. Pecularities of this structure are strong jumps on the background of the exponentially falling function (the dynamical localization). Owing to the correlation of numarical constants with the corresponding space structure , the role of jumps is considerably diffent for various boundary-value problems. The corresponding statistical characteristics of the wave field differ principally one from another (the statistical localization).

For solving statistical problems there is used the imbedding method [1-1], which allows to reformulate boundary-value problems into problems with initial data with respect to auxiliary parameter L - the position of the layer boundary. Problems with initial data are evolutionary ones. For their statistical analysis the standard methods , for example , the equation of Focker-PLank in the diffusion approximation [2-5], can be used.

So , for the problem 1 in the limit case of the half-space ($L_o \to -\infty$) and small,but finite absorption, moments $\langle I^n(x) \rangle$ of the wave field have different form in three regions [6]. In the region near the boundary the intensity moments, beggining from the second one , are growing exponentially deep into the layer and $\langle I(x) \rangle = 1$ (the phenomenon of the stochastc wave parametric resonance). When $\xi \sim \xi_o \sim 4(n-1/2)\ln(n/\beta)$, where $\xi = D(L-x)$, and D is the diffusion coefficient, $\beta = k\gamma/D$, ceases. When $\xi \gg \xi_o$, it turns into localization absorption:

$$\langle I^n(x) \rangle \sim \beta^{-(n-1/2)}\ln\left(\frac{1}{\beta}\right)\ \xi^{-3/2}\ \exp(-\xi/4)\quad.$$

As $\beta \to 0$ ($\gamma \to 0$), the quantity $\xi_o \to +\infty$, and in the limit case of the absorption absence, there is no statistical localization of the energy (e.g., $\langle I(x) \rangle = 1$ in the whole half-space). In this case limits transition $L_o \to +\infty$, $\gamma \to 0$ are permutable.

For the problem 2 there exists [7] the limit fuction

$$\Phi_{loc}(\xi) = \lim_{\substack{\beta \to 0 \\ L_o \to -\infty \\ L \to +\infty}} \lim \langle I(x,x_o) \rangle / \langle I(x_o,x_o) \rangle \ ,\quad \xi = D|x - x_o|\quad,$$

i.e. the statistical energy localization takes place. In spite

of this for small ξ the function $\Phi_{loc}(\xi)$ falls enough quickly, as $\exp(-2\xi)$, and for large ξ $(\xi \gg \pi^2)$ much more slowly, according the localization law:

$$\Phi_{loc}(\xi) \sim \xi^{-3/2} \exp(-\xi/4)$$

For the problem 3 , when the source is on the reflective boundary, there exists also the limit function

$$\Phi_{loc}^{ref}(\xi) = \lim_{\beta \to 0} \lim_{L_o \to -\upsilon} \langle I_{ref}(x,L) \rangle / \langle I_{ref}(L,L) \rangle,$$

and as $\xi \geq 1/3$ we have $\Phi_{loc}^{ref}(\xi) = \Phi_{loc}(\xi)/2$.

For these problems limit transitions over the space and absorption are not permutable.

Equations of the imbedding method have the property of ergodicity with respect to the imbedding parameter. This allows to obtain all statistical characteristics interesting for us, including situations , when the diffusion approximation is not true , by the numerical simulation for one realization $\epsilon(x)$.

Note that the analytical prolongation of stationary solutions with respect to parameter β allows to study the nonstationary problems of the pulse field in the randomly inhomogeneous media [6,7].

For the discussed problems the multi-time reflection results in the accumulating statistical effects, such as statistical energetic localization of the wave field , boundary conditions being played the decisive role for the equation of Helmhotz and localization relations appear to be different. There exist also cases when such situations are simply absent. So, for example, in the boundary-value problem:

$$\frac{d^2}{dx^2} U(x) + k^2[1 + \epsilon(x) + i\gamma]U(x) = 0 \quad ,$$

$$\dot{U}(L) = 1 \quad , \quad U(x) - \frac{i}{k} \frac{d}{dx} U(x) \Big|_{x = L_o} = 0 \quad ,$$

describing the excitation of waves in the medium by surface sources, there are no accumulating statistical effects, and the intensity of the wave field fluctuates weakly around its value when $\epsilon(x)$ is absent [5].

References

[1] G.I. Babkin, V.I. Klyatskin. Wave Motion. 4, 195(1982).

[2] V.I. Klyatskin. Stochastic equations and waves in random inhomogeneous media. Moscow , Nauka, 1980 (in Russian).

[3] V.I. Klyatskin. The imbedding method in the theory of wave propagation. Moscow , Nauka, 1986, (in Russian).

[4] V.I. Klyatskin. Ondes et equations stochastiqes dans les milieus aleatoirement non homogenes. Editions de Physique:Besansan - Cedex, 1985 (in French).

[5] V.I. Klyatskin, "Approximations by delta-correlated random processes and diffussive approximation in stochastic problems", submitted to Lectures in Applied Mathematics.

[6] M.A. Guzev, V.I. Klyatskin, "Plane waves in a layered weakly dissipative randomly inhomogeneous medium", submitted to Waves in Random Media.

[7] V.I. Klyatskin, "Localization and waves in the randomly inhomogeneous media", submitted to Wave Motion.

RECONSTRUCTION OF EVAPORATION DUCT PROFILE FROM SPATIAL STRUCTURE OF THE RADAR BACKSCATTER FROM THE SEA SURFACE

Volkov A.V., Latyshev K.V., Koshel K.V.,
Slavutsky L.A., Shevtsov B.M., Shishkarev A.A.
Pacific Oceanological Institute, 7 Radio St.
Vladivostok, U.S.S.R. 690032

To study electromagnetic waves propagation in waveguides the normal waves method is used. In present paper for reconstruction of waveguide profile from mode eigenvalue spectrum we use WKB-approximation. A similar approach was applied to optical waveguides [1] and in problem of electromagnetic waves scattering from the ungomogenous dielectric layers [2]. The equations for the complex constants of propagation may be obtained from the radiowave path loss. The method suggested for solving inverse problem was used to reconstruct refractive index profile of the evaporation duct [3]. For our analysis we took the experimentally obtained spatial behaviour of the radar signal mean level [4]. Thus the radar observation technique realized makes it possible without using of nonsofisticated equipment on a real time basis to analyze the conditions of the radiowaves propagation near the sea surface.

A wave field in a waveguide can be described by a normal-wave series [5]:

$$\Psi = \sum_n e^{ixt_n} W(z_1, z_2, t_n) \qquad (1)$$

where t_n are complex mode eigenvalues ; x is the distance along the Earth's surface, $W(z_1, z_2, t_n)$ is the altitude function, depending on coordinates z_1 and z_2 of a source and a reciever. A approximate dispersion equation for t is obtained from lacing condition of quasiclassical wave functions [5]:

$$\frac{k}{g} \int_{u \gtrless |t|} \sqrt{\pm(u(z)-t_n)} \, dz = \frac{2}{3}(-\xi_n)^{3/2} \equiv F_n \qquad (2)$$
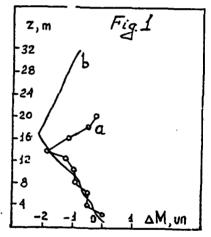
where $u(z) = g (\varepsilon(z)-1+2z/R)$, $g = (kR/2)^{1/3}$, k is the wave number, R – the Earth's radius , $\varepsilon(z)$ is the dielectrical permitivity profile , ξ_n is the roots of Airy-function , $F = \pi(n+1/4)$ at large n. The reversal of a sign in radicand and a change in the limits of integration are assotiated with analytical extending of the solution to the region beyond the waveguide, which corresponds to a penetrate potential barrier in quantum mechanics. Note at once, that equation (2), formally valid at large n, proves acceptable at $n>2$. If imaginary parts of t are not too large $|\Psi(x)|^2$ (z_1 and z_2 are fixed) has reducing spatial oscillations connected with interference between "ca-

ptured" modes. To obtain an equation for eigenvalues $|\Psi(x)|^2$ may be approximated by a reducing trigonometrical functions series accordning to the least nonlinear squares method [6]. If the segment $\Psi(x)$ taking involved at least one period of the spatial oscillations, procedure has numerical stability. To reconstruct the profile of waveguide by the expression obtained for normal-wave spectrum, we used equation (2), which after differentiation over t can be inverted in according with Abel's formula. We obtained an explicit expression for $z(u)$ inside the waveguide. The problem is reduced to obtaining a function $t(F)$ which would run through the turning points $u(z)=t_n$. Each of the complex eigenvalues is matched by two points on the altitudinal dependence $u(z)$. This procedure enables one to reconstruct a monotonously changing difference $\Delta z(u)$ between the waveguide "edges". However, in the real study of radio wave propagation in the atmosphere, one of the $z(u)$ branches is known: for surface waveguides it is the Earth's surface, characterized by impedance boundary conditions, whereas waveguides due to elevated inversion may be regarded as perturbations against the regular refraction $\varepsilon(z)=1$ in (2). The accuracy of obtaining eigenvalues depends on the realization duration $\Psi(x)$. The numerical stability of the method was tested by summing Gaussian noise $V(x)$ with zero average and $\Psi(x)$. For typical case when 2 or 3 modes are" captured" and ratio $|V(x)|/|\Psi(x)|$ is about 10%, the variation of t_n did not exceed 1%. Thus accuracy of reconstruction of the waveguide profile depend mostly on accuracy of computation $z(u)$ with Abel's formula and it does not exceed 10% at $n>2$. In principle the accuracy can be raised to a few percents [1].

The experimental investigations were performed in the northern regions of the Pacific. We used a shipboard navigational station with all-round looking radar aerials wavelengths 3 cm. The transmit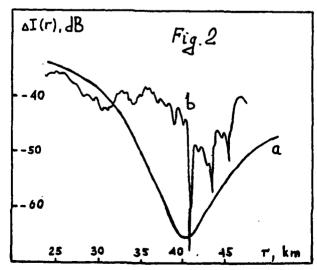ting-recieving radar antennae were placed at an altitude of 25 m (the horizon for a direct ray was about 20 km). Carrying out the experiment we had means to accumulate the echo-pulses from any direction chosen that make it possible to estimate azimuth anisotropy owing to the direction of the wind and the large-scale wave motion. Simultaneously we made direct measurments of the elevation profiles of atmosphere meteorological parameters (temperature and humidity) by means of a radiosond (up to 25 m height). Figure 1a illustrates the typical profiles of the modified refractivity related with a shallow surface guide. To study influence of refraction on the spatial structure of the backscattered signal we plotted dependences of average intensity of radar signals $\Delta I(r)$ in the range of 7–60 km. It took us 8–15 minutes to accumulate 150–300 radar reflected pulses. To the distance r_0 from which the backscattering cross-section doesn't depend on grazing angle one can use a rough estimation $r_0 > 1$ km for a characteristic slope of the surface sea-way $> 1°$. Therefore when

434

r>r$_0$ the sea parameters define only a mean value of intensity of the reflected pulse.The anisotropy of the scattered signal level in azimuthal plane connected with the sea-wave motion didn't exceed a few decibels. Figure 2 shows a modelling path loss (a) and an experimental (b) ΔI(r) for the evaporation duct with the profile illustrated by Figure 1a.These plots correspond to the capture of two modes into the guide channel. The presence of minimum in the beyond-the-horizon region can be explaned by the interference of these two modes. The model calculation for beyond-the-horizon propagption carried out with help of the spectral parameter evolution method [7]. Fig.1b shows the reconstructing refractivity profile. The behaviour of the experimental dependences ΔI(r) from different azimutal directions keeps the same in general. But in many cases a quasiperiodic beat structure can appear and its appearance seems to be connected with unsufficiently long averaging period. Large-scale wave motion (windcaused waves, swell) results in the pulse--position modulation of the radar return with a typical period about a few seconds.

Fig.1

Fig.2

REFERENCES

1. Hertel, P., H.P. Menzlerr,Improved Inverse WKB Proce-
   dure to Reconstruct Refractive Index Profiles of Die-
   lectric Planar Waveguides, Appl. Phys., 44, 75, 1987.
2. Smith, P.R., K.I. Hopcraft, R.E. Burde,A novel method
   for determining dielectric unhomogenety from scatte-
   red electromagnetic radiation, Inv.Probl.,4,235,1988.
3. Rotheram, S.,Radiowave propagation in the evaporation
   duct, Marconi Review , 37, 18-40, 1974.
4. Ko, H., A practical guide to anamalous propagation,
   Microwaves and RF , 24 , 107, 1985.
5. Fok, V.A., Problems of diffraction and propagation of
   the electromagnetic waves (in Russian), Moscow, Sov.
   Radio, 1970.
6. Dennis, I.E., R.B. Schnabel,Numerical methods for un-
   constrained optimization and nonlinear equations,Pre-
   ntice Hall Inc., Englewood Cliffs, New Jersey, 07632.
7. Goland, V.I., K.V. Koshel, Method of evolution of the
   spectral parameter in the problem concerning beyond-
   the-horizon propagation of VHF radiowaves, Radiotekh-
   nika i elektronika (in Russian), 1990 (in press).

AN EFFECTIVE REFRACTIVE INDEX OF A STRATIFIED
RANDOM LAYER

V.D.Gusev, S.M.Golynski

Dept. Physics of the Atmosphere, Physics Faculty,
Moscow State University, 119899 Moscow GSP, USSR,
tel.: 939-32-52

We consider the case when a monochromatic wave with unit amplitude propagates in the z-direction in a one-dimentional random layer. The layer is situated in the area $0 < z < L$. The dielectric constant of the layer's medium is $\varepsilon(z) = 1 + \varepsilon_1(z)$, where $\varepsilon_1(z)$ is a gaussian homogeneous process characterized by $\langle \varepsilon_1 \rangle = 0$ and $\langle \varepsilon_1(z_1)\varepsilon_1(z_2) \rangle = \sigma_\varepsilon^2 R(z_1 - z_2)$. Here the brackets indicate the expected values of the quantaties enclosed and σ_ε^2 is the variance of dielectric constant fluctuations. Outside the layer, we assume $\varepsilon(z) = 1$. The wave field $U(z)$ inside the medium satisfies the Helmholtz equation

$$U''(z) + \kappa^2 \left[1 + \varepsilon_1(z) \right] U(z) = 0 \qquad (1)$$

and the corresponding conditions of continuity for U and U' on the boundaries. Here κ is the free-space wave number and prime denotes the differentiation with respect to z .
We are looking for solution of eq.(1) in the form of progressive waves

$$U(z) = A(z) \, e^{\pm i \kappa \Phi(z)} \qquad (2)$$

Substituting (2) into eq.(1) and equalizing the real and imaginary parts to zero we obtain two equations

$$2A'\Phi' + A\Phi'' = 0, \qquad (3)$$

$$A'' + \kappa^2 \left[\varepsilon - (\Phi')^2 \right] = 0. \qquad (4)$$

The eq.(3) gives us the relation between the amplitude and the eikonal of progressive waves

$$A = \text{Const} \, (\Phi')^{-\frac{1}{2}} \qquad (5)$$

For satisfying the eq.(4) we introduce an effective refractive index m , which is defined by the generalized eikonal equation, namely,

$$(\Phi')^2 = \varepsilon_{\text{eff}} = m^2. \qquad (6)$$

It should be noted that in our approach we do not disregard the first term in the eq.(4). Taking into account (5) and (6) we pass from the eq.(4) to the ordinary nonlinear differential equation of the second order for the effective refractive index

$$2mm'' - 3(m')^2 + 4\kappa^2 m^4 - 4\kappa^2 \varepsilon m^2 = 0 \qquad (7)$$

with the initial conditions $m(z=0) = m_0$ and $m'(z=0) = m_0'$.
Now the general solution of the initial equation (1)

can be represented in the form of two linearly independent progressive waves propagating in opposite directions

$$U(z) = C_1 m^{-1/2} e^{i\kappa\varphi} + C_2 m^{-1/2} e^{-i\kappa\varphi}, \quad \varphi = \int_0^z m(s)ds, \quad (8)$$

where C_1 and C_2 are integration constants defined by the boundary conditions. So for the description of the wave field (8) and its statistical characteristics both in the layer and out of it, it is necessary to find out the statistics of the only unknown function $m(z)$. In general the choice of initial conditions for the eq.(7) is arbitrary because the constants C_1 and C_2 do not depend on changing of m_0 and m_0'. But it is reasonable to use for the definition of m_0 and m_0' the result of the geometrical optics approach (the WKB-method), i.e. $m(z) = \varepsilon^{1/2}(z)$ [1,2]. This choice leads to the coincidence of solutions of the modified method of progressive waves (8) and the WKB-method under the conditions of the WKB-method validity, which were found out in [3]

$$(\kappa a)^2 \gg 1, \quad \sigma_\varepsilon^{-2} \mathcal{D} z \ll 1.$$

Here a is the correlation radius of $\varepsilon_1(z)$ in the z-direction (the scale of inhomogeneities) and $\mathcal{D} = \frac{\kappa^2}{2}\sigma_\varepsilon^2 \int_0^\infty R(s)\cos 2\kappa s\, ds$ plays the role of the diffusion coefficient.

The attempt to represent the solution of the eq.(7) in the form of direct expansion of $m(z)$ in successive powers of the small dimensionless parameter ν ($\nu \sim \sigma_\varepsilon$)

$$m = 1 + \nu m_1 + \nu^2 m_2 + \cdots \quad (9)$$

appeared unsuccessful. The expansion (9) is nonuniform with respect to z. It is only valid under the condition $\mathcal{D}z \ll 1$, which leads to the following form of the effective refractive index mean value ($m_0 = 1$, $m_0' = 0$)

$$\langle m \rangle \approx 1 + \frac{1}{2}\{\mathcal{D}_0 - \mathcal{D}\cos 2\kappa z - \mathcal{D}_1 \sin 2\kappa z\}\sin 2\kappa z,$$

where $\mathcal{D}_0 = \frac{\kappa^2}{2}\sigma_\varepsilon^2 \int_0^\infty R(s)ds, \quad \mathcal{D}_1 = \frac{\kappa^2}{2}\sigma_\varepsilon^2 \int_0^\infty R(s)\sin 2\kappa s\, ds.$

The other way of the solution of the problem in question is connected with the use of the new variable $\theta = m^{-1}$, which satisfies the equation

$$2\theta\theta'' - (\theta')^2 + 4\kappa^2\varepsilon\theta^2 - 4\kappa^2 = 0, \quad (10)$$

$$\theta(z=0) = \theta_0, \quad \theta'(z=0) = \theta_0'.$$

One can easily check that the formal solution of the eq.(10) has a form

$$\theta(z) = \operatorname{ch}\zeta + \operatorname{sh}\zeta \cos(2\kappa z + \varphi), \quad (11)$$

$$\theta'(z) = -2\kappa \operatorname{sh}\zeta \sin(2\kappa z + \varphi), \quad (11')$$

where new functions $\zeta = \zeta(z)$ and $\varphi = \varphi(z)$ are defined by the system of stochastic equations of the first order

$$\zeta' = \kappa\varepsilon_1 \sin(2\kappa z + \varphi), \quad \zeta(0) = \zeta_0, \quad (12)$$

$$\varphi' = \kappa\varepsilon_1[1 + \operatorname{cth}\zeta \cos(2\kappa z + \varphi)], \quad \varphi(0) = \varphi_0.$$

Here the initial values ξ_0 and φ_0 depend on m_0 and m_0'.

The system (12) was obtained in [4,5] by means of other approaches. Its solution is (approximately) markovian two-dimensional process under the condition $\varkappa a \ll 1$. The corresponding Fokker-Planck equation (FPE) can be obtained due to Stratonovich [6] or van Kampen [7]. Let us assume now that the size of fluctuations of the process under consideration is small sufficiently. In this case the statistical characteristics of the problem's solution change slightly at distances of the wavelenth $2\pi/\varkappa$. At the same time there are fast oscillating functions in the r.h.s. of (12). So we can use the method of fast oscillation averaging [5]. After this procedure the coefficients in the convection and diffusion terms of the corresponding FPE do not depend on φ and have forms

$$C_\xi = \tfrac{1}{2}\mathcal{D}\,cth\,\xi \;,\quad C_\varphi = \tfrac{1}{2}\mathcal{D}_1\,sh^{-2}\xi\,(1-ch^2\xi),$$

$$C_{\xi\xi} = \mathcal{D}\;,\quad C_{\xi\varphi} + C_{\varphi\xi} = 0,\quad C_{\varphi\varphi} = \mathcal{D}_0 + \tfrac{1}{2}\mathcal{D}\,cth^2\xi. \tag{13}$$

Integrating the FPE for two-dimensional markovian process with φ and making use of a new variable $u = ch\,\xi$, we come to the FPE describing the probability density $P(u,z)$ [4,5]

$$\frac{\partial P(u,z)}{\partial z} = \mathcal{D}\,\frac{\partial}{\partial u}\left(u^2-1\right)\frac{\partial P(u,z)}{\partial u}\;,\quad P(u,z=0) = \delta(u-u_0). \tag{14}$$

If $\mathcal{E}_1(z=0) = 0$, i.e. $\xi_0 = 0$ and $u_0 = 1$, the solution of (14) is well-known, namely,

$$P(ch\,\xi,z) = \frac{e^{-\mathcal{D}z/4}}{2(2\pi)^{1/2}(\mathcal{D}z)^{3/2}}\int_\xi^\infty dx\,\frac{e^{-x^2/4\mathcal{D}z}}{(ch\,x - ch\,\xi)^{1/2}}. \tag{15}$$

With the help of (15) it is possible to investigate the statistical characteristics of the effective refractive index in the approximation considered. Really, performing the fast oscillation averaging (later on, a swung dash over the letter indicates such averaging) in the formula (11), we have the "smoothed" effective refractive index $\tilde{m} = ch^{-1}\xi$, whose statistics is defined by (15). The results of numerical calculations for different statistical characteristics of $\tilde{m}(z)$ and the wave field $U(z)$ are presented.

The problems of extending of this theory for different values $\varkappa a$ up to $\varkappa a \gg 1$ and of taking into consideration fast oscillations, which can lead to total reflection of radiation in the layer of finite width under the condition $\mathcal{D}z \gg 1$, are discussed also.

References:
1 V.L.Ginzburg, Propagation of Electromagnetic Waves in Plasma (Gordon&Breach, Sci.Publishers, Inc., N.J.,1961)
2 N.Fröman, P.Fröman, JWKB Approximation. Contribution to the Theory (North-Holland Publ. Comp., Amsterdam, 1965)
3 V.D.Gusev, S.M.Golynski, Vestnik Mosk. Univ. Fizika. 31, №5 (1990) 90
4 G.C.Papanicolaou, SIAM J. Appl. Math. 21, №1 (1971) 13
5 V.I.Klyatskin, Invariant Imbedding Method in the Theory of Waves Propagation (Nauka, Moscow, 1986)
6 R.L.Stratonovich, Topics in the Theory of Random Noise II (Gordon&Breach, Sci.Publishers, Inc., N.J.,1967)
7 N.G.van Kampen, Phys.Repts. 24, №3 (1976) 171

Investigations of characteristics of polarized
light, scattered in atmosphere in Ultra-violet.

Efimenko I.M.
Joint counsil "Optics" Academy of Science, Moscow, Pyatnitskaya,
48, TEL 231-06-69, TLX 411576 ASCON SU, FAX 7.095.230.20.81
Ivanov A.N.
Moscow State Technical University, Moscow, 107005,
2 Baumanskaya, 5a, 263-66-56.

Polarimetry has traditionally been used to characterize
the optical properties of an atmospnere by means of Mueller
matrix. This matrix in ultra-violet provides essential input
information into calculations of the light field in planetary
atmospheres. It thus has applications in the fields of clima-
tology, illumination, communications and visibility. But radi-
ation scattered from different surfaces is a necessary and some-
times major part of the complete optical description of whole
radiation field.

In this work there have been many experimental investi-
gations of Mueller matrix for different surfaces: grass, leafs,
asphalt, concrete, (dry and humid) chernozem, snow, ice. It
should be stressed that there were a wide scale of measurements
of snow from flakes to frozen snow crust. In those cases the
internal scattering had different impotance.

Analysis of theoretical and experimental datas of other
authors for atmosphere show that some results for surface
(4 elements of Mueller matrix) could be predicted. Because of
it efforts have been made to measure the entier matrix. These
involve making intensity measurements with various independent
combinations of polarizers and retarders in the incoming and
outgoing light beams. The sixteen matrix elements are obtained
from the frequently small differences between these relatively

441

large measured quantities. A schematic diagram of optical
system is shown in Fig.1.
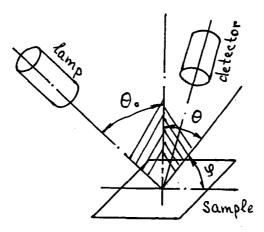
Fig.1 Schematic of the instrument.

The sourse of light is mercurial lamp. Tree wavelegh were used:
$\lambda_L = 0,25 \mu m$, $\lambda_2 = 0,31 \mu m$, $\lambda_3 = 0,36 \mu m$. The optical
geometry was quite simple in consept. The sample was mounted
horizontally. The lamp beam was sent through periscope with
two mirrors which form angle of incidence in vertical plane
required for experiments. The detector was mounted on long arm
that rotated about the sample in the vertical plane. Polarizers
are Glan prisms and retarders are quarterwave plates.

The obtained results were comrared with the same for
ground-glass surface. For the latter the theory of Kirchoff
random surface was used for calculations. Results has shown
that this theory may be fruitfull for estimation of optical
properties of different materials. This theory fails only in
the ranges sufficiently far from specular direction. The cer-
tain experimental results for concrete at $\lambda = 0,31 \mu m$ for an
angle of incidence $\theta_o = 70°$, and azimuth angle $= 0$, is shown
in Fig.2.

442
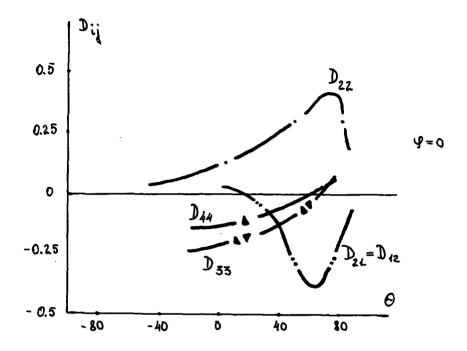
Fig.2 Measured Mueller matrix for concrete.

It can be seen that some elements of Mueller matrix have peak inside the range of specular direction. Only two elements have transition through zero there. These are D33 and D44. When a light beam is reflected by a surface, the Stokes vector of the light beam undergoes a linear transformation to a new Stokes vector. The transformation out of the plane of incidence can be represented not only by Mueller matrix but by matrix of rotation too :

$$
\begin{Vmatrix} I^{\cdot} \\ Q^{\cdot} \\ U^{\cdot} \\ V^{\cdot} \end{Vmatrix} = H(\Psi_1) \begin{Vmatrix} D11 & D12 & D13 & D14 \\ D21 & D22 & D23 & D24 \\ D31 & D32 & D33 & D34 \\ D41 & D42 & D43 & D44 \end{Vmatrix} H(-\Psi_2) \begin{Vmatrix} I \\ Q \\ U \\ V \end{Vmatrix}
$$

where Ψ is azimuth of plane of measurements and $H(\Psi)$ – matrix of rotation

$$H(\psi) = \begin{Vmatrix} 1 & 0 & 0 & 0 \\ 0 & \cos2\psi & \sin2\psi & 0 \\ 0 & -\sin2\psi & \cos2\psi & 0 \\ 0 & 0 & 0 & 1 \end{Vmatrix}$$

In the plane of incidence matrix of rotation converts to matrix with 1 at main diagonal, but when the detector is out of plane of incidence $Hij(\psi)$ have nonzero value.

The most important feature in all measured matrices is the number of zero elements. The normalized matrix elements D12, D21, D22, D33, D44, D34, D43 are much like those of particles in Rayleigh theory. A consistent feature in all measured matrices is the deviation of the D22 element from 1,0. The same effect of deviation D44 from D33 is illustrated at Fig.1. It is important to point that in the plane of incidence D12=D21, D34=D43. Outside of this plane D13, D31, D23, D32, D24, D42 tend to have the same shape as D12 and D34 respectively. Elements D33, D44 are observed to be very similar and reach a maximum of between 0.25 and 0.15 at angles near $\sim 30°$.

Out of the plane of incidence there is the principal difference between the results for horizontally polarized excitations and the results for the vertically polarized excitations. Besides D12 $\neq$ D21, D32 $\neq$ D23, D13 $\neq$ D31. For the same reason it is easy to note that for circullarly polarized light D34 $\neq$ D43. However in all experiments D41 = D14 =0, D42 = D24 =0.

Analyzing all obtained datas for different wavelenghs one can conclude that if albedos of the surface is smaller then the main elements of Mueller matrix in characteristis ranges are stronger. Thus in ultra-violet where albedos is smaller than in IR it is necessary to take into account effects of polarization of light in atmosphere when the problem of visibility is solved.

POSTER SESSION 3

Influence of Scattering on Atmospheric Retrieval Schemes: **P44**
Results Utilizing High Spectral Resolution Simulations

Joseph M. Coughlin

Ball Systems Engineering Division

P.O. Box 1062 Mail Stop CO-7

Boulder, CO 80306 USA

(303) 939-5329

INTRODUCTION

The remote sounding of the atmosphere to retrieve temperature and water vapor profiles has been the subject of a number of papers (Chahine, Smith, etc.). In this paper we present the results of a study to determine the effect uncertainties in the aerosol scattering properties have on the retrieval of temperature and water vapor profiles. We also present the results of a field test in January 1991 to test our atmospheric retrieval algorithms.

We utilize a high spectral resolution line-by-line atmospheric radiative transfer code, Emission Spectra (ES), to compute radiances for different aerosol types and densities. Given uncertainties in the radiance due to variations in the aerosols, we retrieve atmospheric temperature and water vapor profiles using Backus-Gilbert and Chahine relaxation retrieval methods and compare the results.

PROCEDURE

At BSED, we have operational computer programs for the retrieval of atmospheric temperature and water vapor profiles linked to an algorithm for the simulation of atmospheric radiance and transmission.

The radiances used as input to the retrieval algorithms are calculated using a line-by-line radiative transfer algorithm, Emission Spectra (ES). ES is an interactive program for the simulation and analysis of atmospheric spectra. ES calculates the radiances and transmissions using an altitude-based 100 level atmosphere, from 0 to 100 km. For this analysis, the surface was assumed to be black-body radiance. However, the program has an extensive database of emissivities, so a more realistic background could also be calculated. Single-scattered solar radiance is computed for difference aerosols and densities. The aerosol density is specified by the aerosol type and the atmospheric visibility at 0.55 microns. The aerosols are also a source of radiance in the calculations. For this sensitivity analysis, the radiances were calculated at a spectral resolution of 1 cm^{-1} in order to be consistent with a proposed instrument. We were also limited to the 2.0 to 5.0 micron wavelength region. For the temperature

retrievals, the 4.3 micron CO_2 band was utilized.

Since different retrieval algorithms have individual strengths and weaknesses, we have chosen to implement a Chahine relaxation algorithm for retrieving temperature and water vapor profiles and a Backus-Gilbert algorithm for retrieving temperature profiles. This allows us to compare the results from the different algorithms in specific cases. The outputs from the ES program which are used as inputs to these algorithms include the calculated radiances, the weighting functions, and arrays of the transmission as a function of altitude and frequency.

The Backus-Gilbert method (the program is named INVERS) calculates the spectral radiances for an atmosphere with the temperature at a specific level (a so-called tweaked level) displaced by a discrete value. Each level in the atmosphere is tweaked by the same temperature, in our case 2K. The result is a matrix of radiance values showing the effect of temperature variations at different levels. The dimensions of the matrix are the number of radiance channels times the number of tweaked levels. In our case this is a 39 x 100 matrix. The matrix is orthogonalized and inverted to yield the eigenvalues of the matrix. The eigenvalues are then sorted in decreasing magnitude, with negative eigenvalues being discarded. The temperature profile is then corrected using a finite number of eigenvalues. In testing, we have found that if we use the maximum eigenvalue for a few iterations and then gradually increase the number of eigenvalues used, we obtain excellent convergence on the correct solution. Each iteration with successively more eigenvalues will converge to a stable solution, but to speed processing we limit the number of iterations before including smaller eigenvalues. As expected, the difference between successive eignvalues decreases as the solution converges. A maximum of 10 eigenvalues is usually sufficient to reproduce the radiance to less than 0.1%.

Our implementation of the Chahine relaxation method uses ES as a subroutine to calculate the spectral radiances and transmissions for input to its radiance matching algorithm. The Chahine methodology has been described elsewhere and need not be repeated here.

The purpose of this study is to test the sensitivity of the retrieval algorithms to variations in the scattering parameters. The spectral radiances for the "real" atmosphere are first calculated for well-defined conditions to yield a set of "observed" radiances. The temperature profile is then retrieved with the radiances calculated with the same atmospheric model used in the generation of the "observed" set. This gives a baseline temperature profile. The visibility (aerosol density) is then altered in the model atmosphere and the retrieval calculations are repeated. The type of aerosol model is also allowed to vary, which yields those retrieval uncertainties. For consistency in evaluating the different retrieval algorithms, the spectral channels calculated are the same in the Backus-Gilbert and Chahine methods.

RESULTS/CONCLUSIONS

The Backus-Gilbert temperature retrievals more accurately reflect the uncertainties in the aerosols by showing variations in the retrieved temperatures. The Chahine relaxation method does not show these variations as strongly, due mainly to the resolving power of this method as compared to the Backus-Gilbert algorithm. Uncertainties in the types of aerosols, i.e. rural versus urban, show stronger effects than variations in visibility.

For the limited, ideal cases explored here, the Backus-Gilbert algorithm gives more informative results for the temperature retrievals than the Chahine relaxation method. A major drawback of the Backus-Gilbert algorithm is the computation time required. The spectral resolution of 1 cm^{-1} is a disadvantage for the Chahine method due to the width of the weighting functions, but only slightly affects the Backus-Gilbert algorithm. Higher spectral resolution would probably help both algorithms.

The effect of clouds has not yet been considered in our implementation of these algorithms, nor the effect of multiple scattering. A future version of ES will include the effects of multiple scattering, and this study will then be repeated.

BIBLIOGRAPHY

Backus, G.E., and J.F. Gilbert, Numerical Applications of a Formalism for Geophysical Inverse Problems, Geophys. J.R. astr. Soc., 13, 247-276, 1967.

Backus, G.E., and J.F. Gilbert, The Resolving Power of Gross Earth Data, Geophys. J.R. astr. Soc., 16, 169-205, 1968.

Chahine, M.T., A General Relaxation Method for Inverse Solution of the Full Radiative Transfer Equation, JAS, 29, 741-747, 1972.

Finney, S.A., Program Report on Mathematical Techniques, Private Communication, 1990.

Smith, W.L., Iterative Solution of the Radiative Transfer Equation for the Temperature and Absorbing Gas Profile of an Atmosphere, Appl. Opt., 9, 1993-1999, 1970.

ECLIPS: An International Project for Tropospheric Cloud Properties Characterization. The Antarctic Contribution

P45

M. Morandi, V.M. Sacco, L. Stefanutti, F. Castagnoli,
M. Del Guasta

Istituto di Ricerca sulle Onde Elettromagnetiche
del Consiglio Nazionale delle Ricerche
Via Panciatichi 64   I50127 Firenze Italy
tel +39.55.4378512

Introduction

A depolarization lidar [1] has been installed in Antarctica to perform studies on tropospheric clouds at the French base of Dumont D'Urville (66° 40' S, 140° 01' E). The campaigns have proceeded for all 1989 and 1990. This work is performed in the frame of the international program ECLIPS (Experimental Cloud LIdar Pilot Study), promoted under the auspices of the W.M.O [2]. The objectives of this program are:

- a coordinated long term climatological study on cloud physical and optical properties with ground based lidars;
- a study on satellite and lidar data comparison for retrieval of cloud data;
- an improvement of the surface energy balance prediction from satellite data.

Since 1989 coordinated experimental campaigns have been performed. Two ECLIPS campaigns have been carried out, respectively from April 1st to April 30th and from September 15th to October 31st 1989. ECLIPS data are acquired one hour before, twenty minutes during and one hour after the overpasses of NOAA series satellites. A maximum of two set of measurements over the 24 hours were performed. The lidar was shot in this case with a pulse repetition rate of 1 shot/10 sec. and the signatures were averaged each minute. No ECLIPS campaigns took place in 1990, while a next one is planned from March to May 1991.

On a routine basis since January 1989 continuous lidar cloud measurements have been performed: The lidar was fired at a repetition rate of one shot/minute and 10 minute averaged profiles were acquired.

The following ancillary data were available:

- rawinsonde data; Balloon sondes were launched daily;
- ground based meteorological observations performed every three hours by the base meteorological service;
- longwave wideangle (170°) IR and visible radiometric

data;
- wide angle CCD TV images recorder with a time lapse videorecorder.

The 1989 data set has been analyzed and correlated to rawinsonde, radiometric data, and ground based observation. The 1990 data set is now under analysis and only statistical evaluations are presented.
A correlation with satellite data will be also attempted.

Data analysis

The lidar system performs measurements of cloud layers above 500 meters. For lower altitudes a nonlinearity affects the signal, so only cloud bases and thicknesses can be measured. For higher clouds also an evaluation of cloud optical properties can be performed.

A continuous monitoring of the Antarctic Troposphere has been carried out during all 1989 and 1990. The amount of data consists in a production of about 100 MBytes, 70 for 1989 and 30 for 1990.

All the software programs for inverting tropospheric cloud lidar profiles have been written and tested.

A first aim of this study is to produce a quick-look catalog, where daily representations of cloud profiles will be shown for the whole year. Fig. 1 shows an example of these representations for September 21st 1989. In this picture the extinction coefficient profile is shown. Similar pictures can be produced for the backscattering ratio and depolarization profiles.

The measurements are stored in files formed by sequential records. Each record contain an averaged profile. As said before the acquisition integration time is 10 minutes for routine measurements and 1 minute for ECLIPS measurements.

The mean values of the geometrical and optical parameters are computed over 30 or 10 minutes, for routine and ECLIPS measurements respectively. The averaged profile is displayed on the computer's monitor, then the operator can select an appropriate range for the fitting with a molecular atmosphere. The program selects the radiosounding closest to the lidar measurement under analysis and calculate automatically the appropriate molecular atmosphere model. An approximate evaluation of the base and top heights can be also made. Starting from these last selected values, the program analyzes individually each profile and provides the mean value and the standard deviation for both the base and top heights. Then the averaged profile is converted in backscattering coefficient values. A standard backward Klett method [3] is used to calculate the extinction profile. In the case of multi-layer cloud the parameters of each layer can be discriminated.

Conclusions

The parameters evaluated can be summed up in the following table [4,5]:

- bottom, peak and top heights;
- extinction to backscattering ratio;
- backscattering coefficient profile;
- extinction coefficient profile;
- depolarization ratio profile.
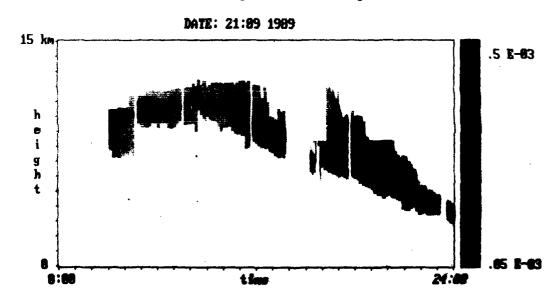
A data base has been organized. All the processed lidar, rawinsonde and ground based observation data are arranged into monthly data sets.

On the basis of the cloud's macrophysical characteristics and their statistical correlation with meteorological parameters and other ancillary data, a cloud classification will be attempted.

An almost complete statistics of the base and top heights, optical depth and integrated backscattering has been performed for the whole year 1989. Further, one of the major aims of such an evaluation is to distinguish liquid-water and ice cloud, on account of their different radiative properties.

A data analysis based on the study and the correlation of several different parameters (such as the depolarization, backscattering and extinction to backscattering ratios and the temperature and humidity profiles), should allow to achieve this objective.

DUMONT D' URVILLE 66 deg 40 min S 140 deg 1 min E

DATE: 21:09 1989

EXTINCTION COEFFICIENT (1/m)

453

References

[1] Sacco V.M. et al "Elastic Backscattering Lidar System for Atmospheric Measurements in Antarctica", Optical and Quantum Electronics, 21 (1989), 215-226.

[2] ECLIPS - Report WCRP/CSIRO Workshop, WMO/TD n. 251 (1988)

[3] Klett J.D. "Stable analytical inversion solution for processing lidar returns", Applied Optics Vol 20 No 2 p 211

[4] Morandi M. et al "Antarctic Tropospheric Cloud Character-ization using an elastic backscattering lidar" SIF Conf. Proc. Vol 20 pp 111 - 120 (1989)

[5] Morandi et al "The Experimental Cloud Pilot Study (ECLIPS): the 1989 campaign at Dumont D'Urville" SIF Conf. Proc. Vol 27 pp 45 - 60 (1990)

A fast atmospheric correction algorithm for small swath angle satellite sensors

F. Lanzl and R. Richter   **P46**

DLR, German Aerospace Research Establishment
Institute for Optoelectronics
D-8031 Oberpfaffenhofen, Germany
Tel. (Germany) 8153-28-785

1. Atmospheric correction in the reflective spectral region

In the spectral region 0.4 - 2.5 μm the images of spaceborne sensors mapping land and ocean surfaces of the earth strongly depend on atmospheric conditions and solar zenith angle. The images contain information about solar radiance reflected at the ground and scattered by the atmosphere.

To infer the spectral reflectance of the earth's surface the atmospheric influence has to be eliminated. The atmosphere modifies the information of the earth's surface in some ways:

- it contributes a signal independent of the earth's surface
- it partly absorbs the ground reflected radiance
- it scatters the ground reflected radiance into the neighbourhood of the observed pixel. Therefore, dark areas surrounded by bright areas appear brighter to the remote observer than to the near observer. This adjacency effect diminishes the image contrast and causes a certain amount of blurring. The effect is especially important for spaceborne sensors of high spatial resolution, e.g. Landsat TM (Thematic Mapper, 30 m spatial resolution) and SPOT (10 - 20 m spatial resolution).

Atmospheric correction is especially useful when comparing multitemporal scenes, since it eliminates the influence of different atmospheres and solar illuminations. Changes in scenes recorded at different times thus correspond to actual changes on the earth's surface and not to changes caused by different atmospheric conditions.

Satellite sensors with a small swath angle are represented by Landsat TM, MSS, and SPOT. For these sensors a fast three-step algorithm is used to calculate the ground reflectance :

1. the ground reflectance $\rho^{(1)}$ is calculated for each spectral band using precomputed atmospheric correction functions a_0 and a_1.
2. an N × N pixel low pass filter is employed to calculate the average reflectance $\overline{\rho}^{(1)}$ in the neighborhood of each pixel to correct the adjacency effect.
3. a precomputed atmospheric function q is used for weighting the difference $\rho^{(1)} - \overline{\rho}^{(1)}$ to account for the strength of the adjacency effect and to obtain the final ground reflectance $\rho^{(2)}$.

Two approximations were made to obtain a fast algorithm:

- the scan angle dependence of the radiance is neglected. All radiances are evaluated for a fixed view angle (center of image, e.g. nadir).
- the slight dependence of global irradiance on ground albedo is neglected. A ground albedo of 30 % is assumed for the global irradiance calculation.

The first step calculates $\rho^{(1)}$ in band i [1, 2]:

$$\rho^{(1)} = \frac{1}{a_1} \left(\frac{\pi\, d^2}{E_s(\lambda_i)\, \cos\theta_s} \left[c_0(i) + c_1(i) \times DN(i) \right] - a_0 \right) \qquad (1)$$

where $L(\lambda_i)$, $E_s(\lambda_i)$, $c_0(i)$, and $c_1(i)$ are radiance in band i, extraterrestrial solar irradiance, offset and slope of calibration coefficients, respectively, λ_i is the center wavelength, θ_s is the solar zenith angle, and d is the Earth - Sun distance in astronomical units, a_0 and a_1 depend on the atmosphere, solar zenith angle, sensor view angle, and spectral band. DN(i) is the digital number in band i.

The second step of the reflectance calculation accounts for the adjacency effect. Here, an N × N low pass filter is applied to get the average reflectance $\bar{\rho}^{(1)}$ in the neighborhood of each pixel.

The final ground reflectance $\rho = \rho^{(2)}$, corrected for the adjacency effect, is obtained from

$$\rho^{(2)} = \rho^{(1)} + q\left(\rho^{(1)} - \bar{\rho}^{(1)} \right) \qquad (2)$$

$$q = \int_{\lambda_1}^{\lambda_2} \frac{\tau_{dif}(\lambda)}{\tau_{dir}(\lambda)}\, \Phi(\lambda)\, d\lambda \qquad (3)$$

where τ_{dif}, τ_{dir}, and Φ are the diffuse transmittance, direct transmittance, and sensor response function, respectively, [2].

A catalog of atmospheric correction functions for Landsat TM, MSS, and SPOT has been compiled. For a wide range of atmospheric conditions and solar zenith angles this catalog enables the conversion of many Landsat and SPOT scenes into ground reflectance images, if the scenes are cloud-free. Besides standard atmospheric conditions the catalog can also contain actual atmospheric data (radiosonde) for specific dates and locations.

The catalog consists of [1, 2]:

- different standard atmospheres (altitude profile of pressure, air temperature, water vapor content, ozone concentration, taken from model LOWTRAN-7, [3, 4]).
- different aerosol types : rural, urban, desert, maritime
- different aerosol concentrations (aerosol optical depth), defined by the ground visibility. The visibility range is 5 - 40 km, i.e. from hazy to very clear conditions.
- different ground elevations: 0, 0.5, 1.0 km above sea level corresponding to pressure levels of about 1010, 960, 900 mbar, respectively. In this way the Rayleigh optical depth for places of different elevation is taken into account.
- solar zenith angles from 20° - 70°.
- The atmospheric correction functions depend on the spectral response of the sensor, thus there are different files for Landsat TM, MSS, and SPOT.
- The atmospheric correction functions also depend on the sensor view angle.

For Landsat TM and MSS all functions of the catalog are evaluated for a nadir view, since the maximum off-nadir scan angle is only 7.5°.
For SPOT seven geometries are offered, because of the tilt capability of the sensor.

456

Fig. 1 shows the effect of the atmospheric correction on a Landsat TM scene of Dresden recorded 5 July 1988.

Figure 1. Landsat TM scene of Dresden, band 1 (450 - 520 nm).

2. Atmospheric correction in the thermal spectral region

In this spectral region Landsat TM band 6 is the only satellite sensor with a small swath angle ($\pm 7.5°$ off nadir). Since this sensor measures the radiance in a single thermal band, the split-window technique cannot be used to eliminate the atmospheric influence. Therefore, the atmospheric correction is based on:

- specification of standard atmospheric conditions or actual atmospheric measurements.
- check of the ground temperature if the temperature of a reference target (e.g. lake) is available.
- neglection of the scan angle effect.

The brightness temperature of the ground is calculated in three steps:

1. the digital number (DN) is converted into radiance L:

$$L = c_0 + c_1 DN \tag{4}$$

where the coefficients for Landsat-5 TM band 6 are $c_0 = 0.124$, $c_1 = 0.00563$ $(mWcm^{-2}sr^{-1}\mu m^{-1})$, [5].

2. The radiance is converted into an equivalent blackbody temperature T_{BB} at the satellite [6]:

$$T_{BB} = \frac{K_2}{K_1 - \ln (c_0 + c_1 DN)} \tag{5}$$

The coefficients K_1 and K_2 depend on the range of blackbody temperatures.

457

3. For two ground surface temperatures T_{S1}, T_{S2} the corresponding at-satellite blackbody temperatures T_{BB1} and T_{BB2} are calculated assuming a fixed surface emissivity of $\varepsilon = 0.98$. The surface temperature T_S corresponding to the at-satellite blackbody temperature is obtained from a linear interpolation:

$$T_S = T_{S1} + \frac{T_{S2} - T_{S1}}{T_{BB2} - T_{BB1}} \, (T_{BB} - T_{BB1}) \tag{6}$$

The error of the linear interpolation is less than 0.2°C in the temperature range specified for the available standard atmospheres below. This corresponds to about half a DN value of TM band 6 and is acceptable.

The calculation of the surface temperature is based on a surface emissivity of 0.98 in TM band 6. This is a typical value for water and vegetated areas. Many natural earth surfaces have emittance values from 0.97 to 0.99. In this range the surface kinetic temperature will deviate less than 0.5°C from the temperature based on the assumption of an emittance of $\varepsilon = 0.98$. Thus, the accuracy is in the range of the noise level of TM band 6.

Typical emittance values for concrete walkway and asphalt paving are 0.966 and 0.956, respectively. Kinetic temperatures of these surfaces can be underestimated by about 0.7°C and 1.2°C, respectively, due to the assumption of an emissivity of 0.98. Still, this is a remarkable improvement compared to the at-satellite blackbody temperature which may differ largely from the surface kinetic temperature.

The influence due to the neglection of the scan angle influence is usually less than 0.1°C for the standard atmospheres of the catalog. It may increase to 0.2°C in some cases.

For the same visibility the difference between the aerosol types (rural, urban, maritime, desert) plays a minor role in the thermal spectral region. The corresponding errors are less than 0.1°C.

The calculations for the standard atmospheric catalog are performed for the ground elevations 0, 0.5, 1 km (above sea level) and the visibilities 5, 7, 10, 15, 23, 40 km. Values in between are obtained by linear interpolation.

References

1. R. Richter, "Atmospheric correction of Landsat TM, MSS, and SPOT images: ATCOR user manual", DLR IB 552-14/90, (1990).
2. R. Richter, "A fast atmospheric correction algorithm applied to Landsat TM images", Int. J. Remote Sensing, Vol. 11:, 159 - 166, (1990).
3. R.G. Isaacs, W.C. Wang, R.D. Worsham, and S. Goldenberg, "Multiple scattering LOWTRAN and FASCODE models", Applied Optics, Vol. 26, 1272 - 1281, (1987).
4. F.X. Kneizys et al., "Users Guide to LOWTRAN 7", Air Force Geophysics Laboratory, AFGL-TR-88-0177, Bedford, MA, (1988).
5. EOSAT, "Landsat Technical Notes", August 1986.
6. S.M. Singh, "Brightness temperature algorithms for Landsat Thematic Mapper Data", Remote Sensing of Environment, Vol. 24, 509 - 512, (1988).

The Radiation near the Boundaries of a Planetary Atmosphere **P47**

W.M.F. Wauben and J.W. Hovenier

Department of Physics and Astronomy, Free University, De Boelelaan 1081, NL−1081 HV Amsterdam, The Netherlands; tel. 020−5484114

Introduction

The polarized radiation emerging from a planetary atmosphere has been intensively studied in the past using various computational methods /see e.g. 1-6/. General methods for calculating the polarized internal radiation of such an atmosphere are relatively new /e.g. 3,5,7/ and there are few results in the literature. The polarized internal radiation contains, however, valuable information on the vertical structure and the composition of an atmosphere. In this paper we discuss results of a border approximation, which uses the emerging radiation – many results of which are already available – as input. In addition, a cubic polynomial approximation is presented, which employs the values and slopes of the radiation at the endpoints. For some cases both approximations of the internal radiation are compared with exact results.

Basic Concepts

The intensity and state of polarization of a beam of light can be fully described by means of the column vector $\mathbf{I} = \{I, Q, U, V\}$, where I, Q, U and V are the Stokes parameters /8,9/. Here $\mathbf{I}$ is called the intensity vector and its first element the intensity.

We consider a plane-parallel homogeneous atmosphere illuminated from above by a parallel beam of light with flux vector $\pi\mathbf{\Phi}$ whose first element, $\pi\Phi_1$, is the flux through a unit area perpendicular to the incident beam. In such an atmosphere, the only spatial dependence is in the vertical direction. To describe this, we use the optical depth, τ, which is zero at the top and equals b, the optical thickness, at the bottom of the atmosphere. The direction in the atmosphere is denoted by: (i) the cosine of the nadir angle, u, while we also use $\mu = |u|$; (ii) the azimuth angle, ϕ, with respect to an arbitrary zero direction measured clockwise when looking upwards. The atmosphere is bounded below by a reflecting ground-surface with albedo A_g. The direction of the unidirectional solar radiation incident at every point at the top of the atmosphere is given by (μ_0, ϕ_0).

The diffuse radiation in the atmosphere is denoted by $\mathbf{I}(\tau, u, \phi)$. The local scattering properties of the atmosphere are described by: (i) the single scattering albedo, a, which is the probability that a photon which interacts within an element of volume will be scattered rather than truly absorbed; (ii) the phase matrix, $\mathbf{Z}(u, u', \phi - \phi')$, which gives the intensity and state of polarization when radiation incident from direction (u', ϕ') is scattered in direction (u, ϕ).

Radiation near the Boundaries

Approximative expressions for the diffuse radiation near the boundaries of the atmosphere have been derived by Stammes et al. /7/ using invariance relations and a first order approximation in optical depth. They found that the downward radiation near the top of the atmosphere $\mathbf{I}(\tau, \mu, \phi)$, where $\tau/\mu \ll 1$, is, approximately, given by

$$\mathbf{I}(\tau, \mu, \phi) = \frac{a\tau}{4\mu} \left\{ \mathbf{Z}(\mu, \mu_0, \phi - \phi_0)\mathbf{\Phi} + \frac{1}{\pi} \int_0^1 d\mu' \int_0^{2\pi} d\phi' \mathbf{Z}(\mu, -\mu', \phi - \phi')\mathbf{I}(0, -\mu', \phi') \right\} \tag{1}$$

and the upward radiation near the top of the atmosphere $\mathbf{I}(\tau, -\mu, \phi)$ by

$$\mathbf{I}(\tau, -\mu, \phi) = \mathbf{I}(0, -\mu, \phi) + \frac{a\tau}{4\mu} \left\{ \frac{4}{a}\mathbf{I}(0, -\mu, \phi) - \mathbf{Z}(-\mu, \mu_0, \phi - \phi_0)\mathbf{\Phi} \right.$$
$$\left. - \frac{1}{\pi} \int_0^1 d\mu' \int_0^{2\pi} d\phi' \mathbf{Z}(-\mu, -\mu', \phi - \phi')\mathbf{I}(0, -\mu', \phi') \right\}. \tag{2}$$

Similarly the downward radiation near the bottom of the atmosphere $\mathbf{I}(\tau, \mu, \phi)$, where $(b - \tau)/\mu \ll 1$, is, approximately, given by

$$\mathbf{I}(\tau, \mu, \phi) = \mathbf{I}(b, \mu, \phi) + \frac{a(b - \tau)}{4\mu} \left\{ \frac{4}{a} \mathbf{I}(b, \mu, \phi) - \mathbf{Z}(\mu, \mu_0, \phi - \phi_0) \exp(-b/\mu_0) \mathbf{\Phi} \right.$$
$$\left. -\frac{1}{\pi} \int_0^1 d\mu' \int_0^{2\pi} d\phi' \left[\mathbf{Z}(\mu, \mu', \phi - \phi') \mathbf{I}(b, \mu', \phi') + \mathbf{Z}(\mu, -\mu', \phi - \phi') \mathbf{I}(b, -\mu', \phi') \right] \right\} \quad (3)$$

and the upward radiation near the bottom of the atmosphere $\mathbf{I}(\tau, -\mu, \phi)$ by

$$\mathbf{I}(\tau, -\mu, \phi) = \mathbf{I}(b, -\mu, \phi) - \frac{a(b - \tau)}{4\mu} \left\{ \frac{4}{a} \mathbf{I}(b, -\mu, \phi) - \mathbf{Z}(-\mu, \mu_0, \phi - \phi_0) \exp(-b/\mu_0) \mathbf{\Phi} \right.$$
$$\left. -\frac{1}{\pi} \int_0^1 d\mu' \int_0^{2\pi} d\phi' \left[\mathbf{Z}(-\mu, \mu', \phi - \phi') \mathbf{I}(b, \mu', \phi') + \mathbf{Z}(-\mu, -\mu', \phi - \phi') \mathbf{I}(b, -\mu', \phi') \right] \right\}. \quad (4)$$

In the above equations the diffuse radiation near the boundaries is given in terms of the incident radiation at the top and bottom, the emerging radiation, and the scattering properties of the constituents of the atmosphere. We shall refer to Eqs. (1)-(4) as the border approximation. If the reflecting ground-surface with albedo A_g is Lambertian, the upward radiation at the bottom of the atmosphere, $\mathbf{I}(b, -\mu, \phi)$, is independent of azimuth and nadir angle and also unpolarized, while its first element is given by

$$I(b, -\mu, \phi) = A_g \left[\frac{1}{\pi} \int_0^1 d\mu' \int_0^{2\pi} d\phi' \mu' I(b, \mu', \phi') + \mu_0 \exp(-b/\mu_0) \Phi_1 \right]. \quad (5)$$

Border Approximation for Isotropic Scattering

In case of isotropic scattering in a homogeneous finite atmosphere bounded below by a black surface, the radiation emerging from the top and the bottom is given in terms of $X-$ and $Y-$functions /cf. 8/. In this case the above equations reduce to

$$I(\tau, \mu) = \frac{a\tau}{4\mu} X(\mu_0) \Phi_1 \quad (6)$$

and

$$I(\tau, -\mu) = I(0, -\mu) \left[1 + \frac{\tau}{\mu} \right] - \frac{a\tau}{4\mu} X(\mu_0) \Phi_1 \quad (7)$$

for the downward and upward radiation near the top of the atmosphere, respectively, and to

$$I(\tau, \mu) = I(b, \mu) \left[1 + \frac{(b - \tau)}{\mu} \right] - \frac{a(b - \tau)}{4\mu} Y(\mu_0) \Phi_1 \quad (8)$$

and

$$I(\tau, -\mu) = \frac{a(b - \tau)}{4\mu} Y(\mu_0) \Phi_1 \quad (9)$$

for the downward and upward radiation near the bottom of the atmosphere, respectively. The border approximation for the radiation near the top of an isotropically scattering, homogeneous semi-infinite atmosphere can be obtained by replacing the $X-$function by the $H-$function.

If a Lambertian reflecting ground-surface with albedo A_g is present, Eqs. (6)-(9) are valid if: (i) $X(\mu_0)$ and $Y(\mu_0)$ are replaced by $X(\mu_0) + 2\mu_0 \beta_0 A_g G(\mu_0)$ and $Y(\mu_0) + 2\mu_0 \alpha_0 A_g G(\mu_0)$, respectively; (ii) an extra term $\mu_0 A_g G(\mu_0)[1 - (b - \tau)/\mu]\Phi_1$ is added to the right of Eq. (9) due to the direct contribution of the radiation incident from below to the upward radiation near the bottom of the atmosphere. Here we used $G(\mu_0) = \{\frac{a}{2}[\beta_0 X(\mu_0) - \alpha_0 Y(\mu_0)] + Y(\mu_0)\}/\{1 - A_g[a(\alpha_0 \alpha_1 - \beta_0 \beta_1) - 2\alpha_1 + 1]\}$, where α_i is the i-th moment of the $X-$function and β_i is the i-th moment of the $Y-$function. Numerous tables for $H-$, $X-$, and $Y-$functions and their moments are available in the literature /cf. 10,11/.

460

Results

Here we will present some results of the border approximation. We use unpolarized incident radiation with $\mu_0 = 0.6$, $\phi_0 = 0°$ and flux π. We assume that no absorption occurs, i.e. $a = 1.0$. The radiation emerging from the atmosphere has been calculated using the adding/doubling method /4/. The border approximation gives the endpoints and derivatives of each of the Stokes parameters at the boundaries of the atmosphere. We have used these endpoints and slopes to fit a cubic polynomial, which we henceforth call the cubic polynomial approximation. The results are compared with exact results of the internal radiation, obtained with an extension of the adding/doubling method /4,7/ (see Figs. 1-3).
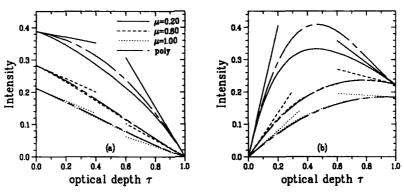

Fig. 1. The intensity as a function of optical depth for three directions showing the border approximation (straight lines), the cubic polynomial approximation, and the exact internal radiation of an isotropically scattering atmosphere with a black ground-surface. The optical thickness $b = 1.0$. Parts (a) and (b) show, respectively, upward and downward radiation. The radiation is azimuth independent.

From Fig. 1 we see that the border approximation is best near the boundaries of the atmosphere and that the approximation is better for vertical directions than for more horizontal ones, as could be expected from Eqs. (1)-(4). The cubic polynomial approximation for isotropic scattering shown in Fig. 1 differ less than 3% from the exact intensities at all optical depths for the upward and downward directions, $\mu = 0.6$ and $\mu = 1.0$. However, this difference increases rapidly for more horizontal directions.
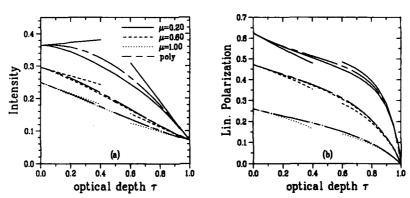

Fig. 2. Same as Fig. 1, but for a Rayleigh scattering atmosphere bounded by a Lambertian reflecting ground-surface with albedo, $A_g = 0.2$, and for upward radiation with azimuth angle, $\phi = 90°$. Parts (a) and (b) show, respectively, the intensity and the degree of linear polarization.

The results for the intensity of a Rayleigh scattering atmosphere (see Fig. 2a) show almost the same

behaviour as for isotropic scattering. The border approximations for the degree of linear polarization, $\sqrt{Q^2 + U^2}/I$, shown in Fig. 2b do not yield straight lines, since only the approximations for the individual Stokes parameters are linear in optical depth. The border approximation gives good results, even for the near horizontal direction $\mu = 0.2$. The cubic polynomial approximation differs for $\mu = 0.2$, less than 0.03, and for the two more vertical directions even less than 0.01 from the exact values for the degree of linear polarization.
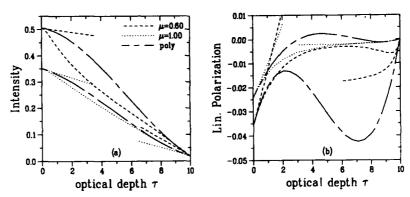

Fig. 3. The intensity (a) and degree of linear polarization (b) as a function of optical depth for the border approximation, the cubic polynomial approximation, and the exact values for two upward directions with $\phi = 0°$. The atmosphere with $b = 10$ consists of Venus cloud particles and is bounded by a Lambertian surface with $A_g = 0.1$.

Finally we show in Fig. 3 results for the intensity and the degree of linear polarization, $-Q/I$, for a Venus atmosphere model consisting of spherical sulfuric-acid cloud droplets with refractive index 1.44 /7,12/. The border approximation and the cubic polynomial approximation differ more from the exact values than for Rayleigh scattering. The cubic polynomial approximation in Fig. 3 differs for the vertical direction, up to about 10% for intensity and 0.005 for the degree of linear polarization.

Conclusions

The border approximation gives sometimes good results, especially near the boundaries but, generally, the cubic polynomial approximation is better. For a thick atmosphere the cubic polynomial approximation may be improved using the eigenmodes of the radiative transfer equation.

References

1. J.E. Hansen, L.D. Travis, *Space Sci. Rev.* **16**, 527 (1974).
2. W.A. de Rooij, *Reflection and Transmission of Polarized Light by Planetary Atmospheres* Thesis, Free University, Amsterdam (1985).
3. R.D.M. Garcia, C.E. Siewert, *J. Quant. Spectrosc. Radiat. Transfer* **36**, 401 (1986).
4. J.F. de Haan, P.B. Bosma and J.W. Hovenier, *Astron. Astrophys.* **183**, 371 (1987).
5. R.D.M. Garcia, C.E. Siewert, *J. Quant. Spectrosc. Radiat. Transfer* **41**, 117 (1989).
6. M.I. Mishchenko, *J. Quant. Spectrosc. Radiat. Transfer* **43**, 163 (1990).
7. P. Stammes, J.F. de Haan and J.W. Hovenier, *Astron. Astrophys.* **225**, 239 (1989).
8. S. Chandrasekhar, *Radiative Transfer*, Oxford University Press, London and New York, 1950 (also Dover, New York, 1960).
9. H.C. van de Hulst, *Light Scattering by Small Particles*, J. Wiley and Sons, New York, 1957 (also Dover, New York, 1981).
10. P.B. Bosma, W.A. de Rooij, *Astron. Astrophys.* **126**, 283 (1983).
11. W.L. Dunn, R.D.M. Garcia, C.E. Siewert, *Astrophys. J.* **260**, 849 (1982).
12. J.E. Hansen, J.W. Hovenier, *J. Atmos. Sci.* **31**, 1137 (1974).

Zhao-xien Zhang

Shanghai Institute of Technical Physics,
Academia Sinica,420 Zhong Shan Bei Yi Road,
Shanghai,China,200083

In this paper a method is provided for inversion of
the atmospheric radiance measured by a channel of a
satellite-borne infrared spectrometer. Because the
atmospheric radiance data were not available, we had to use
the W.L.Smith's polynomial coeffients of the transmittance
of the 15 um CO_2 absorption band for this study. Evident-
ly,this method can be extended to the 4.3 um CO_2 absorption
band.

Considering a horizontal atmosphere divided in N
layers with the highst layer to be refered to as the first
and the layer near the earth surface as the Nth, then the
CO_2 transmittance at the ith level is

$$\tau_i(\gamma) = \prod_i \tau(\gamma, p_i, \frac{q_i+q_{i-1}}{2}, \bar{T}_i) / \tau(\gamma, p_{i-1}, \frac{q_i+q_{i-1}}{2}, \bar{T}_i), \quad (1)$$

where p,T and q are the atmospheric pressure,temperature
and the CO_2 mixing ratio,respectively. The calculation
of $\tau(\gamma,p,q,T)$ is based on the W.L.Smith'th polynomial and
its coefficients C_i (i=0.1,...,8),i.e.

$$\tau = \exp(-\exp W), \quad (2)$$

$$W = C_0 + C_1 X + C_2 Y + C_3 Z + C_4 XY + C_5 XZ + C_6 X^2 + C_7 X^2 Z + C_8 Z^2, \quad (3)$$

where $X=\ln(U(273/T))$, $Y=\ln(p/1000)$, $Z=\ln(T/273)$, $U=(qp/g)\mu_{CO_2}/\mu_r$, and μ_{CO_2} and μ_r are the molecular weights of CO_2 and
air. C's are all the functions of wave number γ. Subs-
tituting $X=\ln U-Z$ into (3), then,

$$a_0 + a_1 Z + a_2 Z^2 + a_3 Z^3 = 0, \quad (4)$$

where a's are the functions of U,W,Y and C's. Leting $p=\bar{p}$
$=p_i/2$, $q=\bar{q}$, (the wave symbol indicates equivalent value), Z
can be solved from (4). Consequently,the equivalent
temperature can be deduced using W.L.Smith's polynomial
representationof CO_2 transmission in condition of non-
homogeneous medium,

$$T = 273\exp(Z) \quad (5)$$

463

In order to inverse the CO_2 mixing ratio accurately, the atmospheric radiative transfer equation in pertubation form was used,

$$\delta_p I_y = \int_{B(p_t)}^{B(p_s)} \delta_p \tau_y(p) dB(p). \tag{6}$$

Where δ_p indicates pertubance, $\delta_p I$ the radiative variation corresponding to pertubance $\delta_p q(p)$ and $\delta_p T(p)$ caused by the variations in $q(p)$ and $T(p)$ relative to their references $q_r(p)$ and $T_r(p)$, respectively. The pertubance $\delta_p \tau(p)$ of $\tau(p)$ was seemed as caused by $\delta_p q_i$ only.

Similar to W.L.Smith's method[1,2], Eq. (19) can be rewritten as the non-liniar iterative formulae

$$\delta_p q^{(j+1)}(y,p) = \delta_p q^{(j)}(p)\left[1 + \frac{\delta_p I_y - \delta_p I_y^{(j)}}{D_y^{(j)}}\right], \tag{7}$$

$$D_y^{(j)} = -\sum_i \delta_p q^{(j)}(p_i)\left[\frac{\partial}{\partial \delta q_i} \delta_p \tau_y(p_i)\right]^{(j)} \Delta_i B_y(p), \tag{8}$$

$$\left[\frac{\partial}{\partial \delta q_i} \delta_p \tau_y(p_i)\right]^{(j)} = \tau_y^{(j)}(p) \ln \tau_y^{(j)}(p)/q^{(j)}(p)$$

$$\cdot \left\{\left[(c_q^{(j)}(y,p))^2(1+\ln \tau_y^{(j)}) + 2(c_6 + c_7 Y) \right.\right.$$

$$\left.\left. -c_q^{(j)}(y,p)\right]\frac{\delta_p q^{(j)}(p)}{q^{(j)}(p)} + c_q^{(j)}(y,p)\right\}, \tag{9}$$

$$c_q^{(j)}(y,p_i) = c_1 + c_4 Y_i + c_5 z_i^{(j)} + 2c_6 x_i^{(j)} + 2c_7 x_i^{(j)} + c_8 z_i^{(j)} z_i^{(j)} \tag{10}$$

Where Δ_i indicates the difference

$$\Delta_i x = x_{i-1} - x_i, \tag{11}$$

In the simulative calculation it was assumed that the CO_2 mixing ratios in the stratosphere and troposphere are 3.45×10^{-4} and 3.5×10^{-4}, respectively, the primary value is 3×10^{-4}, and their reference values were taken as 3.345×10^{-4} and 3.35×10^{-4}, respectively. In addition, it was considered that the inversion error of the atmospheric temperature is $2.2°C(rms)$ and the radiation measurement error 0.25 erg/sec-cm^2-str-cm^{-1}. The atmospheric CO_2 mixing ratios were inversed for 63 channels (with a bandwidth of 5 cm^{-1}) in spectral interval 507.5—817.5 cm^{-1}. The maximal errors of sole channel inversion are 2% for 12 channels. Due to very quick convergence only four iterations were needed.

Refenrence

1. W.L.Smith,"A polynomial representation of carbon dioxide and water vapor transmission", Technical Report, NESC 47,Washington,D.C.,Feb.1969.

2. W.L.Smith,"Iterative solut ion of the radiative transfer equation for the temperature and absorbing gas profiles of an atmosphere",Appl.Opt., 9(1970),9,1993—1999.

R.F.Pueschel, Mail Stop 245-4, NASA Ames Research Center, Moffett Field, CA 94035-1000, Phone: (415) 604 5254.

J.M.Livingston, SRI International, Menlo Park, CA 94025.

M.P.McCormick, NASA Langley Research Center, Hampton, VA 23665

The Stratospheric Aerosol Measurement (SAM II) sun photometer aboard the Nimbus 7 spacecraft has, since 1979, provided a record of 1 μm light extinction due to aerosols in the polar stratospheres (Fig.1).

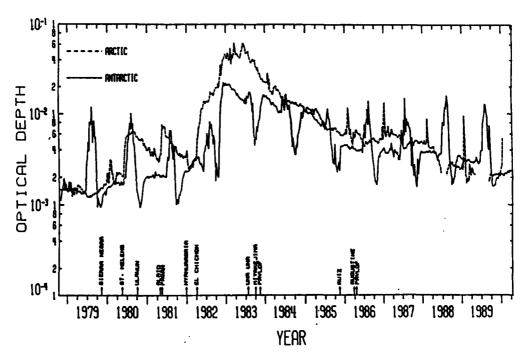
Figure 1: SAM II (1 μm) polar stratospheric optical depths between October 1978 and April 1990.

Typical for this record is an enhancement above background by about one order of magnitude of extinction of radiation at 1 μm wavelength, produced by aerosols in winter when the temperature falls below 200K (McCormick et al., 1982). This enhanced light extinction is due to the formation of a tenuous cloud by the deposition onto the background aerosol of a mixture of water and nitric acid, probably as nitric acid trihydrate (NAT; Pueschel et al., 1991). It follows from Fig. 1 that the optical depth increases caused by these clouds are similar to the one

caused by the Mt.St.Helens 1980 eruption, but are much smaller than the one due to the El Chichon 1982 eruption.

During the Arctic Airborne Stratospheric Expedition (AASE) in 1989 we sampled aerosols aboard the ER-2 aircraft with impactors, and analyzed the samples for particle size and shape by scanning electron microscopy. Fig. 2 shows the size distributions obtained on 24 January in background air (curve a) with log-normal parameters N=3.2 cm^{-3}, r_g=0.10 μm, σ=1.62, and after penetrating a Type 1 polar stratospheric cloud (curve b) with log-normal parameters N=2.2 cm^{-3}, r_g=0.24 μm, σ=1.76. In the background case the air was subsaturated with respect to both ice and NAT; within the cloud the saturation ratio with respect to ice was 80%, and the atmosphere was highly supersaturated with respect to NAT (Pueschel et al., 1991). Because (1) the air was subsaturated with respect to ice, (2) the particles were spherical (Pueschel et al., 1991), and (3) particle size increased by only a factor of three (Fig. 2), we conclude that the aerosol was made up of Type I polar stratospheric cloud particles.
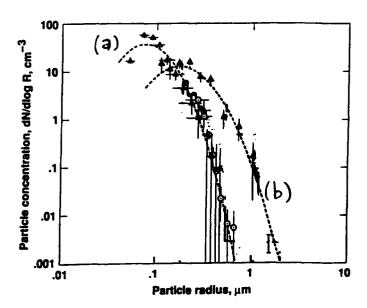

Figure 2: Background aerosol (curve a) and Type I polar stratospheric cloud (curve b) size distributions measured on 24 January 1989 aboard the NASA ER-2 aircraft.

We have computed the optical (extinction) properties of both aerosol size distributions shown in Fig. 2 using Mie theory, assuming a refractive index m=1.52-0i. The results are presented in Fig. 3.
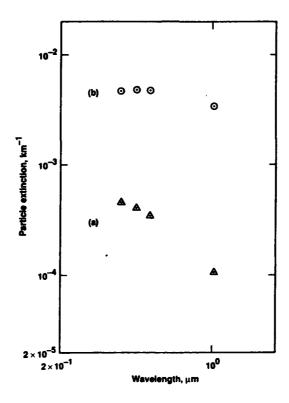
Figure 3: Aerosol light extinction at wavelengths 385, 453, 525 and 1020 nm for the background aerosol (curve a) and the Type I polar stratospheric cloud (curve b).

It follows from Fig. 3 that the light extinction due to the formation of a Type I polar stratospheric cloud is enhanced above background by about one order of magnitude in the visible, and by a factor of about 50 in the near IR. In conjunction with Fig. 1 we conclude that the historic near-IR extinction of the SAM II sun photometer is due primarily to Type I polar stratospheric clouds; a significant concentration of ice crystals typically exceeding 10 µm diameter (Goodman et al., 1989; Dye et al., 1990) would have caused a much greater light extinction than what the satellite has been observing. Implications are that the heterogeneous chemistry that precedes ozone depletion over Antarctica in early spring has to involve Type I polar stratospheric cloud, rather than ice particles. Consequences are that (1) these particles exhibit a larger surface area than would ice crystals (Type II particles) for heterogeneous reactions, and (2) that they are too small to settle out from the stratosphere in the course of a winter season (Toon, 1990). Hence, upon evaporation in spring, they make available NOx gas that can combine with reactive halogen radicals to terminate ozone depletion. For example, ozone-reactive chlorine monoxide can be converted into inert chlorine nitrate.

References:

Dye, J.E., B.W.Gandrud, D.Baumgardner, K.R.Chan, G.V.Ferry, M.Loewenstein, K.K.Kelly, and C.W.Wilson, Observed particle evolution in the polar stratospheric cloud of 24 January, 1989, *Geophys.Res.Lett.*,17,413-416, 1990.

McCormick, M.P., H.M.Steele, P.Hamill, W.P.Chu, and T.J.Swissler, Polar stratospheric cloud sightings by SAM II, *J.Atmos.Sci.*, 39, 328-331, 1982.

Goodman, J., O.B.Toon, R.F.Pueschel, K.G.Snetsinger, and S.Verma, Antarctic stratospheric ice crystals, *J.Geophys.Res.*, 94, 16449-16458.

Pueschel, R.F., G.V.Ferry, K.G.Snetsinger, J.Goodman, J.E.Dye, D.Baumgardner, and B.W.Gandrud, Formation and characteristics of polar stratospheric clouds, *J.Geophys Res.* (submitted, 1991)

Toon, O.B., R.P.Turco, J.Jordan, J.Goodman, and G.V.Ferry, Physical processes in polar stratospheric ice clouds, *J.Geophys.Res.*,94,11359-11380, 1989.

DETERMINATION OF THE ATMOSPHERE   **P̣50**

REFRACTION INDEX BY SATELLITERADIO SIGNALS

B.M.Shevtsov, Pacific Oceanological Institute,

7 Radio St., Vladivostok,USSR,690032

During observations of radio signals from satellites of the navigation system TRANSIT (150 and 400 MHz) over the sea surface not far from the horizon one notes enough frequently signal oscillations more fast than usual interference beats. By contact measurements of the atmosphere radio characteristics there was found the relationship of these oscillations with raised inversion layers. It is possible to show by the solution of the direct problem that fast oscillation are the result of the multipath interferation of the radiation, reflected from the inversion layer. The frequency of fast oscillations is defined by the altitude of the layer bedding,and the amplitude - by the layer reflection factor. This allows to estimate parameters of the inversion layer according to the character of beats (A.N.Bogaturov et.al., DAN AN SSSR, in print, in Russian).

It is possible to solve the inverse problem in the rigorous statement, i.e. to restore the altitude dependence of the atmosphere refraction index by satellite radio observations using the differential method (Shur-algorythm).

Because of the big remoteness of satellites, their radio signals can be regarded as monochromatic plane waves, incident an angle upon the nearsurface inhomogeneous atmosphere layer. Radio signals which pass through the atmosphere inhomogeneities, are received near the Earth surface. It is possible to show, that synchronized amplitude - phase measurements of radio signals over two polarization in dependence on the incidence angle, give the initial data which are necessary for the inverse problem solution by the differential algorythm. However, random influences (the noustability of the satellite transmitter, deposit of ionosphere and atmosphere turbulence) lead to fluctuation of receiving data and put restvictions on the resolution of the restoration method.

SCATTERING BY CONICAL SURFACES OF ARBITRARY CROSS-SECTIONS.
EXACT SOLUTIONS AND HIGH-FREQUENCY ASYMPTOTICS **P51**

V.P.SMYSHLYAEV

Leningrad Department of Mathematical Institute of the USSR Academy of Sciences, Fontanka 27, Leningrad 191011, USSR

1.Introduction. We consider the time-harmonic wave process either in homogeneous acoustic (AC) media, described by the Helmholtz (reduced wave) equation

$$(\Delta + k^2) \, u(\bar{r}) = 0, \tag{1}$$

or in homogeneous electromagnetic (EM) media satisfying the Maxwell equations

$$\nabla \times \bar{E} = ik \, \bar{H} \ , \qquad \mathrm{div} \, \bar{E} = 0$$
$$\nabla \times \bar{H} = -ik \, \bar{E} \ , \qquad \mathrm{div} \, \bar{H} = 0 \tag{2}$$

Let the scattering body be a cone of arbitrary cross-section with vertex in $\bar{r}=(x,y,z) = 0$. The form of the cone is determined by the choice of the subdomain N of the unit sphere remaining after the cutting out of a spherical segment by the cone-obstacle. It is convenient to introduce the system of coordinates $\bar{r}=(r,\omega)$ where $r=|\bar{r}|$ is the distance to the vertex and $\omega =\bar{r}/r$ belongs to N. Let S be the surface of the conical obstacle.

In AC case we suppose that the obstacle is perfectly soft, i.e. $u_{|S} = 0$, or perfectly hard ($\partial u/\partial n_{|S} = 0$, n is the normal to S). In EM case the obstacle is supposed to be perfectly conducting, i.e.

$$(\bar{n} \times \bar{E})_{|S} = 0. \tag{3}$$

We consider the incident wave field generated by the point source $u_0 = e^{ik|\bar{r}-\bar{r}_0|} / 4\pi|\bar{r}-\bar{r}_0|$, $\bar{r}_0=(r_0,\omega_0)$, $\omega_0 \in$ N   in AC case and by the oriented electric (magnetic) dipole in EM case :

$$\bar{E}_0 = \nabla \times \nabla \times \bar{\Pi}, \ \bar{H}_0 = -ik \, \nabla \times \bar{\Pi}, \ \mathrm{or} \ \bar{H}_0 = \nabla \times \nabla \times \bar{\Pi}, \ \bar{E}_0 = +ik \, \nabla \times \bar{\Pi},$$

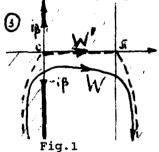$$\bar{\Pi} = \bar{I} \, e^{ik|\bar{r}-\bar{r}_0|} / 4\pi|\bar{r}-\bar{r}_0|, \ \bar{I} \text{ is the vector of polarization.}$$

The case of the plane wave incidence can be treated as the limiting one when $r_0 \to \infty$.

The total wave field should satisfy also the definite conditions at infinity and near the vertex of the cone (and also near the edges of the cone-obstacle if they exist).

We exploit in our considerations the ideas having much in common with ones introduced in [1,Ch.4] for the plane wave incidence.

473

2. Sommerfeld integrals.

AC case. Due to the separation of variables in Helmholtz operator in coordinates (r,ω) the solution of the AC problem can be represented in the form of decomposition by eigenfunctions [2]. Representing the product of Bessel and Hankel functions, appearing in eigenfunctions, by the contour integral we obtain the following representation for the total AC field $G(\bar{r},\bar{r}_0)$:

Fig.1

$$G(\bar{r},\bar{r}_0) = c(rr_0)^{-1/2}$$

$$\int_W H_0^{(1)}(k(r^2+r_0^2-2rr_0\cos s)^{1/2})\Phi(\omega,\omega_0,s)ds \qquad (4)$$

Here $H_0^{(1)}$ is the Hankel function of the first kind, $c=const$, $\Phi(\omega,\omega_0,s)=e^{-iAs}\delta_{\omega_0}$ is the Schwartz kernel of the operator e^{-iAs}, where $A=(-\Delta_\omega+1/4)^{1/2}$ and Δ_ω is the Laplace-Beltrami operator on N with corresponding boundary condition on the boundary ∂N. The integration contour is shown on Fig.1; $\pm i\beta$ where $\beta=(\cosh)^{-1}(\ (r^2+r_0^2)/2rr_0\ )$ are the branch points.

When the incident wave is plane and the direction of incidence is $(-\omega_0)$ we obtain from (4) using the limiting procedure when $r_0\to\infty$

$$u(\bar{r},\omega_0)=c'(kr)^{-1/2}\int_W e^{-ikr\cos s}\,\Phi(\omega,\omega_0,s)ds, \qquad (5)$$

with the same integration contour W and $\beta=+\infty$ [2].

The representations (4) and (5) we call Sommerfeld integrals analogously to the problems of diffraction by wedge.

EM case. The vector diffraction problem can be reduced to the pair of the scalar ones introducing the Debye potentials $u(\bar{r})$ and $v(\bar{r})$:

$$\bar{E} = \nabla \times \nabla \times (u\bar{r}) + ik\,\nabla \times (v\bar{r})$$
$$\bar{H} = \nabla \times \nabla \times (v\bar{r}) - ik\,\nabla \times (u\bar{r}) \qquad (6)$$

If the scalar functions u and v satisfy the Helmholtz equations (1) and the boundary conditions $u|_S=0$, $\partial v/\partial n|_S=0$ then (6) satisfy automatically (2) and (3).

Consequently, to solve the EM diffraction problem it is necessary

1) to determine the solutions u_0 and v_0 of Helmholtz equation satisfying (6) with $(\bar{E}_0,\bar{H}_0)$ in the left hand side;

2) to solve the scalar diffraction problems;

3) to substitute the scalar solutions obtained in (6).

In the case of plane polarized wave incidence [3] the total Debye potentials ku, kv are like in (5) with the functions Φ_D and Φ_N instead of Φ and

$$\Phi_D = e^{-iA_D s} (-\Delta_\omega^D)^{-1} \partial_\xi \delta_{\omega_0}(\omega) \quad , \quad \Phi_N = e^{-iA_N s} (-\Delta_\omega^N)^{-1} (I-P_1) \partial_\eta \delta_{\omega_0}(\omega).$$

Here "D" and "N" denote the Dirichlet and Neumann boundary conditions; P_1 is the ortoprojector $P_1\varphi(\omega) = \int_N \varphi(\omega)d\omega / \int_N d\omega$; ξ and η are the vector fields on N describing the polarization of $\bar{E}_0$ and $\bar{H}_0$.

In the case of dipole source the Debye potentials can be constructed in the form of Sommerfeld integrals like (4).

3. **High-frequerncy asymptotics.** We investigate the exact solutions (4),(5) in a high-frequncy (HF) approximation , i.e. when $kr, kr_0 \gg 1$. We replace in (4) $H_0^{(1)}$ on its asymptotics and deform the contour W into W'(Fig.1). Using the properties of the functions Φ, the complete HF description can be fulfilled combining the stationary-phase and the propagation of singularities of amplitude analysis. This description is in conformity with predictions of J.B.Keller's geometrical theory of diffraction.

The contribution of the stationar point $s=\pi$ yields the formulae for the spherical wave diffracted by the vertex

$$G_{diffr}(\bar{r}, \bar{r}_0) \simeq \frac{e^{ik(r+r_0)}}{2krr_0} \Phi(\omega, \omega_0, \pi) \tag{7}$$

in the case of the point source (for the plane wave incidence the obvious modification of (7) takes place).

In EM case (plane wave incidence) the following formula for diffracted wave takes place :

$$\left. \frac{\bar{E}}{\bar{H}} \right|_{diffr} \simeq \pi \frac{e^{ikr}}{kr} \left[\nabla_\omega \left\{ \begin{matrix} \Phi_D \\ \Phi_N \end{matrix} \right\} \pm \nabla_\omega \left\{ \begin{matrix} \Phi_N \\ \Phi_D \end{matrix} \right\} \times 1_r \right] \tag{8}$$

All the functions Φ_D, Φ_N have the arguments (ω, ω_0, π). The formulae for the spherical wave corresponding to the dipole source are of the similar form.

In cases of circular and elliptic cones and a plane angular sector the diffraction coefficients are expressed in terms of corresponding special functions [2,3]. In general case the numerical calculations could be realized using the reduction to the Laplace equation in the part of unit ball $(r \leq 1, \omega \in N)$ decribed in [1].

[1].V.A.Borovikov, Diffraction by polygons and polyhedrons, Nauka, Moscow, 1966 (in Russian).
[2].V.P.Smyshlyaev, Wave Motion, v.12(4), 329-339 (1990).
[3].V.P.Smyshlyaev, The high frequency diffraction of EM waves by cones of arbitrary cross-sections. Subm."Electomagnetics".

ANOMALOUS INTERFERENCE PATTERN IN PENUMBRA REGION OF P52
OPTICAL GAUSSIAN BEAM DIFFRACTION ON CYLINDER
(ON CORPUSCULAR LIGHT PHENOMENA IN DIFFRACTION)

V.N.Smirnov, G.A.Strokovsky

Research Institute of Physics, Leningrad State University
1, Ulianovskaya str., Leningrad-Petrodvoretz 198904, USSR

The diffraction pattern in penumbra region beyond circular cylinder of radius ρ, illuminated by optical Gaussian beam is represented by oscillating far field ($r \gg \rho$) intensity distribution $I(r,\varphi)$ of diffracted light on observation angles φ [1-3]. Based on the principle of "local field", first introduced by V.A.Fok [4], this distribution is usually interpreted as a result of two-wave interference of "boundary waves", arising from narrow sectors on the cylinder surface. Within fixed observation geometry, any deformation and displacement of dark and bright fringes in diffraction pattern are naturally considered to be connected with variations of phase difference Φ between two narrow sectors on the incident wave phase front, corresponding to the cylinder "edges", i.e. with characteristic of phase front inhomogeneity.

We present the results of anomalous diffraction in penumbra region of Gaussian beam (GB) from the source I (see Fig.1) focused by lens 2 on metallic cylinder 3 in the plane $z=z_c$. The experimentally observed diffraction patterns are anomalous in the sense that deformation and displacement of interference fringes on the screen 5 can not be adequately connected with the appropriate distortions of GB wave front, produced by opaque obstacle 4 (further called "label") in the plane $z=z_l$. Thin metallic filaments of diameters $2\rho=15-80\mu m$ were mounted in the plane $z=z_c$ along X axis and aligned in GB (Z is the propagation axis). The waist width of focused GB was $2w=40\mu m$. Thick metallic wires of diameters $2R=250-2000\mu m$ served as "labels" and were placed on the beam axis at angle ϑ with respect to X axis in the plane $z=z_l$. The case $\vartheta=0$ corresponds to the label parallel to cylinder (LPC) and the case $|\vartheta|>0$ means that the label is inclined from cylinder (LIC).

The schematic view of the parts of diffraction patterns are shown in Fig.2; the initial distribution without label is depicted in Fig.2a. The diffraction pattern with LPC is shown in Fig.2b; it remains practically undisturbed within wide variation range of diameters of cylinders and labels as well as within cylinder translation along Y axis in the range $|\Delta y| \leq 100\mu m$. It is difficult to explain the observed displacement of maxima on half-period by appearance of phase difference $\Phi \equiv \pi$ on the incident wave phase front due to the label, since the experimental situation is purely symmetrical. The same difficulties manifest in the attempts to explain displaced and tilted at angle ϑ maxima in the case of LIC (see Fig.2c). Test experiments with the slit in opaque screen, taken as label (in the

sense of Babinet analogy), proved the absence of phase front deformations in z_e plane by LPC both as wire and slit (Fif.2d) Nevertheless, with inclined slit the diffraction maxima are also tilted at angle ϑ (Fig.2e) as it was with LIC (Fig.2c).

The carried out theoretical analysis in wave optics approximation (Kirchhoff integral) showed that the phase front in the plane z_e remains plane in the case of symmetrical position of label in GB if the observation plane is taken in the waist of "unlabelled" beam. It appears rather doubtful to attribute to the interference (and hence, to wave) phenomena those ones, in which the redistribution of light flux density in space is not defined mainly by changes of phase difference of interfering waves, i.e. by superposition of e.m. fields.
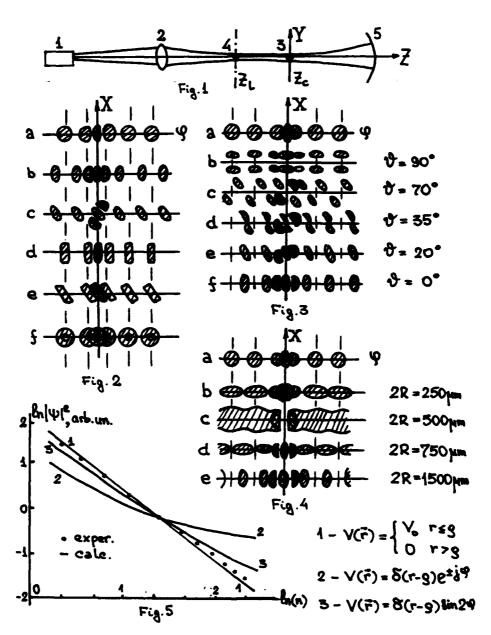
The alternative explanation of anomalous "interference" pattern in penumbra region follows from the analysis of the evolution of diffraction maxima with gradual changes of angle $|\vartheta|=0\div\pi$ in the experiments with LIC (see Figs.3a-f) and gradual changes of LPC middle-section in the range $2R=100\div1500\mu m$ (see Figs.4a-e). Relying on changes in Figs.3-4, one may suppose the intensity redistribution in diffraction pattern with LPC and LIC shows by no means the displacement of former diffraction maxima along ϑ but the formation of new maxima from partly intersected neighboring segments of former maxima. Former maxima happened to be splitted in the middle by shadow from the label and, thus, bright regions are expelled to the places of former minima. As a result, the diffraction pattern from focused GB with $w \approx \rho$ may be interpreted as bundle - the set of practically equidistant discrete directions φ_n (n=1,2..) separated by $\delta\varphi$, along which partly intersected energy fluxes (noninterfering light beams) are propagated after being scattered from the cylinder. The validity of this assumption seems to be clearly seen in the experiments with modified label geometry (see Fig.2e), when the label was represented by opaque circular spot blocking the beam center. To describe phenomenologically the process of scattering in terms of light particles, one may attribute to the scattered beams, taken as some light particles with the pulse $p=\hbar k$, the transversal component of pulse Δp_n as: $|\Delta p_n| \approx p_c |\varphi_n| \approx (h/2\rho)(n-1/2)$; $|\delta\varphi|=h/2\rho p_c$; $\varphi_n = \delta\varphi$ (n-1/2); where p_c is the pulse of incident particle, h - Plank constant, k - wave number. This "corpuscular" approach to the process of diffraction on cylinder is in full agreement with the principle of "local field" [5] and doesn't contradict with propagation of light as wave propagation in free space. Experimental envelope of diffraction maxima (Fig.2a) $I(\varphi_n)$ appeared to be comparable in Fig5 with quantum mechanics calculations of probability maxima $|\psi(\varphi_n)|$ of pulse changes $\Delta p(\varphi_n)$, based on Schrodinger equation in Born approximation, for resonant particle scattering on cylindrical potential $V(r)$.

[1]. V.S.Buldyrev, V.N.Smirnov, G.A.Strokovsky, K.K.Fradkin. Optika i Spektroskopiya (USSR), (1985), 59, p.1255 (Amer.Transl. Optics and Spectr. (1985),59,p.1053).
[2]. V.S.Buldyrev, M.A.Lyalinov, V.N.Smirnov, G.A.Strokovsky, K.K.Fradkin. JETP (USSR), (1990),97,3,p.872.

[3]. P.Langlois,A.Boivin,R.Lessard. Can.J.Phys.,63,p.301(1985)
[4]. V.A.Fok. The problems of diffraction and propagation of waves. (Sov.Radio,1970).
[5]. V.N.Smirnov, G.A.Strokovsky. Proc.Symp."Waves and diffraction" (USSR), 2, p.131.(1990)

Fig.1

Fig.2

Fig.3

$\vartheta = 90°$

$\vartheta = 70°$

$\vartheta = 35°$

$\vartheta = 20°$

$\vartheta = 0°$

Fig.4

$2R = 250 \mu m$

$2R = 500 \mu m$

$2R = 750 \mu m$

$2R = 1500 \mu m$

Fig.5

• exper.
— calc.

$1 - V(\vec{r}) = \begin{cases} V_0 & r \leq g \\ 0 & r > g \end{cases}$

$2 - V(\vec{r}) = \delta(r-g)e^{\pm j\varphi}$

$3 - V(\vec{r}) = \delta(r-g)\sin 2\varphi$

DIFFRACTION OF ELLIPTICAL HERMITE-GAUSSIAN BEAM ON P53
WEDGE-SHAPED DIELECTRIC PLATE AT OBLIQUE INCIDENCE

V.N.Smirnov, G.A.Strokovsky

Research Institute of Physics, Leningrad State University
1, Ulianovskaya str., Leningrad-Petrodvoretz 198904, USSR

The transmission and reflection of elliptical Hermite-Gaussian beams by wedge-shaped dielectric plate at oblique incidence are analyzed taking into account the multiple reflections on plate interfaces. Theoretical results appeared to be in good agreement with experimental dependencies of generation intensity in bleaching resonances of optical ring resonator on orientation of small (<1') wedge in quartz plate.

We consider the plate of thickness $l \gg \lambda$ (λ is the wavelength) with small wedge angle $\chi \ll 1$, placed at a distance z_p from the waist of incident elliptical Hermite-Gaussian beam of amplitude e_{MN}. The wedge plane ζZ (Fig.1) is inclined to XZ plane at angle ψ and normal ν to bisectoral wedge plane is tilted at angle φ with respect to Z (oblique incidence) in QZ plane, which is inclined at angle α to XZ plane. Due to presence of wedge, the transmitted and reflected beams are splitted in a bundle in ζZ plane and within oblique incidence they are also stratified into a comb in QZ plane. One may derive the following expression for cross-term I^{ij} of interfering fields E^i, E^j ($i \neq j = 0,1,..$) of beams, produced by wedge, as ($|\chi| \ll |\varphi|$) :

$$I^{ij}(\varphi)=2Re\{\int\!\!\!\int_{-\infty}^{+\infty} E^i (E^j)^* dxdy\}= 2e_{MN}^2 (1-\rho^2)\rho^{2(i+j)}\cos(2\theta(i-j))L_{MN}^{ij} *$$

$$* \exp\{-(i-j)^2(\tau_x^2+\tau_y^2)\}; \quad \tau_t^2=\left[\frac{\Delta R_t(\alpha)-z\ n\chi R_t(\psi)}{w_{0t}}\right]^2+[kw_{0t} n\chi R_t(\psi)]^2;$$
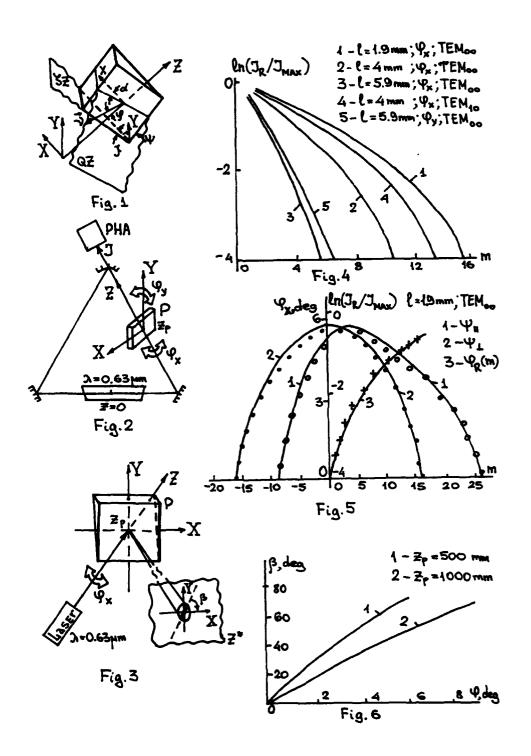
$$R_x(u)=\cos(u); \quad R_y(u)=\sin(u); \quad L_{MN}^{ij}=\lambda_{ij}^x(M)\lambda_{ij}^y(N); \quad (t=x,y) \qquad (1)$$

$$\lambda_{ij}^t(s)= \sum_{\mu=0}^{s} \frac{(-1)^\mu}{\mu!} C_s^\mu \{(j-i)\ \sqrt{2}\tau_t\}^{2\mu}; \quad ; \quad \rho=(\frac{1-n}{1+n})^2; \qquad (2)$$

$\theta= knl\cdot\{1-n(n^2-\sin^2\varphi)^{-1/2}\}$; $\Delta= l\sin\varphi \cdot (n^2-\sin^2\varphi)^{-1/2}$; $k=2\pi/\lambda$; n - refractive index, $w_{0x,0y}$ - waist radii in XZ and YZ planes respectively, M(x),N(y) are indices of Hermite polynoms, * means complex conjugation.

As it follows from (1)-(2), the influence of rotation at angle φ is measured in the scale of waist dimensions $w_{0x,0y}$ (z=0). On the opposite, wedge influence is defined by beam radius at the plate located in $z=z_p$ plane. In general, the influences of tilting angle φ and wedge angle χ are independent only in case of their orientation along orthogonal axes X,Y of incident beam.

For small $|\varphi| \ll 1$ one may apply two-beam interference approximation i,j=0,1 (for transparent dielectrics in optical

Fig. 1

Fig. 2

Fig. 3

$ln(J_R/J_{MAX})$

1 — $l = 1.9$ mm; φ_x; TEM$_{00}$
2 — $l = 4$ mm; φ_x; TEM$_{00}$
3 — $l = 5.9$ mm; φ_x; TEM$_{00}$
4 — $l = 4$ mm; φ_x; TEM$_{10}$
5 — $l = 5.9$ mm; φ_y; TEM$_{00}$

Fig. 4

φ_x, deg $ln(J_R/J_{MAX})$ $l = 1.9$ mm; TEM$_{00}$

1 — $\Psi_{\parallel}$
2 — $\Psi_{\perp}$
3 — $\varphi_R(m)$

Fig. 5

β, deg

1 — $z_p = 500$ mm
2 — $z_p = 1000$ mm

Fig. 6

482

region $\rho \approx 0.04 \ll 1$), thus thecondition $\theta=m\pi$ ($m=0,1,...$) gives the transmission peaks (bleaching resonances), for which $\varphi_R(m)\approx \pm(m\lambda n/l)^{1/2}$, $\Delta \approx l\varphi_R/n$ (m is number of resonance). The presence of wedge $\chi\neq 0$ leads to spatial angular asymmetry $\pm|\varphi_R|$ of transmitted light, arising from either compensational ("+" in eqn.(1)) or additional ("-") contribution of wedge to I^{10} in comparison with plate rotation. In particular case $\alpha\equiv 0$, when $\psi=\pi/2+\alpha$, the angular asymmetry vanishes.

Experimental studies of or reflection and transmission of linear polarized Gaussian beams by dielectric plate were carried out when placing glass plate (P) of thickness $l=0.12\sim 6$mm in optical resonator of ring gas laser (Fig.2) or by illuminating the plate in free space by external laser beam (Fig.3) In ring laser the photoamplifier (PHA) registered the dependencies of generation intensity J in observed bleaching resonances on azimuth (φ_x) and saggital (φ_y) angles of plate rotation for different plate thicknesses and mode indices. In Fig.4 the envelopes of generation intensity peaks $J_R(m)$ for plane parallel plate are normalized to generation intensities without plate. In Fig.5 typical experimental dependencies J_R via resonance number m are depicted for plate $l=1.9$mm, rotating in azimuth plane with orientation of wedge angle $\chi=0.82*10^{-4}$ parallel ($\psi=\psi_\parallel$ $=0$, circles) and perpendicular ($\psi=\psi_\perp$ $=\pi/2$, points) to plane of incidence. In the same figure crosses show the dependence $\varphi_R(m)$ practically indifferent to wedge orientation.

One may relate the mode generation intensity J with diffraction losses q [1], induced by dielectric plate in resonances, as follows:

$$\frac{J}{J_{max}} = \frac{[\varkappa/(\varepsilon+q)]^2-1}{[\varkappa/\varepsilon]^2-1} \ ; \ q_R(m)=1-I^{10}_{MN}(\varphi_R(m))/|e_{MN}|^2; \qquad (3)$$

where $\varkappa$ and ε are gain and initial losses of resonator. Solid curves 1($\psi=0$) and 2($\psi=\pi/2$) in Fig.5, representing the results of numerical calculations, based on (1)-(3) with $\alpha=0$, $n=1.5$, $z=270$mm, $\varkappa=4.7\%$, $\varepsilon=2.2\%$, are in good agreement with experimental data.

The structure of interference pattern of reflected beams was analyzed in free space by studying the dependence of plate tilt in XZ plane on orientation angle β of dark fringes (Fig.3) in observation plane z^*. The experimental curve $\beta(\varphi)$ in Fig.6 fully coincides with analytical formulae $tg(\beta) = =l\varphi/(z\chi)$, that follows from (1)-(2).

The carried out investigations showed the validity of two-beam approximation for description of light diffraction for wedged dielectric plate in optical resonator and uncorrect approach, developed in [2], where no interference phenomena in wedge was taking into account.

References.
[1]. V.N.Smirnov,G.A.Strokovsky. Optika i Spektroskopia, 60, p.1053 (1985) (Amer.Transl. Optics & Spectroscopy, 60, p.652 (1985))
[2] L.Janicievic Год.зб.Физ. Скопje, (1986), 36, p.31.

V.E.Grikurov
Leningrad Branch of Mathematical Institute AS USSR,
Fontanca 27.Leningrad.USSR

Source-excited high-frequency propagation along concave boundaries is known cannot be describe by ray-optical methods due to the accumulation of caustics connected with rays which had undergone multiple reflections. In general, the resulting field near the boundary can be expressed in a sum of few rays plus canonical integral [1]. This canonical integral, in turn, for long propagation distances or/and strong curvature can be reduced to a several whispering gallery modes plus a much smaller integral reminder [2].

The analogous effect arises when the point source is located in the another medium (Ω_1) contacting with the first one (Ω_2) from convex side, provided the critical reflection angle is appeared. In this case refraction on almost tangent angles is presented and the wave field propagating along a boundary by the way described above is excited in medium Ω_1. Due to boundary conditions the concomitant wave field is propagated in Ω_2. The description of this so-called "interfering head wave" have been performed[3,4] and as expected had to be connected with the same canonical integral.

But known formulas become invalid for small distances along the boundary or/and for weak boundary's curvature (in effective sense, see (3) and below), i.e. near the direction of critical reflection. Investigation of this region is an our goal. Note that the limit case of plane interface have been studied previously[5,6] and these results are in agreement with the new canonical integral (4) of given paper.

Traveling to a formulas, necessary notations should be introduced. Let S be a smooth interface between inhomogeneous dielectrics $\Omega_{1,2}$ and parameter α numerates rays generated by a source $M_o \in \Omega_2$, meeting the surface S at points N_α under critical angle. These rays are continued along S by ray optic's way. They can be attended by a family of rays teared away from S at points N

under critical angle too. Let τ be the traveling time from M_o to N and $\zeta = \tau +$ traveling time from N to observation point $M \in \Omega_2$. Set (α, τ, ζ) is the appropriate coordinate system for our problem.

Provided the source is an electric dipole with time dependence $a(t) \cdot \exp\{-ip\vartheta(t)\}$, p is a large parameter, the cross part $E^{\alpha,\tau}$ of e/m field $\overset{*}{E}$ formed due to interference between reflected and head waves near the critical reflection direction is appeared to have a form

$$E^{\alpha,\tau}(M,t) = \text{const} \cdot a(t-\zeta)[p\vartheta'(t-\zeta)]^{3/2} \Phi^{\alpha,\tau}(N_\alpha)\Phi^{\alpha,\tau}(N) \exp\{-ip\vartheta(t-\zeta)\}$$
$$\cdot [\varepsilon_1(M_o)\varepsilon_1(M)J]^{-1/2} G(\gamma,\sigma) \quad [1 + O(p^{-1/7})]. \tag{1}$$

Notations used in (1) are:

$$\Phi^{\alpha,\tau}(N) = \left[\frac{\varepsilon_1}{\mu_1}c_2 \left(Z \cdot \cos\chi_o\right)^{\pm 1}/R_{eff}\right]^{1/2} \cdot \exp\left\{-\int_{N_\alpha}^{N} ds \cdot Z^{\pm 1}/R_{eff}\right\}. \tag{2}$$

ε, μ – dielectric parameters, c – wave speed, χ_o – critical angle. $Z = (\mu_1/\mu_2)\cos\chi_o$:

$$R_{eff}(N) = \left(\frac{1}{\rho} + \frac{1}{c_1} \cdot \frac{\partial c_1}{\partial n}\bigg|_S\right)^{-1} - \tag{3}$$

the effective curvature radios (ρ^{-1} – surface curvature, n – normal to S in Ω_1). Condition $R_{eff} > 0$ is assumed and of great importance for our results; $J(M_o, N_\alpha, N, M)$ – the whole geometrical factor for rays described above (can be calculated in explicit form for homogeneous Ω_2 and arbitrary S); $G(\gamma,\sigma)$ – the new canonical integral of the form

$$G(\gamma,\sigma) = \left(\int_{L_1} \frac{1}{v(\lambda)w_2(\lambda)} + \int_{L_2} \frac{v'(\lambda)}{v(\lambda)} + \int_{L_3} \frac{w_2'(\lambda)}{w_2(\lambda)}\right)\exp\left\{i(\gamma\lambda + \sigma\lambda^2)\right\} d\lambda. \tag{4}$$

where $v(\lambda), w_2(\lambda)$ – Airy functions, $L_1 = (\infty e^{4\pi i/3}, 0)$, $L_2 = (\infty e^{-i\pi/3}, 0)$, $L_3 = (0, \infty e^{2\pi i/3})$; arguments of the function $G(\gamma,\sigma)$ are

$$\gamma(N,t) = \left[\frac{p}{2} \cdot \vartheta'(t-\zeta)\right]^{1/3} \cdot \int_{N_\alpha}^{N} ds / (R_{eff}^2 c_1)^{1/3}. \tag{5}$$

$$\sigma(M_o, N_\alpha, N, M, t) = -\frac{1}{4} \cdot \text{tg}\chi_o \left[\frac{2}{p\vartheta'(t-\zeta)} \quad \frac{c_1^4}{R_{eff}^4}\right]\Big|_{N_\alpha} \cdot \left|\frac{\partial\tau}{\partial\chi}\right|_{\chi=\chi_o}. \tag{6}$$

For small γ (large R_{eff} or/and small distance between N_α and N) the second term in exponent at (4) is essential, and if $R_{eff} \to \infty$ integral $G(\gamma,\sigma)$ transforms to a known expression [5,6] using Weber's function of order 1/2. Otherwise, this term can be neglected (due to it's small asymptotic order) as well as integral over L_1, and the reminder coincides with the canonical integral $G(\gamma)$ of papers[1-4].

References:

1. V.M.Babich & V.S.Buldyrev. Asymptotic Methods of Short Wave Diffraction. Nauka,Moscow.1972.
2. T.Ishihara & L.B.Felsen. High-frequency propagation at long ranges near a concave boundary. Radio Science,vol.23,no.6,pp.997 -1012 (1988).
3. V.S.Buldyrev. Short wave interference in the problem of diffraction on inhomogeneous arbitrary-section cylinder. Radiophys.& Quntum Electron.,vol.10,no.5,pp.874-881 (1967).
4. V.E.Grikurov. Synthetic seismograms for interference wave fronts. Izv. Acad. Sci.USSR. Phys. Solid Earth, vol.16. no.6. pp.413-416 (1980).
5. L.M.Brekhovskikh. Waves in Layered Media. Academic,NY.1980.
6. L.B.Felsen & N.Marcuvitz. Radiation and Scattering of Waves. Prentice-Hall,Enlewood.Cliffs,1973.

B.V. Fortes, F.Yu. Kanev, V.P. Lukin

Institute of Atmospheric Optics SB USSR Acad. Sci.,
1, Akademicheskii avenue, Tomsk, 634055 USSR

The thermal blooming compensation of the laser beam propagated along the horizontal and vertical paths is discussed in the paper. The design of adaptive mirrors is analyzed according to the requirements formulated for the phase corrector.

I. Mathematical description of the beam propagation

The laser beam propagation is described by a system of the differential equations relative to the complex field amplitude E and temperature T

$$2i\kappa \frac{\partial E}{\partial z} = \frac{\partial^2 E}{\partial x^2} + \frac{\partial^2 E}{\partial y^2} + 2\kappa^2 \frac{\partial n}{\partial T} TE, \quad \kappa = \frac{2\pi}{\lambda} \quad (1)$$

$$\cos\beta \frac{\partial T}{\partial x} + \sin\beta \frac{\partial T}{\partial y} = \alpha I(x,y)/(\rho C_p V_\perp) . \quad (2)$$

Here $\cos\beta = V_x/V_\perp$, $\sin\beta = V_y/V_\perp$, $V_\perp$ - is the wind velocity transverse to the beam propagation direction, I is the intensity, C_p is the heat capacity, ρ is the density. The medium nonlinearity is characterized by the parameter

$$R_v = \frac{2\kappa^2 a_0^3 \alpha I_o}{n_o \rho C_p V_\perp} \left(\frac{\partial n}{\partial T}\right), \quad (3)$$

where a_o is the reference radius of the beam. The problem spatial scale along the beam propagation axis is diffractive length $z_d = \kappa a_o^2$.

II. Blooming correction at the horizontal paths

When analyzing the correction of the thermal blooming along the horizontal paths the observation of the beam parameters was carried out at the plane $Z_0 = 0.5 Z_d$. The nonlinear layer length was varied from $Z_{NL} = 0.5 Z_d$ to $Z_{NL} = 0.01 Z_d$. The nonlinearity parameter modulus was varied in the 30 (when $Z_0 = 0.5 Z_d$) to 700(when $Z_0 = 0.01 Z_d$) range. The wind velocity was constant. Phase control was accomplished using an aperture sounding algorithm. The dependence of the compensation efficiency (relative to the increase of energy at the aperture with given dimensions) on the control coordinate basis was determined based on the set of the Zernike polynomials (tilts, defocusing, astigmatism, coma, spherical aberration). The investigations carried out have made it possible to conclude the following:

1. In the conditions of weak nonlinear distortions ($Z_{NL} = 0.5 Z_d$, $|R_v| \leq 10$; $Z_{NL} = 0.1 Z_d$, $|R_v| \leq 20$; $Z_{NL} = 0.01 Z_d$, $|R_v| \leq 250$) the lower aberration compensation, namely, tilts and defocusing provides high quality of the thermal lens correction. The correction of the higher order aberration enable one to enhance the efficiency up to 5%.

2. When increasing the nonlinear distortion the contribution of the higher order polynomials grows. Here, when $Z_{NL} = 0.5 Z_d$, $|R_v| = 30$ compensation of astigmatism, coma and spherical aberration enhances the efficiency by 19%. When $Z_{NL} = 0.1 Z_d$, $|R_v| = 90$ it is enhanced by 32%.

To investigate the efficiency of the thermal blooming compensation taking into account limits of the corrector the flexible mirror model was included as a component of the calculation scheme. The model constructed in the approximation to a thick isotropic plate enabled one to vary a type of the servodrive array and number of its elements. The numerical experiments carried out using this model have shown that

- It is possible to simulate a mirror with the modes of the first and second order and root-mean square error from 5% to 10% in using from 4 to 8 servodrives.

- When using this mirror the efficiency decreases by 10% to 15% in comparison with the ideal corrector.

III. Program blooming correction at the vertical paths

The beam propagation along the vertical paths is considered in the third part of the paper. The variation of the wind direction with the increase of altitudes is described by the profile $\beta(z)$. The reference beam intensity I_0 is selected in such a way that the power of the receiving aperture reaches the largest value. The distortions are assumed to be concentrated at the transmitting aperture plane immediately due to rapid decreasing of the air density:

$$\varphi(x,y) = \frac{2\pi}{\lambda} \int_0^\infty T(x,y,z) \, n'_T(z) \, dz, \quad n'_T = \frac{\partial n}{\partial T} \quad (4)$$

The concept of efficient refraction path length is introduced

$$H_R = \int_0^H R_v(z) / R_v(0) \, dz . \quad (5)$$

To describe the z dependence of the wind velocity direction the function

$$f(\beta) = \frac{1}{H_R R_v(0)} R_v \left(z(\beta) \right) \frac{\partial z}{\partial \beta} , \quad (6)$$

characterizing the distortion distribution in direction and root-mean-square deviation

$$\sigma_v = \left(\int \beta^2 f(\beta) \, d\beta \right)^{-1/2} \quad (7)$$

are introduced. The beam intensity profile at the plane of the emitting aperture $S = \pi a_0^2 = l_0^2$ is given in the forms of the Gaussian beam $I(x,y) = I_0 \exp\left[-(x^2+y^2)/a_0^2\right]$, the hypergaussian beam

$$I(x,y) = I_0 \exp\left[-(x^8+y^8)/l_0^8\right],$$

the supergaussian beam $I(x,y) = I_0 \exp\left[-(x^2+y^2)^4 / (a_0/2)^8\right]$.

The results obtained have made it possible to conclude:

1. The highest power at the target is reached when using the beams with the supergaussian and hypergaussian intensity profiles.

2. The increase of root-mean-square deviation σ_γ from O to π causes the significant (2 to 3 times) growth of the power at the target. In this case the advantage of the filled aperture is remained.

3. With a thin thermal lens compensation the correction efficiency grows simultaneously with increasing the number of classical aberrations being corrected.

4. The use of the nineteen-segment corrector where each element has three degrees of freedom, enables one to obtain the one order increase of the maximum radiation power at the target.

THE DIFFRACTION OF LIGHT BY SMOOTH CONVEX BODY IN INHOMOGENEOUS MEDIA

Ljalinov M.A.

Department of Mathematical Physics, Institute of Physics.
Leningrad University , Uljanovskaja 1-1, Leningrad-Petrodvorec.
198904, USSR.

The interest to a high frequency diffraction in inhomogeneous media is renewed in the recent years owing to the high development of laser technics and its broad application to the control of the technological processes. It´s appeared the possibility of the direct experimental investigations of light diffraction (including the penumbra) with the help of compact laboratory equipment [1].The formulae obtained in the paper may be used for the theoretical simulation of such experiments. The investigation of the scattered e.m. wave near the scattering surface in the case of tangent incidence has been undertaken by V.A.Fock in the numbers of his fundamental papers [2]. The development of Fock´s ideas has led to the application of boundary layer technique to the diffraction problems in inhomogeneous media [3,4].It was developed the technique of "joining " of the local asymptotic series which is used in the present paper.

Let us suppose the inhomogeneous media beyond the convex scattering region with the boundary S being described by the dielectric and magnetic permeabilities $\varepsilon = \varepsilon(\vec{x})$, $\mu = \mu(\vec{x})$, $N^2 = \varepsilon\mu$,depending on observation point $\vec{x}$. The e.m. field $\vec{\mathscr{E}}e^{-i\omega t}$, $\vec{\mathscr{H}}e^{-i\omega t}$,depending on time harmonically, satisfies Maxwell´s equations. The parameter $\omega\mathscr{P}/c_0$ is supposed to be large parameter,

where $\mathscr{P}$ is the characteristic image of inhomogeneoty or characteristic radius of curvature of the scattering surface. We assume that the incident wave is described by the ray series [5]

$$\vec{\mathscr{E}}_i = exp (i\omega\Phi_i(\vec{x})) [\vec{E}_{i0}(\vec{x}) + \vec{E}_{i1}(\vec{x})/ (\omega\mathscr{P}/c_0) + \dots]$$

$$\vec{\mathscr{H}}_i = exp (i\omega\Phi_i(\vec{x})) [H_{i0}(\vec{x}) + H_{i1}(\vec{x})/(\omega\mathscr{P}/c_0) + \dots],$$

where $\Phi_i(x)$ is an eikonal equation solution $(\nabla\Phi_i)^2 = c^{-2}$, E_{ij}, H_{ij} satisfy transport equations. The scattered field $\mathscr{E}_0$, $\mathscr{H}_0$ satisfies the impedance boundary conditions

$$\mathscr{E}^\tau |_S = -q_\varepsilon \mathscr{H}^\alpha |_S$$

$$\mathscr{E}^\alpha |_S = q_\mu^{-1} \mathscr{H}^\tau |_S .$$

where $\vec{\mathscr{E}} = \vec{\mathscr{E}}_0 + \vec{\mathscr{E}}_i$, $\vec{\mathscr{H}} = \vec{\mathscr{H}}_0 + \vec{\mathscr{H}}_i$,(τ , α) are the orthogonal coordinates on the surface S, q are the impedances of the surface, (Im q > 0), depending on the properties of the media inside the surface S.

Let us introduce the coordinate system (τ_0, α_0, t) in the vicinity of the terminator T (the line between the light and shadowed parts of S), α_0 is measured along T, τ_0 is measured along the topographical line on the surface S and it is orthogonal to the curve T ($(\nabla\tau_0)^2 = c^{-2}|_S$, $\tau_0|_S = 0$, $\nabla\tau_0|_S = \nabla\Phi_i|_S$), t is mea-

sured along the curvelinear tangent ray, ariving at the observation point. (τ_0, α_0) is the initial point of the ray. $((\nabla t)^2 = c^{-2}, \nabla t|_S = e_{\tau o}/c|_S, t|_S = \tau_0, |e_{\tau o}^\alpha| = 1)$.Let us introduce the dimensionless reduced coordinate of the boundary layer [4] in penumbra $\gamma = (\omega/2)^{1/3}(c/\mathcal{P}_\tau)^{2/3}|_T \tau_0$, where $\mathcal{P}_\tau$ is the effective radius of curvature in τ-direction

$$\mathcal{P}_\tau = [\rho_\tau^{-1} + \frac{1}{c}\frac{\partial c}{\partial n}]^{-1},$$

$\rho_\tau^{-1} = -b_{\tau\tau}/a_{\tau\tau}$, $a_{\tau\tau}$, $b_{\tau\tau}$ are the coefficients of the first and the second quadratic forms. Half-shadow region is derived by inaqualities: $|\gamma| \le M^{\varepsilon_1}$, $M = (\omega\mathcal{P}_\tau/2c)$, $M \gg 1$, the positive constant ε_1 satisfies the condition $0 < \varepsilon_1 < 1/12$.Omitting unweildy calculations which use the dependance between the coordinate systems, at the highest order we have

$$\begin{bmatrix} \vec{s}_0 \\ \vec{\mathcal{H}}_0 \end{bmatrix} = \frac{exp(\iota\omega[t + \Phi_\iota|_T] + \iota\pi/4)}{(\pi M(\alpha_0))^{1/2}} \sqrt{\frac{(I_S/c)|_T}{(I/c)|_{\tau_0=0}}} \times$$

$$\begin{Vmatrix} A_{11} + \mathcal{O}(M^{-1}) & A_{12} + \mathcal{O}(M^{-1}) & \mathcal{O}(M^{-1}) \\ A_{21} + \mathcal{O}(M^{-1}) & A_{22} + \mathcal{O}(M^{-1}) & \mathcal{O}(M^{-1}) \end{Vmatrix} \begin{bmatrix} \vec{\nu}(s,\alpha_0) \\ \vec{b}(s,\alpha_0) \\ \vec{s}(s,\alpha_0) \end{bmatrix} \quad (1)$$

$$A_{11} = \frac{\cos\theta(s)}{\cos\theta o}(\cos\theta_0 E_{\iota o}^n|_T W(\gamma,Q_\mu) - \sin\theta_0 E_{\iota o}^\alpha|_T W(\gamma,Q_\varepsilon))$$

$$A_{12} = \frac{\sin\theta(s)}{\sin\theta o}(-\sin\theta_0 E_{\iota o}^n|_T W(\gamma,Q_\mu) - \cos\theta_0 E_{\iota o}^\alpha|_T W(\gamma,Q_\varepsilon))$$

$$A_{21} = -\frac{\sin\theta(s)}{\sin\theta o}(-\cos\theta_0 H_{\iota o}^n|_T W(\gamma,Q_\varepsilon) + \sin\theta_0 H_{\iota o}^\alpha|_T W(\gamma,Q_\mu))$$

$$A_{22} = \frac{\cos\theta(s)}{\cos\theta_0}(-\sin\theta_0 H_{\iota o}^n|_T W(\gamma,Q_\varepsilon) - \cos\theta_0 H_{\iota o}^\alpha|_T W(\gamma,Q_\mu)).$$

where I is the devergence of the tangent rays, I_S is the devergence of the surface rays, $E_{\iota o}^n|_T = (\vec{N}.\vec{E}_{\iota o})$, $H_{\iota o}^\alpha|_T = (\vec{e}_{\alpha o}.\vec{H}_{\iota o})$, $e_{\alpha o}$ is the unit vector along the coordinate line α_0, s is the unit vector along the ray and $(\vec{s},\vec{\nu},\vec{b})$ is the right triad of vectors.The angle θ may be derived from Rytov's equation [6]

$$\frac{d\theta}{ds} = \varkappa(s), \quad (2)$$

which describes polarization plain rotation law. s is the ray arclength connected with the t-coordinate by the correlation $dt = c^{-1}ds$, $\varkappa$ is the torsion curvature of the ray. The initial condition for (2) is derived by the orientation of vector $\vec{E}_{\iota o}|_T$: $\theta_0 = \theta(0,\alpha_0)$, $\cos\theta_0 = (\vec{N}.\vec{\nu})$, $\sin\theta_0 = -(\vec{N}.\vec{\nu})$, $\vec{N}$ is the unit normal to S vector. $\vec{E}_{\iota o}|_T = |E_{\iota o}|(\vec{b}\sin\theta_0 + \vec{\nu}\cos\theta_0)|_T$, $\vec{H}_{\iota o}|_T = |H_{\iota o}|(\vec{b}\cos\theta_0 - \vec{\nu}\sin\theta_0)|_T$. The function $W(\gamma,Q)$ has the form

$$W(\gamma,Q) = (i/2) \int_{\mathcal{L}_1} e^{i\gamma\xi + i\xi^2/4M\Psi} \, d\xi - \int_{\mathcal{L}_0} e^{i\gamma\xi} R_0(\xi,Q) \, d\xi + \tag{3}$$

$$+ (-i/2) \int_{\mathcal{L}_2} e^{i\gamma\xi} R_2(\xi,Q) \, d\xi \ .$$

where $R_k(\xi,Q) = \dfrac{v_k'(\xi) - Q\, v_k(\xi)}{w_1'(\xi) - Q\, w_1(\xi)}$, $k = 0;1;2$, $v_0 = v(\xi)$, $v_1 = $

$= w_1(\xi)/(2i)$, $v_2 = w_2(\xi)/(-2i)$ and v, w_1, w_2-are the Airy functions interpreted by Fock [2], $\mathcal{L}_k$ are the integration contours on complex plain , $\mathcal{L}_0 = [0,\infty)$, $\mathcal{L}_1 = (\infty exp(-2\pi i/3),0]$, $\mathcal{L}_2 = (\infty exp(2\pi i/3),0]$. Here $Q_\mu = iM\mu q_\mu|_T$, $Q_\varepsilon = iM\varepsilon q_\varepsilon|_T$, $q_\mu = (\varepsilon_0\mu_0 - 1)^{1/2}/\mu_0$,

$q_\varepsilon = (\varepsilon_0\mu_0 - 1)^{1/2}/\varepsilon_0$, ε_0, μ_0 are the dielectric and magnetic permeabilities inside the surface S.

$$\Psi = \mathcal{P}_\tau \, (K - K_i) \ \left| \frac{\partial \vec{x}(\tau_0,\alpha_0,t)}{\partial \tau_0} \right|^2 / c^2 \Big|_T \ .$$

where K_i, K are the curvatures of the normal cross-sections of the incident and scattered wave fronts corresponding to $\alpha_0 =$ =const.

The formula (3) is valid in the lit penumbra. In the shadowed one ($\tau_0 > 0$) it is advisably to join the incident and scattered field , then the net field $\mathscr{E}$,$\mathscr{H}$ may be described by the same formulae (1),(3), if we change the sign of the first term of (3) and change the integration contour by $\mathcal{L}' = [0, exp(i\pi/3) \infty)$.

The formulae are applicable in the vicinity of light-shadow boundary : $|\gamma| < M^{\varepsilon 1}$ and obtained for the finite (not small) values t ($\omega t > M^2$). However (1) are valid also when t is infinitly increased unless Ψ has the positive value and the devergence I doesn't equal to zero. From the physical point of view it means that the normal curvature of the incident wavefront K_i (α_0=const, τ_0=0) must be less than the normal curvature K of the diffracted wavefront. Beside this it means that in penumbra it mustn't be the regions of focusing of the tangent rays. The formulae (1) are not applicable near the region of irregularity of the tangent rays [7].

[1] Buldyrev V.S., Ljalinov M.A. et. al. J. Experimental and Theoretical Physics, 97(3), 1990, USSR.
[2] Fock V.A. Electromagnetic diffraction and propagation problems. Pergamon, New-York , 454 pp., 1965.
[3] Buslaev V.S. Herald of Leningrad University 13, 1962. USSR.
[4] Babitch V.M., Kirpichnikova N.J. Boundary layer method in the diffraction problems. Leningrad University. Leningrad. 1975. USSR.
[5] Babitch V.M., Buldyrev V.S. Asymptotic methods in shortwave diffraction problems . Nauka. Moscow. 1972. USSR.
[6] Rytov S.M. Reports of AN USSR 18(2) 1938. USSR.
[7] Ljalinov M.A. Heralds of High School. Radiophysics. 33(6), 1990. USSR.

ALEXANDER FEDOTOV; Department of Mathematical Physics,
Institute of Physics, Leningrad University, USSR

1. The applicability conditions of short-wave asymptotics
in case of deterministic problems can be written as

$$\lambda R \ll \ell^2 \quad , \quad \lambda \ell \gg 1 , \tag{1}$$

where λ is a wave-length, ℓ is a typical size of medium in-
homogeneities and R is the distance between the source point
of wave field and the point of the receiver. Investigating
wave propagation in random media with the help of traditional
methods we come to additional restrictions on parameters R .
λ , ℓ . Let us consider, for example, possibilities provid-
ed by geometrical optics approach. In accordance with this ap-
proach one is to calculate the eikonal S for every realiza-
tion of the refraction index using perturbation theory:

$$S = S_0 + \varepsilon S_1 + \varepsilon^2 S_2 + \cdots , \tag{2}$$

where ε is a small parameter, which characterizes fluctuati-
on amplitudes. If R is sufficiently large, coefficients S_κ
appear to be proportional to the powers of the value $\varepsilon R^2/\ell^2$
and thus this value must be small: $\varepsilon R^2/\ell^2 \ll 1$. Coefficients S_κ
show complicated analytical structure and so usually only two
first terms are used. This leads to one more condition.

The use of other traditional methods also leads to such
restrictions. How to avoid the additional conditions ?

R.Dashen proposed to investigate wave propagation in ran-
dom media on the base of path integral calculations (R.Dashen,
J.Math.Phys.20, 894-920, 1979). The main idea was to express
the object of the investigation, for example, wave field in-
tensity, in terms of path integral with fluctuation-independ-
ant measure symbol. In this case averaging over the ensemble
of realizations may be carried explicitly for a wide class of
problems. In result one get path integral which depends on
fluctuations through the second moment of the refraction index.

So the problem is reduced to the calculation of this integral by some approximate method.

For short-wave problems there exists a natural one. It is stationary phase method (A.Fedotov, Papers of conf. "waves & diffraction - 90", Moscow, 381-384, 1990). Relying on it one may obtain formulae containing the determinant of an integro-differential operator - the operator of the second variation of the action. On this stage applicability conditions of the approach appear to be the same as for short-wave asymptotics of field in deterministic media.

In this paper we study short-wave pulse propagation in a fluctuating waveguide. One may obtain that for such problems it is possible to calculate asymptotically the operator determinant as $\varepsilon \to 0$ without additional restrictions on R .

2. Let us formulate the problem mathematically. The wave field P obeys the wave equation

$$(\nabla^2 - n^2(x,z)\, \partial_t^2)\, P(x,z,t) = -e^{-i\omega t}\, h(t)\, \delta(x)\, \delta(z) . \qquad (3)$$

Here $P(x,z,t)$ is field at the point with Cartesian coordinates x , z ; t is the time, $n(x,z)$ is the index of the refraction.

Function $h(t)$ describes the pulse form. We suppose that $h(t)$ is sufficiently smooth and is equal to zero for large t .

To Choose the proper solution of wave equation we require that $P(x,z,t) = P_t'(x,z,t) = 0$ for sufficiently large negative t.

We suppose that

$$n^2(x,z) = V_0(z) + \varepsilon V_1(x,z), \quad 0 < \varepsilon \ll 1 ,$$

where $V_0(z)$ is a function with only one maximum, and $V_1(x,z)$ is random, zero-mean Gaussian function. Let $W(z,z',\, x-x') =$

$= \langle V_1(x,z) V_1(x,z) \rangle$ where angle brackets indicate averaging over the ensemble of random functions V_1 , $W(z,z',-\theta) =$

$= W(z,z',\theta)$ and $W(z,z',\theta) \to 0$ as $\theta \to \infty$.

Due to the properties of $V_0(z)$, refractional waveguide exists in the medium. The function V_1 describes fluctuations.

The problem to be solved is to receive asymptotics of

pulse mean intensity $\langle |P|^2 \rangle$ as $\omega \to \infty$, $\varepsilon \to 0$. This asymptotics is to be applicable when condition (1), usual for deterministic problems is satisfied, i.e. if the distance R is sufficiently large.

3. Let us describe main result of the paper. For this purpose it is necessary to remember that in case of deterministic waveguide with $n^2 = V_0(z)$ ray trajectories are periodic curves, $Z(x,S)$, which period depends on parameter S, $Z(x,S) = Z(x+\mathcal{D}(S),S)$; S is constant along each ray and can be expressed in terms of an angle between its trajectory and X-axis.

As $\omega \to \infty$ and $\varepsilon \to 0$ mean intensity $\langle |P|^2 \rangle$ is approximatelly equal to the sum of contributions of the rays $Z(x,S)$ connecting the source point and the point of the reciever. Each contribution is given by

$$\Gamma \sim \frac{1}{8}\pi\omega^2 \int_{-\infty}^{\infty} d\Delta \, \frac{e^{i\Delta(\Phi(x,z,S)-t)}}{\Im(x,z,S)} \, g(\Delta) \, H(\Delta) \, , \tag{4}$$

$$H(\Delta) = \int_{-\infty}^{\infty} dt' \, e^{i\Delta t'} \, |h(t')|^2 .$$

Here $\Phi(x,z,S)$ and $\Im(x,z,S)$ are eikonal and geometrical divergence of rays $Z(x,S)$ for $V_\perp \equiv 0$,

$$g(\Delta) = A(\Delta) \, e^{-W(\Delta)} \, ,$$

and

$$W(\Delta) = -\frac{\Delta^2 \varepsilon^2}{8} \frac{x}{\mathcal{D}(S)} \int_0^{\mathcal{D}(S)} dx' \int_{-\infty}^{\infty} dx'' \, W(Z(x',S), Z(x'',S), x'-x'') \, ,$$

$$A(\Delta) = (\rho(\Delta)/\mathrm{sh}\,\rho(\Delta))^{1/2} \, ,$$

$$\rho(\Delta) = e^{i\pi/4} \left(\frac{1}{2} W_{12}(S) \mathcal{D}'(S) \Delta \right)^{1/2} \varepsilon x/\mathcal{D}(S) \, ,$$

$$W_{12}(S) = \int_0^{\mathcal{D}(S)} dx' \int_{-\infty}^{\infty} dx'' \frac{dz}{dx}(x',S) \frac{\partial^2 W}{\partial z \partial z'}(z(x',S), z(x'',S), x'-x'') \frac{dz}{dx}(x',S) \, .$$

The formula $g \sim e^{-W}$ can be received by geometrical optics approach; The factor A appears as determinant of an operator in calculations of the path integral for $\langle |P|^2 \rangle$. The formula (4) may be simplified: often the approximation $W \approx 0$ is valid.

A.G.ALENITSYN, A.A.FEDOTOV, Department of Mathematical Physics,
Leningrad State University

The process of wave propagation is assumed to be described
by the wave equation

$$\Delta \, \mathcal{U} - n^2 \frac{\partial^2}{\partial t^2} \mathcal{U} = F(t)\delta(x,y,z-z_0) \tag{1}$$

We may meet such equation in acoustics, optics, seismology and
radio waves theory; in acoustics the function $\mathcal{U}$ is inter-
preted as the sound pressure generated by a point-wise source.

Let us now consider in detail the acoustic problem for a
liquid layer $0 \leqslant z \leqslant d$ which lies upon a liquid (or elastic)
semi-space $z \geqslant d$. Here $0 < z_0 < d$, the cofficient n in
(1) denotes the refraction index; we provide two possibilities:
1) $n = n(z)$ (stratified liquid), 2) $n = n(z, \varepsilon r)$ (quasi-stra-
tified liquid, $0 < \varepsilon \ll 1$, $r = \sqrt{x^2+y^2}$).

The boundary $z = 0$ of the layer is assumed to be free:
$\mathcal{U}|_{z=0} = 0$; at the interface $z = d$ the quantities $\mathcal{U}$
and $\frac{1}{\rho}\frac{\partial u}{\partial z}$ are assumed to be continuous, ρ is the den-
sity of the medium.

The time-modulation factor $F(t)$ in (1) may be either of
simple harmonic type: $F(t) = e^{-i\omega t}$, or of polyharmo-
nic type:

$$F(t) = e^{-i\omega t} \sum_{s=1}^{N} \alpha_s e^{i s \beta t} \qquad . \tag{2}$$

In the simplest case, when $F(t)$ is harmonic, the liquid layer is stratified and the "bottom" $z \geq d$ is liquid, the wave field u may be presented in the well-known normal-modes form:

$$u = e^{-i\omega t} \sum_{m=1}^{M} \psi_m(z_0) \psi_m(z) H_0^{(4)}(\omega \xi_m r) . \tag{3}$$

Here $H_0^{(4)}$ is the Hankel function, ξ_m and ψ_m are, respectively, the eigenvalues and eigenfunctions of the following Sturm-Liouville problem (SLP):

$$\psi''(z) + \omega^2 (n^2(z) - \xi^2) \psi = 0, \quad 0 \leq z \leq d, \tag{4}$$

$$\psi(0) = 0, \quad \rho_0 \psi'(d) + \omega \rho_\infty \sqrt{\xi^2 - n_\infty^2} \, \psi(d) = 0,$$

where ρ_0 and ρ_∞ are the densities in the layer and in the bottom, n_∞ is the refraction index in the bottom.
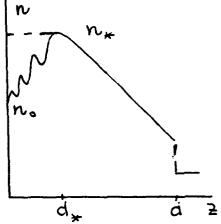
Though there exist many standard numerical methods which allow one to calculate the spectrum $\{\xi_m\}$ and eigenvalues $\{\psi_m\}$ of SLP, in real practicalcases the number M of eigenvalues may achieve some hundreds or even some thousands, so the most of usual algorithms spend too much computer time. Especially this circumstance is essential if ω in (3), or N in (2) are not small, or if the liquid layer is quasi-stratified.

The essence of our approach is as follows. Let the refraction index $n(z)$ behaves as shown at the picture. Consider, for example, the case when the eigenvalues ξ_m belongs to

the interval (n_0, n_*). Then ξ_m satisfies the equation

$$\theta_1(\xi) + \theta_2(\xi) = m$$

where we denoted:

$$\theta_1(\xi) = \frac{\omega}{\pi} \int \sqrt{n^2(z) - \xi^2}\, dz + \frac{1}{4},$$

$$\theta_2(\xi) = \operatorname{arctg}\left(\omega \sqrt{n^2(d_*) - \xi^2}\, \psi(d_*)/\psi'(d_*)\right),$$

and ψ is the solution of the Cauchy problem $\psi(0) = 0, \psi'(0) = 1$ for the equation (4). The term $\theta_1(\xi)$ is similar to integral term in well-known Bohr-quantization rule. The term $\theta_2(\xi)$ corresponds to the interval $0 \leq z \leq d_*$, where $n(z)$ behaves irregularly; this term we calculate by means of numerical finite-difference method.

In general, programs based only on asymptotic formulas are much faster than ones based purely on numerical methods. However such formulas are valid only for sufficiently regular index of refraction. In practice region of irregular behavior of $n(z)$ is relatively small (in z - or ξ-scale), so the combination of asymptotic and **finite** difference methods leads to real-time scale personal computer calculations.

RADIO-THERMAL RADIATION OF THE ATMOSPHERE IN THE PRESENCE OF THE WAVEGUIDE PROPOGATION

B.M.Shevtsov, A.A.Shishkariev
Pacific Oceanological Institute, 7 Radio St,
Vladivostok, USSR, 690032

The angular dependence of the atmosphere thermal radiation into the centimeter range of electromagnetic waves was studied early under the geometric optics approximation [1]. However when the waveguide propagation is present it is necessary to account the diffraction effects. In this paper the spectral analysis of eletromagnetic-wave green function based on the imbedding method, is carried out for the troposphere waveguide. There is also discussed the diffraction problem of the atmosphere thermal radiation.

Let us formulate the problem in the following way, according to [2]. Let us study the spherical layer of the atmosphere with complex dielectric permittivity $\mathcal{E}(r)=1+\mathcal{E}(r)+i\gamma$ over the Earth. When $r<R_0$ (R_0 is the Earth radiues) $\mathcal{E}(r)=\mathcal{E}_0^{\cdot}+i\mathcal{E}_0^{\cdot\cdot}$ and as $r>R_0+H, \mathcal{E}=1$, H is the layer thickness. Every where the magnetic permeability is $\mu=1$. Decomposing the arbitrary system of monochromatic currents into three components $j(r)=j_1+j_2+j_3$ for the spherically layered atmosphere, where j_1 is the radial current component; j_2 and j_3 are horizontal components (eddy and potential respectively). Expressing them in the form $j_1=je_r$, $j_2=$ rot $e_r J$, $j_3=\nabla_\perp G$, where e_r is the radial unit vector in the spherical coordinate system, $\nabla_\perp$ is the angular part of the operator ∇ in the same system,we can decompose the electromagnetic field into three components and introduce scalar potentials $H_1=$ rot $e_r A_1$, $E_2=$ rot $e_r A_2$, $H_3=$ rot $e_r A_3$.Then system of Maxvell`s equations reduces to three scalar wave equations for quantities $A_i (i=1,2,3)$.

If we introduce additional potentials

$$P_1 = \frac{1}{\mathcal{E}} \frac{\partial}{\partial r} = A_1, \quad P_2 = \frac{\partial}{\partial r} A_2, \quad P_3 = \frac{1}{\mathcal{E}} \left[\frac{\partial}{\partial r} A_3 - \frac{4\pi(\mathcal{E}-1)}{c} G \right]$$

and expand A_i and P_i into series with respect to

spherical harmonics $Y_l^m(\theta, \phi)$, we obtain the following equation for series coefficients:

$$
\begin{cases}
\varepsilon(z)\dfrac{dP_1^{m,l}}{dz} + \Phi^2(z)\, A_1^{m,l} = -\dfrac{4\pi}{c}\, j^{m,l}, \\[2mm]
\dfrac{d\, A_1^{m,l}}{dz} - \varepsilon(z)P_1^{m,l} = 0;
\end{cases}
\qquad 1(a)
$$

$$
\begin{cases}
\dfrac{dP_2^{m,l}}{dz} + \Phi^2(z)A_2^{m,l} = -ik_0\dfrac{4\pi}{c}\, J^{m,l}, \\[2mm]
\dfrac{d\, A_2^{m,l}}{dz} - P_2^{m,l} = 0;
\end{cases}
\qquad 1(b)
$$

$$
\begin{cases}
\varepsilon(z)\dfrac{dP_3^{m,l}}{dz} + \Phi^2(z)\, A_3^{m,l} = -\dfrac{4\pi}{c}(\varepsilon-1)\dfrac{\partial}{\partial z}\, G^{m,l} \\[2mm]
\dfrac{d\, A_3^{m,l}}{dz} - \varepsilon(z)P_3^{m,l} = \dfrac{4\pi}{c}(\varepsilon-1)G^{m,l};
\end{cases}
\qquad 1(c)
$$

where $\Phi^2(z) = q^2(z_0)+k_0^2\,\Delta\varepsilon(z)+2k_\perp^2\dfrac{z-z_0}{R_0}$, $q^2(z_0) =$

$k_0^2\varepsilon(z_0)-k_\perp^2$, $k_\perp^2 = l(l+1)/R_0^2$, $\Delta\varepsilon(z)=\varepsilon(z)-\varepsilon(z_0)$, $k_0=\omega/c$

is the wave number, $z=r-R_0$. When obtaining the factor $\Phi^2(z)$, there was used the relationship $z \ll R_0$. We have boundary conditions for the equation (1), which follows from the continuity of potentials.

Let us study equations for the function of the point source:

$$
\frac{d}{dz}\, P(z,z_0)+L(z)A(z,z_0)= \alpha(z_0)\delta(z-z_0), \qquad (3)
$$

$$
\frac{d}{dz}\, A(z,z_0)+K(z)P(z,z_0)=\beta(z_0)\delta(z-z_0),
$$

$$
P(H,z_0)+C(H)A(H,z_0)=0, \quad P(h,z_0)+B(h)A(h,z_0)=0
$$

indexes l,m,i are omitted. Factors L(z) and K(z) are received from the comparison of (3) and (1).

Note, that the density of the source power is $I \propto PA^* = \alpha\beta^*$. Let us choose two normalized solutions

of (3) in the way, that $I=\pm 1$. The second normalizing condition $\alpha/\beta= -C$ follows from the first boundary relationship (2). The two chosed solutions of (3) $I=\pm 1$ correspond to waves going up and down from the source, placed on the sphere of the radius $r=R_0+z_0$. Spherical waves are radiated at an angle with this sphere. This angle can be characterized by the parameter $\Lambda(z_0)$ defined as $Sin^2\Lambda(z_0)=q^2(z_0)/k_0^2\mathcal{E}(z_0)$. The sign of the parameter is chosen according to the sign of I. Any solution of (1) can be expressed by these two normalized solutions of (3).

The boundary-value problem (3) can be reduced to the initial-value problem [2], using the imbedding method. For this purpose let us introduce disignations:

$$A(h+o,h)=A(h), \qquad A(h)/V(h)=\psi(h), \qquad (4)$$

$$A(z,h)/V(h)=\psi(z,h), \text{ where } V(h)=\alpha(h)+B(h)\beta(h);$$

$$A(z,z_0;h)\equiv A(z,z_0), \quad \tilde{A}(h,z_0)=A(z,z_0;h)\big|_{z=h},$$

$$A(z,z_0;h)/V(z_0)N(z_0)=\psi(z,z_0;h),$$

$$\tilde{A}(h,z_0)/V(z_0)N(z_0)=\psi(h,z_0),$$

where $N(z_0)=[1-\beta(z_0)/V(z_0)\psi(z_0)]$.

Fields ψ as $B(h)$ is finite are connected with fields ψ_0 as $B(h)=0$ in the following way

$$\psi(h) = \frac{\psi_0(h)}{1+B(h)\psi_0(h)}, \quad \psi(z,h) = \frac{\psi_0(z,h)}{1+B(h)\psi_0(h)},$$

$$\psi(z,z_0;h)=\psi_0(z,z_0;h)-B(h)\frac{\psi_0(z,h)\psi_0(h,z_0)}{1+B(h)\psi_0(h)},$$

this results from the form of boundary conditions (2). The imbedding equation is

$$\frac{d}{dh}\psi_0(h)=L(h)\psi_0^2(h)-K(h) \qquad (5)$$
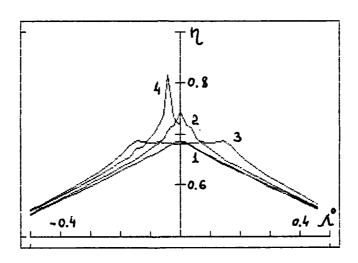
with initial condition $\psi_0(H)=-1/C(H)$.

Two other functions are found by quadratures:

$$\psi_0(z,h)=\psi_0(z)\exp\left\{\int_z^h d_\xi L(\xi)\psi_0(\xi)\right\}, \quad \psi_0(z,z_0;h)= \qquad (6)$$

$$\int_{\min z,z_0}^{h} d_\xi L(\xi)\psi_0(z,\xi)\psi_0(\xi,z_0)+ \begin{cases} \psi_0(z,h)\big|_{h=z_0}\Big/N(z_0)\big|_{B=0,} & z_0\leqslant z, \\ \psi_0(h,z_0)\big|_{h=z,} & z\leqslant z_0 \end{cases}$$

On the upper boundary of the layer z=H the wave can be given in the form $A(H,Z_0)=aw_1(t_H)$, $I_H \propto |a|^2$. The factor of energetic losses is defined as $\eta(\Lambda)=1-I_H$. The radio-brightness temperature is $T=T_0\eta$, where T_0 is the medium temperature.

Calculations of dependences $\eta(\Lambda)$ are given in the figure. They have been carried out for the vertically-polarized wave and the waveguide characteristics $\tilde{\varepsilon}(z)=Q(H_0-Z)$ as $z \leqslant H_0$ and $\tilde{\varepsilon}(z)=0$ as $z > H_0$. There were chosen the next parameters: H=100 m, H_0=15 m, B= 0, γ=2 10^{-8}; 1)Q=0, Z_0=0; 2) Q=2 10^{-7}, Z_0=0; 3) Q=7 10^{-7}, Z_0=0; 4) Q=2 10^{-7}, Z_0=15 m.

REFERENCES

1. A.S.Gurvich, A.T.Ershov, IZV. AN SSSR,FAO, 1979, V.15, № 2, p.218 (in Russian).
2. V.I.Klytskin. The imbedding method in the theory of wave propagation, Nauka, Moscow, 1986,(in Russian).

TO THE THEORY OF NONSTATIONARY WAVE PROBLEMS FOR A LAYERED MEDIA **P60**

A.G.Bugrov, M.A.Guzev, V.I.Klyatskin

Wave processes Lab.,Pacific Oceanological Institute, Far Eastern Branch USSR Academy of Sciences, 7 Radio Street, Vladivostok, 690032, USSR.

Solving the inverse scattering problem associated with the propagation of waves in inhomogeneous media can be simplified by using the method of propagation of singularities [1] and the imbedding method [2-5]. This paper examines the inverse problem when there are the jumps of medium parameters at the boundaries of inhomogeneous slab.

Statement of the problem

We consider the problem of wave incidence on a slab of inhomogeneous medium, which occupies the region $0<x<L$. The wave $\varphi=\vartheta(x-L+c_2 t)$ propagates from the homogeneous region $x>L$, and c_2 is the wave speed in the region $x>L$, c_1- is the wave speed in homogeneous region $x<0$. Inside the slab the wave is described by the equation for the Green's function

$$\left[\frac{1}{c^2(x)} \frac{\partial^2}{\partial t^2} - \frac{\partial^2}{\partial x^2} + \frac{n'(x)}{n(x)} \frac{\partial}{\partial x} \right] G(x,t)= 0 \ , \qquad z_i = n_i c_i \ , \tag{1}$$

$$\left[\frac{z_2}{n(x)} \frac{\partial}{\partial x} + \frac{\partial}{\partial t} \right]G(x,t) \bigg|_{x=L} = 2c_2 \delta(t), \quad \left[\frac{z_1}{n(x)} \frac{\partial}{\partial x} - \frac{\partial}{\partial t} \right]G(x,t) \bigg|_{x=0} = 0,$$

where $n'(x)=dn(x)/dx$, and permittivity $\varepsilon(x)$ ($\mu=0$) is defined by the wave speed in a medium: $\varepsilon(x)=c_2^2 c^{-2}(x)$. The function $G(x,t)$ describes at $n=1$ and $n(x)=\varepsilon(x)$ the electric (E-wave) and magnetic (H-wave) fields, respectively.

We consider the inverse problem which consist in recovering the wave speed profile by using the known time dependence of back-scattered field $G_L(t)=G(L,L;t-t_0)$ on the slab boundary $x=L$.

Wave front proragation and inverse scattering via imbedding equations

The imbedding equations for the boundary value problem (1) may be obtained by considering the slab boundary position L to be variable, and writting equations for the derivatives of the field with respect to L. We present imbedding equations in final form.

The back-scattered field $G_L(t)$ on the slab boundary L at $0<t<2\tau_0$ ($2\tau_0$ is the round trip travel time) has the form $G_L(t)= R_L(t)\vartheta(t)$. Substituting this expression in imbedding equation for $G_L(t)$ yields the relation

$$R_L(0)= 2Z(L)(Z_2+Z(L))^{-1} \tag{2}$$

and the equation for $R_L(t)$ $(t>0)$

$$\left(\frac{\partial}{\partial L} + \frac{2}{c(L)} \frac{\partial}{\partial t} \right) R_L(t) = \frac{n(L)}{2Z_2} (1 - Z_2^2 Z^{-2}(L)) \int_0^t d\tau \frac{\partial R_L(t-\tau)}{\partial t} \frac{\partial R_L(t)}{\partial t} , \quad (3)$$

with initial condition at L=0: $R_0(t) = 2Z_1(Z_1 + Z_2)^{-1}$.

We note that (2) is obvious equality. It shows that reflecting at the moment of wave incidence on the slab is generated by the jump of Z at the boundary L only.

Using (3) we can determine the values of derivatives of $R_L(t)$ in the neighbourhood of t=0. For example, by setting t=0 in (3) we obtain

$$\frac{\partial R_L(t)}{\partial t}\bigg|_{t=0} = - \frac{c(L)}{2} \frac{\partial R_L(0)}{\partial L} = - \frac{Z_2 c(L) Z'(L)}{(Z_2 + Z(L))^2} . \quad (4)$$

Differentiating (3) with respect to t at t=0 gives $\partial^2 R_L(0)/\partial t^2$ associated with $Z''(L)$, etc.

The field $G(x,L;t)$ inside the slab has the structure

$$G(x,L;t) = H(x,L;t) \vartheta(t-\tau_x), \qquad \tau_x = \int_x^L \frac{d\tau}{c(\tau)} , \quad (5)$$

where τ_x is the travel time to depth x. At $t > \tau_x$ the function $H(x,L;t)$ satisfies the imbedding equation, which describes the wave field inside the slab. That equation can be reduced at $t = \tau_x$ to the ordinary differential equation for the wave front amplitude $H(x,L;\tau_x)$, whose solution is

$$H(x,L;\tau_x) = 2 \sqrt{Z(x)Z(L)} \ (Z_2 + Z(L))^{-1}.$$

Thus, the amplitude of wave front (the jump of the field in the moment of wave arrival) is defined by the local value of $Z(x)$.

At $0 < t < 4\tau_0$ the function $G_L(t)$ has the structure

$G_L(t) = R_L(t) \vartheta(t) + F_L(t) \vartheta(t-2\tau_0)$, which describes the jump associated with arrival of the wave reflected by the boundary x=0. As for $R_L(t)$, imbedding equations for $F_L(t)$ and $F_L(2\tau_0)$ may be obtained. This results in

$$F_L(2\tau_0) = 4Z_2 Z(L)(Z_1 - Z(0))(Z_1 + Z(0))^{-1}(Z_2 + Z(L))^{-2}, \quad (6)$$

and the jump of back-scattered field on the boundary L at $t = 2\tau_0$ is defined by local values of $Z(x)$ in the neighbourhoods of reflecting boundaries.

The imbedding equation presented above allows to reconstruct the wave speed profile $c(x)$. The back-scattered field on the slab boundary L is described by $R_L(t)$, expanding of which in Taylor series at t=0 defines the values $c(L)$, $c'(L)$, ets. We must consider now eq.(3) as auxiliary equation and rewrite it for the function $R_x(t)$ with the initial condition $R_x(t)\big|_{x=L} = R_L(t)$.

Since we know the behavior of $c(x)$ $(Z(x))$ in the neibourhood of $x=L$, we can determine $R_x(t)$ at $x=L-\Delta$. Using the time dependence of $R_x(t)$ one can calculate $c(x)$, $c'(x)$, etc. from relations (4)(with L replaced to x). Finally, from the value $G_L(2\tau_0)=R_L(2\tau_0)+F_L(2\tau_0)$ in accordance with (9) we obtain the value Z_1, which characterise the homogeneous half-space $x<0$.

Exact analytical solutions

Imbedding equation presented in this paper allows to obtain two analytical solutions for linear and exponential time dependences of $R_L(t)$, in particular. First, let we have

$$R_L(t)= \alpha\, e^{\beta t}\ , \qquad \alpha(L)= \frac{2Z(L)}{Z_2+Z(L)}\ , \qquad \beta(L)= -\frac{Z_2 Z'(L)}{2n(L)(Z_2+Z(L))}.$$

We consider two polarizations of waves. For the E-wave $(n=1)$ the solution of inverse problem (1) has two branches

$$c(x)= c(L)\left(1 \mp \frac{\xi}{2}\right)^2 , \qquad \xi = \frac{|c'(L)|}{c(L)}\,(L-x)\ . \tag{7}$$

The "$-$" sign corresponds to $c'(L)>0$ and "$+$" sign $-$ to $c'(L)<0$. An interesting feature of solution (7) at $c'(L)>0$ is that the travel time to depth $\xi_0=2$, where $c(x)=0$, is infinity. In this case, the wave travelling to the finit depth $L-x_0=2c(L)/c'(L)$ is reflected by the slab completely.

For the H-wave $(\,n(x)=c_2^2 c^{-2}(x)\,)$ the solution of inverse problem is

$$c(x)= c(L)\left(1 \mp \frac{3}{2}\xi\right)^{2/3}. \tag{8}$$

For the linear time dependence of R_L

$$R_L(t)= \alpha + \beta t\ , \qquad \alpha(L)= \frac{2Z(L)}{Z_2+Z(L)}\ , \qquad \beta(L)= -\frac{Z_2 c(L)Z'(L)}{(Z_2+Z(L))^2}$$

inverse problem solution for both two polarizations has the form

$$\operatorname{arctg}\sqrt{\frac{c(x)}{c_2}} - \sqrt{\frac{c(x)}{c_2}} - \operatorname{arctg}\sqrt{\frac{c(L)}{c_2}} - \sqrt{\frac{c(L)}{c_2}} = \pm\sqrt{\frac{c(L)}{c_2}}\,\frac{|c'(L)|}{c(L)+c_2}\,(L-x),$$

where signs "$+$" and "$-$" are associated with $c'(L)>0$ and $c'(L)<0$, respectively. This solution depends on $c(L)/c_2$ – the wave speed jump at the slab boundary $x=L$.

We note, that an interesting feature of profiles $c(x)$ at $c'(L)>0$ is their waveguide character.

Nonlinear medium

We consider now a nonlinear medium and write the equation for the wave field in the form

511

$$\frac{\partial^2}{\partial t^2}\left[\frac{G(x,t)}{c^2(x,G(x,t))}\right] - \frac{\partial^2}{\partial x^2}G(x,t) = 0, \quad \varphi = \vartheta(t + c_2^{-1}(x-L))/2c_2$$

where $c^2(x,G(x,t))$ describes a medium inhomogenities and a wave field selfaction. In this case $G(x,t) = G(x,L;t)$ and $G_L(t)$ satisfy the imbedding equation with variational derivatives (see e.g.[3]). Equation for $G_L(t)$, for example, has the form

$$\left[\frac{\partial}{\partial L} + \frac{2}{c_2}\frac{\partial}{\partial t}\right]G_L(t) = \frac{\delta(t)}{c_2^2} - \int d\tau \frac{\delta G_L(\tau)}{\delta f(\tau)}\frac{\partial^2}{\partial \tau^2}F(L,G_L(t)), \quad f(t) = \delta(t),$$

$$G_0(t) = \vartheta(t)/2c_2, \quad F(L,G_L(t)) = \left[c_2^2 c^{-2}(L,G_L(t)) - 1\right]G_L(t).$$

The wave field $G_L(+0)$ on the boundary $x = L$ satisfies the equation

$$c_2^2 F(L,G_L(+0)) \, G_L(+0) + 2c_2 G_L(+0) = 1. \tag{9}$$

The unique solution of eq.(9) is determinated from the condition of a connection one with the solution of a linear problem.

When $G_L(+0)$ is known we can find the travel time

$$\tau_x(L) = \int_x^L d\xi \left[c_2^{-1} + F(\xi,G_\xi(+0))\right]$$

and equation for the wave front amplitude :

$$\frac{\partial}{\partial L}\ln G(x,L;\tau_x) = -\left[\frac{dG_L(+0)}{dL}\right]^2 \frac{\partial F(L,s)}{\partial s}\left[s\frac{\partial F(L,s)}{\partial L}\right]^{-1}\Bigg|_{s=G_L(+0)}$$

with the initial condition $G(x,L;\tau_x)\big|_{L=x} = G_x(+0)$.

In a simplest case $F(x,G(x,t)) = \tilde{c}(x)G^k(x,t)$, $|\tilde{c}(x)| \ll 1$, $k > 1$

it is easy to show that $G(x,L;\tau_x)$ depends on $\tilde{c}(x)$ locally as in the linear case.

In conclusion we note that imbedding equations have been obtained for three-dimensional wave problem in [2,3] also.

References

1. R.Burridge, Wave motion 2, 305 (1980).
2. G.I.Babkin, V.I.Klyatskin, Wave Motion 4, 195 (1982).
3 V.I.Klyatskin "Imbedding method in the wave propagation theory", Nauka, Moskow, 1986.
4. J.P.Corones, M.E.Davison, R.J.Krueger, J.Acoust.Soc.Am. 74, 1535 (1983).
5. G.Kristensson, R.J.Krueger, J.Math.Phys. 27, 1667 (1986), 28, 360 (1987).

STATISTICAL THEORY OF RADIATIVE TRANSFER IN LAYERED RANDOM
MEDIA (NONSTATIONARY PROBLEMS) **P61**

M.A. Guzev, V.I. Klyatskin

Pacific Oceanological Institute
Far Eastern Branch USSR Academy of Sciences
7 Radio, Vladivostok, 690032, USSR, Telex: 213121 SVT SU POI

1. Description of various phenomena linked with propagation
of waves in fluctuating natural and artificial media often
demands consideration of boundary wave problems in a nonsta-
tionary formulation.The boundary character of the problems under
cosideration does not allow to use the standard technique of
the statistical analysis. In order to overcome this difficulty
the imbedding method is widely used [1]. In the framework of
the imbedding method the boundary problems are reduced to
initial value problems possessing the dynamic causaulity
property with respect to an auxiliary parameter - it allows to
carry out the statistical analysis on the foundation of the
standard statistical theory apparatus.

Below we consider a number of nonstationary wave problems
for which the corresponding imbedding equations are given. We
investigate the behaviour of the wave field statistical
characteristics and universal features of fluctuating systems
linked with the energy localization.

2. Let a slab of a randomly inhomogeneous medium occupy
the region $L_o \leq x \leq L$ of a homogeneous space and there is
the time-pulse source in some point of the slab. The wave field
$U(x,x_o;t)$ is a solution of the boundary problem

$$\left[\frac{\partial^2}{\partial x^2} - \frac{1}{c^2(x)} \frac{\partial}{\partial t}\left(\gamma + \frac{\partial}{\partial t}\right)\right] U(x,x_o;t) = \frac{2}{c} \delta(x-x_o) \frac{\partial \varphi(t)}{\partial t} ,$$

$$\left[\frac{\partial}{\partial x} + \frac{1}{c} \frac{\partial}{\partial t}\right] U(x,xo;t)\bigg|_{x=L} = 0 , \left[\frac{\partial}{\partial x} - \frac{1}{c} \frac{\partial}{\partial t}\right] U(x,xo;t)\bigg|_{x=L_o} = 0,$$

in which $1/c^2(x) = [1+\epsilon(x)]/c^2$, and $\epsilon(x)$ is the Gaussian white
noise($\epsilon(x) = 0$ outside the slab); parameter γ characterizes
dissipative properties of the medium. If the source is placed
on the right boundary of the slab, we have the problem of the
plane wave $\varphi(t+(x-L)/c)$ be incidence on the slab from the
region $x \geq L$, the boundary condition at $x=L$ being changed:

$$\left[\frac{\partial}{\partial x} + \frac{1}{c} \frac{\partial}{\partial t}\right] U(x,L+0;t)\bigg|_{x=L} = \frac{2}{c} \frac{\partial \varphi(t)}{\partial t} .$$

513

The case $\frac{\partial}{\partial x} U(x,x_o;t)=0$ on the boundary $x=L$ corresponds to the source on the reflected boundary; when $L\to+\infty$, $L_o\to-\infty$ we have the unbounded medium.

3. We are interested in the behaviour of the averaged intensity $\langle I(x,x_o;t)\rangle=\langle U^2(x,x_o;t)\rangle$ over the ensemble realization of the process $\epsilon(x)$ and the energy $E(t)=\int dx \langle I(x,x_o;t)\rangle$ at $t\to\infty, \gamma\to 0$. They are expressed via the two-frequency analogue $\langle I_{\omega,\psi}(x,x_o)\rangle=\langle G_{\omega+\psi/2}(x,x_o)G_{\omega-\psi/2}(x,x_o)\rangle$ of the stationary intensity at small ψ, where $G_{\omega+\psi/2}(x,x_o)$ is the stationary Green function. It has been shown [2] that construction of $\langle I_{\omega,\psi}(x,x_o)\rangle$ at $\psi\to 0$ is reduced to the analytical prolongation of the stationary problem solution with respect to the parameter $\gamma\to(\gamma-i\psi)$ and $\gamma\to(0-i\psi)$ without the absorption.

Calculations for the source in the unbounded medium yield

$$\langle I(x,x_o;+\infty)\rangle=\frac{c}{2\pi}\int_{-\infty}^{+\infty}d\omega\ |\hat{\varphi}(\omega)|^2 D(\omega)\ \Phi_{loc}(\xi)\ ,\quad \xi=D(\omega)|x-x_o|\ ,$$

$$E(+\infty)=\frac{c}{2\pi}\int_{-\infty}^{+\infty}d\omega\ |\hat{\varphi}(\omega)|^2\ ,$$

where $D(\omega)$ is the diffusion coefficient, $\Phi_{loc}(\xi)$ is the localization curve for the stationary problem (see[3]). If the Fourier transformation $\hat{\varphi}(\omega)$ of $\varphi(t)$ falls sufficiently quickly, the averaged intensity in the source point and the total energy appear to be finite. This stands for the presence of the space localization of the intensity. The localization length would be given by the equality

$$l = \int_{-\infty}^{+\infty}d\omega\ |\hat{\varphi}(\omega)|^2\ \times\left[\int_{-\infty}^{+\infty}d\omega\ |\hat{\varphi}(\omega)|^2 D(\omega)\right]^{-1}.$$

Asymptotical behaviour of $\langle I(x,x_o;+\infty)\rangle$ for a smooth time-pulse and a video-pulse has the form:

$$\langle I(x,x_o;+\infty)\rangle\sim|x-x_o|^{-3/2},\quad \langle I(x,x_o;+\infty)\rangle\sim\Phi_{loc}(\xi),\xi=D(\omega_o)|x-x_o|$$

(here ω_o is a carrier frequency)

Acting by analogy with the precedent problem we get the averaged intensity and the the total energy for a source on the reflected boundary [3,4]. In this case the localization length is twice smaller.

514

Let the time-pulse be incident on a half-space of a randomly inhomogeneous medium, then we have [3,5]:

$$\langle I(x,t)\rangle = \frac{1}{\pi t\sqrt{tcd}} \int_{-\infty}^{+\infty} dp \frac{|\hat{\varphi}(p/\sqrt{tcd})|^2}{(2+p^2)^2}\left[p^2 + \frac{2(L-x)}{ct}(1+2p^2+2p^4)\right].$$

$$d = D(\omega)/\omega^2 \quad ;$$

$$E(t) = \frac{1}{\pi\sqrt{tcd}} \int_{-\infty}^{+\infty} dp \frac{|\hat{\varphi}(p/\sqrt{tcd})|^2}{(2+p^2)} \quad .$$

It follows that the averaged intensity increases as the function of (L-x) for not large distance inside the medium. On the boundary x=L the intensity decreases with respect to time, in particular we have the following asymptotical dependence for a smooth time-pulse and a video-pulse correspondingly:

$$\langle I(L,L;t)\rangle \sim t^{-3/2} \quad , \quad \langle I(L,L;t)\rangle \sim t^{-2} \quad .$$

Investigation of the statistical characteristics in a finite thickness slab for the problem of a wave incidence is carried out at $t \gg 2(L-L_0)/c$. In this case the asymptotical behaviour of the wave field have not to depend on an initial value of the nonstationary Green function on the right slab boundary. Then it is easy to obtain the Laplace representation for the stochastic solution of the corresponding imbedding equation. The asymptotical representation of the averaged intensity coincides with the corresponding asymptotical representation for an incident pulse on a half-space [5]. So the wave field jumps are not essential in formation of the statistics, and the accumulating statistical effects are determinated by scattering on random inhomogeneities. Analogous result has been got for a stationary problem [6].

References

[1] V.I. Klyatskin. Ondes et equattions stochastiques dans les milieus aleatoirement non homogenes. Editions de Physique, Besanson - Cedex, 1985.
[2] B.M. Shevtsov, Izv. Vuzov, Radiofizika, 25, 1032 (1982, in Russian).
[3] V.I. Klyatskin, "Localization and waves in the randomly inhomogeneous media", submitted to Wave Motion.
[4] R.Burridge, G.Papanicolaou, P. Sheng, and B. White, SIAM J.Appl. Math, 49,582 (1989).
[5] M.A. Guzev, V.I. Klyatskin, "Plane waves in a layered weakly dissipative randomly inhomogeneous medium", submitted to Waves in Random Media.
[6] V.I. Klyaskin, "Approximations by delta-correlated random **processes and diffussive approximation in stochastic problems", submitted to Lectures in Applied Mathematics.**

INFLUENCE OF LARGE-SCALE SURFACE WAVES ON THE RADAR SEA RETURN AT LOW GRAZING ANGLES **P62**

Volkov A.V., Slavutsky L.A., Shevtsov B.M.
Pacific Oceanological Institute, 7 Radio St.
Vladivostok, U.S.S.R. 690032

Introduction

Radar sensing of the sea surface may be used to get some information about its state and about wind speed and direction. The dominant microwave backscattering is accepted to be produced via the Bragg mechanism [Barric, 1972]. In SHF band the radio-wave backscatering is formed mostly by small-scale ripples on the surface, and the large-scale waves (wind caused waves, swell) result in modulation of the radar return [Bass, Fuks, 1979]. In addition, the large-scale waves causes the change of statistical distribution function of the backscatterred signal amplitude, particularly, its deflection from the Rayleigh one [Trunk,1972]. In this paper we experimentally investigate the influence of the anisotropic large-scale surface waves on temporal-spatial structure of the radar sea echo.

Instrumentation and experimental technique

We used a shipboard surface search radar with two all-round looking aerials (wavelengths 3 and 10 cm, 25 m height) as a source of radio-waves. Along with radar observations we monitored the sea surface by its thermo-microwave radiation at wavelength 1.35 cm. The contribution of ship rolling was accounted with gyro. The radar signal recieved from the direction chosen was directly digitized (with the sampling rate 10 MHz) or recorded by an analogous tape recorder with a band width of 5 MHz. A time interval between repitition radar pulses (0.6-1.2 ms) is sufficiently short to consider the surface as "frozen".At the grazing angles which are less than the usual slopes of the surface roughness, one can accept that the incidence angle change does not influence the structure and characteristics of the reflected pulse. Thus, the technique offered allows to investigate spatial characteristics of the sea surface in the chosen direction.

Analysis of the experimental data

Let $U_n(t)$ be envelope of the radar signal of n-th reflected pulse from a specific direction, and let t be time uniquely connected with the illuminated area distance and grazing angle. σ^2 is the variance of amplitude fluctuations. The statistical properties of $U_n(t)$ are non-uniform over t since for various values of the time t there are various grazing angles and various diameters of the reflected area. To estimate the effect of non-uniformity on the behaviour of $U_n(t)$

we computed the autocorrelation function $R_n(t_0,\tau)$, when the interval of integration exeeding the signal correlation time. We found the fact that change of $R_n(t_0,\tau)$ with t_0 is more appriciable for 10 cm wavelength that appears to be connected with beam divergence in azimuthal plane (which is greater than for 3 cm). The behaviour of $R_n(t_0,\tau)$ doesn't essentially vary as a function of n which fact confirms the stationarity of the surface wave process during a measurment session.

Then we plotted normalized amplitude probability distributions $P(U_n<U_0)$ at grazing angles of the order of 1.5 (t=5 mus) for the waves with the characteristic slope spectrum which is shown in Fig. 1, and we found following. When U_0 is sufficiently low the distribution is closely fitted with the Rayleigh one and deviates from it when U_0 is greater. To appoximate the amplitude probability distribution at high U_0 the wellknown biparameter probability density distribution function appears to be useful:

$$p(U) = \frac{b(\ln 2)U^{b-1}}{G^b} \exp[-(\ln 2)(U/G)^b]$$

where G is a median of the distribution, C=1/b is a shape parameter. When C>0.5 the non-symmetry *changes* and the "tail" of the distribution becomes longer. Such a behaviour matches to the real conditions of the scattering from the sea surface, parameter C being approx. equal to 0.58 for the calm and large swell. It was found that the distribution $P(U_n<U_0)$ for the reflected echo-pulses with 3 cm wavelength does not practically vary at range of the grazing angles from $1°$ to $3°$ and this fact corresponds to behaviour of the correlation function. For the radiosignals. with 10 cm wavelength factor C in the distribution decreases when signal correlation time decreases. Beginning with definite t for both radiowave lengths the fuctions of correlation practically don't change when t increases and the amplitude probability distribution of radar signal is close to the Rayleigh one.

Thus, the initial section of the recieved radar signal which correspond to the grazing angles of $1-3°$ and sufficiently small diameter of the reflected area contains the maximum amount of information about the surface waves, and azimuthal divergence of radiation has a great influence on spatial change of the statistical properties of the radar signal.

To evaluate the azimuthal anisotropy of the backscaterred signal we calculated the variance $\sigma^2(t,\varphi)$ and $C(\varphi)$ as a function of azimuthal sensing angle φ. Energy spectra of the radar signal fluctuations obtained numerically with the help of the Fourier-

transform of the signal envelope are also plotted.

Fig. 2 gives data obtained under conditions of weak wind and large swell (see Fig. 1). Figure shows the result after averaging of the energy spectra of the radar signal fluctuations over 128 echo-pulses (10 cm) from chosen direction ($\varkappa=4\pi f/c$, f is frequency, c= $3\cdot10^8$ m/sec). The direction of swell propagation (most expressed maximum in the spectrum at the angle 100^c) coincides with one of the maxima in $\sigma^2(\varphi)$ plot. The second maximum of $\sigma^2(\varphi)$ is determined by the wind direction.

Fig. 3 (curve 1) shows a similar spectrum for wavelength 3 cm along the wind direction in logarithmic scale (for 200 m swell). It can be seen from the Figure (curve 1) that the spectrum consists of two sections (marked as I and II) which have similar shape and differ from each other in amplitude. Following Dolin and Rodin [Dolin, Rodin, 1980] one can suppose, that the spectrum of backscattered signal is a sum of the surface slope spectrum and its autocorrelation function with certain factors

$$W_{\Delta T}(\varkappa)=4\pi^2 w(\varkappa) \ [a_X^2 W_{\nu_X}(\varkappa)+2a_{XX}^2 \int_{-\infty}^{+\infty} W_{\nu_X}(\varkappa-\varkappa_1)W_{\nu_X}(\varkappa_1)d\varkappa_1]$$

where $\varkappa$ is the surface wave number, $W_{\Delta T}(\varkappa)$ is energy spectrum of fluctuation intensity ΔT, $W_{\nu_X}(\varkappa)$ is energy spectrum of projections of the normal vector to the surface ν_X on a chosen direction X, $w(\varkappa)$ is spatial spectrum of the envelope of the outgoing radar pulse.

For calculation suppose that the first section in the spectrum corresponds to the surface slope spectrum. For rough estimating of a_X and a_{XX} factors suppose that along the sensing direction the surface wave spectrum is concentrated near the harmonic with the spatial wave number $\varkappa$ and amplitude A, and its shape can be approximated by Gauss curve with the half-power width $\Delta\varkappa$. Then

$$\frac{a_X}{a_{XX}} = A\varkappa \ \sqrt{\sqrt{\pi} \ \Delta\varkappa \ D},$$
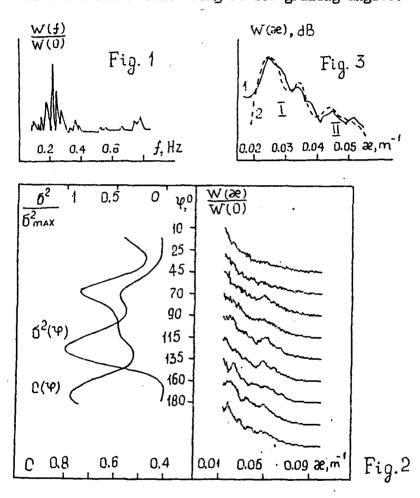
where D is the ratio of the amplitudes of the first and second sections in the spectrum. The result of calculation is shown in Fig. 3 (curve 2).

Thus the spectrum of the reflected radar pulse contains directly the spectrum of the large-scale wave motion, and the experimental data allows you to estimate the nonlinear "detection" effect [Dolin and Rodin, 1980].

Conclusions

All results presented were obtained with the use of nonsophisticated experimental equipment. The influence of the azimuthal beam divergence on the structure of radar signal was analyzed.Our procedure of statistical processing of the recieved backscatter gives enough information about anisotropic large-scale wave motion and permits to envestigate fine structure of the microwave radar scattering at low grazing angles.

Fig. 1

Fig. 3

Fig.2

References
Barric D.E. IEEE Trans., AP-20, N 1, p. 2-10, 1972.
Bass F.G., I.M. Fuks, Wave Scattering From Statistical-
ly Rough Surfaces, 525 pp., Pergamon, New York, 1979.
Dolin L.S., V.V. Rodin. Izv. vuzov, Radiofizika
(in Russian), 23, 79-89, 1980.
Trunk G.V. IEEE, Trans., AES-8, N 2, p. 196-204, 1972.

INFLUENCE OF STRONG-ANISOTROPIC FLUCTUATIONS OF THE REFRACTIVE INDEX ON THE BEYOND-THE-HORIZON PROPAGATION OF SHF

Koshel K.V.
Wave Processes Lab.
Pacific Oceanological Institute
7 Radio St.
Vladivostok
U.S.S.R. 690032

A number of investigators have studied the problem of electromagnetic wave propagation in surface-based or elevated ducts. Nevetheless the determinate modelling doesn't give the exhaustive description of these problems. Particularly, the scattering from the strong-anisotropic in horizontal directions fluctuations of refractive index appers to give an important contribution to the EM field behaviour [1,2].

The propagation of radio waves in gomogeneous atmosphere was considered by Khukhushkin et.al. [2].

They grounded the validity of radial layer model of the fluctuated refractive index profile.. This paper offers the technique to investigate the influence of layered fluctuations of the refractivity on the beyond-the-horizon radio wave propagation in the evaporation duct.

The solution of the given problem in terms of normal wave sum is well-known [1-5]:

$$V(x,y,y',q)=2\sqrt{\pi x}\ e^{i\frac{\pi}{4}}\sum_{n=1}^{\infty} e^{ixt_n}\ \frac{dt_n}{dq}\ f(y',t_n)f(y,t_n) \quad (1)$$

where V is the path loss [3], x,y are dimensionless vertical and horizontal coordinates. In this case the height functions satisfy the following equation [3-5]:

$$\frac{d^2 f(y,t)}{dt^2} + (y+r(y)-t)f(y,t)=0 \quad (2)$$

and the boundary conditions:

$$\frac{df(y,t)}{dy}\bigg|_{y=y_1} + \frac{\omega_1'(t-y_1)}{\omega_1(t-y_1)}\ f(y_1,t)=0$$

$$\frac{df(y_1 t)}{dy}\bigg|_{y=h} + qf(h_1 t)=0 \quad (3)$$

where q is the impedance of the surface, y_1 is the height above which the layer is considered to be gomogeneous, h is the Earth's surface position.

$$r(y,\alpha) = \left[\frac{KR}{2}\right]^{2/3}(\varepsilon(y)-1), \quad (h_1 < y < y_1),$$

$$r(y) = 0, \quad (y_1 < y) \tag{4}$$

and $\omega_1(t) = \pi^{1/2}[Bi(t)+iAi(t)]$ [5].

. With the use of the invariant imbedding method [6] one can obtain the solution of the problem in the following form

$$f(y,t) = \exp\left\{\int_h^y \varphi_\eta(t)\,d\eta\right\},\tag{5}$$

where $\varphi_h(t)$ obey to Riccati equation:

$$\frac{d}{dh}\varphi_h(t) = -\varphi_h^2(t) - (h+r(h)-t), \quad \varphi_{y_1}(t) = -\frac{\omega_1'(t-y_1)}{\omega_1(t-y_1)}.\tag{6}$$

In this case the constants of propagation satisfy the dispersion relationship:

$$\varphi_h(t_n) + q = 0 \tag{7}$$

When the refractivity is suggested to depend on some parameter α ($r \equiv r(y,\alpha)$) one can easy derive from (5),(6),(7) the evolutional equation for $t_n(\alpha)$

$$\frac{dt_n(\alpha)}{d\alpha} = \frac{\int_h^{y_1} f^2(\eta,t_n)\dfrac{\partial r(\eta,\alpha)}{\partial\alpha}\,d\eta}{[\varphi_{y_1}^2 - (t_n-y_1)]f^2(y_1,t_n) + \int_h^{y_1} f^2(\eta,t_n)\,d\eta}\tag{8}$$

. As a boundary condition for (8) we use the solution for gomogeneous medium ($r\equiv 0$), which was obtained by Fok [3]. The norm factor is:

$$\frac{dt_n}{dq} = -\left\{[\varphi_{y_1}^2 - (t_n-y_1)]f^2(y_1,t_n) + \int_h^{y_1} f^2(\eta,t_n)\,d\eta\right\}^{-1}\tag{9}$$

Then solving the system (5),(6),(8) for $r(h,\alpha)$ wich is given in form

$$r(y,\alpha) = (1+\mu^3)(y_2-y) + \left[\frac{KR}{2}\right]^{2/3}(\tilde{\varepsilon}_j(y)(1-\alpha)+\tilde{\varepsilon}_{j+1}(y)\alpha), \quad (h<y<y_2),$$

$$r(y,\alpha)=\left[\frac{KR}{2}\right]^{2/3}(\tilde{\varepsilon}_j(y)(1-\alpha)+\tilde{\varepsilon}_{j+1}(y)\alpha), \quad (y_2 < y < y_1),$$

$$r(y,\alpha)=0, \quad (y > y_1), \tag{10}$$

we obtain numerically solution for (j+1)-th realization of the stochastic function $\tilde{\varepsilon}_j(y)$. Then averaging the sum over realizations we obtain the average characteristics of the path loss. We performed the numerical calculatios for gauss delta-correlated function $\tilde{\varepsilon}(y)$, which presents natural profiles enough correct. We should note now that the method suggested may be used for any another types of profile $\varepsilon(y)$.

Numerical calculations show that considered fluctuations influence especially on the beyond-the-horizon radio wave propagation. It is found that the mean intensity of EM field considerably exeeds one in the case of the undisturbed wavequide and decrease along the Eearth's surface more slowly. It is shown that the field distribution obey to logarithmic normal distribution.

Another important e f fect is a disappearing of the interference structure of the field, two or more normal modes being captured into evaporation duct. The analysis of the field was carried out with some realizations of random refractivity profile.

References

1. Khukhushkin A.W., Freilicher W.D., Fuks I.M., Izv. Vuzov, Radiofizika,1987. V.XXX, № 7, P,811.
2. Khukhushkin A.W., Freilicher W.D., Fuks I.M., Izv. Vuzov, Radiofizika,1983. V.XXXVI, № 7, P,8171.
3. Fok W.A. Problems of diffraction and propagation of electromagnetic waves. Moscow. Sov. Radio, 1970.
4. R.N. Ott. Radio Science, 1981, V.16.№ 6., P.1149-1154.
5. R.N. Ott. J. Math.Phys.1980,№ 21, P.1256-1266.
6. Babkin G.I.,Klyatzkin V.I. Wave Motion, 1982, V.4,P.195.

A STUDY OF APOSTERIORI HOLOGRAPHIC MOIRE TECHNIQUE FOR ESTIMATION OF DEFECTION AREA IN THE DEFECTIVE CURVE OF DIAPHRAGMS/PLATES **P64**

B.N. Gupta, Chandra Shakher and A.K. Nirala

Optics Laboratory

Instrument Design Development Centre

Indian Institute of Technology, Delhi-110016 (INDIA)

ABSTRACT

This communication deals with the use of Aposteriori moire based on double exposure holographic interferometry for measurement of defect affected area in diaphragms and plates.

EXPERIMENTAL ANALYSIS

A posteriori holographic moire can be used for measurement of slopes, curvature and θ-slope fringes. The purpose of this communication is to highlight the potential of posteriori holo-moire for estimation of defective area in diaphragm/ thin plates.

For the purpose of present study, hologram construction geometry assumes normal illumination and observation. Fig.1 and Fig.2 show the holographic interferogram of sound and defective circular diaphragms subjected to uniform pressure difference loading. It has been demonstrated by Chandra Shakher and Aggarwal [1] that a posteriori moire technique is powerful tool for detection of flaws for objects where deformation is radially symmetric . Fig.3 shows the θ-slope fringes when two transparencies made out of such interferograms are slightly rotated about the Center of fringe pattern. θ-slope fringes will be observed and localized in the defect affected areas only. Our

study reveals that rotation about points other than center is more informative. This can be achieved by combining linear translation with rotation. Fig. 4 shows the θ-slope fringe pattern when rotation is about the point other than center. The defect affected area can be easily visualized from this figure.

Further, for precise measurement of defective area in the plates/diaphragms a relative magnification can be used to correct the non-precise application of loading between the interf￮:ograms of sound and defective diaphragms. Fig.5 shows the beat pattern of sound and defective diaphragms . It shows straight away the comparison between the deflection curves of sound and defective diaphragms. We have carried out numerical analysis of double-exposure holographic interferogram. The comparison of theoretical analysis of sound diaphragm and experimental analysis of double exposure holographic interferogram shows very similar curve as given in Fig.5. Experimental results shown in Fig.5 demonstrate defect affected area in diaphragm clearly without doing any numerical analysis.

Discussions

Local changes in stiffness at the defective area will affect the deflection, partial slopes, curvature and θ-slopes. Posteriori holo-moire technique provides capability to use all these parameters to estimate the defective area fast and easily.

Posteriori holo-moire technique can accommodate quite large size engineering objects as well as curved surfaces. Digital image processing for formation of moire pattern has already been

demonstrated by Youren et.al. [2]. Combination of digital image processing and posteriori holo-moire technique looks to be competitive with digital speckle pattern interferometry.

REFERENCES

1. Chandra Shakher and A.K. Aggarwal

    Opt and Laser Technology, $\underline{15}$ (1983) 206-209.

2. Youren, X.V., Vert, C.M. and E.J. Delp

    Opt. Lett. $\underline{8}$ (1983) 452-454.
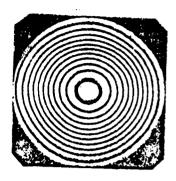
Fig.1: Double Exposure Interferogram
of Non-defective Diaphragm
Subject to Pressure Difference
of 2.1 cm. of water

Fig.2: Double Exposure Inrerferogram
of Deflective Diaphragm
Subject to Pressure
Difference of 2.1 cm. of water

Fig.3: θ-Slope Fringes-Rotation
about Centre of Fringe
Pattern
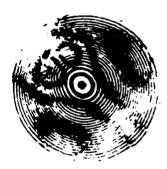
Fig.4: θ-Slope Fringes-Rotation
about a point other than
Centre of Fringe Pattern

Fig.5: Beat Pattern of Interferograms of Defe-
ctive and Non-defective Diaphragms

528

FIELD MEASURED ATTENUATION COEFFICIENT OF CO_2 LASER **P65**

Junbo Wang
Institute of Applied Physics
University of Electronic Science and Technology of China
P.O. Box 83, Chengdu, 610054, P.R. China, (028)333312-2474

Ruizhong Rao
Anhui Institute of Optics and Fine Mechanics
Academia Sinica
P.O. Box 25, Hefei, 230031, P.R. China, (0551)291007

1. INTRODUCTION

CO_2 laser radiation has been widely used in atmospheric optic engineering, especially in communication system and coherent lidar. Many models have been proposed to aid system design. Laboratorial measurements have been done for O_3, CO_2, H_2O and pollutant gases absorption[1]. But, actual attenuations in variety of atmospheric conditions must be known to make a highly reliable system. In 1978 S.T. Hanley et al. reported a field measurement of atmospheric extinctions for HeNe, Nd-YAG, DF and CO_2 lasers in White Sands Missile Rang to compare HITRAN predications[2]. In our University the relative attenuation and turbulence induced fluctuation of CO_2 laser were measured in several places such as Qingdao, Chongqing, Beijing and Tengger Desert of Ninxia provence of China[3][4][5]. To improve our knowledge on the absolute attenuations of CO_2 laser lines, we carried out an out-door measurement in August 1986 in Sichuan Basin, Chengdu City with a computer-aided measurement system. Differ from that of reference [2], the atmospheric conditions in our experiment period were characterized by high relative humidity, high aerosol density and high temperature.

2. DESCRIPTION OF EXPERIMENTAL SYSTEM AND ENVIRONMENT

Our experimental system configuration was shown in FIG.1. The system was separated by 350 m and was 35 m high above ground. At the transmitting side, a CO_2 laser beam, tunable for 40 spectral lines in 00^01-10^00 and 00^01-02^00 band, was modulated by an acoustooptical modulator. Line position was checked up by CO_2 Spectrum Analyzer. Through the modulator, diffracted beam was detected as output monitoring signal V_m, which, after amplifying and demodulating, was transmitted to receiving side and received by a specialized radio system. Un-diffracted beam, with divergent angle 4.4 mrad, was propagated through atmosphere and received by optic antenna (its aperture diameter was 200 mm), and converted to V_r by another electronic apparatus. V_m and V_r was stored by a computer via 7-bit A/D converts in manner of 1 V_m every 800 V_r per second. Attenuations were calculated by:

$$A = ln[C*V_m/V_r/Y(k)]/L, \qquad\qquad 1$$
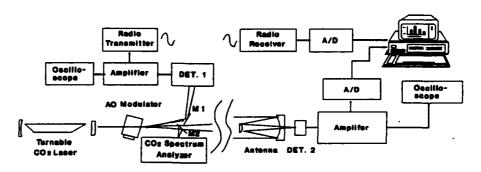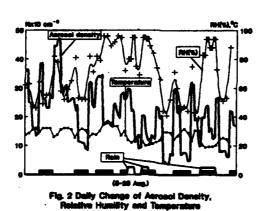
Fig. 1 Sketch of Experiment System

in which, L is propagation distance, C is wavelength-free factor, and Y(k) depends upon wavelength of every spectral line which can be scaled in labo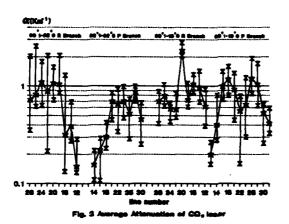ratory. During our experiment, aerosol size distribution and some meteorological parameters ,such as temperature, relative humidity, air pressure and refractive index fluctuation constance C_n^2 were also recorded by hand. Variation of recorded data was: for aerosol density, from 3.6 cm^{-3} to 4.7×10^2 cm^{-3}; relative humidity, 40% to 96%; temperature, $19^0 C$ to $36^0 C$; and C_n^2 0.25–$4.1 \times 10^{-14} m^{-1/3}$. Fig.2 illustrated a typical day-time changes of those parameters.

Fig. 2 Daily Change of Aerosol Density, Relative Humidity and Temperature
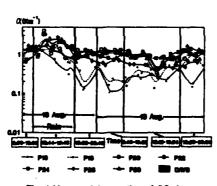
3. MEASURED RESULTS AND DISCUSSION

From August 5 to 30, 1986 we measured the atmospheric attenuation for 4 bands of 40 lines in $00^0 1-10^0 0$ and $00^0 1-02^0 0$

Fig. 3 Average Attenuation of CO₂ laser

transitions of P and R branch. Fig. 3 shows the attenuation of every line of 4 bands of CO_2 laser radiation. The relative attenuation strength is identified to reference [1] and [2], i.e. in 00^01-10^00 transition, $P_{(22)}$ had minor attenuation value to $P_{(18)}$ and $P_{(26)}$, and $R_{(20)}$ was intensely attenuated than other lines. Also, attenuation of $P_{(28)}$ in 00^01-02^00 transition is lager than adjoined lines. We checked our results with those experiential formulas to $P_{(20)}$ of 00^01-10^00 band [6][7][8][9], and found that when relative humidity is not very high(i.e. not exceed 60%), those formulas can be used as estimation of attenuation of $P_{(20)}$ in 00^01-10^00 band.
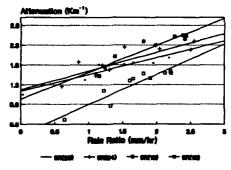
Fig. 4 Measured Attenuation of CO Laser

Fig. 5 Attenuation Vs Rain Ratio

When relative humidity exceed 80%, the predication is fail even if the aerosol density is not very high. If high relative humidity and high aerosol density was encountered at same time, the interaction between air condensation and aerosol causes complexity of absorption, and it is this interaction that played an important role in our attenuation coefficient measurement. Fig. 4 plotted tow days' measured attenuation in rain and sunny day which shows distinct deference between rain and fine day propagation. Fig. 5 shows the relation in attenuation and light rain ratio.

Attenuation is linearly increased with increase of rain ratio. From measured results we can see that to increase the reliability of atmospheric optic system, automatic gain control or adaptive optics is necessary.

4. CONCLUSION

In the summer of Sichuan Basin, both aerosol extinction and water vapor absorption are important factor in CO_2 laser propagation. Measured attenuation coefficient predicts that $P_{(22)}$ of 00^01-10^00 band has lower attenuation than other main output lines so it is appropriate for communication application and coherent Lidar. $R_{(20)}$ of 00^01-10^00 band has the highest attenuation in all of lines of CO_2 laser radiation.

REFERENCE

[1] Tuer, T.W., J.Mudar, J.R. Freeding and G.H. Lindquist, 1980; Atmospheric effects on low-power laser beam propagation, Final report SAM-TR-80-51 under contract F33615-78-C-0627, AD-AO95383(NTIS).

[2] Hanley, S.T., J.A. Dowling, R.F. Horton, et al. 1980; Atmosphere transmission measurement at Whit Sands Missile Range, NRL report 8422, AD-AO92445.

[3] Le Shixiao, et al. 1983; CLEO'83.

[4] Quan Xiecheng et al. 1985; Chinese Laser, Vol.12, No.10, (in Chinese).

[5] Wang Junbo, et al., 1986; Advances in Atmospheric Sciences, Vol. 3 No. 3,.

[6] Duly, W.W., 1983; Laser processing and analysis of materials, Plenum Press, NY, pp 366.

[7] McCoy, J.H., D.B. Rensch, and R.K. Long, 1969; Water vapor continuum absorption of carbon dioxide laser radiation near 10 um, Appl. Opts., Vol. 8, No. 7: 1471-1478.

[8] Chu, T.S., and D.C. Hogg, 1968; Effects of precipitation on propagation at o.63, 3.5, and 10.6 microns, Bell Syst. Tech. J., 47: 724-759.

[9] Hodges, J.A., 1972; Aerosol extinction contribution to atmospheric attenuation in infrared wavelengths, Appl. Opts., 11, No. 10: 2304-2310.

NEAR INFRARED LASER TECHNIQUES FOR ATMOSPHERIC SOUNDING **P66**

T. D. Wilkerson, Institute for Physical Science and Technology

University of Maryland, College Park, MD 20742-2431, USA

(301) 405-4850

U. N. Singh, ST Systems Corporation

4400 Forbes Blvd., Lanham, MD 20706, USA

(301) 794-5000

J. A. McKay, Physical Sciences, Inc.

635 Slaters Lane (#101), Alexandria, VA 22314, USA

(703) 548-6410

(INVITED)

Opportunities for atmospheric measurements by means of near infrared lidar are increasing as better laser and detector technology becomes available. For $\lambda < 1$ μm, examples are the alexandrite and Ti-doped sapphire lasers which can be used for water vapor, pressure, and temperature profiling. There is great interest in the region $\lambda = 1.5 - 5$ μm for reasons of eye safety, predominance of aerosol over Rayleigh scattering, and the presence of molecular absorption lines for DIAL concentration measurements of some pollutants and "greenhouse gases". A tunable laser in this region is $Co:MgF_2$ (1.6 - 2.1 μm). Nd:YAG lasers, though not eyesafe at either 1.06 or 1.32 μm, are pump sources for Raman shifting into the near IR; e.g., to 1.54 μm using high pressure CH_4 as the medium for stimulated Raman scattering. Optical parametric oscillators (OPOs), using lithium niobate or lithium iodate crystals pumped by Nd:YAG, are tunable in the range 1.5 - 4 μm. New solid state lasers containing holmium and thulium emit in the 2 μm region and provide a basis for OPO operation above 4 μm. Optical pumping of lasers by means of diode arrays rather than flash lamps is a technique that is progressing rapidly. The control of energetic solid state laser output ($\lambda = 1.06, 2.1$ μm) by "injection-locking" with low power lasers is providing new sources for coherent Doppler lidar measurements of wind velocity. This offers advantages over the use of CO_2 (10.6 μm) lasers because of greater detection sensitivity and larger aerosol backscatter coefficients. Progress in near infrared laser/lidar techniques and applications is reviewed in this paper.

I.Kolev, O.Parvanov, B.Kaprielov

Institute of Electronics - Bulgarian Academy of Sciences,
72 blvd. Lenin, Sofia 1784, Bulgaria

INTRODUCTION

During last years various remote and conventional tech-
niques are widely used for the investigation of the processes
in the atmospheric boundary layer (ABL) [1]. The lidars allow
profiles of the meteorological parameters to be remotely
obtained with high time and spatial resolutions. The absence
of contact sensors makes them convenient instruments
particularly in two cases:
  1. When investigating transient processes such as for-
mation and destruction of a given atmospheric stratification;
  2. For the observation of interaction areas at the
boundary of different layers where significant changes in the
meteorological parameters behaviour occur.

APPARATUS AND EXPERIMENT

The arrangement used for the present investigation, i.e.
a triple-beam near-vertical sounding lidar and the correlation
measuring methods is well described in [2]. The geometry of
sounding is shown on Fig. 1. Some of the main characteristics
and parameters of the lidar are briefly summarized below:
wavelength   - 532 nm;   pulse energy   - 15-25 mJ;
repetition rate - up to 50 Hz;   pulse duration - 15 nsec;
receivers   - 3 x 150 mm Cassegrain telescopes, f.l.=2250 mm;
interference filters - $\lambda_\bullet$=532 nm, $\Delta\lambda$=0.1 nm;
photodetectors   - 3 x PMP type FEU-84 (USSR);
data acquisition and processing -PC "Pravetz 16" (fully IBM-XT
                                                  compatible).

The pilot balloon measurements were carried out by Yanka
Paneva and Angel Evtimov.

EXPERIMENTAL RESULTS

Lidar measurements of wind velocity profiles by slant
sounding in the ABL accompanied by ground based measurements
and a comparison with radio- and kytoon sounding have been
carried out in the country during 32 hours [4].
In the present paper some preliminary results of two
12-hours lidar measurements of the wind velocity profiles in
the ABL, particularly in case of a convective ABL destruction
are presented. The investigations also include the wind pro-
files during the destruction of the night stable stratifi-
cation over a urban area after the sunrise but they are not
considered here.

On Sept. 24, 1990 the transient process started at 6:30 p.m. and was in progress till a wind shear formation at about 10 p.m.

The lidar measurements were carried out as follow: from 7 p.m. to 11 p.m. every 30 minutes, to 5 a.m. every 2 hours and to 7 a.m. every 30 minutes again. The wind velocity profiles obtained from the lidar data were based on a measurement duration of T=10 min. at a discretization of Δt=0.24 sec. The profiles contain 8 values each at .any distance divisible by 7.5 meters. The last number is determined from the 20 MHz waveform recorder (HP5180A) sample rate.

On Fig. 2 the wind velocity profiles measured by the lidar and by the pilot balloon between 6:30 p.m. and 7 p.m. at Sept. 24, 1990 are shown (the sunset was about 5:40 p.m. local time).

On Fig. 3 analogous profiles are shown but at about 10:30 p.m.

Shown on Fig. 4 is the same comparison at about 1:30 a.m.

The difference between the three wind velocity profiles obtained 1, 5 and 8 hours after the sunset respectively is evident.

DISCUSSION

During the experiments we used the regular standard radio soundings conducted by the Institute of Meteorology and Hydrology (IMH) - Bulgarian Academy of Sciences at 2 a.m., 8 a.m. and 2 p.m. The IMH is in close vicinity to the Institute of Electronics where the lidar is arranged. The kytoon with temperature, humidity and wind speed sensors was also employed but actually at that time it could be used after the convective layer - stable layer transient process completion due to the significant wind speed values (more than 5 m/s) and considerable wind velocity changes by speed and direction.

The pilot balloon observations are the most appropriate for the dynamic processes investigation such as destruction of the convective layer after the sunset. They were conducted near by the lidar synchronously with the lidar soundings. Two to three balloons were launched during one lidar measurement in dependance of the atmospheric condition.
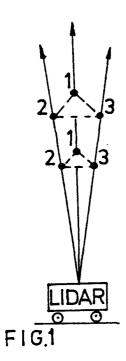
More detailed information about the comparison methods of various means data and the estimation of that comparison is given in [2].

When investigating such processes in the ABL the most appropriate is two or more remote means employing similar measuring methods of the studied parameter to be used [3].

In about an hour after the sunset due to the earth cooling a cooling of the surface air begins which is in progress till the completion of a stable atmosphere stratification. This process is well studied in the surface layers using ground based means but the information about the heights of more than 100-200 meters is still short.

The lidar data on Fig. 2 definitely show the dynamics of the atmosphere, i.e. changes in the wind speed from 1 m/s to 5 m/s (Δv=4 m/s) as well as in the direction in limit of 60 degree (φ=210 deg at H=340 m versus φ=270 deg at H=500 m).
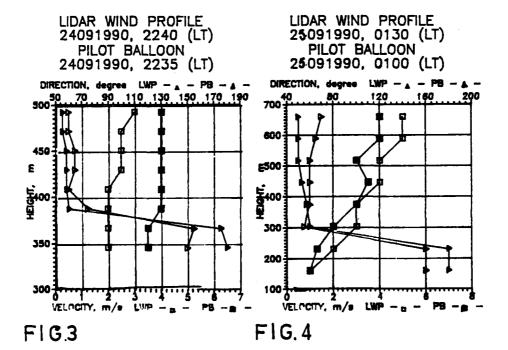
FIG.1

LIDAR WIND PROFILE
24091990, 1900 (LT)
PILOT BALLOON
24091990, 1835 (LT)

FIG.2

LIDAR WIND PROFILE
24091990, 2240 (LT)
PILOT BALLOON
24091990, 2235 (LT)

FIG.3

LIDAR WIND PROFILE
25091990, 0130 (LT)
PILOT BALLOON
25091990, 0100 (LT)

FIG.4

It is not shown on the figure but from the lidar data it is evident that at these heights an aerosol layer exists and the significant changes in the wind speed and direction are near the upper and/or lower boundaries of that layer which is located in the area of the first temperature inversion.

The temperature stratification over the region of Sofia shows a formation of several retentive layers by height [4] under the influence of the orography. Without considering the speed and direction differences between the lidar and pilot balloon data from a methods point of view we assume that they are due to the 30 minutes difference in time between the two measurements. The usual difference of 1-2 m/s and 10-15 deg is seen on Fig. 3.

Fig. 4 shows that the directions shear remains but got about 100 meters down. A uniform increasing of the wind speed from 1 to 5 m/s at heights of 150 to 700 meters is also seen.

Because of the compromise which has to be made between the observation heights number, the time series length and the volume of the computers RAM only a part of the ABL over the region was investigated and this paper does not claim for a thoroughness of the studied processes.

CONCLUSION

In conclusion we shall note that presented investigations show in a good manner the possibilities of the lidar techniques for a study of transient processes and/or of the boundaries of layers with different meteorological characteristics.

During this expedition in autumn 1990 a Raman-lidar and an infrared radiometer have operated simultaneously with the "wind" lidar. A juxtaposition of all obtained data would provide additional information about the processes in the ABL.

REFERENCES

1. Hooper W.P., E.W.Eloranta, 1986, J. Climate and Applied Meteorology, vol. 25, p.p. 900-1001.
2. Kolev I., O.Parvanov, B.Kaprielov, 1988, Applied Optics, vol 27, p.p. 2524-2531.
3. Eloranta E.W., V.L.Schols, 1990, 15-th ILRC, July 23-27, Tomsk, USSR, Abstracts of Papers, Part I, p.p. 227-229.
4. Kolev I., L.Yordaniva, V.Polianov, O.Parvanov, 1988, C. R. Acad. Bulg. Sci., vol. 43 (3), p.p. 37-40.

LITE Simulations using Four Different Retrieval Algorithms **P68**

Mary T. Osborn
ST Systems Corporation
28 Research Drive
Hampton, Virginia 23666
(804) 864-2692

Introduction

LITE, the lidar in-space technology experiment, is being designed by NASA to demonstrate the use of a space-borne lidar system for atmospheric measurements. LITE is currently manifested for flight aboard the space shuttle in 1993. The purpose of this report is to summarize the progress made in evaluating different algorithms for retrieving vertical profiles of aerosol backscatter from expected LITE signal levels. Four of the best known algorithms were chosen and compared at the 0.532 μm wavelength using LITE nighttime parameters. Although only one aerosol model was used for the retrievals in this report, it is fairly representative of some of the aerosol layers LITE will observe.

Aerosol Model

A model of aerosol extinction at 0.55 μm was constructed and converted to vertical profiles of aerosol backscatter mixing ratio at the three LITE wavelengths: 0.532, 0.355, and 1.064 μm. The aerosol model is a composite of the following layers: marine planetary boundary layer, Saharan dust layer, clean free troposphere with thin cirrus cloud layer, and background stratospheric aerosol layer. Simulations, using the LITE parameters for nighttime operation, were used to calculate expected signal and noise levels at the three LITE wavelengths. Signal-to-noise levels expected after horizontal and vertical averaging are shown in Figure 1.
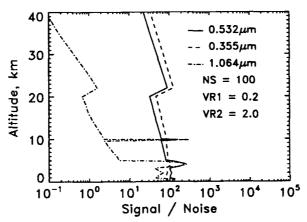
Figure 1. Expected nighttime signal-to-noise levels for the aerosol model described in the text. Signals were averaged horizontally for 100 shots and vertically for 0.2 km between 0 and 20 km and for 2 km between 20 and 40 km.

The Retrieval Problem

The single scattering approximation of the lidar equation can be written in the following form:

$$S(r) = C_L r^{-2} [\beta_a(r) + \beta_m(r)] \Delta r \exp\left\{-2 \int_0^r \sigma_a(r') + \sigma_m(r') + \sigma_g(r') \, dr'\right\} \tag{1}$$

where S is the lidar signal received from range r, C_L is the calibration constant of the lidar system, β_a and β_m are the aerosol and molecular backscatter coefficients, and σ_a and σ_m are the aerosol and molecular extinction coefficients. σ_g represents any gaseous absorption at the wavelength being analyzed (e.g. ozone absorption at 0.532 μm). C_L can be determined by calibrating the lidar signal at an altitude where the aerosol backscatter is assumed minimal or by specifying a known boundary value of scattering ratio, aerosol extinction, etc. β_m and σ_m are calculated from a measured or model molecular density profile and σ_g is usually obtained from a model. This still leaves one equation with two unknowns, β_a and σ_a. Three of the retrieval algorithms chosen reduce (1) to an equation in one unknown by assuming a functional relationship between β_a and σ_a. The fourth algorithm begins with a model aerosol extinction profile which can be updated from the lidar backscatter return (and at that point also assumes a relationship between β_a and σ_a). The four retrieval algorithms were all tested with the same simulated LITE signal profile, perturbed by a profile of normally distributed random errors with standard deviation equal to the expected noise levels. Random errors were inserted into the density model used to calculate molecular backscatter and extinction. Additional errors were included appropriate to the different retrieval techniques.

Russell algorithm

The Russell algorithm (Russell et al., 1979) was evaluated first, since we have extensive experience using this technique (e.g., McCormick et al., 1984). Two-way atmospheric attenuation was estimated from models of aerosol, molecular, and ozone extinction. In our implementation, the aerosol model was updated for two iterations based on the aerosol backscatter calculated from the previous iteration. Random errors were inserted into the retrieval corresponding to expected normalization and transmission errors. The result of the retrieval, plotted as aerosol backscatter mixing ratio, is shown in Figure 2a. The retrieved profile shows excellent agreement with the model except in the upper troposphere, where the narrow vertical resolution and relatively low aerosol content of the atmosphere resulted in a very noisy retrieval.

One of the major advantages of the Russell algorithm is a complete analytic error analysis which helps assess the accuracy of the retrieved aerosol profile. The error bars shown on the retrieved profile in Figure 2a were calculated using this error analysis. Another advantage in using the Russell algorithm for stratospheric measurements is the availability of good models of aerosol extinction from SAGE (Stratospheric Aerosol and Gas Experiment) II satellite observations. SAGE II measurements were also used to normalize (equivalently calibrate) the lidar signal at 32 km to an expected minimum value within an expected uncertainty. The Russell algorithm is most appropriate when the aerosol loading is fairly light (e.g., in the non-volcanic background stratosphere) or when aerosol extinction can be modelled fairly accurately. The Russell algorithm can be used for retrievals of optically thin tropospheric layers by updating the aerosol extinction model using the lidar backscatter return.
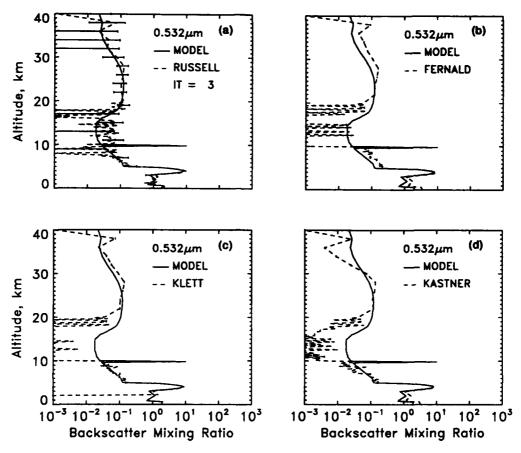
Figure 2. Comparisons between aerosol model and four retrievals using simulated LITE
signal and noise levels. Error bars in 2(a) represent expected 1-sigma uncertainties.

Fernald and Klett algorithms

The Fernald (Fernald, 1984) and Klett (Klett, 1985) algorithms both use analytic
solutions of the lidar equation (1) and iterate through the atmosphere from a near-end
(Fernald) or far-end (Klett) boundary value of backscatter or extinction. In the
implementation of the two algorithms described here, the molecular and aerosol
components of backscatter and extinction were treated separately and the extinction-to-
backscatter ratio was assumed constant within, but allowed to vary between, different
aerosol layers. Aerosol extinction-to-backscatter ratios were overestimated by 50%. For
the Fernald algorithm, the boundary value is easily obtained by assuming no aerosol at
an altitude such as 40 km, where the aerosol is known to be minimal. The result of the
retrieval using the Fernald algorithm is shown in Figure 2b. The results are reasonably
good and show that with moderate aerosol loading, the Fernald algorithm can still provide
good quantitative information about tropospheric aerosol layers. The main disadvantage
of the Fernald algorithm is that the result becomes unstable with iteration through a fairly

541

turbid atmosphere. The result of the retrieval using the Klett algorithm is shown in Figure 2c. The boundary value of aerosol backscatter at 2 km was overestimated by 20%. The Klett algorithm does a good job through turbid tropospheric layers, but iterates in an unstable direction in the case of a spaceborne lidar (even though the results shown here are quite good). The main disadvantage of the Klett algorithm is the difficulty in estimating a boundary value in the highly variable troposphere.

Kastner algorithm

The Kastner algorithm (Kastner et al., 1988) is a true iterative algorithm. A calibration constant is calculated by setting the aerosol terms in equation (1) to zero at an altitude where there is little aerosol. A first guess profile of aerosol backscatter is then chosen and iterated on until the expected and received signal levels are in close agreement. A starting profile equal to 10% of the model aerosol was used here. Aerosol extinction-to-backscatter ratios were overestimated by 50%. The result of the retrieval, after 20 iterations, is shown in Figure 2d. This algorithm also does an acceptable job of retrieving the model aerosol mixing ratio profile. The Kastner algorithm is particularly suitable for a spaceborne lidar since each iteration calculates transmittance downward through the atmosphere. However, retrieval of very turbid tropospheric layers would be difficult unless the aerosol type was well known. Unlike the Klett and Fernald algorithms, the Kastner algorithm does not depend on a particular analytic model of the lidar equation. Thus, multiple scattering effects could be easily incorporated.

Conclusions

All four of the retrieval algorithms studied will be useful for the analysis of LITE lidar data. An important part of the analysis will be the inclusion of auxiliary information obtained from models, previous measurements, SAGE II data, correlative observations, etc. The Russell, Fernald, and Kastner algorithms will be most useful in the stratosphere and upper troposphere. The Klett algorithm is probably the only algorithm capable of retrieving aerosol content below a dense cloud layer. Unfortunately, it will be very difficult to provide a good tropospheric boundary value. The error sources for each algorithm are identifiable and will help in the selection of the most appropriate algorithm.

References

Fernald, F. G.: Analysis of atmospheric lidar observations: some comments. Appl. Opt., 23, 652-653, 1984.

Kastner, M., M. Wiegner, and H. Quenzel: An iterative inversion algorithm to retrieve vertical profile of the atmospheric extinction from backscatter lidar measurements from space. 14th ILRC Abstracts, Italy, 1988.

Klett, J. D.: Lidar inversion with variable backscatter/extinction ratios. Appl. Opt., 24, 1638-1643, 1985.

McCormick, M. P., T. J. Swissler, W. H. Fuller, W. H. Hunt, and M. T. Osborn: Airborne and ground-based lidar measurements of the El Chichon stratospheric aerosol from 90°N to 56°S. Geof. Int., 23-2, 187-221, 1984.

Russell, P. B., T. J. Swissler, and M. P. McCormick: Methodology for error analysis and simulation of lidar aerosol measurements. Appl. Opt., 24, 3783-3797, 1979.

Temperature Profile Retrievals from the SAGE III Occultation   **P69**
Measurements of Atmospheric Oxygen A-Band Spectra

W. P. Chu

NASA Langley Research Center, Mail Stop 475

Hampton, VA 23665-5225

This paper summarizes the results from a detailed sensitivity study utilizing the absorption measurements of oxygen at the visible wavelength region for remote sensing of temperature and pressure profiles. Remote sensing of atmospheric temperature and pressure profiles using the atmospheric limb viewing geometry is generally performed using the absorption or emission properties of some well mixed-gases such as the infrared bands of CO_2 (Gille and House, 1971). In this paper, the utilization of the strong absorptive oxygen A-band spectra located in the visible wavelength region centered at 760 nm is being considered for temperature and pressure sensing application. A preliminary study on this problem was reported by Chu et al. (1990). This paper will expand on the previous study and provide a detailed sensitivity analysis on the temperature retrieval scheme showing the retrieval accuracies, vertical resolution, and improvement in the retrieval accuracy by averaging several retrieval results from measurements at different spectral regions within the oxygen A-band spectra.

There are certain unique features of the oxygen A-band which are well-suited for remote temperature sensing. The line strengths at the center of the absorption band are quite strong; therefore, high signal-to-noise measurements can be obtained at the band center. The number of strong lines in the band is limited to under 200. Therefore, an accurate analytical computation of the measurement parameters can be performed quite efficiently. In addition to the above features, the temperature dependent parameters for the line strengths vary from positive to negative over the A-band spectra. For example, at wavelength far away from the band center, the line strength increases with increasing temperature, while at wavelength close to the band center, the line strength decreases with increasing temperature. This unique sensitivity of the line strength to temperature effect can be utilized for highly accurate temperature profile sensing.

The remote sensing of temperature and pressure profiles utilizing the measurements of the oxygen A-band spectra will be implemented on the Stratospheric Aerosol and Gas Experiment III (SAGE III) instrument. The SAGE III instrument will be an updated version of the SAGE series of flight instruments which have successfully operated on various spacecraft platforms for remote sensing of the atmosphere utilizing the solar occultation technique. The SAGE III instrument follows a long heritage of successful flight missions such as the SAM II, SAGE I, and SAGE II missions in producing global data sets of stratospheric aerosol, ozone, nitrogen dioxide, and water vapor (McCormick et al., 1979; Mauldin et al., 1985). The measurement capability of the SAGE III instrument has been greatly enhanced with the use of a charge-coupled device (CCD) as the photometric detector system. Oxygen A-band spectra will be measured from 740 nm to 780 nm with 2-nm spectral resolution. The extensive spectral measurements outside the oxygen absorption band are

used for the removal of contributions from aerosol and ozone. The radiometric signals at the different spectral channels will be quantized to 14-bit resolution at a rate of 64 samples per second. This will provide extremely accurate measurements of the attenuated solar radiance.

The retrieval scheme employed in this sensitivity study is modeled after the preliminary work (Chu et al., 1990) with some modifications. It is primarily an onion-peeling method with the inversion performed from the topmost height level and proceeding downward, and the solutions are constrained with the ideal gas law and the hydostatic relationship. A pressure value for a reference height level together with an initial temperature profile are used to start the iteration cycles for updating the solutions. The updating is accomplished by adding incremental correction to the current estimated temperature value. The incremental correction value is determined from the residue between the measured absorption versus the computed absorption, scaled by the matrix elements computed from the partial derivative of tangent slant path absorption versus temperature. At each height level, the temperature is updated with the computed matrix element, and the pressure value is accordingly adjusted with the hydrostatic relationship. The updating cycles at each height level are terminated when the calculated and the measured absorption values are within the estimated noise level, and the process will repeat at the next lower height level. A completely inverted profile is then generated when the updating procedure has been applied through all the available height levels.

A procedure for the determination of the pressure value at the reference height level has been developed which utilizes the opposite temperature dependency of the oxygen A-band absorption features. By using measurements from the two spectral channels located at the spectral regions which manifest the opposite temperature effects, two temperature profiles can then be inverted with some arbitrary initial reference pressure value. The reference pressure value can then be updated using the differences between the two temperature profiles. This procedure has been found to provide an accurate estimation of the pressure value for the reference height level.

Sensitivity study on the retrieval method has been performed using synthetic measurements representing different atmospheric conditions. In this study, the emissivity growth approximation (EGA) method is used to generate the synthetic measurements appropriate to the occultation measurement geometry (Gordley and Russell, 1980). Slant path absorption spectra with a spectral resolution of 2-nm as a function of tangent height are calculated at 1-km height intervals. The data base for homogeneous path absorption is computed with a line-by-line scheme together with the Air Force Geophysical Laboratory (AFGL) line compilation.

Individual channel retrievals with noise level of 0.003 appropriate for the instrument design parameters have been studied. The results indicated that temperature profiles generally can be retrieved to an accuray of between 1° to 2° Kelvin, depending on the spectral channels. The corresponding pressure profiles can generally be deduced to an accuracy of about 3 %. There are no significant differences in the retrieval accuracy for inverting the synthetic measurements constructed from temperature profiles at different latitudes and seasons. The accuracy of the retrieved temperature profile can be improved by averaging the different channel retrieval results. Over the oxygen A-band, one can

perform retrievals on seven spectral channel measurements with adequate signal-to-noise level. By averaging the seven retrieval results, one generally can improve the temperature retrieval by a factor of about 2.

Diagnostic study of the temperature retrieval scheme has been performed using the formal approach developed by Rodgers (1990). This study is mainly conducted on the retrieval method rather than the error analysis. The weighting functions, the contributing functions, and the averaging kernels associated with the temperature sensing problem have been studied in detail. The vertical resoluton of the retrieval problem can be estimated from the analysis of the averaging kernel. The averaging kernel calculated for a midlatitude standard temperature profile shows sharp peaks at the corresponding tangent heights, indicating that the achievable vertical resolution is about 1 km over the whole altitude range being studied here.

In conclusion, it is demonstrated that based on the analysis of the retrieval method developed in this paper, accurate temperature and pressure profiles with high vertical resolution can be retrieved from the occultation measurements of oxygen A-band absorption spectra.

References

Chu, W. P., J. C. Larsen, and M. P. McCormick, Pressure and temperature retrievals from the SAGE III/Eos measurements, Optical Remote Sensing of the Atmosphere Topical Meeting, Incline Village, Nevada, February 12-15, 1990.

Gille, J. C., and F. B. House, On the inversion of limb radiance measurements I: Temperature and thickness, J. Atmos. Sci., 28, 1427, 1971.

Gordley, L. L. and J. M. Russell, A fast and accurate radiance algorithm for applications to inversion of limb measurements, in Remote Sensing of Atmospheres and Oceans. Edited by A. Deepak, Academic Press, N. Y., 1980, p. 591.

Mauldin, L. E., N. H. Zaun, M. P. McCormick, J. H. Guy, and W. R. Vaughn, Stratospheric aerosol and gas experiment II instrument: A functional description. Opt. Eng., 24, 307, 1985.

McCormick, M. P., P. Hamill, T. J. Pepin, W. P. Chu, T. J. Swissler, and L. R. McMaster. Satellite studies of the stratospheric aerosol, Bull. Amer. Meteor. Soc., 60, 1038. 1979.

Rodgers, C. D., Characterization and error analysis of profiles retrieved from remote sounding measurements, J. Geophys. Res., 95, 5587, 1990.

LIDAR 1 & 2

Laser Ecological Monitoring of the Atmosphere

V.E. Zuev

Institute of Atmospheric Optics SB USSR Acad.Sci.,
I, Akademicheskii Avenue, Tomsk, 634055, USSR
telephone: (83822) 259303
telex: I33I90 LIDAR SU

(INVITED)

Introduction

At present the ecological problem has become a major world problem whose solution requires obtaining of reliable quantitative data on the environmental conditions including, first of all, the atmosphere as human surroundings and carrier of pollution to the surface of the planet. Thus the problem of ecological monitoring of the atmosphere is of particular concern. An ultimate goal of ecological monitoring is obtaining of statistically proved four-dimensional (three coordinates and time) data array concerning both the main atmospheric pollutants and atmospheric weather producing parameters on a global scale. Only in this case one can be fully confident that the phenomena causing inconvenience to mankind such as destruction of ozone layer of the Earth, greenhouse effect, transboundary transport of atmospheric pollutants will become quantitatively reliable. Simultaneously the corresponding prediction of the state of environment pollutants will be possible.

To this end the methods and technical means should be developed, first of all , for remote sensing of the atmosphere using ground-based, ship-board and spaceborne systems. All these systems are being more and more intensively and effectively developed at present, approval of that can be found taking into account the results of the last three International Laser Radar Conferences/I-3/.

All these aspects are being actively developed at the Institute of Atmospheric Optics. However, in the present report we shall discuss only the part of one of the large programs related to subproject Tropospheric Ozone Research of the project EUROTRAC (a EURECA Environmental Project). In the beginning we enumerate the tasks of this program.

The Problems Solved in the Interests of Subproject TOR

I. Investigation of the Processes of Exchange between Tropospheric and Stratospheric Ozone as well as of Spatio-Temporal Correlations between the Atmospheric Ozone and Aerosol Based on the Use of Lidar Measurements of Ozone and Aerosol Profiles in the Troposphere and Lower Stratosphere.

2. Investigation of Content of Ozone and Other Minor Gases in the Atmospheric Boundary Layers by Means of a Laser Gas Analyzer Based on the Use of CO_2 Tunable Lasers.

3. Investigation of Vertical Ozone Distribution in Tomsk region using in situ Measurements.

4. Investigation of Radiative Situation and Gas Analysis (Including Ozone) of the Atmospheric Boundary Layer Using in situ Sensors.

5. Investigation of Vertical Distribution of the Atmospheric Temperature, Humidity and Aerosol in the Low I km Layer and Their Influence on the Content of Ozone and Other Gases.

6. Laser Monitoring of Tropospheric Aerosol and Its Transfer Associated with Ozone Studies.
7. Airborne Monitoring of Ozone, Other Gases and Aerosols.
8. Research of the Influence of the Cloud Field Characteristics on Ozone Content.
9. Remote Acoustic Monitoring of the Fields of Meteorological Elements in the Atmospheric Boundary Layer.
IO. Investigation of UV Absorption Spectra, Radiative and Nonradiative Constants of O_3, NO_2, SO_2, H_2O and Other Gases for Remote Gas Monitoring.
II. Study of High Resolution IR Spectra of Ozone and a Suite of Trace Gas Constituents of the Troposphere.

Simultaneous Laser Sounding of Vertical Profiles of Ozone and Aerosol

Regular sounding of vertical stratification of aerosol has been conducted at the Institute of Atmospheric Optics starting from I986 on the basis of a stationary lidar with a receiving mirror of I m in diameter at a wavelength of 532 nm (mean radiation power is I W, duration and pulse repetition rate are 200 ns and 3 kHz, respectively). Beginning in December I988 sounding of ozone has been conducted, due to that we developed an UV channel consisted of an excimer laser based on XeCl mixture/4/with rather modest parameters: pulse energy is IO mJ and PRR is I-2 Hz, bandwidth of interference filter is 3.6 nm at λ_T = 308 nm with transmission of 24%. There is also package of programs for data processing and documentation. The wavelength λ_2 = 532 nm was used as a reference one. It took two hours to obtain one profile of ozone. In Fig.I some of the results obtained during first quarter of I989 are presented.
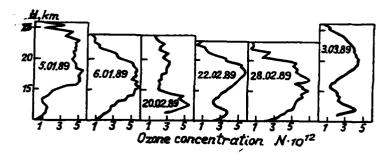
Fig.I. Profiles of the vertical distribution of the ozone concentration (cm-3) for different nights

In the last quarter of I990 the laser sources for ozone and aerosol sounding were changed for the following new ones: an excimer laser XeCl with CH_4 Raman shifted attachment providing radiation with a wavelength of 308 nm, energy per pulse I50 mJ and pulse repetition rate of IOO Hz. In this case 40% of energy is transformed with the attachment into the radiation with a wavelength λ_T= 338 nm which serves simultaneously as a reference one and carries the data on aerosol.

Besides, at aerosol sounding the wavelengths of 532 nm and 780 nm are also used (a titanium-sapphire laser) with energy and pulse repetition rate 50 mJ; 20 Hz and 30 mJ; 20 Hz, respectively.

The above substitution of lasers has changed the lidar potential both quantitatively and qualitatively at sounding of ozone and aerosols since as a result of simultaneous sounding more reliable data on vertical profiles of ozone and on vertical distribution of concentration and aerosol particle size spectra will be obtained.

Figure 2 illustrates the possibilities of sounding of ozone profiles using a modernized lidar.
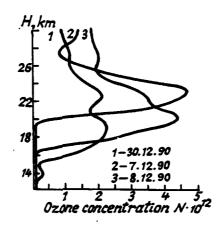
Fig. 2

The Use of Longpath DIAL for Determination of Concentration of Ozone and Other Minor Constituents in the Ground Layer of the Atmosphere

Basically this subprogram is aimed at obtaining the statistically proved data on concentration of ozone molecules and other minor gases in the atmospheric boundary layer including their simultaneous determination by means of CO_2 laser gas analyzers.

The research technique is the long path DIAL of two modifications: I. Stationary path with a retroreflector (total length is I.2 km); 2. Mobile system. Both modifications are supplied with CO_2-frequency tunable lasers including single crystals of $ZnGeP_2$ and $AgGaSe_2$. The technology of growing these crystals was developed at the Institute of Atmospheric Optics. The above crystals provide for multiplication and mixing of the frequencies of CO_2 lasers thus making it possible the generation of synthesized radiation lines with the centers coinciding with center of absorption lines of gases being analyzed. Moreover, in both systems the use of supplementary possibilities of laser gas analysis in the visible and UV spectral range is supposed that should increase the concentration sensitivity of measurements, first of all, of ozone and nitrogen pero-

xide as well as the number of gases being sounded including, e.g., SO_2.

Many years experience in gas analysis with the use of CO_2 lasers has shown the possibility of determining the concentration of a large number of gases in the atmospheric boundary layer (on the planetary scale).

Corresponding measurements are planned to be made in a routine mode with the use of stationary path and mobile facility in various regions of the Western Siberia..

The ultimate goal of the proposed research is obtaining of the array of data of routine monitoring sufficient for corresponding correlation analysis and determination of regularities of complex interaction of concentration fields of ozone molecules and other minor gases defined by the Program EUROTRAC.

During 1991 the measurements of diurnal variations of concentration of O_3, NH_3, C_2H_4, H_2O, CO, CH_4, CH_3OH, C_6H_6, C_4H_8, C_2Cl_4, C_2HCl_3, CCl_2F, $C_2Cl_3F_3$ should be carried out.

References

1. Abstracts, 13-th ILRC, Toronto, Ontario, Canada, 11-15 Aug. 1986, NACA Conference Publication 2431.

2. Abstracts, 14-th ILRC, San-Candido, Italy, 20-24 June, 1988.

3. Abstracts, Parts 1 and 2, 15-th ILRC, Tomsk, USSR, 23-27 July, 1990.

4. A.V.El'nikov, V.V.Zuev, V.N.Marichev and S.I.Tsarego-rodtsev. First Results of Lidar Observations of Stratospheric Ozone above Western Siberia. Atmospheric Optics, v.2, No.9, pp.841-842 (1989).

Calculation and Measurements
of Multiple Scattering Effects
on Lidar and Imaging Applications

Luc R. Bissonnette
Centre de Recherches pour la Défense, Valcartier
P.O. Box 8800, Courcelette, Québec
Canada, G0A 1R0

(INVITED)

1 Proposed Model

The model is based on the time-independent radiative transfer equation for the specific intensity $I(\mathbf{r}, \hat{\mathbf{s}})$ where $\mathbf{r}$ is the position vector and $\hat{\mathbf{s}}$ is the direction unit vector. The total $I(\mathbf{r}, \hat{\mathbf{s}})$ is written as the sum of the reduced and diffuse intensity components, $I_{ri}(\mathbf{r}, \hat{\mathbf{s}})$ and $I_d(\mathbf{r}, \hat{\mathbf{s}})$ respectively. The problem of interest here is that of a collimated beam illuminating a scattering aerosol medium. In this case, $I_{ri}(\mathbf{r}, \hat{\mathbf{s}})$ is given by

$$I_{ri}(\mathbf{r}, \hat{\mathbf{s}}) = I_0(z, \rho)\, e^{-\tau}\, \delta(\omega - \omega_o), \qquad (1)$$

where $I_0(z, \rho)$ is the vacuum irradiance of the incident beam, (z, ρ) are the coordinates parallel and normal to the beam axis, ω and ω_o are the solid angle vectors along $\hat{\mathbf{s}}$ and $\hat{\mathbf{s}}_0$, δ is the delta function such that $\int_{4\pi} d\omega\, \delta(\omega - \omega_o) = 1$, and τ is the optical depth.

No general solution of the radiative transfer equation has yet been obtained. Here, we propose an approximation valid for narrow incident beams. First, the transfer equation is integrated over the solid angle and the individual terms are divided into forward and backward components about the direction $\hat{\mathbf{s}}_0$ of the incident beam. The resulting equation is then separated into a forward and a backward equation. This is a valid transformation that conveniently applies to many practical situations. Because of the narrow beam geometry, the equations are further simplified by making the paraxial approximation. More specifically, the forward and backward flux densities F^+ and F^- are approximated as follows:

$$F^{\pm}(\mathbf{r}) \equiv \int_{(2\pi)\pm} I_d(\mathbf{r}, \hat{\mathbf{s}})\, \hat{\mathbf{s}} \cdot (\pm\hat{\mathbf{s}}_0)\, d\omega \;\simeq\; \pm \int_{(2\pi)\pm} I_d(\mathbf{r}, \hat{\mathbf{s}}) \cos\begin{pmatrix} 0 \\ \pi \end{pmatrix} d\omega. \qquad (2)$$

The approximation of Eq. 2 is justified because $I_d(\mathbf{r}, \hat{\mathbf{s}})$ is peaked in the directions $\hat{\mathbf{s}}_0$ and $-\hat{\mathbf{s}}_0$. This is a consequence of the narrow beam hypothesis. Indeed, because the incident beam is narrow, the highest radiation intensity even at large optical depths is still found in the unscattered or reduced intensity beam I_{ri} which thus constitutes the main source of scattered photons per unit volume. Hence, for observation points $\mathbf{r}$ close to the axis, the diffuse intensity I_d is greatest at angles $\arccos(\hat{\mathbf{s}} \cdot \hat{\mathbf{s}}_0)$ near 0 and π since it is at those angles that the length of the I_{ri} beam seen per unit solid angle is longest.

The resulting equations for $F^{\pm}$ contain additional unknowns: terms that represent the flux in the direction normal to $\hat{\mathbf{s}}_0$. Based on an analogy with turbulent transport, we model these terms

The output functions that can be calculated are the axisymmetric forward and backward diffuse intensities integrated over the field of view Θ, i. e.

$$U^+(z,\rho,\Theta) = 2\pi \int_0^\Theta I_d(\mathbf{r},\theta)\sin\theta\, d\theta; \quad U^-(Z,z,\rho,\Theta) = 2\pi \int_0^\Theta I_d(\mathbf{r},\pi-\theta)\sin(\pi-\theta)\, d\theta. \quad (12)$$

By differentiating the backscattered intensity U^- with respect to Z, one can also derive the lidar backscatter. The required inputs are the power, diameter and divergence of the incident beam, the cloud depth, the medium molecular extinction coefficient, the aerosol extinction and scattering coefficients, and the phase function. The medium properties are allowed to vary along the beam axis but are assumed constant transversely.

2 Sample Results

Validation data were measured in a laboratory simulation experiment described in Ref. 2. Water droplet clouds of adjustable concentrations were produced in a closed chamber 3.2 m long, 1 m wide and 0.75 m high. Forward- and backscatter measurements were made at two wavelengths (1.06 and 10.6 μm) for visible extinction coefficients ranging from 0.25 to 7 m^{-1}.

Figure 1a shows transmitted beam profiles obtained at different optical depths τ for a constant receiver field of view of 140 mrad. We see that the central portion of the beam keeps its Gaussian shape and is virtually unaffected by multiple scattering. The off-axis aureole is due to multiple scattering and increases with optical depth relative to the Beer's law decay rate of $\exp(-\tau)$. The agreement between measurements and calculations is quite good despite the asymmetry in the data caused by a slight tilt of the receiver axis with respect to the incident beam axis.

Figure 1b shows the effect of the receiver field of view for profile measurements performed at approximately the same optical depth. The central core is nearly independent of the field of view since it is made up in large part of the unscattered beam. The off-axis aureole grows rapidly with increasing field of view but eventually levels off as indicated by the smaller difference between 140 and 350 mrad than between 20 and 140 mrad. Again, the calculated profiles fit the measured data very well.

Comparisons were also made with integrated and range-resolved backscatter measurements. Figures 7-14 of Ref. 2 show very good agreement for a variety of cloud geometries and instrument parameters.

The model was also applied to the calculation of the point spread function, i. e. the image of a point source, for imaging through aerosol media. The point spread function and its corresponding Fourier space modulation transfer function are direct measures of the expected image degradation under such conditions. Figure 2 compares the calculated functions with point source images recorded through an atmospheric advection fog at 531 and 921 m. The input parameters to the model were obtained from simultaneous transmission and particle size distribution measurements. The spreading effect due to this large-particle fog is important and very well predicted by the model. It corresponds to a substantial blurring of the small object features. Other results for haze, fog and rain conditions are discussed in Ref. 3.

3 Conclusion

The multiple scattering propagation model of this paper is an approximate solution of the radiative transfer equation valid for narrow incident beam and observation points close to the beam axis. It is not restricted to small-angle scattering. However, the scattering coefficient α_s must be small enough for the scattering geometry to satisfy the paraxial approximation of Eq. 2.

by a diffusion process. This allows relating the unknown normal fluxes to $F^\pm$. More precisely, we write

$$\hat{t} \int_{(2\pi)\pm} I_d(\mathbf{r}, \hat{s}) \hat{s} \cdot \hat{t} \, d\omega = -D^\pm \nabla_\perp F^\pm, \tag{3}$$

where $\hat{t}$ is the unit radial vector in the plane transverse to $\hat{s}_0$, and $D^\pm$ are diffusion coefficients given by

$$D^+ = C^+ \left\{ (z - z') < \sin\theta^+(z') > + \int_{z'}^{z} dz \int_{\eta'}^{\eta} d\eta < \sin\theta^+ > e^{\eta - \eta'} \right\}, \tag{4}$$

$$D^- = C^- (z' - z) < \sin\theta^-(z') > + C^+ \int_{z}^{z'} dz \int_{\eta}^{\eta'} d\eta < \sin\theta^+ > e^{\eta' - \eta}. \tag{5}$$

$D^\pm(z, z')$ are the lateral diffusion coefficients at position z for radiation originally scattered at z'. In Eqs. 4 and 5, $< \sin\theta^+ >$ and $< \sin\theta^- >$ are the average sines of the scattering angle in the forward and backward directions defined by

$$< \sin\theta^+ > = \frac{\int_0^{\pi/2} p(\hat{s}, \hat{s}_0) \sin\theta \, d\theta}{\int_0^{\pi/2} p(\hat{s}, \hat{s}_0) \, d\theta}; \quad < \sin\theta^- > = \frac{\int_{\pi/2}^{\pi} p(\hat{s}, \hat{s}_0) \sin\theta \, d\theta}{\int_{\pi/2}^{\pi} p(\hat{s}, \hat{s}_0) \, d\theta}, \tag{6}$$

$p(\hat{s}, \hat{s}_0)$ is the scattering phase function, η is the forward scattering optical depth,

$$\eta = \int \alpha_s^+ \, dz, \tag{7}$$

with

$$\alpha_s^\pm = \frac{\alpha_s}{4\pi} \int_{(2\pi)\pm} p(\hat{s}, \hat{s}_0) d\omega, \tag{8}$$

the forward and backward components of the scattering coefficient $\alpha_s = \alpha_s^+ + \alpha_s^-$, and $C^\pm$ are constants given by

$$C^+ = 0.080; \quad C^- = \int_{\pi/2}^{\pi} \frac{p(\hat{s}, \hat{s}_0)}{p(-\hat{s}_0, \hat{s}_0)} d\theta. \tag{9}$$

The diffusion model described by Eqs. 3-5 is the main hypothesis undelying the model. It determines how the forward and backward propagating beams spread out due to multiple scattering.

The resulting model equations for the forward and backward fluxes are

$$\frac{\partial F^+}{\partial z} - \nabla_\perp \cdot D^+ \nabla_\perp F^+ + (\alpha_m + \alpha_a + \alpha_s^-)F^+ = \alpha_s^+ I_0(z, \rho) e^{-\tau} + \alpha_s^- F^-, \tag{10}$$

$$-\frac{\partial F^-}{\partial z} - \nabla_\perp \cdot D^- \nabla_\perp F^- + (\alpha_m + \alpha_a + \alpha_s^-)F^- = \alpha_s^- I_0(z, \rho) e^{-\tau} + \alpha_s^- F^+, \tag{11}$$

where α_m is the medium molecular extinction coefficient and α_a is the aerosol absorption coefficient.

Equations 10 and 11 are coupled parabolic partial differential equations. For most applications, we can neglect the backscatter-to-backscatter coupling, i. e. the last term in Eq. 10, and Eqs. 10 and 11 can be solved sequentially. The boundary conditions are $F^+(0, \rho) = F^-(Z, \rho) = F^\pm(z, \infty) = 0$ where Z is the depth of the aerosol cloud. Assuming a Gaussian profile for $I_0(z, \rho)$ and using the method of the Green's function, we can write the solutions in a general analytic integral form. There is not enough space here to list the several expressions and definitions involved. They are given in Ref. 1. The dependence of the flux densities on the receiver field of view is reintroduced *a posteriori* by multiplying the differential contributions to the integral solutions by factors derived from a stochastic representation of the photon paths. The method is described in detail in Ref. 1.

This requires that α_s^{-1} be much greater than the radius of the incident beam, which is the case for most atmospheric applications. The model allows for inhomogeneities along the beam axis and gives solutions for the forward- and backscattered intensities. The calculations require only modest computer memory and time.

The comparisons discussed here and elsewhere (e. g. Refs. 2-3) show good agreement with the measurements obtained over a wide range of experimental conditions. Therefore, the proposed model constitutes a convenient approximation to the radiative transfer equation appicable to many practical transmission and lidar experiments in atmospheric aerosols.

References

[1] L.R. Bissonnette, "Multiscattering Model for Propagation of Narrow Light Beams in Aerosol Media," Appl. Opt. **27**, pp. 2478-2484, 1988.

[2] L.R. Bissonnette, R.B. Smith, A. Ulitsky, J.D. Houston, and A.I. Carswell, "Transmitted Beam Profiles, Integrated Backscatter, and Range-Resolved Backscatter in Inhomogeneous Laboratory Water Droplet Clouds," Appl. Opt. **27**, pp. 2485-2494, 1988.

[3] L.R. Bissonnette, "Blurring Effect of Aerosols on Imaging Systems," SPIE Proc. Vol. 1487 on Propagation Engineering, 1-5 April 1991 (in press).
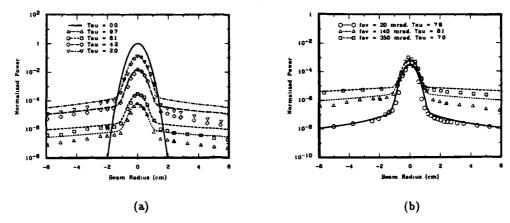
Figure 1: Profiles of a 1.06 μm laser beam after propagation through a 3.2 m long water droplet cloud. The symbols represent the measurements and the curves, the solutions. (a): at a field of view (fov) of 140 mrad but for various optical depths (Tau); (b): at an optical depth near 8.0 but for three different fovs.
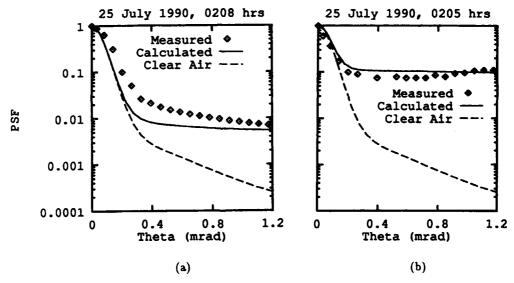
Figure 2: Examples of advection fog point spread functions for a range and extinction coefficient of (a) 531 m and 8.42 km⁻¹, and (b) 921 m and 9.34 km⁻¹. The clear air curve is a fit to experimental data.

Structure In the Atmospheric Pressure Field Observed With An Airborne Lidar

C. L. Korb, G. K. Schwemmer, D. O'C. Starr, C. R. Prasad, H. Walden

NASA/Goddard Space Flight Center, 917
Laboratory for Atmospheres
Greenbelt, Maryland 20771 USA
301-286-6233

H. S. Lee
S. M. Systems and Research Corporation, Landover, Maryland 20785
and
C. Y. Weng
Science Systems and Applications, Inc., Seabrook, Maryland 20706

Structure in the atmospheric pressure field has been observed with an airborne lidar. This paper describes the remote observation of thunderstorm outflow and gravity waves in the lower atmosphere. These observations are the first direct measurement of these phenomena from high accuracy remote measurements of the two-dimensional pressure field. Pressure is a fundamental atmospheric state variable required for virtually all atmospheric applications. The vertical and horizontal structure of the static pressure field characterizes the spatial distribution of mass in the atmosphere. Horizontal gradients of pressure represent the primary physical force leading to atmospheric circulations in the horizontal dimension which include the large-scale general circulation as well as mesoscale phenomena such as sea/land breezes.

The measurements of the atmospheric pressure field[1,2] are made with a differential absorption lidar system[3] utilizing tunable alexandrite lasers to measure absorption in the oxygen A-band near 760 nm. The measurements are made in an absorption trough, a broad region of nearly uniform absorption between two strong oxygen lines. Since the measurement is in the far wing of collision-broadened absorption lines, the result is highly pressure sensitive. The use of a trough region, as opposed to the wing of a single line, greatly reduces the sensitivity of the pressure measurement to the effects of laser frequency instability. An integrated path absorption technique is utilized to determine pressure as a function of altitude. This approach has ~100 times higher sensitivity than a differential ranging method. Oxygen is used as the probe molecule since it is uniformly mixed in the atmosphere and the oxygen A band has strong lines separated by 1-2 cm^{-1} with suitable ground state energy and trough absorption for atmospheric pressure measurement.

Our lidar system utilizes two alexandrite lasers which are continuously tunable from 725 to 790 nm and have a bandwidth of 0.02 cm^{-1} using a birefringent filter and two etalons or a bandwidth of 0.08 cm^{-1} with only one etalon. We have measured the short-term frequency stability of the lasers as <0.005 cm^{-1} and the Q-switched pulse length to be 100-130 nsec. Each laser operates at repetition rates up to 10 Hz with an output energy of 100 or 150 mJ and has a multi-mode spatial intensity distribution.

The output of each in the high resolution mode consists of three axial modes. We have measured the spectral purity of the alexandrite lasers as >99.99%. For airborne measurements, a 40 cm telescope collects the laser energy backscattered from the atmosphere and a multialkali photomultiplier tube serves as the detector. The signals from the photomultiplier are digitized with a 12-bit transient digitizer at a 5 MHz sampling rate. A microprocessor controls the system, displays real time status and absorption data, and records raw data on a 9-track tape recorder.

We made airborne measurements of the atmospheric pressure field in November 1985 and in June 1989 using the Goddard lidar facility on the NASA/Wallops Lockheed Electra aircraft. The average deviation of the earlier aircraft lidar pressure profile data from the radiosonde data is 1.7 mb while the average deviation for the 1989 data was 1.0 mb for a 100 shot average. The two-dimensional pressure field observed by our lidar system between 140 and 90 km off the coast of southern New Jersey on November 20 1985 is shown in Fig. 1. The data consists of 23 contiguous pressure profile measurements. The horizontal resolution of the data is 2 km and the vertical sampling interval is 30 m. The pressure data are shown as a grey scale display for each altitude and location. Gravity wave structure is apparent in the pressure data. A gravity wave is a vertical transverse wave where the air particles move in the vertical as the wave propagates horizontally.

The wave structure was examined in more detail by calculating the corresponding perturbation pressure field. When the mean pressure is removed at each altitude, a coherent wave structure is apparent at a wavelength of approximately 60 km. In addition, a wavelength of approximately 20 km is evident when we remove the linear trend (average horizontal gradient) in the pressure at each altitude as well as the mean pressure to filter out the longer wave features.

Fig. 2 shows the pressure of constant altitude surfaces for a part of the June 1989 flight at 1 km horizontal and 30 m vertical resolution. A large pressure feature is particularly noticeable at the lowest altitude which decreases rapidly at higher altitudes. We believe this feature was due to a thunderstorm outflow, a gust front, associated with a line of thunderstorms about 50 km to the north.

This capability represents a new and exciting tool for remotely probing the atmosphere. It could be used for quantitative analysis of various atmospheric phenomena such as the fine-scale structure in the pressure field or gravity wave structure and propagation. The technique may be extended to high altitude research aircraft platforms and to low earth orbit or polar orbiting satellites for large area or global coverage.

References
1. C. L. Korb and C. Y. Weng, "Differential Absorption Lidar Technique for Measurement of the Atmospheric Pressure Profile," *Appl. Opt.*, **22**, 3759-3770 (1983).
2. C. L. Korb, G. K. Schwemmer, M. Dombrowski, and C. Y. Weng, "Airborne and Ground-based Lidar Measurements of the Atmospheric Pressure Profile," *Appl. Opt.*, **28**, 3015-3020 (1989)
3. G. K. Schwemmer, M. Dombrowski, C. L. Korb, J. Milrod, H. Walden, and R. H. Kagann, "A Lidar System for Measuring Atmospheric Pressure and Temperature Profiles," *Rev. Sci. Instrum.*, **58**, 2226-2237 (1987).
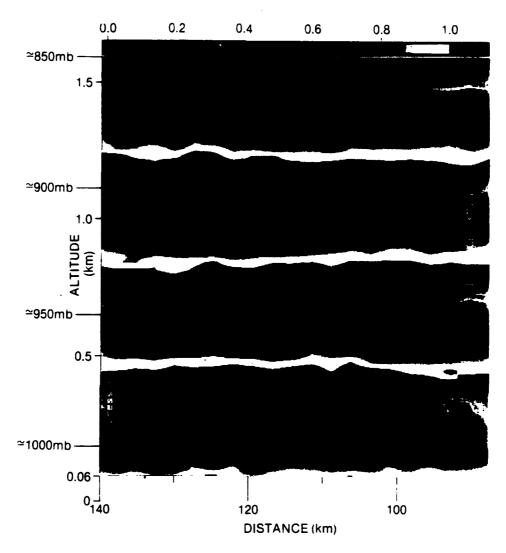
Fig. 1 Two dimensional measurement of the atmospheric pressure field between 140 and 90 km off the coast of Sea Isle, Delaware. The pressure at a given altitude and location is represented by a grey scale. Variations in altitude of constant pressure surfaces can be seen by following a given grey scale horizontally across the figure. The grey scale is repeated four times to enhance the detail in the vertical profile of pressure. The vertical resolution of the data is 30 m and the horizontal resolution is 2 km.
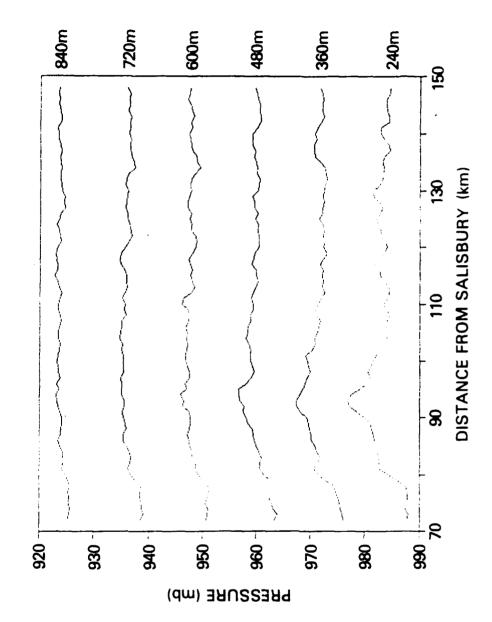
Fig. 2 · Pressure of constant altitude surfaces of the two dimensional pressure field measured by an airborne lidar off the Atlantic Coast showing a thunderstorm outflow.

Measurement of Wind Velocity Spread:
Signal-to-Noise Ratio for Heterodyne Detection
of Laser Backscatter from Aerosol

David L. Fried

the Optical Sciences Company
Placentia, California 92670, USA

In relation to an effort to determine the local variability (in effect the intermittence) of the turbulence induced spread in wind velocity in a small and inaccessible region — in particular a region one on more kilometers above the ground — we have carried out an analysis of the expected performance of a CW, heterodyne detection, 10 μm wavelength laser radar used to make such measurements. At this wavelength essentially all of the backscatter signal power is due to scattering from aerosol particles. Since these particles move with the wind velocity the doppler shift they impart to the backscattered laser radiation will be indicative of the wind velocity. Only the component of wind velocity parallel (or antiparallel) to the laser radar's line-of-sight would be sensed, showing up in the doppler shift in the heterodyne beat frequency signal. The CW operation of the laser radar allows a very high doppler frequency (or wind velocity) resolution, but also has the consequence that timing can not be used to provide range resolution. The range/range-resolution of the system is nominally provided by the focusing of the transmitter:receiver optics at some range of interest with the range-resolution being provided by the depth-of-focus of the optics.

In operation a one or two second sample of heterodyne signal data would be recorded and processed to provide an estimate of the power spectral density (PSD) to be associated with that signal sample.[*] We would interpret the width of this estimated PSD as indicating the spread of wind velocities within a region of the atmosphere whose location and size is defined by the focal distance and by the diffraction limited spot width and depth-of-focus respectively — all determined by the optics settings.

In evaluating this system's performance we have developed analytic and numerical results addressing the following questions;

- For a thin layer of aerosol at a range corresponding to exactly the range at which the optics are focused, what is the value of the signal-to-noise ratio to be associated with the heterodyne signal?

- How does the heterodyne signal power vary with the range to a thin layer of aerosol?

- For a space filling distribution of aerosol how does the total signal power compare with that from a unit thickness (in effect a thin) layer at the range at which the optics are focused? This is a ratio defining the "effective" thickness for a space filling aerosol distribution.

- For the above two questions we also wanted to know how the answers are affected by the laser transmitter's diameter being significantly smaller than the receiver's diameter.

- Finally, considering both the shot-noise in the heterodyne signal (as represented by the signal-to-noise ratio) and the random nature of the aerosol backscatter signal *per se*, we have evaluated the fractional accuracy of the PSD estimates for each frequency

---

[*] An estimate of the white noise PSD of the local oscillator shot-noise would be separately evaluated and would be subtracted from the PSD calculated from the signal sample. It is the difference that is considered to be the PSD of the backscatter signal.

resolution cell of the result — as a function of the measurement time (i.e. the length of the heterdyne signal sample that is processed) and the bandwidth associated with the frequency resolution of the PSD result.

With regard to the first question we find that the heterodyne signal-to-noise power ratio, $(SNR_P)_{Het}$, is most conveniently expressed in terms of the incoherent detection signal-to-noise power ratio, $(SNR_P)_{Inco}$, to be associated with the same laser transmitter, aerosol layer, collection optics, and detector quantum efficiency. We find that

$$(SNR_P)_{Het} = 0.91924(SNR_P)_{Inco}.$$

The fact that the coefficient is so much less than the factor of two normally considered to relate heterodyne and incoherent detection, derives from the extended distribution of the laser illumination on the aerosol layer and the reduced heterodyne detection efficiency in the "wings" of this region — a deficiency incoherent detection does not suffer from (and a deficiency which would not be manifested if we were working with a single point target rather than an *extended layer* of aerosol particles as the target).

The results shown in Fig. 1 address the second question and the relevant part of the fourth question. Taking $\dot{N}_{BF}$ as a measure, in units of photo-detection-events per second, of the amplitude of the heterodyne beat-frequency signal we get

$$(\dot{N}_{BF})^2 = 16\eta^2[(h\nu)\lambda]^{-2}\mathcal{N}\sigma\Delta z \; P_{LO}P_T(\tfrac{1}{4}\pi D_R^2)^3 g(D_R^2/\lambda, z, R_R, R_T, D_T/D_R),$$

where η denotes quantum efficiency, $h\nu$ the energy per laser photon, λ the laser wavelength, $\mathcal{N}$ the aerosol particle density, σ the backscatter cross-section (in units of area times inverse solid angle) of an individual aerosol particle, Δz the thickness of the aerosol layer, P_{LO} the local oscillator power, P_T the transmitted laser power, D_R the receiver diameter, z the range to the aerosol layer, R_R the range at which the receiver optics is focused, R_T the range at which the transmitter optics is focused, and D_T the transmitter diameter. The function g is defined by the equations

$$g(a,b,c,d,e) = b^{-4}e^{-2}\int_0^\infty x dx \left|f(ae^2(d^{-1} - b^{-1}), ae^2 b^{-1}; e^{-1}x)\right|^2 \left|f(a(c^{-1} - b^{-1}), ab^{-1}; x)\right|^2$$

$$f(\alpha, \beta; u) = 2\int_0^1 x dx J_0(\pi\beta ux)\exp\left(\frac{\pi i}{4}\alpha x^2\right).$$

The function g is shown in Fig. 1 for the case of $\lambda = 10.0\ \mu$m, $D_R = 1.0$ m, $R_T = R_R = 1.0$ km, with $D_T/D_R = 10^0$, $10^{-1/3}$, $10^{-2/3}$, 10^{-1}. The narrower and higher curves correspond to the larger values of D_T/D_R. We may consider g to be a measure of the way the heterodyne signal power varies with the range to the aerosol layer.

The third question as well as the relevant part of the fourth question is addressed by integrating g over all possible aerosol layer ranges and dividing that by the value of g (for a unit thickness layer) at the range where the optics are focused — this value of g being calculated for $D_T/D_R = 1.0$. In Fig. 2 we show this result for the same four cases treated in Fig. 1. Depending on the value of D_T/D_R, the effective backscatter depth varies from about 72 m to as little as 8.8 m, the larger values of this effective backscatter depth corresponding to the larger values of D_T/D_R.

The fifth question is treated by assuming that the local oscillator shot noise as well as the (aerosol randomness induced) laser signal fluctuations can be modeled as gaussian random variables. The subject for analysis is formulated by considering that the PSD calculation proceeds by means of the signal processing hardware shown in Fig. 3. The heterodyne beat frequency signal is amplified and directed to each of a number of channels, defined by a narrow band filter, each channel/filter centered at a different frequency, and each having a bandwidth, Δf — which may be considered to correspond to the frequency resolution of the measured PSD results. Each of the filtered signals
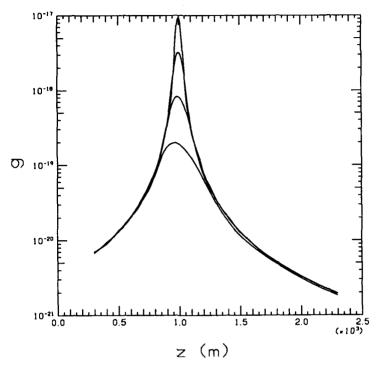
Figure 1. Range Dependence of Heterodyne Signal Power.
Results are shown for $D_T/D_R = 10^0$, $10^{-1/3}$, $10^{-2/3}$, and 10^{-1} — the higher valued curves corresponding to the larger values of D_T/D_R.

is squared and then integrated over a time, T, corresponding to the length of the samples of the heterodyne beat frequency signal — one or two seconds. The output of each of these integrators (i.e. the channel outputs) represent the estimates of the value of the PSD for that channel/filter center-frequency. It is the fractional variability of a channel's output, F, for a fixed wind velocity pattern — i.e. the rms value of the output variation divided by the expected value — that we have evaluated to answer the fifth question. We find that

$$F = (T\Delta f)^{-1/2} \left[1 + (\text{SNR}_P)^{-2}\right]^{1/2}.$$

Here the signal-to-noise ratio should be evaluated considering only the fraction of the aerosol particles in the effective backscatter range which particles are moving with a velocity which results in a doppler shift matched to the channel's pass-band.
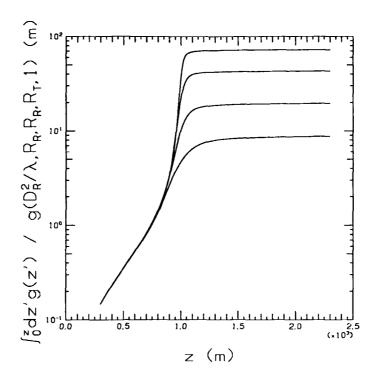
Figure 2. Normalized Total Heterodyne Signal Power for an Aerosol Distribution Extending from the Ground Up to Some Upper Limit. Results are shown for $D_T/D_R = 10^0$, $10^{-1/3}$, $10^{-2/3}$, and 10^{-1} — the higher curves corresponding to the larger values of D_T/D_R. The normalization factor corresponds to a unit thickness aerosol layer at $z \cong 1.0$ km (the range at which the optics are focused), the normalization factor being calculated for $D_T/D_R = 10^0$ — so the limiting values correspond to an effective thickness for an infinite extent aerosol distribution.
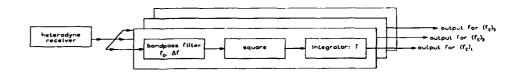
Figure 3. PSD-Estimation Signal Processor

Enhanced Backscattering in Laser Radar Signatures [*]

Zu-Han Gu, Richard S. Dummer and James Jafolla
Surface Optics Corporation, P.O. BOX 261602, San Diego, CA 92126, U.S.A.

Alexei A. Maradudin
University of California, Physics Department, Irvine, CA92717, U.S.A.

One of the most interesting phenomena associated with the scattering of light from a randomly rough surface is that of enhanced backscattering. This is the presence of a well-defined peak in the retroreflection direction in the angular distribution of the intensity of the incoherent component of the light scattered from such a surface. This enhanced backscattering was predicted in perturbation-theoretic calculations of the incoherent scattering of light from a weakly rough metal surface ,[1-3] and was subsequently observed experimentally .[4] For rougher surfaces the effect has also been observed experimentally ,[5-7] and studied theoretically by a variety of approaches .[8-10]

Consideration of enhanced backscattering (i.e. opposition effect) can be critically important in computing laser radar signatures. This is illustrated by the comparison of two signature models of the same missile - one developed using measured bidirectional reflectance data at one degree away from the retro-direction and the other developed from monostatic measurement data in a true retro-direction. The unique instrument used to obtain for field laser reflectance data, the reflectance data itself which are compared with numerical calculation, and the software ensemble used to develop the signature are described and discussed.

REFERENCES

1. V. Celli, A.A. Maradudin, A.M. Marvin, and A.R.McGurn, "Some Aspects of Light Scattering from a Randomly Rough Metal Surface," J. Opt. Soc. Am. A.2, 2225 (1985).

2. A.R. McGurn and A.A. Maradudin, "Localization Effects in the Elastic Scattering of Light from a Randomly Rough Surface," J. Opt. Soc. Am. B.4,910 (1987).

3. A.R. McGurn, A.A. Maradudin and V. Celli, "Localization Effects in the Scattering of Light from a Randomly Rough Grating," Phys. Rev. B31, 4866 (1985).

4. Zu-Han Gu, Richard S. Dummer, A. A. Maradudin and A. R. McGurn , "The Experimental Investigation of the Opposition Effect in the Scattering of Light From a Random Rough Metal Surface," Applied Optics, Vol. 28, No. 3, 537-543, (February 1989).

5. K.A. O'Donnell and E.R. mendez, "Experimental Study of Scattering from Characterized Random Surfaces," J. Opt. Soc. Am. A 4, 1194 (1987).

6. J.C. Dainty, M.J. Kim and A.J. Sant, "Measurements of Angular Scattering by Randomly Rough Metal and Dielectric Surfaces," in "Scattering in Volumes and Surfaces," Edited by M. Nieto-Vesperinas and J.C. Dainty, (1989).

7. David A. Haner and Robert T. Menzies, "Reflectance Characteristics of Reference materials used in lider hard target calibration," Applied Optics, Vol. 28, No. 5, 857-864, (March 1989).

8. P. Tran and V. Celli, "Monte Carlo Calculation of Backscattering for a Randomly Rough Grating," J. Opt. Soc. Am. A-5, 1635 (1988).

9. A.A. Maradudin, E.R. Mendez, and T. Michel, "Backscattering Effects in the Elastic Scattering of P-Polarized Light," Optics Lett. 14, 151 (1989).

10. M. Nieto-Vesperinas and J.M. Soto-Crespo, "Monte Carlo Simulations for Scattering of Electromagnetic Waves from Perfectly Conductive Random Rough Surfaces," Optics Lett. 12, 979-981 (1987).

Enhancement of Backscattered Intensity for a Bistatic LIDAR Operating in Atmospheric Turbulence

J. Fred Holmes
Department of Applied Physics and Electrical Engineering
Oregon Graduate Institute
19600 N.W. von Neumann Drive
Beaverton, OR 97006-1999 USA
(503) 690-1132

SUMMARY

The enhancement of received intensity backscattered through the turbulent atmosphere is not a new topic. Researchers in the U.S.S.R. have been doing experimental and analytic work on this topic for around fifteen years. They have investigated plane, spherical wave, and beam wave sources with point, mirror, retroreflective and diffuse targets for a monostatic lidar. Their analytical approach was to solve the parabolic wave equation subject to the paraxial approximation. This work is reviewed in detail in a book entitled "LIDAR in a Turbulent Atmosphere," by Banakh and Mironov[1] which also contains an extensive list of U.S.S.R. references. Their results are in terms of integrals of confluent hypergeometric functions, and consequently are difficult to evaluate and interpret physically.

Some very recent work was done by Jakeman, et al.,[2,3] and by Welch and Phillips.[4] The former involved analysis and experimental work for enhanced backscattering through a random phase screen and the latter involved computer simulation of enhanced backscatter by a phase screen. In this paper, the extended Huygens-Fresnel formulation is used to develop a formulation for the backscattered intensity as a function of separation between the transmitter axis and a point receiver for a bistatic lidar operating in atmospheric turbulence, with a beam wave source, a diffuse target and including the correlation between the turbulence on the outgoing and return paths. This approach yields a compact solution involving the integral of a non-oscillating simple exponential function that is easily evaluated numerically, is valid for turbulence levels up to the onset of saturation, and is physically easy to interpret.

Using the extended Huygens-Fresnel principle, the intensity at the receiver can be written as

$$I(p) = \frac{T_o^2 U_o^2 \alpha_o^2}{\pi L^2} \int dR' \exp[-R'^2 + 4C_\chi(o, p - R'\alpha_o)] \tag{1}$$

where for uniform turbulence the log amplitude covariance C_χ is given by

$$C_\chi(o, p - R'\alpha_o) = 2.386 \left(\frac{\alpha_o}{\rho_o}\right)^{5/3} \int_0^1 dt$$

$$\int_0^\infty du' u'^{-8/3} \sin^2\left(\frac{u't(1-t)}{2\Omega}\right) J_o\left(u' \, |\bar{p}/\alpha_o - R'| \, (1-t)\right) \tag{2}$$

and where $\rho_o^{-5/3} = 0.546 \, L k^2 C_n^2$, L is the path length, k is the wave number, C_n^2 is the strength of turbulence, α_o is the outgoing Gaussian beam radius, U_o is the outgoing beam amplitude, T_o is the target reflectivity. P is the off-axis location of the receiver

and $\Omega = \alpha_o^2 k/L$. That the turbulence dependent part of the result only depends on C_χ which represents the incoherent fluctuations due to the turbulence is somewhat surprising. It appears that while intensity enhancement requires correlation of the atmospheric perturbations along the forward and return paths, it is an incoherent effect.

A backscattered intensity enhancement function can be defined as

$$BIEF(\bar{p}) = \frac{I(p)}{I(\infty)} \tag{3}$$

Since when p gets large, C_χ approaches zero,

$$I(\infty) = \frac{T_o^2 U_o^2 \alpha_o^2}{L^2} \tag{4}$$

which corresponds to independent turbulence on the outgoing and return paths. Using Eqs.(1) and (4) in (3),

$$BIEF(\bar{p}) = \frac{1}{\pi} \int dR' \exp\left[-R'^2 + 4C_\chi(o, p - R'\alpha_\theta)\right] \tag{5}$$

The above result is compact, relatively easy to evaluate (see reference 5 for evaluation of C_χ) and shows that the backscatter intensity enhancement is due solely to the log-amplitude fluctuations.

By examining Eqs. (1) and (5), the relative effect of the parameters can be found. The exponential part of the integrand in (5) can be written as the following product.

$$\exp(-R'^2)\exp(4C_\chi(o, \bar{p} - R'\alpha_o))$$

The first term starts at unity and as R' increases, it decreases exponentially to zero with a scale size equal to α_o. The log amplitude covariance can be positive or negative, but since it will be integrated over all values of R and θ_R (angle variable associated with dR), the net effect will always be positive. Consequently, the last factor starts out $\geq$ unity and as $R'\alpha_o$ increases, it decreases to unity with a scale size equal to $(L/k)^{1/2}$. It appears then that the maximum effect is for $\alpha_o << (L/k)^{1/2}$ and for $\alpha_o >> (L/k)^{1/2}$ the BIEF approaches unity. This conclusion has been confirmed by evaluating Eq. (5).

There are two other considerations that needs to be discussed. In examining Eq. (5) it is observed that the covariance contribution is proportional to $1/\rho_o$. Consequently as ρ_o approaches zero, it would appear that the BIEF approaches a large value. There are however two reasons why this does not happen. The first is that ρ_o cannot decrease much below the size of the inner scale. The second is that as ρ_o decreases, saturation of scintillation starts to occur and C_χ is no longer proportional to $1/\rho_o$. Consequently, there will be some maximum value for the BIEF. It should also be noted that the results of this paper are only good up to the onset of saturation.

Equation (5) has been evaluated for the case, $\lambda = 10.6$ μm and 1.06 μm, L = 4000 m, $\alpha_o = 0.05$ m and for (σ_χ^2), the log-amplitude variance, equal to 0.227. This is just at the onset of saturation and corresponds to $\rho_o = (L/k)^{1/2}$. The results are shown versus p/α_o, the normalized off-axis distance, in figure (1). The effect is stronger for the 10.6 μm wavelength due to the sensitivity of C_χ to $(L/k)^{1/2}$ which goes up with wavelength.

Acknowledgement

References

1. V. A. Banakh and V. L. Mironov, *Lidar in a Turbulent Atmosphere*, Artech House, Boston and London, 1987.

2. E. Jakeman, "Enhanced backscattering through a deep random phase screen," J. Opt. Soc. Am. A, Vol. 5, October 1988.

3. P. R. Tapster, A. R. Weeks, and E. Jakeman, "Observation of backscattering enhancement through atmospheric phase screens," J. Opt. Soc. Am. A, Vol. 6, April 1989.

4. Gisele Welch and Ronald Phillips, "Simulation of enhanced backscatter by Gisele Welch and Ronald Phillips, "Simulation of enhanced backscatter by a phase screen," J. Opt. Soc. Am. A., Vol. 7, April 1990.

5. V. S. Rao Gudimetla, J. Fred Holmes and Richard A. Elliott, "A Two-point joint-density function of the intensity for a laser-generated speckle field after propagation through the turbulent atmosphere," J. Opt. Soc. Am. A, Vol. 7, June 1990.
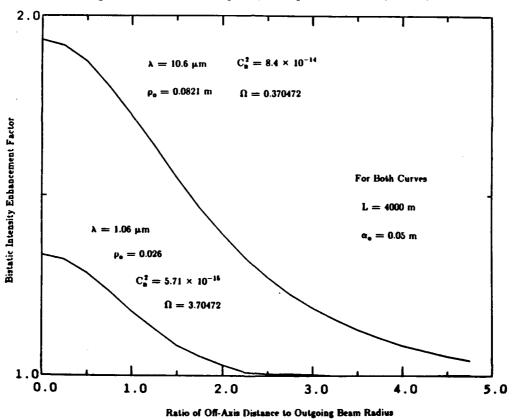
Figure 1 - Bistatic backscattered intensity enhancement factor as a function of transmitter and receiver spacing.

Depolarization Effect by Nonspherical Particles on the Lidar Signal

C. Flesia*, A. Mugnai+, L. Stefanutti++

* Institut of Atmospheric Physics ETH, CH-8093, Zurich, Switzerland
and Observatoire Cantonal de Neuchâtel, CH-2000, Neuchâtel, Switzerland.
+ Istituto di Fisica dell'Atmosfera, CNR, CP 27 - 00044 Frascati, Italy
++ IROE/CNR, Florence, Italy

It is well known that lidar measurements can provide information on atmospheric aerosols and clouds. To this end, the vertical profiles of the backscattered intensity measured by lidar must be transformed into the vertical profiles of the extinction and backscattering coefficients by inversion of the lidar equation. Then, under certain conditions, size and/or concentration of the scattering particles can be derived. However, a very important aspect of the inversion of the lidar signal concerns the physical interpretation of the inversion results and thus the real possibility to derive the optical and physical parameters of the scattering particles from the analysis of the backscattered radiation. Moreover, the accuracy of the results of the inversion of the lidar equation is directly dependent upon the sensitivity of the system to the physical assumptions. Two mayor assumptions are usually made:
a) the scattering particles are spheres
b) the multiple scattering contributions can be neglected

However, atmospheric particles are usually nonspherical. Thus, an additional problem arises from the fact that, in most real physical situations shape, as well as size and nature (i.e., refractive index) of the scattering particles contribute to the lidar signal in a way which is not known "a priori" and which can not be resolved by means of the lidar signal itself. In particular, the orientation of the nonspherical scatterers plays an important role on the intensity of the lidar return, while their geometrical shape may have in some cases an influence stronger than their dimension. In addition, the multiple scattering effect for optically thick clouds may confuse even more the interpretation of the lidar signal. A typical and very important example is the fact that clouds made by big crystals with a low optical density and clouds made by small crystals or droplets with high optical density may produce similar lidar signals.

The basic idea of this work is to investigate the potential of combined backscatter and depolarization information for deriving the optical parameters of clouds together with size and physical phase of the cloud particles. In particular, the main advantage of lidar depolarization measurements would be to distinguish between clouds made of "spherical" liquid water droplets and clouds made of nonspherical ice crystals. Following this way, some tests on the simulated lidar return have been carried out in order to investigate the influence of cloud particles deformation and orientation on the parallel and perpendicular backscattered intensity.

In order to do so, we consider a rather general class of particles which can be continuously deformed from a sphere. These " Chebyshev Particles" [1] are obtained by rotating the curve $r_s = r_0[1 + \epsilon T_n(cos\theta_s)]$ about the vertical axis $\theta_s = 0$. Here, r_0 is the radius of the unperturbed sphere, T_n is then the $n^{(th)}$ Chebyshev polynomial, and ϵ is the deformation parameter. Fig 1 shows a T_2 particle for different deformations. The depolarization of the lidar return has been investigated as a function of the deformation parameter ϵ for different orientations and sizes of water droplets between 0.5 and 5 μm. To this end, extinction and backscattering coefficients of the scattering droplets have been computed by means of the Extended Boundary Condition Method [1]. Moreover, in order to study the information capabilities of a depolarization signal in the case of a real atmospheric measurement, the lidar signal-to-noise ratio has been evaluated as a function of the deformation parameter ϵ , for different measurement conditions (daytime, nighttime measurement, different fields of view, etc.).

The results show that as soon as a little deformation is introduced, the depolarization of the lidar signal may become considerable. In particular, the depolarization as a function of the deformation parameter ϵ shows maxima as high as 49% that depend on particle size. The deformation giving a first depolarization peak is usually rather small and it decreases when the the particle radius increases. This dependence seems to be almost linear, at least for the deformations and sizes that we have investigated. As an example, fig 2 shows the parallel (a) and perpendicular (b) backscattered intensities and the depolarization percentage $((I_\perp/(I_\perp + I_\parallel)) * 100)$ as a function of a positive deformation parameter ϵ for a T_2 "prolate spheroid" (see fig. 1a,b) with a volume equal to that of a sphere of radius $r_{ev} = 0.5$ μm. The particles are, i.e. their symmetry axis is, randomly orientated in a plane perpendicular to the incoming linearly polarized radiation ($\lambda = 0.532\mu m$). The value of ϵ giving the first maximum of depolarization is found to be $\epsilon = 0.15$ for T_2 water particles with $r_{ev} = 0.5$ μm while it is as low as $\epsilon = 0.09$ for the same particles with $r_{ev} = 1$ μm. A second maximum for these last particles is found for $\epsilon = 0.19$.

In conclusion, the existence of such high depolarization maxima indicates that a large concentration of slightly nonspherical particles may play a crucial role on the depolarization effect even if no multiple scattering is taken into account. Moreover, since even a small deformation may produce a considerable depolarization effect, interpretation of a strong depolarization in terms of presence of ice crystals in clouds and the consequent characterization of their microphysical properties must be considered very carefully.

REFERENCES

[1] A. Mugnai, W.J. Wiscombe : Appl. Opt. 25, 1235-1244, (1986)
[2] C. Flesia, A. Mugnai, L. Stefanutti : Proceedings of "3th Workshop Italian Research on Antarctic Atmosphere", Porano (1990), in press.

$T_2(\epsilon)$ *CHEBYSHEV PARTICLES*

$T_2(0.10)$ $T_2(0.20)$
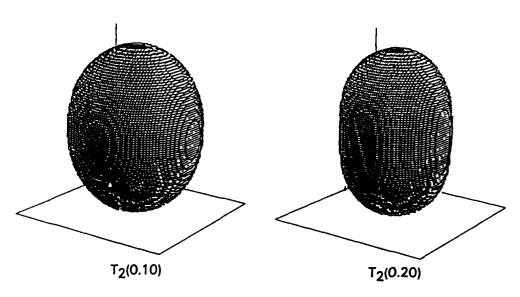
Fig. 1
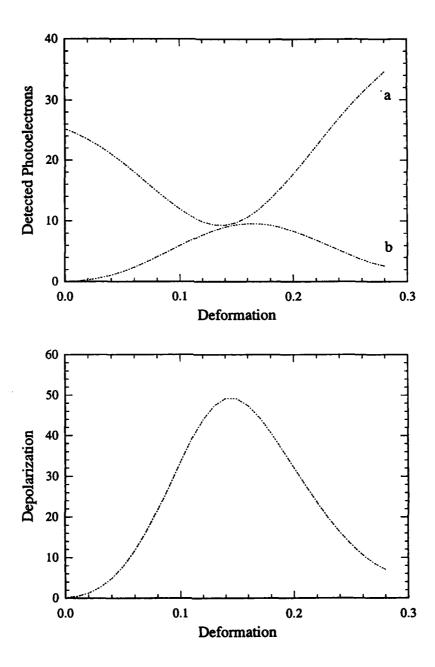
Fig. 2

TWO YEARS MEASUREMENTS OF POLAR STRATOSPHERIC CLOUDS BY MEANS OF A DEPOLARIZATION LIDAR

L. Stefanutti, M. Morandi, M. Del Guasta, F. Castagnoli
Istituto di Ricerca sulle Onde Elettromagnetiche del CNR
via Panciatichi 64, 501277 Firenze, Italy

S. Godin, G. Megie
Service d' Aeronomie du CNRS
Universite` Pierre et Marie Curie
Jussieu, Paris, France

J. Brechet, P. Nisol
Expeditions Polaires Francaises

1-Introduction

A depolarization lidar has been operational at the French base of Dumont d' Urville since January 1988, under a Italo-French cooperative program between IROE-CNR and SA-CNRS, within the Italian National Program foe Antarctic Research and the French Territoires Antartiques et Australes Fran-caises. Background stratospheric aerosols and Polar Strato-spheric Clouds have been measured during the last two years. Polar Stratospheric Clouds are of primary importance in the chemistry of the Antarctic Stratosphere. It has been demon-strated that on the surface of such clouds heterogeneous chemical reactions occur, with the transformation of the reservoir gas $ClONO_2$ into active chlorine species and with the trapping of HNO_3 into the solid phase in the cloud. Such clouds may play an essential role also in the processes of dehydration of the Stratosphere. By computing the Backscat-tering Ratio R and the Depolarization Ratio D Polar Strato-spheric Clouds were identified and classified into different types. Here we report the results obtained during the two Antarctic winter campaigns.

2-Instrumentation and measurement technique

A depolarization Lidar, designed and build at IROE-CNR [1] has been installed at the French base of Dumont d' Urville in January 1989. The system had been tested the year before at the Italian Base of Terra Nova Bay during the Antarctic summer [2]. The system uses a Nd-YAG laser operating at the second harmonic. Two receiving channels collect the two polarizations parallel and perpendicular to the emitted laser beam. A narrow band interference filter with 0.15 nm width is mounted on the receiving channel. The field of view of the receiver is 0.6 mrad full angle, just a little larger than the full divergency of the laser beam, which is of the order of 0.5 mrad. This way daytime measurements can be performed up to heights of 30 km. A computer data link via INMARSAT between Dumont d' Urville and Europe has been established, which allowed to transmit the data regularly to IROE and SA.
    Stratospheric lidar measurements have been carried out

during the summer time and spring with a frequency of at least one measurement per week. During 1990 different measurements of stratospheric profiles have been carried out on each clear day. Frequency of the measurements have been intensified during the Antarctic winter and spring, in order to evidence the possible occurrence of Polar Stratospheric Clouds.

Ancillary data were the local meteorological data, the Rowinsonde data, and wide angle CCD TV images. In the case of the TV images some attempts to monitor PSCs were carried out during the month of September 1989, but with little success.

3-Evaluated parameters

Backscattering ratio R and depolarization ratio D have been measured. The scattering ratio is defined as:

$$R=(\beta_M+\beta_R)/\beta_R$$

since the system used has two separate receiving channels it was convenient to introduce a p and s backscattering ratio, referred to the two different polarization planes.

For the depolarization ratio a more complex consideration has been made. Generally the depolarization ratio is considered the ratio between the s component of the lidar signal and the p component. With such definition the depolarization ratio may vary between 0 and ∞, which does not seem to have much physical sense, therefore we preferred to consider the ratio between the s component of the signal and the sum of the p and s component. This way the depolarization ratio may vary between 0 and 1. In the case of stratospheric measurements a further consideration has to be done: in the presence of PSCs the scattering ratio is never very high, as it occurs for tropospheric clouds. It varies between 1.5 and 10, consequently the Rayleigh contribution to the signal is large. In order to evidence the effect of the Mie scattering on the lidar signal it was considered more meaningful to define as depolarization ratio, the ratio between the s component of the Mie backscattered signal versus the sum of the p and s Mie backscatterd signals:

$$D=P_{SM}/(P_{SM}+P_{pM})$$

In the evaluation of the Depolarization Ratio it is extremely important to perform a good calibration of the lidar system. Both the relative gain between the two channels and the system depolarization ratios have to be carefully measured. An other source of error turned out to be electrical induced noise into the lidar signature. All these quantities have been taken into account in evaluating the lidar data.

4-Data evaluation

Stratospheric Background aerosols have been measured all through 1989 and 1990. From a first analysis there was no substantial change in the stratospheric loading. Scattering ratios of the order of 1.15 are typical. During the antarctic winter a good evaluation of the loading becomes quite complex as it becomes very important to fit the data with the correct molecular atmosphere. Due to the peculiar temperature profile of the winter and early springtime atmosphere, and to the time lapse between the lidar measurement and the Rawinsonde data, large errors in the correct evaluation of the loading can be performed. This occurs as long as the loading remains low with an integrated backscattering, computed between 12 and 25 km, of the order of $1.5 \ 10^{-4}$. In such conditions errors of the order of 100% can be easily committed. This large value of the error seems in agreement with what obtained by other groups (Jäger, McCormick etc, Workshop on Lidar intercalibration, Obninsk, USSR, July 1990). When the loading is stronger, as in the presence of Polar Stratospheric Clouds, the error becomes much smaller. PSCs have been measured at Dumont d' Urville between July and September of 1989 [3] and 1990. Typical values of Scattering ratios, between 1.5 and 5 have been measured and Depolarization Ratios ranging between 0 and 30% have been computed. A distinction between two types of Nitric Acid Trihydrate Clouds ($HNO_3.3H_2$) have been evidenced. In fact two cases occur frequently, often simultaneously at different heights: clouds presenting a low scattering ratio, not larger than 2, and a high depolarization ratio, larger than 10 % and cases with scattering ratios larger than 2, but negligible depolarization ratios. These clouds have been classified by Browell and others respectively as Type Ia and Type Ib PSCs. They occur with stratospheric temperatures of the order of $190-195^{o}K$, and consequently it is difficult to confuse them with Type II ice water clouds, which should generally occur at lower temperatures.

During the month of September 1989 very high cirrus clouds were observed, with cloud base in the range of 9 km and cloud top up to above 13 km. It may be recalled that the Tropopause height in the Polar regions is generally much lower than in the rest of the planet, at altitudes typically of 8 km. While, from the Rawinsonde data, the cloud bottom seems always warm, with temperatures of the order of $220^{o}K$, the cloud top is generally very cold with temperatures of the order of $190^{o}K$. Such clouds penetrate a few kilometers into the Stratosphere. Ozone vertical profiles for that period were not available, but it might be reasonable to think that such clouds may be chemically active and may be considered like PSCs of Type II. They present generally a quite high scattering ratio, of the order of 4 and depolarization ratios of the order of 30%, constant from the cloud bottom to the cloud top.

5-Conclusions

Lidar depolarization technique has proven to be a very efficient and reliable tool for the investigation of the characteristics of the polar Stratosphere. In January 1991 such system has been replaced by a more complex Ozone lidar, capable to measure simultaneously Ozone vertical profiles from 2 Km to 40 Km and PSCs with the depolarization technique. This system will operate within the Network for Detection of Stratospheric Changes. The Depolarization Backscattering lidar will operate from November 1991 to March 1992 in Sodankyla, in northern Finland in the frame of the European Arctic Stratospheric Ozone Experiment (EASOE), planned by the European Community to verify the occurrence of heterogeneous chemistry in the northern hemisphere.

6-Bibliography

[1] V.M. Sacco, F.. Castagnoli, M. Morandi, L. Stefanutti: "Elastic backscattering lidar system for atmospheric measurements in Antarctica", Optical and Quantum Electronics, 21 (1989), 215-226

[2] L. Stefanutti, M. Del Guasta, M. Morandi, V.M. Sacco, L. Zuccagnoli: "The application of Lidar for the Antarctic Stratospheric Research", SIF: Conference Proceedings Vol. 20 "Italian Research on Antarctic Atmosphere", M. Colacino, G. Giovannelli and L. Stefanutti (Eds.), Bologna, 1989 161-170

[3] L. Stefanutti, M. Morandi, M. Del Guasta, S. Godin, G. Megie, J. Brechet, J. Piquard: "Polar Stratospheric Cloud Observations over the Antarctic Continent at Dumont d' Urville", Jour. Geophys. Res. accepted for publication

AUTHORS' INDEX

INTERNATIONAL COMMISSION FOR OPTICS

BUREAU 1990 - 1993

President
Dainty J.C., *Imperial College, London, UK*

Past President
Goodman J.W., *Stanford University, USA*

Secretary-General
Chavel P., *CNRS, Orsay, France*

Treasurer
Hariharan P., *CSIRO, West Lindfield, Australia*

Vice-Presidents
Asakura T., *Hokkaido University, Sapporo, Japan*
Consortini A., *Università di Firenze, Italy*
Lanzl F., *Inst. for Optoel., Oberpfaffenhofen, Germany*
Lupkowicz G., *MOM Globios, Budapest, Hungary*
Rebane K., *Acad. of Sci., Moscow, USSR*
Sincerbox G.T., *IBM Almaden Res. Ctr., San Jose, USA*
Velzel C.H.F., *Philips CFT, Eindhoven, The Netherlands*
Yzuel M.J., *Univ. Autonoma de Barcelona, Spain*